STRESSES AND DEFORMATIONS IN IMPULSE WATER TURBINES.

THESIS PRESENTED FOR THE DEGREE OF

DOCTOR OF PHILOSOPHY OF THE

UNIVERSITY OF GLASGOW

by

IAIN B. MACDUFF, B.Sc.

17, LARCHFIELD ROAD,
BEARSDEN,
GLASGOW.

JULY, 1969.

ProQuest LLC.
789 East Eisenhower Parkway
P.O. Box 1346
Ann Arbor, MI 48106 – 1346

ABSTRACT

This thesis concerns the theoretical and experimental investigation of the working stresses and deformations in the Turgo impulse wheel and, to a lesser extent, in the Pelton wheel. These wheels are the only impulse water turbines in common use.

Directly relevant publications are very few. The most recent significant paper, which discusses a limited experimental analysis of the approximate jet loading stresses in a Pelton bucket, was issued in 1934. A much more recent Russian publication is much less informative. It appears that no theory has been advanced to explain the working stress behaviour of the buckets of these water wheels, and that no attempt has been made at rational theoretical stress analyses for their strength design. Impulse water turbine buckets are of shell form, and are critical components from the strength aspect.

An Introduction sketches the background to the investigation and indicates that potential advantages in respect of design and performance are attendant on a realistic knowledge of the working stresses. The literature is reviewed and a cursory glance given at indirectly pertinent publications relating to the stress analyses of other types of water turbine.

The Turgo impulse wheel, which is a side-jet wheel incorporating a rim round the buckets, is described in Chapter 2, and the bucket geometry is discussed. It is shown that the bucket shape approximates reasonably to that of part of a shell of revolution of varying thickness.

Assuming an idealised but realistic bucket and rim geometry, approximate theoretical analyses are developed in Chapter 3, to determine the order-of-magnitude of the centrifugal and jet loading stresses in a working/

working Turgo wheel. These analyses are based mainly on elementary energy methods, and assume that the buckets behave as beams. Albeit approximate, the calculations reliably reveal the dominance of centrifugal action, the maximum approximate centrifugal stress being about twice the corresponding maximum approximate jet loading stress. Both maxima occur on the bucket edges.

Chapter 4 presents the experimental stress analyses of a Turgo wheel. The strain measurements comprise static loading tests on separate single buckets, centrifugal tests using slip rings, with the wheel spinning in the dry condition, and approximate jet loading tests on the stationary wheel, the loading being simulated by mechanical means. Most of the important predictions of the approximate theoretical analyses are confirmed. It is demonstrated that the stress behaviour of a bucket under working conditions, approximates reasonably to that of a toroidal shell subjected to in-plane bending.

An approximate theoretical solution is derived in Chapter 5, for the stresses and deformations in a varying-thickness open toroidal shell under in-plane bending, a case which does not seem to have been treated. This derivation is founded on the work of R. A. Clark, dealing with theoretical stress analyses of pipe-bends and thin toroidal shells. Clark's approximate non-homogeneous complex differential equation and a given approximate particular integral are relevant. An asymptotic solution for the complementary function is then found, using a method developed by R. E. Langer. Applications of the general solution to simplified cases are performed using the special functions tabulated by L. N. Osipova and S. A. Tumarkin. The stress behaviour indicated by this shell theory, fits well with the working stress behaviour measured on Turgo wheel buckets.

In Chapter 6 comparison is made between theoretical and experimental/

experimental results for the working Turgo impulse wheel. An approximate rigidity factor from the shell theory of Chapter 5, is applied to some of the calculations of Chapter 3 to modify the beam analyses to take shell behaviour into account. Reasonably good correspondence is found between theory and experiment.

In Chapter 7 shell theory is applied in an approximate manner to the case of the Pelton bucket subjected to jet loading. The solution derived in Chapter 5 is used in conjunction with existing toroidal shell solutions due to Clark. The results compare quite well with results from strain measurements on a Pelton bucket subjected to simulated jet loading by mechanical means.

The implications of the results of the investigation are considered in Chapter 8, in relation to the designs and duties of these two types of impulse water turbine.

A Bibliography is given.

Considering the early remarks regarding lack of knowledge in this field, insofar as these paragraphs indicate, this entire work in its essence, and the underlying concepts, are original to the author.

STRESSES AND DEFORMATIONS IN IMPULSE WATER TURBINES

CONTENTS

		Page No.
ABSTRACT		-i-
NOMENCLATURE		-x-
CHAPTER 1	INTRODUCTION AND REVIEW OF LITERATURE RELATING TO THE STRENGTH OF WATER TURBINES	-1-
1.A.	INTRODUCTION	-2-
1.B.	REVIEW OF LITERATURE RELATING TO THE STRENGTH OF WATER TURBINES	-8-
CHAPTER 2	THE TURGO IMPULSE WHEEL AND ITS GEOMETRY	-16-
CHAPTER 3	APPROXIMATE THEORETICAL ANALYSES FOR THE CENTRIFUGAL AND JET LOADING STRESSES AND DEFORMATIONS IN A TURGO IMPULSE WHEEL	-26-
3.A.	THEORETICAL ASSUMPTIONS	-29-
3.B.	APPROXIMATE STRESSES AND DEFORMATIONS DUE TO CENTRIFUGAL LOADING	-34-
3.B.i	The free rotating condition of the rim	-36-
3.B.ii	The free rotating condition of the hub-with-buckets	-37-
3.B.iii	Assembly condition — assembly actions on the rim	-49-
3.B.iv	Assembly condition — assembly actions on the hub-with-buckets	-56-
3.B.v	Assembly condition at the bucket/rim junction — evaluation of assembly actions and total centrifugal stresses	-79-

		Page No.
3.C.	APPROXIMATE STRESSES AND DEFORMATIONS DUE TO JET LOADING	-86-
3.C.i	The distribution of loading on a bucket due to jet action	-89-
3.C.ii	The rimless jet-loaded bucket condition	-92-
3.C.iii	Assembly condition— assembly actions on the rim of the remainder of the wheel	-96-
3.C.iv	Assembly condition— assembly actions on the bucket	-102-
3.C.v	Assembly condition at the bucket/rim junction —evaluation of assembly actions and total jet loading stresses	-109-
3.D.	COMPARISON OF CENTRIFUGAL AND JET LOADING APPROXIMATE STRESSES AND DEFORMATIONS, AND COMBINATION OF CENTRIFUGAL AND JET LOADING APPROXIMATE STRESSES	-116-
CHAPTER 4	EXPERIMENTAL INVESTIGATIONS OF THE CENTRIFUGAL AND APPROXIMATE JET LOADING STRESSES AND DEFORMATIONS IN A TURGO IMPULSE WHEEL	-121-
4.A.	PRELIMINARY EXPERIMENTAL INVESTIGATION ON SEPARATE SINGLE BUCKETS	-123-
4.A.i	Strain measurements on separate single buckets subjected to various loadings	-126-
4.A.ii	Analysis of strains to determine actions on a meridional section of a bucket	-131-
4.A.iii	Examination of strains pertinent to the behaviour of a bucket under torsion	-138-
4.B.	MEASUREMENT OF CENTRIFUGAL STRESSES IN $16\frac{1}{2}$ in. p.c.d. TURGO WHEEL	-140-
4.B.i	Centrifugal stress measurement using electrical resistance strain gauges and slip rings	-142-
4.B.ii	Centrifugal stresses on the buckets	-146-

		Page No.
4.B.iii	Centrifugal stresses on the rim	-152-
4.B.iv	Centrifugal stresses on the hub	-154-
4.B.v	Check on results by dynamic recording of centrifugal strains	-155-
4.B.vi	Corresponding centrifugal stresses in $16\frac{1}{2}$ in. cast steel Turgo Wheel	-158-
4.C.	MEASUREMENT OF APPROXIMATE JET LOADING STRESSES IN $16\frac{1}{2}$ in.p.c.d. TURGO WHEEL	-159-
4.C.i	Approximate jet loading stresses on the buckets	-162-
4.C.ii	Approximate jet loading stresses on the rim	-166-
4.C.iii	Approximate jet loading stresses on the hub	-168-
4.C.iv	Corresponding approximate jet loading stresses in $16\frac{1}{2}$ in.cast steel Turgo Wheel	-169-
4.D.	COMPARISON AND COMBINATION OF CENTRIFUGAL AND APPROXIMATE JET LOADING STRESSES IN $16\frac{1}{2}$ in.p.c.d. TURGO WHEEL	-170-
CHAPTER 5	THEORETICAL ANALYSIS OF THE STRESSES AND DEFORMATIONS IN AN OPEN TOROIDAL SHELL SUBJECTED TO IN-PLANE BENDING	-173-
5.A.	GENERAL SOLUTION FOR OPEN TOROIDAL SHELL OF VARYING THICKNESS	-177-
5.A.i	Solution of the shell differential equation	-181-
5.B.	APPLICATION OF THE SOLUTION TO THE OPEN TOROIDAL SHELL OF CIRCULAR CROSS-SECTION AND UNIFORM THICKNESS	-193-
5.C.	NUMERICAL APPLICATION OF THE ANALYSIS TO PARTICULAR CIRCULAR SECTION, UNIFORM THICKNESS OPEN TOROIDAL SHELLS ASSOCIATED WITH THE GEOMETRY OF IMPULSE WATER TURBINE BUCKETS	-200-
CHAPTER 6	THE TURGO IMPULSE WHEEL. APPROXIMATE METHOD OF MODIFYING THEORETICAL ANALYSIS TO TAKE ACCOUNT OF THE SHELL BEHAVIOUR OF THE BUCKET. COMPARISON OF THEORETICAL AND EXPERIMENTAL RESULTS	-206-

		Page No.
6.A.	APPROXIMATE METHOD OF MODIFYING THEORETICAL ANALYSIS TO TAKE ACCOUNT OF THE SHELL BEHAVIOUR OF THE BUCKET	-207-
6.B.	COMPARISON OF THEORETICAL AND EXPERIMENTAL RESULTS	-212-
6.B.i	Comparison of theoretical and experimental centrifugal actions and stresses	-213-
6.B.ii	Comparison of theoretical and experimental approximate jet loading stresses	-216-
6.B.iii	Comparison of theoretical and experimental maximum stress ratios	-221-
CHAPTER 7	THE PELTON WHEEL. APPLICATION OF SHELL THEORY TO DETERMINATION OF THE APPROXIMATE JET LOADING STRESSES AND DEFORMATIONSIN THE BUCKET. COMPARISON OF THEORETICAL AND EXPERIMENTAL RESULTS	-222-
7.A.	APPLICATION OF SHELL THEORY TO THE ANALYSIS OF THE APPROXIMATE JET LOADING STRESSES IN A PELTON BUCKET	-225-
7.A.i	Approximate theoretical analysis of the effectiveness of the "circumferential" reinforcing rib on a Pelton half-bucket	-237-
7.B.	MEASUREMENT OF APPROXIMATE JET LOADING STRESSES IN A BUCKET OF A 21 in.p.c.d. PELTON WHEEL. COMPARISON WITH THEORETICAL RESULTS	-241-
CHAPTER 8	IMPLICATIONS OF RESULTS IN RELATION TO THE DUTIES AND THE STRENGTH DESIGN OF TURGO IMPULSE WHEELS AND PELTON WHEELS	-246-
8.A.	VARIATIONS OF NORMAL WORKING STRESSES IN IMPULSE WATER TURBINES, WITH SIZE AND WITH HEAD	-248-
8.B.	IMPLICATIONS OF RESULTS IN RELATION TO THE DUTIES AND STRENGTH DESIGN OF TURGO IMPULSE WHEELS	-251-

		Page No.
8.C.	IMPLICATIONS OF RESULTS IN RELATION TO THE STRENGTH DESIGN OF PELTON WHEELS	-255-
8.D.	COMMENTARY WITH REFERENCE TO FUTURE WORK DERIVING FROM THESE INVESTIGATIONS	-257-
APPENDICES		-261-
APPENDIX 1.	Properties of the "equivalent" parabolic section of the bucket, pertinent to the approximate theoretical analyses for centrifugal and jet loading stresses and deformations in a Turgo Impulse Wheel	-262-
APPENDIX 2.	Properties of the "equivalent" rectangular section of the rim, pertinent to the approximate theoretical analyses for centrifugal and jet loading stresses and deformations in a Turgo Impulse Wheel	-269-
APPENDIX 3.	(a) Solution of the non-uniform torsion differential equation for assembly action F_R on the bucket, (b) Derivation of the non-uniform torsion strain-energy components of displacement $\delta_{r2}^{F_R}$ by the dummy load method, both pertinent to the approximate theoretical analyses of Chapter 3	-271-
APPENDIX 4.	Brittle lacquer technique	-276-
APPENDIX 5.	The rotating wedge: a method of obtaining strain-free locations in a centrifugal field	-279- (see pocket attached to inside of back cover)
APPENDIX 6.	Analysis of measured strains to determine centrifugal actions on four meridional sections of bucket of $16\frac{1}{2}$ in. aluminium Turgo Wheel, rotating at 1,300 r.p.m.	-280-
APPENDIX 7.	A more realistic approximate theoretical analysis of the jet loading stresses in the buckets of the Turgo Impulse Wheel	-282-

Page No.

BIBLIOGRAPHY -286-

ACKNOWLEDGMENTS

FIGURES Figs. are numbered and are distributed in consecutive order, as appropriate, throughout the typescript. Fig.9 (oversize) is in the pocket on the back cover of the thesis.

NOMENCLATURE.

THE FOLLOWING NOMENCLATURE IS COMMON THROUGHOUT:

E	Young's modulus.
ν	Poisson's ratio.

Two different sets of nomenclature are adopted, one set applicable to chapters 2, 3, 4 and 6, the other to chapters 5 and 7.

THE FOLLOWING NOMENCLATURE APPLIES TO CHAPTERS 2, 3, 4 and 6:-

(NOMENCLATURES, PERTINENT TO PROPERTIES OF CROSS-SECTIONS OF EQUIVALENT BUCKET AND EQUIVALENT RIM, ARE PRESENTED IN APPENDICES 1 AND 2).

θ	Angle in plane of wheel, defining points on line of centroids of equivalent bucket, or, "Circumferential" angle locating "meridional" cross-sections of bucket, Figs.9 and 12.
D	Density of material.
G	Modulus of rigidity.
F_R, F_T, F_A	Assembly forces - radial, tangential and axial - at junction point of equivalent rim and equivalent bucket.
$(F_T \cdot q), M_P$	Assembly moments in plane of wheel, at junction point of equivalent rim and equivalent bucket.
M_R, M_T	Assembly moments, about a radius, and about a tangent, at junction point of equivalent rim and equivalent bucket.
σ_{c1}	Circumferential stress in equivalent rim, in free rotating condition.

q	Radius of line of centroids of rim, $= \sqrt{k^2 + h^2 - 2kh\cos(\alpha+\beta)}$, Fig.15.
ω	Angular velocity of wheel.
g	Gravitational constant, 32.2 ft/sec^2.
$M_\theta, P_\theta, V_\theta$ (beam treatment)	Bending moment, direct force and shearing force in plane of wheel, at Θ on equivalent bucket, due to free rotating condition, or due to rimless jet loaded condition.
"with suffixes 2, and with $T_{\theta 2}$	Bending moment, direct force, shearing force and torque at Θ, due to assembly condition.
M_θ (shell treatment)	"Circumferential" stress couple or bending moment per unit length of bucket or shell mid-surface, Fig.50.
$k, h, \alpha, \beta, \rho$	Radii and angles relating to geometry of arc of centroids of equivalent bucket, Fig.15.
A	Area of parabolic meridional cross-section of equivalent bucket, Appendix 1.
σ_b, σ_d, τ	Bending stress, normal, direct or membrane stress and shear stress.
M_b, P_d, V, T	Bending moment, direct force, shearing force and torque.
Δ	Linear displacement due to free rotating condition or due to rimless jet loaded condition. Suffixes R, T - radial, tangential.
Φ	Angular displacement due to free rotating condition, or due to rimless jet loaded condition. Suffix P - in plane of wheel.
δ	Linear displacement due to assembly action or actions. Suffixes R, T, A - radial, tangential, axial.

ϕ (always with suffix or suffixes)	Angular displacement due to assembly action or actions. Suffixes R, T, P - about a radius, about a tangent, in plane of wheel.
Suffix 1 :-	where used with actions, stresses and displacements, refers to the rim.
Suffix 2 :-	where used with actions, stresses and displacements, refers to the hub-with-buckets. Where used with a displacement, e.g. Δ_{T2}, the displacement invariably refers to the junction point on the equivalent bucket.
H_R	Radial force per bucket on hub outer surface, due to free rotating condition.
$\nu, \gamma, \lambda, \mu$	Radius and angles relating to geometry of arc of centroids of equivalent bucket, and its connection to hub, Fig.17. These quantities can all be expressed in terms of k, h, α, β.
r_H	Any radius of hub.
$\sigma_R', \sigma_C', \sigma_A'$	Stresses in hub, radial, circumferential and axial. Suffixes O, I - outer surface, inner surface.
Suffix H	Due to hub.
Suffix TOT	Total.
A', B'	Lamé constants.
F_R'	$\frac{\text{Number of buckets} \times F_R}{2\pi q}$, correspondingly for F_T', M_R', M_T' in terms respectively of F_T, M_R, M_T
$\sigma_{C1}^{F_R}$	Circumferential stress in equivalent rim due to assembly action F_R.
$\tau_1^{F_T \& (F_T \cdot q)}$	Shear stress in equivalent rim due to assembly action F_T - and $-(F_T \cdot q)$.

$\tau_1^{M_R}$	Shear stress in equivalent rim due to assembly action M_R.
$\sigma_{b1}^{M_T}$	Bending stress in equivalent rim due to assembly action M_T.
d	Axial distance between centroid G of equivalent bucket section and bucket/rim junction point G_1, Figs. 11, 12, 21.
Ω	$(\alpha - \theta)$, Fig. 21.
ϕ (without suffix)	Angle of twist of equivalent bucket section due to non-uniform torsion.
J, Γ	St. Venant torsion constant, and warping constant, of parabolic section of equivalent bucket, Appendix 1.
$\tau_{sv}, \sigma_z, \tau_z$	St. Venant shear stress, warping restraint direct stress and warping restraint shear stress due to non-uniform torsion.
H, P	Coefficients in fundamental non-uniform torsion differential equation; $H = GJ/k$, $P = E\Gamma/k^3$, Appendix 3.
K	Constant in solution of fundamental non-uniform torsion differential equation; $K = \sqrt{H/P}$, Appendix 3.
$M_3, N_3, L_3, F_3, S_3,$ $M_4, N_4, L_4, F_4,$ M_5, L_5, F_5	Constants in solution of fundamental non-uniform torsion differential equation, Appendix 3.
U	Total strain energy.
Q	Dummy load, applied in analysis of equivalent bucket displacements.
W_θ	Loading intensity in plane of wheel, at θ on equivalent bucket subjected to jet loading.
ϵ	Normal or direct strain.

N_θ (shell treatment) — "Circumferential" stress resultant or normal force per unit length of bucket or shell mid-surface, Fig.50.

X_M or x, Y_M or Y, s_M, ξ (shell treatment) — Co-ordinates and parameters associated with a point on mid-line of meridional section of an actual bucket, Fig.50 and Appendix 6.

t_M (shell treatment) — Thickness of bucket at point (X_M, Y_M) or (x, Y), Fig.50 and Appendix 6.

M_{YM} or M_Y, M_{XM} or M_X, P_M or P' — Total bending moment and direct force actions on a meridional section of an actual bucket, Figs.50, 67 and Appendix 6.

THE FOLLOWING NOMENCLATURE APPLIES TO CHAPTERS 5 AND 7, AND PERTAINS TO THEORETICAL ANALYSES OF STRESSES AND DEFORMATIONS IN AN OPEN TOROIDAL SHELL, e.g. FIG.88:-

m — Circumferential in-plane bending moment applied to shell, Fig.88.

M_A — Uniformly distributed, rotationally symmetrical, meridional stress couple on inlet edge of theoretical (open toroidal shell) Pelton half-bucket, Figs. 106, 109; CLARK[9].

r, θ, z — Cylindrical co-ordinates of a point on shell mid-surface, Fig.88.

ξ — Independent variable throughout analyses. Parameter in representation of a meridian of shell mid-surface, Fig.88. Angular meridional co-ordinate pertinent to shell of circular mid-surface meridian, Fig.89.

α — $\left[(r')^2 + (z')^2 \right]^{\frac{1}{2}}$, where prime $'$ denotes differentiation with respect to ξ. For shell of circular mid-surface meridian, $\alpha = b =$ radius of circular meridional cross-section, Fig.89

r_N	Radius of cylindrical neutral surface of shell under in-plane bending.
ΔK	Change of in-plane curvature of shell due to bending moment m.
v, u	Circumferential and radial linear displacements of a point on shell mid-surface, Figs. 88(d), 109(a).
β	Rotational displacement of a tangent to a mid-surface meridian of shell, Figs. 88(a), (b), 109(a). Real component of complex dependent variable of differential equation, basic to toroidal shell edge couple analysis, CLARK[9]
k	Dimensionless constant basic to analysis of shell subjected to in-plane bending. $v = k r \theta$ and k = constant x m/E for a particular shell geometry.
$N_\theta, N_\xi, Q, M_\theta, M_\xi$	Normal stress resultants circumferential and meridional, transverse shear stress resultant, and stress couples circumferential and meridional, on shell element, Fig. 88(e).
I	Second moment of area of shell meridional cross-section, about an axis through the centroid perpendicular to plane of shell, e.g. Fig. 90.
ρ	Shell rigidity factor, expressing in-plane bending rigidity resulting from shell theory analysis, as a ratio of that resulting from beam theory analysis.
ε	Normal or direct strain.
$\sigma_{S.MAX}$, $\sigma_{B.MAX}$	Maximum normal stresses in shell under in-plane bending, resulting from shell theory analysis and beam theory analysis respectively.
σ_θ , σ_ξ	Normal stresses in shell, circumferential and meridional.

$Z = X + iY$ — Complex dependent variable of differential equation basic to analysis of shell under in-plane bending.

$h = h_o \bar{h}$ — Varying shell thickness. Suffix o denotes thickness at $\xi = 0$, Fig.88. For shell of uniform thickness, $\bar{h} = 1$.

$\lambda = \frac{b}{a}$ — pertinent to shell of circular mid-surface meridian, Fig.89. a is radius from axis of revolution to centre of shell meridional cross-section. b is meridional radius of cross-section.

μ — Definitive shell parameter of relatively large magnitude. $\mu = [12(1-\nu^2)]^{\frac{1}{2}} \frac{\alpha_o z_o''}{r_o h_o}$ for general shell, where suffix o denotes value of quantity at $\xi = 0$, Fig.88.

$\mu = [12(1-\nu^2)]^{\frac{1}{2}} \frac{b^2}{a h_o}$ for shell of circular mid-surface meridian, Fig.89.

ω — $= \int_0^{\xi} \bar{\Phi}^{\frac{1}{2}} . d\xi = \int_0^{\xi} \left[\frac{1}{\bar{h}} \left(\frac{\sin\xi}{1+\lambda\sin\xi} \right) \right]^{\frac{1}{2}} . d\xi$, pertinent to shell of circular mid-surface meridian.

x — $\mu^{\frac{1}{3}} \left(\frac{3}{2} \omega \right)^{\frac{2}{3}}$

$\bar{Q}$ — $\frac{(\frac{3}{2}\omega)^{\frac{1}{6}}}{(\omega')^{\frac{1}{2}}}$, where prime $'$ denotes differentiation with respect to ξ.

Ψ — Imaginary component of complex dependent variable of differential equation, basic to toroidal shell edge couple analysis, CLARK[9].

CHAPTER 1.

INTRODUCTION AND REVIEW OF LITERATURE RELATING TO THE STRENGTH OF WATER TURBINES.

1A. INTRODUCTION

The water turbine is the most reliable form of prime mover. It is also probably the form of prime mover about which, in general, least is known regarding its strength, and in the design of which, therefore, strength considerations have featured to the least extent. The plentiful literature on water turbine design seldom refers to design for strength. This somewhat paradoxical situation implies that water turbines in general are "overdesigned" and carry large inherent "factors of safety", a result perhaps of the derivation of some of their dimensions from manufacturing strictures rather than from working-strength criteria.

One reason for the relative rarity of publications on the strength of water turbines is that the associated problems are ones of considerable complexity and difficulty, both experimentally and theoretically. Measurement of stresses in the hostile environment of working conditions is a major undertaking requiring preliminary experimental investigations, and prior resolution of a number of attendant experimental difficulties. Of the basic components common to water turbines, namely vanes, hub and rim, this last being absent on some types, it is the vanes which present the most complex problems in a theoretical stress analysis.

Although, in a broad sense, the vanes of impulse turbines are of shell form, those of radial-flow or Francis turbines are of part-shell, part-plate form, and those of propeller or Kaplan turbines are of plate form, general lack of symmetry and variations of vane curvatures, thickness and boundary shape, to say nothing of applied loading, give rise in many instances to major complications in solutions attempted on the basis of normal shell and plate theory. Indeed the pessimistic view "that/

"that any attempt to produce usable stress calculations is doomed to failure from the very outset", has been expressed by investigators SURBER AND SCHWEIZER [1], reporting in 1960 an experimental investigation of the stresses in a Francis turbine. This however is a rather jaundiced outlook condemning effort in the theoretical direction. It is made to look a little silly, by the fact that several Russian workers [2,3] had published theoretical calculations of the stresses in a Francis turbine in 1953 and 1957, these calculations being based mainly on simple bending and thin-walled beam theories and being to some extent in agreement with experimental results.

Of this neglected family of water turbines, for whose strength relatively little concern has been shown, the impulse turbine is the most neglected member. It appears that there are only two publications [4,5] in existence, dealing directly with the stresses encountered in the buckets or vanes of a Pelton wheel. The familiar Pelton wheel is, of course, by far the most common type of impulse water turbine, having dominated the scene since its basic form was invented by Lester A. Pelton of the U.S.A., about 1880. Since 1919, however, it has had a minor rival in the Turgo impulse wheel, the invention of Eric Crewdson, Great Britain. This impulse turbine is a side-jet wheel (Fig.1) so, unlike the Pelton wheel, it is subject to a small axial thrust. Also, unlike the normal Pelton, the jet straddles more than one bucket and the wheel carries a rim. Until about 1949, the Turgo wheel had been manufactured exclusively by Messrs. Gilbert Gilkes and Gordon Ltd., Kendal, England, but since then it has been manufactured by the Russians [6] as well as by the Kendal firm.

At least three other types of impulse water turbine have been under development in Russia [5] but these have not gone into general production in that country, and are virtually unknown outside it. The Pelton wheel and the Turgo wheel are the only types of impulse water turbine in general use, so that, since no published work exists concerning the strength of the/

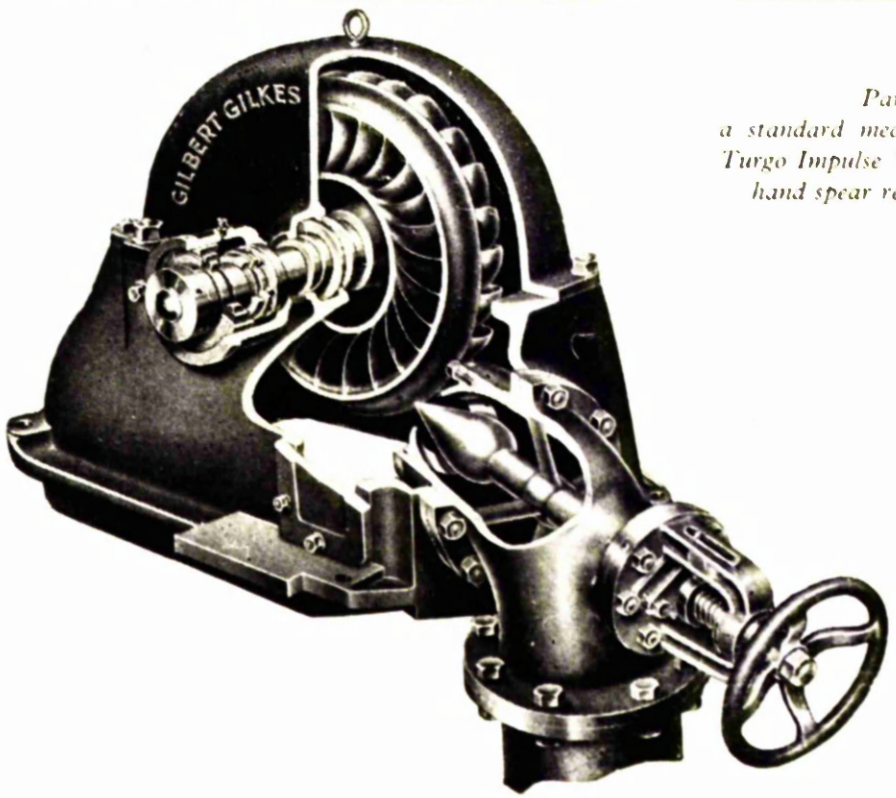

Part section of a standard medium power Turgo Impulse Wheel with hand spear regulator.

FIG. 1.

the Turgo wheel, the literature[4,5] previously cited, which describes experimental investigations, appears to represent the extent of knowledge regarding the strength of the buckets of this class of water turbine.

In design, the dimensions of the buckets of these impulse wheels are determined largely irrespective of considerations of strength. The shape of the bucket surface swept by the water-jet is determined solely from hydraulic considerations, and to a lesser degree the geometry of the unswept surface is also so determined, since it must be such as to avoid interference with the flow on and from the swept surface of the adjacent bucket. To this extent the bucket thickness is a function of the flow design, but in addition it is influenced by manufacturing aspects.

The Turgo wheel is, and always has been, produced as an integral casting and the modern Pelton wheel is also manufactured in this form. In the smallest sizes the buckets must be of a certain minimum thickness to be cast successfully. This restriction influences the sizes of larger wheels since it is common practice simply to scale-up proportionately particularly in respect of the thickness dimension. A "reinforcing" rib is commonly incorporated lengthwise on the unswept surface of the Pelton bucket, and appears to be dimensioned such that it doubles the thickness locally. Some manufacturers indicate that after the bucket shape and thickness have been determined in the fashion described, calculations based on simple bending theory are executed to "check" the bucket sections for strength.

Concern on the part of the British manufacturers, over the strength aspects of the Turgo impulse wheel, has been stimulated recently by the desire to use existing designs for operation at considerably higher ratings than formerly. The possibility of adopting such a course of action was apparently indicated by Russian practice. Mention of the

Turgo/

Turgo wheel occurs more widely in the Russian literature on water turbines, than in the English counterparts, where it features evidently in only one hydraulics text-book[7] in which the description is of an out-of-date version. It is gratifying to find that KOVALEV AND KVYATKOVSKIY [6] give credit to Crewdson for the invention of the original form of the Turgo wheel and to Jackson for the improved modern design. It was Earnest Jackson, lately chief engineer of Messrs. Gilbert Gilkes and Gordon Ltd., who introduced the Turgo wheel to Russian technology after the last war, by supplying a visiting Russian technical mission with a considerable quantity of relevant data.

Under Jackson's guidance, Messrs. Gilbert Gilkes and Gordon Ltd., have produced a design of high hydraulic efficiency and the firm wishes to exploit the improved qualities of this design under heads in excess of those formerly regarded as limiting. In more than forty years' experience of manufacturing and servicing Turgo wheels, report of failure for strength reasons is unknown to the company, so cautious extension to higher ratings seems a reasonable proposition. Higher ratings incur higher wheel speeds and jet loads thus highlighting the problem of strength, in consideration of which, knowledge of the stresses induced in the wheel is the first essential. At the invitation of the company, investigations have been conducted by the author with a view to obtaining this knowledge and an exposition of these investigations, concerning the stresses and deformations in the current design of Turgo impulse wheel, comprises the greater portion of this volume.

Under normal working conditions all water turbines are subjected to dual loading from hydrodynamic and centrifugal actions. On the buckets of impulse turbines the hydrodynamic or jet loading is an intermittent action, so that a possible mode of failure to be considered is corrosion fatigue. By using materials of high corrosion resistance and good/

good fatigue properties, a degree of protection against corrosion fatigue is provided, and in this respect impulse turbines possess an inherent advantage, being manufactured mainly in bronze and stainless steel.

To view in perspective the problems associated with the determination of stresses in the Turgo wheel, particularly on the experimental side, it was highly desirable at the outset to have some idea of the relative magnitudes of the maximum centrifugal and jet loading stresses for normal working conditions, and of the magnitude of the maximum centrifugal stress for the runaway or overspeed condition. A wheel of medium size was of primary interest. Theoretical order-of-magnitude analyses were developed and applied to estimate the normal working centrifugal and jet loading stresses. These calculations indicated stresses of a credible order, with the maximum centrifugal stress almost twice the corresponding maximum jet loading stress. Although essentially, and to a considerable degree, approximate, the nature of these calculations was also such that the indication of the relative maximum stress magnitudes could be taken as fairly accurate. This result had bearing on subsequent experimental work and indicated that, although an experimental stress analysis under actual working conditions was not contemplated in these investigations, such a test may hardly be necessary at all.

In view of the predominance of the centrifugal stress component, highlighted for the overspeed condition, a wheel of the size considered, supplied by the makers, was spun in a centrifugal test rig and the resulting strains were measured. Subsequently, on the stationary wheel, the jet loading was simulated in an approximate manner by mechanical means and the corresponding strains were measured.

In order to examine the behaviour of the buckets as shells, strains were measured on separately-cast single buckets subjected to various relevant loadings. The basic shell behaviour was observed to be generally somewhat akin to that of a pipe-bend or toroidal shell subjected to in-plane bending./

bending. On the basis of the work of CLARK [8,9], a theoretical solution was derived for the case of an open toroidal shell of varying thickness subjected to in-plane bending, and particular applications of this solution indicated theoretical results which approximated to the experimentally-determined behaviour of the single buckets and of the buckets on the wheel. The duties and the design of the Turgo impulse wheel were examined in the light of all the theoretical and experimental results which had been obtained concerning the stresses and deformations.

It was perceived that, with the addition of some existing shell theory, the open toroidal shell solution which had been derived, would also be applicable in an approximate manner to the case of the Pelton bucket under jet loading. Analysis of such a case was carried out on this basis and, for experimental comparison, corresponding strains were measured on a Pelton bucket subjected to simulated jet loading by mechanical means. Consideration was given to the implications of the results in relation to the design of Pelton wheels.

1B. REVIEW OF LITERATURE RELATING TO THE STRENGTH OF WATER TURBINES

During the investigations several publications came to light referring to strength aspects of water turbinesother than impulse wheels. Many of these publications were not directly pertinent to the problems under examination. Those, however, considered to be worth recording, are mentioned in this review.

In comparison to the abundant literature dealing with the strength aspects of steam and gas turbines and pump impellers, publications relating to the strength of water turbines are few in number. This is clearly illustrated in the bibliography of LÖFFLER [10] where, among more than one-hundred-and-thirty titles of references dealing with stresses and strains in rotating components, there is none referring to the strength of water turbines. Similarly in BIBLIOGRAPHY 17 [11] of THE BRITISH HYDROMECHANICS RESEARCH ASSOCIATION, of a total of seventy-two references, mostly pertaining to stresses in rotating discs, only five relate to the strength aspects of water turbines. None of these five concerns impulse turbines.

The earliest significant publication relating to the strength of an impulse turbine appears to be that of PERRIG [4]. Published in 1934, ten years before the advent of the electrical resistance strain gauge, and based on experimental methods somewhat crude by modern standards, it is still the most informative paper on the subject.

In order to reduce jet loading stresses in Pelton wheel buckets, and so combat corrosion fatigue, PERRIG proposed that rims might be fitted to connect the tips of the buckets. In the Federal Materials Testing Laboratory in Zurich, under the direction of Professor Ros, tests were/

were carried out to measure bucket stresses on a large Pelton wheel with and without rims. Huggenberger extensometers were arranged along the splitter or inlet edge of a bucket, along an outlet edge on the unswept or convex side, and on a reinforcing rib. The wheel was locked in a stationary position and simulated jet loading was applied to the swept surface of the test bucket by small hydraulic jacks, the reactions of which were carried on the reinforcing ribs of the neighbouring bucket. The magnitude of the simulated loading was equal to the resultant jet force on a bucket for the maximum power condition of the wheel, and stresses were measured for this magnitude of loading applied by the jacks in two different positions.

Since the reactions of the hydraulic jacks were taken on the adjacent bucket, the validity of this system of loading, as representative of jet loading, is somewhat questionable for the wheel fitted with rims, where the resultant actions on the test bucket are statically indeterminate. However, for the wheel without rims, where the resultant actions on the test bucket are statically determinate, the loading system is reasonably valid. The unrimmed wheel, of course, has been by far the more common form over the last thirty years, the rimmed Pelton apparently having failed to "catch-on", although it is mentioned and illustrated by EDEL [5] and by NECHLEBA [12].

Fig.2 taken from PERRIG, indicates the results in the form of stress distributions plotted along various portions of the test bucket. The most interesting values are the stresses parallel to the edges for the wheel without rims, as given on the plan view of the swept surface of the test bucket. Position I of the jacks corresponds to the greater bending moment on the bucket in the plane of the wheel, and induces tensile stress along the splitter or inlet edge varying linearly from almost zero to the maximum measured stress of 860 kg/cm^2 (12,200 lb/in^2). In contrast, there /

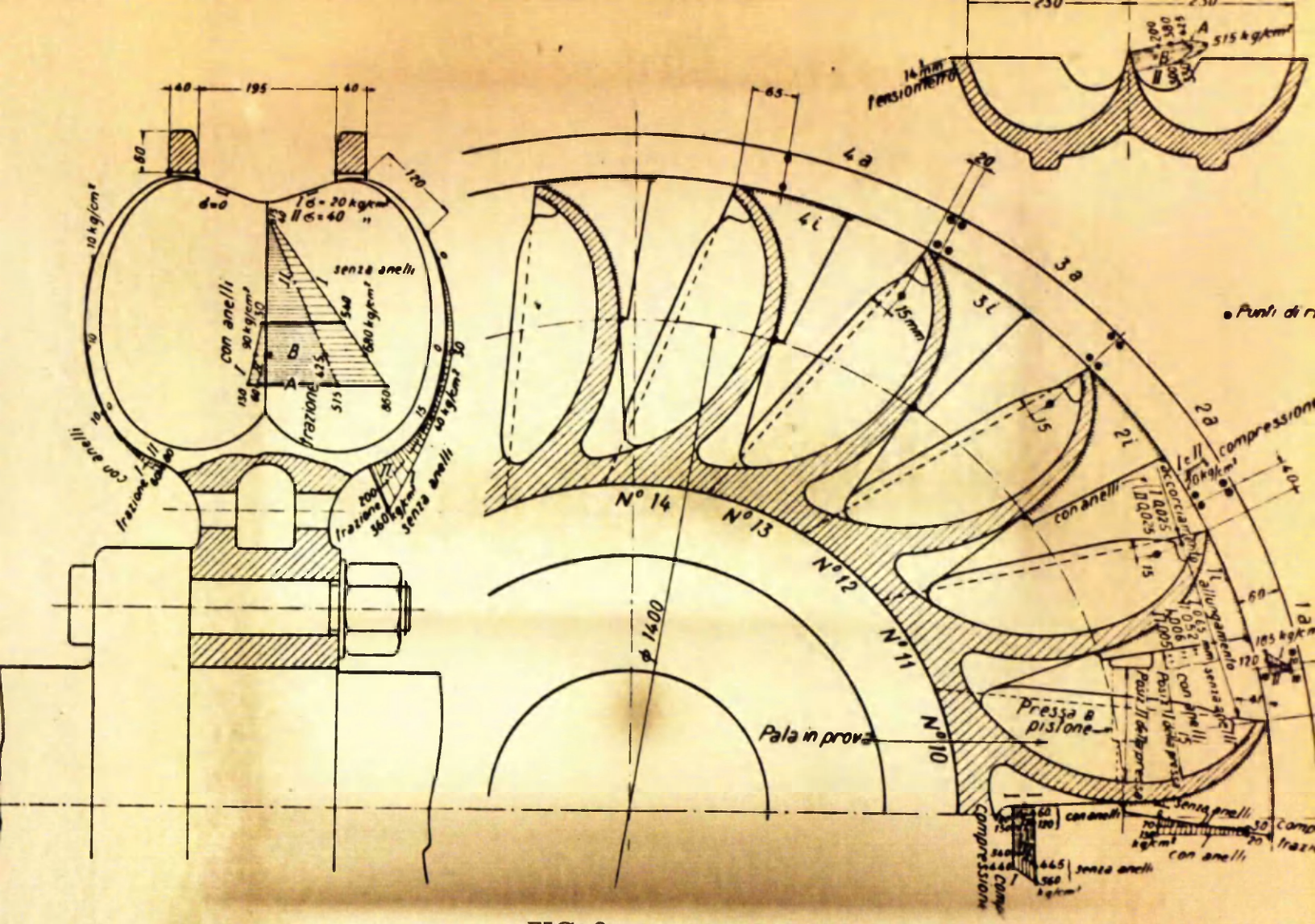

FIG. 2.

STRESSES MEASURED ON A 1400 mm.p.c.d. PELTON WHEEL SUBJECTED TO SIMULATED JET LOADING (PERRIG [4]).

ITALIAN	ENGLISH
CON ANELLI	WITH RIMS
SENZA ANELLI	WITHOUT RIMS
TRAZIONE	TENSION
COMPRESSSIONE	COMPRESSION
PALA IN PROVA	BUCKET UNDER TEST
PRESSA A PISTONE	HYDRAULIC JACKS
POSIZ. I DELLA PRESSA	POSITION I OF JACKS
POSIZ. II DELLA PRESSA	POSITION II OF JACKS
TENSIOMETRO	EXTENSOMETER
1 kg/cm^2	14.22 lb/in^2

there is correspondingly a very small tensile stress, less than 40 kg/cm^2, (570 lb/in^2) along most of the length of the unswept or convex side of the outlet edge. Unfortunately no measurements seem to have been made of the stresses along the swept or concave side of an outlet edge.

High factors of safety are said by QUICK [13] to be customary in design of Pelton wheels, but he gives no indication regarding the basis of these safety factors and of design procedures for strength. The problem of the stress analysis of the Pelton bucket is mentioned only to emphasise its difficult nature. Interesting photographs are, however, presented, illustrating various shapes of Pelton bucket and showing how the shape has evolved during sixty years.

NECHLEBA [12] considers a bolted Pelton bucket in two different positions relative to the jet and determines the resultants of the centrifugal and jet forces on the bucket. The bolts are then designed for shear and crushing. The complete calculation is of normal standard design form and nothing at all is mentioned concerning the strength of the bucket itself. Bolted buckets are relatively rare nowadays, the modern trend being towards integrally cast Pelton wheels.

The Russians, aware of difficulties associated with the theoretical approach, have carried out experimental work relating to the strength of Pelton wheels and including a strain-gauge test of limited scope on a full-scale working turbine. This work is described in the book by EDEL [5] which also presents a history of the development of the impulse turbine, portrays a Turgo impulse wheel and treats its hydraulic aspects. At the Leningrad Metal Works (LMZ - Leningradskii metallicheskii zavod) a strain-gauge test under working conditions was performed on a single-jet model Pelton wheel with bolted buckets. Strain-gauges which, together with leads, were waterproofed and protected, were located on the/

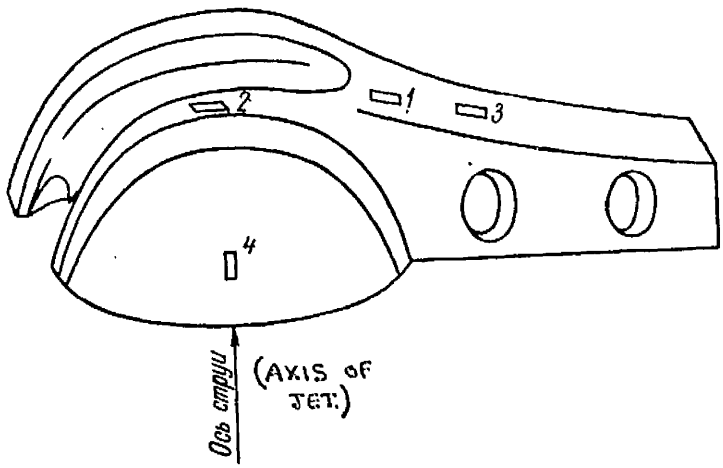

Схема расположения тензометрических датчиков (*1—4*) на лопасти при прочностных испытаниях экспериментальной турбины.

FIG. 3. DIAGRAM OF LAYOUT OF STRAIN GAUGES 1 TO 4 ON (PELTON) BUCKET, FOR STRENGTH TEST ON EXPERIMENTAL TURBINE. (EDEL[5]).

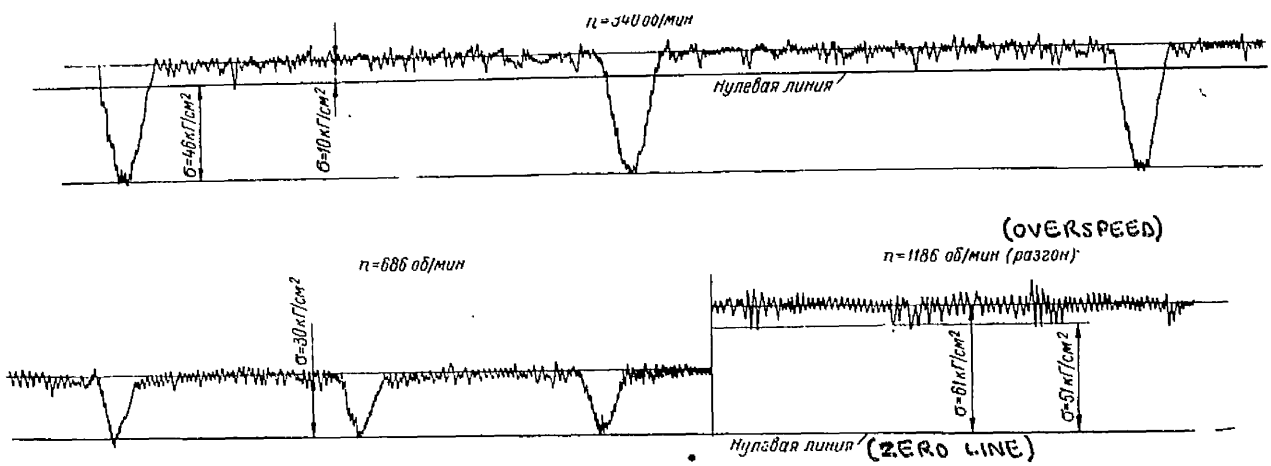

Осциллограммы напряжений в хвостовой части лопасти по данным лабораторных испытаний при трех значениях чисел оборотов.

FIG. 4. OSCILLOGRAM OF STRESSES ON BRACKET OF (PELTON) BUCKET, FOR THREE SIGNIFICANT SPEEDS, - LABORATORY TEST RESULTS. (EDEL[5]).

the unswept surfaces of a bucket and on the attachment bracket as shown on Fig.3. Testing was carried out at various wheel speeds and with the wheel stationary at various positions relative to the jet, the strain signals being recorded via slip-rings, amplifiers and oscillograph. Location 3 on the attachment bracket (Fig.3) showed the maximum stress for the locations examined, and Fig.4 indicates the recordings of this stress for three wheel speeds, 340 r.p.m., 686 r.p.m. and the runaway speed 1186 r.p.m. The centrifugal component of the stress at this location is tensile while the intermittent jet loading component is compressive. As might be expected this latter component practically disappears at the overspeed of 1186 r.p.m. The values of stresses at the other locations are not quoted, but are said to have been very small.

The full-scale service test was conducted on a four-jet, cast steel Pelton wheel of 1950 mm p.c.d. installed at the Khramskoy hydro-electric power station. Single strain-gauges and rosettes were mounted at unswept locations on a bucket, the layout being as shown on Fig.5. Techniques of waterproofing and protecting gauges and leads, and of recovering strain signals were essentially similar to those adopted in the test previously described. Various working conditions obtained, including running at maximum power. The values of stress at most of the locations are not quoted, but on the body of the bucket the stresses are indicated as having been very small, and again, the maximum stress of the locations examined, a value of 300 kg/cm^2 (4270 lb/in^2), is said to have been found on the attachment bracket, at gauge 28, Fig.5.

It is evident from PERRIG'S results, Fig.2, and from the author's findings, presented subsequently, that both of these strain-gauge tests under working conditions have been inadequate in respect of locations explored for strains. High strains are found along the bucket edges, as indeed/

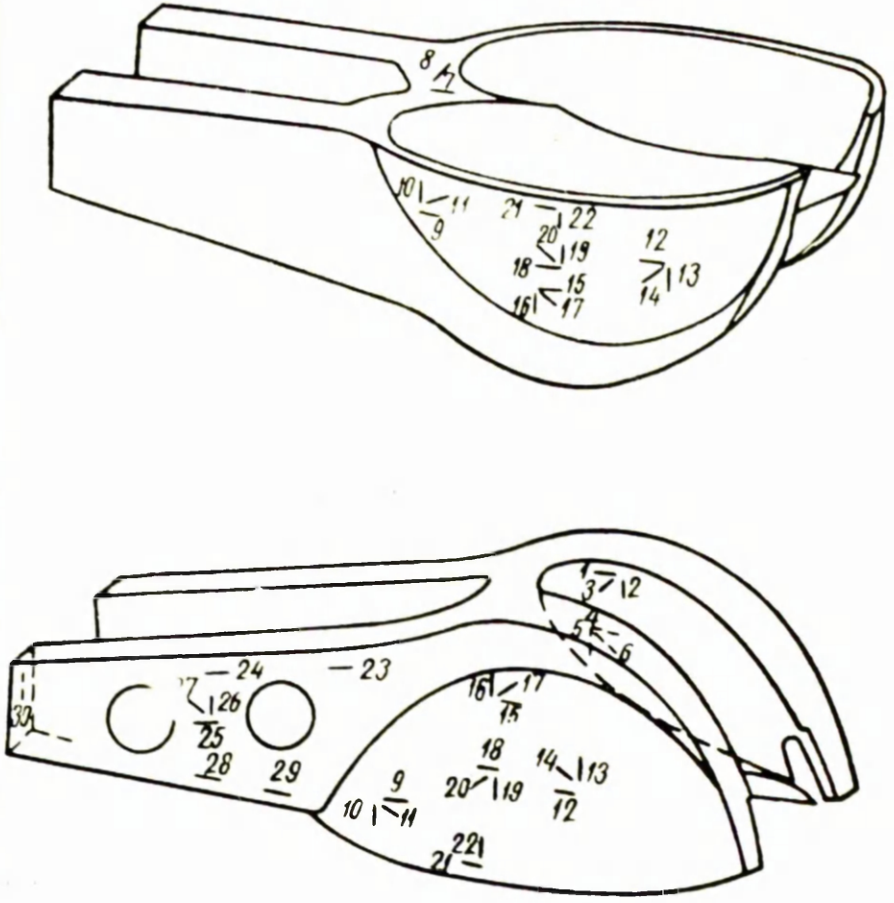

FIG. 5. DIAGRAM OF LAYOUT OF STRAIN GAUGES ON BUCKET OF WORKING (PELTON) WHEEL. (EDEL[5]).

Схема расположения тензометров на лопасти рабочего колеса.

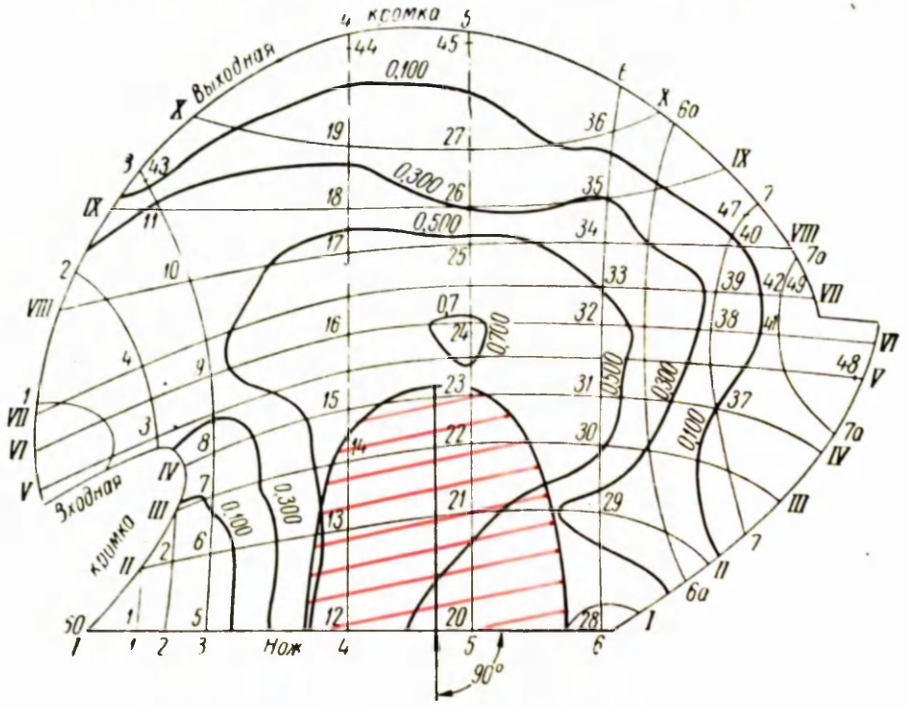

Приближенная развертка поверхности ковша лопасти с изобарами, полученными при исследовании неподвижной лопасти.

FIG. 6. APPROXIMATE DEVELOPED SWEPT HALF-SURFACE OF (PELTON) BUCKET, SHOWING ISOBARS (kg/cm^2), FOUND FROM MEASUREMENTS WITH BUCKET STATIONARY. RED AREA IS DEVELOPED HALF-JET SECTION. (EDEL[5]).

indeed the predominantly bending action of the loading would suggest, and less high, but appreciable values are found on the swept surfaces. Although these locations may be very difficult to explore under working conditions, any such test in which no attempt is made to do so, is relatively worthless, since it will almost certainly not record the maximum stress and other significant stresses in the bucket. Comparison of the maxima in EDEL'S tests, 61 kg/cm^2 and 300 kg/cm^2, with PERRIG'S maximum measured stress of 860 kg/cm^2, demonstrates this likelihood, even allowing for some differences in loading conditions and geometry. The LMZ model test seems to have been singularly lacking, the application of a strain-rosette, for example, having been neglected at location 4 (Fig.3).

Other data given by EDEL include a useful diagram of the pressure distribution measured on a small stationary Pelton bucket under jet action. This diagram is reproduced as Fig.6 and shows isobars plotted over the developed swept surface of a half-bucket, with sections indicated. Details of the bucket and sections are also given in the book permitting profiles of pressure distribution to be drawn for various sections. A description is given of a test in which the bolted buckets of a stationary Pelton wheel were struck with a hammer and the resulting vibration was recorded with a view to determining the effect of various adjustments of the bolts on the natural frequencies of the buckets. The only mention of design procedure for strength is the presentation of formulae, based on simple bending theory, for calculating the sizes of bolted bucket attachment brackets of rectangular cross-section. Allowable stresses are quoted for these items and the procedure is of normal standard design form. A bibliography of seventy-eight references is appended, the majority of them Russian publications.

The strength aspects of radial-flow or mixed-flow turbines of the Francis type have been examined by several investigators. SURBER AND SCHWEIZER [1]/

SCHWEIZER [1] describe techniques used in an experimental stress analysis of a model runner subjected to centrifugal loading and then to several static loadings, all in the dry condition, while NECHLEBA [12] presents a very approximate theoretical treatment, based on simple bending theory, for the hydrodynamic stresses in the vanes. Data of greater significance are given by Russian authors. GRANOVSKIY ET AL [2] and ARONSON [3] indicate fairly rigorous theoretical analyses for centrifugal stresses in the rim, and for working stresses in the vanes and rim, ARONSON'S calculations showing fair comparison with measured stresses. An experimental centrifugal stress analysis of a model runner is detailed by KUSTANOVICH AND IGNATEVA [14]. This test was similar to one carried out by SURBER AND SCHWEIZER [1], who do not indicate any of their results, whereas KUSTANOVICH AND IGNATEVA [14] quote many results, transforming from model values to equivalent stresses to be expected in full-size turbines. PRIGOROVSKII ET AL [15] give an account of a full-scale experimental investigation in which strains and pressures were recorded on a 5450 mm. diameter runner under service conditions. Testing techniques, conditions and results are depicted. The book by PRIGOROVSKII [16] draws together much of the Russian work, and utilises the data of ARONSON [3], KUSTANOVICH AND IGNATEVA [14] and PRIGOROVSKII ET AL [15] in the presentation of additional theoretical and experimental stress analyses for all components of this class of turbine. Several extensive pertinent bibliographies are given in this book which should be regarded as a key reference.

Axial-flow propeller or Kaplan turbines have received a fair amount of attention in respect of strength considerations. NECHLEBA [12] and RUUD [17] derive expressions for the hydrodynamic and centrifugal stresses on sections of a blade by the application of simple bending theory, the section at the blade-hub junction being regarded as critical. The/

The approximate hydrodynamic stresses at this section have been examined experimentally by OSTERWALDER [18] who simulated the loading on the blade-surface statically by means of dead-weights. The results of this experimental analysis are not reported. Again, as for the other classes of turbine, Russian work predominates. In their book GRANOVSKIY ET AL [2] give a simple bending theoretical treatment of the hydrodynamic stresses on blade sections and detail standard form design calculations for blade-to-shaft bolt arrangements. Shallow-shell theory is derived in the book by SMIRNOV [19], to which others have contributed, and this theory is applied to the calculation of working stresses and vibrations in the blade. A frozen-stress photoelasticity analysis of a model blade loaded with dead-weights is described, and the results are compared with relevant theoretical values. A number of full-scale investigations have been conducted under service conditions, some of them on 6 600 mm. diameter turbines on which strains, pressures and vibrations were measured. RUDASHEVSKII AND NEMM [20], KOVALEV [21], and KOVALEV ET AL [22], describe techniques used in such tests and present many results obtained under various conditions. PRIGOROVSKII'S book [16] summarises much of the relevant work published in the U.S.S.R. and describes further experimental stress analyses of models and of full-size turbines loaded statically under laboratory conditions. Contours of stress and pressure on blade surfaces are illustrated on several graphs which, together with the other content, including useful bibliographies, render this volume an important source of data.

Two Russian reviews are of interest. KOVALENKO [23] surveys one-hundred-and-twelve publications dealing with theory of plates and shells as applied to turbomachinery. Only one of the references reviewed however, deals directly with water turbines, being concerned with the Kaplan turbine, but another reference cited, that of TUMARKIN [24], presents/

presents methods of analysis which may be applicable to any of the reaction water turbines. TUMARKIN'S book[24] examines the stresses in fans on a theoretical basis. The book by KOVALEV AND KVYATKOVSKIY[6] reviews several pertinent topics including the hydraulic investigation of impulse turbines, being Pelton and Turgo wheels, investigations performed on water turbines under service conditions, and investigations relating to the strength of water turbines. A historical survey of the development of the water turbine between 1738 and 1957 is presented together with a chronological bibliography of two-hundred-and-twenty references.

The references which relate to reaction turbines of Francis and Kaplan types, and which have been quoted in the foregoing paragraphs, are not directly pertinent to the problems associated with the strength aspects of impulse turbines. It is evident however that some of the techniques employed in the model and full-scale experimental stress analyses of these reaction turbines, would be applicable, perhaps with slight modification, to similar experimental stress analyses of impulse turbines.

CHAPTER 2.

THE TURGO IMPULSE WHEEL AND ITS GEOMETRY.

THE TURGO IMPULSE WHEEL AND ITS GEOMETRY

The Turgo impulse wheel is a high capacity, medium-to-high head, free jet impulse water turbine designed and manufactured, outside the U.S.S.R., by Messrs. Gilbert Gilkes and Gordon Ltd., Kendal, England[25]. Its invention by CREWDSON[26] was announced in 1921 when it was described as a development of the axial-flow Girard turbine with a jet of the Pelton type. The arrangement of turbine, nozzle and casing is shown in Fig.1 in which the turbine is of an early design. As shown, the jet enters the turbine from the side making an angle of about 20° with the plane of the wheel, and strikes three buckets, practically filling three inlet passages. Discharge takes place at the opposite side of the wheel, the water then falling by gravity to the tail race. The turbine, which is always manufactured as an integral casting in bronze or stainless steel, according to its duty and size, incorporates a rim offset to the inlet side as indicated in the diametral section, Fig.7. Other illustrations of the wheel depicted in Fig.7, which relates to the current design, are to be found in Figs. 55 and 56 of Chapter 4, Figs. 55(a) and 55(b) in particular showing respectively the curvatures of the inlet and outlet edges of the buckets.

The nozzle is identical to that used for a Pelton wheel and produces a solid, well-formed jet. In comparison with the equivalent Pelton wheel, which is one driven by the same jet or alternatively subject to the same head and developing approximately the same B.H.P., the Turgo wheel is about half the diameter of the Pelton and rotates at about twice its speed. It is slightly less efficient than the Pelton, but offers less wind-resistance. For maximum efficiency in both types of impulse wheel, the pitch-circle* peripheral/

* The radius of the pitch-circle is the perpendicular distance from the wheel axis to the centre-line of the jet.

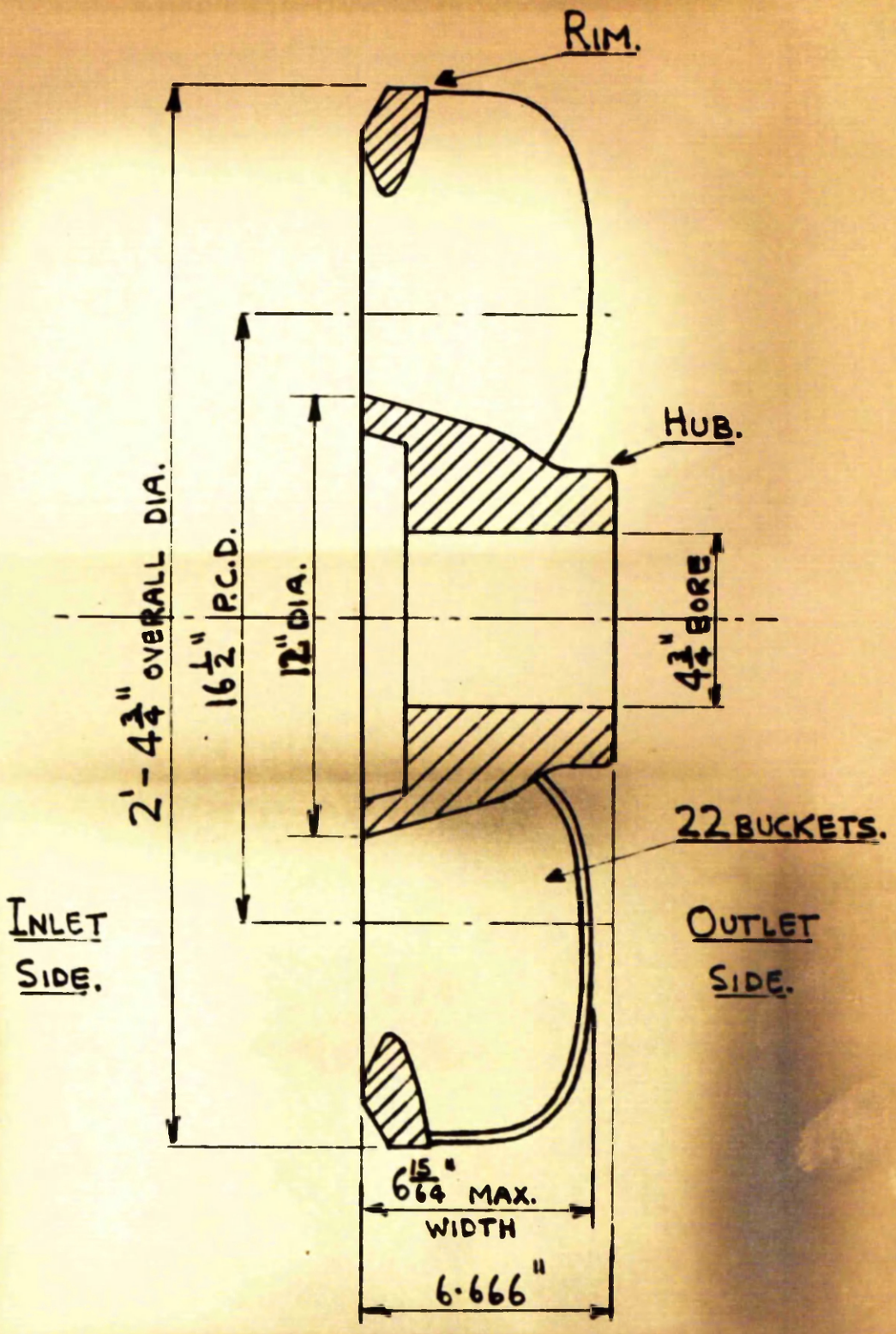

FIG. 7. DIAMETRAL SECTION OF 16½ IN. P.C.D.

TURGO IMPULSE WHEEL OF CURRENT DESIGN.

peripheral speed should be theoretically half the speed of the jet, but in practice the normal working wheel peripheral speed of both turbines is slightly less than half the jet speed. If, while operating under constant head, the brake-load is removed from the wheel and the governing mechanism fails, then the overspeed or runaway condition occurs in which the wheel peripheral speed approaches the speed of the jet. The runaway speed of the Turgo wheel is approximately 80% above the normal working speed [25]. The largest Turgo impulse wheel manufactured by the Kendal firm is of 36 in.p.c.d. and about 6 ft.overall diameter and develops 4,600 B.H.P. at approximately 600 r.p.m. under normal working conditions.

For experimental investigation, Messrs. Gilbert Gilkes and Gordon supplied the writer with a $16\frac{1}{2}$ in.p.c.d. (2 ft.,4.3/4 in.overall diameter) Turgo impulse wheel of current design in cast aluminium. Unfortunately separate single buckets for this size of wheel were unavailable, but two single buckets for other sizes were supplied, one for an 18 in.p.c.d. current design wheel and one for a 33 in.p.c.d. early (obsolete) design wheel. Both separate single buckets were in cast aluminium and were integral with segments of hub for the purpose of mounting.

In the current design, the buckets of the $16\frac{1}{2}$ in.wheel are geometrically similar to those of an 18 in.wheel. The single aluminium bucket for this latter size is shown together with a white plaster replica, in Fig.8, which indicates clearly the high curvatures of the bucket both in the plane of the wheel and in planes perpendicular to the plane of the wheel. Outward from the hub the outlet edge of the bucket, for the most part, follows the general curvature in the plane of the wheel while the inlet edge rather departs from this, as is shown particularly in Fig.8(a). The inlet edge is quite sharp of course, but along the outlet edge the bucket thickness is fairly constant at about $\frac{1}{4}$ in., as may be seen in Figs./

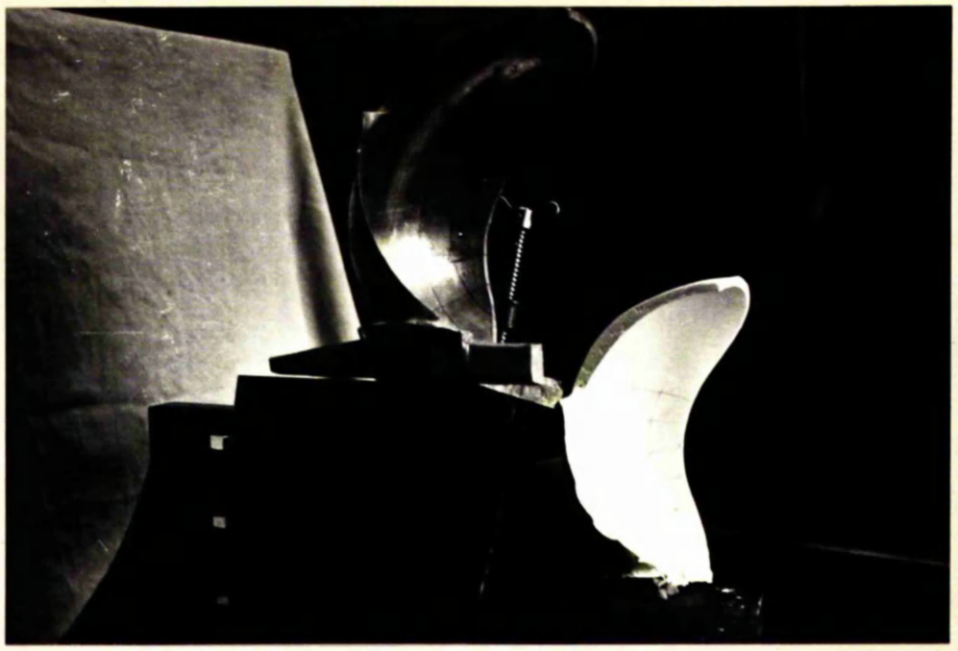

(a) LOOKING ON INLET SIDE, AND SHOWING SWEPT SURFACES.

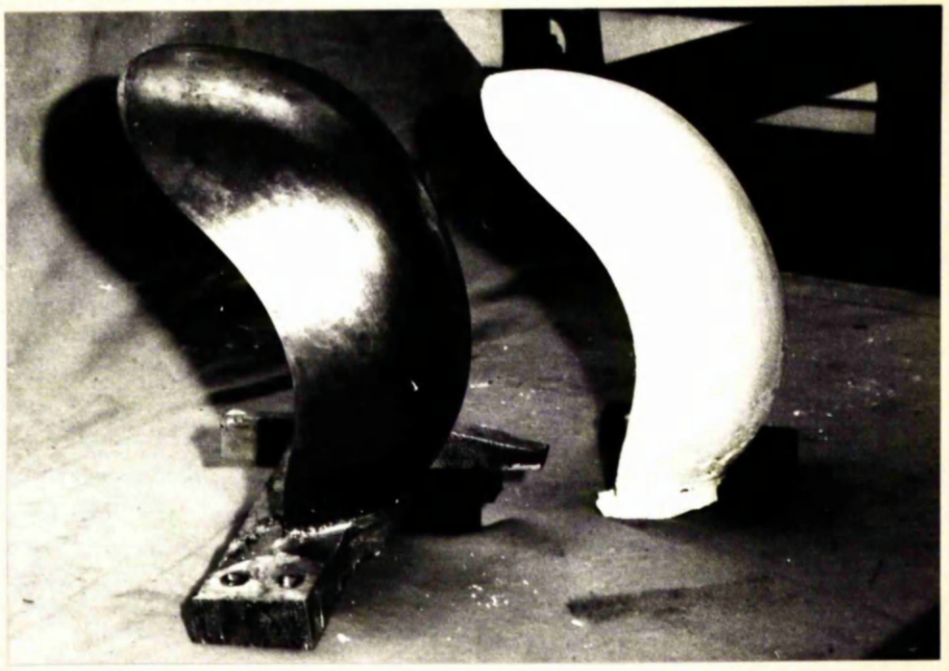

(b) LOOKING ON OUTLET SIDE AND SHOWING UNSWEPT SURFACES.

FIG. 8. SINGLE ALUMINIUM BUCKET FOR 18 in. p.c.d. TURGO IMPULSE WHEEL, AND WHITE PLASTER REPLICA.

Figs.9 and 10(a). Fig. 8(a) and Figs. 55(b) and 56(b) of Chapter 4 show that the bucket attaches to the rim over a long "line of contact", one bucket appearing to "overlap" another on the outlet side of the rim. Alternatively, this may be expressed by saying that the rim, at all its cross-sections, is integral on the outlet side with one bucket or with two buckets.

One of the manufacturing drawings for the $16\frac{1}{2}$ in. wheel is shown as Fig.9.* In its original form from the makers, this drawing comprised View X, the diametral section, on which details of hub and rim are given, and the important View Y which shows sections of the bucket in planes parallel to the plane of the wheel at the stations 0, 2, 4, ...13 of View X. All of these bucket sections are related to an axial datum line which passes through point 0 on View Y, point 0 being the intersection of the pitch-circle and inlet edge. The intersections of the parallel planes, containing sections 2, 4, ...13 of View Y, with this axial datum line, are shown in View Y as points 2, 4, ...13 on the pitch-circle, point 2 being the datum point for section 2, point 4 the datum point for section 4, etc. Thus if radii Z0, Z2, Z4, ...Z13 were superposed in View Y, that is points 0, 2, 4, ...13 on the pitch-circle all coinciding, the corresponding sections 0, 2, 4, ...13 would appear in correct relation to each other. As well as showing the inlet edge, View Y shows a considerable length of the outlet edge much of which lies in a plane approximately parallel to the plane of the wheel, as can be seen in View X. The corresponding manufacturing drawing for an 18 in.p.c.d. wheel is very similar to Fig.9. Similar sections 0, 2, 4, ...13 are shown and dimensions are proportionately greater.

To assist examination of bucket geometry, replicas of the aluminium bucket for an 18 in. wheel were made in fine modelling plaster. The aluminium bucket, coated with silicone release agent, was used as pattern/

*Fig. 9 is in pocket attached to inside of back cover.

pattern suitably arranged in a mould box, and a mould was cast round the bucket in hard-setting silicone rubber. After setting, the mould was cut carefully to release the bucket and was then cleaned, coated with release agent and re-assembled and sealed ready to receive the cast of liquid plaster for the replica bucket. Several plaster replicas were made, some of them being shown in Figs. 8 and 10. Careful measurements and the application of templets confirmed their accurate correspondence with the geometry of the aluminium bucket.

Extensive use was made of templets to record curvatures in various planes at many points on the swept and unswept surfaces of the 18 in.wheel aluminium and plaster replica buckets. The survey of curvatures, together with thickness measurements, indicated the following:-

(a) The curvatures in planes parallel to the plane of the wheel, pertaining to the sections 0, 2, 4, ...13 shown on the manufacturing drawing, are faithfully reproduced on the actual bucket.

(b) As may be practically discerned by eye, e.g. in Fig.8, the bucket shape for the most part approximates somewhat roughly to that of part of a shell of revolution, the axis of which is parallel to the wheel axis. With the exception of part of the inlet edge, the curvatures of the bucket in planes parallel to the plane of the wheel, represent approximately the circumferential curvatures of this shell of revolution. This may be seen on the manufacturing drawing for the 18 in.wheel, just as in Fig.9, where the long boundaries of sections 2, 4, 6, ...13 approximate to circular arcs. From examination of these sections and of View X of Fig.9, together with Fig.8 showing general bucket shape, it may be said that section 6 represents approximately the "equator" of the corresponding shell of revolution. Therefore taking the plane of section 6, View Y, as the "equatorial" plane/

plane of the shell, the centre of the circular arc which approximates to the concave or swept boundary of section 6, locates the axis of revolution of the shell. In View Y of Fig.9 this circular arc is indicated and shown dotted, so locating the axis of the corresponding shell of revolution at centre Z_1. Although Fig.9 refers, of course, to the $16\frac{1}{2}$ in. wheel, exactly similar observations apply to the corresponding drawing for the bucket of the 18 in. wheel.

(c) With reference to View Y, Fig.9, the planes of sections 0, 2, 4, 6, ...13 may be called circumferential planes. Planes perpendicular to these and passing through Z_1, thus containing the axis of revolution, are evidently meridional planes, and it is roughly in such meridional planes that many of the highest curvatures of the bucket occur, both on swept and unswept surfaces. Again Fig.8 indicates that this feature is practically discernable by eye. At most points on the bucket surfaces it is evident that, to a reasonable degree of approximation, the principal curvatures lie in such meridional planes and in planes perpendicular to meridional planes, as is the case in a shell of revolution.

It is instructive to inspect sections of the bucket in meridional planes. In View Y, Fig.9, the lines of intersection of meridional planes with the "equatorial" plane of section 6, may be used to specify the angular positions of the meridional planes relative to a datum. The datum is chosen as that meridional plane which intersects the "equatorial" plane along trace $Z_1 G_1$, shown dotted, and so the position of any meridional plane is defined by the relevant value of angle Θ^*. The determination of datum $Z_1 G_1$ is indicated in Chapter 3. Meridional sections of the bucket at $\Theta = 74^\circ$ and at $\Theta = 86^\circ$ are shown for the $16\frac{1}{2}$ in. wheel in View W of Fig.9. These sections are constructed from the circumferential sections/

* See Nomenclature.

sections of View Y and from View X as follows, e.g. for the meridional section at $\Theta = 74^{\circ}$, :-

(1) From View X, stations 0, 2, 4, ...13 are projected into View W as the same stations, 0, 2, 4, ...13. These stations are, of course, traces of the circumferential planes.

(2) In View Y, with reference to section 6, angle $\Theta = 74^{\circ}$ is measured and $Z_1 b$ is drawn to cut radius Z6 in $6'$ and to cut section 6 in points a and b. Angle γ which $b6'$ makes with $Z6'$, is measured. For this meridional section then, point $6'$ on radius Z6 locates an axial datum line for all the other circumferential sections of View Y. In View W, any line perpendicular to stations 0, 2, 4, ...13 is drawn to represent this axial datum. In this view, the intersection of the axial datum line with station 6 then locates point $6'$ and lengths $6'a$ and ab are measured along station line 6, equal respectively to $6'a$ and ab of View Y. Thus in View W, points a and b are located as points on the two surfaces of the meridional section at $\Theta = 74^{\circ}$.

(3) Now considering section 4 of View Y, $Z4'$ is measured along radius Z4 to equal $Z6'$, locating datum point $4'$ relative to this circumferential section 4. Then line $4'e$ is drawn to make angle γ with $Z4'$, cutting section 4 in points d and e. In View W, point $4'$ is located at the intersection of the axial datum line with station 4, so lengths $4'd$ and de are measured along station line 4, equal respectively to $4'd$ and de of View Y. Thus in View W, points d and e are located as points on the two surfaces of the meridional section at $\Theta = 74^{\circ}$.

(4) Exactly similar procedure as in (3) is applied correspondingly in turn to sections 0, 2, 8, 10, 12 and 13 of View Y, thus giving points/

points f, g, h, j, k, l, m, n, p, q, r and s as points on the two surfaces of the meridional section at $\Theta = 74^{\circ}$.

(5) Length 13' t from View Y, together with projection from View X in the region of line G at the outlet edge, then locate the outlet edge points t and u in View W for the meridional section at $\Theta = 74^{\circ}$, which is finally revealed by joining the appropriate points f, h, d, a, k, etc., and g, j, e, b, etc., with smooth curves.

For the bucket of the $16\frac{1}{2}$ in. wheel, in addition to the meridional sections at $\Theta = 74^{\circ}$ and at $\Theta = 86^{\circ}$ shown in Fig.9, three other meridional sections, constructed as described, are shown in Figs. A6.1(a), A6.3(a) and A6.4(a) of Appendix 6. These respectively are for $\Theta = 57^{\circ}$, $\Theta = 92^{\circ}$ and $\Theta = 111^{\circ}$.

Using exactly the same method of construction on the corresponding manufacturing drawing, a similar set of five meridional sections was drawn for the bucket of the 18 in. wheel. One such section, in the region of the bucket in way of the pitch-circle, is shown in Fig.45 of Chapter 4. Like the corresponding sections of the $16\frac{1}{2}$ in. wheel bucket, these sections were from the main body of the bucket clear of the rim.

It was a matter of some consequence to determine how closely these constructed meridional sections would correspond with their counterparts on the actual bucket. Accordingly one of the plaster replica buckets for the 18 in. wheel was appropriately marked-off on the basis of measurements from the manufacturing drawing, and corresponding sections were cut through the replica. The sections were cut carefully by hand, using a fine hacksaw lightly applied. Fig.10(a) illustrates one replica appropriately marked-off and another, of better surface quality, which has been sectioned correspondingly. A typical meridional section of this latter/

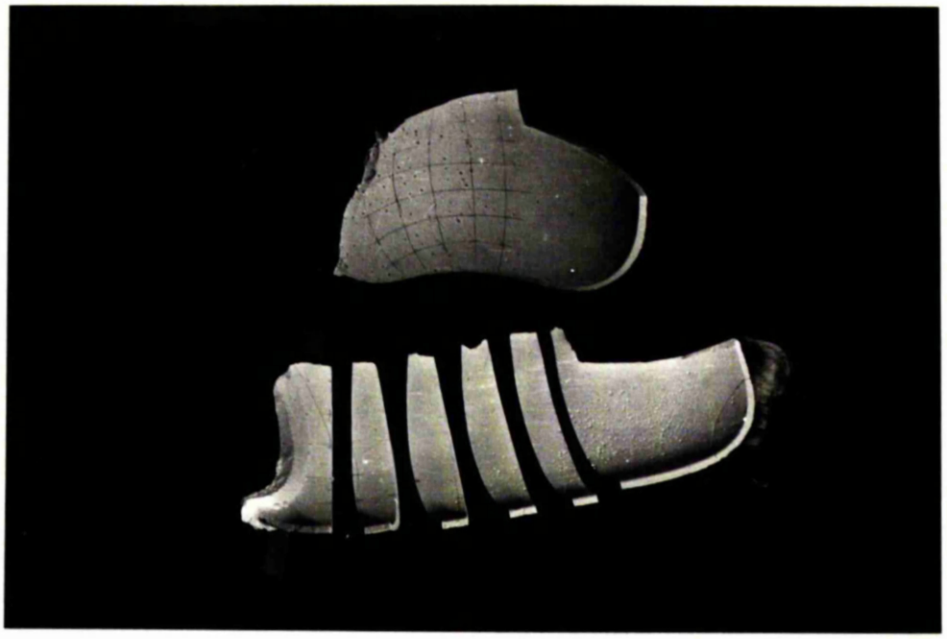

(a) LOOKING ON SWEPT SURFACES, ONE REPLICA SECTIONED MERIDIONALLY, THE OTHER MARKED-OFF MERIDIONALLY AND CIRCUMFERENTIALLY.

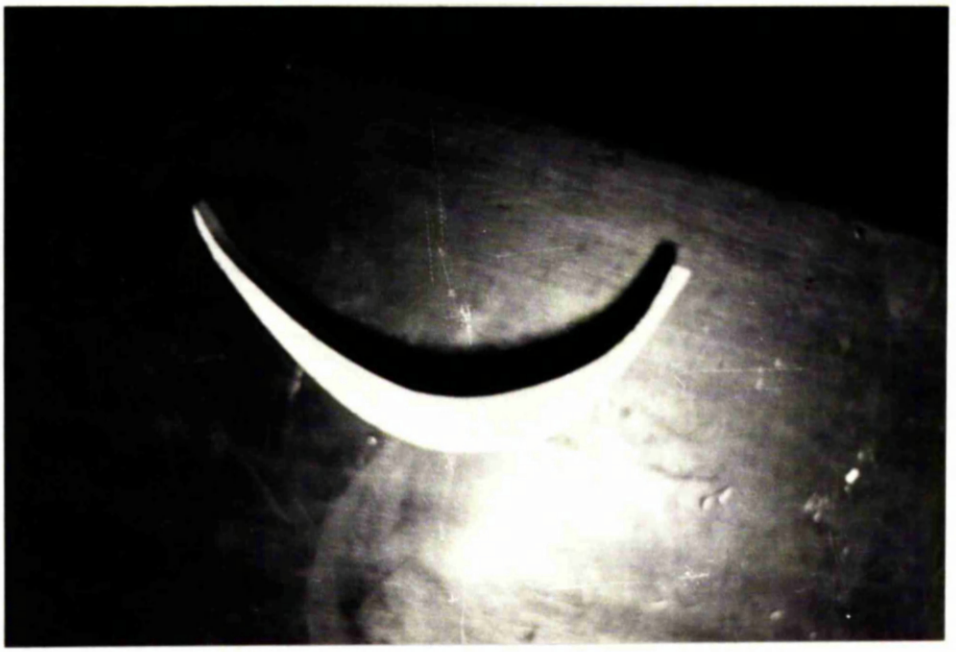

(b) VIEW ON A MERIDIONAL SECTION OF REPLICA.

FIG 10. PLASTER REPLICAS OF BUCKET FOR 18 in.p.c.d. TURGO WHEEL.

latter model is shown in Fig.10(b) from which the section may be seen to resemble the constructed section of Fig.45. Comparison of the meridional sections constructed from the manufacturing drawing, with their counterparts on the sectioned replica, showed good correspondence especially in respect of general curvatures. There were minor differences in thickness at one or two points.

Concerning the bucket for the $16\frac{1}{2}$ in.wheel, inspection of the five meridional sections for values of Θ equal to 57°, 74°, 86°, 92° and 111° (Figs. A6.1(a), 9; A6.3(a) and A6.4(a)) shows that these sections are generally quite similar, the only marked differences in shape occurring at, and in the region of, the inlet edge. This is also evident from the general appearance of the bucket, e.g. as Fig.8(a) indicates. Meridional sections of the bucket in way of the rim have, of course, no portions in the region of the inlet edge, as may be seen from Views X and Y, Fig.9, but apart from this, these sections mainly resemble the corresponding parts of the five full meridional sections shown. All the meridional sections lack symmetry, as might be expected, but the "average" shape of section is one not very far from symmetrical about a plane parallel to the plane of the wheel.

The areas were measured and the centroids were located for the five full meridional sections of the $16\frac{1}{2}$ in.wheel bucket, and the following were established:-

(a) All the sections have almost the same area. The area of the largest is just over 6% greater than the area of the smallest.

(b) The centroids all lie within 1/8 in.of a common plane which is parallel to the plane of the wheel. The trace of this plane lies between the traces at stations 6 and 8 of View W, Fig.9. Alternatively, it may be said that all the centroids are located at almost the same distance from the plane of the inlet edge.

(c) /

(c) The projections of the centroids on this common plane, and also on the "equatorial" plane of section 6 (View Y of Fig.9), lie within 3/16 in.of a circular arc, centre Z_1. This arc is the same in the common plane as in the plane of section 6, and is of radius slightly less than that of the arc shown in View Y as approximating to the concave boundary of section 6.

In comparing the bucket shape to that of part of a shell of revolution, which, of course, exhibits identical meridional sections, a degree of approximation is incurred which is not unreasonable. The meridional sections of the bucket all correspond fairly closely in respect of section thickness. It is evident that the thickness of a meridional section varies from inlet edge to outlet edge in a rather pronounced manner, so the shell of revolution comparable to the shape of the bucket, is a shell of revolution of varying thickness.

CHAPTER 3.

APPROXIMATE THEORETICAL ANALYSES FOR THE CENTRIFUGAL AND JET LOADING STRESSES AND DEFORMATIONS IN A TURGO IMPULSE WHEEL.

APPROXIMATE THEORETICAL ANALYSES FOR THE CENTRIFUGAL AND JET LOADING STRESSES AND DEFORMATIONS IN A TURGO IMPULSE WHEEL.

These approximate analyses have been developed mainly to estimate the orders-of-magnitude of the centrifugal and jet loading stresses in a Turgo wheel, and so to provide comparison between the approximate stress maxima for the two types of loading under normal working conditions. Additional aims have been to enhance the effectiveness of subsequent strain measurement by indicating probable regions of significant stress, and to investigate bases on which methods of design for strength might be founded.

The approximate theories are derived in completely general form, and since the number of buckets is standardised at 22 for the current design, and geometrical similarity applies over a wide range of sizes, significant expressions are set-down non-dimensionally as far as possible. Separate analyses are, of course, presented for centrifugal loading and jet loading but the derivations are on similar lines, comprise common matter and for the most part, share a common nomenclature.

The $16\frac{1}{2}$ in.p.c.d. wheel, being of medium size and of interest experimentally, is the subject of the numerical applications of the theoretical analyses. The dimensions of the wheel are shown in Figs.7 and 9. Throughout the analyses, numerical calculations are shown for this wheel under its maximum rated service head of 700 ft.[25], and also, where appropriate, at the corresponding overspeed, the wheel material being cast steel. In relation to the experimental work, reference is also made to a similar wheel in aluminium, subjected to the same service conditions. The pertinent conditions and the relevant physical and mechanical properties of the two materials are indicated in Table 1.

TABLE 1.

WORKING CONDITIONS AND PROPERTIES OF MATERIALS PERTINENT TO NUMERICAL CALCULATIONS FOR 16½ in. p.c.d. TURGO WHEEL.

Maximum rated head = 700 ft.	
Normal working condition.(25)	Overspeed.(25)
1013 B.H.P. at 1300 r.p.m.	2340 r.p.m.

Material of Wheel.	Physical and Mechanical Properties.			
	Density. D lb/in.^{3}	Young's Modulus. E lb/in.^{2}	Modulus of Rigidity. G lb/in.^{2}	Poisson's Ratio. ν
Cast Steel *	0.285	30×10^6	11.4×10^6	0.31
Aluminium+	0.095	11.3×10^6	4.3×10^6	0.31

* Properties for cast steel are taken from relevant literature.

\+ All properties for aluminium, except G, were measured from material from the same cast as the wheel used in experimental work. G is calculated from E and ν.

3A. THEORETICAL ASSUMPTIONS

The assumptions made concerning the geometry of the wheel, are listed below. These are based largely on the findings of the examination of typical wheel geometry, presented in the previous chapter.

(1) All meridional sections of the bucket are identical being parabolic in shape and symmetrical about a plane parallel to the plane of the wheel. The curvature and thickness of the parabolic symmetrical section approximate respectively to the curvature and thickness of the "average" meridional section of the bucket, which is a meridional section in the region of the pitch circle, e.g. for the $16\frac{1}{2}$ in. wheel of Fig.9, the "average" meridional section is at about $\Theta = 86^{\circ}$ or $\Theta = 92^{\circ}$. The "equivalent" parabolic section is obtained from this average meridional section as follows, e.g. with reference to Fig.11 which shows in dotted lines the meridional section at $\Theta = 92^{\circ}$ for the $16\frac{1}{2}$ in. wheel:-

The origin of the parabola which forms the mid-line of the equivalent section is located at O, the intersection of the mid-line of the average meridional section with line Ox in the plane of the wheel. Ox bisects the total width of the average section and forms the x-axis, Oy being the y-axis. The general equation of the parabola with respect to these axes is $y^2 = 4ax$, and the parabola selected is the one judged as approximating to the mid-line of the average section in the best balanced manner. The parabola shown is for $a = 1.32$ in. Thickness t of the equivalent parabolic section is a linear function of x, where $t = mx + c$. The value of c is taken as the thickness of the average meridional section at $x = 0$, and m is found from the condition that at x_{MAX}, t is/

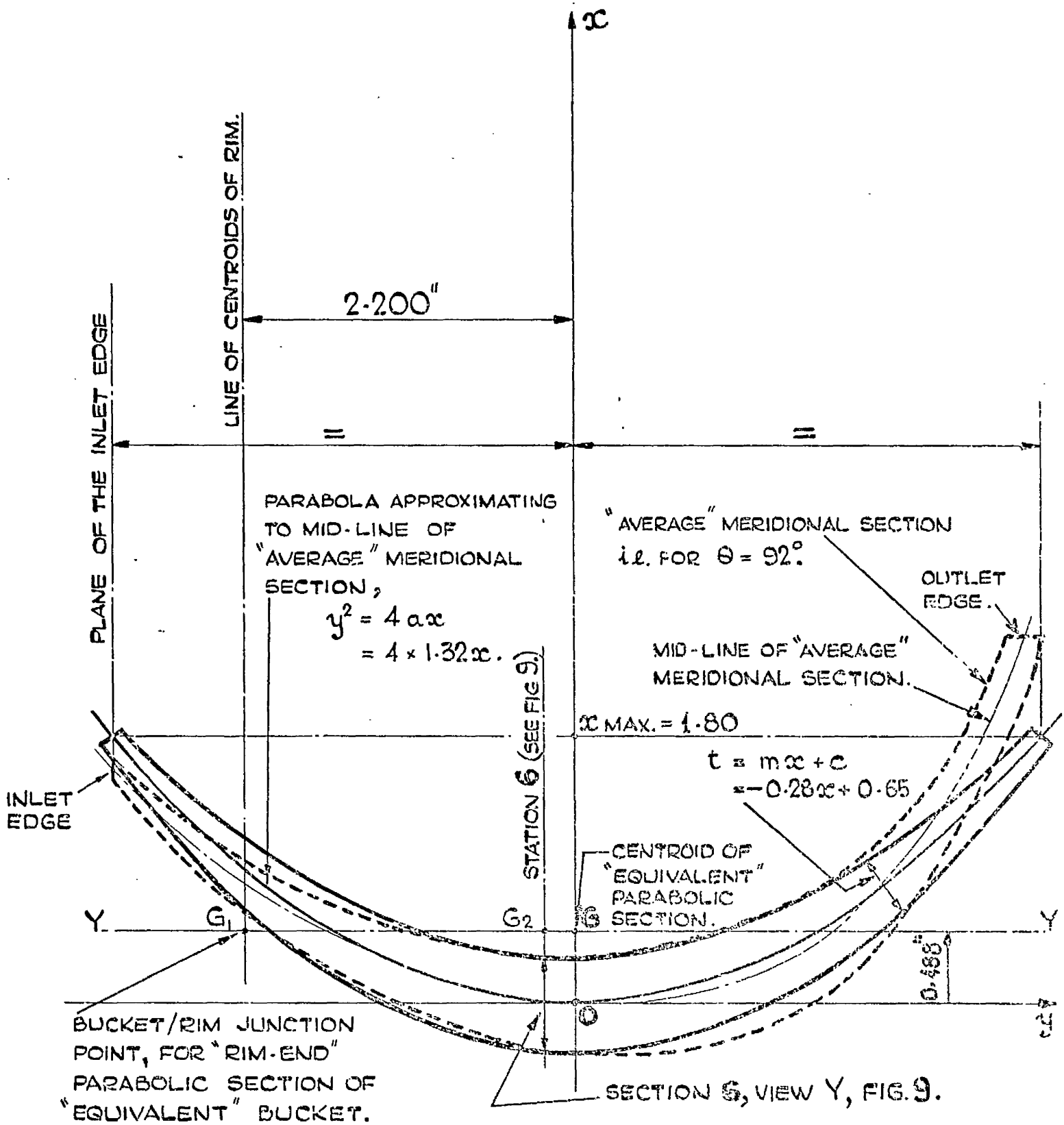

FIG. 11. "AVERAGE" MERIDIONAL SECTION OF BUCKET AT $\theta = 92°$ AND "EQUIVALENT" PARABOLIC SECTION, FOR $16\frac{1}{2}$" P.C.D. TURGO WHEEL. SEE APPENDIX 1 FOR PROPERTIES OF THE "EQUIVALENT" PARABOLIC SECTION.

is taken as the mean of the thicknesses at the edges of the average meridional section. For the section shown, $t = -0.28x + 0.65$. The parabolic section with linearly-varying thickness approximates fairly closely to the average meridional section. For such an equivalent section, all the properties relevant to the analyses may be derived mathematically with reasonable facility. These properties are given in Appendix 1, from which the location of G, Fig.11, is found. G is the centroid of the equivalent parabolic section.

(2) The locus of the centroids of the identical equivalent parabolic sections of the bucket is a circular arc in the plane of the wheel, e.g. containing Ox, Fig.11. This circular arc is located as follows, e.g. for the $16\frac{1}{2}$ in. wheel:-

In Fig.11, the projection of G on station 6 is G_2, which locates the "height" of the centroid relative to section 6. At $\Theta = 92^\circ$ in View Y of Fig.9, G_2 is then easily located relative to section 6 and the required circular arc is then drawn with centre Z_1 and radius Z_1G_2. The circular arc is shown dotted in Fig.9 and is indicated as the line of centroids of the equivalent parabolic meridional sections. From View X of Fig.9, the centroid G_R of the rim-section may be found and so the projection of the line of centroids of the rim may be drawn in View Y as shown. The line of centroids of the parabolic sections intersects the line of centroids of the rim at G_1 in View Y, at which point the former line terminates. Line Z_1G_1 then forms a zero datum for measurement of angle Θ, as has been indicated in the previous chapter. The other termination of the circular arc of centroids of parabolic sections is at G_3 where the arc intersects the trace of the junction of the hub with section 6. Arc $G_1G_2G_3$ is then the line of centroids of the "equivalent" bucket of parabolic sections. No part of this equivalent bucket extends beyond G_1.

(3) /

(3) The rim is of rectangular cross-section, of area approximately equal to that of the actual rim-section. The depth of the rectangular section lies in a plane parallel to the plane of the wheel, and is twice the breadth. The centroids of actual and "equivalent" rectangular rim coincide. In View X, Fig.9, the equivalent rectangular section is shown dotted for the rim of the $16\frac{1}{2}$ in.wheel. The degree of the approximation is evidently reasonable.

The rectangular section rim and parabolic section bucket join at one point only, the joint being rigid. This bucket/rim junction point is at the centroid of the rim-section and, for the $16\frac{1}{2}$ in.wheel, is shown as G_1 in View Y, Fig.9, and as G_R in View X. In relation to the parabolic section at the "rim-end" termination of the equivalent bucket, the junction point is shown as G_1 in Fig.11.

(4) The hub is a thick cylinder of the same bore as the actual hub, and of length equal to the total width of the average meridional section of the bucket (see e.g. Fig.11). The outer radius is measured from the centre of the wheel to the "hub-end" termination point of the circular line of centroids of the parabolic section bucket, e.g. for the $16\frac{1}{2}$ in.wheel, the outer radius of the thick cylinder hub is the line joining Z to G_3 in View Y, Fig.9.

The bucket, over its total width, is rigidly joined to the outer surface of the hub.

Fig.12 illustrates and summarises these geometrical assumptions with application to the $16\frac{1}{2}$ in.wheel. The bucket is replaced by its equivalent parabolic section bucket, and the rim by its equivalent rectangular section rim. In the line diagram these are represented by their lines of centroids, which also represent bucket and rim in many parts of the analyses. The bucket and rim are rigidly connected only at point G_1. The hub is replaced by its equivalent thick cylinder to which the buckets are/

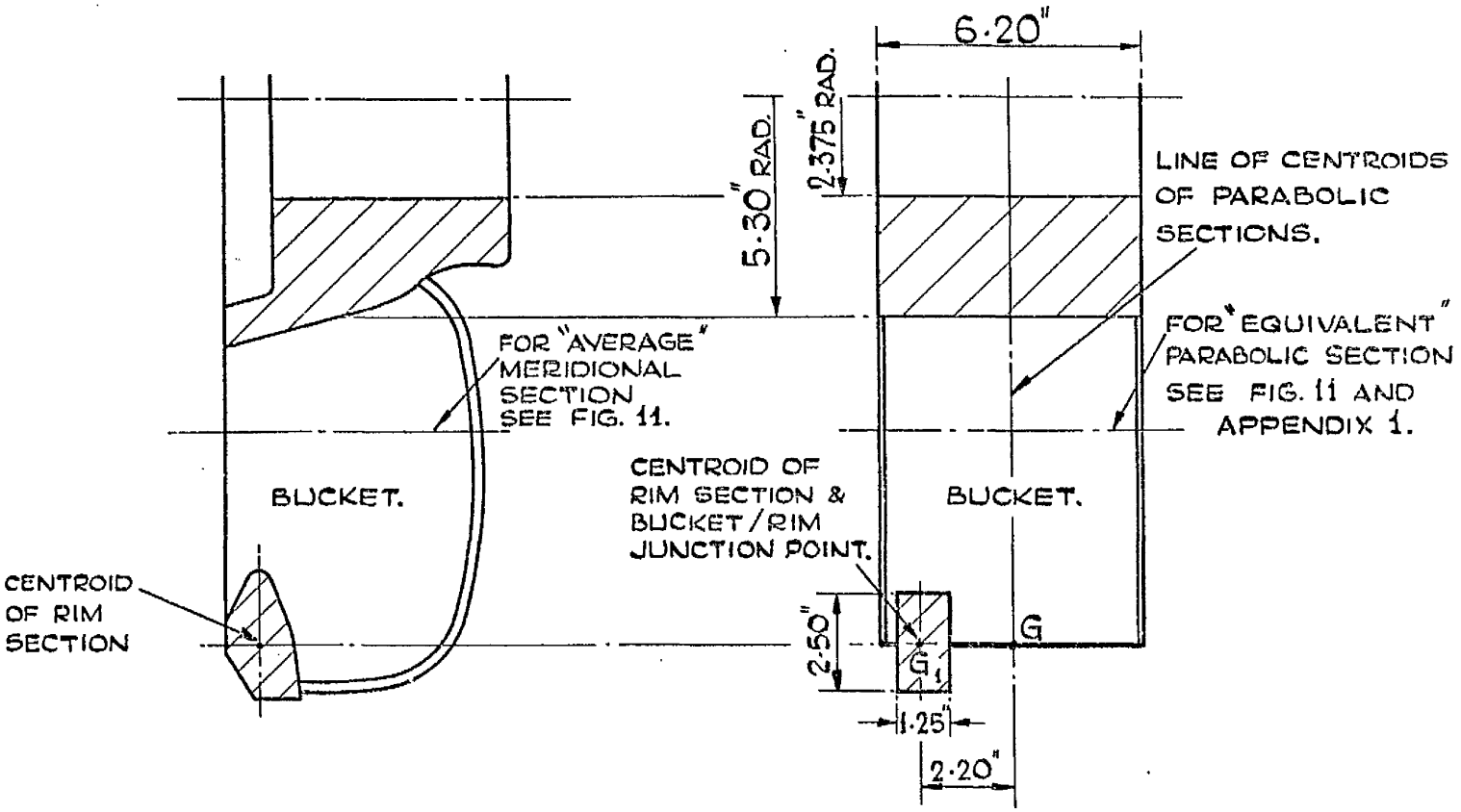

DIAMETRAL SECTION OF ACTUAL WHEEL.

DIAMETRAL SECTION OF WHEEL GEOMETRY ASSUMED FOR THEORETICAL ANALYSES.

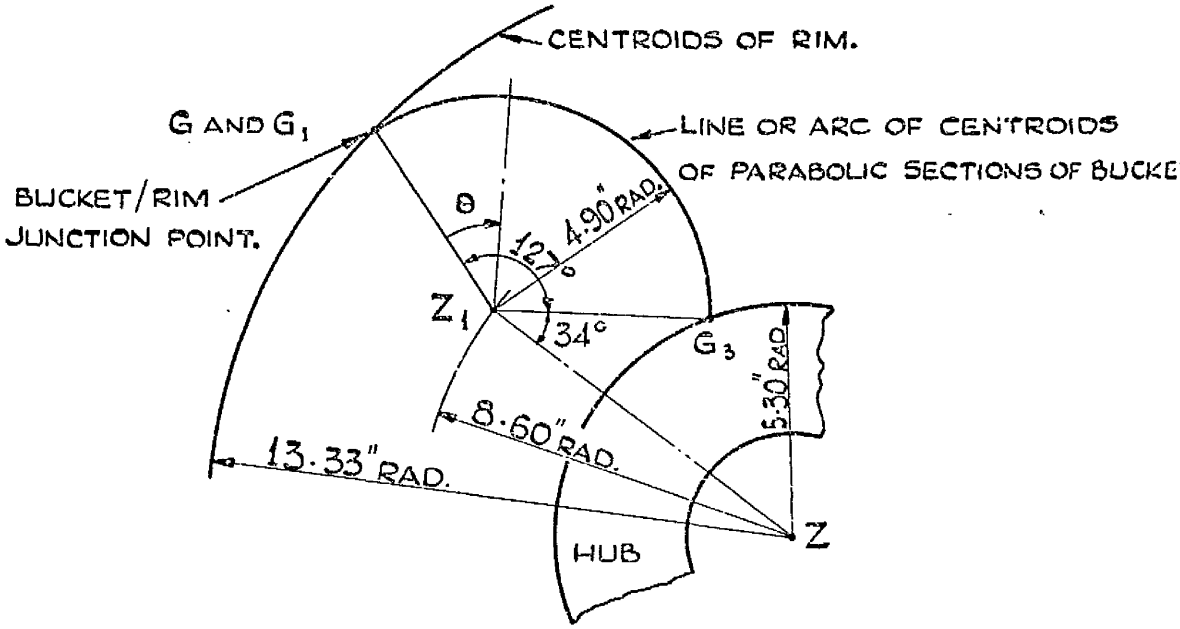

LINE DIAGRAM ELEVATION, LOOKING AT INLET SIDE, AND SHOWING ASSUMED GEOMETRY. BUCKET AND RIM ARE REPRESENTED BY THEIR LINES OF CENTROIDS. (DIMENSIONS TAKEN FROM FIG. 9.)

FIG. 12. ASSUMED GEOMETRY, WITH DIMENSIONS, PERTINENT TO APPROXIMATE THEORETICAL ANALYSES FOR $16\frac{1}{2}$" P.C.D. TURGO WHEEL.

are rigidly joined.

The main assumptions made concerning the elastic behaviour of the assumed components are now listed:-

(1) The bucket behaves as a thin beam curved in the plane of the wheel, and the corresponding theories of bending, torsion, shear and direct force are applicable. These theories are appropriate to the open parabolic cross-section of the beam, for which section the properties relevant to the theories are given in Appendix 1.

The geometry assumed for the bucket is clearly that for part of a shell of revolution, to which allusion is made in the previous chapter. Shell behaviour is not assumed in these analyses, but is considered in subsequent chapters. There it is shown that it may be possible to develop approximate shell behaviour analyses by initially assuming beam behaviour, proceeding on the lines indicated in this chapter, and appropriately introducing factors to modify the beam analyses to take shell behaviour into account. The approach would be akin to pipework flexibility analysis in which beam behaviour is basically assumed and factors are introduced to take account of the shell behaviour of pipe-bends. The assumption then that the bucket behaves as a beam is basic as an initial approximation.

Following chapters indicate that the beam approximation in itself, is not unreasonable. Similar approximations are made in the analyses of certain cylindrical shell roofs[27, 28], pipe-bends and straight pipes[29]. For long cylindrical shell roofs, solutions based on the beam assumption are close to those based on shell behaviour in respect of the significant actions. The beam approximation made here for the bucket, however, is not such a close one, since it neglects transverse actions and moments along the edges which are seen later to be fairly important.

(2)/

(2) The rim behaves as a thin ring and the corresponding theories of bending, shear and direct force apply. This assumption is pertinent only to the analysis for centrifugal loading. The corresponding assumption for the jet loading analysis is given subsequently.

(3) The hub behaves as a thick cylinder. All actions on it are neglected save those of radial force and centrifugal load, and for those the appropriate form of the Lamé theory applies. This assumption is pertinent only to part of the analysis for centrifugal loading of the wheel. For jet loading the hub is assumed to be rigid and to carry negligible stresses.

The assumptions made concerning the loading applied to the bucket by jet action are given later.

3B. APPROXIMATE STRESSES AND DEFORMATIONS DUE TO CENTRIFUGAL LOADING

The rim is initially regarded as detached from the buckets, and the separated rim and hub-with-buckets rotate at the angular velocity of the wheel. This is called the "free rotating condition" in which actions are set-up in the separate rim and hub-with-buckets due to centrifugal loading. These actions, all in the plane of the wheel, are statically determinate and, with respect to the wheel axis, are rotationally symmetrical and self-equilibrating. The stresses in the two separate parts are calculated for this condition. The radial deflection of the rim is also calculated, and, using strain-energy methods the displacements are determined at the bucket-tip which is the bucket/rim junction point on the hub-with-buckets. These displacements are radial and tangential deflections and a rotation in the plane of the wheel. In the free rotating condition, discontinuities of displacement exist between the separated rim and the bucket-tip of the hub-with-buckets. These discontinuities of displacement are determined.

To eliminate the displacement discontinuities and now assemble the rotating rim and hub-with-buckets at the junction point, forces and moments must be applied there on the two parts. These forces and moments are called "assembly actions" and this second condition is called the "assembly condition". Since the rim is offset to the inlet side of the wheel, there are assembly actions not only in the plane of the wheel but also in planes perpendicular to the plane of the wheel. With regard to the rim itself (the same applies to the hub-with-buckets itself) these assembly actions must be self-equilibrating and rotationally symmetrical with respect to the axis of the wheel. Taking account also of the fact that the rim is incapable/

incapable of exerting restraint against its own linear tangential and axial displacements, it is clear that the assembly actions are four in number, F_R, F_T - and - $(F_T.q)$, M_R and M_T as indicated diagrammatically in Fig.13. Combined force-and-moment assembly action F_T -and- $(F_T.q)$ is associated with rotation at the junction point in the plane of the wheel and the fact that the joint there between rim and bucket-tip is assumed rigid. For each assembly action and for the separate rim and hub-with-buckets, the displacement/action relations relevant respectively to the rim and to the junction point on the hub-with-buckets, are determined. For this, the assembly actions are assumed uniformly distributed on the rim, and strain-energy methods are applied in respect of the junction point on the hub-with-buckets. The assembly condition simultaneous equations are written. These are based on equilibrium and compatibility of displacements for assembly of the two parts at the junction point. Inserting the previously derived displacement/action relations, solution of the simultaneous equations gives the magnitudes and directions of the four assembly actions. The stresses due to the assembly actions are then calculated.

Total stresses and displacements are determined by superimposing appropriately the values for the free rotating condition and the values for the assembly condition.

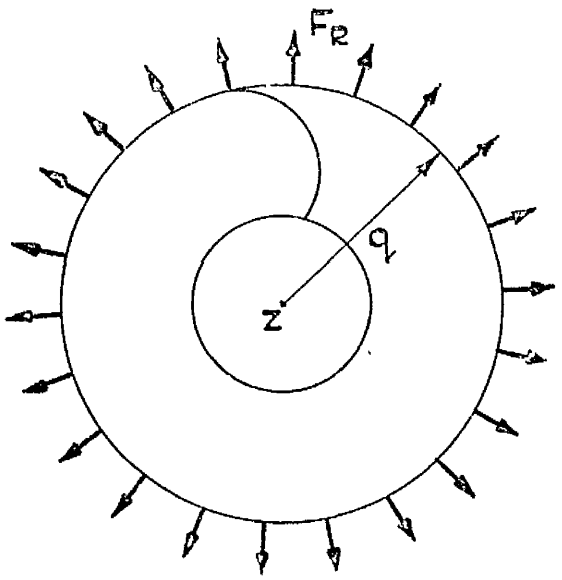

F_R = ASSEMBLY FORCE IN RADIAL DIRECTION.

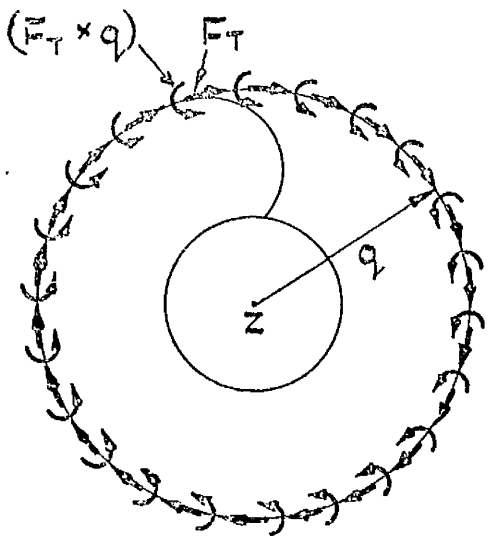

F_T = ASSEMBLY FORCE IN TANGENTIAL DIRECTN

$(F_T \times q)$ = ASSEMBLY MOMENT IN THE PLANE OF THE WHEEL

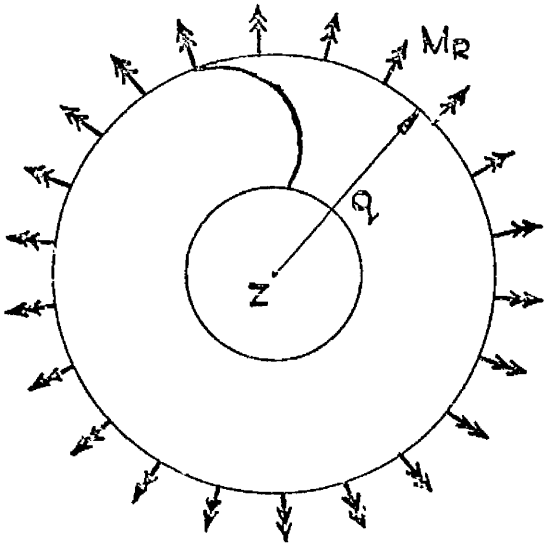

M_R = ASSEMBLY MOMENT ABOUT A RADIUS.

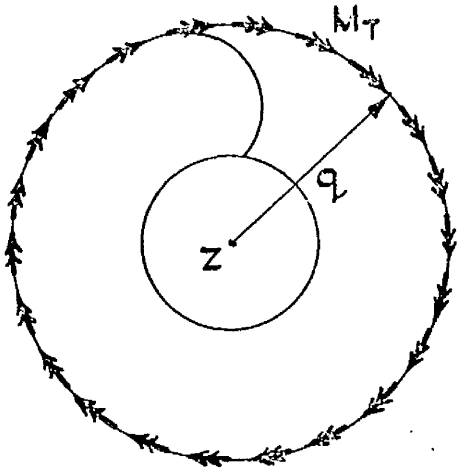

M_T = ASSEMBLY MOMENT ABOUT A TANGENT.

DOUBLE-ARROW ON MOMENT VECTOR IS RELATED TO MOMENT DIRECTION BY R.H. SCREW RULE

THUS F_R AND F_T -AND- $(F_T \times q)$ ACT IN THE PLANE OF THE WHEEL,

AND M_R AND M_T ACT IN PLANES PERPENDICULAR TO THE PLANE OF THE WHEEL.

FIG. 13. DIAGRAMMATIC SKETCH OF THE FOUR ASSEMBLY ACTIONS (ALL +VE AS SHOWN AT JUNCTION-POINT OF RIM AND BUCKET-TIP. (CENTRIFUGAL LOADING).

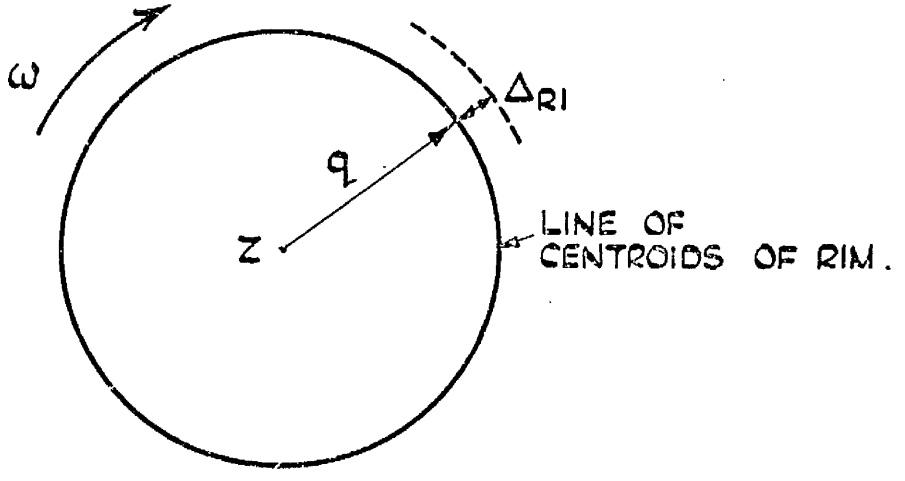

FIG. 14. DIAGRAM OF FREE ROTATING RIM.

3B i The free rotating condition of the rim

With reference to Fig.14, from equilibrium of a rim segment, it is readily shown that the circumferential stress σ_{c1} is tensile (+) and is given by:-

$$\sigma_{c1} = \frac{D}{g} \omega^2 q^2 . \qquad (3B.1)$$

From the corresponding circumferential strain, the radial deflection of all points on the rim is outwards (+) and is given by:-

$$\Delta_{R1} = q \cdot \frac{\sigma_{c1}}{E} . \qquad (3B.2)$$

For the $16\frac{1}{2}$ in. cast steel wheel at normal working speed:-

$\sigma_{c1} = +2430$ lb/in.^{2} and $\Delta_{R1} = +1080 \times 10^{-6}$ ins.

3B ii The free rotating condition of the hub-with-buckets

Referring to Fig.15, at any section of the bucket at angle θ, the actions due to centrifugal loading are bending moment M_θ, direct force P_θ and shearing force V_θ, all in the plane of the wheel. To determine these, consider element $k.d\xi$ at point B, at angle ξ from θ as shown. The centrifugal force on this element is $\frac{DA\,k.d\xi}{g}.\omega^2 r$, so due to such elements, the actions on a section of the bucket at θ are given by:-

$$M_\theta = \int_{\xi=0}^{\xi=\theta} \frac{DA\,k.d\xi}{g}\,\omega^2 r.f = \frac{DA\,k\omega^2}{g}\int_0^\theta r.f.d\xi.$$

$$P_\theta = \int_{\xi=0}^{\xi=\theta} \frac{DA\,k.d\xi}{g}\,\omega^2 r.\cos\psi = \frac{DA\,k\omega^2}{g}\int_0^\theta r.\cos\psi.d\xi.$$

$$V_\theta = \int_{\xi=0}^{\xi=\theta} \frac{DA\,k.d\xi}{g}\,\omega^2 r.\sin\psi = \frac{DA\,k\omega^2}{g}\int_0^\theta r.\sin\psi.d\xi.$$

By trigonometry it can be shown that:-

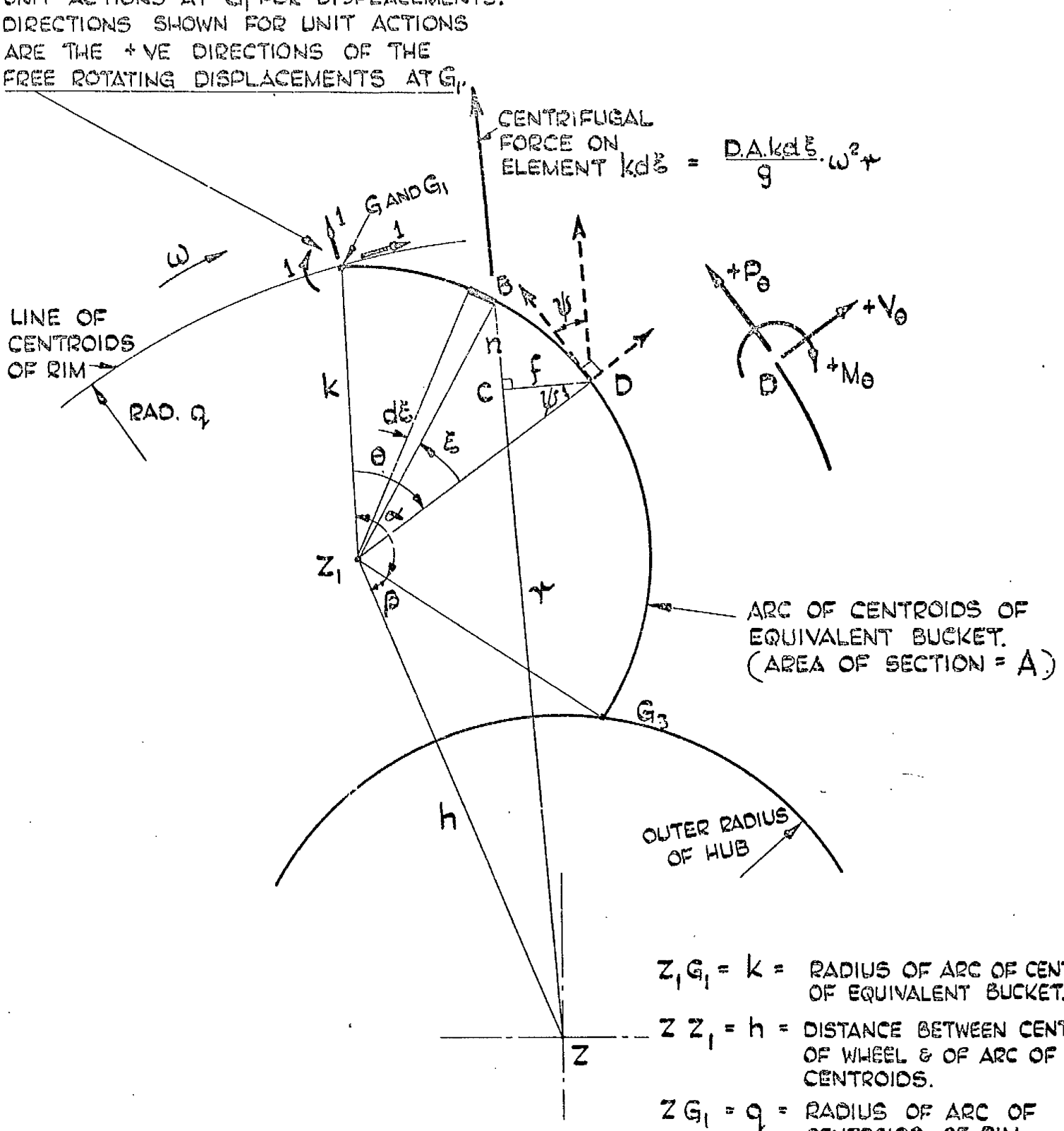

$Z_1G_1 = k$ = RADIUS OF ARC OF CENTROID OF EQUIVALENT BUCKET.

$Z\,Z_1 = h$ = DISTANCE BETWEEN CENTRES OF WHEEL & OF ARC OF CENTROIDS.

$ZG_1 = q$ = RADIUS OF ARC OF CENTROIDS OF RIM.

$$= \sqrt{k^2 + h^2 - 2k.h.\cos(\alpha+\beta)}$$

$ZB = r$, $CD = f$, $BC = n$,

$\left(\alpha + \beta - \frac{\pi}{2}\right) = \rho$.

FIG. 15. DIAGRAM OF FREE ROTATING BUCKET ON HUB, SHOWING BASIS FOR ANALYSIS OF THE BUCKET FOR THIS CONDITION.

that:- $$r.f = kh\cos(\rho-\theta) + k^2\cos(\rho-\theta).\sin(\rho-\theta+\xi) - k\left[k\sin(\rho-\theta)+h\right]\cos(\rho-\theta+\xi),$$

$$r.\cos\psi = h\cos(\rho-\theta) + k\sin\xi ,$$

$$r.\sin\psi = h\sin(\rho-\theta) + k\cos\xi ,$$

where $$\rho = \left(\alpha+\beta-\frac{\pi}{2}\right).$$

Direct integration then gives:-

$$M_\theta = \frac{DAk^3\omega^2}{g}\left\{\frac{h}{k}\left[\theta\cos(\rho-\theta)+\sin(\rho-\theta)-\sin\rho\right]+1-\cos\theta\right\} \quad (3B.3)$$

$$P_\theta = \frac{DAk^2\omega^2}{g}\left\{\frac{h}{k}\theta\cos(\rho-\theta)+1-\cos\theta\right\} \quad (3B.4)$$

$$V_\theta = \frac{DAk^2\omega^2}{g}\left\{\frac{h}{k}\theta\sin(\rho-\theta)+\sin\theta\right\} \quad (3B.5)$$

Corresponding stresses in the bucket due to these free rotating actions, may be calculated from the elementary expressions of the general type:-

for bending stress, $$\sigma_b = \pm\frac{M_b.\ell}{I} \quad (3B.6)$$

for direct stress, $$\sigma_d = \frac{P_d}{A} \quad (3B.7)$$

for shear stress $$\tau = \frac{V}{I}\left(\frac{\bar{Q}}{t}\right) \quad (3B.8)$$

where M_b, P_d and V are given by the appropriate expressions (M_θ, P_θ, V_θ here) /

($M_\theta, P_\theta, V_\theta$ here) and where I, ℓ $\bar{Q}$ and t are given by the appropriate properties of the section. General properties I, ℓ, $\bar{Q}$ and t are defined in Appendix 1 from which the appropriate properties may be calculated. The signs of stresses are interpreted in relation to the directions of the actions.

Regarding the buckets as fully-fixed to the hub, which is assumed for this part of the analysis not to displace at all, the free rotating displacements at the bucket-tip or junction point G_1 Fig.15, are radial deflection Δ_{R2}, tangential deflection Δ_{T2} and rotation Φ_{P2} in the plane of the wheel. These may be found by the strain-energy unit load method which is based on Castigliano's Theorem.

To determine radial deflection Δ_{R2}, unit radial force is applied at bucket-tip G_1 as shown in Fig.15. Considering total strain-energy due to bending, direct force and shear, by the unit load method, Δ_{R2} is given by:-

$$\Delta_{R2} = \int_0^\alpha \frac{M_\theta . m_\theta . k . d\theta}{E I_{YY}} + \int_0^\alpha \frac{P_\theta . p_\theta . k . d\theta}{EA} + K_x \int_0^\alpha \frac{V_\theta . v_\theta . k . d\theta}{GA} \qquad (3B.9)$$

for which expression the section properties are defined and derived in Appendix 1, and where $M_\theta, P_\theta, V_\theta$ are given by equations (3B.3), (3B.4) and (3B.5),

m_θ = bending moment at θ due only to unit radial load at G_1,
$= +1 . f_{\xi=\theta}$,

p_θ = direct force at θ due only to unit radial load at G_1,
$= +1 . \cos \psi_{\xi=\theta}$,

v_θ = shearing force at θ due only to unit radial load at G_1,
$= +1 . \sin \psi_{\xi=\theta}$.

By/

By trigonometry it can be shown that:-

$$f_{\xi=\theta} = \frac{k^2}{q}\left\{\frac{h}{k}\left[\cos(\beta-\theta) - \cos\beta\right] + \sin\theta\right\} \quad ,$$

$$\cos\psi_{\xi=\theta} = \frac{k}{q}\left\{\frac{h}{k}\cos(\beta-\theta) + \sin\theta\right\} \quad ,$$

$$\sin\psi_{\xi=\theta} = \frac{k}{q}\left\{\frac{h}{k}\sin(\beta-\theta) + \cos\theta\right\} \quad .$$

m_θ, p_θ and v_θ are therefore obtained directly. Products $(M_\theta.m_\theta)$, $(P_\theta.p_\theta)$ and $(V_\theta.v_\theta)$ are all found as functions of θ. Substituting into equation (3B.9) and integrating directly gives:-

$$\begin{aligned}
\Delta_{R2} = \frac{DAk^6\omega^2}{gEI_{rr}q}\Bigg\{ & \frac{h^2}{k^2}\Big[\frac{\alpha}{4}(\alpha+\sin 2\beta) - \frac{\alpha}{2}\sin 2(\alpha+\beta) - \sin(\alpha+\beta).(\sin\beta+\alpha\cos\beta) \\
& + \sin^2(\alpha+\beta) - \frac{5}{8}\cos 2(\alpha+\beta) + \cos(\alpha+2\beta) - \frac{3}{8}\cos 2\beta\Big] \\
& - \frac{h}{k}\Big[\frac{\alpha^2}{4}\cos(\alpha+\beta) + 2\alpha\sin(\alpha+\beta) - \frac{\alpha}{4}\sin(\alpha-\beta) \\
& - 2\sin\alpha.\sin(\alpha+\beta) - \frac{1}{4}\sin\alpha.\sin\beta\Big] \\
& + \frac{1}{4}\cos 2\alpha - \cos\alpha + \frac{3}{4}\Bigg\} \\
+ \frac{Dk^4\omega^2}{gEq}\Bigg\{ & \frac{h^2}{k^2}\Big[\frac{\alpha}{4}(\alpha+\sin 2\beta) - \frac{1}{8}\cos 2\beta + \frac{1}{8}\cos 2(\alpha+\beta)\Big] \\
& - \frac{h}{k}\Big[\Big(\frac{\alpha^2}{4}+\frac{7}{8}\Big)\cos(\alpha+\beta) + \frac{\alpha}{4}\big\{2\sin(\alpha+\beta) - \sin(\alpha-\beta)\big\} + \frac{1}{8}\cos(\alpha-\beta) - \cos\beta\Big] \\
& + \frac{1}{4}\cos 2\alpha - \cos\alpha + \frac{3}{4}\Bigg\} \\
+ K_\chi\frac{Dk^4\omega^2}{gGq}\Bigg\{ & \frac{h^2}{k^2}\Big[\frac{\alpha}{4}(\alpha-\sin 2\beta) + \frac{1}{8}\cos 2\beta - \frac{1}{8}\cos 2(\alpha+\beta)\Big] \\
& - \frac{h}{k}\Big[\frac{\alpha^2}{4}\cos(\alpha+\beta) + \frac{\alpha}{4}\big\{2\sin(\alpha+\beta) + \sin(\alpha-\beta)\big\} - \frac{1}{4}\sin\alpha.\sin\beta\Big] \\
& - \frac{1}{4}\cos 2\alpha + \frac{1}{4}\Bigg\}
\end{aligned} \qquad (3B.10)$$

Tangential deflection Δ_{T2} is found in similar fashion, from a strain-energy equation with R.H.S. similar to that of equation (3B.9) but pertinent to unit tangential force applied at G_1, Fig.15. The corresponding expressions for m_θ, p_θ and v_θ are:-

$$m_\theta = + 1.n_{\xi=\theta} \quad ,$$

$$p_\theta = - 1.\sin\psi_{\xi=\theta} \quad ,$$

$$v_\theta = + 1.\cos\psi_{\xi=\theta} \quad .$$

By trigonometry:-

$$n_{\xi=\theta} = \frac{k^2}{q}\left\{1 - \cos\theta - \frac{h}{k}\left[\sin(\rho-\theta) - \sin\rho\right]\right\} \quad ,$$

and $\sin\psi_{\xi=\theta}$ and $\cos\psi_{\xi=\theta}$ are as given previously for Δ_{RZ}. $m_\theta, p_\theta, v_\theta$ are therefore obtained, and direct integration in the corresponding equation of the form of equation (3B.9) gives:-

$$\Delta_{T2} = \quad /$$

$$\Delta_{T2} = \frac{DAk^6\omega^2}{gEI_{rrq}}\left\{\frac{h^2}{k^2}\left[\frac{\alpha}{2}\left(\frac{1}{2}\cos 2\beta - 1\right) - \alpha\cos(\alpha+\beta)\left\{\cos(\alpha+\beta)+\cos\beta\right\}\right.\right.$$
$$\left.-3\cos(\alpha+\beta)\left\{\sin\beta - \sin(\alpha+\beta)\right\} - \frac{3}{8}\left\{\sin 2(\alpha+\beta) - \sin 2\beta\right\}\right]$$
$$-\frac{h}{k}\left[\frac{\alpha^2}{4}\sin(\alpha+\beta) + \frac{\alpha}{4}\left\{\cos(\alpha-\beta) - 4\cos\beta\right\} + \frac{7}{8}\sin(\alpha+\beta)\right.$$
$$\left.-\frac{1}{8}\sin(\alpha-\beta) - \sin\beta\right]$$
$$\left.+\frac{1}{4}\sin 2\alpha - 2\sin\alpha + \frac{3}{2}\alpha\right\}$$

$$-\frac{Dk^4\omega^2}{gEq}\left\{\frac{h^2}{k^2}\left[-\frac{\alpha}{4}\cos 2\beta - \frac{1}{8}\sin 2\beta + \frac{1}{8}\sin 2(\alpha+\beta)\right]\right.$$
$$+\frac{h}{k}\left[\left(\frac{\alpha^2}{4} - \frac{7}{8}\right)\sin(\alpha+\beta) + \frac{\alpha}{4}\left\{2\cos(\alpha+\beta) + \cos(\alpha-\beta)\right\}\right.$$
$$\left.+\frac{1}{8}\sin(\alpha-\beta) + \sin\beta\right]$$
$$\left.-\frac{1}{4}\sin 2\alpha + \sin\alpha - \frac{1}{2}\alpha\right\}$$

$$+K_x\cdot\frac{Dk^4\omega^2}{gGq}\left\{\frac{h^2}{k^2}\left[-\frac{\alpha}{4}\cos 2\beta - \frac{1}{8}\sin 2\beta + \frac{1}{8}\sin 2(\alpha+\beta)\right]\right.$$
$$+\frac{h}{k}\left[\left(\frac{1}{8} - \frac{\alpha^2}{4}\right)\sin(\alpha+\beta) + \frac{\alpha}{4}\left\{\cos(\alpha-\beta) - 2\cos(\alpha+\beta)\right\}\right.$$
$$\left.+\frac{1}{8}\sin(\alpha-\beta)\right]$$
$$\left.-\frac{1}{4}\sin 2\alpha + \frac{1}{2}\alpha\right\}$$

(3 B.11)

For the rotation Φ_{P2} in the plane of the wheel, unit moment is applied in that plane, at junction point G_1 as shown in Fig.15. The corresponding form of the strain-energy equation similar to equation (3B.9), gives the required rotation. The relevant unit actions at Θ are:-

$$m_\Theta = +1, \qquad p_\Theta = v_\Theta = 0,$$

and direct integration in the appropriate strain-energy unit load equation gives:-

$$\Phi_{P2} = \frac{DAk^4\omega^2}{gEI_{YY}}\left\{\frac{h}{kL}\left[\alpha\cos\beta+\alpha\cos(\alpha+\beta)+2\sin\beta-2\sin(\alpha+\beta)\right]-\sin\alpha+\alpha\right\} \tag{3B.12}$$

For numerical application to the $16\frac{1}{2}$ in. cast steel wheel at normal working speed, the values of the relevant properties of the equivalent parabolic section are given in Appendix 1, and the values of the radii and angles pertinent to the assumed bucket geometry are given in Fig.12. The distributions of the free rotating actions M_Θ, P_Θ and V_Θ with Θ, are shown for this case in Fig.16. These are calculated from equations (3B.3), (3B.4) and (3B.5). The maximum free rotating stresses (+ tensile) in the bucket, due to these actions, are determined on the basis of equations (3B.6), (3B.7) and (3B.8) and are as follows:-

due to M_Θ:- $\sigma_{b\,MAX.} = +12,850$ lb/in^2 at inlet and outlet edges of bucket, at $\Theta = 92^\circ$,

due to P_Θ :- $\sigma_{d\,MAX.} = +1,300$ lb/in^2 at $\Theta = 112^\circ$,

due to V_Θ :- $\tau_{MAX.} = 2,460$ lb/in^2 fairly near neutral axis YY of the section, at $\Theta = 127^\circ$.

The maximum free rotating total normal stress $\underline{\sigma_{MAX.} = +14,050 \text{ lb/in}^2}$ at the bucket edges at about $\Theta = 92^\circ$.

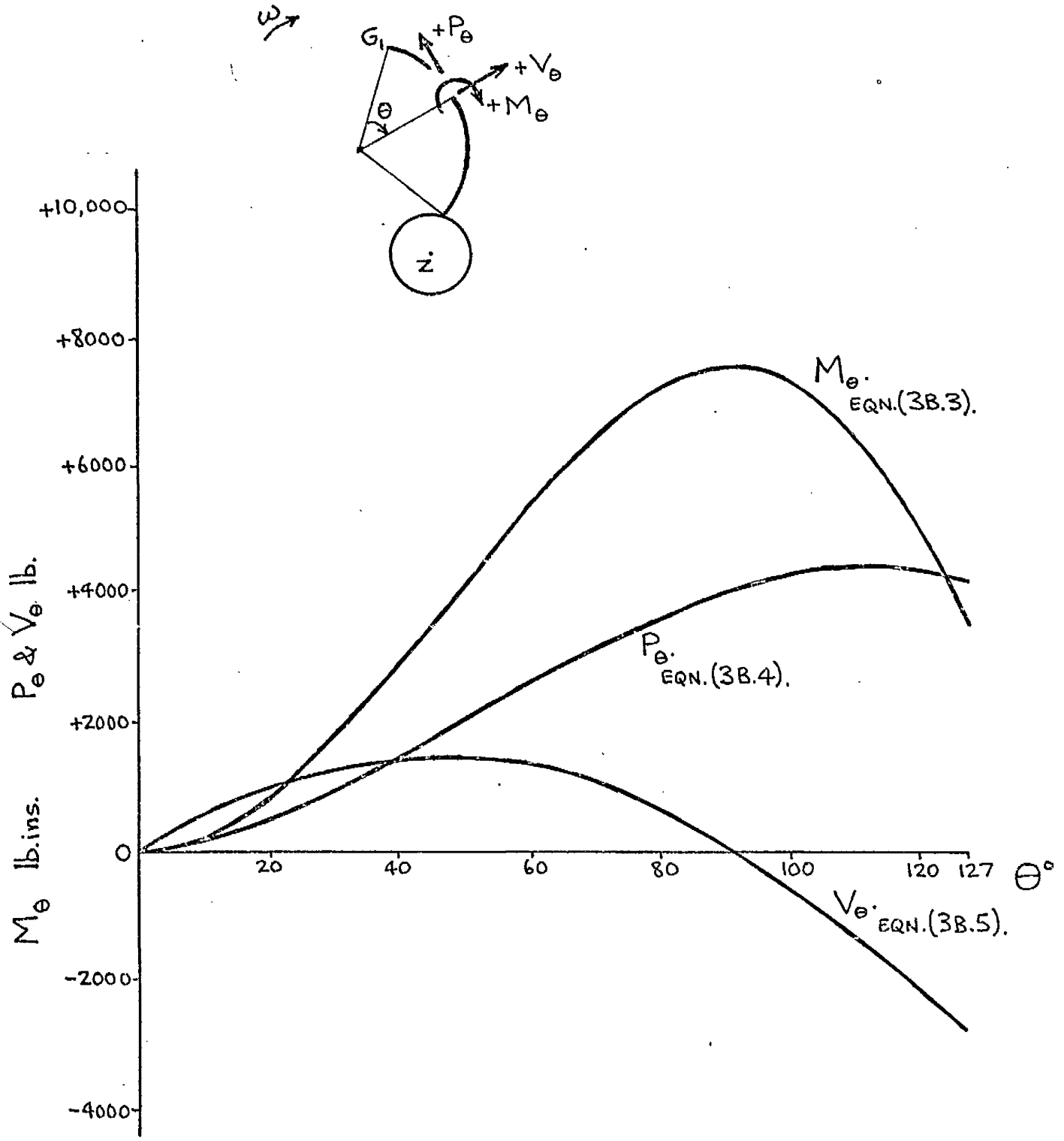

FIG 16. DISTRIBUTIONS OF FREE ROTATING ACTIONS $M_\theta, P_\theta, V_\theta$ WITH θ ON THE EQUIVALENT BUCKET OF THE $16\frac{1}{2}$ IN. CAST STEEL TURGO WHEEL AT NORMAL WORKING SPEED.

These stresses in the bucket are of quite credible order for free rotation of a rimless wheel. The dominant action is clearly M_θ. It is also evident that the shear stress may be neglected since it is zero in the region of the maximum total normal stress and even for its maximum value, is of comparatively small order.

From equations (3B.10), (3B.11) and (3B.12), the free rotating displacements of the junction point G_1 on the bucket, relative to the outer surface of the hub, are found respectively to be:-

radial deflection	$\triangle_{R2} = +\ 7{,}980 \times 10^{-6}$ ins
tangential deflection	$\triangle_{T2} = +\ 11{,}020 \times 10^{-6}$ ins
rotation in the plane of the wheel	$\Phi_{P2} = +\ 2{,}080 \times 10^{-6}$ rads

The +ve directions of these free rotating displacements are indicated on Fig.15.

The separate contributions of the bending, direct force and shear strain-energy terms of equations (3B.10) and (3B.11) to the value of $\triangle_{R2}$ and $\triangle_{T2}$ are of interest. The contributions respectively are 88%, 3% and 9% of the total for $\triangle_{R2}$, and 96.3%, 0.3% and 3.4% of the total for $\triangle_{T2}$. It is evident that the bending strain-energy terms are dominant and that strain-energy due to the force actions might reasonably be disregarded in an initial estimate type of calculation.

The hub of the free rotating hub-with-buckets, is itself subjected to centrifugal action and carries loading on the outer surface due to the centrifugal action on the buckets. The buckets are assumed to be rigidly connected to the outer surface of the hub. The outer surface centrifugal loading per bucket may be determined by two methods illustrated in Fig.17.

(a) The loading per bucket is given by the values of $M_{\theta=\alpha}$, $P_{\theta=\alpha}$ and $V_{\theta=\alpha}$ calculated from equations (3B.3), (3B.4) and (3B.5). These actions on the hub are shown dotted in Fig.17(a). The radial force per bucket on the hub outer surface is then H_R, given by:-

$$H_R = P_{\theta=\alpha}.\sin(\beta+\gamma) + V_{\theta=\alpha}.\cos(\beta+\gamma) \quad , \tag{3B.13}$$

where $$\sin\gamma = \frac{k\sin\beta}{\sqrt{k^2+h^2-2kh\cos\beta}}$$

ΣH_R due to all the buckets is a self-equilibrating system. Similarly since $H_T.\sqrt{k^2+h^2-2kh\cos\beta} = M_{\theta=\alpha}$, where H_T is the tangential force per bucket on the outer surface, Fig.17(a), the system $\Sigma(H_T\text{-and-}M_{\theta=\alpha})$ due to all the buckets is a self-equilibrating system. It is exactly similar in kind to the assembly action system F_T-and-$F_T.q$ discussed previously. Stresses and deformations of the hub due to the system H_T-and-$M_{\theta=\alpha}$ are neglected, and only the radial force system is considered.

(b) Referring to Fig.17(b), the centrifugal force F_c, due to a whole bucket, acts at centroid G_4 of the arc G_1G_3 and is given by:-

$$F_c = \frac{DAk\alpha}{g}.\omega^2 v$$

where

$$v = ZG_4 = \sqrt{h^2 + \frac{k^2\sin^2\frac{\alpha}{2}}{\frac{\alpha^2}{4}} - \frac{2hk\sin\frac{\alpha}{2}}{\frac{\alpha}{2}}\cos\left(\frac{\alpha}{2}+\beta\right)} \quad .$$

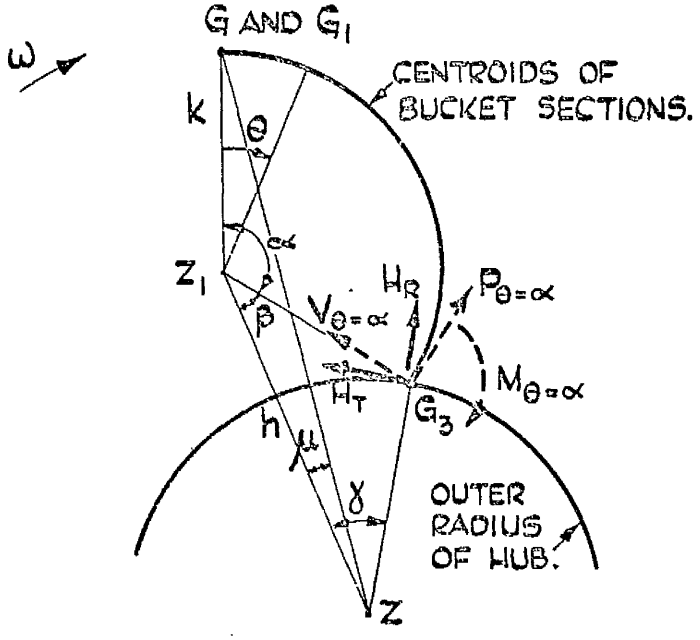

ZG_3 = OUTER RADIUS OF HUB.

$$= \sqrt{k^2 + h^2 - 2kh.\cos\beta}$$

METHOD (a), BY MEANS OF $M_{\theta=\alpha}$, $P_{\theta=\alpha}$ AND $V_{\theta=\alpha}$ (SHOWN DOTTED) CALCULATED FROM EQUATIONS (38.3) (38.4) AND (38.5).

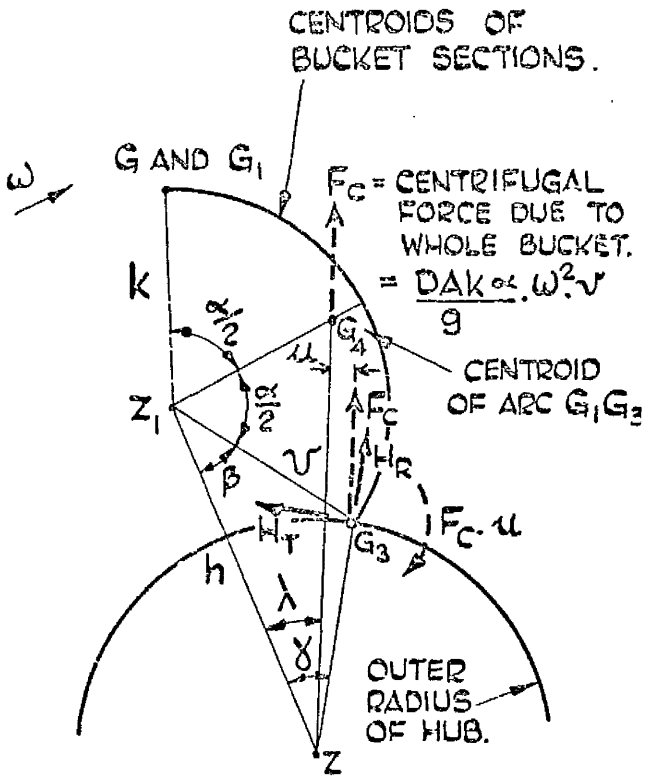

$$ZG_4 = \nu.$$

$$Z_1G_4 = \frac{k.\sin\frac{\alpha}{2}}{\frac{\alpha}{2}}.$$

METHOD (b), BY CONSIDERING THE CENTRIFUGAL FORCE F_C DUE TO THE WHOLE BUCKET, AT CENTROID G_4 OF THE BUCKET AR

FIG. 17. TWO METHODS OF DETERMINING THE FREE ROTATING CENTRIFUGAL LOADING PER BUCKET ON THE OUTER SURFACE OF THE HUB.

For the loading per bucket on the hub, F_c is transferred to G_3 giving at G_3, force F_c and moment $F_c.u$, both shown dotted. The radial force per bucket on the hub outer surface is then H_R, given by:-

$$H_R = \frac{DAk\alpha}{g}\omega^2 v\cos(\gamma-\lambda) \qquad (3B.14)$$

where $$\sin\lambda = \frac{k\sin\frac{\alpha}{2}}{v.\frac{\alpha}{2}}\sin\left(\frac{\alpha}{2}+\beta\right).$$

Distance u is given by $$u = \sqrt{k^2+h^2-2kh\cos\beta}.\sin(\gamma-\lambda).$$

One method may be used to check the other. Also, method (b) provides a check on the analysis of the free rotating actions on the bucket since, e.g. $M_{\theta=\alpha} = F_c.u$.

For the hub as a thick cylinder rotating at angular velocity ω and carrying uniformly distributed radial surface loading, the stresses (+ tensile) at any radius r_H are given, according to the appropriate form of the Lamé theory, by the equations:-

$$\left.\begin{aligned}
&\text{radial stress,} \quad \sigma_R' = A' + \frac{B'}{r_H^2} - \frac{1}{8}\frac{3-2\nu}{1-\nu}\frac{D}{g}\omega^2 r_H^2 ,\\
&\text{circumferential stress,} \quad \sigma_c' = A' - \frac{B'}{r_H^2} - \frac{1}{8}\frac{1+2\nu}{1-\nu}\frac{D}{g}\omega^2 r_H^2 ,\\
&\text{axial stress,} \quad \sigma_A' = \frac{\nu}{4(1-\nu)}\frac{D}{g}\omega^2\left(r_{HO}^2 + r_{HI}^2 - 2r_H^2\right).
\end{aligned}\right\} \qquad (3B.15)$$

The total radial force due to the buckets is assumed uniformly distributed over the outer surface, while the bore is free, so that constants A' and B' are determined from the boundary conditions:-

$$\sigma_{RO}' = +\frac{\text{No. of buckets.} \times H_R}{2\pi r_{HO} \times \text{Length of hub.}} \quad \text{and} \quad \sigma_{RI}' = 0 .$$

The radial deflection (+ outwards) of the outer surface is given by:-

$$\Delta_{RO} = \frac{r_{HO}}{E}\left[\sigma'_{CO} - \nu(\sigma'_{RO} + \sigma'_{AO})\right] \tag{3B.16}$$

Δ_{RO} is a whole body displacement of the bucket in the direction ZG_3 Fig.17(a), giving rise, at junction point G_1 on the bucket, to radial and tangential deflections:-

$$\left.\begin{aligned}\Delta_{RH} &= \Delta_{RO}\cos(\gamma-\mu)\\ \Delta_{TH} &= \Delta_{RO}\sin(\gamma-\mu)\end{aligned}\right\} \tag{3B.17}$$

where $$\sin\mu = \frac{k\sin(\alpha+\beta)}{\sqrt{k^2+h^2-2kh\cos(\alpha+\beta)}}$$

The +ve directions of Δ_{RH} and Δ_{TH} are those indicated on Fig.15.

The total free rotating displacements at junction point G_1 on the bucket are therefore $\Delta_{R2\,TOT}$, $\Delta_{T2\,TOT}$ and Φ_{P2} where:-

$$\left.\begin{aligned}\Delta_{R2\,TOT} &= \Delta_{R2} + \Delta_{RH}\\ \Delta_{T2\,TOT} &= \Delta_{T2} + \Delta_{TH}\end{aligned}\right\} \tag{3B.18}$$

For the $16\frac{1}{2}$ in. cast steel wheel at normal working speed, with reference to Fig.12 for the pertinent geometry and dimensions, the maximum free rotating stress in the hub is the circumferential stress at the bore:-

$$\sigma'_{CI} = + 1,680 \text{ lb/in.}^2$$

and

$$\Delta_{RH} = + 120 \times 10^{-6} \text{ ins}$$

$$\Delta_{TH} = + 60 \times 10^{-6} \text{ ins}$$

The total free rotating displacements at junction point G_1 on the bucket/

bucket are therefore:-

$$\Delta_{R2\,TOT} = + 8{,}100 \times 10^{-6} \text{ ins}$$

$$\Delta_{T2\,TOT} = + 11{,}080 \times 10^{-6} \text{ ins}$$

$$\Phi_{P2} = + 2{,}080 \times 10^{-6} \text{ rads.}$$

all +ve as shown on Fig.15.

On Fig.18 these displacements are compared with Δ_{R1} so illustrating the free rotating discontinuities of deflection and rotation in the plane of the wheel at the bucket/rim junction point. From this it is clear that, in the rotating-assembled condition, the rim will effectively restrain the bucket-tip in a radially-inward sense. The maximum stress in the hub of the rotating wheel therefore, would be expected to be less than the relatively small free rotating value of + 1,680 lb/in^2. The hub radial displacement contributes less than 2% of the values of $\Delta_{R2\,TOT}$ and $\Delta_{T2\,TOT}$. These indications reasonably justify having neglected the system H_T - and - $M_{\theta=\alpha}$ in the foregoing, and the intention to neglect all stresses and deformations in the hub in the following.

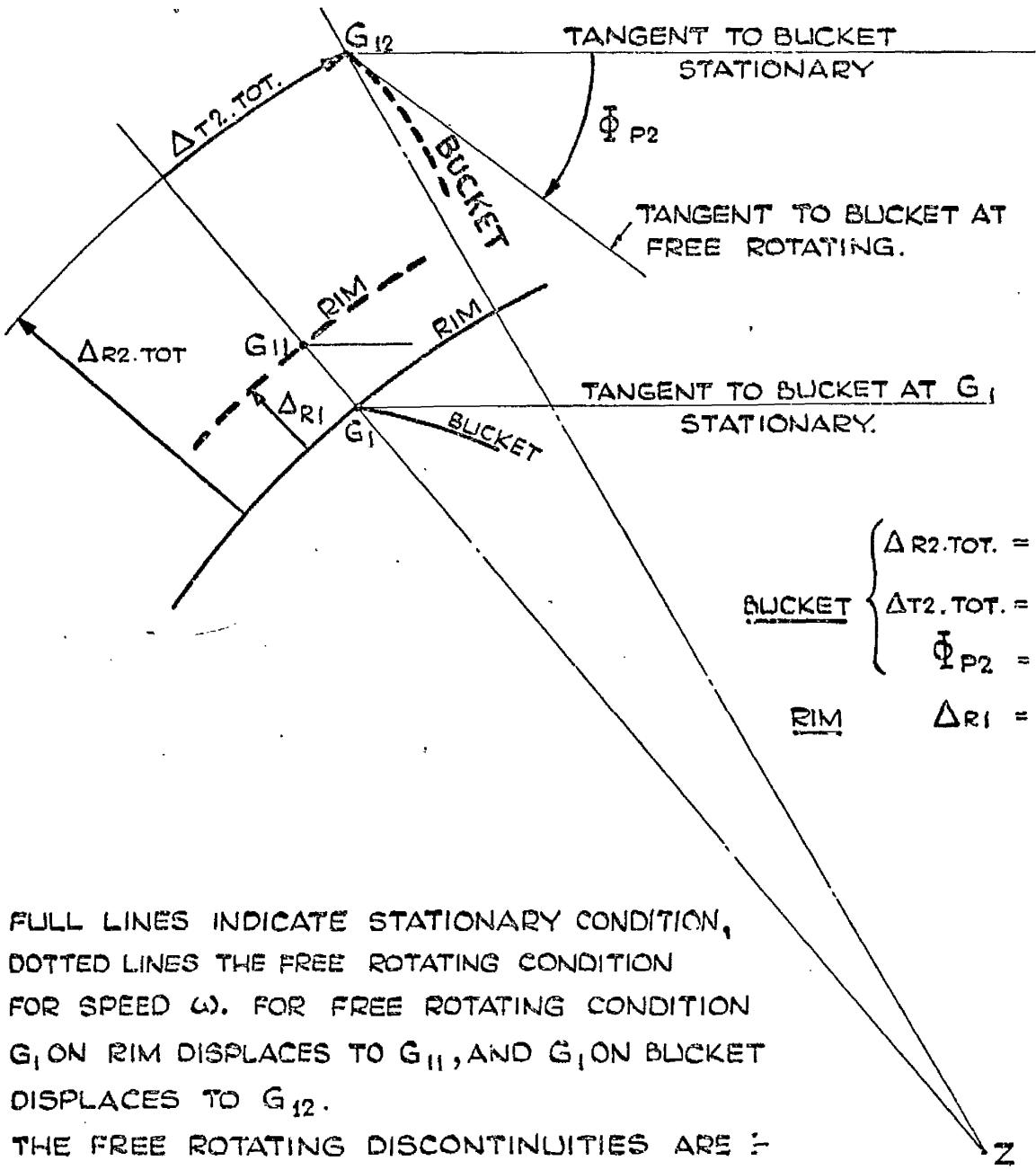

BUCKET
$\Delta_{R2.TOT.} = +8,100 \times 10^{-6}$ INS.
$\Delta_{T2.TOT.} = +11,080 \times 10^{-6}$ INS.
$\Phi_{P2} = +2,080 \times 10^{-6}$ RADIAN

RIM
$\Delta_{R1} = +1,080 \times 10^{-6}$ INS.

FULL LINES INDICATE STATIONARY CONDITION, DOTTED LINES THE FREE ROTATING CONDITION FOR SPEED ω. FOR FREE ROTATING CONDITION G_1 ON RIM DISPLACES TO G_{11}, AND G_1 ON BUCKET DISPLACES TO G_{12}.
THE FREE ROTATING DISCONTINUITIES ARE :-
$(\Delta_{R2.TOT.} - \Delta_{R1})$, $\Delta_{T2.TOT.}$, Φ_{P2}.

FIG. 18. DIAGRAM ILLUSTRATING THE FREE ROTATING DISCONTINUITIES OF DISPLACEMENT BETWEEN RIM AND BUCKET, AT THE BUCKET/RIM JUNCTION POINT, FOR $16\frac{1}{2}$" CAST STEEL TURGO WHEEL AT NORMAL WORKING SPEED.

3B iii Assembly condition - assembly actions on the rim

The assembly actions on the rim at the bucket/rim junction points are F_R, F_T -and-($F_T.q_v$), M_R and M_T as shown in Fig.13. For the purpose of deriving the stresses and deformations which these actions induce in the rim, the actions are replaced by their equivalents, uniformly distributed on the rim. Thus,

F_R lb. is replaced by F_R' lb/in. where $F_R' = \frac{\text{No. of buckets x } F_R}{2\pi q_v}$,

and F_T, M_R and M_T are replaced respectively by F_T', M_R' and M_T' with similar relationships.

Action F_R.

From equilibrium of a rim segment it is readily shown that the circumferential stress $\sigma_{c1}^{F_R}$, the sign of which is easily determined in relation to the direction of F_R, is given by:-

$$\sigma_{c1}^{F_R} = \frac{q_v}{A_1} F_R' \qquad (3B.19)$$

where A_1 is the cross-sectional area of the rim, (Appendix 2).

From the corresponding circumferential strain, the radial deflection of all points on the rim is in the same direction as F_R and is given by:-

$$\delta_{R1}^{F_R} = \frac{q_v^2}{EA_1} F_R' \qquad (3B.20)$$

Action F_T -and-($F_T.q_v$).

Due to this combined force-and-moment action, the actions on a section of the rim are all in the plane of the rim, and may be found by reasoning based on rotational symmetry. A more direct approach is by application of a general method of solution derived by BIEZENO AND GRAMMEL[30]. /

GRAMMEL [30]. This method and other similar powerful methods of BIEZENO AND GRAMMEL[30] are applicable to thin circular rings having a principal axis of the cross-section in the plane of the ring. Using BIEZENO AND GRAMMEL'S [30] notation and with reference to Fig.19, the method applies to this case as follows:-

The rim is sectioned at $\phi = 0$ and internal actions N_0, Q_0, M_0 and $N_{2\pi}, Q_{2\pi}, M_{2\pi}$ are applied at the sectioned ends. The resultant complete system of forces and moments is now changed into another system, Fig.19(b), as follows:-

(1) Each force and each moment is multiplied by the coefficient $\phi/2\pi$ corresponding to its position. The quantities N_0, Q_0, M_0 acting on the left face of the section $\phi = 0$ thus vanish, whereas $N_{2\pi}, Q_{2\pi}, M_{2\pi}$ on its right face remain undiminished.

(2) Each "reduced" applied tangential force $\frac{\phi}{2\pi} \cdot F_T' \cdot q\, d\phi$ is accompanied by a radial force $\frac{\mu}{2\pi} \cdot F_T' \cdot q\, d\phi$ inward, at the same position ϕ. μ is a dimensionless constant related to the properties of the rim section, the radius of the rim and the elastic constants.

(3) Each "reduced" applied moment $\frac{\phi}{2\pi} \cdot F_T' \cdot q^2\, d\phi$ is accompanied by a radial force $\frac{\nu}{\pi q} \cdot F_T' q^2\, d\phi$ outward, at the same position ϕ. ν is a dimensionless constant similar to μ.

According to the derivation of the method, which is based on strain-energy theorems, this reduced substitute system is in equilibrium; consequentiy, the unknown actions $N_{2\pi}, Q_{2\pi}, M_{2\pi}$ acting on the right face of the section $\phi = 0$ are obtained explicitly by the conditions of equilibrium that

I. /

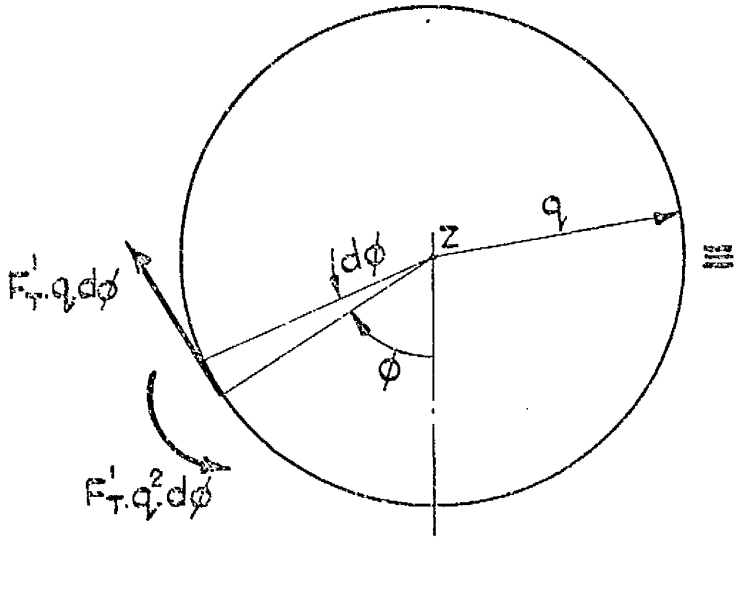

(a)

ACTUAL APPLIED UNIFORMLY DISTRIBUTED SYSTEM ON A TYPICAL ELEMENT.

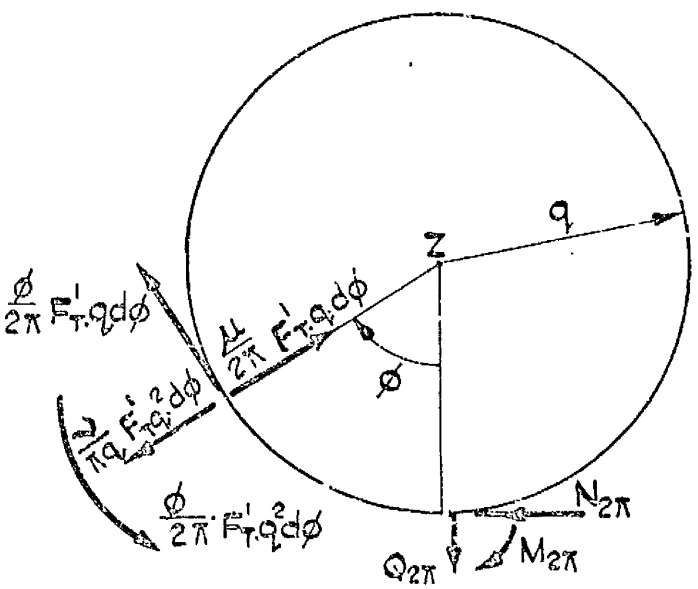

(b)

REDUCED SUBSTITUTE APPLIED UNIFORMLY DISTRIBUTED SYSTEM ON ELEMENT, AND INTERNAL SYSTEM ACCORDING TO BIEZENO & GRAMMEL'S METHOD OF ANALYSIS.

(30)

FIG. 19. METHOD OF BIEZENO & GRAMMEL APPLIED TO THE ANALYSIS OF ACTIONS ON A RIM SECTION, DUE TO THE ASSEMBLY ACTION F_T - AND - $(F_T.q)$ ON THE RIM. (EXCEPT FOR THE ASSEMBLY ACTION AND RADIUS q, THE NOTATION USED HERE IS THAT OF B. & G.).

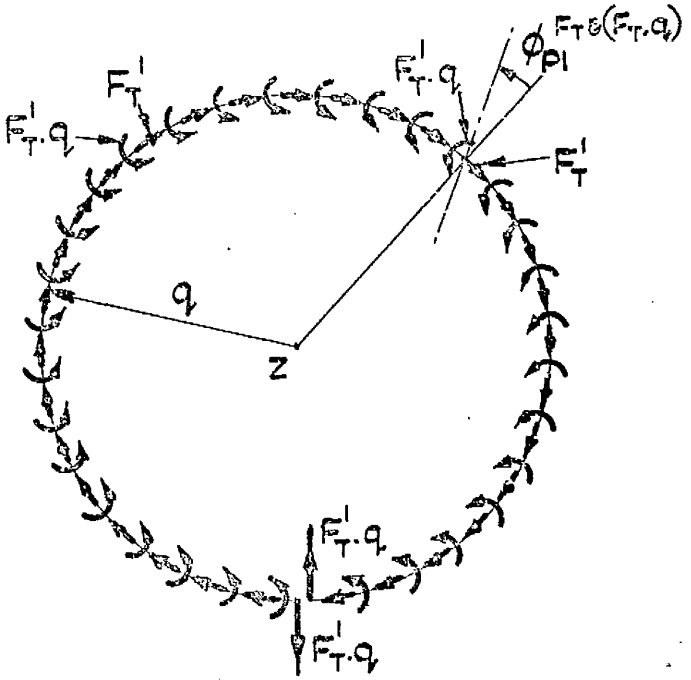

$$F'_T = \frac{\text{NO. OF BUCKETS} \times F_T}{2\pi q}$$

FIG. 20. SHEARING FORCE $F'_T.q$ ON A SECTION AND ROTATIONAL DEFORMATION $\phi_{PI}^{F_T \& (F_T.q)}$ OF THE RIM, DUE TO ASSEMBLY ACTION F_T - AND - $(F_T.q)$ ON THE RIM.

I. the sum of all forces acting in the direction of $N_{2\pi}$ is zero,

II. the sum of all forces acting in the direction of $Q_{2\pi}$ is zero,

III. the sum of all moments about the point $\phi = 0$ is zero.

Referring to Fig.19(b) and applying conditions I, II and III :-

$$N_{2\pi} + \int_0^{2\pi} \frac{\phi}{2\pi} F_T' q . d\phi . \cos\phi + \int_0^{2\pi} \left(\frac{\nu}{\pi q} F_T' q^2 . d\phi - \frac{\mu}{2\pi} F_T' q . d\phi \right) \sin\phi = 0. \qquad \text{I.}$$

$$\therefore N_{2\pi} = 0 .$$

$$Q_{2\pi} - \int_0^{2\pi} \frac{\phi}{2\pi} F_T' q . d\phi . \sin\phi + \int_0^{2\pi} \left(\frac{\nu}{\pi q} F_T' q^2 . d\phi - \frac{\mu}{2\pi} F_T' q . d\phi \right) \cos\phi = 0. \qquad \text{II}$$

$$\therefore Q_{2\pi} = - F_T' . q .$$

$$M_{2\pi} - \int_0^{2\pi} \frac{\phi}{2\pi} F_T' q^2 . d\phi - \int_0^{2\pi} \left(\frac{\nu}{\pi q} F_T' q^2 . d\phi - \frac{\mu}{2\pi} F_T' q . d\phi \right) q \sin\phi$$

$$+ \int_0^{2\pi} \frac{\phi}{2\pi} F_T' . q . d\phi . q (1 - \cos\phi) = 0. \qquad \text{III}$$

$$\therefore M_{2\pi} = 0 .$$

The only action induced on a rim section then is shearing force $F_T' \cdot q$ as shown in Fig.20. The resulting shear stress distribution on the section corresponds to that of simple beam theory and is given by:-

$$\tau_1^{F_T \& (F_T \cdot q)} = \frac{\overline{Q}_{Y'}}{I_{x'x'} \cdot b_1} F_T' \cdot q \qquad (3B.21)$$

The properties of the rim rectangular section are defined and given in Appendix 2.

It is evident that the only deformation of the rim induced by action F_T - and - $(F_T \cdot q)$ is angular deformation in the direction of the moment $(F_T \cdot q)$. This is consistent with the shearing action radially on a rim section, Fig.20, and with its complementary shearing action circumferentially. This rotational deformation $\phi_{P1}^{F_T \& (F_T \cdot q)}$ (reverting to thesis nomenclature) of all points on the rim, is easily determined by equating the work done on an element of length ds_1, of the rim, to the strain-energy stored in the corresponding elementary volume, in terms of the shear stress distribution $\tau_1^{F_T \& (F_T \cdot q)}$. Thus:-

$$\frac{1}{2}(F_T' \cdot q) \cdot ds_1 \cdot \phi_{P1}^{F_T \& (F_T \cdot q)} = ds_1 \int_{A_1} \frac{(\tau_1^{F_T \& (F_T \cdot q)})^2}{2G} dA_1 = \frac{ds_1}{2G} K_{Y'} \frac{(F_T' \cdot q)^2}{A_1} ,$$

giving :-

$$\phi_{P1}^{F_T \& (F_T \cdot q)} = \frac{K_{Y'}}{G A_1} F_T' \cdot q \qquad (3B.22)$$

the rotation being in the direction of moment $(F_T \cdot q)$.

Action M_R.

Due to this moment action about radii, or in tangential planes, the actions on a section of the rim are all in planes perpendicular to the plane/

plane of the rim. A general method of determining such transverse internal actions in rings has also been derived by BIEZENO AND GRAMMEL[30] In application, it is essentially similar to the method indicated for the previous assembly action, and the initial results obtained from its application to this particular problem are such as could not have been determined from considerations of rotational symmetry. These results are the following transverse internal actions on the section, (using BIEZENO AND GRAMMEL'S [30] notation) :-

Shearing force perpendicular to plane of the rim, $Q_{2\pi} = -M_R'(1-\mathcal{U})$,

Twisting moment in plane of the section, $W_{2\pi} = \mathcal{U} M_R' \cdot q$,

where $\mathcal{U}$ is a dimensionless constant related to the properties of the rim section and the radius of the rim. For the proportions of the rim, $\mathcal{U}$ has been found to be less than $\frac{1}{400}$ and so the contributions of twisting moment $W_{2\pi} = \mathcal{U} M_R' \cdot q$ to the resulting total stresses and deformation have been found to be negligible. $\mathcal{U}$ therefore may be taken as zero, so $W_{2\pi} = 0$, and the only significant action on the section is shearing force M_R' perpendicular to the plane of the rim. The resulting shear stress distribution on the section is given by:-

$$\tau_1^{M_R} = \frac{\overline{Q}_{x'}}{I_{y'y'} \cdot d_1} M_R' \qquad (3B.23)$$

The deformation of the rim induced by action M_R, is solely angular deformation in tangential planes in the direction of moment M_R. This case resembles the previous one very closely, and similarly by equating work done to strain-energy stored for an elementary length of rim, the rotational deformation $\phi_{R1}^{M_R}$ of all points on the rim, due to assembly action M_R, is found to be given by:-

$$\phi_{R1}^{M_R} = \frac{K_{x'}}{G A_1} M_R' \qquad (3B.24)$$

the rotation being in the direction of moment M_R.

Action M_T.

This case may be analysed in a fashion exactly similar to that of the previous assembly action, employing BIEZENO AND GRAMMEL [30] for the internal actions, and equating work done to strain-energy stored for the deformation. It is however, well-documented of itself, [31, 32] and indeed is specially treated by BIEZENO AND GRAMMEL [30] at some length, under the heading "Inversion of rings". The following results are quoted from these sources. The only internal action on a section is:-

Bending moment about radius, or in tangential plane $M_T'.q$.

Referring to Appendix 2 and Fig. A2.1 thereof, the corresponding circumferential bending stress distribution on the section is given by:-

$$\sigma_{b1}^{M_T} = \pm \frac{x'}{I_{Y'Y'}} M_T' q \qquad (3B.25)$$

The appropriate sign may be determined by considering the actions $M_T' q$ on a diametral section of the rim in relation to the direction of M_T, e.g. for M_T as shown in Fig.13, the uppermost face of the rim is in compression.

The only deformation of all points on the rim is angular deformation $\phi_{T1}^{M_T}$ in the plane of the section in the direction of moment M_T. This is given by:-

$$\phi_{T1}^{M_T} = \frac{q^2}{E I_{Y'Y'}} M_T' \qquad (3B.26)$$

the rotation being in the direction of moment M_T.

The simplicity in regard of the displacement/action relations associated with the four assembly actions is noteworthy. There is only one deformation corresponding to each action, the deformation being in the direction of the action. With reference to Fig.12 for dimensions and to/

to Appendix 2 for section properties, the displacement/action relations relevant to the assembly condition of the rim of the $16\frac{1}{2}$ in. cast steel wheel are given, for subsequent use, as follows:-

$$\delta_{R1}^{F_R} = 0.49832 \times 10^{-6} F_R \quad , \quad \text{from equation (3B.20)}$$

$$\phi_{P1}^{F_T \& (F_T \cdot q)} = 0.11772 \times 10^{-6} F_T \quad , \quad " \quad " \quad (3B.22)$$

$$\phi_{R1}^{M_R} = 0.00881 \times 10^{-6} M_R \quad , \quad " \quad " \quad (3B.24)$$

$$\phi_{T1}^{M_T} = 3.82364 \times 10^{-6} M_T \quad , \quad " \quad " \quad (3B.26)$$

The directions are those of the respective assembly actions shown in Fig.13, $\phi_{P1}^{F_T \& (F_T \cdot q)}$ being in the direction of moment $(F_T \cdot q)$.

3B iv Assembly condition - assembly actions on the hub-with-buckets

In general terms, the assembly actions on the bucket at the bucket/rim junction point are F_R, F_T - and - $(F_T \cdot q_v)$, M_R and M_T as shown in Fig.13. The bucket is assumed to be rigidly connected to the rigid hub. As exemplified for F_R in Fig.21, each assembly action comprises a statically determinate system in respect of the bucket attached to the hub, and assembly forces F_R and F_T in general induce, on any section of the bucket at θ, bending moments $M_{\theta Y2}$ and $M_{\theta X2}$ respectively about axes YY and Ox of the section, direct force $P_{\theta 2}$, shearing force $V_{\theta x2}$ in axis Ox, and twisting moment $T_{\theta 2}$ about the shear centre C_S. Assembly moments $(F_T \cdot q_v)$, M_R and M_T in general induce only some of the moment actions on a section at θ.

The general pertinent displacements of the junction point, induced by these assembly actions, are the linear radial and tangential deflections δ_{R2} and δ_{T2}, and the rotations, in the plane of the wheel, about a radius and about a tangent, ϕ_{P2}, ϕ_{R2}, ϕ_{T2}. Linear axial displacement is of no interest, the rim being free to displace axially as a whole-body according to the dictates of the attached buckets.

To analyse the actions induced at θ (and therefore the stresses) and the displacements at the junction point, the assembly actions are, of course, treated individually, assembly moment $(F_T \cdot q_v) = M_P$ being handled separately from assembly force F_T, although the two are components of one assembly action. Either comprises a statically determinate system in respect of the bucket attached to the hub. Separate treatment is convenient and has advantages with regard to the subsequent jet loading analysis. It is not necessary to carry out analyses to find all the displacements due to all the actions. Having derived some displacements/

ANALYSES IN THE CASES OF THE OTHER ASSEMBLY ACTIONS WHICH ARE SHOWN HERE AT G_1 ON THE BUCKET, FOLLOW SIMILAR LINES TO THE ANALYSES IN THE CASE OF F_R.

SECTION OF BUCKET AT $\theta = 0, \Omega = \alpha$.

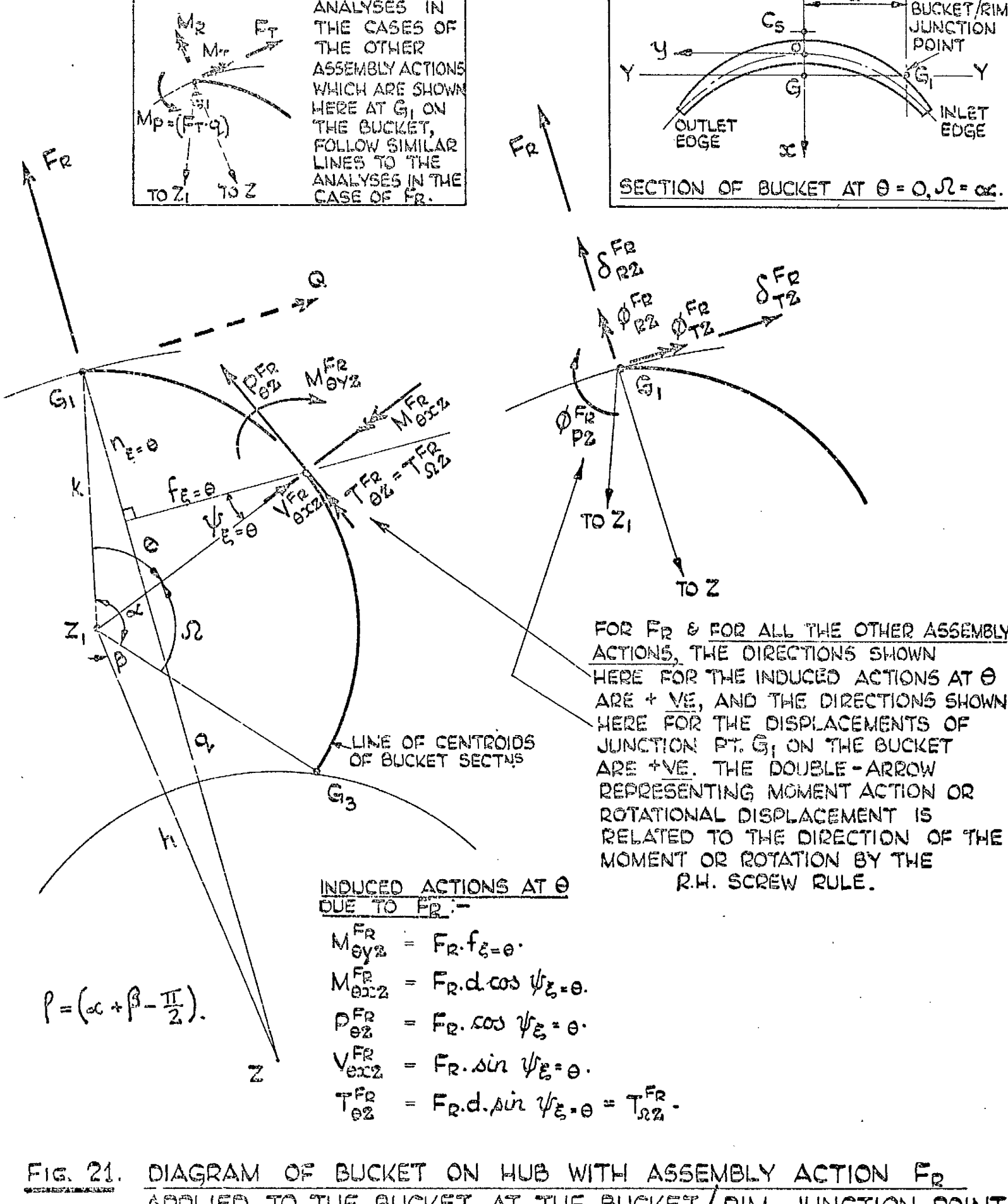

FOR F_R & FOR ALL THE OTHER ASSEMBLY ACTIONS, THE DIRECTIONS SHOWN HERE FOR THE INDUCED ACTIONS AT θ ARE + VE, AND THE DIRECTIONS SHOWN HERE FOR THE DISPLACEMENTS OF JUNCTION PT. G_1 ON THE BUCKET ARE +VE. THE DOUBLE-ARROW REPRESENTING MOMENT ACTION OR ROTATIONAL DISPLACEMENT IS RELATED TO THE DIRECTION OF THE MOMENT OR ROTATION BY THE R.H. SCREW RULE.

INDUCED ACTIONS AT θ DUE TO F_R:-

$$M^{F_R}_{\theta Y Z} = F_R \cdot f_{\xi=\theta}.$$

$$M^{F_R}_{\theta X Z} = F_R \cdot d \cdot \cos \psi_{\xi=\theta}.$$

$$P^{F_R}_{\theta Z} = F_R \cdot \cos \psi_{\xi=\theta}.$$

$$V^{F_R}_{\theta X Z} = F_R \cdot \sin \psi_{\xi=\theta}.$$

$$T^{F_R}_{\theta Z} = F_R \cdot d \cdot \sin \psi_{\xi=\theta} = T^{F_R}_{\Omega Z}.$$

FIG. 21. DIAGRAM OF BUCKET ON HUB WITH ASSEMBLY ACTION F_R APPLIED TO THE BUCKET AT THE BUCKET/RIM JUNCTION-POINT G_1, AND SHOWING THE INDUCED ACTIONS AT θ ON THE BUCKET AND THE PERTINENT DISPLACEMENTS OF THE JUNCTION POINT. ANALYSES IN THE CASES OF THE OTHER ASSEMBLY ACTIONS ARE SIMILAR.

displacements due to some actions, other displacements due to other actions may be inferred by the application of Maxwell's Reciprocal Theorem.

Action F_R.

With reference to Fig.21, the actions induced on a section of the bucket at Θ are $M_{\theta Y2}^{F_R}$, $M_{\theta X2}^{F_R}$, $P_{\theta 2}^{F_R}$, $V_{\theta X2}^{F_R}$ and $T_{\theta 2}^{F_R}$ as shown. Quantities $f_{\xi=\theta}, n_{\xi=\theta}, \sin\psi_{\xi=\theta}, \cos\psi_{\xi=\theta}$ have already been derived (before equations (3B.10) and (3B.11) so the actions are given by:-

$$M_{\theta Y2}^{F_R} = F_R \cdot \frac{k^2}{q}\left\{\frac{h}{k}\left[\cos(\rho-\theta) - \cos\rho\right] + \sin\theta\right\} \tag{3B.27}$$

$$M_{\theta X2}^{F_R} = F_R \cdot d \cdot \frac{k}{q}\left\{\frac{h}{k}\cos(\rho-\theta) + \sin\theta\right\} \tag{3B.28}$$

$$P_{\theta 2}^{F_R} = F_R \cdot \frac{k}{q}\left\{\frac{h}{k}\cos(\rho-\theta) + \sin\theta\right\} \tag{3B.29}$$

$$V_{\theta X2}^{F_R} = F_R \cdot \frac{k}{q}\left\{\frac{h}{k}\sin(\rho-\theta) + \cos\theta\right\} \tag{3B.30}$$

$$T_{\theta 2}^{F_R} = T_{\Omega 2}^{F_R} = F_R \cdot d\,\frac{k}{q}\left\{\frac{h}{k}\sin(\rho-\theta) + \cos\theta\right\} \tag{3B.31}$$

For $M_{\theta Y2}^{F_R}$, $M_{\theta X2}^{F_R}$, $P_{\theta 2}^{F_R}$, $V_{\theta X2}^{F_R}$ the corresponding stresses are given, in terms of F_R by appropriate application of equations (3B.6), (3B.7) and (3B.8), interpreting signs of stresses in relation to the directions of the actions and therefore of F_R.

The stresses induced by torque $T_{\theta 2}^{F_R} = T_{\Omega 2}^{F_R}$ are analysed by application of the theory of non-uniform torsion of thin-walled open-section beams/

beams [33, 34]. Due to restraint of warping of the section, direct stresses arise on the section as well as shear stresses. The values of these stresses at a section are not proportional to the torque on the section. This theory is developed by TIMOSHENKO AND GERE [33] and by ARGYRIS [34], assuming that the member under torsion is straight, and the theory is here applied to a member, the shear-centre axis of which is curved to a considerable degree. However, this is consistent with the basic assumption in these analyses, that the bucket behaves as a thin beam. Moreover, experimental evidence is adduced subsequently which, for a single bucket under torsion, reveals stresses very similar in kind to those predicted by the application of the theory.

The theory is generally derived [33, 34] for a member with a fully-fixed end as origin of co-ordinates. For application to the bucket therefore, it is more convenient to take angle $\Omega = \alpha - \Theta$, Fig.21, as independent variable rather than Θ. The basic differential equation [33, 34] of the theory of non-uniform torsion is given, for application to general torsion of the bucket, by:-

$$T_{\Omega z} = GJ\frac{d\phi}{k.d\Omega} - E\Gamma\frac{d^3\phi}{k^3.d\Omega^3} \qquad (3B.32)$$

where $T_{\Omega z}$ is the torque and ϕ (always without suffix) the angle of twist at any section at Ω. The resulting stresses on the bucket parabolic section at Ω are given by:-

$$\tau_{sv} = G\frac{d\phi}{k.d\Omega}(mx+c) \qquad (3B.33)$$

for the St. Venant shear stress,

$$\sigma_z = -E\frac{d^2\phi}{k^2.d\Omega^2}\,y\left(\frac{y^2}{12a} - e_s\right) \qquad (3B.34)$$

for the warping restraint direct stress,

$$\tau_z = E\frac{d^3\phi}{k^3 d\Omega^3}\cdot\frac{4a^{\frac{1}{2}}}{(mx+c)}\cdot J(y) \qquad (3B.35)$$

for the warping restraint shear stress. Function $J(y)$ is given in Appendix 1.

In these stress equations the derivatives give the stress variations with Ω along the line of centroids, Fig.21. The terms following the derivatives give the stress distributions along the boundaries of the parabolic section (see Appendix 1 and Fig.A1.1). For σ_z and τ_z these latter terms also give the distributions along the mid-parabolic-line of the section, since the stress distributions over the thickness t (Fig.A1.1) are uniform. St. Venant shear stress τ_{sv} however, is linearly distributed over section thickness being zero on the mid-line.

For action F_R, fundamental differential equation (3B.32) takes the form:-

$$T_{\Omega z}^{F_R} = GJ\frac{d\phi}{k.d\Omega} - E\Gamma\frac{d^3\phi}{k^3.d\Omega^3} = F_R\left(M_3\sin\Omega + N_3\cos\Omega\right) \qquad (3B.36)$$

where

$$M_3 = d.\frac{k}{q}\left(\frac{h}{k}\sin\beta + \sin\alpha\right)$$

$$N_3 = d.\frac{k}{q}\left(-\frac{h}{k}\cos\beta + \cos\alpha\right) .$$

The equation has similar form for the other assembly actions which induce torsion.

The solution of this differential equation for the pertinent boundary conditions is given in Appendix 3. From this solution and with reference to equations (3B.33), (3B.34) and (3B.35), the non-uniform torsion stresses are found to be given by:-

$$\tau_{sv}^{F_R} = G\frac{(mx+c)}{k}.\left\{K\left(L_3e^{K\Omega} - F_3e^{-K\Omega}\right) + \frac{N_3\cos\Omega + M_3\sin\Omega}{H+P}\right\}F_R \qquad (3B.37)$$

$$\sigma_z^{F_R} = -E\frac{y}{k^2}\left(\frac{y^2}{12a} - e_s\right)\left\{K^2\left(L_3 e^{K\Omega} + F_3 e^{-K\Omega}\right) - \frac{N_3\sin\Omega - M_3\cos\Omega}{H+P}\right\} F_R \qquad (3B.38)$$

$$T_z^{F_R} = E\frac{4a^{\frac{1}{2}}}{k^3(mx+c)}\,J(y)\left\{K^3\left(L_3 e^{K\Omega} - F_3 e^{-K\Omega}\right) - \frac{N_3\cos\Omega + M_3\sin\Omega}{H+P}\right\} F_R \qquad (3B.39)$$

where $H = \frac{GJ}{k}$, $P = \frac{E\Gamma}{k^3}$, $K = \sqrt{\frac{H}{P}}$,

$$L_3 = \frac{N_3\sin\alpha - M_3\cos\alpha - KN_3 e^{-K\alpha}}{K^2(H+P)(e^{K\alpha} + e^{-K\alpha})}$$

$$F_3 = \frac{N_3\sin\alpha - M_3\cos\alpha + KN_3 e^{K\alpha}}{K^2(H+P)(e^{K\alpha} + e^{-K\alpha})}$$

The sign convention adopted for non-uniform torsion analysis is that of TIMOSHENKO AND GERE [33]. Warping w of the parabolic section is defined in Appendix 1 in accordance with this sign convention, for which positive torque $T_{\Omega z}$ is that shown on the section at Ω in Fig.21. For F_R outwards as shown, the torque at $\Omega = \alpha$, that is on the section at the junction point, is also positive. In correspondence to the sign convention, the equivalent parabolic cross-section of the bucket stands in relation to the x , y axes of Appendix 1 such that the inlet edge of the section lies in the negative y field, the outlet edge in the positive y field, as shown in Fig.21. For warping restraint direct stress σ_z , + emerging from analysis indicates tension, - indicates compression.

Action F_R as already indicated, causes five pertinent displacements of junction point G_1 on the bucket, Fig.21. These displacements/

displacements are, in general, derived using strain-energy methods based on Castigliano's Theorem, the procedure being partly the same as that applied for the free rotating bucket displacements. Similar forms apply for the strain-energy expressions for bending, direct force and shear. Here, however, non-uniform torsion strain-energy [33, 35] must also be included, and the total strain energy of the bucket is given by:-

$$\mathcal{U} = \int_0^{\alpha} \frac{(M_{\theta Y Z}^{F_R})^2 k.d\theta}{2EI_{YY}} + \int_0^{\alpha} \frac{(M_{\theta X Z}^{F_R})^2 k.d\theta}{2EI_{OX}} + \int_0^{\alpha} \frac{(P_{\theta Z}^{F_R})^2 k.d\theta}{2EA} + K_x \int_0^{\alpha} \frac{(V_{\theta X Z}^{F_R})^2 k.d\theta}{2GA}$$

$$+ \int_0^{\alpha} \frac{GJ}{2} \left(\frac{d\phi}{k.d\Omega} \right)_{F_R}^2 k.d\Omega + \int_0^{\alpha} \frac{E\Gamma}{2} \left(\frac{d^2\phi}{k^2.d\Omega^2} \right)_{F_R}^2 k.d\Omega \quad ,$$

expressing, for convenience, the first four terms as functions of Θ and the last two terms, which give the strain-energy of non-uniform torsion, as functions of Ω . The first four expressions are given in terms of the internal actions, which have been found previously as functions of applied loading F_R , but the non-uniform torsion expressions are in terms of the deformation ϕ due to F_R , with the result that the unit load method cannot be applied throughout. Resort has to be made in the general case, to another version of the same principle, namely, the dummy load method, in which an additional load Q is applied at the required point in the direction of the required displacement. The total strain energy of the system $\mathcal{U}_{TOT}$ is then expressed in terms of actions and/or deformations caused by Q and the applied loading, of both of which the actions and/or deformations are linear functions. The required displacement is then given by the operation $\left(\frac{\partial \mathcal{U}_{TOT}}{\partial Q} \right)_{Q=0}$.

Applied/

Applied for a general displacement due to F_R on the basis of the strain-energy equation above, the displacement is given by:-

$$\left(\frac{\partial u_{F_R+Q}}{\partial Q}\right)_{Q=0} = \int_0^{\alpha} \frac{M_{\theta Y2}^{F_R}\cdot\left(\frac{\partial M_{\theta Y2}^{F_R+Q}}{\partial Q}\right)k.d\theta}{EI_{YY}} + \int_0^{\alpha} \frac{M_{\theta X2}^{F_R}\cdot\left(\frac{\partial M_{\theta X2}^{F_R+Q}}{\partial Q}\right)k.d\theta}{EI_{OX}}$$

$$+ \int_0^{\alpha} \frac{P_{\theta 2}^{F_R}\left(\frac{\partial P_{\theta 2}^{F_R+Q}}{\partial Q}\right)k.d\theta}{EA} + K_x \int_0^{\alpha} \frac{V_{\theta x2}^{F_R}\left(\frac{\partial V_{\theta x2}^{F_R+Q}}{\partial Q}\right)k.d\theta}{GA}$$

$$+ \int_0^{\alpha} \frac{GJ}{k}\left(\frac{d\phi}{d\Omega}\right)_{F_R}\cdot\frac{\partial}{\partial Q}\left[\left(\frac{d\phi}{d\Omega}\right)_{F_R+Q}\right]d\Omega + \int_0^{\alpha} \frac{E\Gamma}{k^3}\left(\frac{d^2\phi}{d\Omega^2}\right)_{F_R}\cdot\frac{\partial}{\partial Q}\left[\left(\frac{d^2\phi}{d\Omega^2}\right)_{F_R+Q}\right]d\Omega$$

(3B.40)

The first four integrals, in which the internal actions are readily expressible in terms of F_R and Q, are exactly equivalent to those derivable by the unit load method. Hence for the pertinent displacements at the junction point due to F_R, these non-torsion terms are derived on the unit load basis rather than on the dummy load basis, since many of the relevant "unit" internal actions are given previously in the free rotating condition analysis of the bucket. To integrate the non-uniform torsion terms, the torque $T_{\Omega 2}^{F_R+Q}$ due to Q and the applied loading F_R, is readily written as a function of Ω and is substituted in the non-uniform torsion differential equation (3B.32) giving an equation similar to (3B.36). This equation is then solved subject to the corresponding boundary conditions, giving $\left(\frac{d\phi}{d\Omega}\right)_{F_R+Q}$ and $\left(\frac{d^2\phi}{d\Omega^2}\right)_{F_R+Q}$ as functions of Ω, also of course linear in F_R and Q. Partial derivatives of these with/

with respect to Q are obtained directly, $\left(\frac{d\phi}{d\Omega}\right)_{F_R}$ and $\left(\frac{d^2\phi}{d\Omega^2}\right)_{F_R}$ are found for $Q = 0$, and the derivatives, all then as functions of Ω are inserted appropriately under the integral signs, multiplied and integrated directly. This procedure for obtaining the non-uniform torsion strain-energy components of the displacements is exemplified in Appendix 3 for a general case, that of $\delta_{T2}^{F_R}$, the tangential displacement of the junction point due to F_R. The determination of a displacement in the direction of the applied action is, of course, more simply obtained by direct application of Castigliano's Theorem, e.g. $\delta_{R2}^{F_R} = \frac{\partial U}{\partial F_R}$, in which cases the non-uniform torsion terms are found more easily.

The following five displacements of the junction point G_1 on the bucket, Fig.21, due to F_R, have been found as indicated. They are positive in the directions shown on Fig.21, and are given by:-

$$\delta_{R2}^{F_R} = \frac{F_R k^5}{q^2 E I_{YY}} \left\{ \frac{h^2}{k^2}\left[\frac{\alpha}{2} + \alpha\sin^2(\alpha+\beta) + \frac{3}{4}\sin 2(\alpha+\beta) - 2\sin(\alpha+\beta)\cos\beta + \frac{1}{4}\sin 2\beta\right] \right.$$
$$\left. + \frac{h}{k}\left[2\sin(\alpha+\beta)\cos\alpha + \frac{1}{2}\sin(\alpha-\beta) - \alpha\cos(\alpha+\beta) - \frac{3}{2}\sin(\alpha+\beta)\right] + \frac{\alpha}{2} - \frac{1}{4}\sin 2\alpha \right\}$$

$$+ \frac{F_R k^3}{q^2 E}\left(\frac{d^2}{I_{ox}} + \frac{1}{A}\right)\left\{ \frac{h^2}{k^2}\left[\frac{\alpha}{2} - \frac{1}{4}\sin 2(\alpha+\beta) + \frac{1}{4}\sin 2\beta\right] - \frac{h}{k}\left[\alpha\cos(\alpha+\beta) - \sin\alpha.\cos\beta\right] \right.$$
$$\left. + \frac{\alpha}{2} - \frac{1}{4}\sin 2\alpha \right.$$

$$+ \frac{F_R K_x k^3}{q^2 GA}\left\{ \frac{h^2}{k^2}\left[\frac{\alpha}{2} + \frac{1}{4}\sin 2(\alpha+\beta) - \frac{1}{4}\sin 2\beta\right] - \frac{h}{k}\left[\alpha\cos(\alpha+\beta) + \sin\alpha.\cos\beta\right] + \frac{\alpha}{2} + \frac{1}{4}\sin 2\alpha \right\}$$

$$+ \quad \text{(on next page)},$$

$$+F_R H\Bigg\{\frac{K}{2}\left(L_3^2 e^{2K\alpha}-F_3^2 e^{-2K\alpha}\right)-2K^2L_3F_3\alpha-\frac{K}{2}\left(L_3^2-F_3^2\right)$$

$$+\frac{2KL_3e^{K\alpha}}{(H+P)(K^2+1)}\left[N_3(K\cos\alpha+\sin\alpha)+M_3(K\sin\alpha-\cos\alpha)\right]$$

$$+\frac{2KF_3e^{-K\alpha}}{(H+P)(K^2+1)}\left[N_3(K\cos\alpha-\sin\alpha)+M_3(K\sin\alpha+\cos\alpha)\right]$$

$$+\frac{2(N_3^2+M_3^2)\alpha+(N_3^2-M_3^2)\sin2\alpha-2N_3M_3\cos2\alpha}{4(H+P)^2}$$

$$-\frac{2K}{(H+P)(K^2+1)}\left[KN_3(L_3+F_3)-M_3(L_3-F_3)\right]+\frac{N_3M_3}{2(H+P)^2}\Bigg\}$$

$$+F_R P\Bigg\{\frac{K^3}{2}\left(L_3^2e^{2K\alpha}-F_3^2e^{-2K\alpha}\right)+2K^4L_3F_3\alpha-\frac{K^3}{2}\left(L_3^2-F_3^2\right)$$

$$-\frac{2K^2L_3e^{K\alpha}}{(H+P)(K^2+1)}\left[N_3(K\sin\alpha-\cos\alpha)-M_3(K\cos\alpha+\sin\alpha)\right]$$

$$+\frac{2K^2F_3e^{-K\alpha}}{(H+P)(K^2+1)}\left[N_3(K\sin\alpha+\cos\alpha)-M_3(K\cos\alpha-\sin\alpha)\right]$$

$$+\frac{2(N_3^2+M_3^2)\alpha-(N_3^2-M_3^2)\sin2\alpha+2N_3M_3\cos2\alpha}{4(H+P)^2}$$

$$-\frac{2K^2}{(H+P)(K^2+1)}\left[KM_3(L_3-F_3)+N_3(L_3+F_3)\right]-\frac{N_3M_3}{2(H+P)^2}\Bigg\} \qquad (3.B.41)$$

where, in the non-uniform torsion terms:-

$$K=\sqrt{\frac{H}{P}}\quad,\qquad H=\frac{GJ}{k}\quad,\qquad P=\frac{E\Gamma}{k^3}$$

$$M_3=d\frac{k}{q}\left(\frac{h}{k}\sin\beta+\sin\alpha\right)\quad;\qquad N_3=d\frac{k}{q}\left(-\frac{h}{k}\cos\beta+\cos\alpha\right),$$

$$L_3=\frac{N_3\sin\alpha-M_3\cos\alpha-KN_3e^{-K\alpha}}{K^2(H+P)(e^{K\alpha}+e^{-K\alpha})},\qquad F_3=\frac{N_3\sin\alpha-M_3\cos\alpha+KN_3e^{K\alpha}}{K^2(H+P)(e^{K\alpha}+e^{-K\alpha})}.$$

$$\delta_{T2}^{F_R} = \frac{F_R k^5}{q^2 E I_{YY}} \left\{ \frac{h^2}{k^2} \left[\frac{\alpha}{2} \sin 2(\alpha+\beta) + \frac{3}{4}\cos 2(\alpha+\beta) + \sin(\alpha+\beta)\sin\beta - \cos(\alpha+\beta)\cos\beta + \frac{1}{4}\cos 2\beta \right] \right.$$

$$+ \frac{h}{k} \left[\sin(\alpha+\beta)\sin\alpha + \cos(\alpha+\beta)\cos\alpha - \frac{1}{2}\cos(\alpha-\beta) - \alpha\sin(\alpha+\beta) - \frac{3}{2}\cos(\alpha+\beta) + \cos\beta \right.$$

$$\left. + \frac{1}{4}\cos 2\alpha - \cos\alpha + \frac{3}{4} \right]$$

$$+ \frac{F_R k^3}{4q^2} \left(\frac{K_\chi}{GA} - \frac{d^2}{E I_{o\chi}} - \frac{1}{EA} \right) \left\{ \frac{h^2}{k^2} \left[\cos 2(\alpha+\beta) - \cos 2\beta \right] + 4\frac{h}{k}\sin\alpha\sin\beta - \cos 2\alpha + 1 \right\}$$

$$+ F_R H \left\{ \frac{K}{2}\left(L_3 L_4 e^{2K\alpha} - F_3 F_4 e^{-2K\alpha} \right) - K^2 \left(L_4 F_3 + L_3 F_4 \right)\alpha - \frac{K}{2}\left(L_3 L_4 - F_3 F_4 \right) \right.$$

$$+ \frac{K e^{K\alpha}}{(H+P)(K^2+1)} \left[\left(L_4 N_3 + L_3 M_3 \right)\left(K\cos\alpha + \sin\alpha \right) + \left(L_4 M_3 - L_3 N_3 \right)\left(K\sin\alpha - \cos\alpha \right) \right]$$

$$+ \frac{K e^{-K\alpha}}{(H+P)(K^2+1)} \left[\left(F_4 N_3 + F_3 M_3 \right)\left(K\cos\alpha - \sin\alpha \right) + \left(F_4 M_3 - F_3 N_3 \right)\left(K\sin\alpha + \cos\alpha \right) \right]$$

$$+ \frac{2 M_3 N_3 \sin 2\alpha + \left(M_3^2 - N_3^2 \right)\left(1 - \cos 2\alpha \right)}{4(H+P)^2}$$

$$\left. - \frac{K}{(H+P)(K^2+1)} \left[K\left(L_4 + F_4 \right) N_3 + K\left(L_3 + F_3 \right) M_3 - \left(L_4 - F_4 \right) M_3 + \left(L_3 - F_3 \right) N_3 \right] \right\}$$

$$+ F_R \cdot P \left\{ \frac{K^3}{2}\left(L_3 L_4 e^{2K\alpha} - F_3 F_4 e^{-2K\alpha} \right) + K^4 \left(L_4 F_3 + L_3 F_4 \right)\alpha - \frac{K^3}{2}\left(L_3 L_4 - F_3 F_4 \right) \right.$$

$$- \frac{K^2 e^{K\alpha}}{(H+P)(K^2+1)} \left[\left(L_4 N_3 + L_3 M_3 \right)\left(K\sin\alpha - \cos\alpha \right) - \left(L_4 M_3 - L_3 N_3 \right)\left(K\cos\alpha + \sin\alpha \right) \right]$$

$$+ \frac{K^2 e^{-K\alpha}}{(H+P)(K^2+1)} \left[\left(F_4 N_3 + F_3 M_3 \right)\left(K\sin\alpha + \cos\alpha \right) - \left(F_4 M_3 - F_3 N_3 \right)\left(K\cos\alpha - \sin\alpha \right) \right]$$

$$- \frac{2 M_3 N_3 \sin 2\alpha + \left(M_3^2 - N_3^2 \right)\left(1 - \cos 2\alpha \right)}{4(H+P)^2}$$

$$\left. - \frac{K^2}{(H+P)(K^2+1)} \left[\left(L_4 + F_4 \right) N_3 + \left(L_3 + F_3 \right) M_3 + K\left(L_4 - F_4 \right) M_3 - K\left(L_3 - F_3 \right) N_3 \right] \right\} \qquad (3B.42),$$

where, in the non-uniform torsion terms:-

$K, H, P, M_3, N_3, L_3, F_3$ are the same as for $\delta_{R2}^{F_R}$, and where:-

$$L_4 = \frac{M_3\sin\alpha + N_3\cos\alpha - K M_3 e^{-K\alpha}}{K^2(H+P)\left(e^{K\alpha} + e^{-K\alpha} \right)}, \qquad F_4 = \frac{M_3\sin\alpha + N_3\cos\alpha + K M_3 e^{K\alpha}}{K^2(H+P)\left(e^{K\alpha} + e^{-K\alpha} \right)}.$$

$$\phi_{P2}^{F_R} = \frac{F_R k^3}{q E I_{YY}} \left\{ \frac{h}{k} \left[\cos\beta - \cos(\alpha+\beta) - \alpha \sin(\alpha+\beta) \right] - \cos\alpha + 1 \right\} \qquad (3B.43)$$

$$\begin{aligned}
\phi_{R2}^{F_R} = & -\frac{F_R k^3 d}{4 q^2 E I_{ox}} \left\{ \frac{h^2}{k^2} \left[\cos 2(\alpha+\beta) - \cos 2\beta \right] + 4 \frac{h}{k} \sin\alpha \sin\beta - \cos 2\alpha + 1 \right\} \\
& + F_R \frac{H}{d} \left\{ \begin{array}{l}
\frac{K}{2} \left(L_3 L_4 e^{2K\alpha} - F_3 F_4 e^{-2K\alpha} \right) - K^2 \left(L_4 F_3 + L_3 F_4 \right) \alpha - \frac{K}{2} \left(L_3 L_4 - F_3 F_4 \right) \\
+ \frac{K e^{K\alpha}}{(H+P)(K^2+1)} \left[(L_4 N_3 + L_3 M_3)(K\cos\alpha + \sin\alpha) + (L_4 M_3 - L_3 N_3)(K\sin\alpha - \cos\alpha) \right] \\
+ \frac{K e^{-K\alpha}}{(H+P)(K^2+1)} \left[(F_4 N_3 + F_3 M_3)(K\cos\alpha - \sin\alpha) + (F_4 M_3 - F_3 N_3)(K\sin\alpha + \cos\alpha) \right] \\
+ \dfrac{2 M_3 N_3 \sin 2\alpha + (M_3^2 - N_3^2)(1 - \cos 2\alpha)}{4 (H+P)^2} \\
- \dfrac{K}{(H+P)(K^2+1)} \left[K(L_4 + F_4) N_3 + K(L_3 + F_3) M_3 - (L_4 - F_4) M_3 + (L_3 - F_3) N_3 \right]
\end{array} \right\} \\
& + F_R \frac{P}{d} \left\{ \begin{array}{l}
\frac{K^3}{2} \left(L_3 L_4 e^{2K\alpha} - F_3 F_4 e^{-2K\alpha} \right) + K^4 \left(L_4 F_3 + L_3 F_4 \right) \alpha - \frac{K^3}{2} \left(L_3 L_4 - F_3 F_4 \right) \\
- \frac{K^2 e^{K\alpha}}{(H+P)(K^2+1)} \left[(L_4 N_3 + L_3 M_3)(K\sin\alpha - \cos\alpha) - (L_4 M_3 - L_3 N_3)(K\cos\alpha + \sin\alpha) \right] \\
+ \frac{K^2 e^{-K\alpha}}{(H+P)(K^2+1)} \left[(F_4 N_3 + F_3 M_3)(K\sin\alpha + \cos\alpha) - (F_4 M_3 - F_3 N_3)(K\cos\alpha - \sin\alpha) \right] \\
- \dfrac{2 M_3 N_3 \sin 2\alpha + (M_3^2 - N_3^2)(1 - \cos 2\alpha)}{4 (H+P)^2} \\
- \dfrac{K^2}{(H+P)(K^2+1)} \left[(L_4 + F_4) N_3 + (L_3 + F_3) M_3 + K(L_4 - F_4) M_3 - K(L_3 - F_3) N_3 \right]
\end{array} \right\}
\end{aligned}$$

(3B.44),

where, in the non-uniform torsion terms:-

$K, H, P, M_3, N_3, L_3, F_3 L_4$ and F_4 are the same as for $\delta_{T2}^{F_R}$.

$$\phi_{T2}^{F_R} = -\frac{F_R k^3 d}{q^2 E I_{ox}}\left\{\frac{h^2}{k^2}\left[\frac{\alpha}{2} - \frac{1}{4}\sin 2(\alpha+\beta) + \frac{1}{4}\sin 2\beta\right] - \frac{h}{k}\left[\alpha\cos(\alpha+\beta) - \sin\alpha.\cos\beta\right] + \frac{\alpha}{2} - \frac{1}{4}\sin 2\alpha\right.$$

$$- F_R\frac{H}{d}\left\{\frac{K}{2}\left(L_3^2 e^{2K\alpha} - F_3^2 e^{-2K\alpha}\right) - 2K^2 L_3 F_3\alpha - \frac{K}{2}\left(L_3^2 - F_3^2\right)\right.$$

$$+ \frac{2KL_3 e^{K\alpha}}{(H+P)(K^2+1)}\left[N_3(K\cos\alpha+\sin\alpha) + M_3(K\sin\alpha-\cos\alpha)\right]$$

$$+ \frac{2KF_3 e^{-K\alpha}}{(H+P)(K^2+1)}\left[N_3(K\cos\alpha-\sin\alpha) + M_3(K\sin\alpha+\cos\alpha)\right]$$

$$+ \frac{2(N_3^2+M_3^2)\alpha + (N_3^2-M_3^2)\sin 2\alpha - 2N_3M_3\cos 2\alpha}{4(H+P)^2}$$

$$\left.\left. - \frac{2K}{(H+P)(K^2+1)}\left[KN_3(L_3+F_3) - M_3(L_3-F_3)\right] + \frac{N_3M_3}{2(H+P)^2}\right\}\right.$$

$$- F_R\frac{P}{d}\left\{\frac{K^3}{2}\left(L_3^2 e^{2K\alpha} - F_3^2 e^{-2K\alpha}\right) + 2K^4 L_3 F_3\alpha - \frac{K^3}{2}\left(L_3^2 - F_3^2\right)\right.$$

$$- \frac{2K^2 L_3 e^{K\alpha}}{(H+P)(K^2+1)}\left[N_3(K\sin\alpha-\cos\alpha) - M_3(K\cos\alpha+\sin\alpha)\right]$$

$$+ \frac{2K^2 F_3 e^{-K\alpha}}{(H+P)(K^2+1)}\left[N_3(K\sin\alpha+\cos\alpha) - M_3(K\cos\alpha-\sin\alpha)\right]$$

$$+ \frac{2(N_3^2+M_3^2)\alpha - (N_3^2-M_3^2)\sin 2\alpha + 2N_3M_3\cos 2\alpha}{4(H+P)^2}$$

$$\left.\left. - \frac{2K^2}{(H+P)(K^2+1)}\left[KM_3(L_3-F_3) + N_3(L_3+F_3)\right] - \frac{N_3M_3}{2(H+P)^2}\right\}\right.$$

(3B.45),

where, in the non-uniform torsion terms:-

K, H, P, M_3, N_3, L_3 and F_3 are the same as for $\phi_{R2}^{F_R}$.

Action F_T. (of assembly action F_T - and - $(F_T.q)$.)

Analyses for induced actions at Θ and for displacements at G_1 due to F_T, follow, in the main, similar lines to the analyses in the case of F_R. With reference to Fig.21 for the relevant geometry and sign conventions, the induced actions at Θ and the displacements at junction point G_1 are as follows:-

$$M_{\theta Y2}^{F_T} = \frac{F_T.k^2}{q}\left\{\frac{h}{k}\left[\sin\rho - \sin(\rho-\theta)\right] + 1 - \cos\theta\right\} \tag{3B.46}$$

$$M_{\theta x2}^{F_T} = -\frac{F_T dk}{q}\left\{\frac{h}{k}\sin(\rho-\theta) + \cos\theta\right\} \tag{3B.47}$$

$$P_{\theta 2}^{F_T} = -\frac{F_T k}{q}\left\{\frac{h}{k}\sin(\rho-\theta) + \cos\theta\right\} \tag{3B.48}$$

$$V_{\theta x2}^{F_T} = \frac{F_T k}{q}\left\{\frac{h}{k}\cos(\rho-\theta) + \sin\theta\right\} \tag{3B.49}$$

$$T_{\theta 2}^{F_T} = T_{\Omega 2}^{F_T} = \frac{F_T dk}{q}\left\{\frac{h}{k}\cos(\rho-\theta) + \sin\theta\right\} \tag{3B.50}$$

Corresponding stresses, in terms of F_T, are obtained in the same way as for F_R, the non-uniform torsion stresses being given by:-

$$\tau_{sv}^{F_T} = \frac{G(mx+c)}{k}\left\{K\left(L_4 e^{K\Omega} - F_4 e^{-K\Omega}\right) + \frac{M_3\cos\Omega - N_3\sin\Omega}{H+P}\right\}F_T \tag{3B.51}$$

$$\sigma_z^{F_T} = -E\frac{y}{k^2}\left(\frac{y^2}{12a} - e_s\right)\left\{K^2\left(L_4 e^{K\Omega} + F_4 e^{-K\Omega}\right) - \frac{M_3\sin\Omega + N_3\cos\Omega}{H+P}\right\}F_T \tag{3B.52}$$

$$\tau_z^{F_T} = E\frac{4a^{\frac{1}{2}}}{k^3(mx+c)}\,J(y)\left\{K^3\left(L_4 e^{K\Omega} - F_4 e^{-K\Omega}\right) - \frac{M_3\cos\Omega - N_3\sin\Omega}{H+P}\right\}F_T$$

(3B.53)

where K, H, P, M_3, N_3, L_4 and F_4 are as given for the case of F_R.

$$\delta_{R2}^{F_T} = F_T\cdot\frac{\delta_{T2}^{F_R}}{F_R}$$

(3B.54)

by Maxwell's Reciprocal Theorem.

$$\delta_{T2}^{F_T} = \frac{F_T k^5}{q^2 E I_{YY}}\left\{\frac{h^2}{k^2}\left[\frac{\alpha}{2} + \alpha\cos^2(\alpha+\beta) - \frac{3}{4}\sin 2(\alpha+\beta) + 2\cos(\alpha+\beta)\sin\beta - \frac{1}{4}\sin 2\beta\right]\right.$$

$$+\frac{h}{k}\left[2\cos(\alpha+\beta)\sin\alpha - \frac{1}{2}\sin(\alpha-\beta) - 3\alpha\cos(\alpha+\beta) + \frac{3}{2}\sin(\alpha+\beta) - 2\sin\beta\right]$$

$$\left.+\frac{3}{2}\alpha + \frac{1}{4}\sin 2\alpha - 2\sin\alpha\right.$$

$$+\frac{F_T k^3}{q^2 E}\left(\frac{d^2}{I_{ox}} + \frac{1}{A}\right)\left\{\frac{h^2}{k^2}\left[\frac{\alpha}{2} + \frac{1}{4}\sin 2(\alpha+\beta) - \frac{1}{4}\sin 2\beta\right] - \frac{h}{k}\left[\alpha\cos(\alpha+\beta) + \sin\alpha.\cos\beta\right] + \frac{\alpha}{2} + \frac{1}{4}\sin 2\alpha\right\}$$

$$+\frac{F_T K_x k^3}{q^2 G A}\left\{\frac{h^2}{k^2}\left[\frac{\alpha}{2} - \frac{1}{4}\sin 2(\alpha+\beta) + \frac{1}{4}\sin 2\beta\right] - \frac{h}{k}\left[\alpha\cos(\alpha+\beta) - \sin\alpha.\cos\beta\right] + \frac{\alpha}{2} - \frac{1}{4}\sin 2\alpha\right\}$$

$$+F_T H\left\{\frac{K}{2}\left(L_4^2 e^{2K\alpha} - F_4^2 e^{-2K\alpha}\right) - 2K^2 L_4 F_4\alpha - \frac{K}{2}\left(L_4^2 - F_4^2\right)\right.$$

$$+\frac{2K L_4 e^{K\alpha}}{(H+P)(K^2+1)}\left[M_3(K\cos\alpha + \sin\alpha) - N_3(K\sin\alpha - \cos\alpha)\right]$$

$$+\frac{2K F_4 e^{-K\alpha}}{(H+P)(K^2+1)}\left[M_3(K\cos\alpha - \sin\alpha) - N_3(K\sin\alpha + \cos\alpha)\right]$$

$$+\frac{2(M_3^2+N_3^2)\alpha + (M_3^2 - N_3^2)\sin 2\alpha + 2M_3 N_3\cos 2\alpha}{4(H+P)^2}$$

$$\left.-\frac{2K}{(H+P)(K^2+1)}\left[KM_3(L_4+F_4) + N_3(L_4 - F_4)\right] - \frac{M_3 N_3}{2(H+P)^2}\right\}$$

+ (on next page),

$$+F_T P\left\{\begin{array}{l}\frac{K^3}{2}\left(L_4^2 e^{2K\alpha}-F_4^2 e^{-2K\alpha}\right)+2K^4 L_4 F_4\alpha-\frac{K^3}{2}\left(L_4^2-F_4^2\right)\\ -\frac{2K^2 L_4 e^{K\alpha}}{(H+P)(K^2+1)}\left[M_3(K\sin\alpha-\cos\alpha)+N_3(K\cos\alpha+\sin\alpha)\right]\\ +\frac{2K^2 F_4 e^{-K\alpha}}{(H+P)(K^2+1)}\left[M_3(K\sin\alpha+\cos\alpha)+N_3(K\cos\alpha-\sin\alpha)\right]\\ +\frac{2(M_3^2+N_3^2)\alpha-(M_3^2-N_3^2)\sin 2\alpha-2M_3N_3\cos 2\alpha}{4(H+P)^2}\\ +\frac{2K^2}{(H+P)(K^2+1)}\left[-KN_3(L_4-F_4)+M_3(L_4+F_4)\right]+\frac{M_3N_3}{2(H+P)^2}\end{array}\right\}$$

(3B.55),

where, in the non-uniform torsion terms:-

K, H, P, M_3, N_3, L_4 and F_4 are as given for the case of F_R.

$$\phi_{P2}^{F_T}=\frac{F_T K^3}{qEI_{YY}}\left\{\frac{h}{k}\left[\sin(\alpha+\beta)-\sin\beta-\alpha\cos(\alpha+\beta)\right]-\sin\alpha+\alpha\right\}$$

(3B.56)

$$\phi_{R2}^{F_T} = \frac{F_T k^3 d}{q^2 E I_{ox}} \left\{ \frac{h^2}{k^2}\left[\frac{\alpha}{2} + \frac{1}{4}\sin 2(\alpha+\beta) - \frac{1}{4}\sin 2\beta\right] - \frac{h}{k}\left[\alpha\cos(\alpha+\beta) + \sin\alpha.\cos\beta\right] + \frac{\alpha}{2} + \frac{1}{4}\sin 2\alpha \right\}$$

$$+ F_T \frac{H}{d} \left\{ \begin{array}{l} \frac{K}{2}\left(L_4^2 e^{2K\alpha} - F_4^2 e^{-2K\alpha}\right) - 2K^2 L_4 F_4 \alpha - \frac{K}{2}\left(L_4^2 - F_4^2\right) \\ + \frac{2KL_4 e^{K\alpha}}{(H+P)(K^2+1)}\left[M_3(K\cos\alpha + \sin\alpha) - N_3(K\sin\alpha - \cos\alpha)\right] \\ + \frac{2KF_4 e^{-K\alpha}}{(H+P)(K^2+1)}\left[M_3(K\cos\alpha - \sin\alpha) - N_3(K\sin\alpha + \cos\alpha)\right] \\ + \frac{2\left(M_3^2+N_3^2\right)\alpha + \left(M_3^2 - N_3^2\right)\sin 2\alpha + 2M_3N_3\cos 2\alpha}{4(H+P)^2} \\ - \frac{2K}{(H+P)(K^2+1)}\left[KM_3(L_4+F_4) + N_3(L_4 - F_4)\right] - \frac{M_3N_3}{2(H+P)^2} \end{array} \right\}$$

$$+ F_T \frac{P}{d} \left\{ \begin{array}{l} \frac{K^3}{2}\left(L_4^2 e^{2K\alpha} - F_4^2 e^{-2K\alpha}\right) + 2K^4 L_4 F_4 \alpha - \frac{K^3}{2}\left(L_4^2 - F_4^2\right) \\ - \frac{2K^2 L_4 e^{K\alpha}}{(H+P)(K^2+1)}\left[M_3(K\sin\alpha - \cos\alpha) + N_3(K\cos\alpha + \sin\alpha)\right] \\ + \frac{2K^2 F_4 e^{-K\alpha}}{(H+P)(K^2+1)}\left[M_3(K\sin\alpha + \cos\alpha) + N_3(K\cos\alpha - \sin\alpha)\right] \\ + \frac{2\left(M_3^2+N_3^2\right)\alpha - \left(M_3^2 - N_3^2\right)\sin 2\alpha - 2M_3N_3\cos 2\alpha}{4(H+P)^2} \\ - \frac{2K^2}{(H+P)(K^2+1)}\left[-KN_3(L_4 - F_4) + M_3(L_4 + F_4)\right] + \frac{M_3N_3}{2(H+P)^2} \end{array} \right\}$$

(3B.57),

where, in the non-uniform torsion terms:-

K, H, P, M_3, N_3, L_4 and F_4 are as given for the case of F_R.

$$\phi_{T2}^{F_T} = \frac{F_T k^3 d}{4q^2 E I_{ox}} \left\{ \frac{h^2}{k^2}\left[\cos 2(\alpha+\beta) - \cos 2\beta\right] + 4\frac{h}{k}\sin\alpha.\sin\beta - \cos 2\alpha + 1 \right\}$$

$$-F_T\frac{H}{d}\left\{ \begin{array}{l} \frac{K}{2}\left(L_3L_4e^{2K\alpha} - F_3F_4e^{-2K\alpha}\right) - K^2\left(L_4F_3+L_3F_4\right)\alpha - \frac{K}{2}\left(L_3L_4 - F_3F_4\right) \\ + \frac{Ke^{K\alpha}}{(H+P)(K^2+1)}\left[\left(L_4N_3+L_3M_3\right)\left(K\cos\alpha+\sin\alpha\right) + \left(L_4M_3-L_3N_3\right)\left(K\sin\alpha-\cos\alpha\right)\right] \\ + \frac{Ke^{-K\alpha}}{(H+P)(K^2+1)}\left[\left(F_4N_3+F_3M_3\right)\left(K\cos\alpha-\sin\alpha\right) + \left(F_4M_3-F_3N_3\right)\left(K\sin\alpha+\cos\alpha\right)\right] \\ + \frac{2M_3N_3\sin 2\alpha + \left(M_3^2-N_3^2\right)\left(1-\cos 2\alpha\right)}{4(H+P)^2} \\ - \frac{K}{(H+P)(K^2+1)}\left[K\left(L_4+F_4\right)N_3 + K\left(L_3+F_3\right)M_3 - \left(L_4-F_4\right)M_3 + \left(L_3-F_3\right)N_3\right] \end{array} \right.$$

$$-F_T\frac{P}{d}\left\{ \begin{array}{l} \frac{K^3}{2}\left(L_3L_4e^{2K\alpha} - F_3F_4e^{-2K\alpha}\right) + K^4\left(L_4F_3+L_3F_4\right)\alpha - \frac{K^3}{2}\left(L_3L_4-F_3F_4\right) \\ - \frac{K^2e^{K\alpha}}{(H+P)(K^2+1)}\left[\left(L_4N_3+L_3M_3\right)\left(K\sin\alpha-\cos\alpha\right) - \left(L_4M_3-L_3N_3\right)\left(K\cos\alpha+\sin\alpha\right)\right] \\ + \frac{K^2e^{-K\alpha}}{(H+P)(K^2+1)}\left[\left(F_4N_3+F_3M_3\right)\left(K\sin\alpha+\cos\alpha\right) - \left(F_4M_3-F_3N_3\right)\left(K\cos\alpha-\sin\alpha\right)\right] \\ - \frac{2M_3N_3\sin 2\alpha + \left(M_3^2-N_3^2\right)\left(1-\cos 2\alpha\right)}{4(H+P)^2} \\ - \frac{K^2}{(H+P)(K^2+1)}\left[\left(L_4+F_4\right)N_3 + \left(L_3+F_3\right)M_3 + K\left(L_4-F_4\right)M_3 - K\left(L_3-F_3\right)N_3\right] \end{array} \right.$$

(3B.58),

where, in the non-uniform torsion terms:-

$K, H, P, M_3, N_3, L_3, F_3, L_4$ and F_4 are as given for the case of F_R.

Action $M_P = (F_T.q)$. (of assembly action F_T - and - $(F_T.q)$).

Referring to Fig.21, the induced action at Θ and the displacements at junction point G_1 are as follows:-

$$M_{\theta Y2}^{M_P} = -M_P \tag{3B.59}$$

from which corresponding stresses, in terms of M_P, may be calculated via equation (3B.6).

$$\delta_{R2}^{M_P} = -M_P.\frac{\phi_{P2}^{F_R}}{F_R} \tag{3B.60}$$

by Maxwell's Reciprocal Theorem.

$$\delta_{T2}^{M_P} = -M_P.\frac{\phi_{P2}^{F_T}}{F_T} \tag{3B.61},$$

similarly.

$$\phi_{P2}^{M_P} = -M_P.\frac{kc}{EI_{YY}} \tag{3B.62}.$$

For the centrifugal loading analyses, $M_P = F_T.q$ in the above four equations.

Action M_R

The induced actions at Θ and the displacements at junction point G_1, Fig.21, are as follows:-

$$M_{\theta x2}^{M_R} = -M_R\frac{k}{q}\left\{\frac{h}{k}\sin(\rho-\theta)+\cos\theta\right\} \tag{3B.63}$$

$$T_{\theta 2}^{M_R} = T_{\Omega 2}^{M_R} = M_R\frac{k}{q}\left\{\frac{h}{k}\cos(\rho-\theta)+\sin\theta\right\} \tag{3B.64}$$

Corresponding/

Corresponding stresses, in terms of M_R, are obtained in the same way as for F_T, the non-uniform torsion stresses being given by:-

$$\tau_{sv}^{M_R} = \frac{\tau_{sv}^{F_T}}{F_T} \times \frac{M_R}{d} \tag{3B.65}$$

$$\sigma_z^{M_R} = \frac{\sigma_z^{F_T}}{F_T} \times \frac{M_R}{d} \tag{3B.66}$$

$$\tau_z^{M_R} = \frac{\tau_z^{F_T}}{F_T} \times \frac{M_R}{d} \tag{3B.67}$$

by comparison of equations (3B.64) and (3B.50), and by equations (3B.51), (3B.52) and (3B.53).

$$\delta_{R2}^{M_R} = M_R \cdot \frac{\phi_{R2}^{F_R}}{F_R} \tag{3B.68}$$

by Maxwell's Reciprocal Theorem.

$$\delta_{T2}^{M_R} = M_R \cdot \frac{\phi_{R2}^{F_T}}{F_T} \tag{3B.69},$$

similarly.

$$\phi_{R2}^{M_R} = \frac{\delta_{T2}^{M_R}}{d} \tag{3B.70}$$

$$\phi_{T2}^{M_R} = -\frac{\delta_{R2}^{M_R}}{d} \tag{3B.71}$$

Action M_T

With reference to Fig. 21, the induced actions at Θ and the displacements at junction point G_1 are as follows:-

$$M_{\theta z 2}^{M_T} = -M_T \frac{k}{q}\left\{\frac{h}{k}\cos(\beta-\theta)+\sin\theta\right\} \tag{3B.72}$$

$$T_{\theta 2}^{M_T} = T_{\Omega 2}^{M_T} = -M_T \frac{k}{q}\left\{\frac{h}{k}\sin(\beta-\theta)+\cos\theta\right\} \tag{3B.73}$$

Corresponding stresses, in terms of M_T are obtained in the same way as for F_R, the non-uniform torsion stresses being given by:-

$$\tau_{sv}^{M_T} = -\frac{\tau_{sv}^{F_R}}{F_R} \times \frac{M_T}{d} \tag{3B.74}$$

$$\sigma_z^{M_T} = -\frac{\sigma_z^{F_R}}{F_R} \times \frac{M_T}{d} \tag{3B.75}$$

$$\tau_z^{M_T} = -\frac{\tau_z^{F_R}}{F_R} \times \frac{M_T}{d} \tag{3B.76},$$

by comparison of equations (3B.73) and (3B.31), and by equations (3B.37), (3B.38) and (3B.39).

$$\delta_{R2}^{M_T} = M_T \cdot \frac{\phi_{T2}^{F_R}}{F_R} \tag{3B.77}$$

by Maxwell's Reciprocal Theorem.

$$\delta_{T2}^{M_T} = M_T \cdot \frac{\phi_{T2}^{F_T}}{F_T} \tag{3B.78},$$

similarly.

$$\phi_{R2}^{M_T} = \frac{\delta_{T2}^{M_T}}{d} \qquad (3B.79)$$

$$\phi_{T2}^{M_T} = -\frac{\delta_{R2}^{M_T}}{d} \qquad (3B.80)$$

In the strain-energy analyses for the displacements of junction point G_1 due to the assembly actions, no account is taken of displacement components due to the free warping of the bucket cross-section containing G_1 at $\theta = 0$. Such components in the region of G_1 are readily derived from the non-uniform torsion solutions for the assembly actions, e.g. as in Appendix 3(a), and from the expression for warping w given in Appendix 1. For the numerical application, calculations were performed to determine the appropriate warping displacement components in the region of G_1, associated with each pertinent assembly action. As might reasonably have been expected, these were all found to be negligibly small in comparison with the corresponding assembly action displacements calculated from the expressions derived in this section.

With reference to Fig.12 for dimensions, to Appendix 1 for section properties and to Fig.21 for sign convention, the displacement/action relations at junction point G_1 on the bucket, relevant to the assembly condition of the hub-with-buckets of the $16\frac{1}{2}$ in. cast steel wheel, are given, for subsequent use, as follows:-

$\delta_{R2}^{F_R} = +\ 8.75688 \times 10^{-6} F_R$, from equation (3B.41)

$\delta_{T2}^{F_R} = +\ 8.03753 \times 10^{-6} F_R$, " " (3B.42)

$\phi_{P2}^{F_R} = +\ 1.32147 \times 10^{-6} F_R$, " " (3B.43)

$\phi_{R2}^{F_R} = +\ 0.95256 \times 10^{-6} F_R$, " " (3B.44)

$\phi_{T2}^{F_R} = -\ 1.81235 \times 10^{-6} F_R$, " " (3B.45)

$$\delta_{R2}^{F_T} = + \ 8.03753 \times 10^{-6} F_T \ , \quad \text{from equation (3B.54)}$$

$$\delta_{T2}^{F_T} = + \ 19.44856 \times 10^{-6} F_T \ , \quad " \quad " \quad (3B.55)$$

$$\phi_{P2}^{F_T} = + \ 1.79787 \times 10^{-6} F_T \ , \quad " \quad " \quad (3B.56)$$

$$\phi_{R2}^{F_T} = + \ 3.75568 \times 10^{-6} F_T \ , \quad " \quad " \quad (3B.57)$$

$$\phi_{T2}^{F_T} = - \ 0.95256 \times 10^{-6} F_T \ , \quad " \quad " \quad (3B.58)$$

$$\delta_{R2}^{M_P} = - \ 17.64013 \times 10^{-6} F_T \ , \quad " \quad " \quad (3B.60)$$

$$\delta_{T2}^{M_P} = - \ 24.01328 \times 10^{-6} F_T \ , \quad " \quad " \quad (3B.61)$$

$$\phi_{P2}^{M_P} = - \ 6.27435 \times 10^{-6} F_T \ , \quad " \quad " \quad (3B.62)$$

putting $M_P = (F_T \cdot q)$ here.

$$\delta_{R2}^{M_R} = + \ 0.95256 \times 10^{-6} M_R \ , \quad \text{from equation (3B.68)}$$

$$\delta_{T2}^{M_R} = + \ 3.75568 \times 10^{-6} M_R \ , \quad " \quad " \quad (3B.69)$$

$$\phi_{R2}^{M_R} = + \ 1.70713 \times 10^{-6} M_R \ , \quad " \quad " \quad (3B.70)$$

$$\phi_{T2}^{M_R} = - \ 0.43298 \times 10^{-6} M_R \ , \quad " \quad " \quad (3B.71)$$

$$\delta_{R2}^{M_T} = - \ 1.81235 \times 10^{-6} M_T \ , \quad " \quad " \quad (3B.77)$$

$$\delta_{T2}^{M_T} = - \ 0.95256 \times 10^{-6} M_T \ , \quad " \quad " \quad (3B.78)$$

$$\phi_{R2}^{M_T} = - \ 0.43298 \times 10^{-6} M_T \ , \quad " \quad " \quad (3B.79)$$

$$\phi_{T2}^{M_T} = + \ 0.82380 \times 10^{-6} M_T \ , \quad " \quad " \quad (3B.80)$$

It is of interest to examine the separate contributions to these displacements, of the various strain-energy terms. Table 2 gives the percentage contributions of the strain-energy terms to the pertinent multi-term displacements.

Table 2

Contributions of the various strain-energy terms to the assembly action displacements of the bucket junction point.

Displacement	Percentage contribution to displacement by strain-energy of:-					
	Bending in plane of wheel, or about axis YY of section.	Bending about axis Ox of section.	Direct force.	Shearing force.	Non-uniform torsion.	
					1st term. (St. Venant torsion term).	2nd term. (Warping restraint term).
$\delta_{RZ}^{F_R}$	48	1	1	5	39	6
$\delta_{TZ}^{F_R}$	71	< 1	< 1	1	31	-5
$\phi_{RZ}^{F_R}$	-	-1	-	-	117	-16
$\phi_{TZ}^{F_R}$	-	3	-	-	84	13
$\delta_{TZ}^{F_T}$	53	< 1	< 1	4	38	4
$\phi_{RZ}^{F_T}$	-	1	-	-	90	9

The predominant strain-energy term for the deflections is clearly that due to bending in the plane of the wheel, with the St. Venant torsion component of non-uniform torsion also very significant. This latter term is, of course, predominant for the rotations. The warping restraint component of non-uniform torsion is small in comparison with the St. Venant torsion component, being about 1/7th of the latter or less. It is evident throughout that only strain-energy of in-plane bending and strain-energy of non-uniform torsion need be considered, and that the other three terms can be neglected.

3B v Assembly condition at the bucket/rim junction - evaluation of assembly actions and total centrifugal stresses

The free rotating discontinuities to be eliminated by assembly at the bucket/rim junction, are all in the plane of the wheel, and are as illustrated in Fig.18. With regard to in-plane displacements, assembly is assumed to be achieved at position G_{1A} Fig.22, at which point the final position of the tangent to the bucket is $G_{1A}T$. The assembly actions F_{R2}, F_{T2}, etc., on the bucket, initially at G_{12}, therefore induce displacements δ_{R2}, δ_{T2} and ϕ_{P2} as shown. Considering the assembly actions F_{R1}, F_{T1}, etc. on the rim, initially at G_{11}, none of these actions is, of course, associated with tangential displacement, which the rim may sustain as a whole-body rotation, without deformation, about the wheel axis Z. For assembly at G_{1A} therefore, the rim rotates about Z as a whole-body, from G_{11} to G'_{11}, or through the angle $\gamma_1 = \dfrac{\Delta_{T2,TOT} + \delta_{T2}}{q}$. The assembly actions F_{R1}, F_{T1}, etc., now initially at G'_{11}, induce deformations δ_{R1} and ϕ_{P1} of the rim for assembly and compatibility of deflection and rotation, at G_{1A}. The order in which the whole-body displacement and the assembly action displacements of the rim are considered to take place, is, of course, immaterial, and assembly action deformations δ_{R1} and ϕ_{P1} could be considered firstly, displacing G_{11} to G''_{11} with appropriate tangent position $G''_{11}T''$, whole body rotation γ_1 subsequently taking place to G_{1A} and $G_{1A}T$. With reference to Fig.22 then, on the assumption that the joint between rim and bucket is rigid, the following equations must be satisfied for compatibility of the in-plane displacements:-

$$\delta_{R1} + \Delta_{R1} = \delta_{R2} + \Delta_{R2\,TOT} \qquad (3B.81)$$

$$\phi_{P1} - \frac{\Delta_{T2,TOT} + \delta_{T2}}{q} = \phi_{P2} - \Phi_{P2} \qquad (3B.82)$$

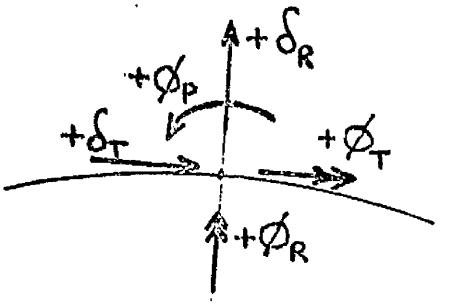

SIGN CONVENTION FOR IN-PLANE & TRANSVERSE PLANES ASSEMBLY ACTION DISPLACEMENTS.

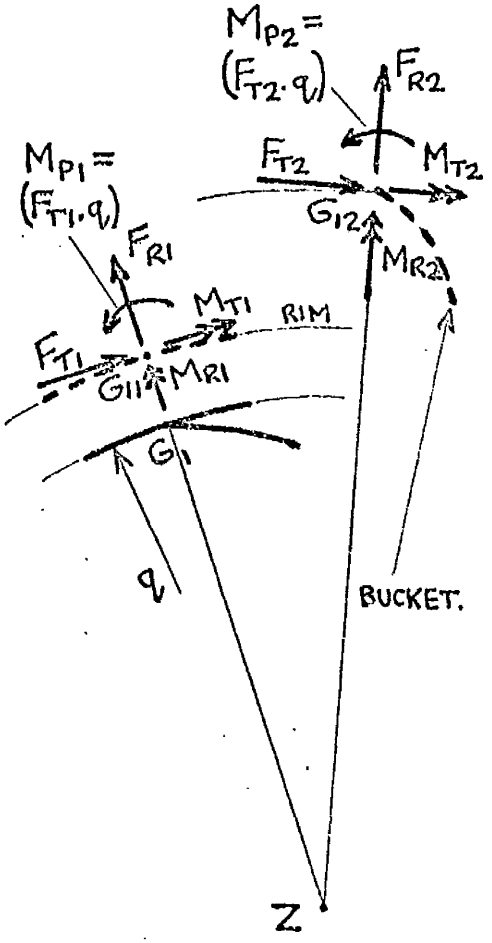

ASSEMBLY ACTIONS, SUFFIX 1 ON RIM, SUFFIX 2 ON BUCKET, CAUSING FINAL ASSEMBLY OF ROTATING RIM & BUCKET AT G1A & G1A T.
THE ASSEMBLY ACTIONS AS SHOWN ARE +VE.

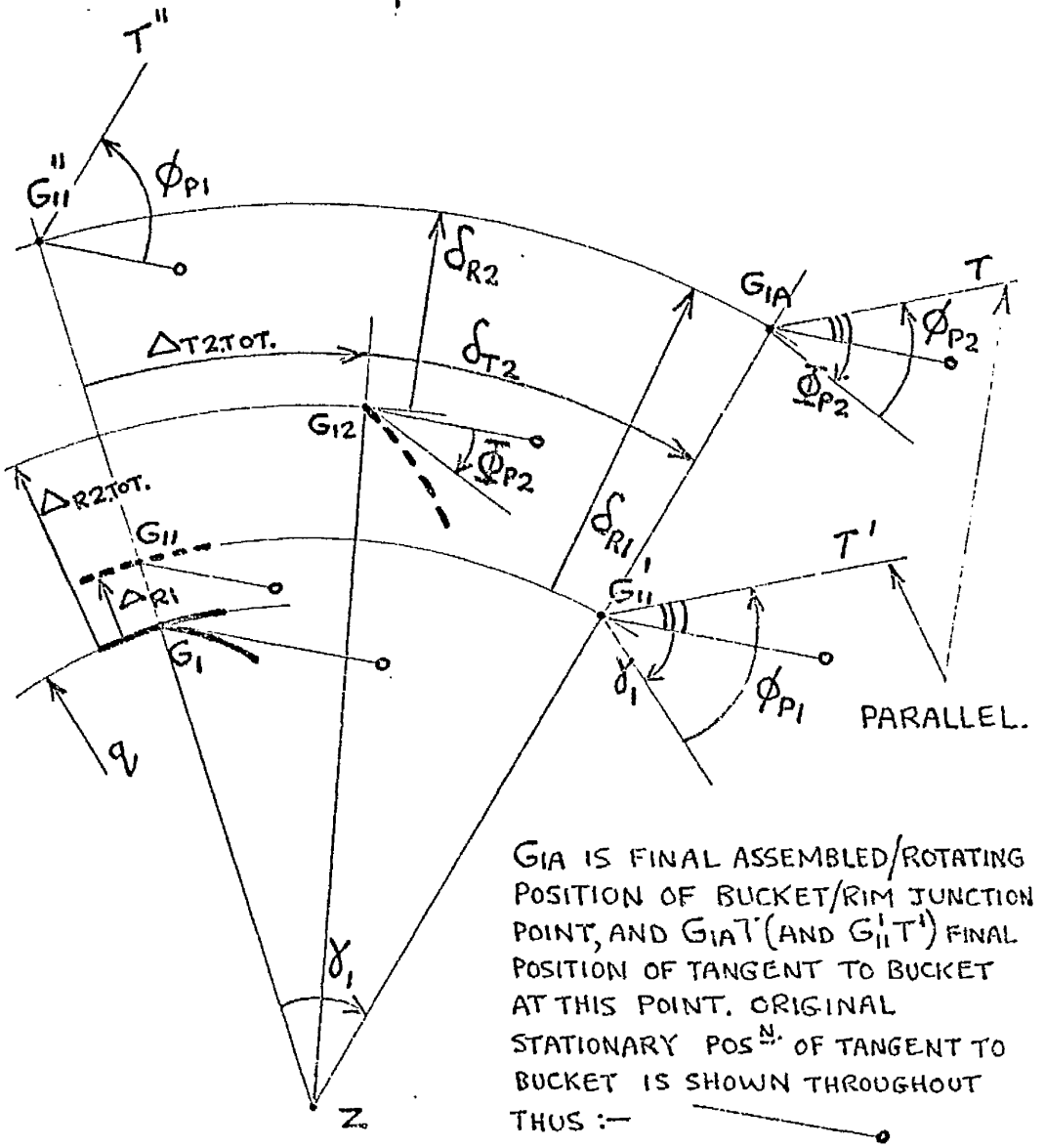

G1A IS FINAL ASSEMBLED/ROTATING POSITION OF BUCKET/RIM JUNCTION POINT, AND G1A T' (AND G11' T1') FINAL POSITION OF TANGENT TO BUCKET AT THIS POINT. ORIGINAL STATIONARY POSN. OF TANGENT TO BUCKET IS SHOWN THROUGHOUT THUS :—

ANALYSIS OF FREE ROTATING & ASSEMBLY ACTION DISPLACEMENTS IN PLANE OF WHEEL, FOR COMPATIBILITY IN ASSEMBLED/ROTATING CONDITION.
FREE ROTATING DISPLACEMENTS TO POINTS G11 & G12 ARE AS IN FIG. 18.

FIG. 22. DIAGRAM SHOWING THE ASSEMBLY ACTIONS & THE ANALYSIS OF DISPLACEMENTS IN THE PLANE OF THE WHEEL FOR THE ASSEMBLED/ROTATING CONDITION OF BUCKET AND RIM AT THE JUNCTION POINT.

The sign convention pertinent to the in-plane and transverse planes assembly action displacements is given in Fig.22.

Since there are no free rotating discontinuities in the transverse planes, the assembly action displacements of bucket and of rim in the transverse planes, must be equal for compatibility. If ϕ_{R1} and ϕ_{T1} are the assembly action displacements of the rim, and ϕ_{R2} and ϕ_{T2} the assembly action displacements of the bucket, then for compatibility of the transverse displacements:-

$$\phi_{R1} = \phi_{R2} \tag{3B.83}$$

$$\phi_{T1} = \phi_{T2} \tag{3B.84}$$

For equilibrium in the assembled condition:-

$$F_{R1} + F_{R2} = 0 \tag{3B.85}$$

$$F_{T1} + F_{T2} = 0 \tag{3B.86}$$

$$M_{R1} + M_{R2} = 0 \tag{3B.87}$$

$$M_{T1} + M_{T2} = 0 \tag{3B.88}$$

The sign convention pertinent to the assembly actions is given in Fig.22.

In the compatibility equations (3B.81) to (3B.84) the assembly action displacements comprise, in general, components due to all the assembly actions, e.g. $\delta_{R2} = \delta_{R2}^{F_{R2}} + \delta_{R2}^{F_{T2}} + \delta_{R2}^{M_{P2}=(F_{T2}\cdot q)} + \delta_{R2}^{M_{R2}} + \delta_{R2}^{M_{T2}}$, taken algebraically according to sign convention. So by means of the displacement/action relations derived in sections 3B iii and 3B iv, these compatibility equations may be written in terms only of the assembly actions F_{R1}, F_{R2}, etc. and of the free rotating discontinuities. The eight compatibility and equilibrium simultaneous equations (3B.81) to (3B.88) are then solved directly to find the eight assembly actions F_{R1}, F_{R2}, etc. in magnitude and direction.

The corresponding assembly action stresses are subsequently calculated/

calculated from the appropriate expressions of sections 3B iii and 3B iv. Appropriate superposition of the assembly action stresses and the free rotating stresses of sections 3B i and 3B ii, finally determines the total centrifugal stresses in bucket and rim.

For the $16\frac{1}{2}$ in. cast steel Turgo wheel at normal working speed, all the terms relevant to the application of the compatibility and equilibrium simultaneous equations have already been derived numerically. Therefore, in accordance with the sign conventions of Figs.21 and 22, these equations are as follows:-

$$0.49832\,F_{R1} = 8.75688\,F_{R2} + 8.03753\,F_{T2} - 17.64013\,F_{T2} + 0.95256M_{R2} - 1.81235\,M_{T2} + (8100 - 1080). \quad (3B.81).$$

$$0.11772\,F_{T1} - \frac{11,080}{13.329} - \frac{1}{13.329}\left\{8.03753\,F_{R2} + 19.44856\,F_{T2} - 24.01328F_{T} + 3.75568\,M_{R2} - 0.95256\,M_{T2}\right\}$$
$$= -1.32147\,F_{R2} - 1.79787\,F_{T2} + 6.27435\,F_{T2} - 2080. \quad (3B.82).$$

$$0.00881\,M_{R1} = 0.95256\,F_{R2} + 3.75568\,F_{T2} + 1.70713\,M_{R2} - 0.43298\,M_{T2}. \quad (3B.83).$$

$$3.82364\,M_{T1} = -1.81235\,F_{R2} - 0.95256\,F_{T2} - 0.43298\,M_{R2} + 0.82380\,M_{T2} \quad (3B.84).$$

$$F_{R1} + F_{R2} = 0 \quad (3B.85).$$

$$F_{T1} + F_{T2} = 0 \quad (3B.86).$$

$$M_{R1} + M_{R2} = 0 \quad (3B.87).$$

$$M_{T1} + M_{T2} = 0 \quad (3B.88).$$

Solving/

Solving these equations gives:-

$F_{R2} = -561.07$ lb., $F_{T2} = +211.38$ lb.,

$\therefore M_{P2} = (F_{T2}.q) = +2821.32$ lb.ins., $M_{R2} = -200.64$ lb.ins.,

$M_{T2} = -193.97$ lb.ins.

The corresponding assembly actions, suffix 1, on the rim, have the same values as these, but have opposite signs.

Total centrifugal stresses in the bucket

Knowing the magnitudes and directions of the assembly actions on the bucket, the induced actions $M_{\theta Y2}$, $M_{\theta X2}$, $P_{\theta 2}$ and $V_{\theta X2}$ due to all the assembly actions are readily determined, $M_{\theta Y2}$ from equations (3B.27), (3B.46) and (3B.59), $M_{\theta X2}$ from equations (3B.28), (3B.47), (3B.63) and (3B.72), $P_{\theta 2}$ from equations (3B.29) and (3B.48), and $V_{\theta X2}$ from equations (3B.30) and (3B.49). The distribution of $M_{\theta Y2}$ with θ is shown in Fig.23, together with the corresponding in-plane free rotating bending moment M_{θ} from Fig.16. Superposition of M_{θ} and $M_{\theta Y2}$ gives the total centrifugal in-plane bending moment $M_{\theta Y.TOT}$ as indicated. Similar distributions with θ are given in Fig.24(a) for direct forces $P_{\theta 2}$, P_{θ} from Fig.16, and their algebraic sum $P_{\theta.TOT}$, the total centrifugal direct force. The variation with θ of bending moment $M_{\theta X2}$ induced only by the assembly actions, is plotted in Fig.24(b), from which $M_{\theta X2}$ is evidently small in comparison with $M_{\theta Y.TOT}$ of Fig.23. Graphs may likewise be drawn for shearing forces $V_{\theta X2}$ and V_{θ}, from Fig.16. Superposition gives $V_{\theta X.TOT}$ which, in general, has been found to be less than V_{θ}. The resulting shear stresses have been calculated and are of little significance, so these shearing forces are not considered further.

The induced non-uniform torsion shear and direct stresses due to all the assembly actions, may also be found from the relevant equations of section/

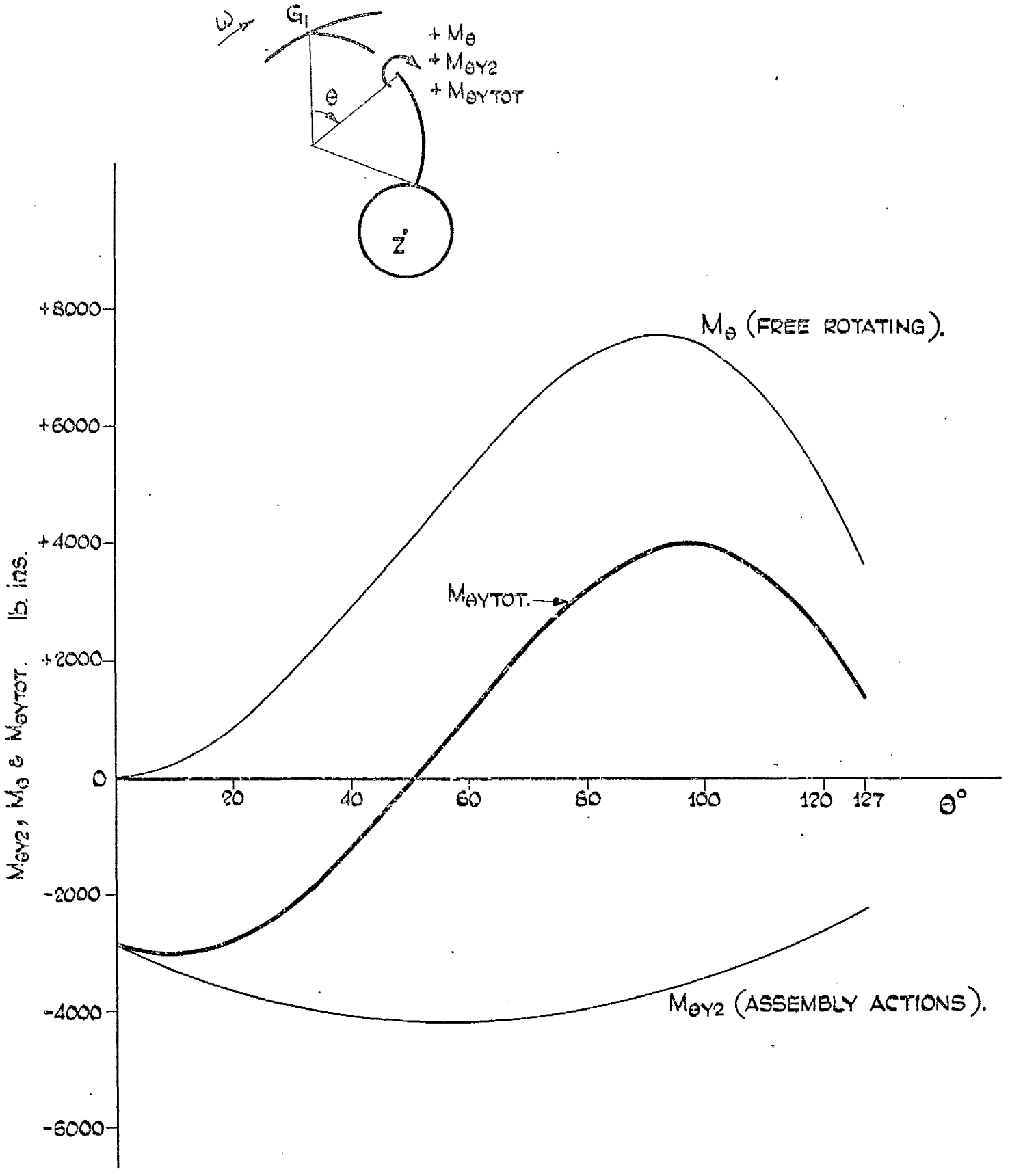

FIG 23. DISTRIBUTIONS WITH θ OF IN-PLANE BENDING MOMENTS, $M_{\theta Y2}$ DUE TO ASSEMBLY ACTIONS, M_θ FREE ROTATING (FIG. 16) AND THEIR RESULTANT $M_{\theta YTOT}$, ALL ON THE EQUIVALENT BUCKET OF THE $16\frac{1}{2}$ IN CAST STEEL TURGO WHEEL AT NORMAL WORKING SPEED. $M_{\theta YTOT}$ IS THE TOTAL CENTRIFUGAL IN-PLANE BENDING MOMENT ON THE BUCKE

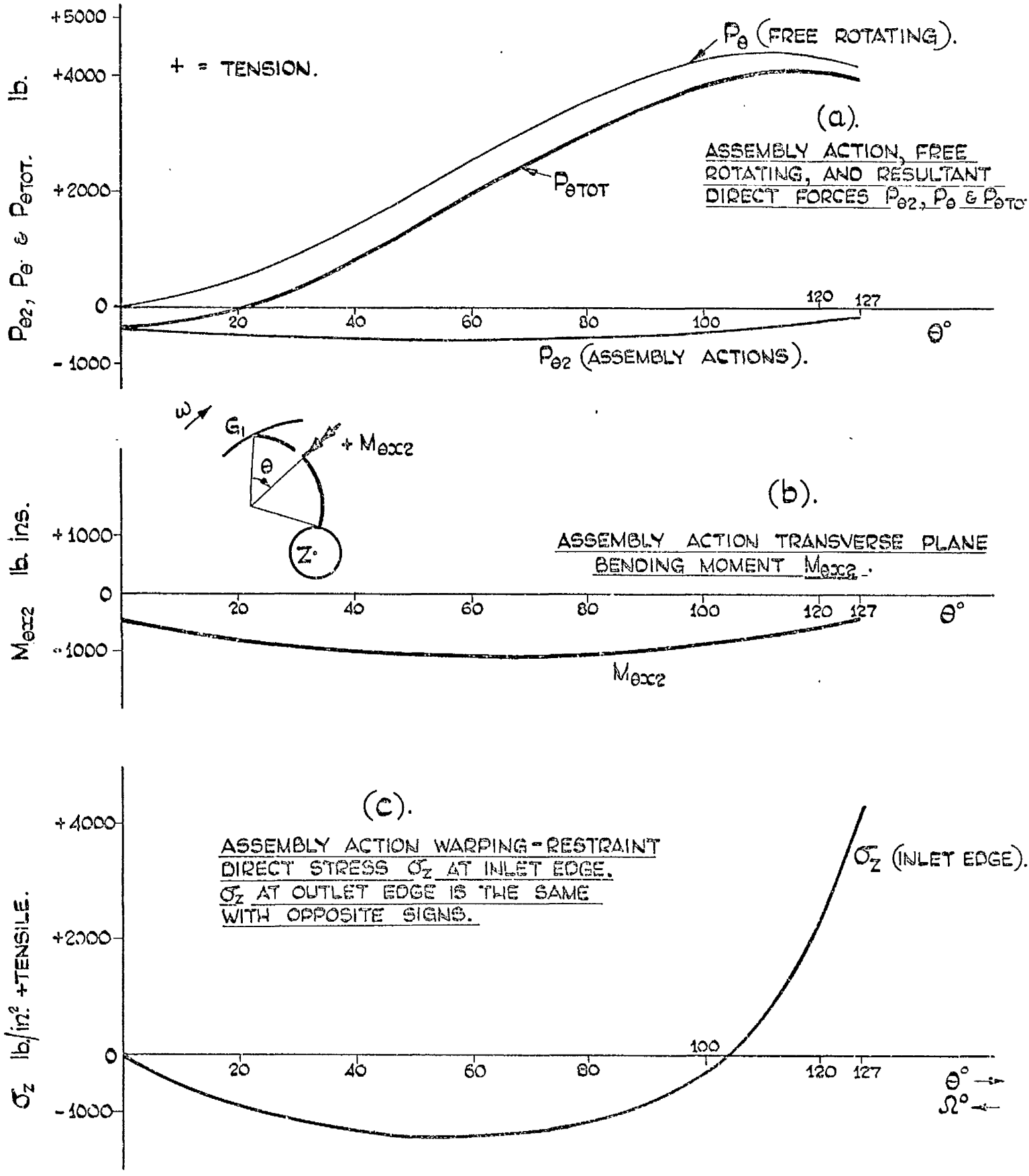

FIG. 24. DISTRIBUTIONS WITH θ OF DIRECT FORCES $P_{\theta 2}$, P_θ (FROM FIG. 16) AND THEIR RESULTANT $P_{\theta TOT}$, BENDING MOMENT M_{exc2} AND WARPING-RESTRAINT DIRECT STRESS σ_z AT INLET EDGE, ALL ON THE EQUIVALENT BUCKET OF THE 16½ IN. CAST STEEL TURGO WHEEL AT NORMAL WORKING SPEED. (CENTRIFUGAL LOADING).

section 3B iv. The St.Venant torsion and the warping restraint shear stresses $\tau_{S.V.}$ and τ_z respectively, have been determined and found to be of negligible significance. The warping restraint direct stresses σ_z however, are appreciable, having been calculated from equations (3B.38), (3B.52), (3B.66) and (3B.75). These stresses are maximum on the bucket edges and the distribution with Θ (or Ω) of σ_z on the inlet edge is shown in Fig.24(c). Fig.25 depicts the distribution of σ_z over the parabolic cross-section of the equivalent bucket at $\Theta = 127^\circ$, ($\Omega = 0$).

The direct stresses due to $M_{\theta Y.TOT}$, $M_{\theta XZ}$ and $P_{\theta.TOT}$ are simply determined by appropriate application of equations (3B.6) and (3B.7). $M_{\theta Y.TOT}$ is found to be by far the dominant action in regard to stresses and, since maximum bending stresses occur there, the bucket edges are critical as the locations of the maximum total direct stresses on the cross-section. Total direct stresses on the edges are calculated by algebraic superposition of the appropriate stresses due to $M_{\theta Y.TOT}$, $M_{\theta XZ}$ and $P_{\theta.TOT}$ together with the appropriate edge values of σ_z. Fig.26 shows the variation with Θ of the total direct stresses on the inlet and outlet edges of the bucket. Overall, the outlet edge is more highly stressed in tension than the inlet edge. The maximum centrifugal stress in the bucket, 8,750 lb/in.^{2} tension, occurs on the outlet edge at about $\Theta = 94^\circ$, which, from Fig.9, is in the vicinity of the pitch circle. Comparing this value with the corresponding maximum free rotating direct stress of + 14,050 lb/in.^{2} at about the same location, it is clear that the effect of rim restraint on the bucket is a reduction of some 38% in the maximum free rotating stress.

Total centrifugal stresses in the rim

Knowing the magnitudes and directions of the assembly actions F_{R1}, F_{T1}, etc. on the rim, the corresponding direct stresses are determined from/

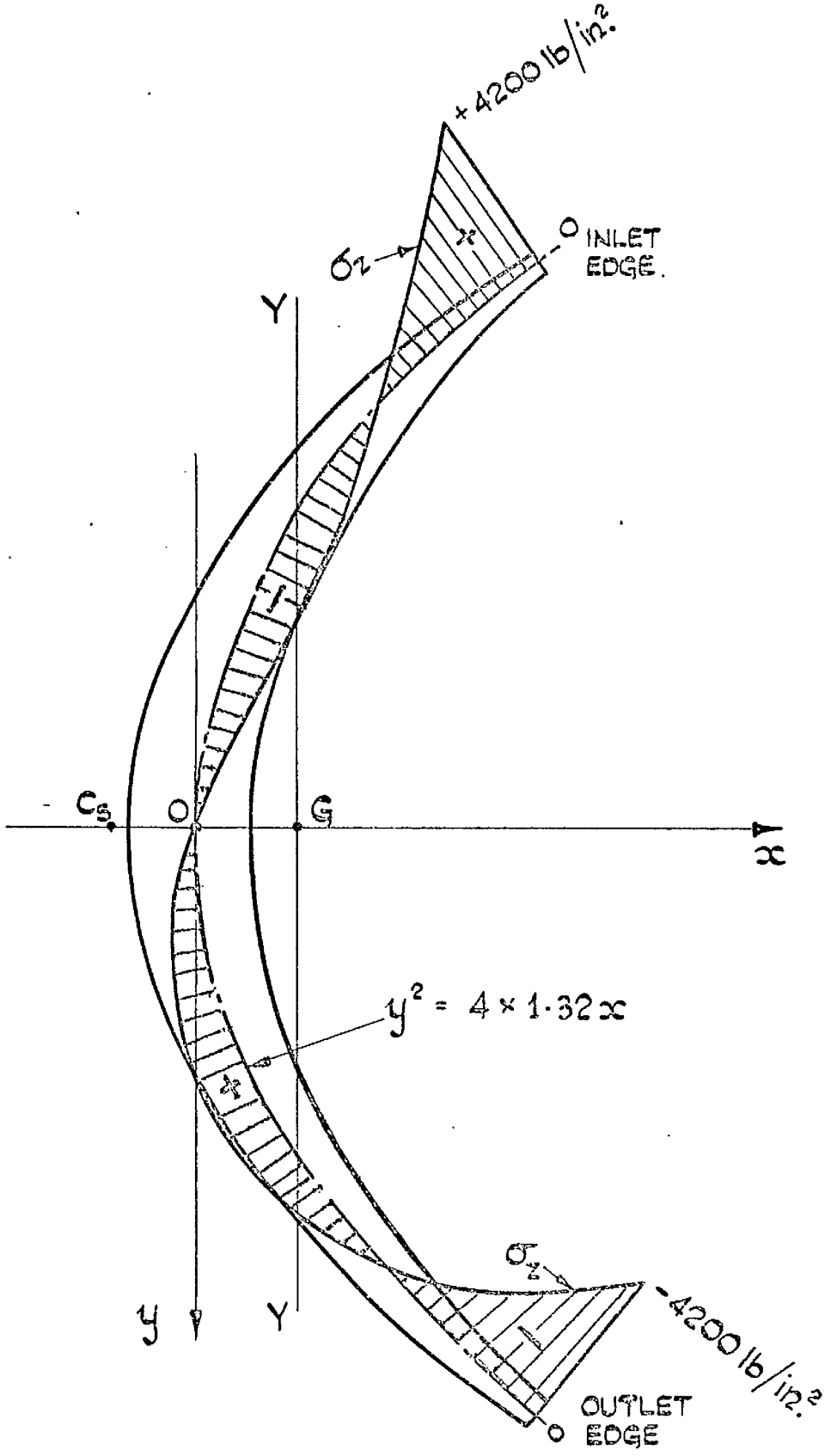

FIG. 25. DISTRIBUTION OF ASSEMBLY ACTION WARPING-RESTRAINT DIRECT STRESS σ_z (+ TENSILE) OVER THE PARABOLIC CROSS-SECTION OF THE EQUIVALENT BUCKET, AT $\theta = 127°$. ($\Omega = 0$), FOR THE $16\frac{1}{2}$ IN. CAST STEEL TURGO WHEEL AT NORMAL WORKING SPEED. (CENTRIFUGAL LOADING.).

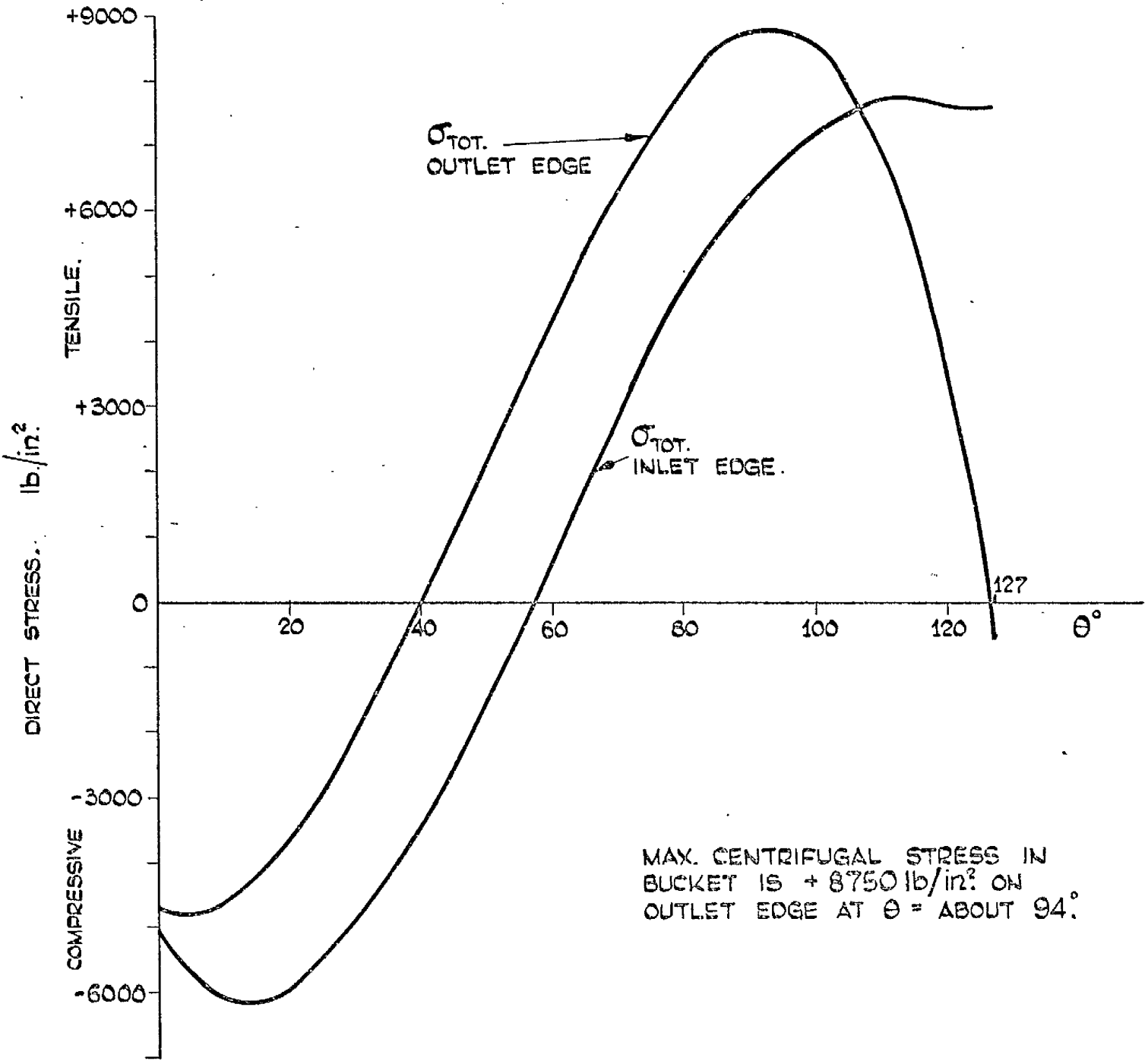

FIG. 26. DISTRIBUTION WITH θ OF THE TOTAL CENTRIFUGAL DIRECT STRESSES ON THE INLET AND OUTLET EDGES OF THE EQUIVALENT BUCKET OF THE $16\frac{1}{2}$ IN. CAST STEEL TURGO WHEEL AT NORMAL WORKING SPEED.

from equations (3B.19) and (3B.25), and the shear stresses from equations (3B.21) and (3B.23). The latter stresses have been found to be negligibly small, the maximum value not exceeding 400 lb/in^2. The assembly action direct stresses are superposed on the free rotating direct stress of + 2430 lb/in^2, to give the total direct stress distribution over the equivalent rim section as indicated in Fig.27. The linear distribution arises from the bending moment about $Y'Y'$, induced by "inversion moment" assembly action M_{T1} which acts about the rim section as shown.
The maximum centrifugal stress in the rim is 4100 lb/in^2 circumferential tension over the complete outlet side.

Total centrifugal stresses in the hub

As previously mentioned, and as confirmed by the assembly action analysis, due to the rim restraint, the maximum centrifugal stress in the hub would be expected to be less than 1680 lb/in^2 tension, this being the maximum free rotating stress which occurs at the bore.

From a survey of the method of calculation, it is noteworthy that:-

(1) All the induced actions on the bucket at Θ, due to the free rotating condition and due to the assembly condition, are directly proportional to $D.\omega^2$. So the free rotating stresses, the assembly action stresses, and therefore the total stresses are directly proportional to $D.\omega^2$. This applies also to the rim.

(2) The free rotating stresses are independent of the elastic constants, but the assembly action stresses are dependent on ν, so the total stresses are functions of ν. For materials of the same, or nearly the same ν, the same stresses will be determined, other factors being constant.

The maximum centrifugal stress of + 8750 lb/in^2, or about + 4 T/in^2, in the 16½ in.cast steel Turgo wheel at normal working speed, is of reasonable order, and occurs in a fairly small localised region of the bucket/

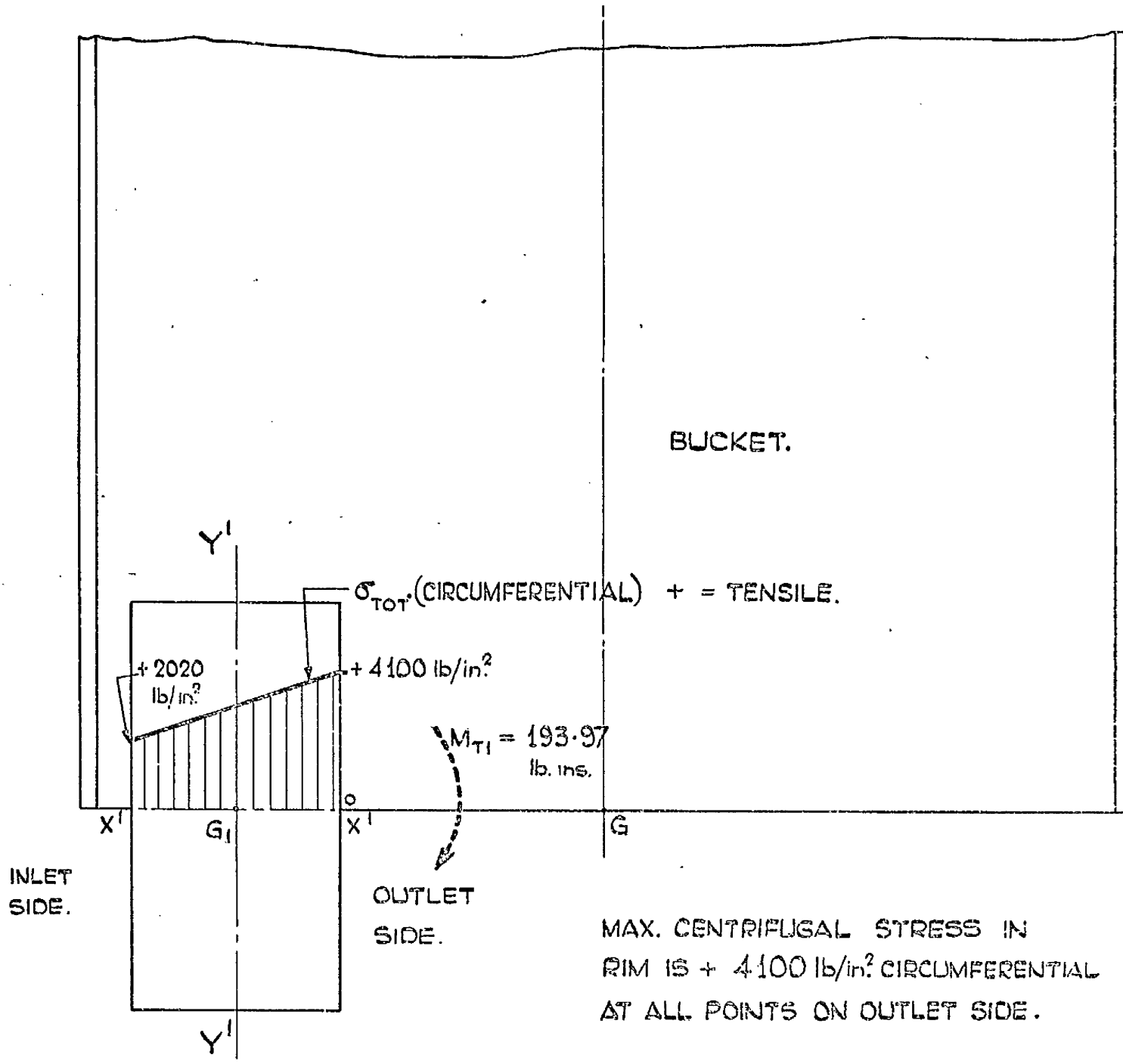

FIG. 27. DISTRIBUTION OF THE TOTAL CENTRIFUGAL DIRECT STRESSES (CIRCUMFERENTIAL) ON THE EQUIVALENT RIM CROSS-SECTION, FOR THE 16½". CAST STEEL TURGO WHEEL AT NORMAL WORKING SPEED.

bucket outlet edge. Together with some reasonable value for the corresponding jet loading stress, which might be guessed at this stage, it is not as high as would be expected to lead to failure at the normal working condition. Referring to Table 1, the corresponding maximum centrifugal stress at overspeed, when the jet loading stress is zero, is given by:-

$$+ 8{,}750 \times \left(\frac{2340}{1300}\right)^2 = + 28{,}400 \text{ lb/in}^2 \doteqdot + 12.7 \text{ T/in.}^2$$

This value of stress, obtaining perhaps only once or a few times in the service life of the wheel, would also be unlikely to lead to failure.

With reference to the subsequent experimental analyses of the $16\frac{1}{2}$ in. cast aluminium Turgo wheel, pertinent approximate theoretical centrifugal actions, stresses and displacements are easily determined from the corresponding values calculated for the cast steel wheel. Table 1 indicates that both materials have the same value of Poisson's Ratio $\nu = 0.31$, and that the aluminium has density D equal to one-third that of steel. For the same normal working speed of 1,300 r.p.m., therefore, the actions and stresses in the aluminium wheel will be one-third of the corresponding values for the steel wheel. In the aluminium wheel, actions $M_{\theta x.TOT}$, $P_{\theta.TOT}$, $M_{\theta x2}$ and total direct stresses on the bucket edges and in the rim are all of particular interest. Although these stresses appear small in comparison with the corresponding ones in the steel wheel, the associated strains will be of similar order in the two wheels, since Young's Modulus E for the aluminium is little more than one-third that for the steel.

3C. APPROXIMATE STRESSES AND DEFORMATIONS DUE TO JET LOADING

In the absence of any information regarding the distribution of loading on a Turgo wheel bucket subject to jet action, a reasonable loading distribution is assumed, in the light of data, from Fig.6 and from EDEL[5], pertinent to jet action on a stationary Pelton bucket. The comparatively small axial component of the jet force is neglected and the assumed loading acts solely in the plane of the wheel, identically distributed on three adjacent buckets.

The three jet-loaded buckets are initially considered as detached from the rim at the junction points, being rigidly connected to the hub, itself assumed rigid and fully-supported, that is, keyed to the turbine driving shaft. This is called the "rimless jet-loaded bucket condition" in which actions, statically determinate and all in the plane of the wheel, are set-up only in the three adjacent buckets due to the applied jet loading. This condition corresponds very closely to the "free rotating condition" of the buckets in section 3B ii, and the stresses at Θ in the bucket and the displacements at the junction point on the bucket are calculated in identical fashion to those of that section. The junction point displacements of a rimless jet-loaded bucket are of course, radial and tangential deflections and a rotation in the plane of the wheel, just as in the free rotating condition. In the rimless jet-loaded condition, however, these displacements also represent the discontinuities of displacement between the bucket-tip of the jet-loaded bucket and the junction point on the rim of the "remainder of the wheel". The remainder of the wheel comprises of course, a wheel less the three adjacent loaded buckets, and since the hub is assumed rigid and fully-supported, the remainder of the wheel in this condition, carries no loading whatsover and does not displace.

To/

To eliminate the displacement discontinuities, the "assembly condition" is incurred. This resembles its counterpart for centrifugal loading in part 3B, but differs essentially in that the assembly actions here are neither rotationally symmetrical nor self-equilibrating. They are, of course, mutually equilibrating in the same sense as are those of the centrifugal loading analysis, that is in the sense expressed by equations (3B.85) to (3B.88). Unlike the rim in the centrifugal loading analysis, the rim of the remainder of the wheel is integral with, and supported by, all the unloaded buckets which are rigidly connected to the fully-supported rigid hub. The assembly actions at a jet-loaded bucket/rim junction point are thus fully three-dimensional, being six in number, - forces F_R, F_T, F_A, radial, tangential and axial respectively, and moments M_P, M_R, M_T, in the plane of the wheel, about a radius and about a tangent respectively, as illustrated diagrammatically in Fig.28. At each of the three junction points G_1, G_{1B} and G_{1C}, six such assembly actions obtain. The values of corresponding actions at the three junction points will be different in general.

Considering the junction points on the rim of the remainder of the wheel, it is evident that the derivation, for each assembly action, of the displacement/action relations relevant to these junction points on this very highly redundant structure, is a task of very formidable magnitude, no matter whether strain-energy methods or other methods of derivation are applied. In a current design Turgo wheel, the rim on the remainder of the wheel connects to nineteen buckets. It is clearly totally impracticable therefore, to attempt to derive the pertinent displacement/action relations in general terms, and hardly less impracticable to attempt to calculate their values numerically for particular applications. Moreover, were such a derivation or calculation to be carried out, the subsequent assembly conditions at the junction points would present a correspondingly complex calculation. Such an approach, even via computer methods, is patently/

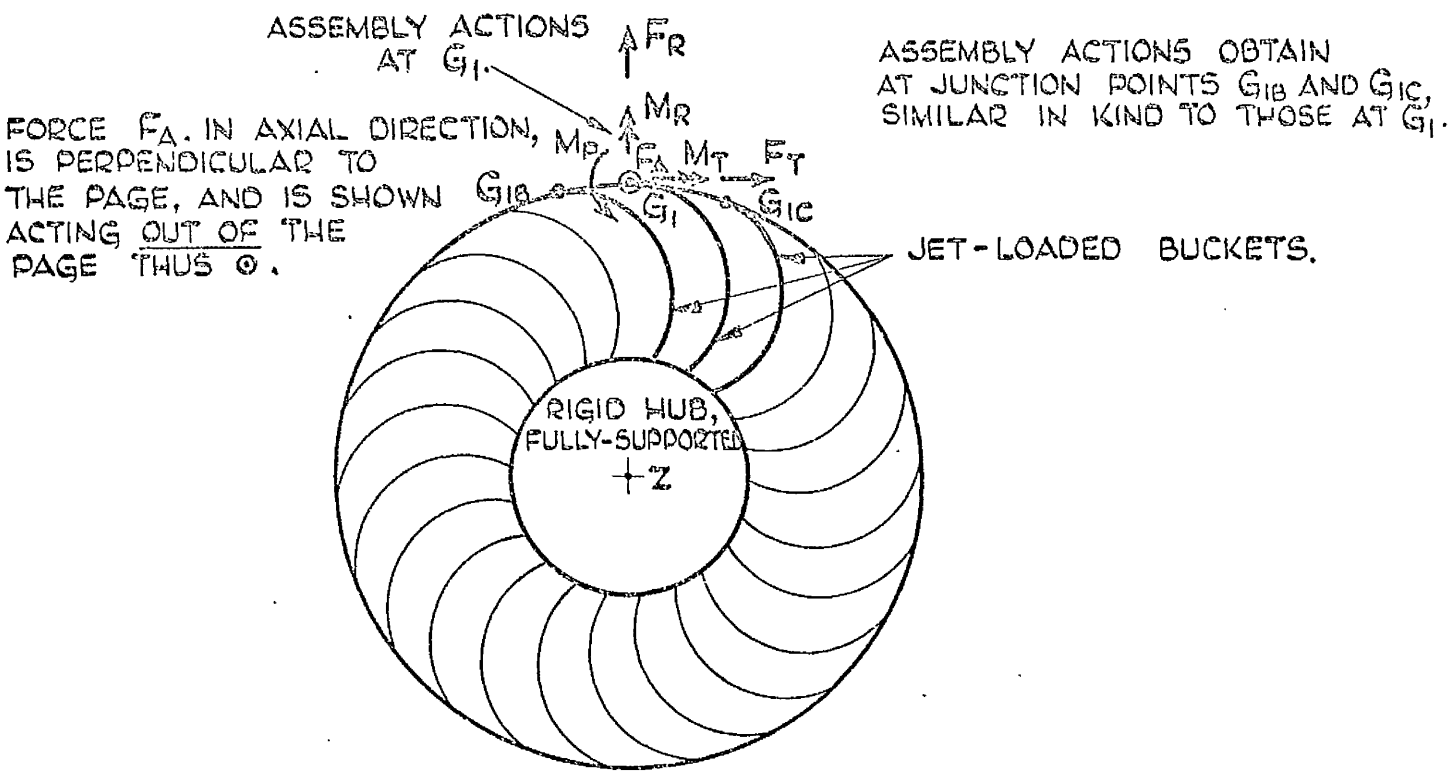

FIG. 28. DIAGRAMMATIC SKETCH OF THE SIX ASSEMBLY ACTIONS AT JUNCTION-POINTS OF RIM AND TIPS OF THE JET-LOADED BUCKETS.

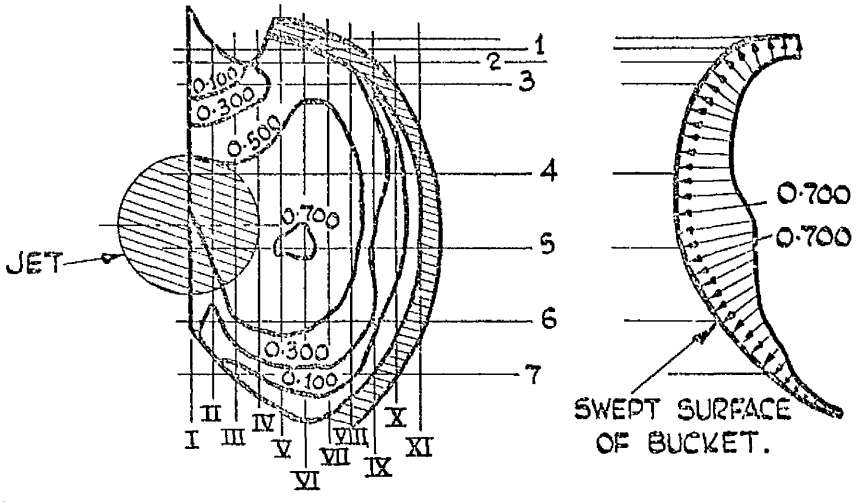

(a). PLAN VIEW OF HALF-BUCKET OF FIG. 6, SHOWING THE SAME PRESSURE CONTOURS AND SECTIONS.

PRESSURE DISTRIBUTION PROFILE AT SECTION VI.

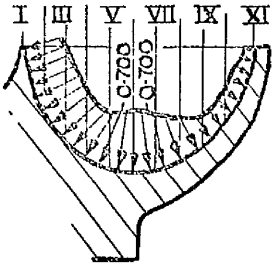

PRESSURE DISTRIBUTION PROFILE AT SECTION 5.

ISOBAR UNITS ARE kg/cm^2. ($1 kg/cm^2 = 14.2 lb/in^2$)

FIG. 29. CONTOURS AND PROFILES OF MEASURED PRESSURE DISTRIBUTION DUE TO JET ACTION ON A STATIONARY PELTON BUCKET; AFTER EDEL.[5]

patently inappropriate to this essentially simple approximate analysis and cannot reasonably be entertained. For simplicity therefore, it is assumed that corresponding assembly actions are identical on the three buckets at G_1 G_{1B} and G_{1C}, so necessitating analysis for only one jet-loaded bucket. It is further assumed, subsequent to a reasoned case, that the remainder of the wheel may be simulated by a fully-fixed arch, of the rim radius and cross-section, subtending an angle of 180^{o} at the wheel axis and with the pertinent junction point at its apex. Using strain-energy methods, the displacement/action relations relevant to this junction point are then obtained for each assembly action.

For the junction point on the jet-loaded bucket, rigidly connected to the rigid hub, most of the displacement/action relations have been derived previously for the centrifugal loading analysis, and so are extracted from section 3B iv. The other displacement/action relations, e.g. associated with axial displacements and with axial force F_A, are determined in exactly similar fashion to those of section 3B iv.

The twelve assembly condition simultaneous equations together with the displacement/action relations, provide on solution, the magnitudes and directions of the six assembly actions. The assembly action stresses and hence the total jet-loading stresses, are then calculated for locations on the bucket and for the junction point on the rim.

To investigate the rationality of the "arch" assumption, pertaining to the assembly actions on the rim of the remainder of the wheel, the assembly condition calculation is repeated for the hypothetical case of a fully-fixed support at the bucket junction point, and again for the hypothetical case of restraint provided only by two buckets rigidly attached to the hub, co-linear with the jet-loaded bucket but rigidly connected to it only at the junction point. The former case is obviously a more stiff restraint than would be applied by the remainder of the wheel, the latter a more flexible restraint. Results derived from the "arch" assumption are compared with results determined on these two bases.

3C i The distribution of loading on a bucket due to jet action

No investigation has yet been made of the distribution of pressure due to jet action on a bucket of a Turgo impulse wheel. The pressure distribution will vary as the bucket rotates, and it may reasonably be assumed that the critical condition in respect of jet loading stresses will be that corresponding to the development of the maximum value of the resultant jet force on the bucket. Fig.6, taken from EDEL[5], shows contours of measured pressure distribution, due to jet action on a stationary Pelton bucket in a condition roughly corresponding to that for maximum jet force on an identical rotating bucket. The contours are drawn on the developed swept surface of a half-bucket. Details of the geometry of this Pelton bucket are given by EDEL[5] and have enabled the more meaningful Fig.29 to be constructed. The pressure contours of Fig.6 are transferred to a plan view of the half-bucket, Fig.29(a), which shows the same sections as Fig.6. From this plan view and from details of the sections, profiles of pressure distribution are constructed at section VI and at section 5 as shown, section VI being roughly the mid-half-bucket section in the plane of the wheel, and section 5 being roughly the section tangential to the pitch circle. It is evident that the pressure peak occurs in the "hollow" of the half-bucket, roughly in way of the pitch circle. Clearly this is a fairly predictable result.

It is not unreasonable to assume that the pressure distribution on a Turgo wheel bucket for the condition of the development of maximum resultant jet force, will be somewhat similar in character to that depicted in Fig.29. The axial component of the jet force on the Turgo wheel bucket is comparatively small and may be neglected, so the loading intensity on the bucket may reasonably be assumed not to vary in the axial direction. This may also be expressed by saying that the loading intensity distribution over any meridional parabolic section of the equivalent bucket, may be assumed/

assumed to be uniform, a condition remotely simulating the approximately corresponding condition in Fig.29. The more important jet loading intensity distribution on the bucket in the plane of the wheel, is a function of angle Θ and, for the maximum jet force condition, is assumed to be given by the expression:-

$$W_\theta = \frac{W_{\theta=\frac{\alpha}{2}}}{1-\cos\frac{\alpha}{2}}\left[\cos\left(\frac{\alpha}{2}-\theta\right)-\cos\frac{\alpha}{2}\right] \qquad (3C.1),$$

W_θ being the jet loading intensity on the bucket in the plane of the wheel, at any angle Θ.

The variation of W_θ with Θ is indicated on Fig.30. The peak loading intensity is of course $W_{\theta=\frac{\alpha}{2}}$ and occurs in the "hollow" of the equivalent bucket, but offset a little from the pitch circle towards the bucket tip G_1. In character, this assumed loading intensity distribution is seen to be reasonably similar to the approximately corresponding pressure distribution profile of Fig.29.

Since it is assumed that there is no variation in loading intensity over meridional sections, the resultant torque about the wheel axis due to loading intensity distribution W_θ, may be determined straightforwardly. As the wheel efficiency is high, around 84%, and as the axial component of the jet force has been neglected, it is reasonable to equate this torque to one-third of $T_{B.H.P.}$, the brake horse power torque, for the purpose of calculating the value of $W_{\theta=\frac{\alpha}{2}}$ in a particular application. Three adjacent buckets are of course, assumed to be identically loaded by the jet. Thus from Fig.30:-

$$\left\{\int_0^{\alpha} W_\theta . k . d\theta . \cos\left(\frac{\alpha}{2}-\theta\right)\right\} h . \sin\left(\frac{\alpha}{2}+\beta\right) = \frac{T_{B.H.P.}}{3},$$

which, on substituting from equation (3C.1) and integrating, gives:-

$$W_{\theta=\frac{\alpha}{2}} . kh \frac{(\alpha-\sin\alpha).\sin\left(\frac{\alpha}{2}+\beta\right)}{2\left(1-\cos\frac{\alpha}{2}\right)} = \frac{T_{B.H.P.}}{3} \qquad (3C.2),$$

in which/

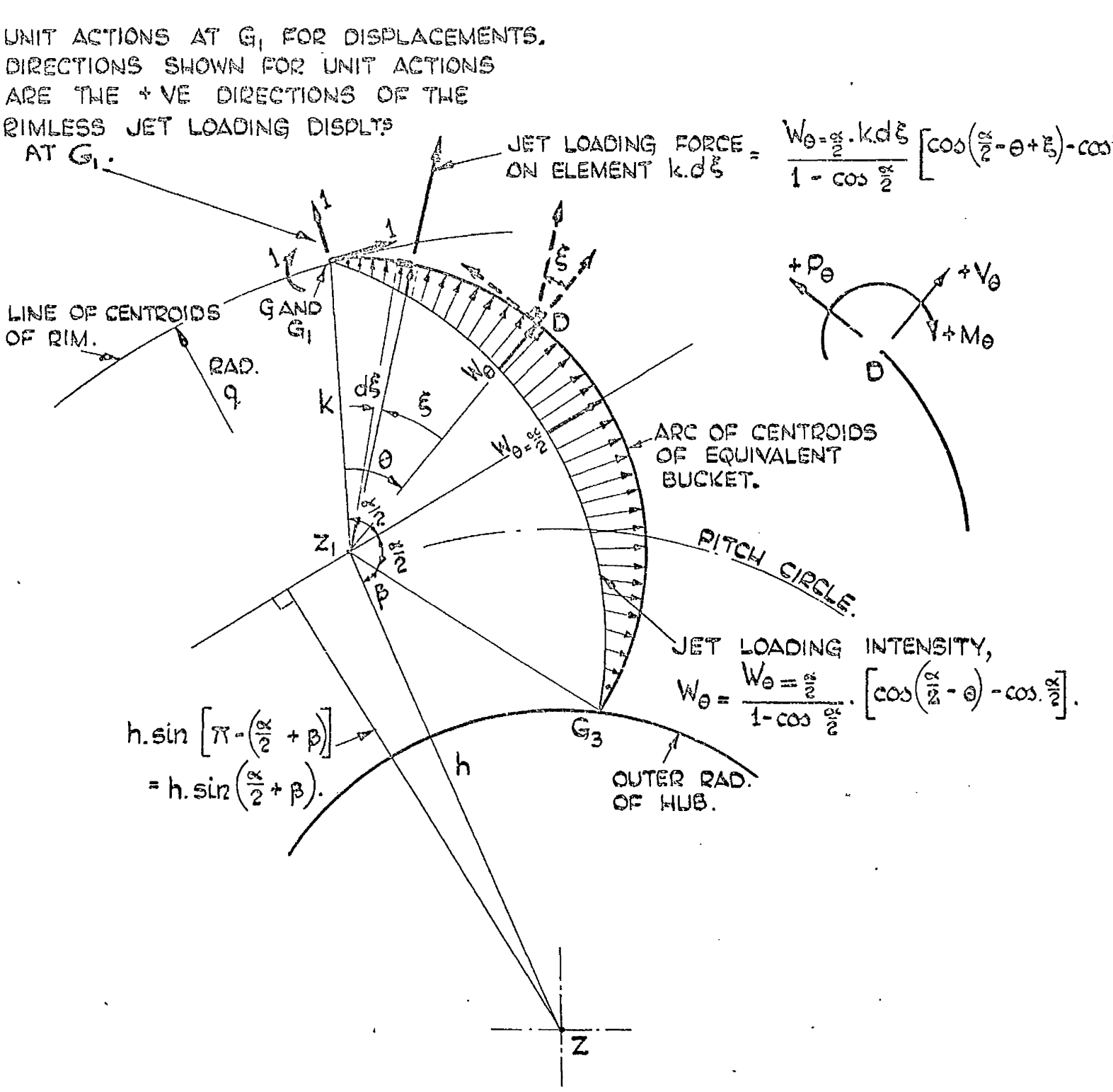

FIG. 30. DIAGRAM OF RIMLESS JET-LOADED BUCKET ON RIGID, FULLY-SUPPORTED HUB, SHOWING ASSUMED JET LOADING INTENSITY DISTRIBUTION W_θ, AND BASIS FOR ANALYSIS OF THE BUCKET FOR THIS CONDITION.

in which $$T_{B.H.P.} = \frac{(B.H.P.) \times 33000}{2\pi\,(R.P.M.)} \text{ lb. ft.}$$

From Table 1, the $16\frac{1}{2}$ in. cast steel Turgo wheel develops 1,013 B.H.P. at 1,300 R.P.M. under normal working conditions. The corresponding value of $W_{\theta=\frac{\alpha}{2}}$ is found from equation (3C.2) to be $W_{\theta=\frac{\alpha}{2}} =$ 306.82 lb/in., referring to Fig.12 for the dimensions appropriate to the assumed geometry.

3C ii The rimless jet-loaded bucket condition

Referring to Fig.30, at any section of the bucket at angle Θ the actions due to jet loading are bending moment M_θ, direct force P_θ and shearing force V_θ all in the plane of the wheel. Considering element $k.d\xi$ at angle ξ from Θ as shown, these actions on the bucket are given by:-

$$M_\theta = \int_0^\theta \frac{W_{\theta=\frac{\alpha}{2}}.k.d\xi}{1-\cos\frac{\alpha}{2}}\left[\cos\left(\frac{\alpha}{2}-\theta+\xi\right)-\cos\frac{\alpha}{2}\right]k.\sin\xi = \frac{W_{\theta=\frac{\alpha}{2}}.k^2}{1-\cos\frac{\alpha}{2}}\int_0^\theta\left[\cos\left(\frac{\alpha}{2}-\theta+\xi\right)-\cos\frac{\alpha}{2}\right]\sin\xi.d\xi$$

giving,

$$M_\theta = \frac{W_{\theta=\frac{\alpha}{2}}.k^2}{1-\cos\frac{\alpha}{2}}\left\{\frac{1}{2}\left[\cos\left(\frac{\alpha}{2}-\theta\right)-\theta\sin\left(\frac{\alpha}{2}-\theta\right)\right]-\cos\frac{\alpha}{2}\left(1-\frac{1}{2}\cos\theta\right)\right\} \qquad (3C.3)$$

$$P_\theta = \int_0^\theta \frac{W_{\theta=\frac{\alpha}{2}}.k.d\xi}{1-\cos\frac{\alpha}{2}}\left[\cos\left(\frac{\alpha}{2}-\theta+\xi\right)-\cos\frac{\alpha}{2}\right]\sin\xi = \frac{W_{\theta=\frac{\alpha}{2}}.k}{1-\cos\frac{\alpha}{2}}\int_0^\theta\left[\cos\left(\frac{\alpha}{2}-\theta+\xi\right)-\cos\frac{\alpha}{2}\right]\sin\xi.d\xi \ ,$$

giving,

$$P_\theta = \frac{W_{\theta=\frac{\alpha}{2}}.k}{1-\cos\frac{\alpha}{2}}\left\{\frac{1}{2}\left[\cos\left(\frac{\alpha}{2}-\theta\right)-\theta\sin\left(\frac{\alpha}{2}-\theta\right)\right]-\cos\frac{\alpha}{2}\left(1-\frac{1}{2}\cos\theta\right)\right\} \qquad (3C.4)$$

$$V_\theta = \int_0^\theta \frac{W_{\theta=\frac{\alpha}{2}}.k.d\xi}{1-\cos\frac{\alpha}{2}}\left[\cos\left(\frac{\alpha}{2}-\theta+\xi\right)-\cos\frac{\alpha}{2}\right]\cos\xi = \frac{W_{\theta=\frac{\alpha}{2}}.k}{1-\cos\frac{\alpha}{2}}\int_0^\theta\left[\cos\left(\frac{\alpha}{2}-\theta+\xi\right)-\cos\frac{\alpha}{2}\right]\cos\xi.d\xi \ ,$$

giving,

$$V_\theta = \frac{W_{\theta=\frac{\alpha}{2}}.k}{2\left(1-\cos\frac{\alpha}{2}\right)}\left\{\theta\cos\left(\frac{\alpha}{2}-\theta\right)-\cos\frac{\alpha}{2}.\sin\theta\right\} \qquad (3C.5)$$

Corresponding stresses may be calculated by appropriate application of equations (3B.6), (3B.7) and (3B.8) respectively, the signs of stresses being interpreted in relation to the directions of the actions.

Regarding the buckets as fully-fixed to the rigid fully-supported hub, the rimless jet loading displacements at the bucket-tip or junction point G_1, Fig.30, are radial deflection Δ_{R2}, tangential deflection Δ_{T2} and rotation Φ_{P2} in the plane of the wheel. These displacements are found by the unit load method considering total strain-energy of the bucket due to bending, direct force and shear. They are positive in the directions of the corresponding unit loads shown at G_1 in Fig.30, and are given by:-

$$\Delta_{R2} = \frac{W_{\theta=\frac{\alpha}{2}} \cdot k^5}{(1-\cos\frac{\alpha}{2})qEI_{YY}} \left\{ \begin{array}{l} \frac{\alpha^2}{8}\left[\cos\frac{\alpha}{2} - \frac{h}{k}\cos\left(\frac{\alpha}{2}+\beta\right)\right] \\ +\frac{\alpha}{8}\left[\frac{h}{k}\left\{2\sin\left(\frac{\alpha}{2}+\beta\right) + 14\cos\frac{\alpha}{2}\sin(\alpha+\beta) + \sin\left(\frac{\alpha}{2}-\beta\right)\right\} + 2\sin\frac{\alpha}{2} - \sin\frac{3\alpha}{2}\right] \\ +\frac{h}{k}\left[\frac{3}{16}\left\{\cos\left(\frac{\alpha}{2}-\beta\right) - \cos\left(\frac{3\alpha}{2}+\beta\right)\right\} - 2\sin\frac{\alpha}{2}\sin(\alpha+\beta)\right. \\ \qquad -\cos\frac{\alpha}{2}\left\{\cos\beta - \frac{1}{8}\cos(\alpha-\beta) - \frac{7}{8}\cos(\alpha+\beta) + \frac{1}{2}\sin\alpha.\sin(\alpha+\beta)\right\} \\ \left. \qquad +\cos\frac{\alpha}{2}\left(\cos\alpha - \frac{1}{8}\cos 2\alpha\right) - \frac{11}{16}\cos\frac{\alpha}{2} - \frac{3}{16}\cos\frac{3\alpha}{2}\right\} \end{array} \right.$$

$$+ \frac{W_{\theta=\frac{\alpha}{2}} \cdot k^3}{(1-\cos\frac{\alpha}{2})qEA} \left\{ \begin{array}{l} \frac{\alpha^2}{8}\left[\cos\frac{\alpha}{2} - \frac{h}{k}\cos\left(\frac{\alpha}{2}+\beta\right)\right] \\ +\frac{\alpha}{8}\left[\frac{h}{k}\left\{2\sin\left(\frac{\alpha}{2}+\beta\right) + 2\cos\frac{\alpha}{2}\sin(\alpha+\beta) + \sin\left(\frac{\alpha}{2}-\beta\right)\right\} + 2\sin\frac{\alpha}{2} - \sin\frac{3\alpha}{2}\right] \\ +\frac{h}{k}\left[\frac{3}{16}\left\{\cos\left(\frac{\alpha}{2}-\beta\right) - \cos\left(\frac{3\alpha}{2}+\beta\right)\right\} - \cos\frac{\alpha}{2}\left\{\cos\beta - \frac{1}{8}\cos(\alpha-\beta) - \frac{7}{8}\cos(\alpha+\beta)\right.\right. \\ \left. \qquad +\cos\frac{\alpha}{2}\left(\cos\alpha - \frac{1}{8}\cos 2\alpha\right) - \frac{11}{16}\cos\frac{\alpha}{2} - \frac{3}{16}\cos\frac{3\alpha}{2}\right\} \end{array} \right.$$

$$+ \frac{K_x W_{\theta=\frac{\alpha}{2}} \cdot k^3}{2(1-\cos\frac{\alpha}{2})qGA} \left\{ \begin{array}{l} \frac{\alpha^2}{4}\left[\cos\frac{\alpha}{2} - \frac{h}{k}\cos\left(\frac{\alpha}{2}+\beta\right)\right] + \frac{\alpha}{4}\left[\frac{h}{k}\left\{2\cos\frac{\alpha}{2}\sin(\alpha+\beta) - \sin\left(\frac{\alpha}{2}-\beta\right)\right\} + \sin\frac{3\alpha}{2}\right] \\ +\frac{h}{k}\left[\frac{1}{8}\left\{\cos\left(\frac{3\alpha}{2}+\beta\right) - \cos\left(\frac{\alpha}{2}-\beta\right)\right\} - \frac{1}{2}\cos\frac{\alpha}{2}\cdot\sin\alpha.\sin\beta\right] \\ \qquad +\frac{1}{4}\cos\frac{\alpha}{2}\left(\cos 2\alpha - \frac{3}{2}\right) + \frac{1}{8}\cos\frac{3\alpha}{2} \end{array} \right.$$

(3C.6)

$$\Delta_{T2} = \frac{W_{\theta=\frac{\alpha}{2}} \cdot k^5}{(1-\cos\frac{\alpha}{2})qEI_{YY}} \left\{ \begin{array}{l} \frac{\alpha^2}{8}\left[\frac{h}{k}\sin\left(\frac{\alpha}{2}+\beta\right)+\sin\frac{\alpha}{2}\right] \\ +\frac{\alpha}{8}\left[\frac{h}{k}\left\{2\cos\left(\frac{\alpha}{2}+\beta\right)+14\cos\frac{\alpha}{2}\cos(\alpha+\beta)-\cos\left(\frac{\alpha}{2}-\beta\right)\right\}-16\cos\frac{\alpha}{2}+\cos\frac{3\alpha}{2}\right] \\ +\frac{h}{k}\left[\frac{3}{16}\left\{\sin\left(\frac{\alpha}{2}-\beta\right)+\sin\left(\frac{3\alpha}{2}+\beta\right)\right\}-2\sin\frac{\alpha}{2}\cos(\alpha+\beta)\right. \\ \left.+\cos\frac{\alpha}{2}\left\{\sin\beta+\frac{1}{8}\sin(\alpha-\beta)-\frac{7}{8}\sin(\alpha+\beta)-\frac{1}{2}\sin\alpha\cos(\alpha+\beta)\right\}\right] \\ +\cos\frac{\alpha}{2}\left(\frac{3}{2}\sin\alpha-\frac{1}{8}\sin 2\alpha\right)+\frac{29}{16}\sin\frac{\alpha}{2}-\frac{3}{16}\sin\frac{3\alpha}{2} \end{array} \right\}$$

$$+\frac{W_{\theta=\frac{\alpha}{2}} \cdot k^3}{(1-\cos\frac{\alpha}{2})qEA} \left\{ \begin{array}{l} \frac{\alpha^2}{8}\left[\frac{h}{k}\sin\left(\frac{\alpha}{2}+\beta\right)+\sin\frac{\alpha}{2}\right] \\ +\frac{\alpha}{8}\left[\frac{h}{k}\left\{2\cos\left(\frac{\alpha}{2}+\beta\right)+2\cos\frac{\alpha}{2}\cos(\alpha+\beta)-\cos\left(\frac{\alpha}{2}-\beta\right)\right\}-4\cos\frac{\alpha}{2}+\cos\frac{3\alpha}{2}\right] \\ +\frac{h}{k}\left[\frac{3}{16}\left\{\sin\left(\frac{\alpha}{2}-\beta\right)+\sin\left(\frac{3\alpha}{2}+\beta\right)\right\}+\cos\frac{\alpha}{2}\left\{\sin\beta+\frac{1}{8}\sin(\alpha-\beta)-\frac{7}{8}\sin(\alpha+\beta)\right\}\right] \\ +\cos\frac{\alpha}{2}\left(\sin\alpha-\frac{1}{8}\sin 2\alpha\right)-\frac{3}{16}\left(\sin\frac{\alpha}{2}+\sin\frac{3\alpha}{2}\right) \end{array} \right\}$$

$$+\frac{K_x W_{\theta=\frac{\alpha}{2}} \cdot k^3}{2(1-\cos\frac{\alpha}{2})qGA} \left\{ \begin{array}{l} \frac{\alpha^2}{4}\left[\sin\frac{\alpha}{2}+\frac{h}{k}\sin\left(\frac{\alpha}{2}+\beta\right)\right]+\frac{\alpha}{4}\left[\frac{h}{k}\left\{2\cos\frac{\alpha}{2}\cos(\alpha+\beta)+\cos\left(\frac{\alpha}{2}-\beta\right)\right\}-2\cos\frac{\alpha}{2}-\cos\frac{3\alpha}{2}\right. \\ \left.-\frac{h}{k}\left[\frac{1}{8}\left\{\sin\left(\frac{3\alpha}{2}+\beta\right)+\sin\left(\frac{\alpha}{2}-\beta\right)\right\}+\frac{1}{2}\cos\frac{\alpha}{2}\cdot\sin\alpha\cdot\cos\beta\right]\right. \\ \left.+\frac{1}{4}\cos\frac{\alpha}{2}\sin 2\alpha+\frac{1}{8}\left(\sin\frac{\alpha}{2}+\sin\frac{3\alpha}{2}\right)\right. \end{array} \right\}$$

(3C.7)

$$\Phi_{P2} = \frac{W_{\theta=\frac{\alpha}{2}} \cdot k^3}{(1-\cos\frac{\alpha}{2})EI_{YY}} \left\{2\sin\frac{\alpha}{2}+\frac{1}{2}\cos\frac{\alpha}{2}\left(\sin\alpha-3\alpha\right)\right\}$$

(3C.8)

For numerical application to the $16\frac{1}{2}$ in.cast steel wheel under normal working conditions, Fig.31 illustrates the distributions with Θ of the rimless jet loading actions M_θ, P_θ and V_θ on the bucket. The maximum rimless jet loading stresses (+ tensile) due to these actions are as follows:-

due to M_θ :- $\sigma_{b\,MAX} = +14,450$ lb/in.^{2} at inlet and outlet edges of bucket, at $\Theta = 127^\circ$

due to P_θ :- $\sigma_{d\,MAX} = +500$ lb/in^2 at $\Theta = 127^\circ$

due to V_θ :- $\tau_{MAX} = 1,200$ lb/in^2 fairly near neutral axis YY of the section, at $\Theta = 95^\circ$.

The maximum rimless jet loading total normal stress $\underline{\sigma_{MAX.} = +14,950 \text{ lb/in}^2}$ at the bucket edges at $\Theta = 127^\circ$.

These stresses in the bucket are of quite credible order for jet loading of a rimless wheel. It is evident that M_θ is the dominant action, and that the shear stress is of negligible significance.

From equations (3C.6), (3C.7) and (3C.8) the rimless jet loading displacements of the junction point G_1 on the bucket, relative to the hub, are found respectively to be:-

radial deflection $\Delta_{R2} = +4,420 \times 10^{-6}$ ins.

tangential deflection $\Delta_{T2} = +9,660 \times 10^{-6}$ ins.

rotation in the plane of the wheel $\Phi_{P2} = +1,380 \times 10^{-6}$ rads.

The bending strain-energy terms of the deflections are highly dominant and the other terms may readily be neglected.

Since the remainder of the wheel is unloaded in this condition and so does not displace, these displacements Δ_{R2}, Δ_{T2} and Φ_{P2}, all +ve as shown on Fig.30, represent at the bucket/rim junction point, the jet loading discontinuities of deflection and rotation in the plane of the wheel, between the jet-loaded bucket and the rim on the remainder of the wheel.

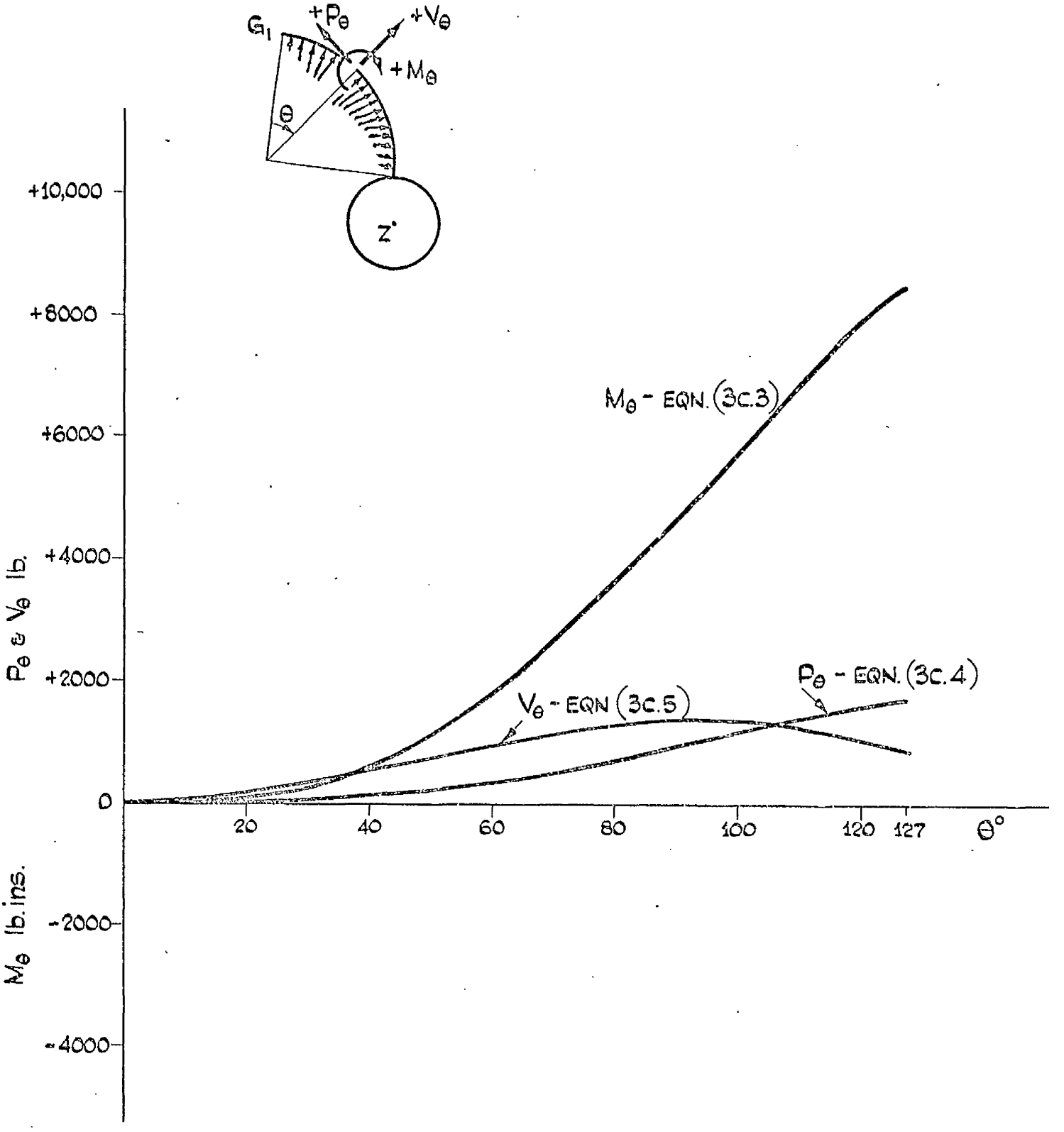

FIG. 31. DISTRIBUTIONS OF RIMLESS JET LOADING ACTIONS M_θ, P_θ, V_θ WITH θ ON THE EQUIVALENT BUCKET OF THE $16\frac{1}{2}$ IN. CAST STEEL TURGO WHEEL UNDER NORMAL WORKING CONDITIONS.

3C iii Assembly condition - assembly actions on the rim of the remainder of the wheel

With reference to Fig.28, it is assumed for simplicity that the assembly actions at bucket/rim junction points G_{1B} and G_{1C} will be identical in magnitudes and directions to the corresponding assembly actions at junction point G_1. The assembly actions at these three junction points on the rim of the remainder of the wheel are thus F_R, F_T, F_A, M_P, M_R and M_T as shown in Fig.28 and also in Fig.32(a). In the latter figure it is evident that the rim carrying these 3 identical sets of assembly actions, is supported by the 19 unloaded buckets.

Considering any one of these 3 junction points on the rim, say G_1, it may reasonably be assumed as a simple approach, that the assembly actions at this one junction point are sustained by one-third of the unloaded buckets, i.e. by 6 unloaded buckets say, as indicated in Fig. 32(b). So for one junction point only, the rim is supported by 6 buckets. If now, the buckets I and II, Fig.32(b), were considered to be removed as shown in Fig.32(c), the resulting system would in general be less stiff in respect of the assembly action displacements at junction point G_1 and would correspond to that of an arch, subtending an angle of 180° at the wheel axis Z, elastically-supported at G_{1D} and G_{1E}, and with the assembly actions applied at G_1, the apex of the arch. To compensate for the effects of removal of buckets I and II, and so attempt to simulate approximately the stiffness associated with the system Fig.32(b), the arch supports at G_{1D} and G_{1E} may reasonably be regarded as fully-fixed rather than elastic. Thus system Fig.32(d), a fully-fixed arch of the rim radius and cross-section, is assumed to represent system Fig.32(b) in respect of the displacements and internal actions induced at junction point G_1 on the rim, by the assembly actions applied there.

By/

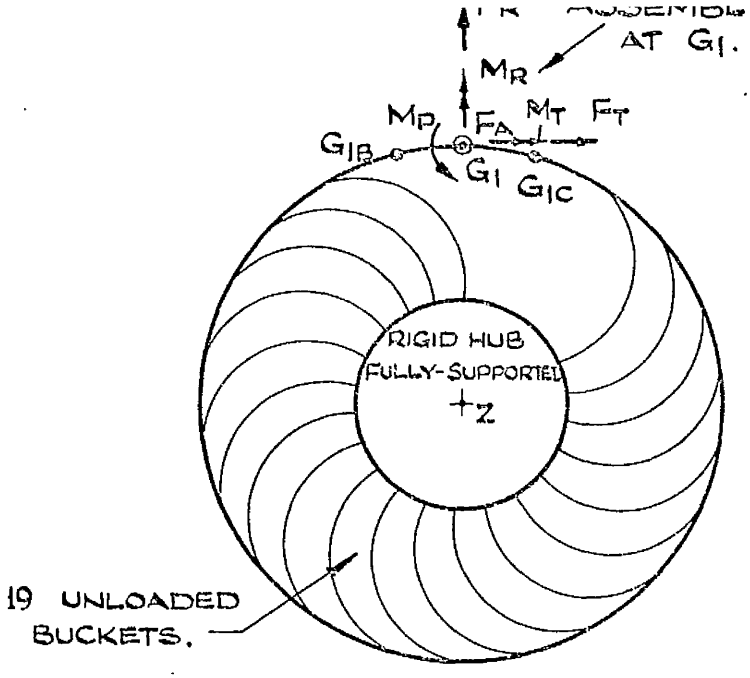

(a). RIM ON REMAINDER OF WHEEL. ASSUME ASSEMBLY ACTIONS AT JUNCTION POINTS G_{1B} AND G_{1C} WILL BE IDENTICAL TO THOSE AT JUNCTION POINT G_1.

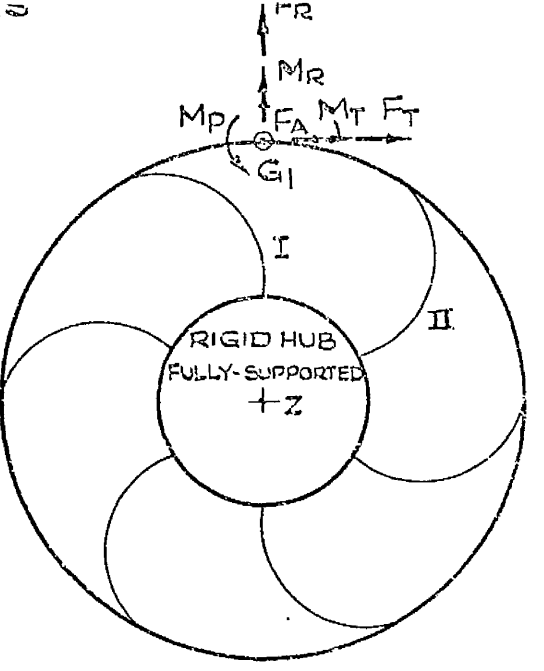

(b). IN RESPECT OF ONE JUNCTION POINT ONLY, SAY G_1, AND OF THE ASSEMBLY ACTIONS THEREON, ASSUME RIM SUPPORTED BY ONE-THIRD OF UNLOADED BUCKETS, SAY BY 6 BUCKETS.

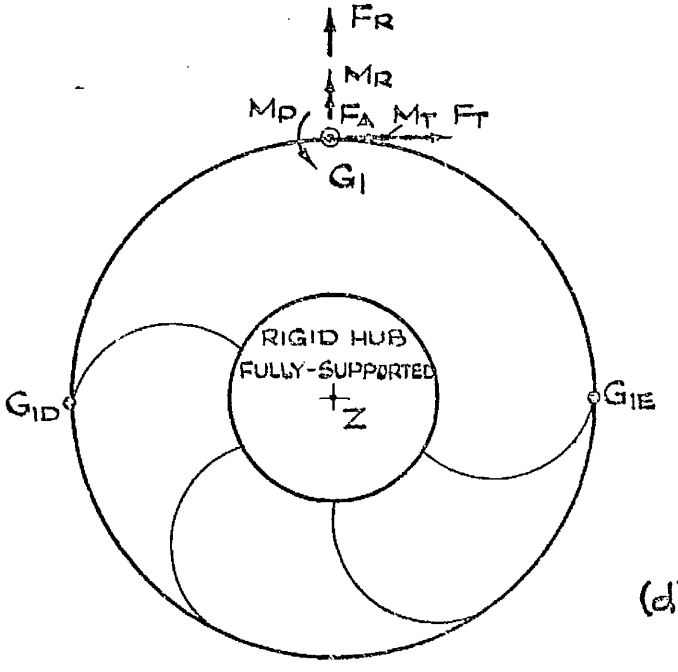

(c). ASSUME BUCKETS I AND II REMOVED. G_{1D} G_1 G_{1E} IS A CIRCULAR ARCH, ELASTICALLY-SUPPORTED AT G_{1D} AND G_{1E}, AND LOADED AT APEX G_1 BY THE ASSEMBLY ACTIONS.

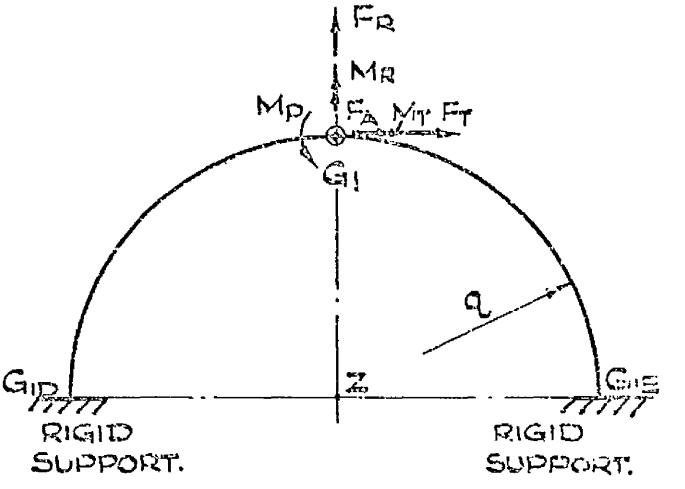

(d). TO ATTEMPT TO COMPENSATE FOR REMOVAL OF BUCKETS I AND II, ASSUME G_{1D} AND G_{1E} ARE FULLY-FIXED SUPPORTS. THIS SYSTEM OF A FULLY-FIXED 180° ARCH, OF THE RIM RADIUS AND CROSS-SECTION REPLACES SYSTEM (b).

ALL THE ASSEMBLY ACTIONS ARE +VE AS SHOWN.

FIG. 32. DIAGRAM ILLUSTRATING THE SEQUENCE OF THE ASSUMPTIONS MADE TO SIMPLIFY DERIVATION OF THE DISPLACEMENT/ACTION RELATIONS, AND OF THE INTERNAL ACTIONS, PERTINENT TO THE ASSEMBLY ACTIONS ON THE RIM OF THE REMAINDER OF THE WHEEL. (JET LOADING).

By this very considerably simplified approach it is relatively easy to obtain in general terms, the displacement/action relations and the induced actions pertaining to the assembly actions at junction point G_1 on the rim. As a substitute for the actual rim-on-remainder-of-wheel system, typified by Fig.32(a) but showing disparity in the 3 sets of assembly actions, the assumed-arch system of Fig.32(d) might be expected to exhibit less stiffness in general, than the very highly redundant actual system, in respect of the assembly action displacements at junction point G_1. In consequence it would be likely to offer less restraint with regard to the jet loading bucket/rim displacement discontinuities.

For a fully-fixed thin circular arch carrying in-plane or transverse forces or moments at the apex, the induced actions and displacements at the apex are readily derived using strain-energy methods. Several of the cases represented by Fig.32(d) and the assembly actions thereof, are standard cases which have received treatment widely, e.g. by ROARK [32] and by PIPPARD [36]. Concerning each assembly action at the arch apex G_1, the relevant displacement/action relations and the internal actions induced at G_1 are presented below. These have been determined by application of Castigliano's Theorem, the unit load method and Maxwell's Reciprocal Theorem, assuming the rim-arch to be thin and considering strain-energy of bending and also, where applicable, strain-energy of torsion. The sign convention pertinent to the assembly action displacements at G_1, in general, is indicated on Fig.33(a), and the sign convention pertinent to the induced internal actions at G_1, in general, is indicated on Fig.33(b). With reference to this latter figure and to Fig.A2.1 (Appendix 2), which shows the rim cross-section and its principal axes $Y'Y'$ and $X'X'$, the internal actions induced at G_1 by these assembly actions, are, in general, direct force P_1, shearing forces $V_{Y'1}$ and $V_{X'1}$, bending moments $M_{X'1}$ and $M_{Y'1}$ and torque T_1. The associated stresses/

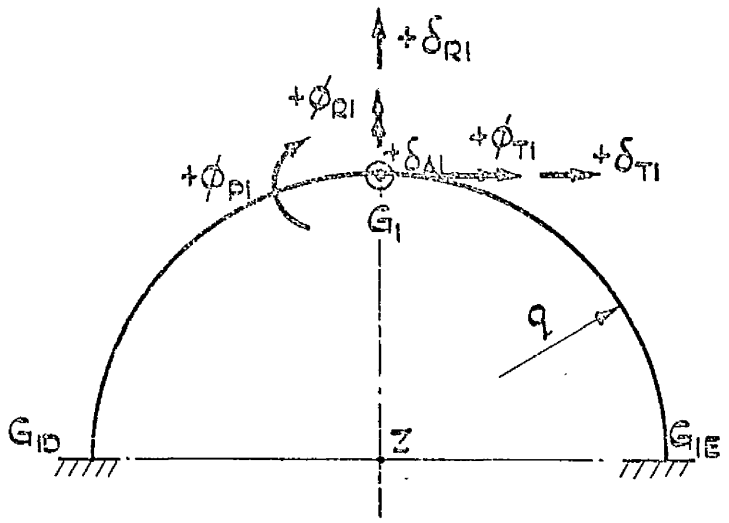

(a).

SIGN CONVENTION PERTINENT TO THE GENERAL DISPLACEMENTS AT JUNCTION POINT G_1.

δ_{A1} THUS ⊙ IS OUT OF THE PAGE.

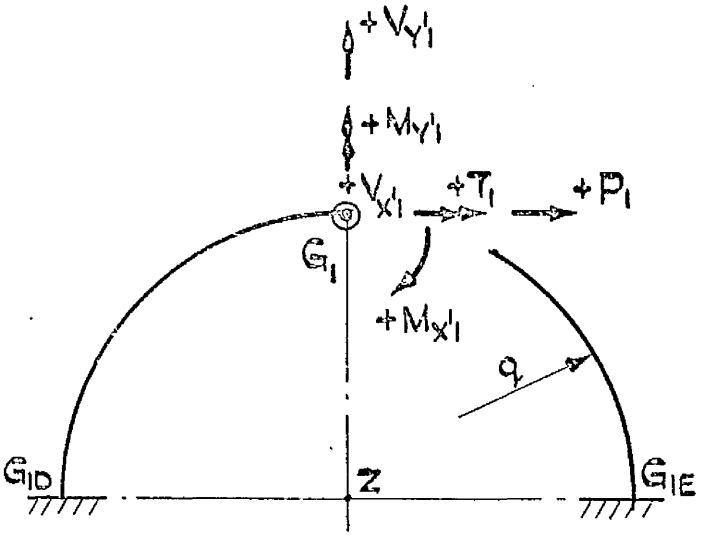

(b).

SIGN CONVENTION PERTINENT TO THE GENERAL INTERNAL ACTIONS INDUCED AT JUNCTION POINT G_1.

$V_{X'1}$ THUS ⊙ IS OUT OF THE PAGE.

FIG. 33. RIM ON REMAINDER OF WHEEL REPLACED BY FULLY-FIXED 180° ARCH OF THE RIM RADIUS AND CROSS-SECTION:— SIGN CONVENTIONS PERTINENT TO THE DISPLACEMENT/ACTION RELATIONS AND TO THE INTERNAL ACTIONS AT JUNCTION POINT G_1 DUE TO THE SIX ASSEMBLY ACTIONS APPLIED THERE. (JET LOADING.)

stresses are determined straightforwardly, those due to T_1 by way of a standard treatment [31]:-

Action F_R

$$\left.\begin{aligned} P_1^{F_R} &= \frac{4-\pi}{\pi^2-8}\, F_R \\ V_{Y'1}^{F_R} &= \tfrac{1}{2} F_R \\ M_{X'1}^{F_R} &= \frac{2\pi-6}{\pi^2-8}\, F_R \cdot q \end{aligned}\right\} \qquad (3C.9)$$

$$\delta_{R1}^{F_R} = \frac{F_R \cdot q^3}{E I_{x'x'}} \cdot \frac{\pi^3 - 20\pi + 32}{8(\pi^2-8)} \qquad (3C.10)$$

Action F_T

$$\left.\begin{aligned} P_1^{F_T} &= \tfrac{1}{2} F_T \\ V_{Y'1}^{F_T} &= \frac{1}{\pi} F_T \end{aligned}\right\} \qquad (3C.11)$$

$$\delta_{T1}^{F_T} = \frac{F_T \cdot q^3}{E I_{x'x'}} \cdot \frac{3\pi^2 - 8\pi - 4}{8\pi} \qquad (3C.12)$$

$$\phi_{P1}^{F_T} = \frac{F_T \cdot q^2}{E I_{x'x'}} \cdot \frac{\pi^2 - 2\pi - 4}{4\pi} \qquad (3C.13)$$

Action M_P

$$\left.\begin{aligned} V_{Y'1}^{M_P} &= -\frac{2}{\pi} \cdot \frac{M_P}{q} \\ M_{X'1}^{M_P} &= -\tfrac{1}{2} M_P \end{aligned}\right\} \qquad (3C.14)$$

$$\delta_{T1}^{M_P} = \frac{M_P \cdot q^2}{E I_{x'x'}} \cdot \frac{-\pi^2 + 2\pi + 4}{4\pi} \qquad (3C.15)$$

$$\phi_{P1}^{M_P} = \frac{M_P \cdot q}{E I_{x'x'}} \cdot \frac{8 - \pi^2}{4\pi} \qquad (3C.16)$$

Action F_A

$$\left.\begin{aligned} V_{x'1}^{F_A} &= \frac{1}{2} F_A \\ M_{y'1}^{F_A} &= \frac{1}{\pi} F_A \cdot q \end{aligned}\right\} \qquad (3C.17)$$

$$\delta_{A1}^{F_A} = \frac{F_A \cdot q^3}{E I_{y'y'}} \cdot \frac{\pi^2(1+3\Lambda) - 8\pi\Lambda - 4(1+\Lambda)}{8\pi} \qquad (3C.18)$$

$$\phi_{T1}^{F_A} = \frac{F_A \cdot q^2}{4 E I_{y'y'}} \cdot \frac{\pi^2(1+\Lambda) - 4\pi\Lambda - 4(1-\Lambda)}{2\pi} \qquad (3C.19)$$

where $\Lambda = \dfrac{E I_{y'y'}}{G J_1}$.

Action M_R

$$\left.\begin{aligned} V_{x'1}^{M_R} &= \frac{M_R}{q} \cdot \frac{\pi^2(1+\Lambda) - 4[1 - \Lambda(1-\pi)]}{(\pi-2)[\pi^2(1+\Lambda) - 8\Lambda]} \\ M_{y'1}^{M_R} &= \frac{1}{2} M_R \\ T_1^{M_R} &= M_R \cdot \frac{2[(3-\pi)\Lambda - 1]}{\pi^2(1+\Lambda) - 8\Lambda} \end{aligned}\right\} \qquad (3C.20)$$

$$\phi_{R1}^{M_R} = \frac{M_R \cdot q}{E I_{Y'Y'}} \cdot \frac{\pi^3(\pi-2)(1+2\Lambda+\Lambda^2) - 4\pi\Lambda(5\pi\Lambda+2\pi-18\Lambda+4) - 4\pi(\pi-2) - 64\Lambda(\Lambda-1)}{2(\pi-2)[\pi^2(1+\Lambda)-8\Lambda]}$$

(3C.21)

where $\Lambda = \frac{E I_{Y'Y'}}{G J_1}$

Action M_T

$$\left.\begin{aligned} M_{Y'1}^{M_T} &= \frac{1-\Lambda}{\pi(1+\Lambda)} M_T \\ T_1^{M_T} &= \frac{1}{2} M_T \end{aligned}\right\}$$

(3C.22)

$$\delta_{A1}^{M_T} = \frac{M_T \cdot q^2}{4 E I_{Y'Y'}} \cdot \frac{\pi^2(1+\Lambda) - 4\pi\Lambda - 4(1-\Lambda)}{2\pi}$$

(3C.23)

$$\phi_{T1}^{M_T} = \frac{M_T \cdot q}{4 E I_{Y'Y'}} \cdot \frac{\pi^2(1+\Lambda)^2 - 4(1-\Lambda)^2}{2\pi(1+\Lambda)}$$

(3C.24)

where $\Lambda = \frac{E I_{Y'Y'}}{G J_1}$

For the $16\frac{1}{2}$ in. cast steel wheel, referring to Appendix 2 for section properties, the displacement/action relations relevant to the assembly condition of the rim on the remainder of the wheel, are as follows:-

$\delta_{R1}^{F_R} = + 0.56583 \times 10^{-6} F_R$, from equation (3C.10)

$\delta_{T1}^{F_T} = + 0.91782 \times 10^{-6} F_T$, " " (3C.12)

$\phi_{P1}^{F_T} = - 0.11971 \times 10^{-6} F_T$, " " (3C.13)

$\delta_{T1}^{M_P} = + 0.11971 \times 10^{-6} M_P$, " " (3C.15)

$$\phi_{P1}^{M_P} = - 0.04059 \times 10^{-6} M_P \text{ , from equation (3C.16)}$$

$$\delta_{A1}^{F_A} = + 48.78861 \times 10^{-6} F_A \text{ , " " (3C.18)}$$

$$\phi_{T1}^{F_A} = + 4.11868 \times 10^{-6} F_A \text{ , " " (3C.19)}$$

$$\phi_{R1}^{M_R} = + 0.27213 \times 10^{-6} M_R \text{ , " " (3C.21)}$$

$$\delta_{A1}^{M_T} = + 4.11868 \times 10^{-6} M_T \text{ , " " (3C.23)}$$

$$\phi_{T1}^{M_T} = + 0.83890 \times 10^{-6} M_T \text{ , " " (3C.24) .}$$

3C iv Assembly condition — assembly actions on the bucket

Of the general assembly actions F_R, F_T, F_A, M_P, M_R and M_T on the bucket at the bucket/rim junction point G_1, Fig.28, all but axial force F_A have priorly been the subject of analysis in section 3B iv, for derivation of the induced actions at Θ on the bucket and of displacement/action relations pertaining to the bucket-tip G_1. The entire section 3B iv with $M_P \neq (F_T \cdot q)$ is therefore incorporated as part of this section. Analysis of the assembly condition relevant to jet loading however, requires the addition of axial-displacement/action relations at G_1 for assembly actions dealt with in 3B iv, together with the displacement/action relations at G_1 and the induced actions at Θ relevant to assembly action F_A. Derivation of this additional data is carried out on lines exactly similar to 3B iv, and results in the expressions presented below. The sign convention for displacements at G_1 on the bucket is that of Fig.21, with the addition that positive general axial deflection δ_{A2} is outward from the page, exactly like its counterpart δ_{A1} on the rim, as shown in Fig.33(a). Induced shearing force $V_{\Theta Y2}^{F_A}$ is positive outward from the page. The assembly actions at G_1 on the bucket, are positive as shown on Figs.21 and 28:-

Action F_R

$$\delta_{A2}^{F_R} = \frac{F_R . d . k^3}{q E I_{o\alpha}} \left\{ \frac{\alpha}{2} \left[\frac{h}{k} \cos(\alpha+\beta) - 1 \right] - \frac{1}{4} \frac{h}{k} \left[\sin(\alpha+\beta) + \sin(\alpha-\beta) \right] + \frac{1}{4} \sin 2\alpha \right\}$$

+(on next page),

$$+F_R H\begin{cases}\frac{K}{2}\left(F_5F_3e^{-2K\alpha}-L_5L_3e^{2K\alpha}\right)+K^2(F_3L_5+F_5L_3)\alpha\\ -\frac{Ke^{K\alpha}}{(H+P)(K^2+1)}\left[(L_5N_3+L_3N_4)(K\cos\alpha+\sin\alpha)+(L_5M_3+L_3M_4)(K\sin\alpha-\cos\alpha)\right]\\ -\frac{Ke^{-K\alpha}}{(H+P)(K^2+1)}\left[(F_5N_3+F_3N_4)(K\cos\alpha-\sin\alpha)+(F_5M_3+F_3M_4)(K\sin\alpha+\cos\alpha)\right]\end{cases}$$

$$+\frac{(M_3N_4+N_3M_4)(\cos2\alpha-1)-(N_3N_4-M_3M_4)\sin2\alpha-2(N_3N_4+M_3M_4)\alpha}{4(H+P)^2}$$

$$-\frac{M_5}{H}\left[L_3(e^{K\alpha}-1)+F_3(e^{-K\alpha}-1)\right]+\frac{M_5}{H(H+P)}\left[M_3(\cos\alpha-1)-N_3\sin\alpha\right]$$

$$+\frac{K}{2}(L_3L_5-F_3F_5)+\frac{K\left[KN_3(L_5+F_5)+KN_4(L_3+F_3)-M_3(L_5-F_5)-M_4(L_3-F_3)\right]}{(H+P)(K^2+1)}$$

$$+F_R P\begin{cases}\frac{K^3}{2}\left(F_3F_5e^{-2K\alpha}-L_3L_5e^{2K\alpha}\right)-K^4(F_3L_5+L_3F_5)\alpha\\ +\frac{K^2e^{K\alpha}}{(H+P)(K^2+1)}\left[(L_5N_3+L_3N_4)(K\sin\alpha-\cos\alpha)-(L_5M_3+L_3M_4)(K\cos\alpha+\sin\alpha)\right]\\ -\frac{K^2e^{-K\alpha}}{(H+P)(K^2+1)}\left[(F_5N_3+F_3N_4)(K\sin\alpha+\cos\alpha)-(F_5M_3+F_3M_4)(K\cos\alpha-\sin\alpha)\right]\end{cases}$$

$$-\frac{(M_3N_4+N_3M_4)(\cos2\alpha-1)-(N_3N_4-M_3M_4)\sin2\alpha+2(N_3N_4+M_3M_4)\alpha}{4(H+P)^2}$$

$$+\frac{K^3}{2}(L_3L_5-F_3F_5)+\frac{K^2\left[KM_3(L_5-F_5)+KM_4(L_3-F_3)+N_3(L_5+F_5)+N_4(L_3+F_3)\right]}{(H+P)(K^2+1)}$$

(3C.25),

where, in the non-uniform torsion terms:-

K, H, P, M_3, N_3, L_3 and F_3 are the same as in section 3B iv, and where:-

$$M_4 = k\sin\alpha\ , \qquad N_4 = k\cos\alpha\ , \qquad M_5 = -(k+e_s+\bar{x})\ ,$$

$$L_5 = -\frac{HN_4+(H+P)M_5}{KH(H+P)(e^{2K\alpha}+1)}\ , \qquad F_5 = \frac{HN_4+(H+P)M_5}{KH(H+P)(e^{-2K\alpha}+1)}\ .$$

Action F_T

$$\delta_{AZ}^{F_T} = \frac{F_T d k^3}{q E I_{ox}} \left\{ -\frac{\alpha}{2}\frac{h}{k}\sin(\alpha+\beta) - \frac{1}{4}\frac{h}{k}\left[\cos(\alpha+\beta) - \cos(\alpha-\beta)\right] + \frac{1}{4}(1-\cos 2\alpha) \right\}$$

$$+ F_T H \left\{ \begin{array}{l} \frac{K}{2}(F_5 F_4 e^{-2K\alpha} - L_4 L_5 e^{2K\alpha}) + K^2(F_4 L_5 + F_5 L_4)\alpha \\ -\frac{K e^{K\alpha}}{(H+P)(K^2+1)}\left[(L_5 M_3 + L_4 N_4)(K\cos\alpha + \sin\alpha) + (L_4 M_4 - L_5 N_3)(K\sin\alpha - \cos\alpha\right. \\ -\frac{K e^{-K\alpha}}{(H+P)(K^2+1)}\left[(F_5 M_3 + F_4 N_4)(K\cos\alpha - \sin\alpha) + (F_4 M_4 - F_5 N_3)(K\sin\alpha + \cos\alpha)\right. \\ +\frac{(M_3 M_4 - N_3 N_4)(\cos 2\alpha - 1) - (M_3 N_4 + N_3 M_4)\sin 2\alpha - 2(M_3 N_4 - N_3 M_4)\alpha}{4(H+P)^2} \\ -\frac{M_5}{H}\left[L_4(e^{K\alpha} - 1) + F_4(e^{-K\alpha} - 1)\right] - \frac{M_5}{H(H+P)}\left[N_3(\cos\alpha - 1) + M_3\sin\alpha\right] \\ +\frac{K}{2}(L_4 L_5 - F_4 F_5) + \frac{K\left[K M_3(L_5 + F_5) + K N_4(L_4 + F_4) + N_3(L_5 - F_5) - M_4(L_4 - F_4)\right.}{(H+P)(K^2+1)} \end{array} \right\}$$

$$+ F_T P \left\{ \begin{array}{l} \frac{K^3}{2}(F_4 F_5 e^{-2K\alpha} - L_4 L_5 e^{2K\alpha}) - K^4(F_4 L_5 + L_4 F_5)\alpha \\ +\frac{K^2 e^{K\alpha}}{(H+P)(K^2+1)}\left[(L_5 M_3 + L_4 N_4)(K\sin\alpha - \cos\alpha) - (L_4 M_4 - L_5 N_3)(K\cos\alpha + \sin\alpha)\right] \\ -\frac{K^2 e^{-K\alpha}}{(H+P)(K^2+1)}\left[(F_5 M_3 + F_4 N_4)(K\sin\alpha + \cos\alpha) - (F_4 M_4 - F_5 N_3)(K\cos\alpha - \sin\alpha)\right] \\ -\frac{(M_3 M_4 - N_3 N_4)(\cos 2\alpha - 1) - (M_3 N_4 + N_3 M_4)\sin 2\alpha + 2(M_3 N_4 - N_3 M_4)\alpha}{4(H+P)^2} \\ +\frac{K^3}{2}(L_4 L_5 - F_4 F_5) + \frac{K^2\left[K M_4(L_4 - F_4) - K N_3(L_5 - F_5) + M_3(L_5 + F_5) + N_4(L_4 + F_4)\right]}{(H+P)(K^2+1)} \end{array} \right\}$$

(3C.26),

where, in the non-uniform torsion terms:-

K, H, P, M_3, N_3, L_4 and F_4 are the same as in section 3B iv, and M_4, N_4, M_5, L_5 and F_5 are the same as for $\delta_{AZ}^{F_R}$.

Action M_R

$$\delta_{AZ}^{M_R} = \frac{\delta_{AZ}^{F_T}}{F_T \cdot d} \cdot M_R \qquad (3C.27)$$

Action M_T

$$\delta_{AZ}^{M_T} = -\frac{\delta_{AZ}^{F_R}}{F_R \cdot d} \cdot M_T \qquad (3C.28)$$

Action F_A

With reference to Figs. 21 and 28, the actions induced on a section of the bucket at Θ are:-

$$V_{\theta Y Z}^{F_A} = F_A \qquad (3C.29)$$

$$M_{\theta x z}^{F_A} = -F_A k \sin\theta \qquad (3C.30)$$

$$T_{\theta z}^{F_A} = T_{\Omega 2}^{F_A} = F_A \left\{ k(1-\cos\theta) + \bar{x} + e_S \right\} \qquad (3C.31)$$

Corresponding stresses, in terms of F_A, are obtained by the same methods used in section 3B iv for the cases of F_R and F_T. The non-uniform torsion stresses are given by:-

$$\tau_{SV}^{F_A} = G\frac{mx+c}{k}\left\{K\left(F_5 e^{-K\Omega} - L_5 e^{K\Omega}\right) - \frac{N_4\cos\Omega + M_4\sin\Omega}{H+P} - \frac{M_5}{H}\right\} F_A \qquad (3C.32)$$

$$\sigma_z^{F_A} = -E\frac{y}{I^2}\left(\frac{y^2}{12a} - e_S\right)\left\{-K^2\left(F_5 e^{-K\Omega} + L_5 e^{K\Omega}\right) + \frac{N_4\sin\Omega - M_4\cos\Omega}{H+P}\right\} F_A \qquad (3C.33)$$

$$\tau_z^{F_A} = E\frac{4a^{\frac{1}{2}}}{k^3(mx+c)} \cdot J(y)\left\{K^3\left(F_5 e^{-K\Omega} - L_5 e^{K\Omega}\right) + \frac{N_4\cos\Omega + M_4\sin\Omega}{H+P}\right\} F_A \qquad (3C.34)$$

where $K, H, P, M_4, N_4, M_5, L_5$ and F_5 are the same as for $\delta_{AZ}^{F_R}$.

$$\delta_{R2}^{F_A} = \frac{\delta_{A2}^{F_R}}{F_R} \cdot F_A$$

(3C.35)

by Maxwell's Reciprocal Theorem.

$$\delta_{T2}^{F_A} = \frac{\delta_{A2}^{F_T}}{F_T} \cdot F_A$$

(3C.36),

similarly.

$$\phi_{R2}^{F_A} = \frac{\delta_{A2}^{M_R}}{M_R} \cdot F_A$$

(3C.37),

similarly.

$$\phi_{T2}^{F_A} = \frac{\delta_{A2}^{M_T}}{M_T} \cdot F_A$$

(3C.38),

similarly.

$$\delta_{A2}^{F_A} = \frac{F_A . K_y . k\alpha}{GA} + \frac{F_A k^3}{2EI_{ox}}\left(\alpha - \tfrac{1}{2}\sin 2\alpha\right)$$

$$+ F_A H\left\{\frac{K}{2}\left[L_5^2\left(e^{2K\alpha}-1\right) - F_5^2\left(e^{-2K\alpha}-1\right)\right] - 2K^2 L_5 F_5 \alpha + \frac{2M_5}{H}\left[L_5\left(e^{K\alpha}-1\right) + F_5\left(e^{-K\alpha}-1\right)\right]\right.$$

$$+ \frac{2KL_5 e^{K\alpha}}{(H+P)(K^2+1)}\left[N_4(K\cos\alpha+\sin\alpha) + M_4(K\sin\alpha-\cos\alpha)\right]$$

$$+ \frac{2KF_5 e^{-K\alpha}}{(H+P)(K^2+1)}\left[N_4(K\cos\alpha-\sin\alpha) + M_4(K\sin\alpha+\cos\alpha)\right]$$

$$+ \frac{M_5}{H^2(H+P)}\left[2HM_4 + M_5(H+P)\alpha\right] - \frac{2K\left[KN_4(L_5+F_5) - M_4(L_5-F_5\right.}{(H+P)(K^2+1)}$$

$$\left. + \frac{2(M_4^2+N_4^2)\alpha + (N_4^2-M_4^2)\sin 2\alpha - 2M_4N_4(\cos 2\alpha - 1)}{4(H+P)^2}\right.$$

+ (on next page),

$$+F_A P\Bigg\{\frac{K^3}{2}\left[L_5^2(e^{2K\alpha}-1)-F_5^2(e^{-2K\alpha}-1)\right] + 2K^4 L_5 F_5 \alpha$$

$$-\frac{2K^2 L_5 e^{K\alpha}}{(H+P)(K^2+1)}\left[N_4(K\sin\alpha-\cos\alpha)-M_4(K\cos\alpha+\sin\alpha)\right]$$

$$+\frac{2K^2 F_5 e^{-K\alpha}}{(H+P)(K^2+1)}\left[N_4(K\sin\alpha+\cos\alpha)-M_4(K\cos\alpha-\sin\alpha)\right]$$

$$-\frac{2K^2\left[KM_4(L_5-F_5)+N_4(L_5+F_5)\right]}{(H+P)(K^2+1)}$$

$$+\frac{2(M_4^2+N_4^2)\alpha-(N_4^2-M_4^2)\sin 2\alpha + 2M_4N_4(\cos 2\alpha-1)}{4(H+P)^2}$$

(3C.39),

where, in the non-uniform torsion terms:-

K, H, P, M_4, N_4, M_5, L_5 and F_5 are the same as for $\delta_{AZ}^{F_R}$.

The additional displacement/action relations at junction point G_1 on the bucket, relevant to the jet loading assembly condition of the bucket of the $16\frac{1}{2}$ in. cast steel wheel, are given below. These are supplementary to the values already quoted at the end of section 3B iv:-

$$\delta_{AZ}^{F_R} = +0.29253 \times 10^{-6}\ F_R\ ,\quad \text{from equation (3C.25)}$$

$$\delta_{AZ}^{F_T} = +17.22563 \times 10^{-6}\ F_T\ ,\quad \text{from equation (3C.26)}$$

$$\begin{cases} \delta_{RZ}^{M_P} = -1.32184 \times 10^{-6}\ M_P\ , & \text{from equation (3B.60)} \\ \delta_{TZ}^{M_P} = -1.80086 \times 10^{-6}\ M_P\ , & \text{" \quad " \quad (3B.61)} \\ \phi_{PZ}^{M_P} = -0.47053 \times 10^{-6}\ M_P\ , & \text{" \quad " \quad (3B.62),} \end{cases}$$

since $M_P \neq (F_T \cdot q)$ here.

$$\delta_{AZ}^{M_R} = + \ 7.83425 \times 10^{-6} M_R, \text{ from equation (3C.27)}$$

$$\delta_{AZ}^{M_T} = - \ 0.13293 \times 10^{-6} M_T, \text{ from equation (3C.28)}$$

$$\begin{cases} \delta_{RZ}^{F_A} = + \ 0.29253 \times 10^{-6} F_A, \text{ from equation (3C.35)} \\ \delta_{TZ}^{F_A} = + \ 17.22563 \times 10^{-6} F_A, \text{ " " (3C.36)} \\ \delta_{AZ}^{F_A} = + \ 43.15268 \times 10^{-6} F_A, \text{ " " (3C.39)} \\ \phi_{RZ}^{F_A} = + \ 7.83425 \times 10^{-6} F_A, \text{ " " (3C.37)} \\ \phi_{TZ}^{F_A} = - \ 0.13293 \times 10^{-6} F_A, \text{ " " (3C.38)} . \end{cases}$$

3C v Assembly condition at the bucket/rim junction - evaluation of assembly actions and total jet loading stresses

The discontinuities arising from the rimless jet-loaded bucket condition, and to be eliminated by assembly at the bucket/rim junction are Δ_{R2}, Δ_{T2} and Φ_{P2} as given in section 3C ii. These are all in the plane of the wheel, as illustrated in Fig.34 in which, with regard to in-plane displacements, assembly is assumed to be achieved at position G'_{1A}. At this point the final position of the tangent to the bucket is $G'_{1A}t$. Assembly actions F_{R1}, F_{T1}, etc. on the rim on the remainder of the wheel, initially at G_1, therefore induce displacements δ_{R1}, δ_{T1}, ϕ_{P1}, and assembly actions F_{R2}, F_{T2}, etc. on the bucket, initially at G'_{12}, therefore induce displacements δ_{R2}, δ_{T2}, ϕ_{P2} as shown. Assuming the bucket/rim joint to be rigid, compatibility of the in-plane displacements, Fig.34, requires that:-

$$\delta_{R1} = \delta_{R2} + \Delta_{R2} \tag{3C.40}$$

$$\delta_{T1} = \delta_{T2} + \Delta_{T2} \tag{3C.41}$$

$$\phi_{P1} = \phi_{P2} - \Phi_{P2} \tag{3C.42}$$

If, in the transverse planes, the assembly action displacements of rim on remainder of wheel, and of bucket, are respectively δ_{A1}, ϕ_{R1} ϕ_{T1} and δ_{A2}, ϕ_{R2}, ϕ_{T2}, then for compatibility of the transverse displacements:-

$$\delta_{A1} = \delta_{A2} \tag{3C.43}$$

$$\phi_{R1} = \phi_{R2} \tag{3C.44}$$

$$\phi_{T1} = \phi_{T2} \tag{3C.45}$$

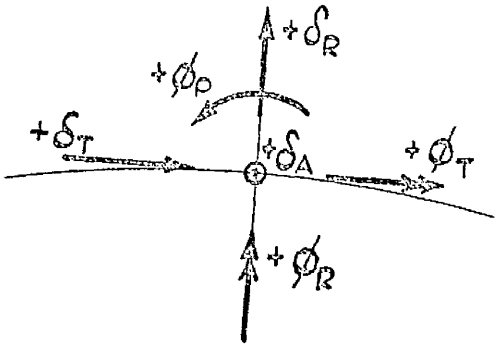

SIGN CONVENTION FOR IN-PLANE & TRANSVERSE PLANES ASSEMBLY ACTION DISPLACEMENTS.

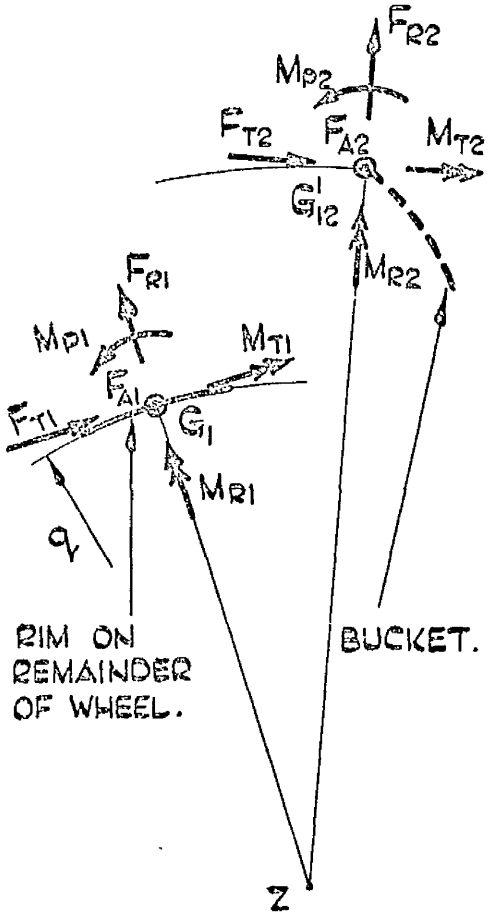

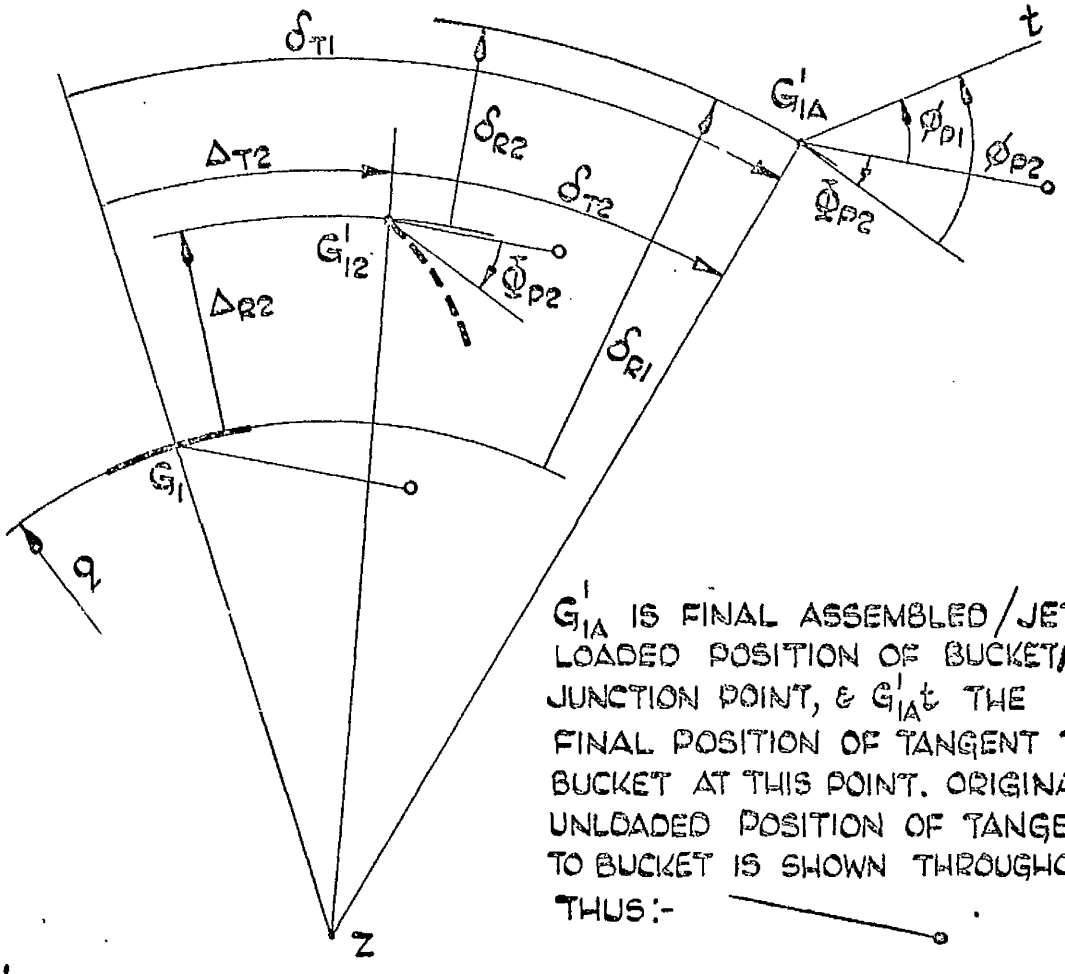

G'_{1A} IS FINAL ASSEMBLED/JET-LOADED POSITION OF BUCKET/RIM JUNCTION POINT, & $G'_{1A}t$ THE FINAL POSITION OF TANGENT TO BUCKET AT THIS POINT. ORIGINAL UNLOADED POSITION OF TANGENT TO BUCKET IS SHOWN THROUGHOUT THUS:-

ASSEMBLY ACTIONS, SUFFIX 1 ON RIM ON REMAINDER OF WHEEL, SUFFIX 2 ON BUCKET, CAUSING FINAL ASSEMBLY OF RIM & JET-LOADED BUCKET AT G'_{1A} AND $G'_{1A}t$.

THE ASSEMBLY ACTIONS AS SHOWN ARE + VE.

ANALYSIS OF RIMLESS JET LOADING & ASSEMBLY ACTION DISPLACEMENTS IN PLANE OF WHEEL, FOR COMPATIBILITY IN ASSEMBLED/JET-LOADED CONDITION. RIMLESS JET LOADING DISPLACEMENTS OF BUCKET TO POINT G'_{12} ARE Δ_{R2}, Δ_{T2} AND $\bar{\Phi}_{P2}$ AS SHOWN.

FIG. 34. DIAGRAM SHOWING THE ASSEMBLY ACTIONS AND THE ANALYSIS OF DISPLACEMENTS IN THE PLANE OF THE WHEEL FOR THE ASSEMBLED/JET-LOADED CONDITION OF BUCKET & RIM AT THE JUNCTION POINT.

For equilibrium in the assembled condition, referring to Fig.34:-

$$F_{R1} + F_{R2} = 0 \qquad (3C.46)$$

$$F_{T1} + F_{T2} = 0 \qquad (3C.47)$$

$$F_{A1} + F_{A2} = 0 \qquad (3C.48)$$

$$M_{P1} + M_{P2} = 0 \qquad (3C.49)$$

$$M_{R1} + M_{R2} = 0 \qquad (3C.50)$$

$$M_{T1} + M_{T2} = 0 \qquad (3C.51)$$

Appropriate substitution of the displacement/action relations of sections 3C iii, 3B iv and 3C iv enables the twelve compatibility and equilibrium simultaneous equations (3C.40) to (3C.51) to be solved for the twelve assembly actions F_{R1}, F_{R2}, etc. The corresponding assembly action stresses are readily determined and are superposed appropriately on the rimless jet loading stresses to give the total jet loading stresses in the bucket. The total jet loading stresses in the rim at the junction point are those due only to the assembly actions.

For the $16\frac{1}{2}$ in.cast steel Turgo wheel under normal working conditions, all terms relevant to the application of the compatibility and equilibrium simultaneous equations have already been derived numerically. Substituting therefore, in accordance with the sign conventions of Figs. 33(a), 21 and 34, and solving, the assembly actions on the bucket are found to be:-

$F_{R2} = +\ 46.74$ lb. $\qquad F_{T2} = -\ 708.39$ lb. $\qquad F_{A2} = +\ 41.73$ lb.

$M_{P2} = +\ 432.85$ lb.in. $\qquad M_{R2} = +\ 1148.74$ lb.in. $\qquad M_{T2} = -\ 163.03$ lb.in.

The corresponding assembly actions suffix 1, on the rim on the remainder of the wheel, have the same values as these but have opposite signs.

Total jet loading stresses in the bucket

Having evaluated the assembly actions on the bucket, the induced actions $M_{\theta Y2}$, $M_{\theta X2}$, $P_{\theta 2}$, $V_{\theta X2}$ and $V_{\theta Y2}$ due to all the assembly actions, are easily found from the relevant equations of sections 3B iv and 3C iv. The distribution of $M_{\theta Y2}$ with Θ is shown in Fig.35, with the corresponding in-plane rimless jet loading bending moment M_θ from Fig.31, and their resultant $M_{\theta Y.TOT}$, the total jet loading in-plane bending moment. Distributions with Θ of $P_{\theta 2}$, P_θ from Fig.31, and their resultant $P_{\theta.TOT}$, of $M_{\theta X2}$ and of non-uniform torsion direct stress σ_z (inlet edge) are illustrated respectively in (a), (b) and (c) of Fig.36. Shear stresses arising from $V_{\theta X2}$ and V_θ of Fig.31, from $V_{\theta Y2}$ and from non-uniform torsion have all been found to be negligibly small.

Action $M_{\theta Y.TOT}$ is the dominant action in regard to stresses, and the bucket edges are critical as the locations of the maximum total direct stresses on the cross-section. Fig.37 shows the variation with Θ of the total direct stresses on the edges of the bucket. Overall, the outlet edge is more highly stressed than the inlet edge. The maximum jet loading stress in the bucket, 4800 lb/in^2 tension, occurs on the outlet edge at $\Theta = 127^\circ$, which is at the junction of the outlet edge with the hub. In comparison with the corresponding maximum rimless jet loading direct stress of + 14,950 lb/in^2 at the same location, the effect of the restraint on the bucket by the rim on the remainder of the wheel, is evidently a reduction of some 68% in the maximum rimless jet loading stress.

There is an interesting parallel between these calculated jet loading stresses on the edges of a Turgo wheel bucket, and the stresses measured by PERRIG[4], Fig.2, on the edges of a Pelton bucket under simulated jet loading. If PERRIG'S values for the bucket on the Pelton wheel with rims are accepted, it is evident from Fig.2 that the addition of rims reduces the maximum measured stress in the bucket from + 860 kg/cm^2 (12,200 lb/in^2) to + 130 kg/cm^2, a reduction of some 85%. This compares with/

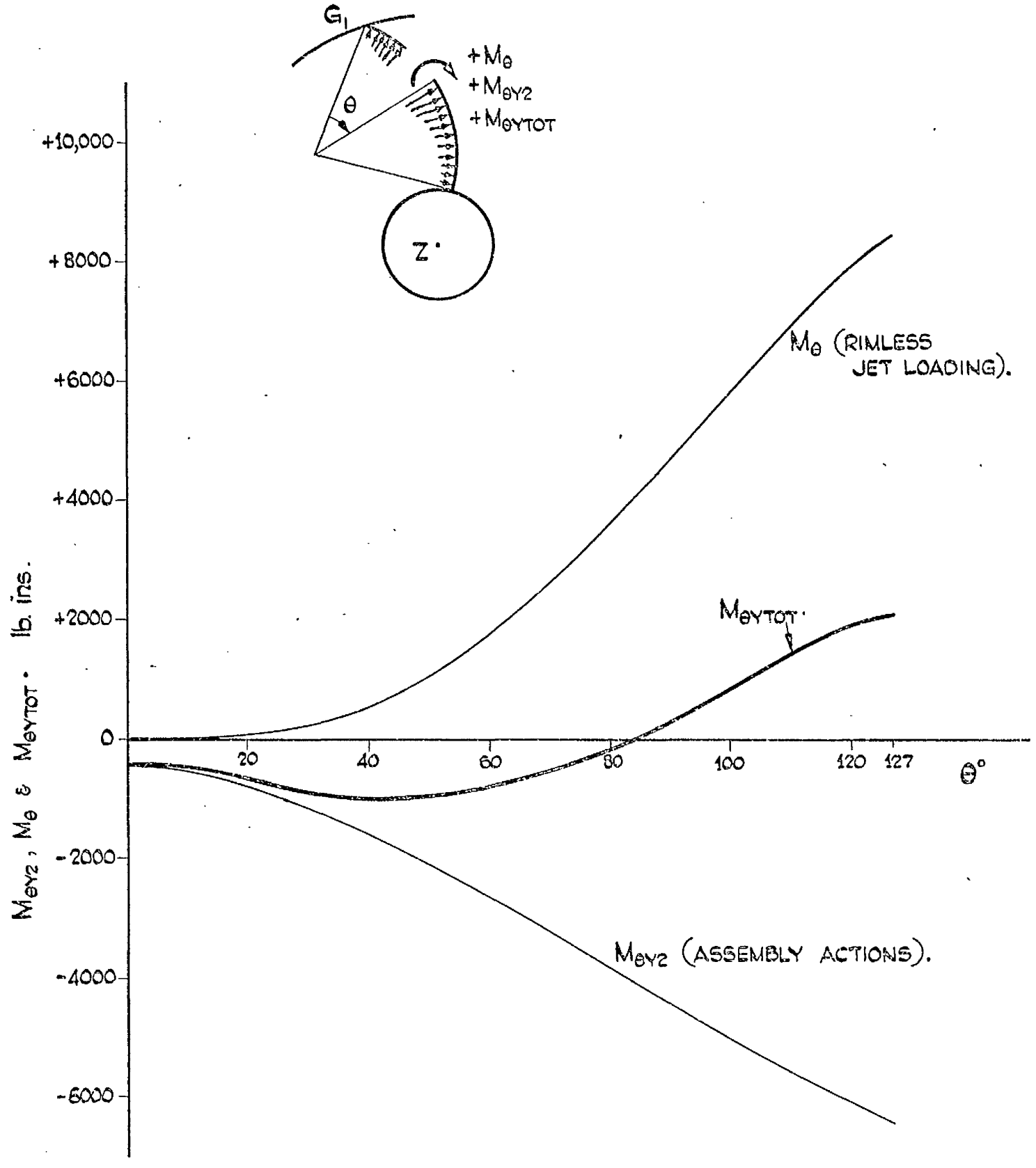

FIG. 35. DISTRIBUTIONS WITH θ OF IN-PLANE BENDING MOMENTS, $M_{\theta y2}$ DUE TO ASSEMBLY ACTIONS, M_θ RIMLESS JET LOADING (FIG. 31), AND THEIR RESULTANT $M_{\theta yTOT}$, ALL ON THE EQUIVALENT BUCKET OF THE $16\frac{1}{2}$ IN. CAST STEEL TURGO WHEEL UNDER NORMAL WORKING CONDITIONS. $M_{\theta yTOT}$ IS THE TOTAL JET LOADING IN-PLANE BENDING MOMENT ON THE BUCKET.

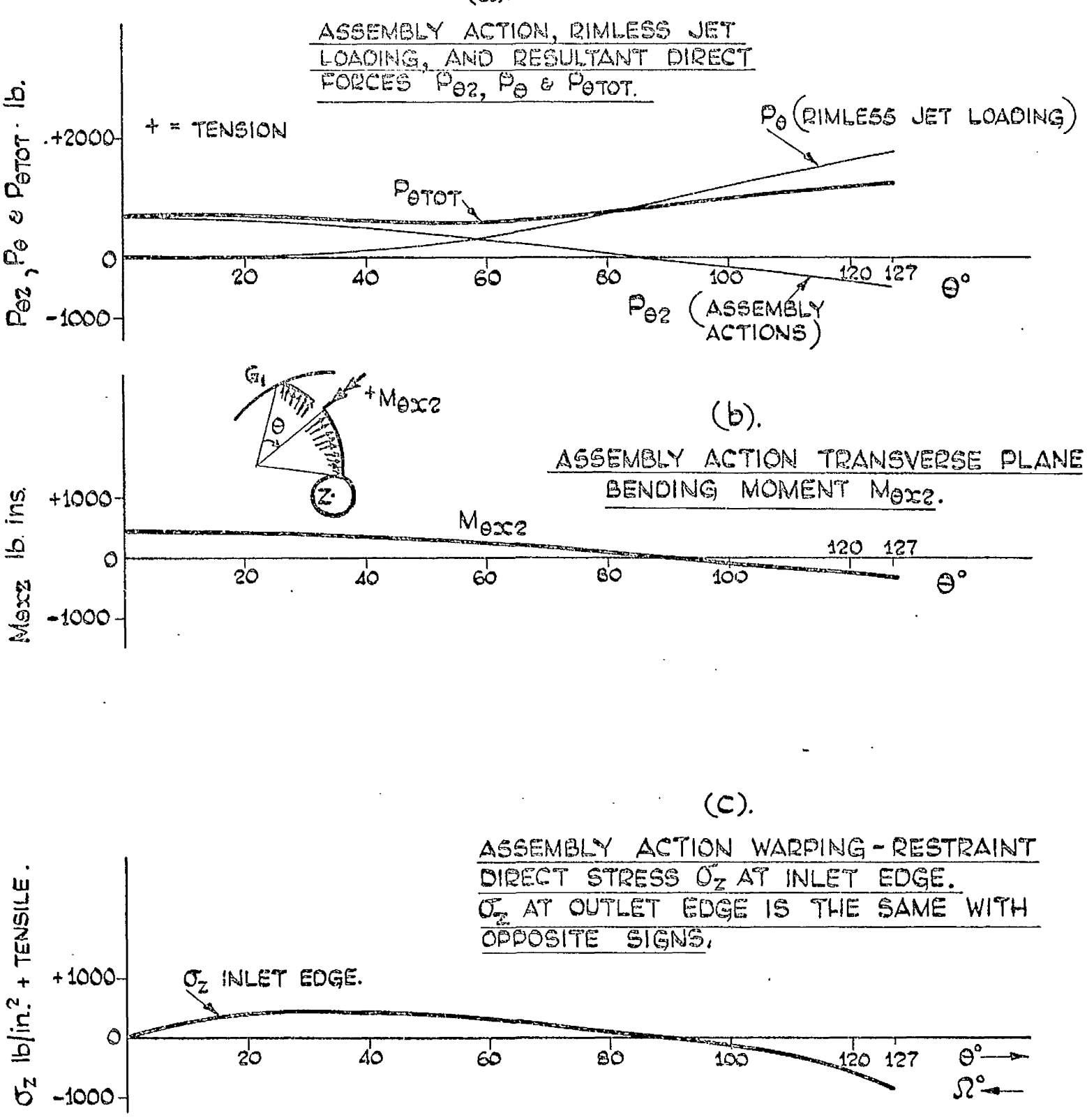

Fig. 36. DISTRIBUTIONS WITH θ OF DIRECT FORCES $P_{\theta z}$, P_θ (FROM Fig. 31) AND THEIR RESULTANT $P_{\theta TOT}$, BENDING MOMENT $M_{\theta x z}$ AND WARPING-RESTRAINT DIRECT STRESS σ_z AT INLET EDGE ALL ON THE EQUIVALENT BUCKET OF THE $16\frac{1}{2}$ IN. CAST STEEL TURGO WHEEL UNDER NORMAL WORKING CONDITIONS. (JET LOADING).

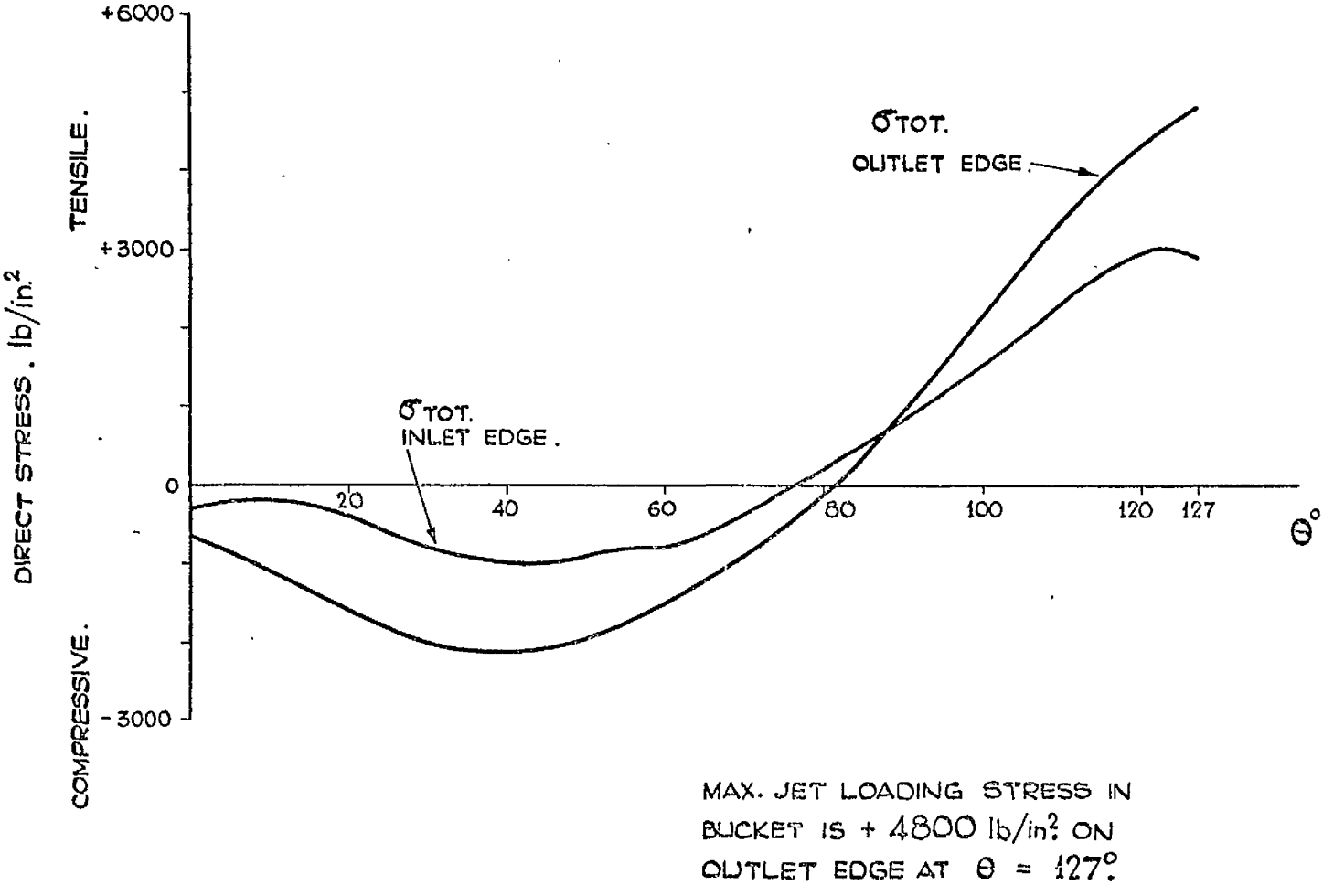

FIG. 37. DISTRIBUTION WITH θ OF THE TOTAL JET LOADING DIRECT STRESSES ON THE INLET AND OUTLET EDGES OF THE EQUIVALENT BUCKET OF THE 16½" CAST STEEL TURGO WHEEL UNDER NORMAL WORKING CONDITIONS.

with the reduction of some 68% calculated for the case of the Turgo wheel bucket. Regarding this analysis for the Turgo wheel bucket therefore, measurements in a roughly parallel situation confirm that restraint on a bucket, by a rim arrangement on the remainder of the wheel, has a very significant reducing influence on the value of the maximum rimless jet loading stress in the bucket.

Total jet loading stresses in the rim

The only loading on the rim on the remainder of the wheel is that of the assembly actions at junction point G_1, Fig.32(d). On account of the assumptions illustrated in Fig.32 and which culminate in the treatment of the rim on remainder of wheel as a 180° fully-fixed arch, it is unrealistic to consider stresses at any point other than junction point G_1 on this system. Knowing the magnitudes and directions of assembly actions F_{R1}, F_{T1}, etc., corresponding internal actions at G_1 on the rim are found from the pertinent equations of section 3C iii, and so the stresses there are determined. The total direct stresses (circumferential) at the extreme fibres of the rim junction point cross-section are indicated on Fig.38, the shear stresses on this section having been found to be negligible. The maximum jet loading stress in the rim is 1350 lb/in^2 circumferential tension at the outer radius/outlet side edge of the section containing the point of junction with the jet-loaded bucket.

With regard to restraint exerted on the jet-loaded bucket by the rim on the remainder of the wheel, the rationality of the treatment of the latter as a 180° fully-fixed arch, may be assessed by comparing the results with those derived from assumptions of an unrealistically stiff restraint and of an unrealistically flexible restraint. Since the dominant action on the bucket under jet loading is clearly in-plane bending, it is a sufficient basis of assessment to compare the resulting values of total in-plane bending moment $M_{\theta Y.TOT}$. Curve I, Fig.39, shows $M_{\theta Y.TOT}$ determined/

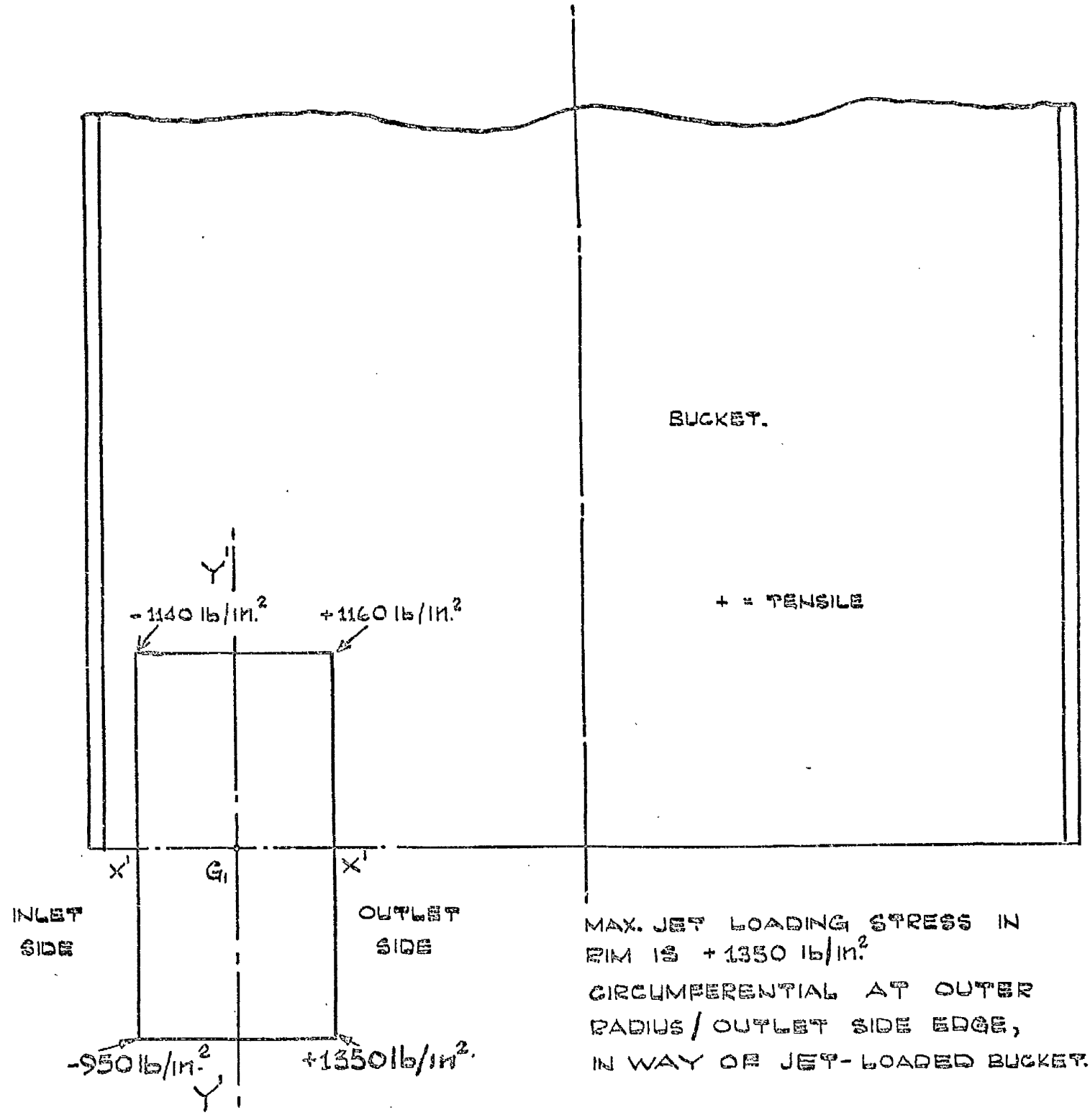

FIG.38. VALUES OF THE TOTAL JET LOADING DIRECT STRESSES (CIRCUMFERENTIAL) ON THE EQUIVALENT RIM CROSS-SECTION, FOR THE 16½ IN. CAST STEEL TURGO WHEEL UNDER NORMAL WORKING CONDITIONS. THE VALUES ARE AT THE EXTREME FIBRES OF THE CROSS-SECTION WHICH CONTAINS G1, THE POINT OF JUNCTION WITH THE JET-LOADED BUCKET.

I / $M_{\theta Y TOT.}$, ASSUMING BUCKET/RIM RESTRAINT TO BE A FULLY-FIXED 180° ARCH. (FROM FIG. 35).

II / $M_{\theta Y TOT.}$, " " " " TO BE A FULLY-FIXED SUPPORT.

III / $M_{\theta Y TOT.}$, " " " " TO BE A SYSTEM OF TWO CO-LINEAR BUCKETS.

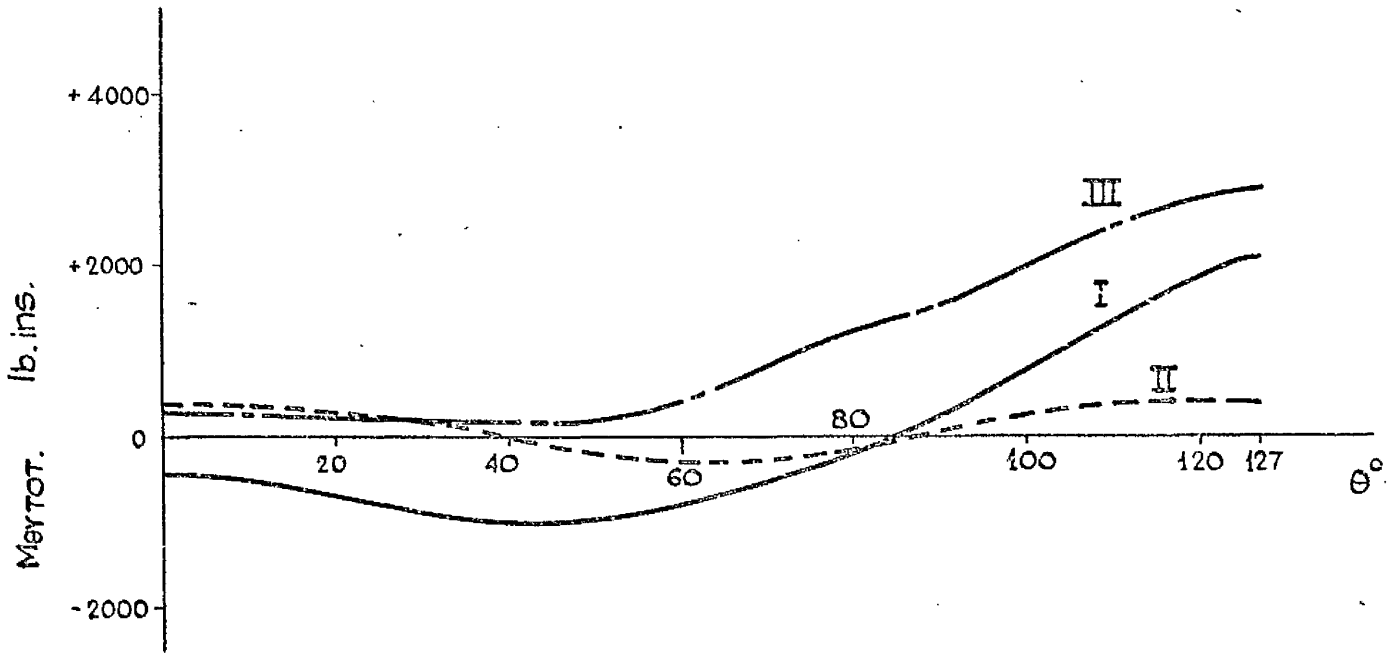

FIG. 39. DISTRIBUTIONS OF $M_{\theta Y TOT.}$ WITH θ, ON THE EQUIVALENT BUCKET OF THE 16½" CAST STEEL TURGO WHEEL UNDER NORMAL WORKING CONDITIONS. COMPARISON OF ASSUMPTIONS REGARDING RESTRAINT EXERTED AT BUCKET/RIM JUNCTION. (JET LOADING).

determined from the "arch" assumption, this curve being transferred directly from Fig.35. For the assumption of a fully-rigid restraint, which of course is unrealistically stiff, the left-hand sides (suffix 1) of the displacement compatibility equations (3C.40) to (3C.45) become zero, and the pertinent assembly actions are evaluated on this basis. This is a useful case to consider now, not only for purposes of comparison, but also since the results provide a partial check on the formulation of the simultaneous equations of the prior calculation. Among other characteristic features, the resultant transverse actions on the bucket are found to be zero, the results being obtained:-

$$F_{A2} = 0, \qquad M_{R2} + F_{T2}.d = 0, \qquad M_{T2} - F_{R2}.d = 0,$$

all as they should be. The $M_{\theta Y.TOT}$ distribution with Θ for the fully-rigid restraint case is shown as curve II on Fig.39.

The unrealistically flexible restraint is somewhat imaginary but possesses double virtues of being obviously unrealistically flexible and of giving results very easily derivable from those for fully-rigid restraint. It comprises restraint provided by two buckets rigidly attached to the hub, co-linear with the jet-loaded bucket, but both rigidly connected to it only at the junction point. Clearly such an imaginary system would be expected to offer less restraint at junction point G_1 than that of Fig.32(b). In each of the relevant displacement compatibility equations (3C.40) to (3C.45), for every assembly action term, suffix 2, on the right-hand side, e.g. $+ 8.75688 \times 10^{-6} F_{R2}$, there is on the left-hand side a corresponding assembly action term, suffix 1, with the coefficient halved, e.g. $+ \frac{1}{2} \times 8.75688 \times 10^{-6} F_{R1}$. In view of the equilibrium equations (3C.46) to (3C.51), the net effect is that the six compatibility equations are the same as those for fully-rigid restraint, with left-hand sides zero, but with the numerical terms for Δ_{R2}, Δ_{T2} and Φ_{P2} multiplied by $\frac{2}{3}$. Hence the relevant assembly actions are $\frac{2}{3}$ of the corresponding assembly actions for the fully-rigid restraint case. Curve III, Fig.39, gives the values for $M_{\theta Y.TOT}$ for this "two co-linear buckets" restraint case.

It/

It is evident from Fig. 39 that in respect of the maximum values of $M_{\theta Y.TOT}$, which occur at $\theta = 127^{\circ}$, curve I of $M_{\theta Y.TOT}$ derived from the "arch" assumption for rim restraint, lies between curves II and III of $M_{\theta Y.TOT}$ values for the two extreme restraint cases. This indication, together with the experimental data of PERRIG, previously cited, provide support for the "arch" assumption as a reasonably realistic and useful approximation.

From a survey of the method of calculation it is noteworthy that:-

(1) All the induced actions on the bucket at θ, due to the rimless jet loading condition and due to the assembly condition, are directly proportional to $W_{\theta=\frac{\alpha}{2}}$. So the rimless jet loading stresses, the assembly action stresses, and therefore the total stresses are directly proportional to $W_{\theta=\frac{\alpha}{2}}$. The actions and stresses at the junction point section of the rim are also directly proportional to $W_{\theta=\frac{\alpha}{2}}$.

(2) The rimless jet loading stresses are independent of the elastic constants, but the assembly action stresses are dependent on ν, so the total stresses are functions of ν. For materials of the same, or nearly the same ν, the same stresses will be determined, other factors being constant.

The maximum jet loading stress of + 4800 lb/in.^{2}, or about + 2.1 T/in.^{2}, in the $16\frac{1}{2}$ in. cast steel Turgo wheel under normal working conditions, is of reasonable order, and occurs in a fairly small localised region of the bucket outlet edge. Appropriate superposition of the graphs of Figs. 26 and 37 indicates that the total maximum normal working stress (centrifugal + jet loading) is about + 10,800 lb/in.^{2}, or just less than + 5 T/in.^{2}, a value not as high as would be expected to lead to failure.

Concerning the subsequent experimental analyses of the $16\frac{1}{2}$ in. cast aluminium Turgo wheel, since this material has the same value of ν as the/

the cast steel, the pertinent approximate theoretical jet loading actions and stresses are exactly the same as those calculated for the cast steel wheel, for the same value of the jet loading parameter $W_{\theta=\frac{\pi}{2}}$.

3D COMPARISON OF CENTRIFUGAL AND JET LOADING APPROXIMATE STRESSES AND DEFORMATIONS, AND COMBINATION OF CENTRIFUGAL AND JET LOADING APPROXIMATE STRESSES

Application of the analyses to the $16\frac{1}{2}$ in.cast steel Turgo wheel shows that the bucket edges are the critical locations of high stress, exhibiting the stress maxima. From Figs.26 and 37 the maxima are as follows:-

Normal working conditions:
- Maximum centrifugal stress = + 8750 lb/in^2
- Maximum jet loading stress = + 4800 lb/in^2
- $\therefore$ ratio, $\frac{\text{Max. centrif. stress}}{\text{Max.jet load.stress}} = 1.82$

Overspeed condition:- Maximum centrifugal stress = + 28,400 lb/in^2

Centrifugal stress is clearly dominant at normal working conditions and is critically important at overspeed.

Considering normal working conditions, the governing action in respect of both centrifugal and jet loading maximum stresses is in-plane bending of the bucket. The predominance of the maximum centrifugal stress is predictable from the results of the free rotating and rimless jet loading conditions of the bucket. The edge direct stresses for these two conditions are compared in Fig.40 and the associated displacement discontinuities at the bucket junction point are compared as follows:-

free rotating condition	rimless jet loading condition
$\Delta_{R2.TOT} - \Delta_{R1} = + 7020 \times 10^{-6}$ in	$\Delta_{R2} = + 4420 \times 10^{-6}$ in
$\Delta_{T2.TOT} = + 11,080 \times 10^{-6}$ in	$\Delta_{T2} = + 9660 \times 10^{-6}$ in
$\Phi_{P2} = + 2,080 \times 10^{-6}$ rads	$\Phi_{P2} = + 1380 \times 10^{-6}$ rads

It is evident that the stress maxima for the two conditions are of similar/

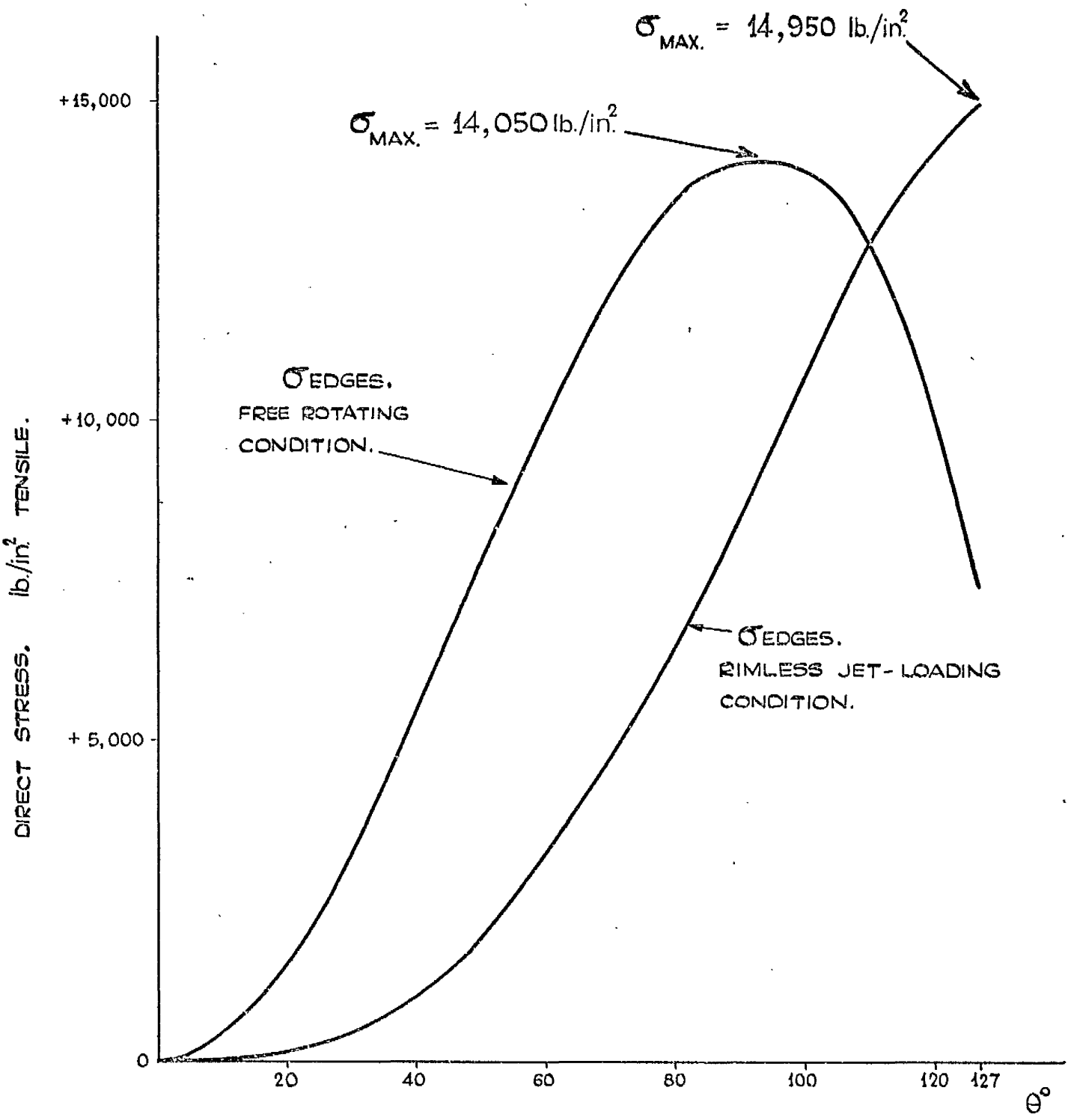

FIG. 40. COMPARISON OF THE DISTRIBUTIONS WITH θ OF THE DIRECT STRESSES ON THE BUCKET EDGES FOR THE FREE ROTATING CONDITION AND FOR THE RIMLESS JET LOADING CONDITION OF THE EQUIVALENT BUCKET OF THE 16½" CAST STEEL TURGO WHEEL, UNDER NORMAL WORKING CONDITIONS.

similar value, but the displacement discontinuities are significantly greater for the free rotating condition than for the rimless jet loading condition, a feature in accordance with the edge stress variations. Now for the assembly conditions at the junction point, even on a qualitative basis it may be seen that the restraint offered by the rim in the centrifugal loading case, where the rim cannot restrain tangential deflection, will be considerably less than the restraint exerted by the rim, supported by all the unloaded buckets, in the jet loading case. It would therefore be expected that the total maximum centrifugal stress would exceed the total maximum jet loading stress, perhaps by a margin somewhat more than that estimated.

In comparing the two cases from this viewpoint, it must be noted that the distribution of jet loading on the bucket has been assumed in the absence of directly pertinent data, so the degree of approximation associated with the rimless jet loading calculation is greater than that associated with the centrifugal counterpart. However, it is reasonable to consider that any other appropriate jet loading distribution should exhibit roughly the same magnitude, position and direction of the resultant jet force on the bucket, so giving about the same value of maximum stress for the rimless jet loading condition. Thus a similar comparison in the magnitudes of the total centrifugal and jet loading stress maxima would be looked for.

With regard to the assembly conditions for the centrifugal loading and jet loading cases, the comparative effectiveness of the restraints exerted respectively by the rim and by the rim on the remainder of the wheel, may be gauged from the $M_{\theta Y2}$ curves of Figs. 23 and 35 in relation to the respective M_{θ} curves. The restraint in the case of jet loading is the much more effective one. This has already been illustrated in sections 3B v and 3C v where, in the former, the rim restraint reduces the maximum free/

free rotating stress by only about 38% while in the latter, the actions of the rim on the remainder of the wheel reduce the maximum rimless jet loading stress by some 68%. It is also interesting to compare the values found in the two cases for the total tangential deflections of the bucket/rim junction point, (Figs. 22 and 34):-

centrifugal loading condition	jet loading condition
$\Delta_{T2.ToT} + \delta_{T2} = +5020 \times 10^{-6}$ in	$\Delta_{T2} + \delta_{T2} = +690 \times 10^{-6}$ in

In the centrifugal loading case the rim restraint permits almost 50% of the free rotating tangential deflection of the bucket to occur, while in the jet loading case the restraint of the rim on the remainder of the wheel permits less than 10% of the rimless jet loading tangential deflection to take place. This demonstrates the essential difference in the characters of the two restraints.

As already mentioned, in respect of the assumed jet loading distribution, the degree of approximation of the jet loading analysis is greater than that of the centrifugal loading analysis. This is of course also the case in respect of the comparative restraints producing assembly, where for centrifugal loading, the rim is fairly realistically treated, but where, for jet loading the rim on the remainder of the wheel is assumed to be replaced by a 180° fully-fixed arch - a system simpler than the actual system. Both analyses are approximate in respect of the geometry assumed and of the assumption of beam behaviour of the buckets in place of actual shell behaviour. A noteworthy geometrical assumption is that of point contact between bucket and rim at their junction. The actual contact is over a long "line", part of which subtends an angle of $\Theta \simeq 45^{\circ}$ at Z_1. (Fig. 9). These and other assumptions are factors to be considered when assessing these calculated results in the light of corresponding experimental data.

In/

In light of the indication that centrifugal stress is predominant for normal working conditions of the $16\frac{1}{2}$ in. cast steel Turgo wheel, and also in light of the magnitude of the maximum centrifugal stress at overspeed, it is rational as well as practically convenient to conduct subsequent corresponding experimental stress analyses on this size of wheel, mainly as follows:-

(1) By spinning the wheel in the dry condition in a centrifugal test rig, and measuring the centrifugal stresses.

(2) By attempting to simulate the jet loading by mechanical means on the stationary wheel, and measuring the approximate jet loading stresses.

These experimental stress analyses are such as would require to be completed in any case, prior to embarking on considerations of an experimental investigation under actual working conditions, were such an investigation to be contemplated. However, the results of the approximate theoretical analyses indicate that a test under working conditions may hardly be necessary at all and that the experiments in the dry condition, both of which are shown to be necessary, may suffice. Reservations on this point must presently be maintained, of course, in view of ignorance concerning the relevant jet loading distribution and in view of the fact that under normal working conditions, the associated stress component is a cyclic one superimposed on the steady centrifugal stress.

The centrifugal and jet loading stresses on the edges of the bucket of the $16\frac{1}{2}$ in. wheel are indicated respectively on Figs. 26 and 37, from which the cyclic jet loading stress component may be superimposed on the corresponding steady centrifugal stress component, enabling the combinations to be examined. The combined stresses on the edges, taken from these two Figs., are shown on Fig. 41, from which it is seen that under/

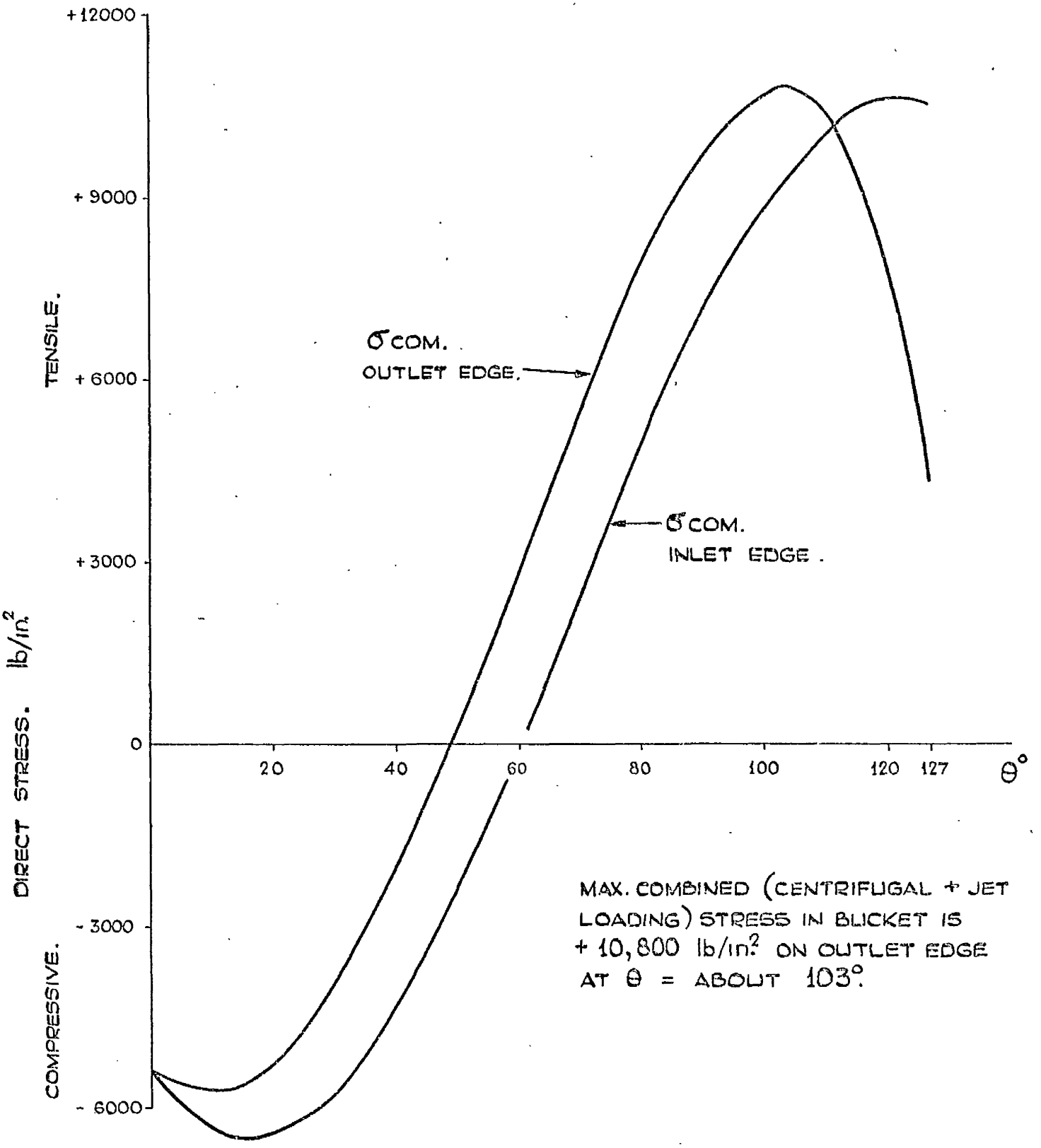

FIG. 41. DISTRIBUTION WITH θ OF THE COMBINED (CENTRIFUGAL + JET LOADING) DIRECT STRESSES ON THE INLET AND OUTLET EDGES OF THE EQUIVALENT BUCKET OF THE 16½" CAST STEEL TURGO WHEEL UNDER NORMAL WORKING CONDITIONS. (FROM FIGS. 26 & 37).

under normal working conditions the maximum combined (centrifugal + jet loading) stress in the $16\frac{1}{2}$ in. wheel is + 10,800 lb/in^2 (+ 4.8 T/in^2) and occurs on the outlet edge of the bucket at Θ = about 103°. From Figs. 27 and 38, the corresponding maximum combined stress in the rim is + 5,450 lb/in^2 at the outlet side/outer radius corner of the bucket junction point section . The maximum stress in the wheel and the stresses of Figs.26, 27, 37, 38 and 41 are all of quite credible order. Steady and cyclic stresses of these comparatively small values would be expected when it is considered that in 20 years of normal working life, such a wheel will withstand, in corrosive conditions, more than 10^{10} cycles of combined stress.

The main conclusions from this chapter are summarised as follows:-

(1) For the $16\frac{1}{2}$ in. cast steel Turgo wheel under normal working conditions:-

(a) Centrifugal stress is predominant, the maximum centrifugal stress being about twice the maximum jet loading stress. Both maxima occur on the outlet edge of the bucket.

(b) For both loadings, the most significant stresses occur on the bucket edges, along which the stress distributions are quite distinctive.

(c) For both loadings the most significant action on the bucket is in-plane bending (bending in the plane of symmetry of the equivalent bucket. This plane is also the plane of the wheel).

(d) These indications provide considerable guidance for subsequent experimental investigations.

(2) The analyses may be applied to estimate the approximate centrifugal and jet loading stresses and deformations in any size of current design Turgo impulse wheel, under any conditions of speed and power. They may thus be used as a basis for studying the approximate effects on the stresses, of alterations in duty and design.

CHAPTER 4.

EXPERIMENTAL INVESTIGATIONS OF THE CENTRIFUGAL AND APPROXIMATE JET LOADING STRESSES AND DEFORMATIONS IN A TURGO IMPULSE WHEEL.

EXPERIMENTAL INVESTIGATIONS OF THE CENTRIFUGAL AND APPROXIMATE JET LOADING STRESSES AND DEFORMATIONS IN A TURGO IMPULSE WHEEL

The major experimental investigations were conducted on the $16\frac{1}{2}$ in. current design Turgo impulse wheel made in aluminium. Guided by the indications from the approximate theoretical stress analyses of the previous chapter, these investigations comprised measurement of the centrifugal strains, followed by measurement of the approximate jet loading strains. In the latter test the approximate jet loading was simulated by mechanical means. In both tests strains were measured at a large number of locations. It was important to set out to explore these many locations, having in mind that the local quantitative results afforded by the experimental analyses, would be inherently of the most direct significance.

Prior to these strain measurements however, an experimental study was undertaken to measure the strains in separate single aluminium buckets under various pertinent loadings. The main objects were to examine the behaviour of the bucket as a shell, and to investigate the estimation of actions on a meridional cross-section of the bucket, from corresponding strain measurements at the section. These matters had important bearing on the subsequent centrifugal and simulated jet loading experimental stress analyses.

The adoption of cast aluminium as the material of these experimental components was on grounds of economy only. Aluminium would not be used for wheels in service. For the rôles taken by the experimental components it proved to be a perfectly adequate material, being found to be linear-elastic to a limit of 6.2 T/in^2 for both the wheel and the separate single buckets.

4A PRELIMINARY EXPERIMENTAL INVESTIGATION ON SEPARATE SINGLE BUCKETS

For the aluminium of the two separate single buckets, the values of Young's Modulus E and Poisson's Ratio ν were found to be:-

$$E = 10.9 \times 10^6 \text{ lb/in}^2 \qquad \nu = 0.3$$

The choice of loadings to be applied to the single buckets was guided mainly by results of the approximate theoretical stress analyses of the previous chapter, supported by general reasoning as to the likely behaviour of a bucket in a working wheel. These indicated that the loadings most relevant to the actual working behaviour should be such as to induce bending in the plane of the wheel as the predominant action on the bucket. It was therefore decided to examine the stresses and deformations of the single buckets under loading by forces approximately tangential and approximately radial, and by a pure moment in the plane of the wheel.

To provide for proper transmission of loading, the bucket for the 18 in.wheel, which is the aluminium bucket of Fig.8, was bolted appropriately at its hub-portion to an L-shaped bracket fabricated from structural steelwork, and an L-shaped plinth of reinforced concrete was cast integral with the hub-portion of the 33 in.wheel bucket. These mountings for the buckets may be seen in Figs.42 and 43.

Before application of strain gauges to the buckets, a test of limited scope was conducted, in which the 18 in.wheel bucket was coated with brittle lacquer and subsequently subjected to approximately tangential loading. One of the important objects of this was to gain experience in brittle lacquer technique prior to its application to investigations on the $16\frac{1}{2}$ in.wheel. The technique, finally developed and used, is detailed in Appendix 4. The strain-sensitivity of the lacquer in this brief test

was/

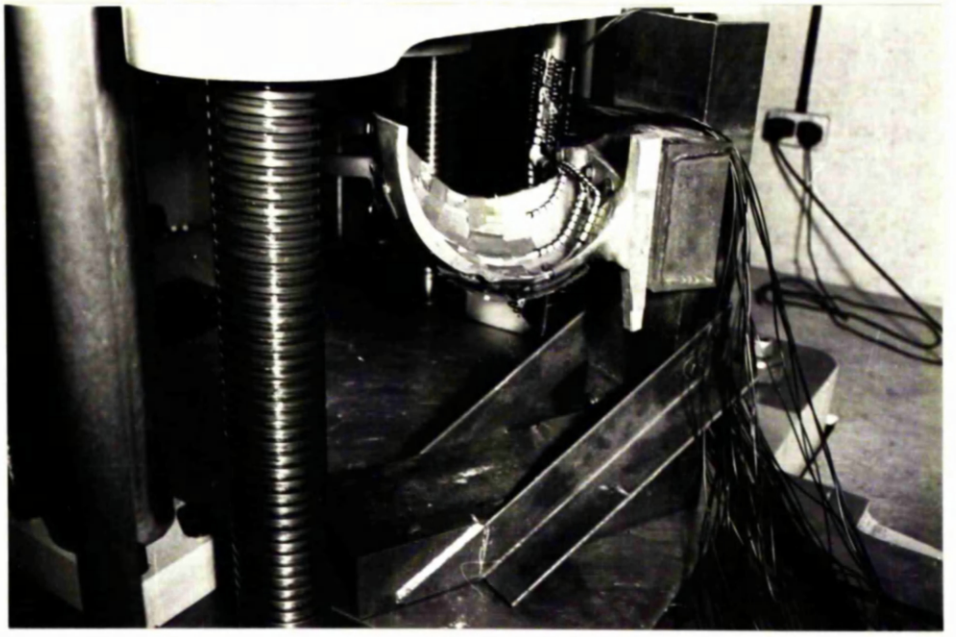

(a) LOOKING ON SWEPT SURFACE OF BUCKET FROM INLET SIDE.

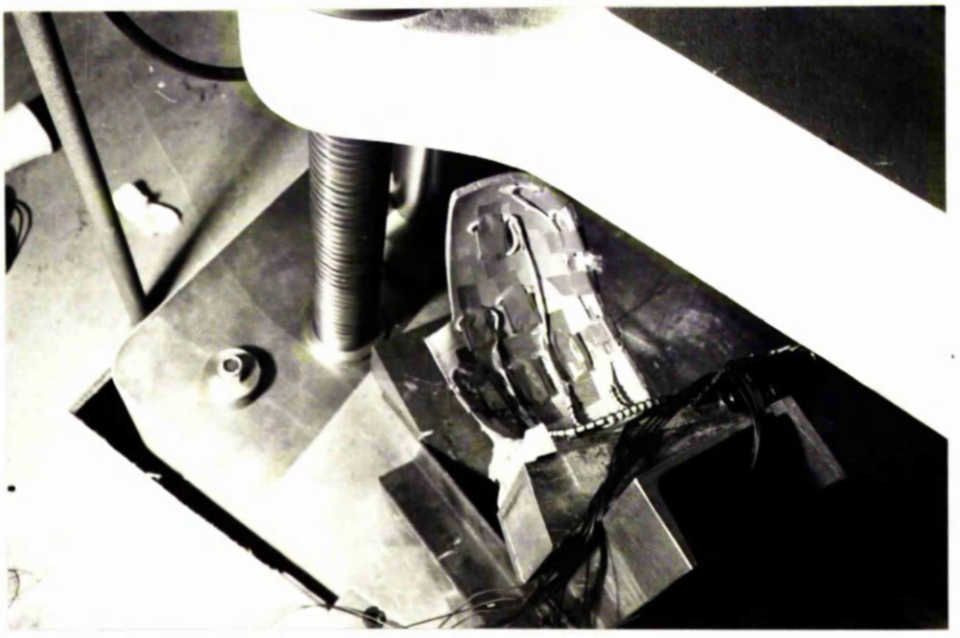

(b) LOOKING DOWN ON SWEPT SURFACE OF BUCKET.

FIG. 42. SINGLE ALUMINIUM BUCKET FOR 18 in.p.c.d. TURGO WHEEL, MOUNTED ON L-SHAPED BRACKET. BUCKET CARRIES STRAIN GAUGES, WIRED AND COVERED, AND IS READY FOR LOADING IN THE ADJACENT COMPRESSION TESTING MACHINE.

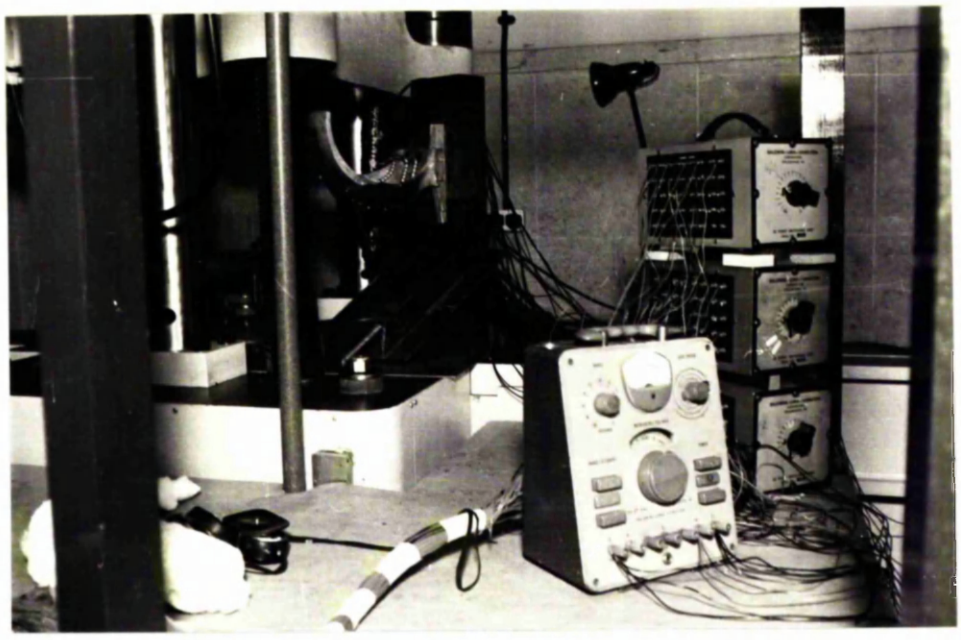

(a) SINGLE ALUMINIUM BUCKET OF FIG. 42, TOGETHER WITH BALDWIN-LIMA-HAMILTON STRAIN MEASURING INSTRUMENT AND SWITCH-BOXES.

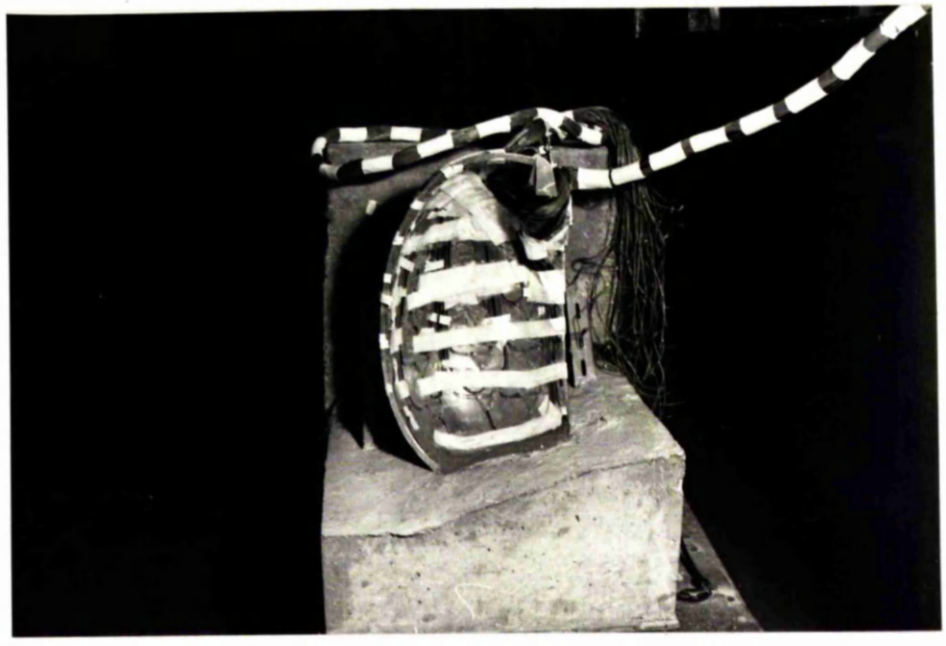

(b) SINGLE ALUMINIUM BUCKET FOR 33 in. p.c.d. TURGO WHEEL (EARLY OBSOLETE DESIGN) MOUNTED ON L-SHAPED REINFORCED CONCRETE PLINTH. BUCKET CARRIES STRAIN GAUGES, WIRED AND COVERED. FOR CONDITIONS SHOWN, SOME OF THESE GAUGES SERVE AS COMPENSATORS WHEN GAUGES ON 18 in. WHEEL BUCKET OF (a) ABOVE, ARE ACTIVE.

FIG. 43.

was found to be about 0.0007. The lacquered bucket on its bracket, was placed in a compression testing machine, somewhat as shown in Figs.42 and 43(a) and a concentrated force, roughly in the tangential direction (with respect to an 18 in.wheel) was applied to the bucket tip. The loading was exactly the same as the approximately tangential loading indicated subsequently in detail in section 4A i.

First cracking of the brittle lacquer occurred at the inlet edge of the bucket on the swept surface, for an approximately tangential force of 400 lb. Photograph, Fig.44(a) shows this condition, while Fig.44(b) indicates the extent of the cracking of the lacquer around this same region, when the force had been increased to 700 lb. At about 500 lb, cracking of the lacquer was also found at two regions on the outlet edge, one on the swept surface roughly on the same meridional section which contained the points of first cracking at the inlet edge, the other on the unswept surface where the outlet edge joined the hub-portion. It was noteworthy throughout the test that, although there was fairly extensive cracking at both edges on the swept surface, there was no evidence of cracking at corresponding points at the edges on the unswept surface.

Knowing the lacquer strain-sensitivity to be about 0.0007, a rough quantitative assessment of the strains in some regions of the bucket, was able to be made for this loading condition. For instance, with reference to Fig.44, it could be said that:-

(a) At 400 lb. the strain at the first crack region on the inlet edge was about 0.0007 tensile.

(b) At 700 lb. the maximum tensile strain on the boundary of the cracked region shown on the swept surface, was about 0.0007.

However, apart from the experience gained in brittle lacquer technique, the value of this short test with regard to bucket behaviour under this loading, was in showing that the bucket edges, mainly on the swept/

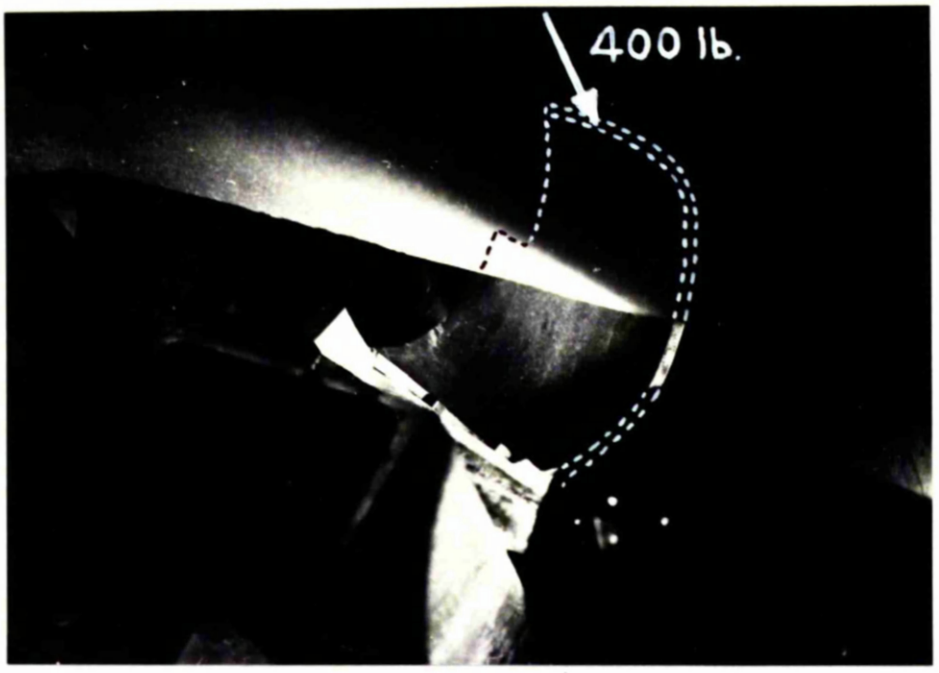

(a) FIRST CRACKING OF BRITTLE LACQUER OCCURS AT INLET EDGE ON SWEPT SURFACE. APPROXIMATELY TANGENTIAL FORCE = 400 lb.

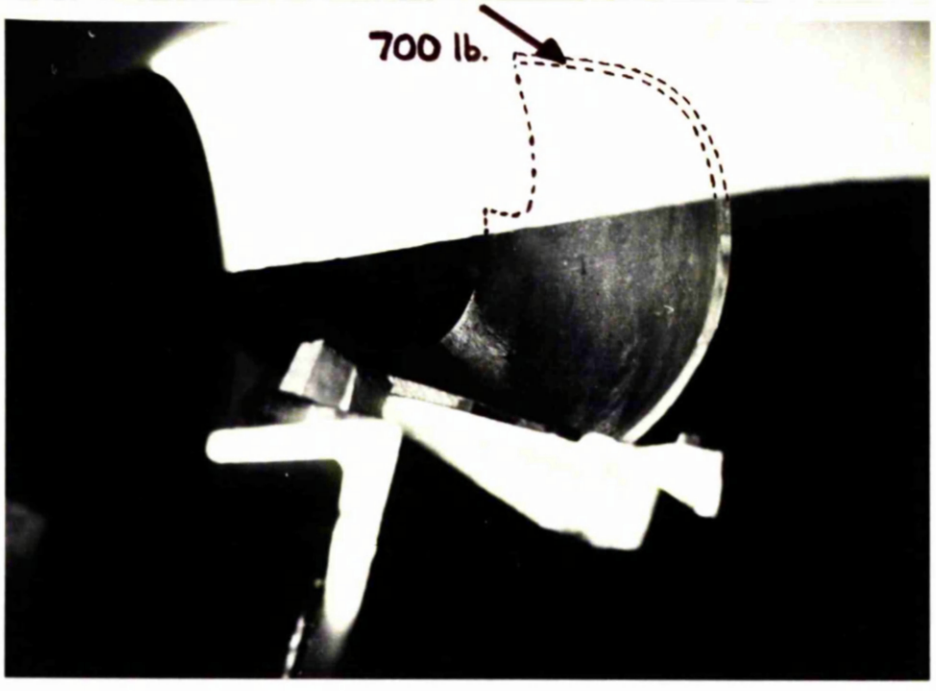

(b) EXTENT OF CRACKING OF LACQUER ON SWEPT SURFACE FOR APPROXIMATELY TANGENTIAL FORCE = 700 lb.

FIG. 44. SINGLE ALUMINIUM BUCKET FOR 18 in. TURGO WHEEL, COATED WITH BRITTLE LACQUER AND LOADED IN TESTING MACHINE BY APPROXIMATELY TANGENTIAL FORCE AT BUCKET TIP. ILLUMINATION SHOWS CRACKING OF LACQUER (LIGHT PARTS AT, AND EXTENDING FROM, INLET EDGE) AND DETAILS HAVE BEEN ADDED TO PHOTOGRAPHS TO CLARIFY THEM AND INDICATE LOADS.

swept side, were the locations of greatest tensile strains, and that at corresponding points at the edges, on the opposite side, the strains were smaller or compressive. This was the first indication, albeit qualitative, of the action of bending moments along the bucket edges. The test also showed, to a small extent, the directions of principal strains on the swept surface. For example it is interesting to note, from the direction of cracking in Fig.44(b) that, for this loading, the principal tensile strains in the region indicated, are roughly perpendicular to the line of the bucket/hub junction rather than perpendicular to a meridional section. This can be seen more clearly if Fig.44(b) is examined in conjunction with Fig.10(a), especially with the unsectioned plaster bucket thereof, on which meridional sections are marked.

4A i Strain measurements on separate single buckets subjected to various loadings

Since it pertained to the current design, the bucket for the 18 in. Turgo wheel was of the greater interest. Electrical resistance strain gauges of 0.25 in gauge length were affixed to this bucket at selected locations, some of which are detailed on Fig.45. Gauge pairs were used at locations on the edges and 45° rosettes at locations remote from the edges. Accurate positioning of the gauges on the bucket was achieved on the basis of measurements taken from the manufacturing drawing (similar to Fig.9) and from the whole and sectioned plaster replicas, Figs.8 and 10. These latter were of particular value for pin-pointing locations on the unswept surface opposite, through the thickness, to selected locations on the swept surface. As indicated in Fig.45, gauges were concentrated particularly on the boundaries of a meridional section of the bucket in the region of the pitch circle — the "average" meridional section of Chapter 3. On the amplified manufacturing drawing (see View Y, Fig.9), this section was specified by $\Theta = 86^{\circ}$.

Similar strain gauges were applied to the 33 in. wheel bucket in a somewhat similar layout. On both buckets, wires were connected to the gauges which were then suitably covered as protection from draughts. Figs.42 and 43 show the components just prior to a loading test on the 18 in. wheel bucket, with strain gauges covered and wires run. Fig.43(a) also shows the strain measuring instrument and switch boxes which were used. The strain bridge and the three switch boxes were of the Baldwin-Lima-Hamilton types. Connections were so arranged that when one bucket was under loading, with its strain gauges active, gauges on the other served as compensators.

On/

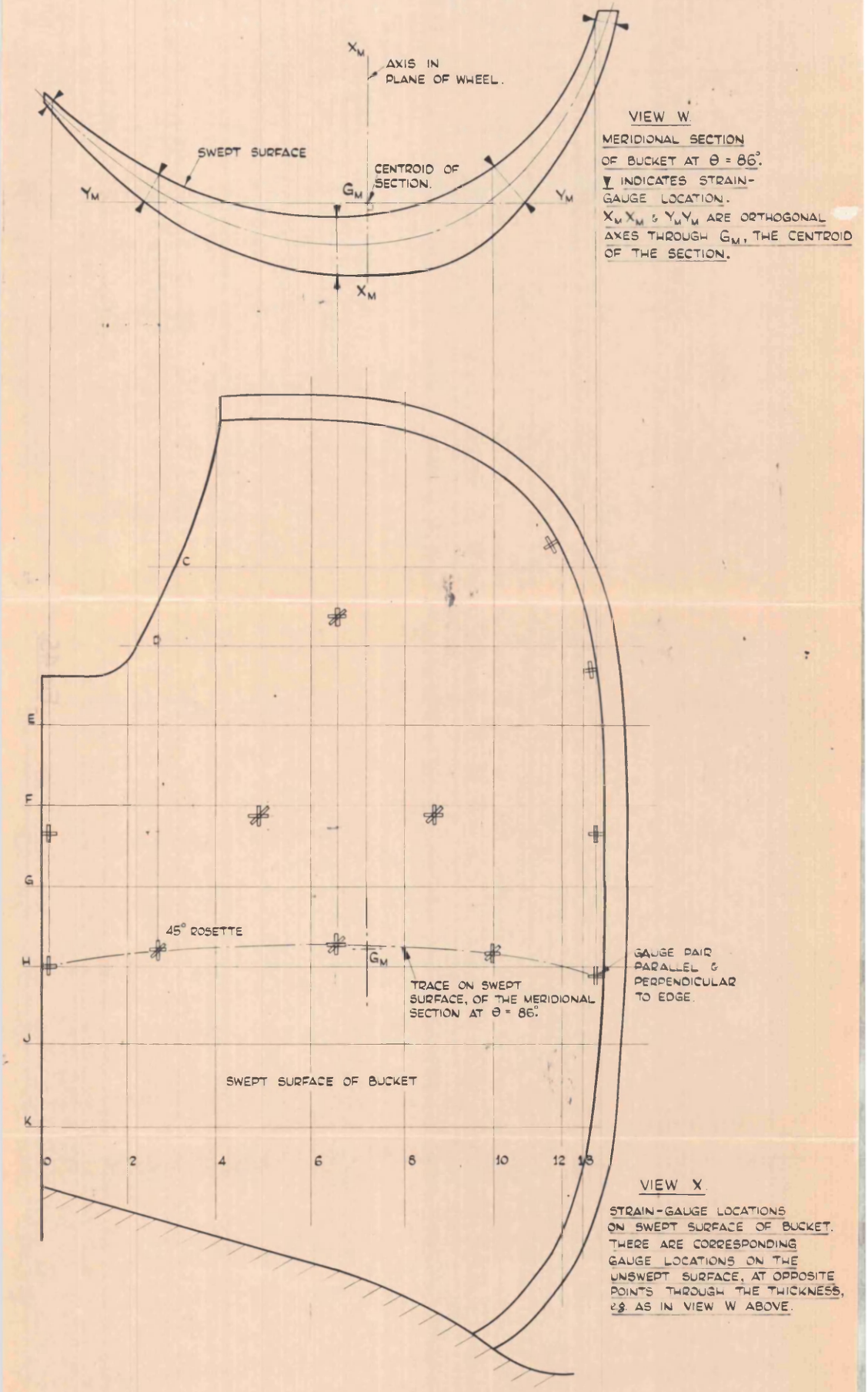

VIEW W

MERIDIONAL SECTION OF BUCKET AT $\theta = 86°$.
▼ INDICATES STRAIN-GAUGE LOCATION.
$X_M X_M$ & $Y_M Y_M$ ARE ORTHOGONAL AXES THROUGH G_M, THE CENTROID OF THE SECTION.

VIEW X

STRAIN-GAUGE LOCATIONS ON SWEPT SURFACE OF BUCKET. THERE ARE CORRESPONDING GAUGE LOCATIONS ON THE UNSWEPT SURFACE, AT OPPOSITE POINTS THROUGH THE THICKNESS, e.g. AS IN VIEW W ABOVE.

FIG 45.

STRAIN-GAUGE LOCATIONS ON SINGLE SEPARATE ALUMINIUM BUCKET FOR 18 IN. P.C.D. TURGO WHEEL.

VIEWS SHOWN CORRESPOND TO VIEWS X & W OF FIG. 9.

FULL SIZE.

On the bucket of the 18 in.wheel, strains were measured for loading by pure moment in the plane of the wheel, and by forces approximately tangential and approximately radial (with respect to the wheel), applied at the bucket tip. The moment was effected as shown in Fig.46, by applying equal and opposite vertical forces to the ends of a bar which was grooved to fit tightly on the bucket tip. Araldite adhesive was used to make a temporary but sufficiently strong joint between bar and bucket. The approximately tangential and approximately radial forces at the bucket tip were applied by a compression testing machine in which the bucket, on its bracket, had been suitably arranged, for example somewhat as indicated in Figs.42 and 43(a). The directions and points of application of these forces on the bucket are specified in Figs.47 and 48. There they are referred to the three-dimensional orthogonal axes $X_M X_M$, $Y_M Y_M$, $Z_M Z_M$, pertaining to the $\Theta = 86^\circ$ meridional section of the bucket, the centroid G_M of this section, Fig.45, being the origin of axes. The arrangements of these force directions substantially parallel and perpendicular to the meridional section, were achieved only after painstaking setting-up procedures in the compression machine.

Loading and unloading were applied incrementally, strains being read correspondingly. The readings throughout were found to be linear-elastic. The results, in the form of principal stresses at the meridional section locations, are shown in Figs.46, 47 and 48 for the maximum values of the three loadings. These results typify the strain behaviour of the bucket. The tendencies and behaviour indicated were fully confirmed by the results from all the other gauges.

Strains were measured on the obsolete design bucket for the 33 in. wheel, under approximately tangential and approximately radial forces applied at the tip. The characteristics of the results obtained were exactly similar to those exhibited by the results of the corresponding tests on the 18 in.wheel bucket.

It/

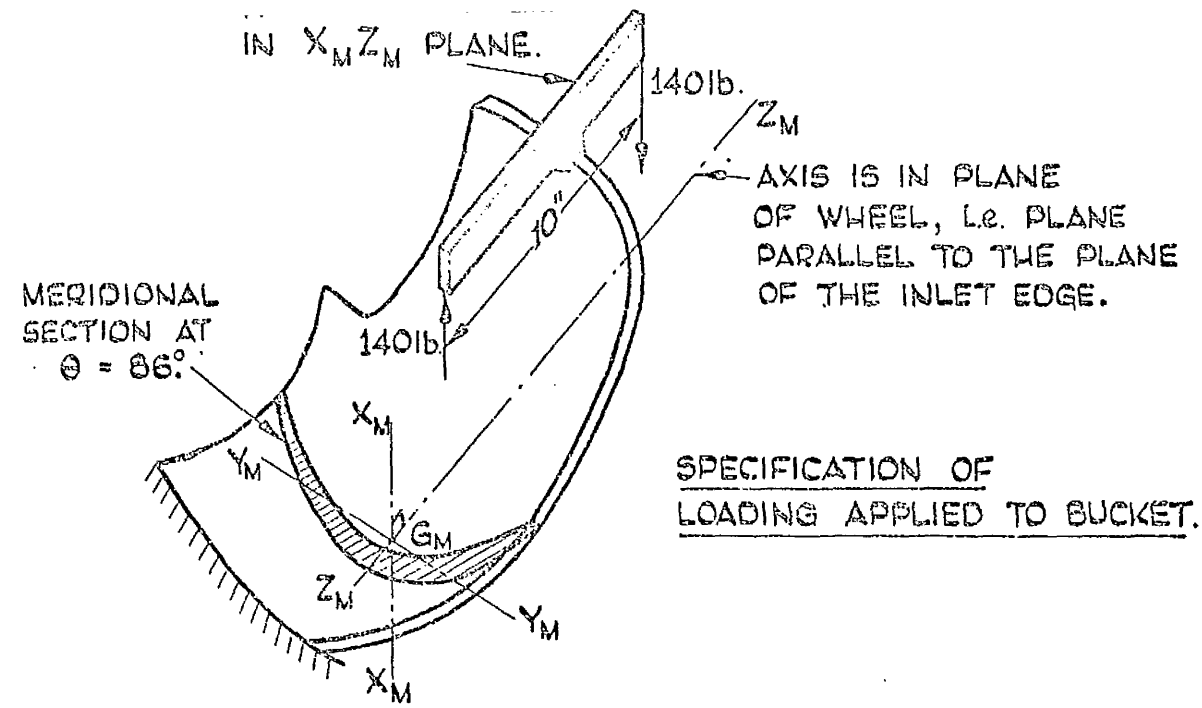

SPECIFICATION OF LOADING APPLIED TO BUCKET.

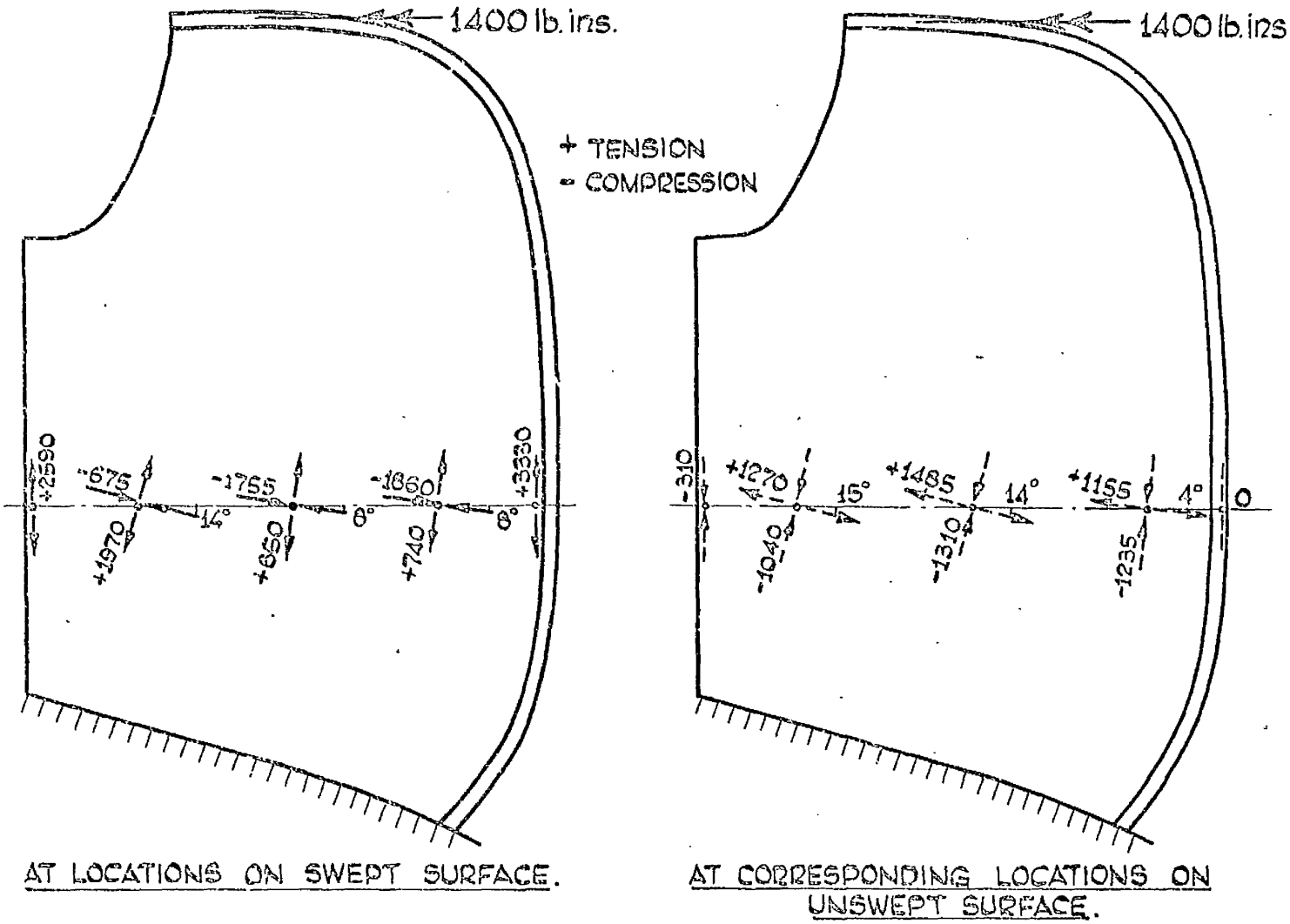

AT LOCATIONS ON SWEPT SURFACE.

AT CORRESPONDING LOCATIONS ON UNSWEPT SURFACE.

Fig. 46. PRINCIPAL STRESSES (lb./in.^{2}) ON SINGLE ALUMINIUM BUCKET FOR 18 IN. P.C.D. TURGO WHEEL, DUE TO LOADING BY PURE BENDING MOMENT OF 1400 lb. ins. IN THE PLANE OF THE WHEEL. THE STRESSES ARE SHOWN AT THE LOCATIONS ON THE $\theta = 86°$ MERIDIONAL SECTION, (Fig. 45) FOR THE MAXIMUM VALUE OF THIS LOADING.

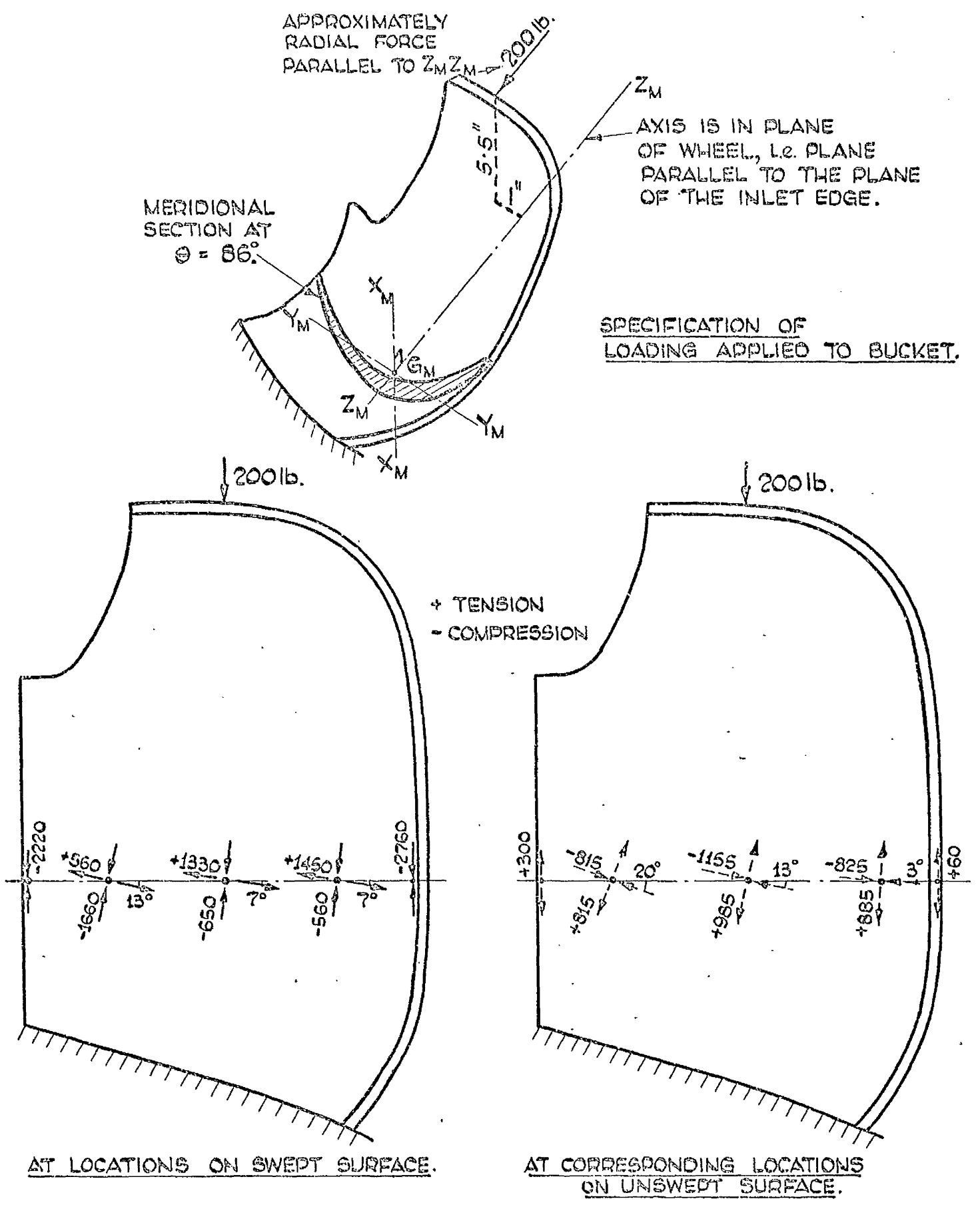

Fig. 47. PRINCIPAL STRESSES (lb./in.²) ON SINGLE ALUMINIUM BUCKET FOR 18 IN. P.C.D. TURGO WHEEL, DUE TO LOADING BY APPROXIMATELY RADIAL FORCE (WITH RESPECT TO WHEEL) OF 200 lb. THE STRESSES ARE SHOWN AT THE LOCATIONS ON THE $\Theta = 86°$ MERIDIONAL SECTION, (FIG. 45) FOR THE MAXIMUM VALUE OF THIS LOADING.

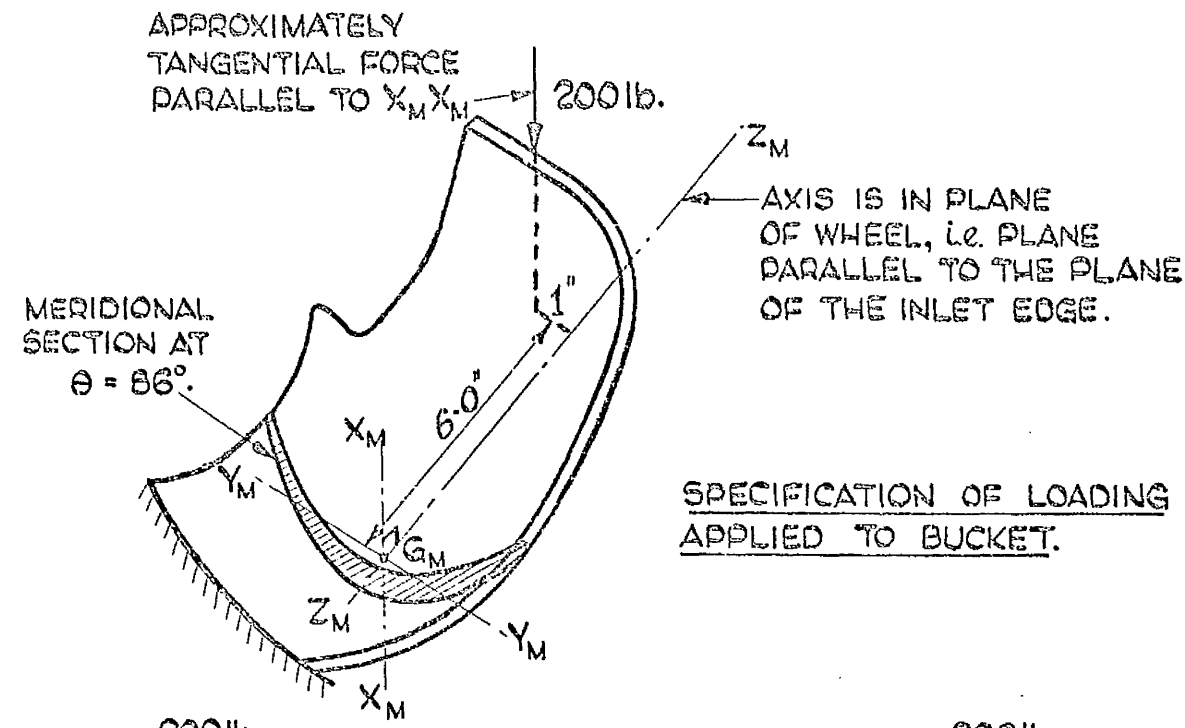

SPECIFICATION OF LOADING APPLIED TO BUCKET.

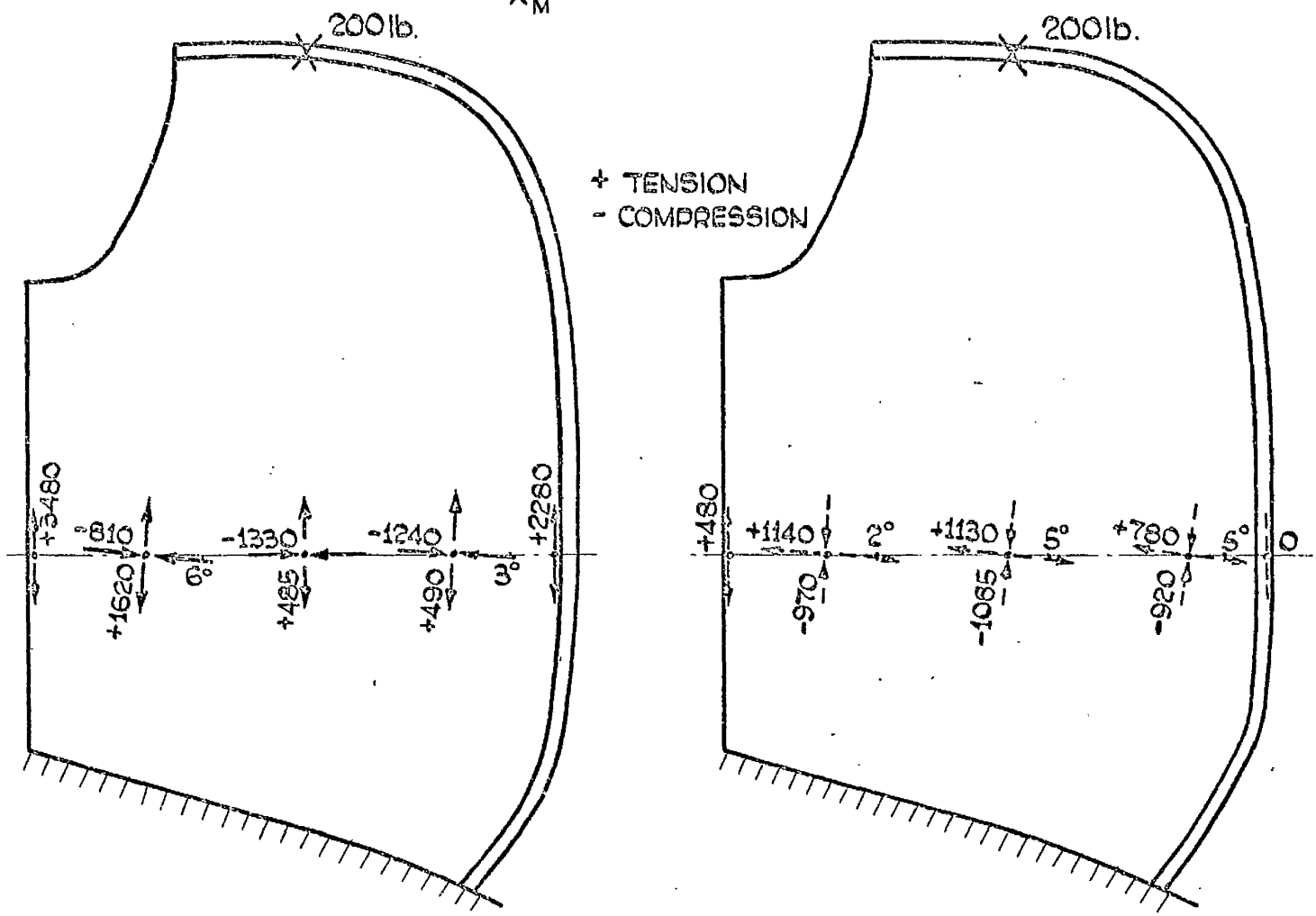

AT LOCATIONS ON SWEPT SURFACE.

AT CORRESPONDING LOCATIONS ON UNSWEPT SURFACE.

FIG. 48. PRINCIPAL STRESSES (lb/in²) ON SINGLE ALUMINIUM BUCKET FOR 18 IN. P.C.D. TURGO WHEEL, DUE TO LOADING BY APPROXIMATELY TANGENTIAL FORCE (WITH RESPECT TO WHEEL) OF 200lb. THE STRESSES ARE SHOWN AT THE LOCATIONS ON THE θ = 86° MERIDIONAL SECTION, (FIG. 45) FOR MAXIMUM VALUE OF THIS LOADING.

It is clear from Figs.46, 47 and 48 that the principal stress directions on both surfaces, at the meridional section, are not far from being parallel and perpendicular to the plane of the wheel, or alternatively, are almost circumferential and meridional. There is a common slight deviation from the circumferential and meridional towards the parallel and perpendicular to the line of the bucket/hub junction, this tendency being most in evidence at the locations nearest this junction. For purposes of discussion, however, it is not unreasonable to say that the principal planes are substantially circumferential and meridional.

The most remarkable feature throughout is the presence, remote from the edges, of appreciable meridional stress, of sign opposite to that of the corresponding circumferential stress. At the majority of the non-edge locations the meridional stress has the higher magnitude. The signs of the meridional stresses on the two surfaces for a given loading, show that the meridional section deforms mainly by bending, the meridional curvature changing in a sense opposite to that of the corresponding change in the circumferential or in-plane curvature. For instance, in the cases, Figs.46 and 48, where the applied in-plane bending moment tends to reduce the circumferential curvature, the meridional curvature is increased (meridional compression on the swept surface, tension on the unswept). The situation is vice-versa in the case, Fig.47, where the applied in-plane bending moment tends to increase the circumferential curvature.

In all three loading cases both edges of the bucket show the same general stress behaviour and the highest stresses on the section occur at the edge locations on the swept surface. These stresses are, of course, parallel to the edges and the corresponding stresses on the unswept surface are either small or zero. This indicates the presence of significant bending moments and membrane forces along both edges, the signs of the bending and membrane stresses being similar on the swept/

swept surface, dissimilar on the unswept surface. For pure moment and radial force loadings, Figs.46 and 47, maximum stress is on the outlet edge, but for tangential force loading, Fig.48, maximum stress is on the inlet edge. It is shown later that the edge results for this last case reflect, to some degree, the influence of torsion on the bucket as well as that of in-plane bending. The outlet edge stresses for all cases may have been somewhat affected by the fact that the application of the loadings was directly on this edge, albeit at points remote from the $\Theta = 86^{\circ}$ meridional section. However, any effects due to this are shown to have been small by the similarity in the stress behaviour at both edges and by results of the subsequent centrifugal and simulated jet loading experimental stress analyses.

As was to be expected, for all three loadings the stresses perpendicular to the edges, the edge meridional stresses, were found to be very small and virtually zero.

It is interesting to note that the prior brittle lacquer test result represented by Fig.44(a), is quite well confirmed by the maximum stress result of the case, Fig.48, linearly extrapolated to 400 lb loading. Indeed, all the indications of the brittle lacquer test are well substantiated by the results of the strain measurements for this case.

For actions on the bucket producing predominantly bending in the plane of the wheel, these test results of Figs.46, 47 and 48 show that the shell behaviour of the bucket is very similar to that of a toroidal shell under in-plane bending. This is particularly so in respect of the deformation of meridional sections. The behaviour under bending of the closed toroidal shell or pipe-bend is well documented. The publication of the M. W. KELLOGG CO.[41] for example, illustrates how the originally circular section deforms elliptically under both senses of in-plane bending, and under out-of-plane bending. The meridional section deformations/

deformations of the pipe-bend under in-plane bending and of the Turgo wheel bucket under bending in the plane of the wheel, are compared diagrammatically in Fig. 49. It is evident that the bucket deforms in the same way as the part of the pipe-bend which it resembles geometrically, namely the part outermost from the centre of revolution of the bend.

The behaviour under corresponding conditions, of an open toroidal shell shaped like this outermost portion, forms a better comparison with the bucket behaviour which has been recorded. The general qualitative reasoning used by some investigators, for example CLARK & REISSNER[42], to explain the meridional deformation under in-plane bending of the closed toroidal shell, can be applied equally to this corresponding open toroidal shell case, and shows that in respect of meridional section deformation, the open toroidal shell behaves similarly to the bucket. The open toroidal shell case is treated analytically in the succeeding chapter.

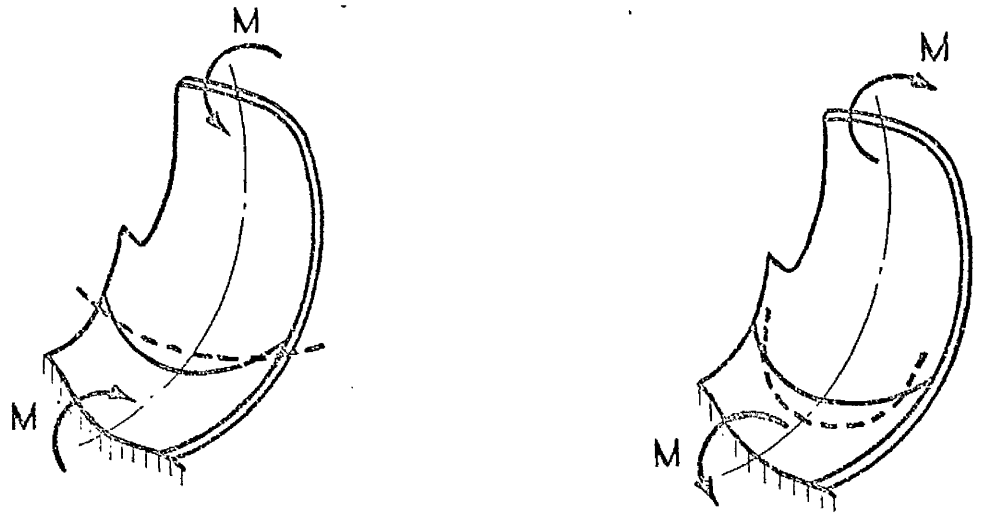

BUCKET OF TURGO WHEEL SUBJECTED TO PURE BENDING IN THE PLANE OF THE WHEEL.

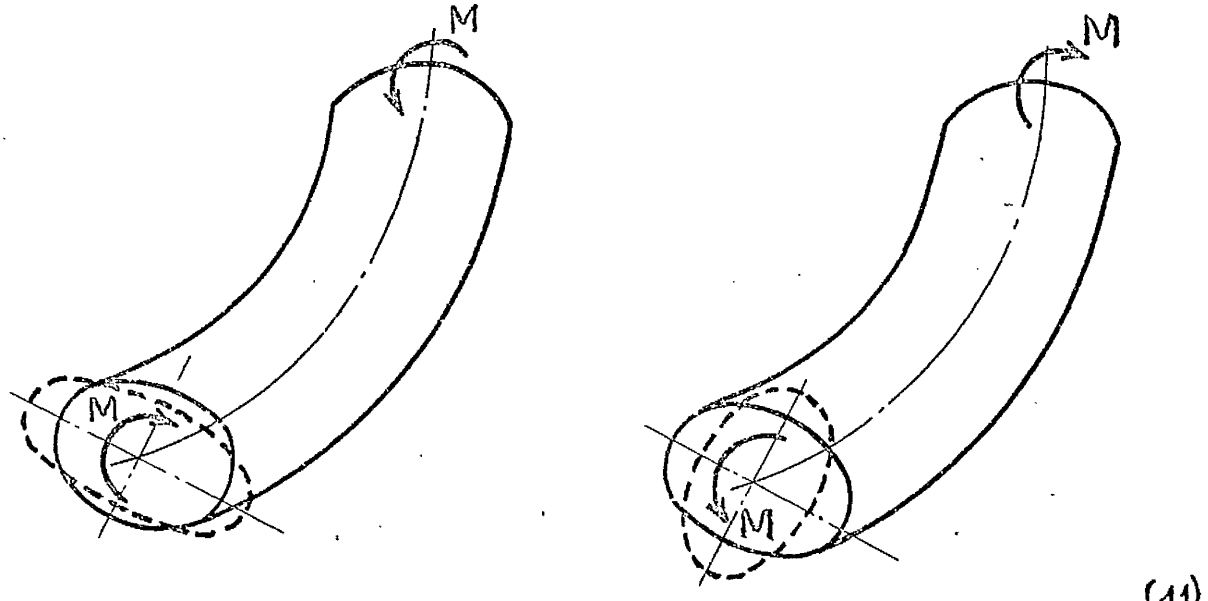

PIPE - BEND SUBJECTED TO PURE IN-PLANE BENDING.

FIG. 49. COMPARISON OF DEFORMATIONAL BEHAVIOUR OF A TURGO WHEEL BUCKET UNDER BENDING IN THE PLANE OF THE WHEEL, WITH THAT OF A PIPE-BEND UNDER IN-PLANE BENDING. DOTTED LINES SHOW DIAGRAMMATICALLY, THE DEFORMED SHAPES OF MERIDIONAL SECTIONS DUE TO MOMENT M.

4A ii Analysis of strains to determine actions on a meridional section of a bucket

It is variously accepted [43, 68] that thin shell theory applies to shells of which the geometry lies within the limitations:-

$$\frac{\text{thickness at a point}}{\text{minimum radius of curvature of mid-surface at the point}} \leq \frac{1}{20}, \text{ or } \frac{1}{10}.$$

Despite the fact that either ratio is obviously exceeded at some points on it (see, for example, the sections of Fig.9), it is assumed for simplicity that the Turgo wheel bucket behaves as a thin elastic shell, and hence in particular here, that the distribution of normal stress through the thickness is linear. Photoelastic investigations by FESSLER AND STANLEY [44] and FESSLER AND ROSE [45] on models of torispherical drumheads under pressure, show that the through-thickness stress distribution may depart grossly from the linear at points on a shell where the above ratio is of the order of 1. However, on a shell where the ratio is about $\frac{1}{3}$, the stress distribution is indicated as approaching fairly closely to the linear. Although the cases cited are not precisely comparable with those of the bucket, when it is considered that the ratio does not exceed about 1/5 at any point on a Turgo wheel bucket, and is of the order of 1/20 or less at many locations on it, the assumption of linear stress distribution through the bucket thickness may be regarded as reasonable.

For any meridional section of a bucket, if the stresses normal to the section (i.e. the circumferential stresses) are known on the swept and unswept surfaces, the corresponding membrane and bending stress components σ_d and σ_b are simply obtained. Referring to the meridional section Fig.50, for any point along the mid-line at distance S_M from the inlet edge datum, let the circumferential direct force and bending/

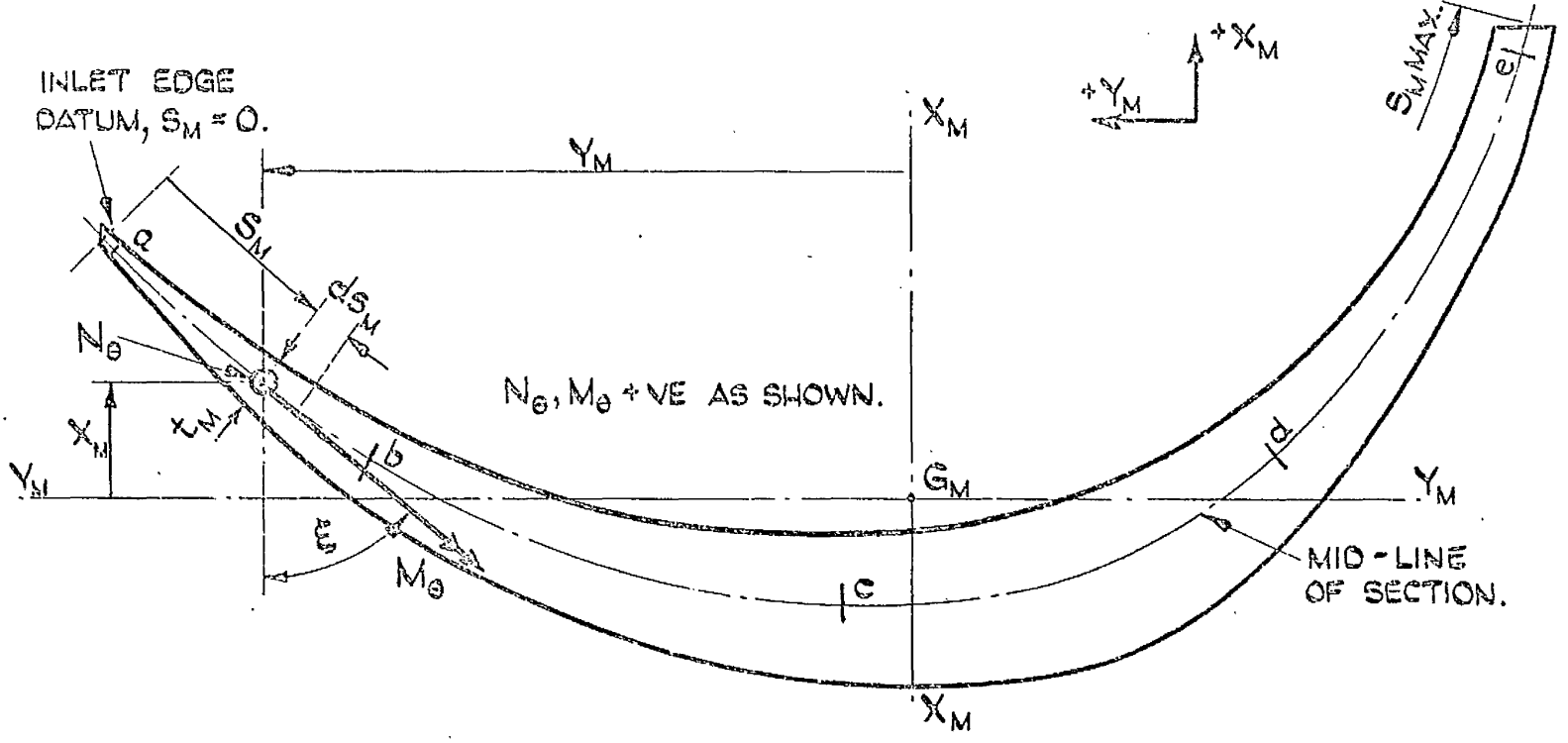

(a). FULL SIZE DRG. OF A MERIDIONAL SECTION SHOWING UNIT ACTIONS N_θ & M_θ AT A POINT ON THE MID-LINE, & INDICATING THE PARAMETERS OF THE POINT RELEVANT TO THE ANALYSIS. THIS PARTICULAR SECTION EXEMPLIFYING THE TREATMENT IS THE $\theta = 86°$ MERIDIONAL SECTION OF THE 18 IN. WHEEL BUCKET. POINTS a,b,c,d,e ON MID-LINE CORRESPOND TO THE STRAIN-GAUGE LOCATIONS OF VIEW W, FIG. 45, & ARE THE POINTS AT WHICH SURFACE STRESSES, NORMAL TO THE SECTION, ARE KNOWN.

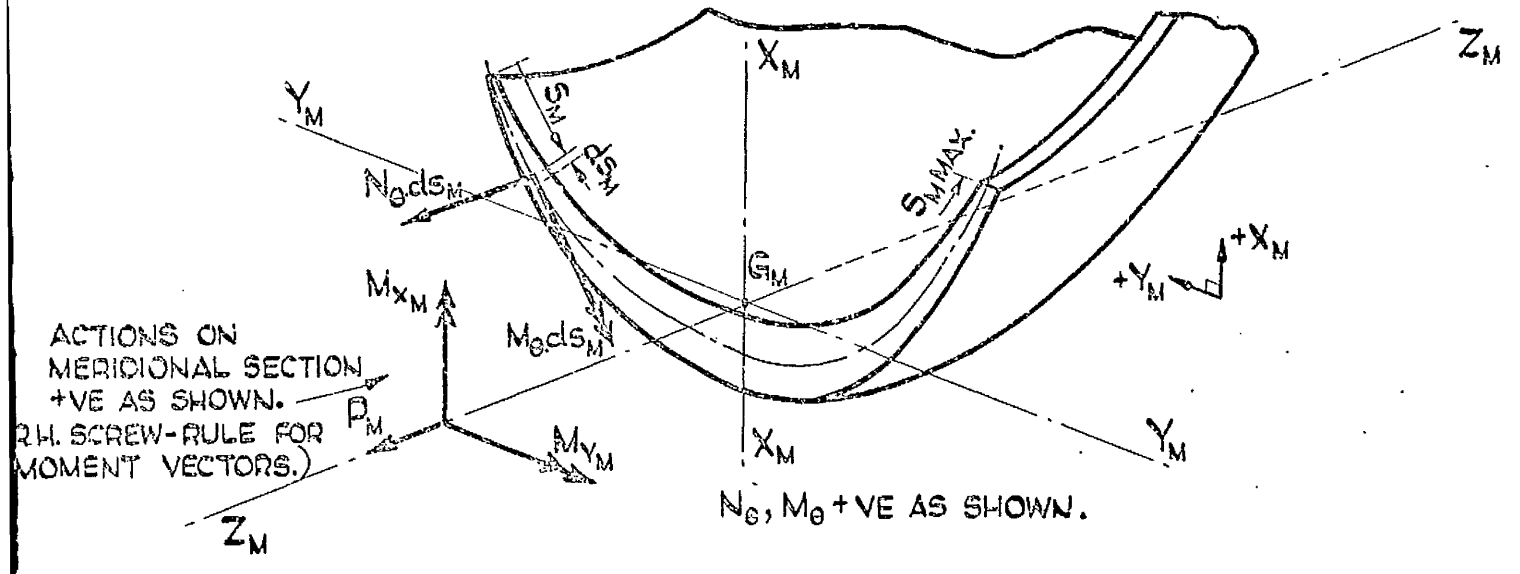

(b). PICTORIAL VIEW OF SECTION & BUCKET SHOWING ACTIONS ON ELEMENT ds_M OF MID-LINE, AND TOTAL ACTIONS M_{Y_M}, M_{X_M} AND P_M ON THE SECTION.

FIG. 50. MERIDIONAL SECTION OF A BUCKET WITH BASIS INDICATED FOR DERIVATION OF ACTIONS ON THE SECTION FROM SURFACE STRESSES. AT THE SECTION.

bending moment per unit length be N_θ and M_θ respectively, in notation appropriate to thin shell treatment. These unit actions may be found from the corresponding membrane and bending stresses via the equations:-

$$N_\theta = \sigma_d . t_M \ , \qquad M_\theta = \frac{\sigma_b . t_M^2}{6} \tag{4A.1}$$

where t_M is the corresponding thickness of the bucket.

The total direct force action P_M on the section, Fig.50(b), is then given by:-

$$P_M = \int_0^{s_M MAX} N_\theta . ds_M \tag{4A.2}$$

and, with respect to axes $Y_M Y_M$ and $X_M X_M$, the total bending moment actions M_{YM} and M_{XM} on the section, Fig.50(a) and (b), are given respectively by:-

$$M_{YM} = \int_0^{s_M MAX} N_\theta . X_M . ds_M + \int_0^{s_M MAX} M_\theta . \sin\xi . ds_M \tag{4A.3}$$

and

$$M_{XM} = \int_0^{s_M MAX} N_\theta . Y_M . ds_M - \int_0^{s_M MAX} M_\theta . \cos\xi . ds_M \tag{4A.4}$$

It is evident that, knowing the distributions of σ_d and σ_b with s_M along the mid-line, and knowing the section geometry from a full scale drawing, e.g. Fig.50(a), graphs of all the terms or products within the integral signs may be plotted to a common base of s_M. Evaluation of the integrals may then be carried out using Simpson's Rule or graphical integration, or simply by direct measurement with planimeter of the areas under the curves. The corresponding actions P_M, M_{YM} and M_{XM} on the meridional section are thus obtained.

The above analysis for determining actions on a meridional section from the surface stresses at the section, has been applied to the results of/

of the tests on the 18 in.wheel bucket. Since the correct actions on the $\Theta = 86^{\circ}$ meridional section were known from equilibrium, (see pictorial views of Figs.46, 47 and 48) a check on the accuracy of the method was available. The accuracy was of interest in relation to the number of locations on the section at which strains had been measured, or alternatively, to the number of values of S_M for which the initial stress data were known. The latter number was five as is shown in View W, Fig.45 and in Fig.50(a), and it was hoped that this would provide an adequate distribution of σ_d and σ_b over the section. The analysis was also under consideration for use in the subsequent strain-gauge investigations on the $16\frac{1}{2}$ in.wheel, particularly in regard to the results of the centrifugal test.

Application of the analysis to the results of the 18 in.wheel bucket, was carried out as described below and, as illustrated in Figs.51 (a), (b) and (c), is exemplified by the treatment of the 1400 lb.in. pure bending moment loading case, in respect of the $\Theta = 86^{\circ}$ meridional section:-

(1) The normal circumferential stresses on the two surfaces of the section were calculated from the readings of the strain-gauges perpendicular and parallel to the section. As was expected, the values obtained were only of slightly smaller magnitudes than the corresponding principal stresses indicated on Fig.46.

(2) At each of the corresponding five points on the mid-line of the section, Fig.50(a), the membrane and bending stresses σ_d and σ_b normal to the section, were found by:-

σ_d = half the algebraic sum of the surface normal stresses,

σ_b = half the algebraic difference of the surface normal stresses.

(3) From Fig.50(a), graph Fig.51(a) was drawn, S_M being set out as base line, and the values of σ_d and σ_b were plotted as abscissae at the appropriate locations on S_M. Smooth direct curves were drawn through the plotted points as shown.

(4) /

FIG. 51(a). ANALYSIS FOR ACTIONS ON $\theta = 86°$ MERIDIONAL SECTION OF 18 IN. WHEEL BUCKET, UNDER 1400 lb.ins. PURE MOMENT, (FIG. 46). DISTRIBUTIONS OF σ_d & σ_b WITH S_M ALONG MID-LINE, DERIVED FROM MEASURED STRAINS PERTINENT TO POINTS a,b,c,d & e. (SEE FIG. 50(a)). THICKNESS VARIATION t_M IS ALSO SHOWN.

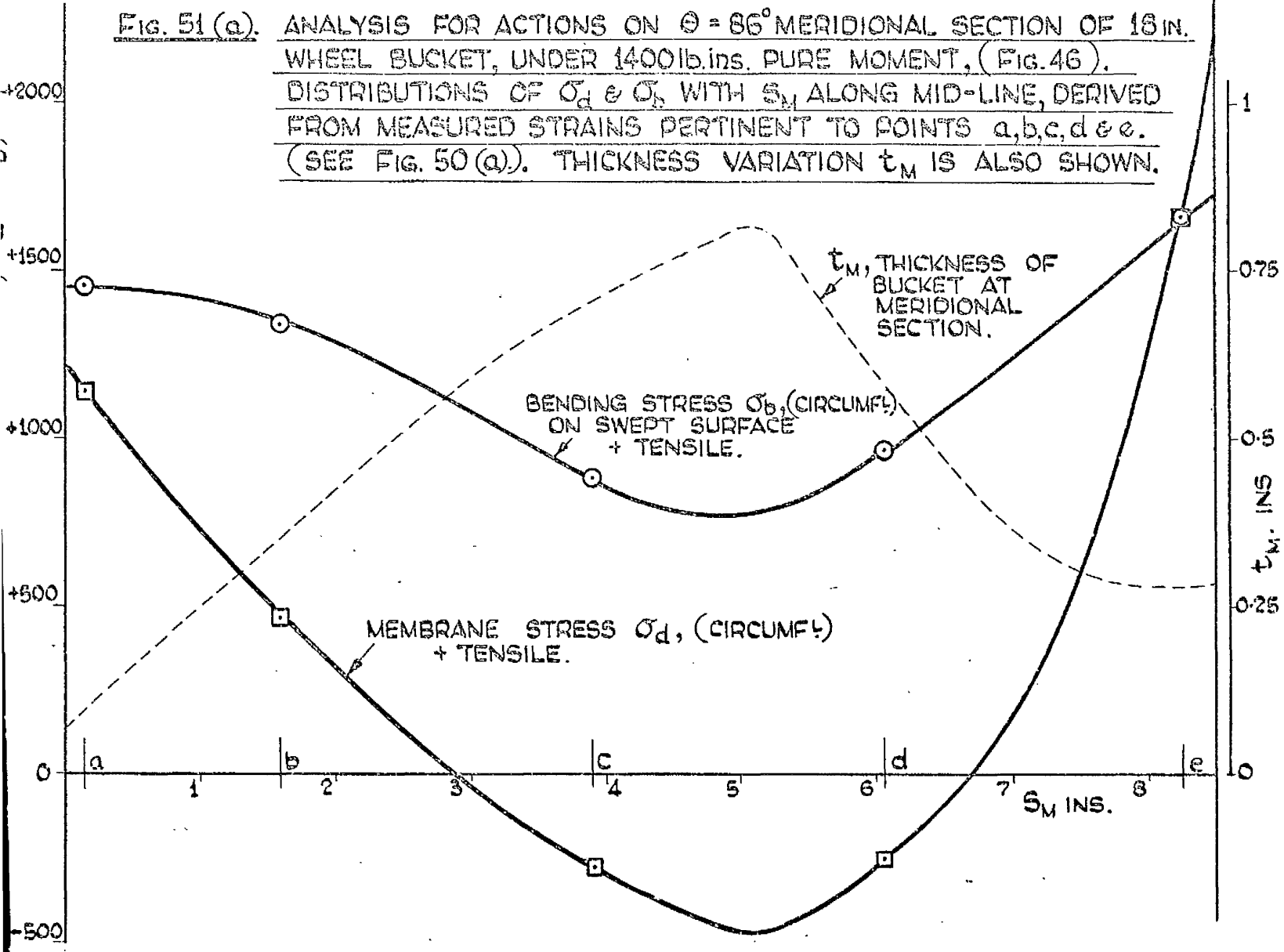

FIG 51(b). ANALYSIS FOR ACTIONS ON $\theta = 86°$ MERIDIONAL SECTION OF 18 in. WHEEL BUCKET, UNDER 1400 lb.ins. PURE MOMENT, (FIG 46). DISTRIBUTIONS OF UNIT ACTIONS N_θ & M_θ WITH S_M, DERIVED FROM ABOVE CURVES VIA EQNS. (4A.1).

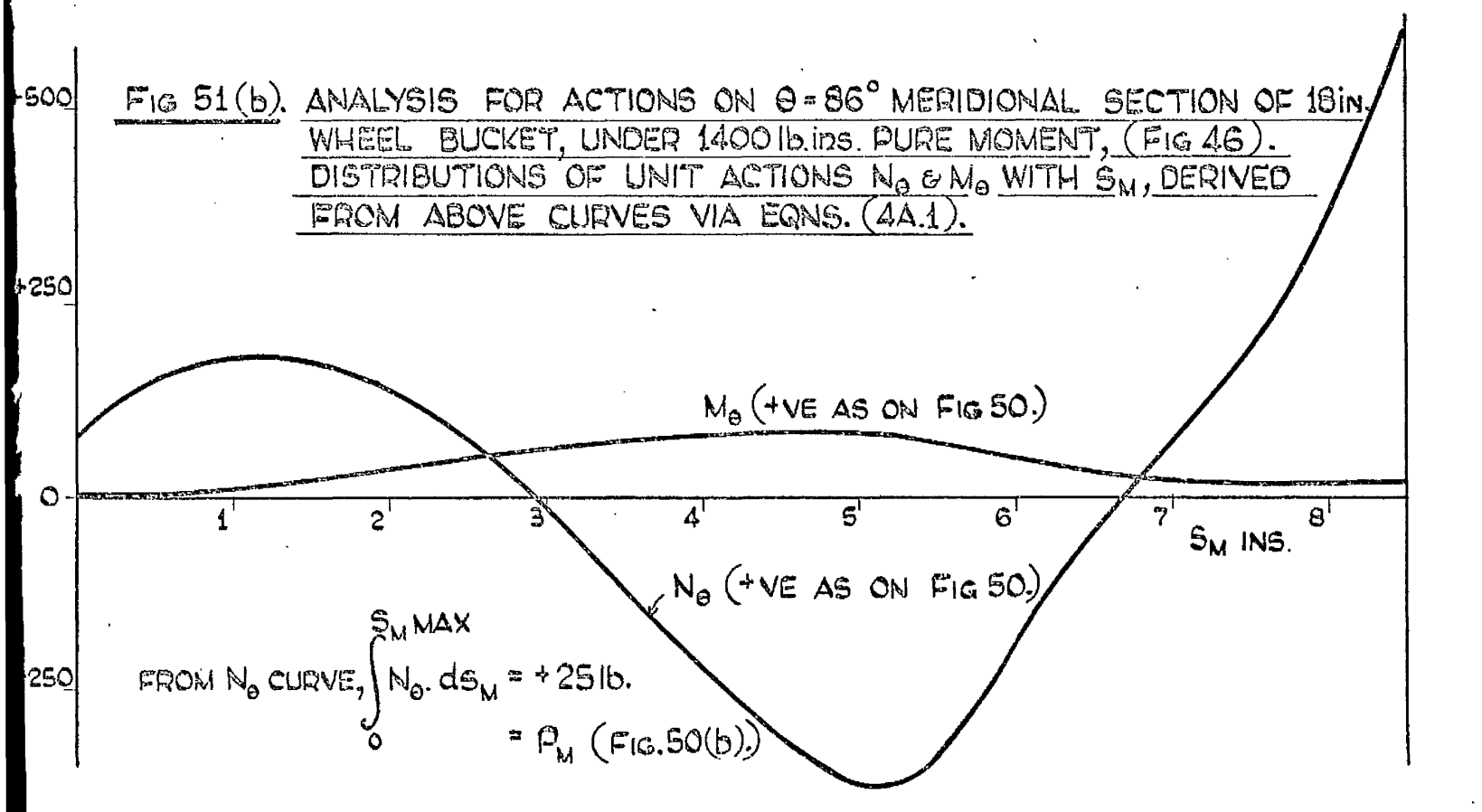

FROM N_θ CURVE, $\int_0^{S_M\,MAX} N_\theta \cdot ds_M = +25$ lb.

$= P_M$ (FIG. 50(b)).

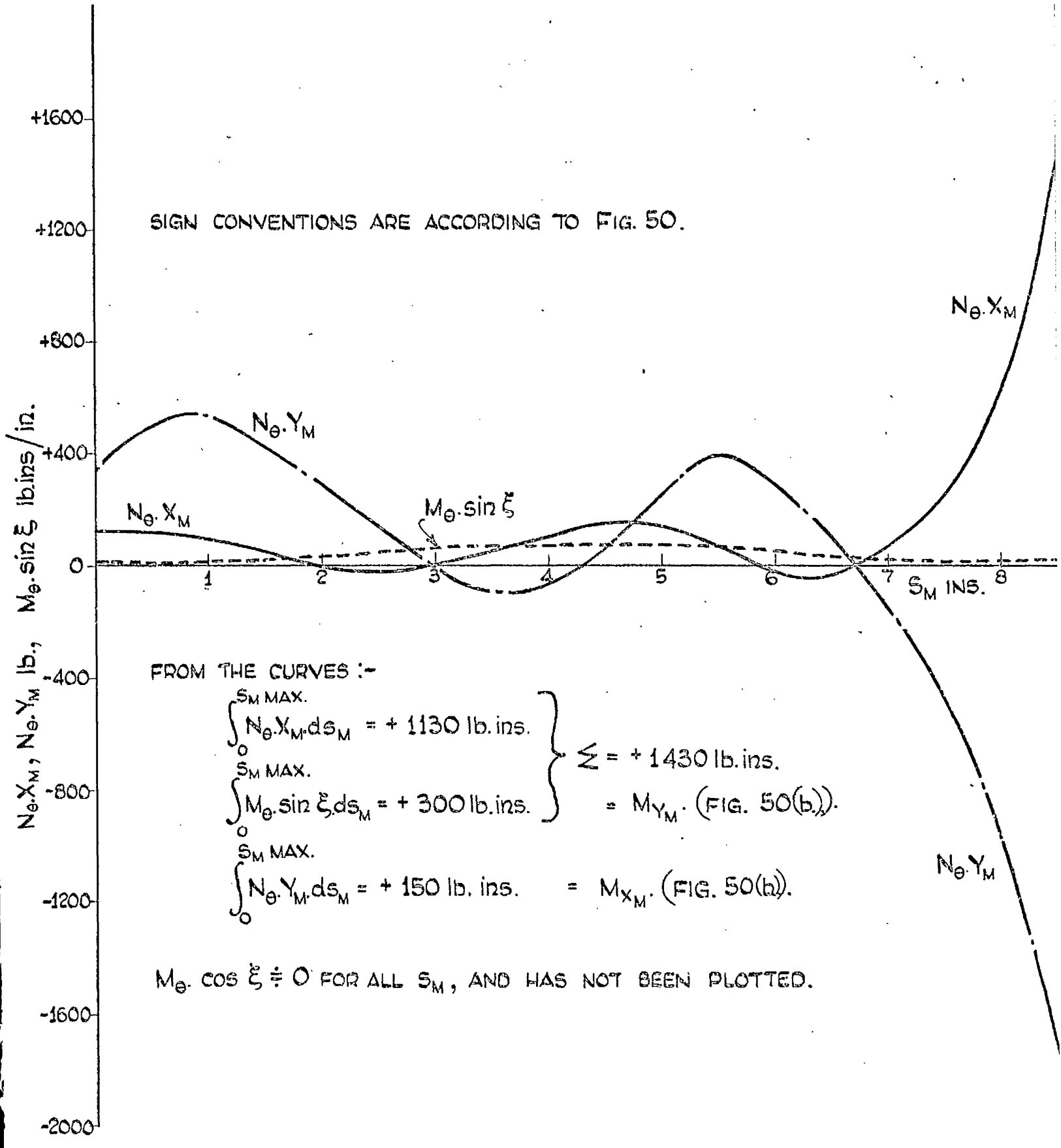

FIG. 51(c). ANALYSIS FOR ACTIONS ON $\theta = 86°$ MERIDIONAL SECTION OF 19 IN. WHEEL BUCKET, UNDER 1400 lb. ins. PURE MOMENT, (FIG. 46). DISTRIBUTIONS OF $N_\theta.X_M$, $M_\theta.\sin\xi$, $N_\theta.Y_M$ WITH S_M. DERIVED FROM THE CURVES FIG. 51(b), AND FROM THE MID-LINE GEOMETRY FIG. 50(a).

(4) For many values of s_M, Fig.50(a), the parameters t_M, X_M, Y_M, ξ, pertinent to the mid-line of the section, were measured from the Fig., and then plotted on a base of s_M, e.g. as shown for t_M on Fig.51(a).

(5) From the curves of this latter Fig., N_θ and M_θ were calculated via equations (4A.1) and graphed with s_M, as illustrated in Fig.51(b). By measuring the area under the appropriate curve, $\int_0^{s_{M\,MAX}} N_\theta . ds_M$ was evaluated.

(6) From the curves of Fig.51(b) and from the plot of the mid-line parameters, products $N_\theta X_M$, $M_\theta \sin\xi$, $N_\theta Y_M$, were determined. These were graphed with s_M giving Fig.51(c). Product $M_\theta . \cos\xi$ was also calculated, but was found throughout to be small in comparison with the other products and was therefore neglected. By measuring areas under the appropriate curves, $\int_0^{s_{M\,MAX}} N_\theta . X_M . ds_M$, $\int_0^{s_{M\,MAX}} M_\theta \sin\xi . ds_M$ and $\int_0^{s_{M\,MAX}} N_\theta . Y_M . ds_M$ were evaluated. This was actually carried out on graphs to greater scales than those of Fig.51(c), which is presented to illustrate the procedure. The values of all the integrals pertinent to this case are shown on Figs.51(b) and (c). These correspond to the total actions on the section, according to equations (4A.2), (4A.3) and (4A.4).

The corresponding results of the other tests on the 18 in. wheel bucket, reference Figs.47 and 48, have been analysed exactly as above.

The values of all the actions obtained by these analyses are compared with the corresponding correct equilibrium values in the following table:-

Table 3 /

Table 3.

Tests on bucket for 18 in. Turgo wheel.

Comparison of actions on a meridional section, obtained by analysis of measured strains, with the corresponding correct actions for equilibriu

Loading on bucket	Action on $\Theta = 86^\circ$ meridional section, ref. Fig. 50(b)					
	M_{YM} lb. in.		M_{XM} lb. in.		P_M lb.	
	Derived from strain measurement	Correct from equilibrium	Derived from strain measurement	Correct from equilibrium	Derived from strain measurement	Correct from equilibrium
1400 lb. in. pure bending moment Fig. 46	+ 1430	+ 1400	+ 150	0	+ 25	0
200 lb., approx.ly radial force Fig. 47	- 1100	- 1100	- 300	- 200	- 225	- 200
200 lb., approx.ly tangential force Fig. 48	+ 1240	+ 1200	+ 400	0	- 15	0

It is evident from the table that the analysis from measured strains, as presented, results in the determination of action M_{YM} with excellent accuracy, and of action P_M with quite good accuracy. Action M_{XM} is much less accurately determined. One possible reason for this poor accuracy in one moment as compared with the other, is the natures of the products $N_\theta X_M$ and $N_\theta Y_M$, typified in the curves of Fig. 51(c). There the area under $N_\theta X_M$ comprises mainly positive portions, so any error associated/

associated with one portion, say towards the inlet edge, will be reflected as a relatively small fraction of the total. The area under $N_\theta Y_M$, however, comprises much larger and roughly equal positive and negative portions. An error associated with one such portion would be expected to be proportionately greater than the corresponding error in $N_\theta X_M$, and would be reflected as a relatively large percentage of the total area, itself comparatively small. Thus the determination of M_{xM} will be more sensitive to the accuracy inherent in the initial curve of σ_d, e.g. as in Fig.51(a), and in the initial specification of the section geometry, e.g. Fig.50(a). The table indicates a consistent trend in the error in M_{xM}, which error may be associated with the strain results or the shapes of the σ_d curves in the region of the inlet edge. For the tangential force loading where, as is shown later, the influence of torsion on the section is also present, the stresses at the inlet edge, Fig.48, are considerably higher than at the outlet edge. This seems to have exacerbated the corresponding error in M_{xM}.

The shapes of the initial membrane and bending stress curves, e.g. Fig.51(a), are of obvious importance to the accuracy of the analysis. The curves in the Fig., and for the other two loading cases, have been drawn smoothly and directly through the plotted points. Since action M_{xM} is of minor concern both in these tests and in relation to bucket behaviour in a working wheel, the form of the analysis presented, based on measured strains pertinent to five points on the section mid-line, is regarded as reasonably satisfactory.

It is interesting to note from Fig.51(c), that on the meridional section, the resistance to the in-plane bending moment M_{YM} is provided mainly by the membrane action of the bucket, reflected in $\int_0^{s_M MAX.} N_\theta . X_M . ds_M = +1130$ lb. in. The following table gives the data pertinent to this result and to the other results:-

Table 4.

Tests on bucket for 18 in. Turgo wheel.

Membrane and bending actions on meridional section.

Loading on bucket	Percentage of in-plane bending moment M_{Y_M} on $\theta = 86^{\circ}$ meridional section, taken by:-	
	Membrane action $\int_0^{s_{M\,MAX}} N_\theta . X_M . ds_M$	Bending action $\int_0^{s_{M\,MAX}} M_\theta . \sin\xi . ds_M$
1400 lb. in. pure bending moment, Fig.46	79	21
200 lb., approximately radial force, Fig.47	75	25
200 lb., approximately tangential force, Fig.48	79	21

The distribution of membrane unit force N_θ over the section, Fig.51(b), is not unlike the corresponding stress distribution, which would be given by assuming simple beam behaviour.

4A iii Examination of strains pertinent to the behaviour of a bucket under torsion

Of the three types of loading applied to the 18 in. wheel bucket, only the approximately tangential force, Fig. 48, acted transversely with respect to the $\Theta = 86^{\circ}$ meridional section, and so was the only loading likely to cause any significant effects due to torsion to be exhibited. The occurrence in this case, of maximum stress on the inlet edge, in contrast to the results for the pure bending moment loading case Fig. 46, where maximum stress is shown on the outlet edge, was suspected as reflecting the influence of torsion on the section. The suspicion was confirmed by the results of two further approximately tangential force tests, in which the same force on the bucket tip, Fig. 48, was applied at different distances in relation only to axis $Z_M Z_M$. In this way, the only action which was varied on the section was the torque. The edge stresses for all three approximately tangential force tests are indicated on Fig. 52, which also shows the force positions relative to $Z_M Z_M$. As the torque changes with increasing distance of the 200 lb. force from $Z_M Z_M$, so the inlet edge stresses increase on both surfaces and the outlet edge swept surface stress reduces. Conversely, it is evident that, if the approximately tangential force were to be applied at zero distance from $Z_M Z_M$, or a little to the right of this axis, Fig. 52, the outlet edge would exhibit the maximum stress on the section, and a force position could be found for which the ratio $\left(\frac{\text{outlet edge swept surface stress}}{\text{inlet edge swept surface stress}}\right)$ would equal the corresponding ratio for the pure bending moment loading case, Fig. 46.

The approximately tangential force of 200 lb, Fig. 48, exerts an in-plane bending moment M_{Y_M} of 1200 lb. in. on the $\Theta = 86^{\circ}$ meridional section. As indicated previously, the strains of this case have been analysed/

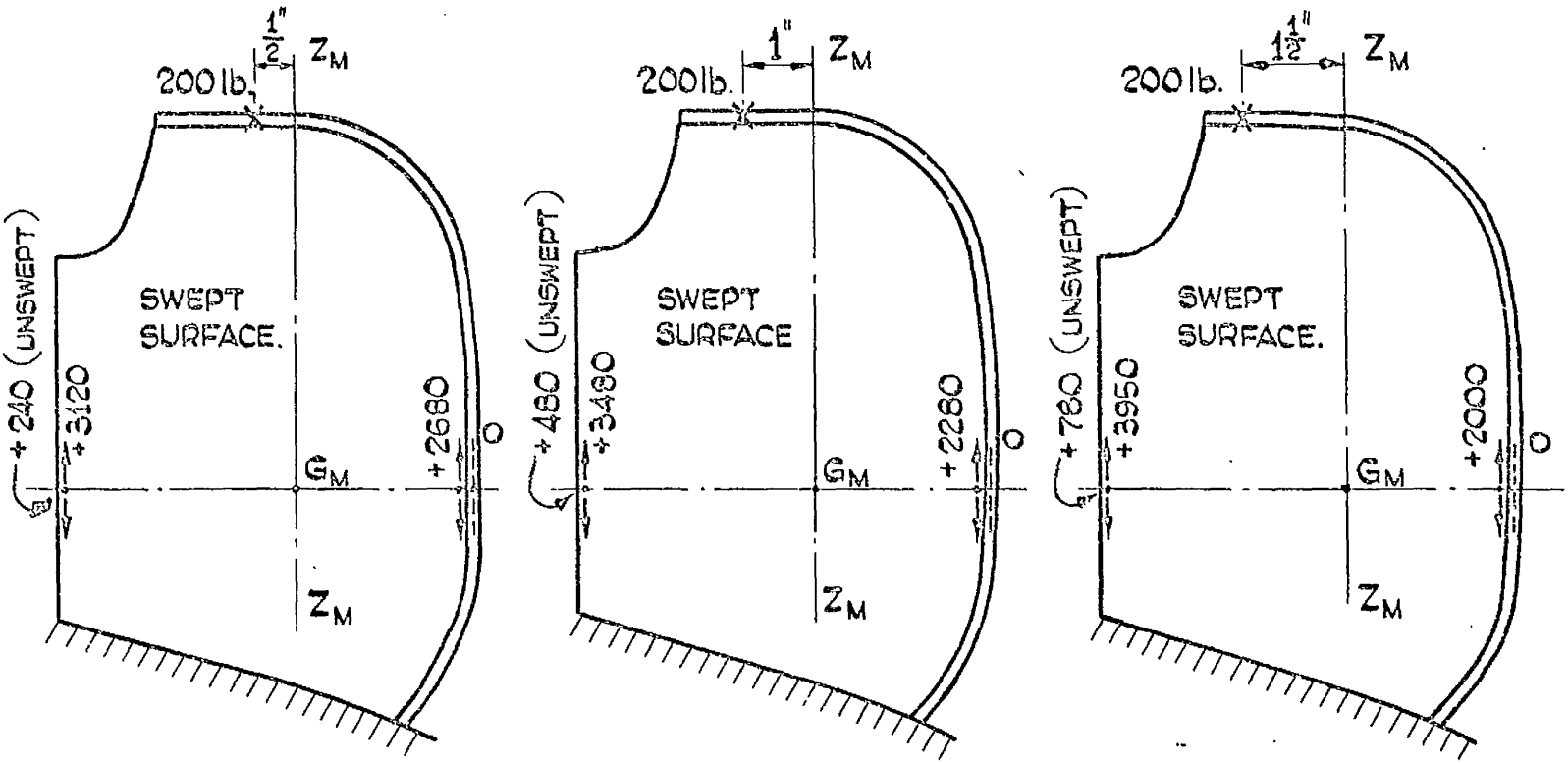

FIG. 52. STRESSES (lb./in²) AT THE EDGES, ON BOTH SURFACES OF THE $\theta = 86°$ MERIDIONAL SECTION, FOR 200 lb. APPROXIMATELY TANGENTIAL FORCE APPLIED AT TIP OF THE 18 IN. WHEEL BUCKET, AT THREE DIFFERENT POSITIONS RELATIVE TO AXIS $Z_M Z_M$:

analysed for the derivation of actions on the section. It is instructive to compare the measured bending and membrane stress distributions, σ_b and σ_d, over the section for this case, with the corresponding stress distributions for the case of 1200 lb.in. pure bending moment loading, the stress results for this latter having been extracted by direct proportion from the values of Fig.51(a). The comparisons are shown on Fig.53, where the more interesting of the two is undoubtedly the membrane stress comparison Fig.53(b). It is not unreasonable to assume that the σ_d curve for 1200 lb.in.pure moment loading, also represents the effect of the 1200 lb.in. in-plane bending moment exerted by the 200 lb.tangential force. The difference in ordinates, therefore, between the two σ_d curves, represents the membrane stress distribution due to the 200 lb.transverse force and to torsion on the section induced by this force. Membrane stress due to transverse force will clearly be of small consequence, so that the difference in ordinates between the curves, as indicated on Fig.53(b), is approximately the membrane stress distribution due mainly to torsion on the section.

This membrane stress distribution due mainly to torsion, has been replotted over the actual $\Theta = 86^{\circ}$ meridional section of the bucket, as shown in Fig.54. Comparing this Fig. with Fig.25, there is a remarkable resemblance between the distribution of torsion membrane stress over an actual bucket section and that of theoretical warping restraint direct stress over an equivalent parabolic section of bucket. Moreover, the signs of the torsion membrane stresses (+ at inlet, - at outlet) are in accordance with the directions of the torque distribution over the bucket from tip to root, if the problem is viewed in the light of the theory of non-uniform torsion of thin-walled open-section beams [33, 34]. Clearly, although the bucket is of pronounced shell form, its behaviour under torsion is not so very different from that of a straight beam of similar meridional section.

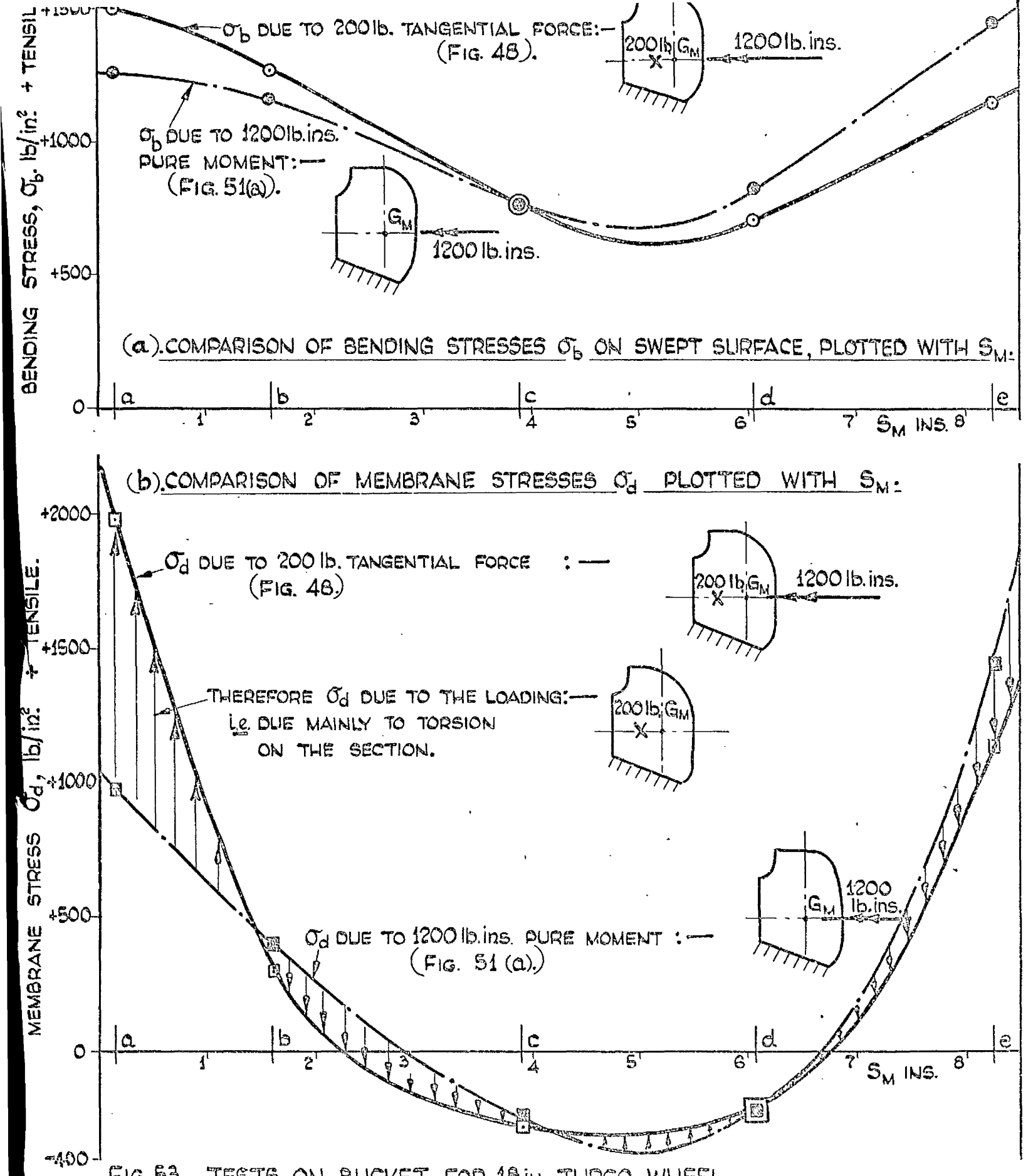

FIG. 53. TESTS ON BUCKET FOR 18 IN. TURGO WHEEL. COMPARISON OF BENDING AND MEMBRANE STRESS DISTRIBUTIONS OVER $\theta = 85°$ MERIDIONAL SECTION, FOR 200 lb. APPROXIMATELY TANGENTIAL FORCE LOADING CASE, FIG. 48, AND 1200 lb. ins. PURE BENDING MOMENT LOADING CASE, (FROM FIG 51(a)).

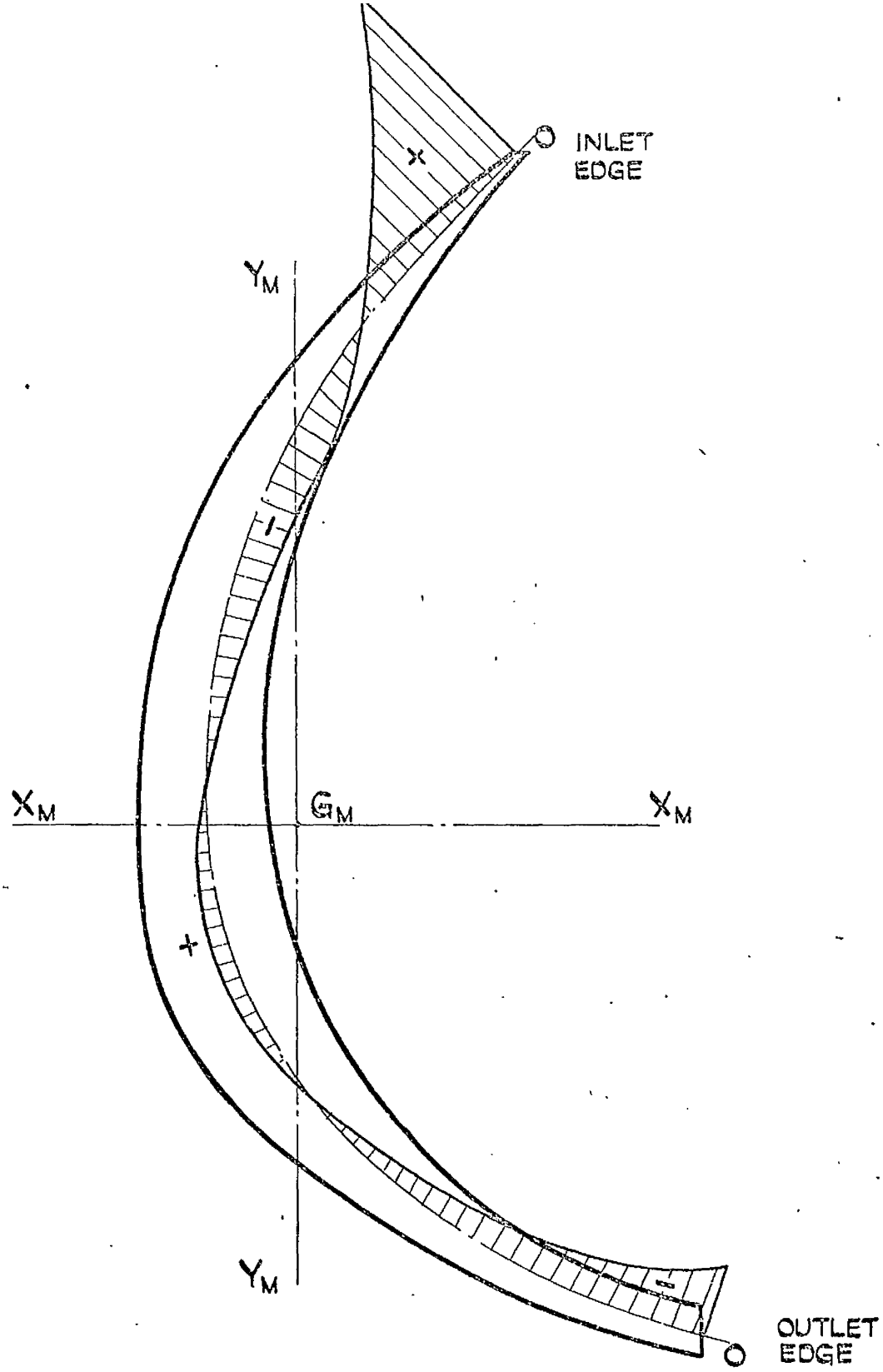

FIG. 54. MEMBRANE STRESS DISTRIBUTION OVER $\theta = 86°$ MERIDIONAL SECTION OF 18 IN. TURGO WHEEL BUCKET, DUE MAINLY TO TORSION ON THE SECTION INDUCED BY 200 lb. APPROXIMATELY TANGENTIAL FORCE LOADING. (FIG 48). THE DISTRIBUTION, SHOWN PLOTTED TO SCALE OVER THE SECTION MID-LINE, IS TAKEN FROM FIG. 53 (b).

4B MEASUREMENT OF CENTRIFUGAL STRESSES IN $16\frac{1}{2}$ in.p.c.d. TURGO WHEEL

The choice of size of aluminium wheel for experimental stress analysis was a compromise mainly between two factors. The wheel had to be small consistent with economy, but also had to be sufficiently large to allow ease of access to all surfaces of interest for the installation of strain gauges.

The density and the elastic constants of the wheel material were measured. These are given in Table 1, Chapter 3.

A spinning test rig was manufactured and consisted basically of a bedplate with bearings which carried a steel shaft. One end of the shaft was coupled directly to the drive unit— a variable speed A.C. motor incorporating a speed regulator. The other end, which was 1.15/16 in. diameter and overhung or cantilevered, bore the dynamically-balanced wheel and other rotating parts when the latter were required. As the bore of the wheel hub was $4\frac{3}{4}$ in (Figs.7 and 9), mounting of the wheel on the overhung shaft was achieved via a flanged steel sleeve on which the hub was a sliding fit. The sleeve was keyed to the shaft, and its flange was connected to the inlet side face of the wheel hub by four steel driving pins which engaged in radial slots cut in the hub face. The arrangement of pins in radial slots was designed so as to provide positive drive, but to incur no restraint against radial deformation of the wheel. In the same way, a flat ring screwed to the sleeve on the outlet side, served to locate the wheel axially but with sufficient clearance to allow any axial deformation of the wheel to occur freely. The wheel/sleeve assembly was axially located on the shaft by means of spacer rings, a washer and a nut on the screwed overhung end. The wheel may be seen mounted in the spinning test rig in Fig.59.

Prior/

Prior to commencing strain gauge installation, a brittle lacquer centrifugal test was conducted on the wheel. The technique largely followed the general description given in Appendix 4. The lacquered wheel and calibration bars were stoved in a large closed oven, cooled slowly and removed. Fairly speedily, 3 calibration bars were tested while simultaneously the wheel was fitted on the overhung shaft of the spinning test rig, care being taken to avoid touching the lacquered areas. To prevent contact with draughts while spinning, a lacquered sector of the wheel was appropriately masked-off with tape, but another nominally identical lacquered sector was left uncovered. The wheel was spun at incrementally increasing speeds, with intervals at stationary to permit examination of the lacquer for cracking. The maximum speed which the motor would attain, 1920 r.p.m., was achieved without any cracking of the lacquer, either on the masked-off sector or on the exposed sector, being found on subsequent examination. After the remaining calibration bars were tested all results from the bars were plotted on an appropriate graph, and the strain-sensitivity of the lacquer was obtained. The results are graphed on Fig.A4.1, from which the strain-sensitivity is seen to be about $0.0005 \pm 20\%$. Although this brittle lacquer test on the wheel was somewhat abortive, it did indicate that, at 1920 r.p.m., the maximum tensile strain on the wheel was most unlikely to exceed 0.0006.

4B i Centrifugal stress measurement using electrical resistance strain gauges and slip rings

After the brittle lacquer test the wheel was removed from the shaft of the spinning test rig. It was then cleaned and mounted on a stand, Figs.55 and 56, for installation of strain gauges.

The use of slip rings to recover signals from strain gauges on rotating pieces, is a topic on which there is a considerable literature.[1, 5, 14, 15, 20, 21, 22, 46 - 57 incl.] A circuit system in wide use is that of the full rotating bridge which is designed specifically to minimise the possible effects of slip ring "noise". This system formed the basis of the strain gauge circuit, Fig.57, which was adopted for the Turgo wheel tests. In the full rotating bridge, as well as the active gauge, the three inactive gauges of the basic four-arm bridge are mounted on the rotating side. The slip rings lie outwith the bridge, being in series only with the power supply and galvanometer of the strain meter, where the influence of the rings on the strain indication is negligible, provided their resistance is relatively low.

A problem associated with the use of the full rotating bridge, is that suitable locations for the inactive gauges require to be found or provided on the rotating parts. None of the various solutions, which investigators have adopted, was regarded as suitable for this application. A new solution, devised by the author[57], was used. This new method, which provides strain-free locations in the centrifugal field, consists in mounting the inactive gauges axially on the segmented circumference of a thin disc, made from the same cast of material as the Turgo wheel, with which the disc rotates. Figs.55(b) and 56(b) show the segmented disc on the outlet side of the wheel during attachment and wiring of the strain gauges. In Fig.59(b) it is shown installed on the outlet side of the wheel in the spinning test rig. In this photograph the disc is covered with black tape.

Together/

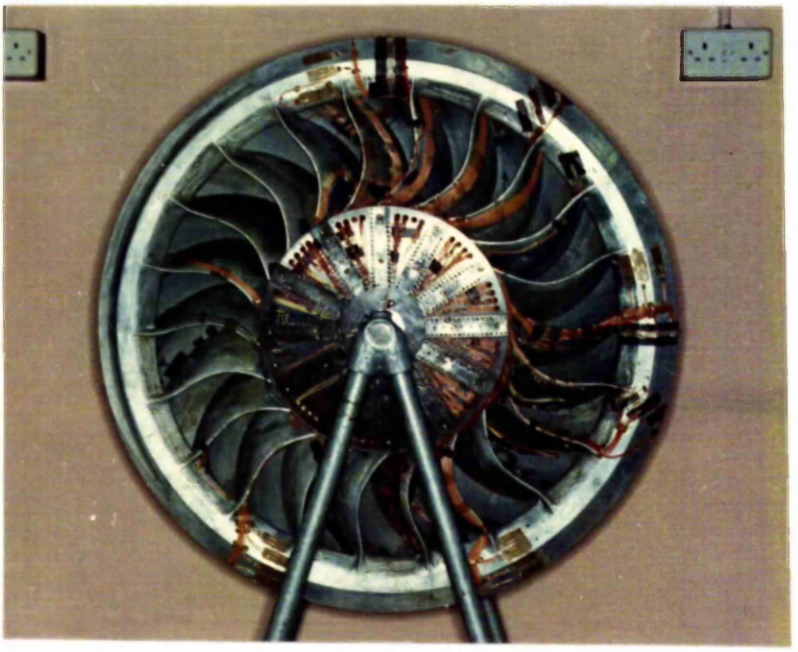

(a) LOOKING ON INLET SIDE AND SHOWING TUFNOL TERMINAL BOARD TO WHICH ALL STRAIN GAUGES ON WHEEL ARE CONNECTED.

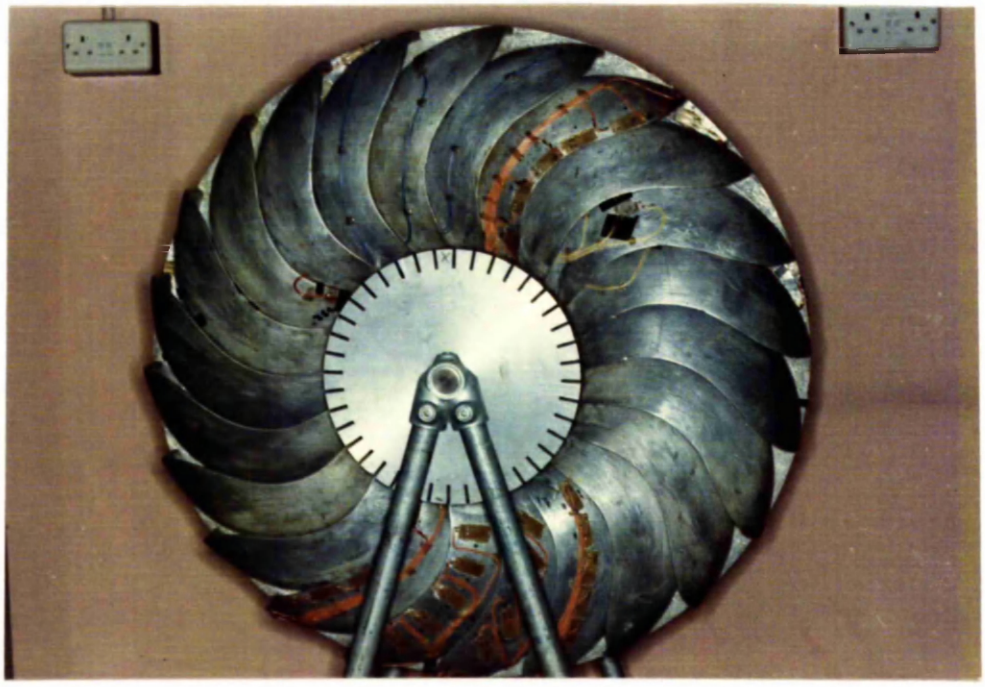

(b) LOOKING ON OUTLET SIDE AND SHOWING ALUMINIUM SEGMENTED DISC WHICH CARRIES COMPENSATING AND RATIO-ARM STRAIN GAUGES.

FIG. 55. $16\frac{1}{2}$ in. ALUMINIUM TURGO WHEEL ON STAND, DURING INSTALLATION AND WIRING OF STRAIN GAUGES.

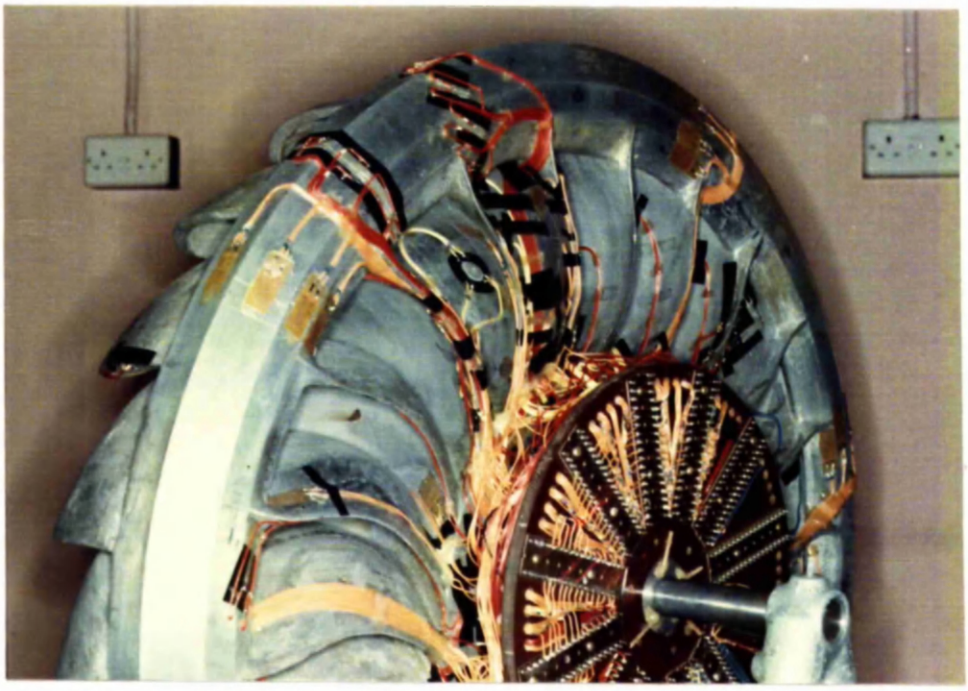

(a) LOOKING ON INLET SIDE AND SHOWING TUFNOL TERMINAL BOARD TO WHICH ALL STRAIN GAUGES ON WHEEL ARE CONNECTED.

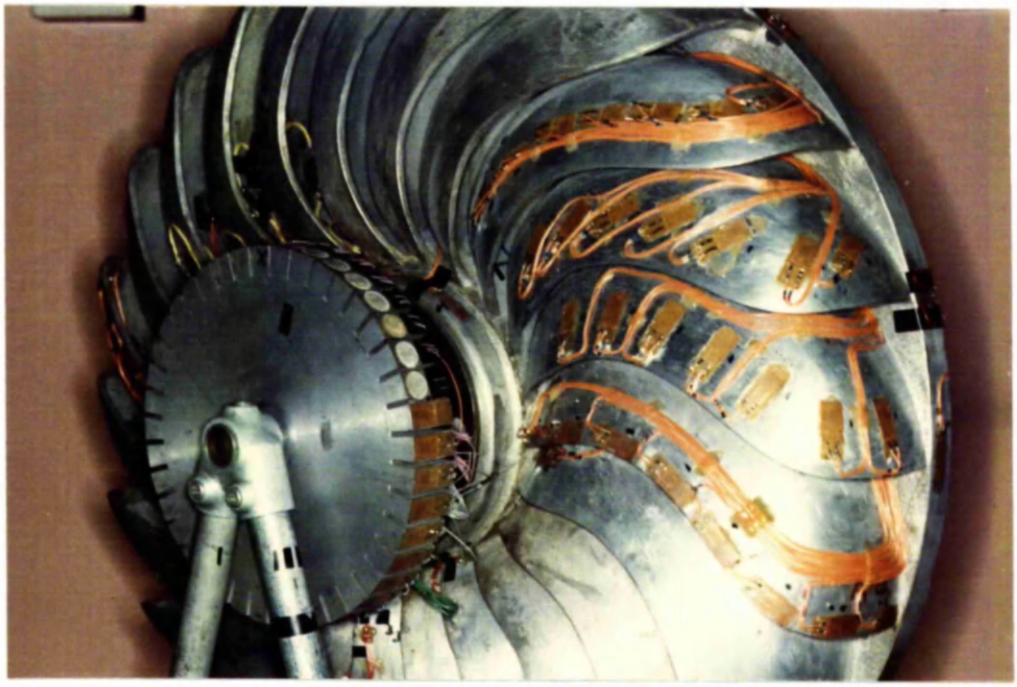

(b) LOOKING ON OUTLET SIDE AND SHOWING ALUMINIUM SEGMENTED DISC WHICH CARRIES COMPENSATING AND RATIO-ARM STRAIN GAUGES.

FIG. 56. $16\frac{1}{2}$ in. ALUMINIUM TURGO WHEEL ON STAND, DURING INSTALLATION AND WIRING OF STRAIN GAUGES.

Together with associated considerations, a description of the segmented disc method for inactive gauge locations is presented in Appendix 5, which comprises the author's publication.

Installation and wiring of strain gauges on the wheel and segmented disc were completed with both these components on the stand, Figs.55 and 56. All wires were arranged to run to the Tufnol terminal board shown on the inlet side of the wheel. The 219 gauges mounted on the wheel were of 0.125 in.and 0.25 in.gauge lengths and between 0.10 in.and 0.20 in.gauge width, and comprised many singles, rosettes, and singles mounted in rosette orientations at nominally identical locations (Fig.56). Details of the strain gauge locations are indicated in subsequent sections which present the strain measurement results. On the buckets, many single gauges were located along the edges on both swept and unswept surfaces. For the most part, gauge pairs were not used at the edges, in view of the results of the tests on the single buckets (section 4A i), and owing to the difficulties associated with locating a pair accurately together at an edge. Other locations on the buckets were on meridional sections, and at possible stress concentration points at bucket/rim and bucket/hub junctions. On the rim, gauges were located mainly at points on full rim-sections, as far as possible in way of the rim junctions with the inlet and outlet edges. Gauges were arranged circumferentially, axially and radially as appropriate, on the surfaces of the hub, as far as access would permit. The hub bore was inaccessible. To provide checks on results, some gauges were duplicated at nominally identical locations on the buckets, rim and hub.

The wheel, segmented disc and terminal board were transferred to the overhung shaft of the spinning test rig, the disc being arranged on the outlet side of the wheel, the terminal board on the inlet side near the end of the shaft. A dog-drive on this end was coupled to the rotor of the slip ring/

ring unit which stood on a separate mounting, as shown in Figs.58 and 59. The slip ring unit was a commercially manufactured one specifically designed for use with strain gauges. It provided 11 conducting channels together with a split-channel for revolution counting.

Details of the centrifugal test strain gauge circuit are shown on Fig.57 for one of the four similar banks of active, compensating and ratio-arm gauges. The strain meter and switch leads on the stationary side were connected via the 11 channels of the slip ring unit, to terminals S1 to S11 on the terminal board. Three slip ring channels were occupied by the power leads and common galvanometer lead, leaving 8 for active gauge connections, so allowing 8 active gauges to be read per test run. Only 8 compensating and 2 ratio-arm gauges were therefore necessary in each gauge bank as shown in Fig.57, the compensators and ratio-arms being mounted on the segmented disc. The wires from these were taken through the wheel passages directly to the terminal board. Also all the leads from the active gauges on the wheel passed directly to the terminal board, where changes of connections were effected between runs. Referring to Fig.57, for a typical test run the following connections were made:-

DI1 and DI1 both to S1, DI2 to S2, DI3 to S3, DA1 ----DA8 respectively to S4 ----S11, and DC1 ----DC8 also respectively to S4 ----S11. The test run was then made for active gauges DA1 ----DA8, and on completion of the run DA1 ----DA8 were disconnected from S4 ---- S11 and replaced there by other 8 active gauge connections DA9 ---- DA16. A test run was then made for active gauges DA9 ---- DA16, and so on.

The wires on the rotating side were stuck down with epoxy glue and taped, and all gauges were covered with felt and tape.

At any setting of the motor regulator a virtually constant speed was maintained, so steady-state, direct-reading strain meters of the Baldwin-Lima-Hamilton/

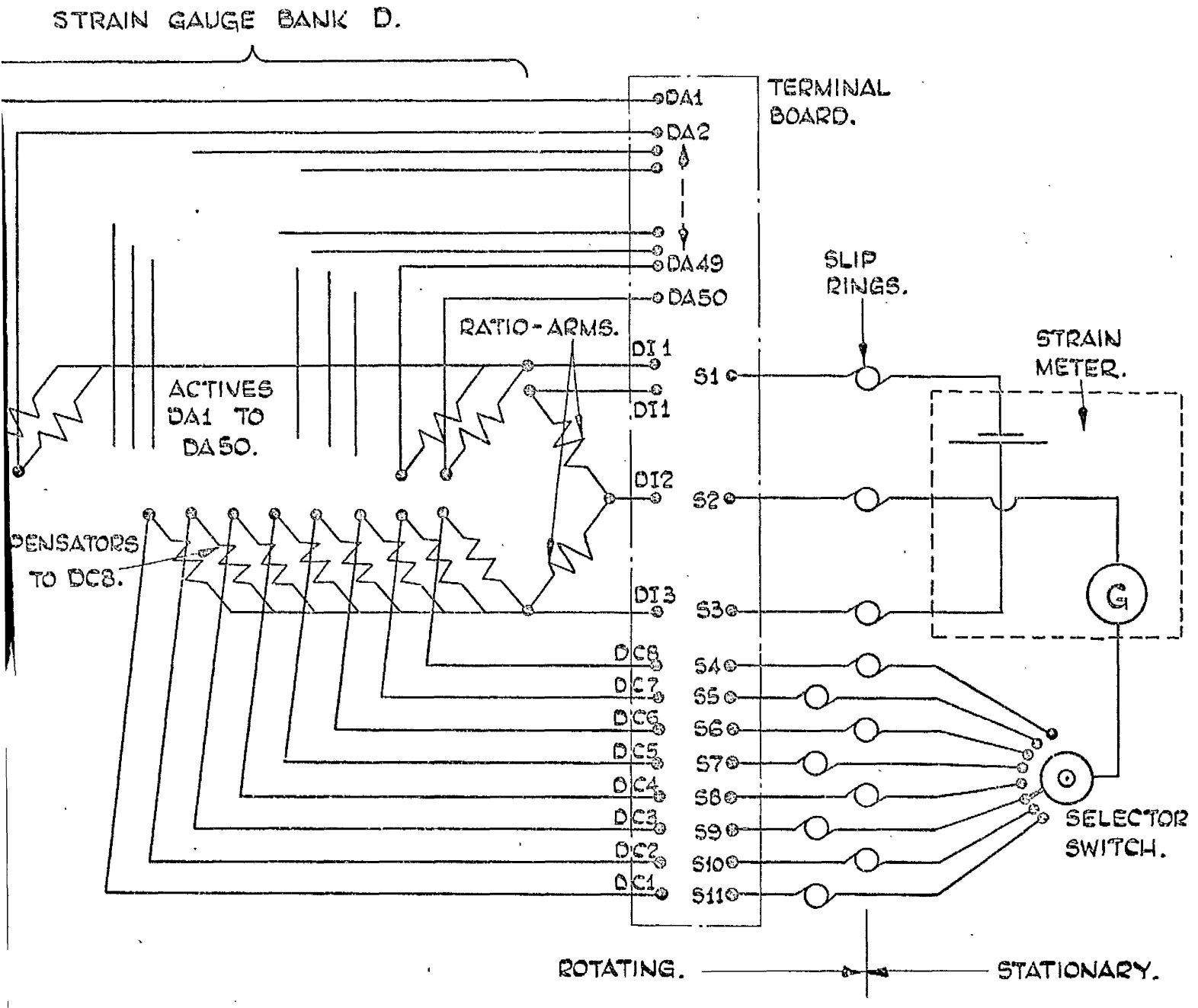

ACTIVE GAUGES DA1 TO DA50 ARE ON WHEEL.

COMPENSATORS DC1 TO DC8 AND RATIO-ARM GAUGES ARE ON SEGMENTED DISC.

FIG. 57. DIAGRAM OF STRAIN GAUGE CIRCUIT USED FOR MEASUREMENT OF CENTRIFUGAL STRESSES IN $16\frac{1}{2}$ IN. ALUMINIUM TURGO WHEEL.

Lima-Hamilton and Huggenberger types were used for centrifugal strain indication. These were found to be perfectly satisfactory. A subsequent check, described later, in which an S.E. Laboratories ultra-violet dynamic-strain recorder was used, fully confirmed important results obtained with the steady-state instruments, both in respect of the strain magnitudes indicated and of the steadiness of the readings.

Speed was measured by tachometer and digital pulse counter, this latter being operated via the counting channel of the slip ring unit.

Figs 58 and 59 show the wheel in the spinning test rig ready for a test run. The former Fig. gives two views of the wheel, slip ring unit and pulse counter, the gauges and wires on the wheel being taped. The terminal board is also shown taped, as it was for each test run. Fig.59(a) shows the wheel in the rig, the slip ring unit, the motor and speed regulator and the Baldwin strain meter and switch box. In Fig.59(b) the strain meter has been replaced by the u.v. dynamic-strain recorder.

In a test run, strains at a location were measured at 3 speeds, about 770 r.p.m., about 900 r.p.m. and about 1300 r.p.m., the normal working speed. Subsequent to tests with the wheel in the working condition as shown in Figs.58 and 59, the complete wheel was masked-off with tape to eliminate windage. Many of the more significant strains were re-measured for this condition, but it was found that the elimination of windage had no appreciable effect.

All the measured centrifugal strains showed accurate linear variation with the square of the speed. Fig.60 shows a graph of measured strain v $(\text{r.p.m.})^2$ for a few gauge locations, including the most significant ones.

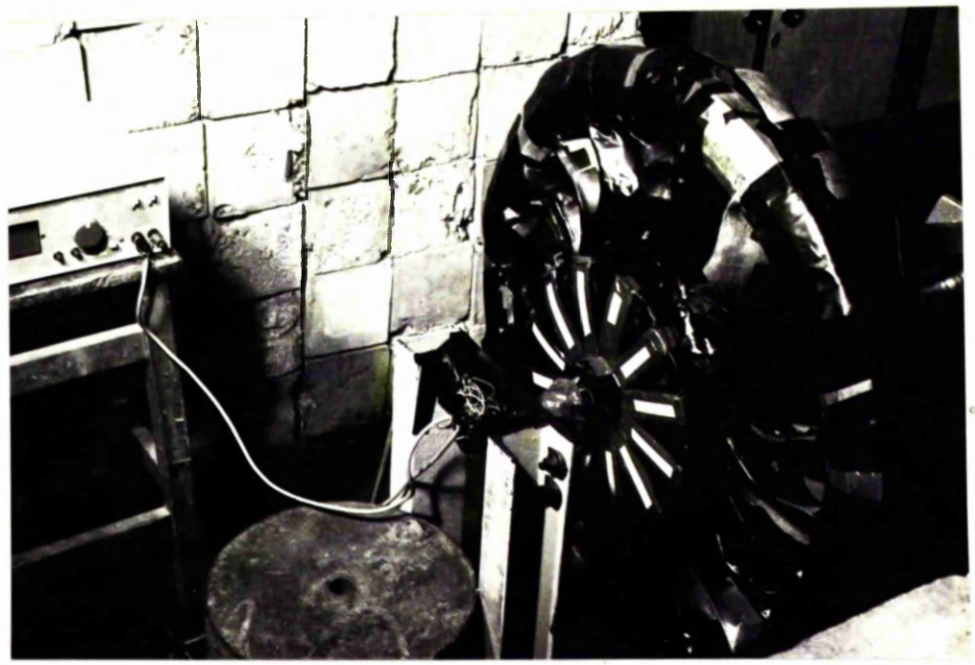

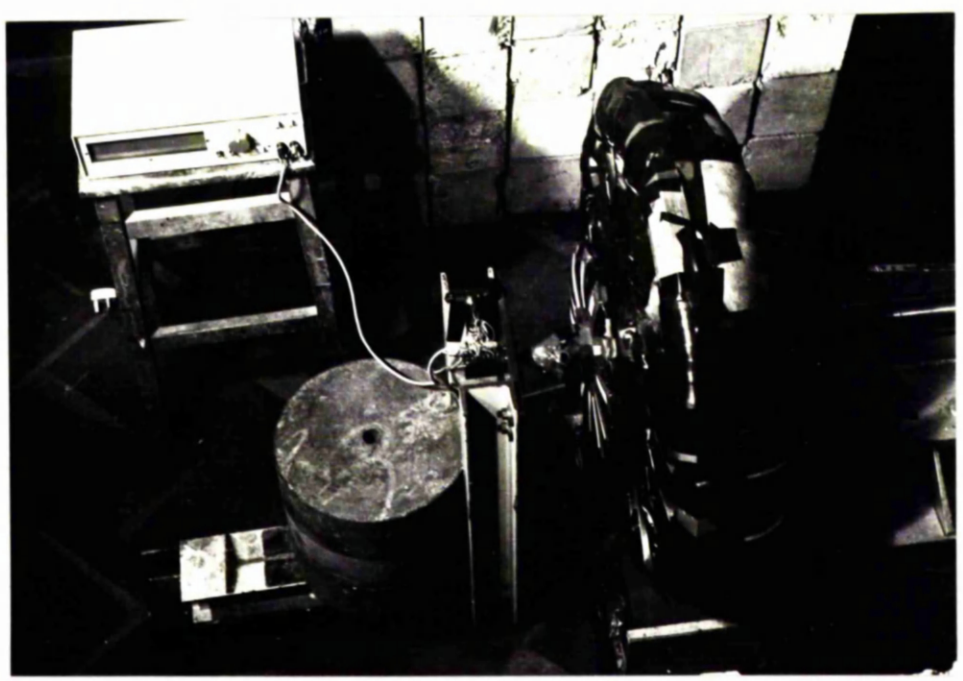

FIG.58. TWO VIEWS OF $16\frac{1}{2}$ in. ALUMINIUM TURGO WHEEL IN RIG READY FOR CENTRIFUGAL TEST. THE TAPED TERMINAL BOARD, SLIP RING UNIT AND PULSE COUNTER ARE SHOWN.

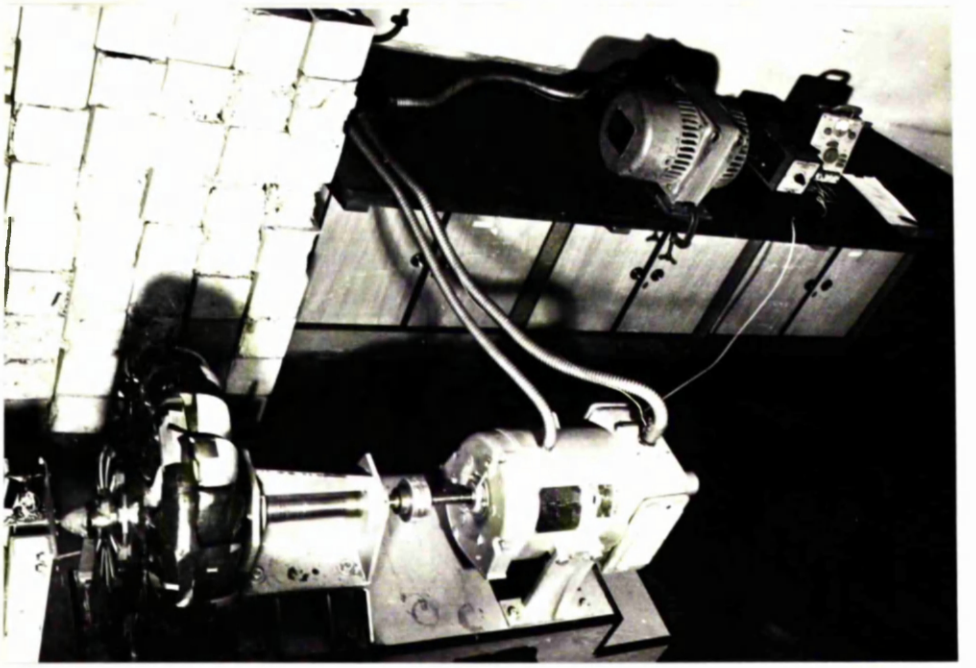

(a) VIEW SHOWING SLIP RING UNIT, BALDWIN-LIMA-HAMILTON STRAIN METER AND SWITCH-BOX.

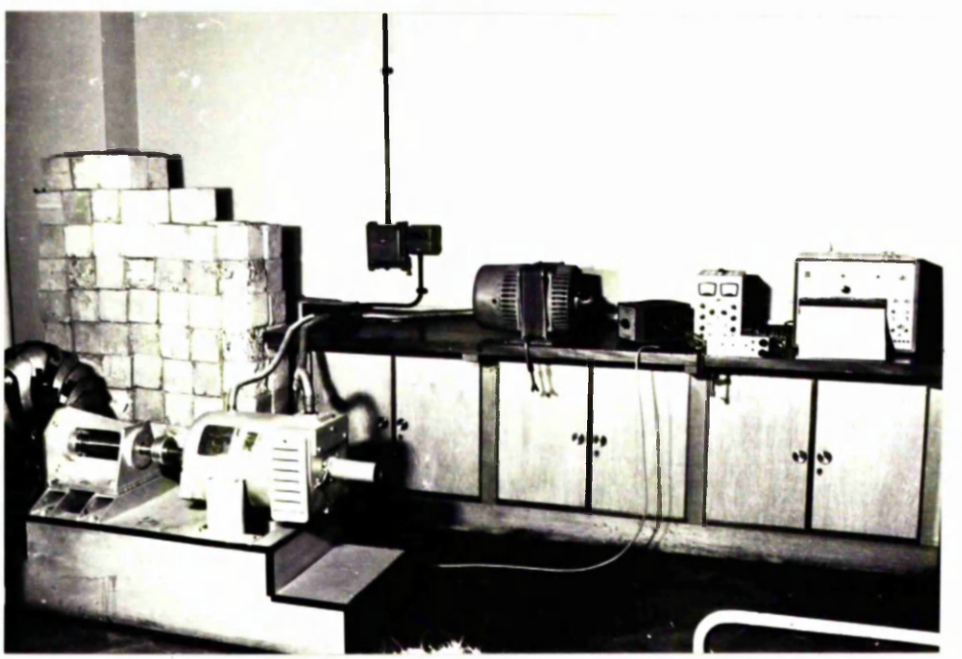

(b) VIEW SHOWING TAPED SEGMENTED DISC ADJACENT TO OUTLET SIDE OF WHEEL, AND SHOWING S.E. LABORATORIES ULTRA-VIOLET DYNAMIC-STRAIN RECORDING EQUIPMENT.

FIG. 59. $16\frac{1}{2}$ in. ALUMINIUM TURGO WHEEL IN RIG READY FOR CENTRIFUGAL TEST. THE DRIVING MOTOR AND SPEED REGULATOR ARE SHOWN.

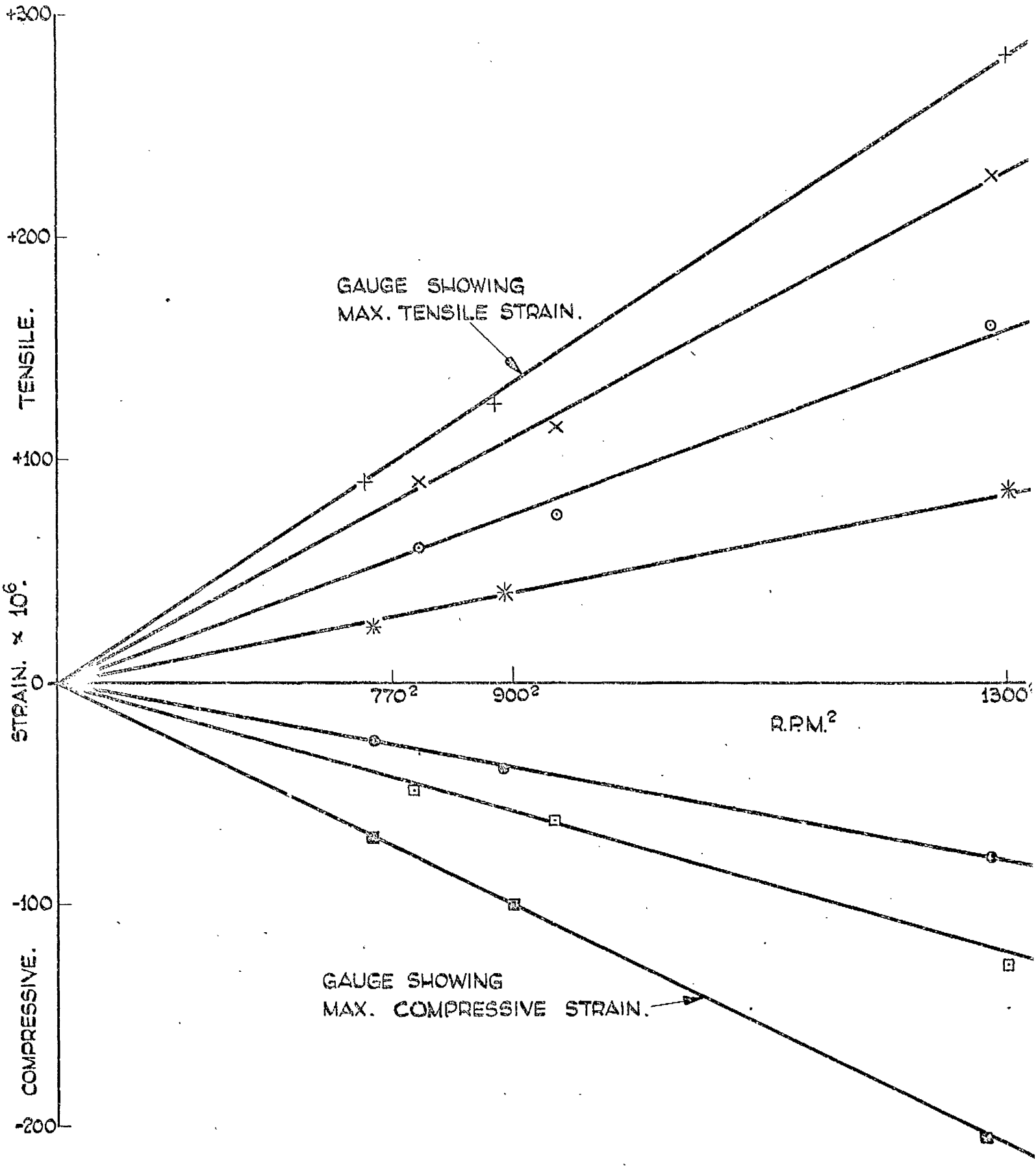

FIG. 60. GRAPHS OF MEASURED CENTRIFUGAL STRAIN v SQUARE OF WHEEL SPEED (R.P.M.)², TYPICAL OF THE STRAIN GAUGE READINGS FOR THE TEST ON THE 16½ IN. ALUMINIUM TURGO WHEEL.

4B ii Centrifugal stresses on the buckets

The main measured centrifugal stresses on the buckets of the $16\frac{1}{2}$ in. aluminium Turgo wheel are presented in Figs.61, 62, 63 and 64. These results pertain to the normal working speed of 1300 r.p.m., which was the maximum speed attained in the tests.

The results for the edges are plotted as edge stress distributions, in Figs.61 and 62, the former showing the values read on the swept surfaces of the edges, the latter the values at corresponding points on the unswept surfaces of the edges.

The principal stresses on the surfaces at points remote from the edges are indicated in Figs.63 and 64, the former Fig. for points on the swept surface, the latter for, in the main, corresponding points on the unswept surface. The principal stresses mostly refer to points on four meridional sections of the bucket (at $\Theta = 57^{\circ}, 74^{\circ}, 92^{\circ}, 111^{\circ}$ - Fig.9) and at junctions of the bucket with rim and with hub. Some edge stress values have been repeated in these two Figs., mainly at points of interest in relation to indicated non-edge stresses.

There is a marked contrast in magnitudes between the stresses on the swept surfaces of the bucket edges Fig.61, and those on the unswept surfaces of the edges, Fig.62. The former stresses are, in general, much higher than the latter— a circumstance indicative of the presence of bending moments and membrane forces along the edges. For the most part, bending and membrane stresses are of similar signs on the swept surfaces, and are of dissimilar signs on the unswept surfaces. The maximum measured centrifugal stress on the wheel, 3160 lb/in^2 tensile, occurs on the swept surface of the outlet edge, as shown on Fig.61, and lies on the same meridional section ($\Theta = 92^{\circ}$, Fig.63) as the highest measured stress on the/

the inlet edge — a value of 2600 lb/in^2 tensile, on the swept surface. These stresses occur on the bucket edges in the region of the pitch circle (Fig.9). Despite the different geometries of inlet and outlet edges, it is clear from Figs.61 and 62 that, over the region of the bucket between hub and inner radius of rim, the general stress behaviour of one edge is fairly similar to that of the other.

Figs. 63 and 64 show that, at points on meridional sections, principal stresses in the main, lie roughly parallel and perpendicular to the plane of the wheel (or circumferential and meridional). On the sections $\Theta = 74^\circ, 92^\circ, 111^\circ$, the mainly circumferential principal stresses on the swept surface are tensile and the accompanying meridional stresses are compressive, while the situation is largely vice-versa on the unswept surface. The circumferential and meridional stresses on these sections are of comparable magnitudes on the average and, at individual points, the meridional stress is frequently the greater. It is evident that, over this region of the bucket, bending in the plane of the wheel reduces the circumferential curvature, with consequent deformation of the meridional sections by bending, increasing the meridional curvature. This behaviour is very similar to that found in the tests on single buckets (section 4A i) and in particular closely resembles the indications presented in Figs.46 and 48.

Of the non-edge and non-junction stresses, the highest values occur on the meridional section at $\Theta = 92^\circ$ where the edge stresses are also highest. The meridional section principal stress results, Figs.63 and 64, together with the edge stress results of Figs.61 and 62, clearly establish that bending in the plane of the wheel is the most significant action on the bucket.

The principal stresses on the meridional section at $\Theta = 57^\circ$, Figs.63 and 64, and the edge stresses, particularly at inlet, on this same section, reflect/

reflect the influence of the rim. The natures of the principal stresses and their generally smaller magnitude in comparison to the values of principal stresses on the other meridional sections, and the comparatively high compressive stresses on the inlet edge near the rim, indicate the restraining effect of the rim, in opposition to the tendency of the bucket to bend radially outwards in the plane of the wheel. To some extent too, these inlet edge compressive stresses may arise due to the geometry of the edge local to its junction with the rim (see e.g. Fig.56(a)). Further evidence of the restraint due to the rim is to be seen in the region of the outlet edge/rim junction, Figs.63 and 64. The swept surface stresses + 2200 lb/in^2 and + 740 lb/in^2, together with the respective corresponding unswept surface stresses -580 lb/in^2 and - 1390 lb/in^2, show the strong tendency of the bucket to bend outwards in this region, the rim restraint countering this tendency. Along the outlet edge from the rim, outward bending of the edge does indeed occur, as the edge stresses show in Figs.61 and 62.

The effect of bending action in the plane of the wheel is discernible in the stresses on the bucket at its junction with the hub, Figs.63 and 64. The tendency for "meridional" bending of this junction "section" however, is restrained by the hub, and thus gives rise to comparatively high tensile stresses on the unswept surfaces of the edges near their junctions with the hub, Fig.62. This may be contrasted with the edge stresses more remote from the hub, e.g. at $\Theta = 111^\circ$, Figs.63, 64 and 61, where meridional bending apparently takes place unrestrained.

Many of the stress readings presented in Figs.61, 62, 63 and 64, including the maximum measured centrifugal stress, represent values which have been confirmed by duplicate gauges at nominally identical locations. This also applies to the stresses measured on rim and hub. Some of the single gauges arranged in rosette orientations, e.g. as shown on/

on the unswept surfaces of buckets in Fig.56(b), played the duplicate rôle in relation to composite rosettes. The maximum difference in strains indicated by duplicates was of the order of 35%, and referred to small strain values.

Owing to the reasonably thorough centrifugal strain survey, it is rational to conclude that the maximum measured stress of 3160 lb/in^2 tensile, will be of the order of the actual maximum centrifugal stress on the wheel. The measured value would be expected to be somewhat less than the actual maximum stress since the gauge indicating the value was close to the bucket edge, but could not, of course, be right on the edge. The other readings on Figs.61 and 63 show that the stress gradients in the maximum stress region are fairly appreciable. It is likely also that, in the stress concentration regions at outlet edge junctions with hub and rim, where stresses of + 2600 lb/in^2 on unswept surface (Fig.62) and + 2200 lb/ on swept surface (Fig.61) were indicated respectively, the measured values will be exceeded by the actual local maxima. This, of course, is an inherent characteristic of strain gauge results from non-uniform strain areas

It is of interest to compare the maximum measured stress with the indications of the brittle lacquer centrifugal test. Extrapolating to the relevant speed of 1920 r.p.m., the maximum measured strain would have been

$$\frac{3160}{11.3 \times 10^6} \times \left(\frac{1920}{1300}\right)^2 = \quad 0.0006 \ ,$$

equal to the upper limit of the strain sensitivity of the lacquer in the test. In the maximum stress area then, the lacquer might have been just on the point of cracking. It seems likely that, if a speed only a little in excess of 1920 r.p.m. had been attainable, cracking of the brittle lacquer would have occurred and been evident at the maximum stress location.

Most of the edge locations where stresses were measured, can readily be related to, and so defined by, angle Θ (Figs.9 and 12).

Fig./

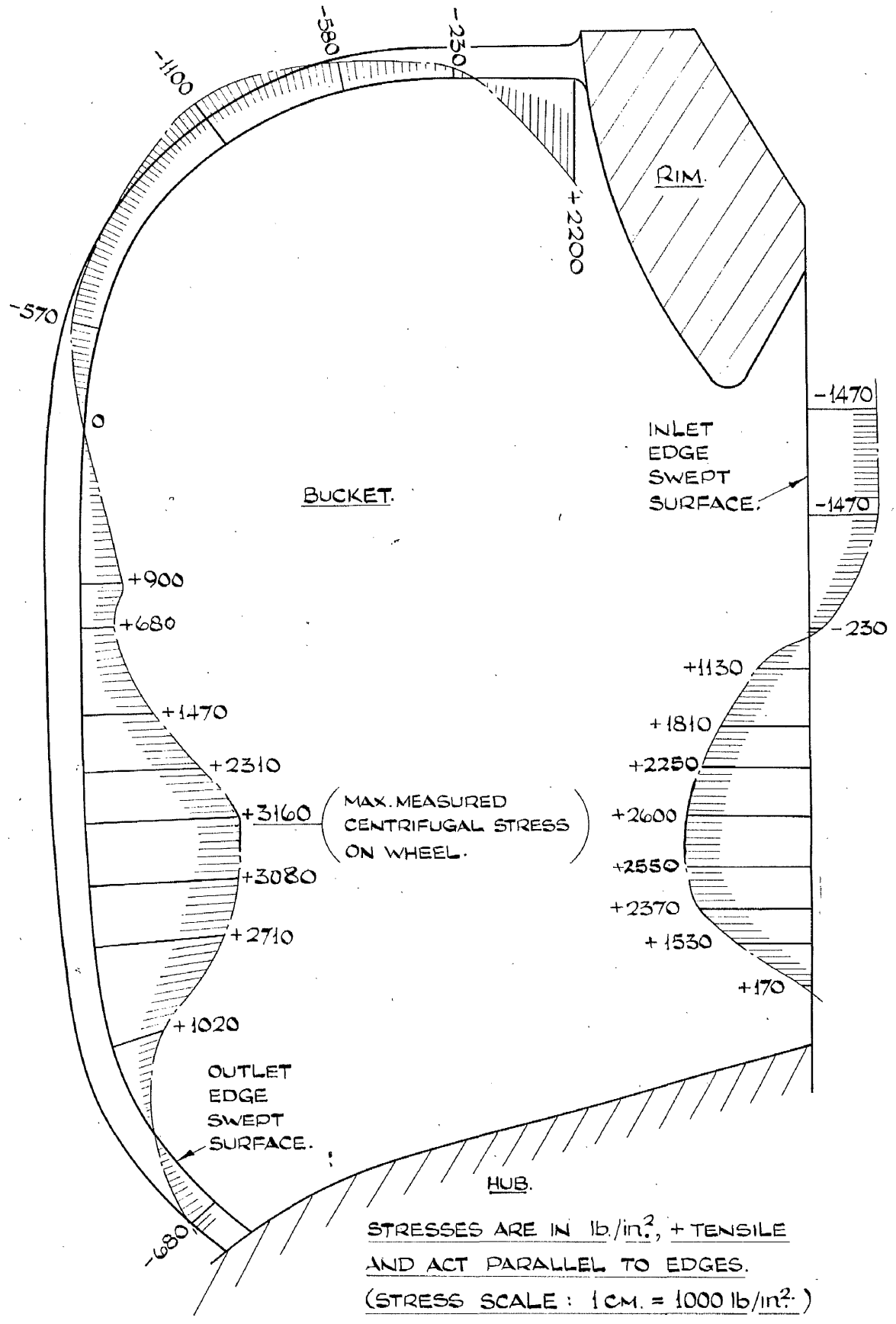

FIG. 61. MEASURED CENTRIFUGAL STRESSES ON THE SWEPT SURFACES OF THE INLET AND OUTLET EDGES OF A BUCKET OF THE $16\frac{1}{2}$ IN. ALUMINIUM TURGO WHEEL, ROTATING AT 1300 R.P.M.

FIG. 62 SHOWS STRESSES AT CORRESPONDING POINTS ON THE UNSWEPT SURFACES. FULL SIZE.

FIG. 61.

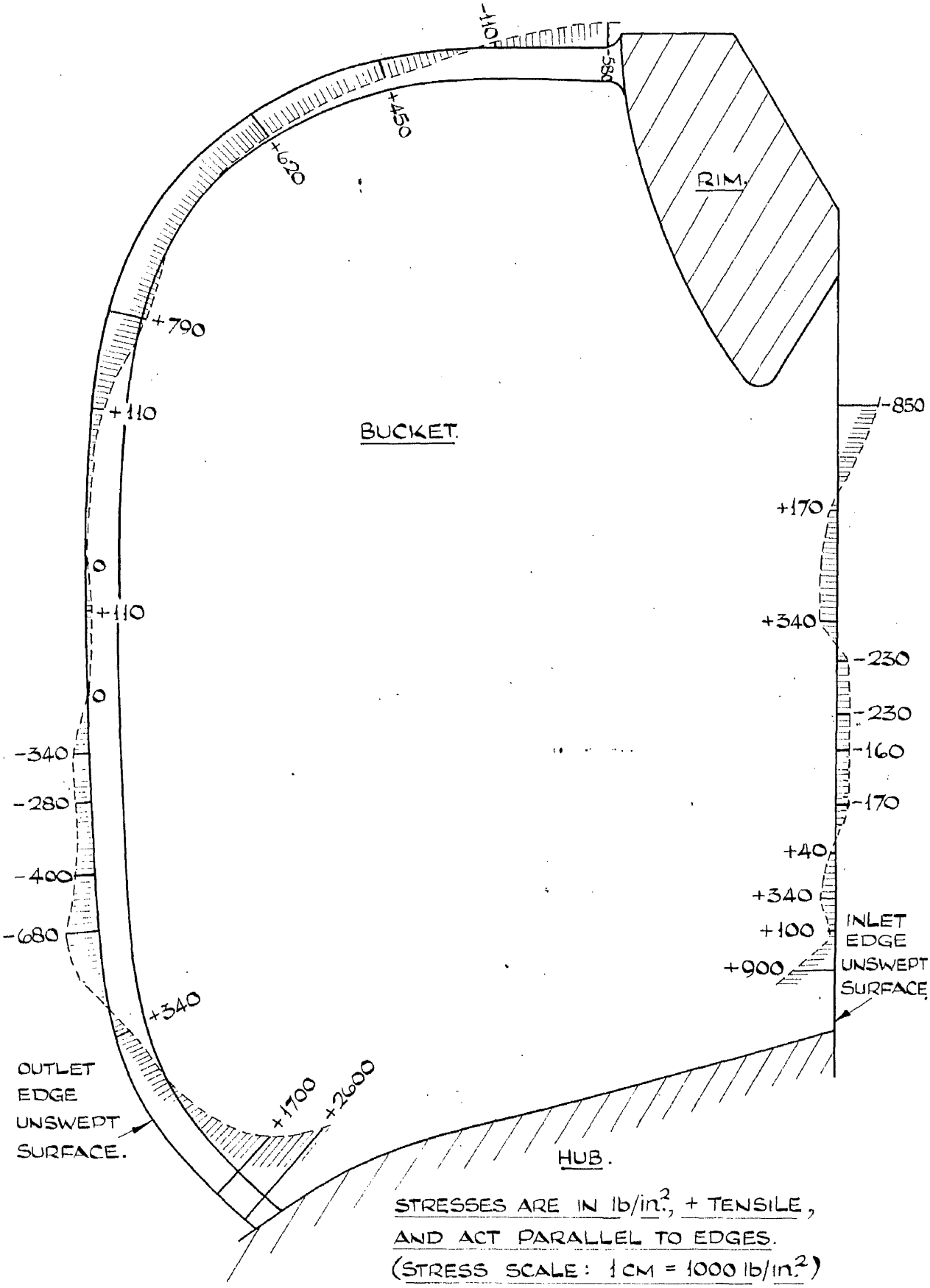

FIG. 62. MEASURED CENTRIFUGAL STRESSES ON THE UNSWEPT SURFACES OF THE INLET AND OUTLET EDGES OF A BUCKET OF THE $16\frac{1}{2}$ IN. ALUMINIUM TURGO WHEEL, ROTATING AT 1300 R.P.M.
FIG. 61 SHOWS STRESSES AT CORRESPONDING POINTS ON THE SWEPT SURFACES.

FULL SIZE.

FIG. 62.

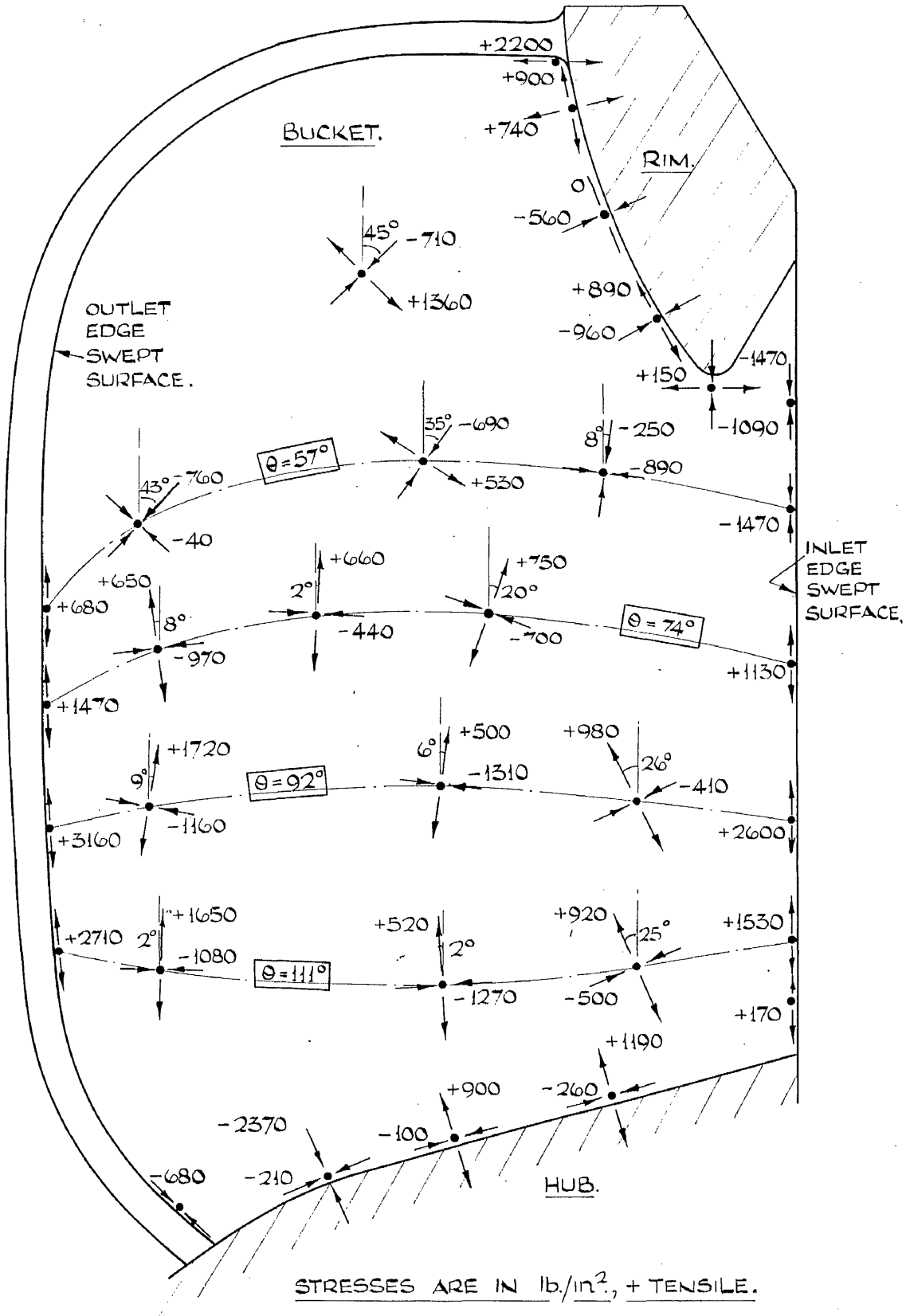

FIG. 63. MEASURED CENTRIFUGAL PRINCIPAL STRESSES ON SWEPT SURFACE OF BUCKET OF 16½ IN. ALUMINIUM TURGO WHEEL, ROTATING AT 1300 R.P.M. THE STRESSES ARE MAINLY AT POINTS ON FOUR MERIDIONAL SECTIONS (θ = 57°, 74°, 92°, 111° – FIG. 9.) AND AT RIM AND HUB JUNCTIONS WITH THE BUCKET.

FIG. 64 SHOWS PRINCIPAL STRESSES MAINLY AT CORRESPONDING POINTS ON UNSWEPT SURFACE.

FULL SIZE.

FIG. 63.

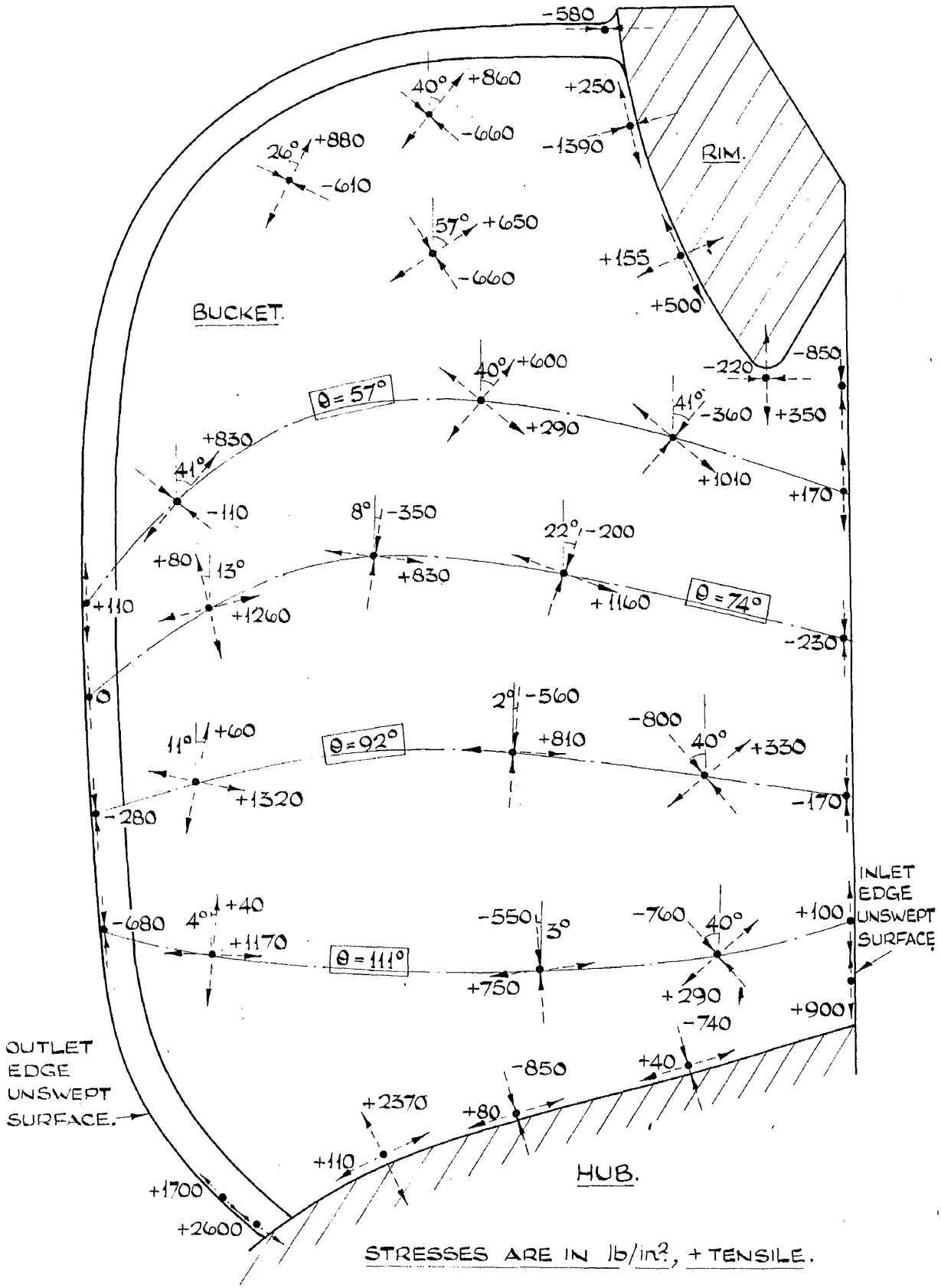

FIG. 64. MEASURED CENTRIFUGAL PRINCIPAL STRESSES ON UNSWEPT SURFACE OF BUCKET OF 16½ IN. ALUMINIUM TURGO WHEEL ROTATING AT 1300 R.P.M. THE STRESSES ARE MAINLY AT POINTS ON FOUR MERIDIONAL SECTIONS ($\theta = 57°, 74°, 92°, 111°$ – FIG. 9.) AND AT RIM AND HUB JUNCTIONS WITH THE BUCKET.

FIG. 63 SHOWS PRINCIPAL STRESSES MAINLY AT CORRESPONDING POINTS ON SWEPT SURFACE.

FULL SIZE.

FIG. 64.

Fig.65 shows the inlet and outlet edge locations in correct relation to $Z_1 G_1$ the Θ - datum, and to arc $G_1 G_3$. The values of Θ pertinent to the locations are measured from this Fig. so permitting the construction of Fig.66 which presents the distributions with Θ of the measured centrifugal stresses on the bucket edges.

From the measured stresses at meridional sections $\Theta = 57^\circ, 74^\circ, 92^\circ, 111^\circ$, Figs.63 and 64, corresponding bending moment and direct force actions on the sections have been derived by the method established in section 4A ii. The relevant results, diagrams and derivations are given in Appendix 6, in which Table A6.1 presents a summary of the derived experimental actions. Fig.67 has been drawn from the Table and shows the distributions of the experimental centrifugal actions with Θ over the bucket. The actions are as follows:-

M_Y :- bending moment in the plane of the wheel; corresponds to M_{YM} of Fig.50(b).

P' :- direct force in the plane of the wheel; corresponds to P_M of Fig.50(b).

M_X :- bending moment in transverse plane; corresponds to M_{XM} of Fig.50(b).

As stated in Appendix 6, for uniformity in all four sections and for subsequent direct comparison with corresponding theory, the bending moments have been referred to axes YY and XX (see Appendix 6, e.g. Fig.A6.1(a)) origin G, the centroid of the equivalent parabolic section (Fig.11) rather than to the corresponding axes through G_M, (Fig.50) the centroid of each meridional section.

It is natural that the general shapes of the curves of Fig.67, especially the curve M_Y should correspond roughly to the shapes of the swept surface edge stress curves of Fig.66. Each experimental point on Fig.67 reflects the overall circumferential stresses on a meridional section, but it is evident from the Figs. presenting the analyses in Appendix 6/

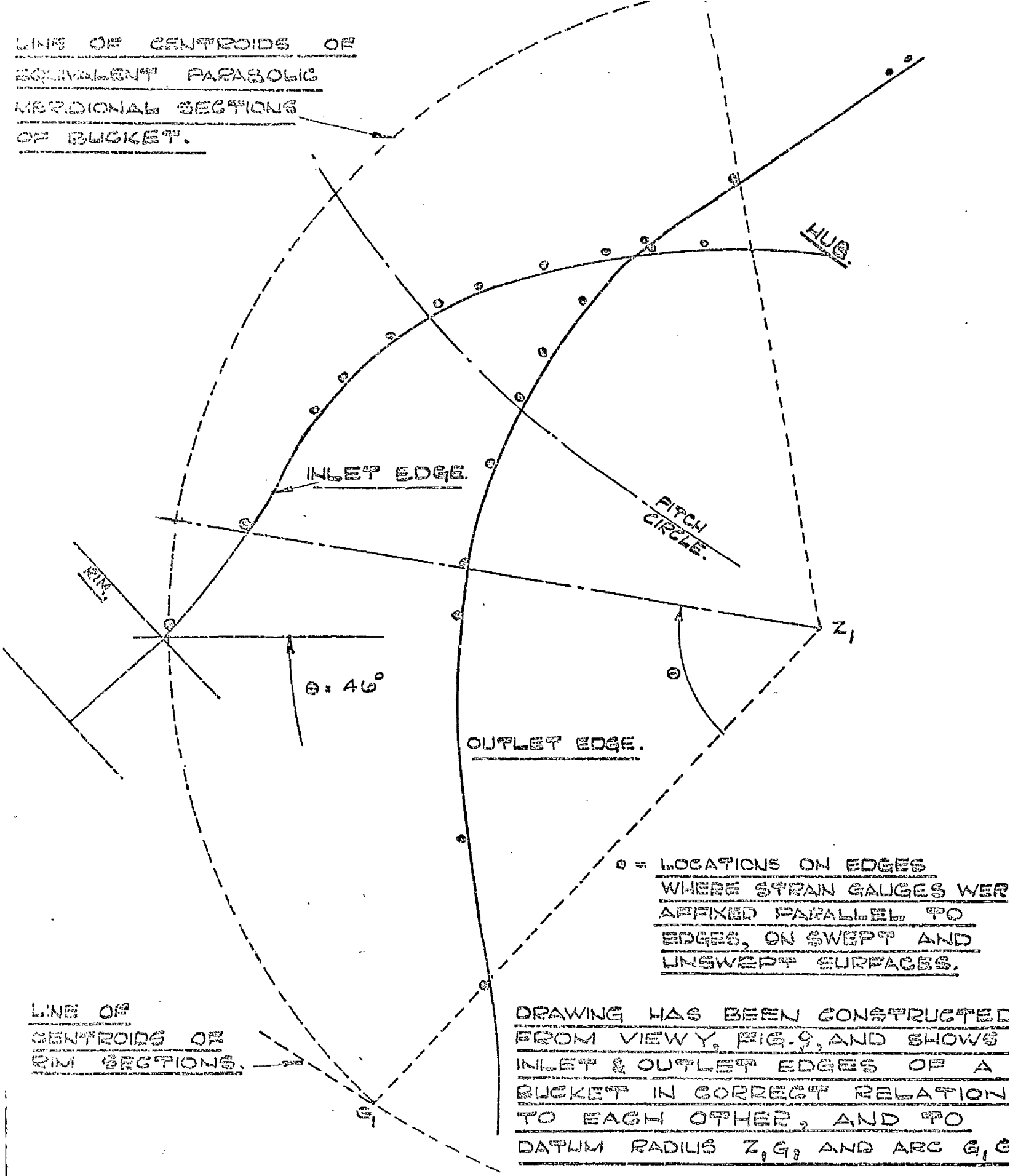

FIG. 65. LOCATIONS, DEFINED BY THE APPROPRIATE VALUES OF ANGLE θ, (REF. FIGS. 9 & 12), WHERE STRESSES WERE MEASURED ON EDGES OF BUCKET OF 16½ IN. ALUMINIUM "TURGO" WHEEL. FULL SIZE.

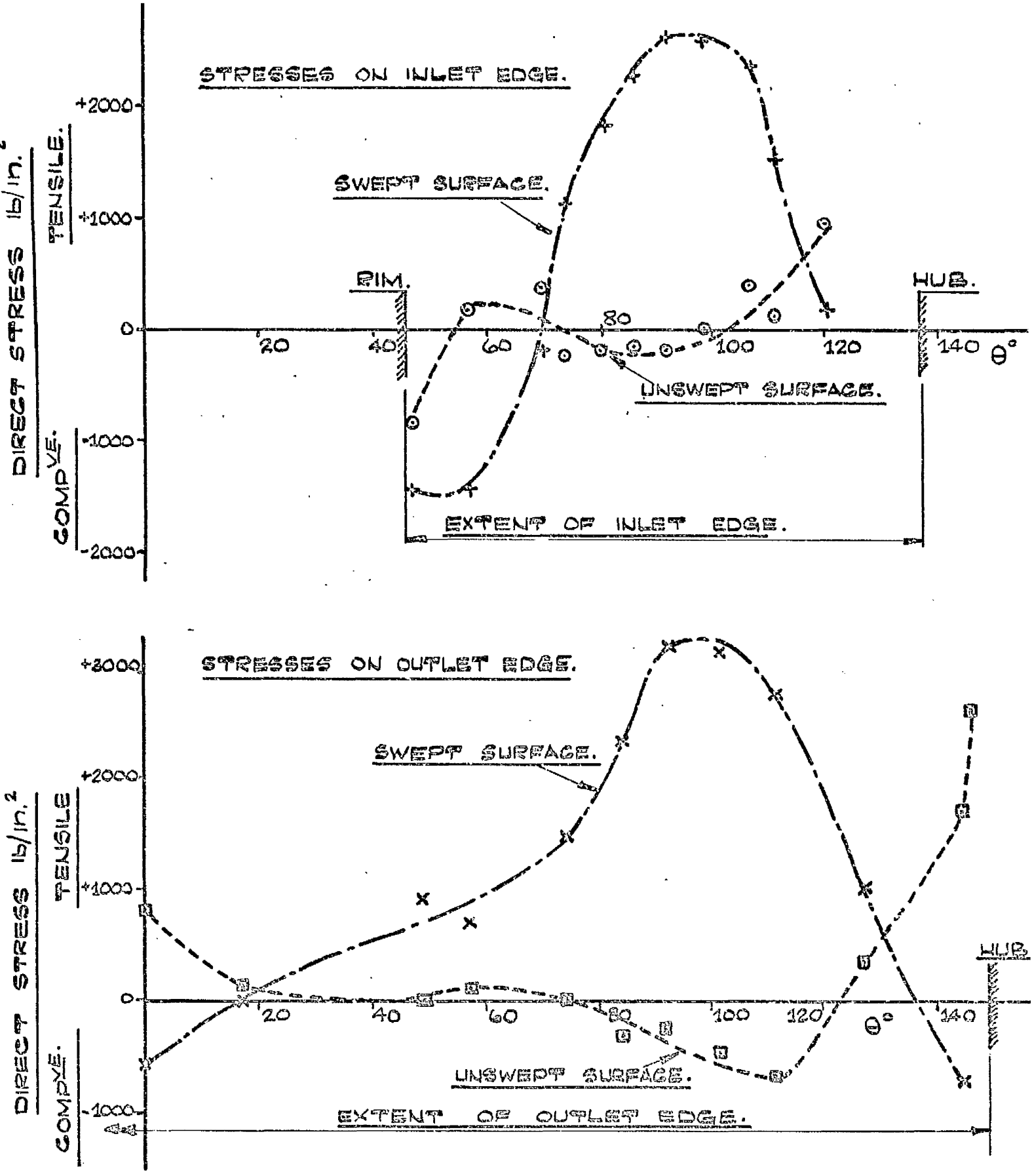

FIG. 66. DISTRIBUTION WITH θ (REF. FIG 65.) OF MEASURED CENTRIFUGAL STRESSES ON SWEPT AND UNSWEPT SURFACES OF THE INLET AND OUTLET EDGES OF BUCKET OF 16½ IN. ALUMINIUM TURGO WHEEL, ROTATING AT 1300 R.P.M.

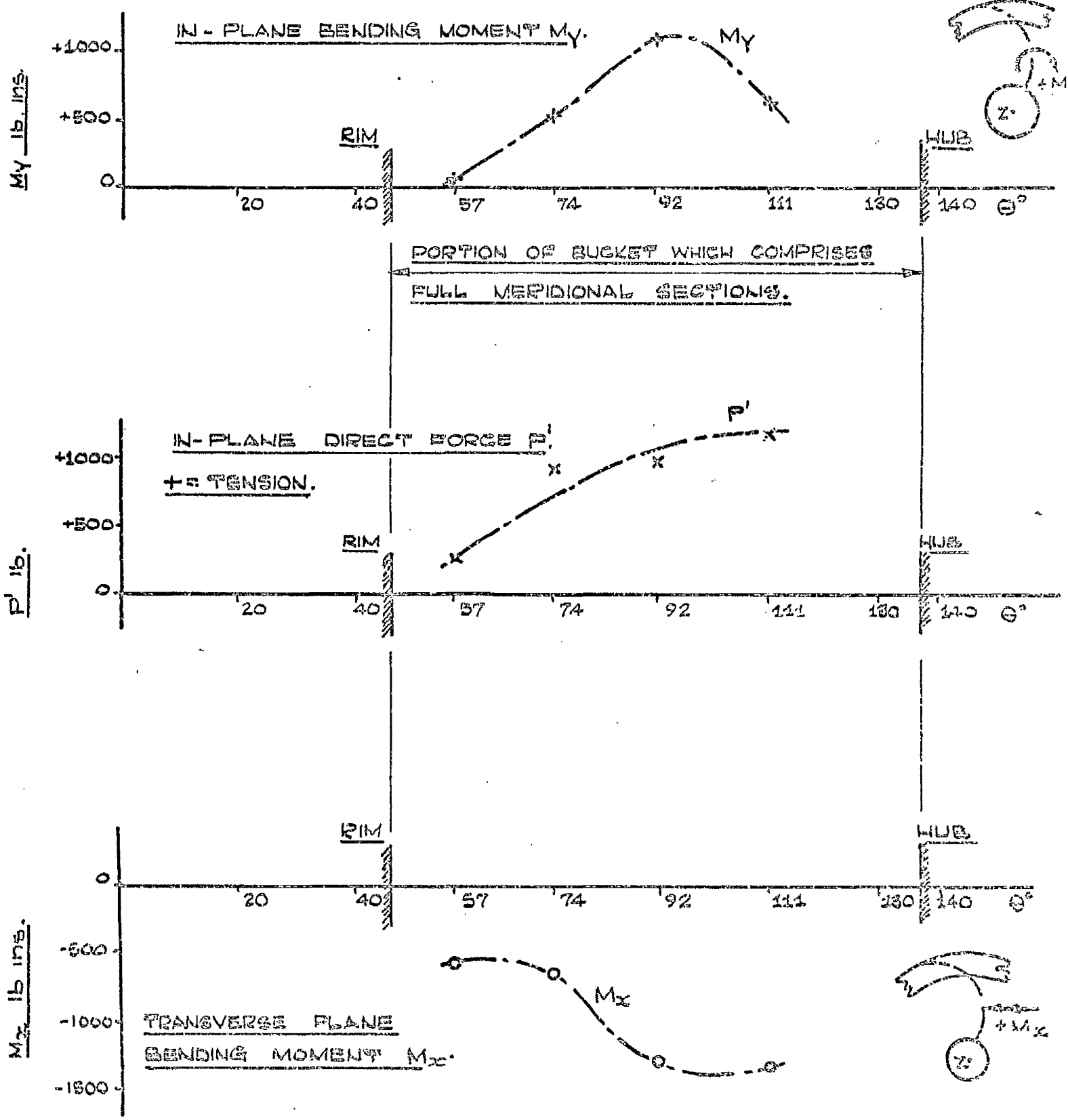

FIG. 67. DISTRIBUTION WITH θ OF CENTRIFUGAL ACTIONS, — IN-PLANE BENDING MOMENT My, IN-PLANE DIRECT FORCE P', AND TRANSVERSE PLANE BENDING MOMENT Mx, — ON MERIDIONAL SECTIONS OF BUCKET OF 16½IN. ALUMINIUM TURBO WHEEL, ROTATING AT 1300 R.P.M.

THE ACTIONS HAVE BEEN DERIVED FROM THE MEASURED CENTRIFUGAL STRESSES AT THE SECTIONS.

(REF. APPENDIX 6, FIGS. 50, 63 AND 64).

6; that the edge stresses are dominant factors in determining the actions, in particular, bending moments M_Y and M_x. This is also evident, of course, in the analyses for the single bucket tests, section 4A ii, Fig.51. A noteworthy feature of all the N_θ, M_θ graphs of Fig.51 and of Appendix 6, is the very small values of shell edge bending moments M_θ in comparison with the corresponding relatively large values of shell edge membrane forces N_θ. On account of the relative thinness of the bucket edges however, corresponding bending stresses and membrane stresses are generally of the same order.

The resistance to in-plane bending moment M_Y on meridional sections, is shown in Appendix 6 to be mainly due to membrane action of the bucket. The results are summarised in Table A6.2 of the Appendix. This finding is also in accord with the single bucket test indications. The proportions of M_Y at $\theta = 57^\circ$, Table A6.2, are remarkable in that the membrane and bending actions are of opposite signs. Fig.A6.1(d) however, shows that over most of this section $N_\theta x$ and $M_\theta \sin\xi$ are both - ve, and that much the greatest fraction of the + ve membrane action is due to the outlet edge stresses at $S_{M MAX}$. This section, of all four, is the "most unsymmetrical" (Fig.A6.1(a)) and is the most subject to the influence of the rim. The proportionately high bending action may be related to the fact that the section is "flatter" or less crescent-shaped than the other sections, particularly towards the inlet edge.

4B iii Centrifugal stresses on the rim

The centrifugal stresses measured on the rim of the $16\frac{1}{2}$ in. aluminium Turgo wheel are shown in Fig.68. These are principal stresses in the main and refer to two rim sections A and B, in way of bucket inlet edge and outlet edge junctions respectively.

It is evident that, almost throughout these data, the major principal stresses are tensile and circumferential or nearly so (with respect to the rim and the wheel axis). On the whole, the stresses are appreciably different at comparable locations on the two sections — a circumstance which would seem to demonstrate the influence of the bucket junctions. The stresses on the inlet side of the rim, adjacent to the bucket inlet edge junction, show evidence of radial "push" on the rim by the bucket inlet edge. The values on the outlet side and on the outer face of the rim, adjacent to the bucket outlet edge junction, show evidence of radial "pull" on the rim by the bucket outlet edge. Both of these indications are consistent with the corresponding stresses locally on the bucket edges, Figs.61 and 62.

The maximum measured stress on the rim, 2150 lb/in^2 tensile, is circumferential and occurs on the outlet side near the outlet side/outer face edge of the rim at the junction with the bucket outlet edge. In general, for both sections A and B, the outlet side stresses are much higher than those on the outer face. The outer face stresses, in turn, are much higher than the stresses on the inlet side. These remarks are best illustrated with reference to Fig.69 which shows the measured circumferential stresses plotted as distributions over the two rim sections A and B. Since the major principal stresses of Fig.68 are circumferential or nearly so, the plotting of the circumferential stress distributions of Fig.69 is justified

and/

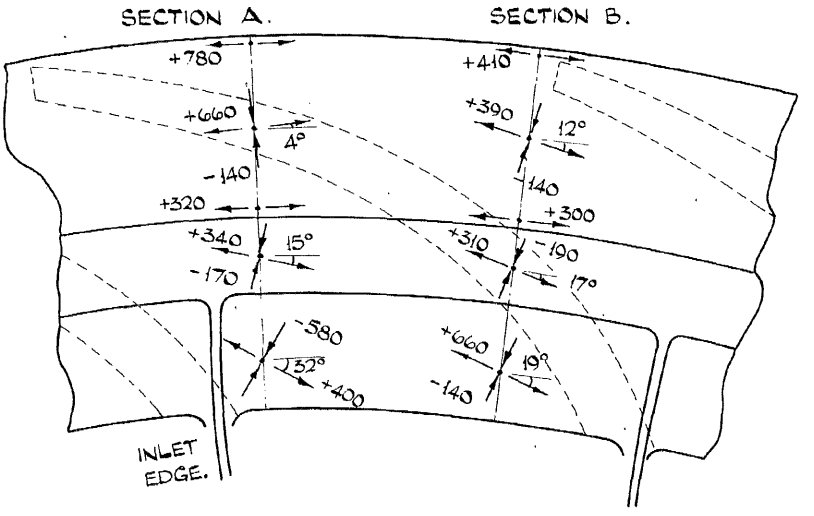

PRINCIPAL STRESSES ON INLET SIDE OF RIM.

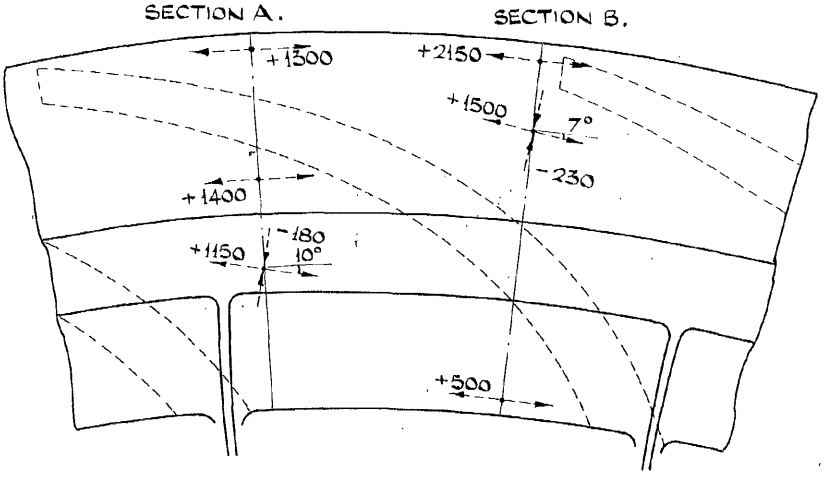

PRINCIPAL STRESSES ON OUTLET SIDE OF RIM.

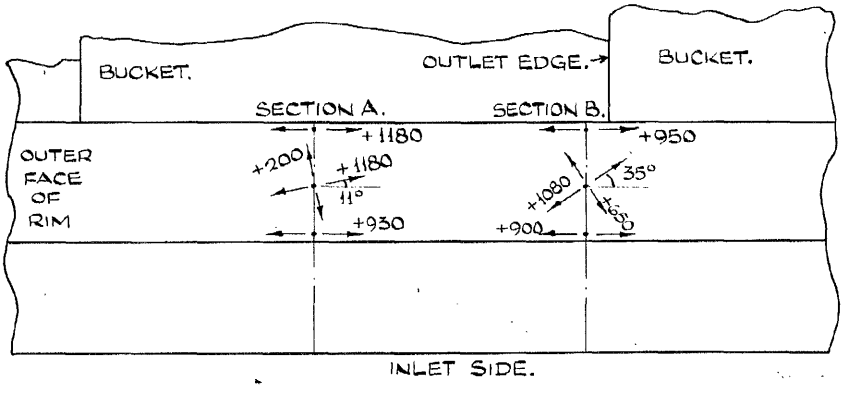

PRINCIPAL STRESSES ON OUTER FACE OF RIM.

STRESSES ARE IN lb./in^2., + TENSILE.

SECTION A - IN WAY OF BUCKET INLET EDGE JUNCTION.

SECTION B - IN WAY OF BUCKET OUTLET EDGE JUNCTION.

FIG. 68. MEASURED CENTRIFUGAL PRINCIPAL STRESSES ON TWO SECTIONS A & B OF RIM OF 16½ IN. ALUMINIUM TURGO WHEEL, ROTATING AT 1300 R.P.M. FULL SIZE.

FIG. 68.

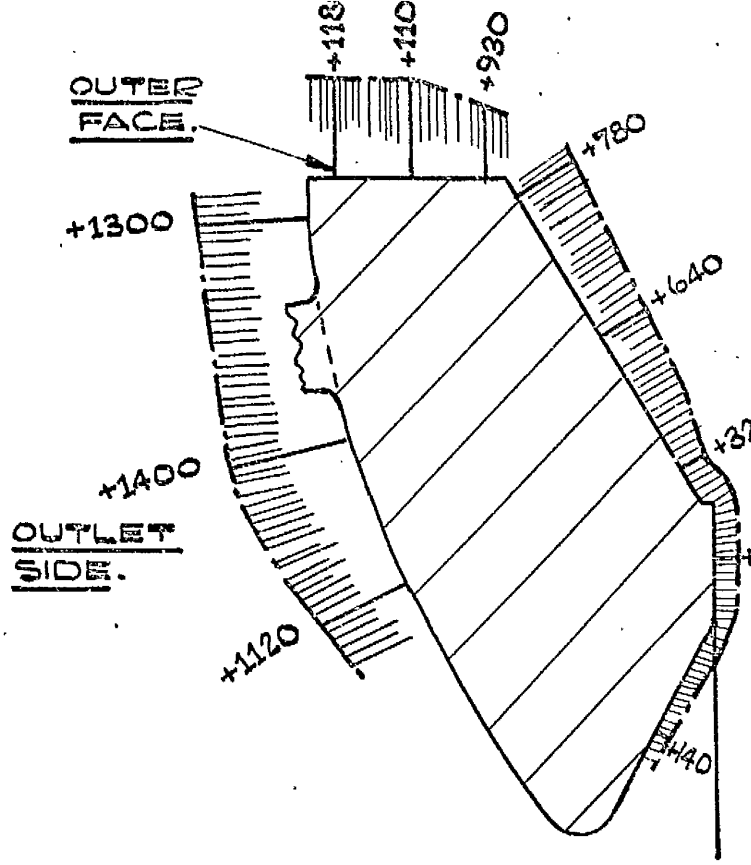

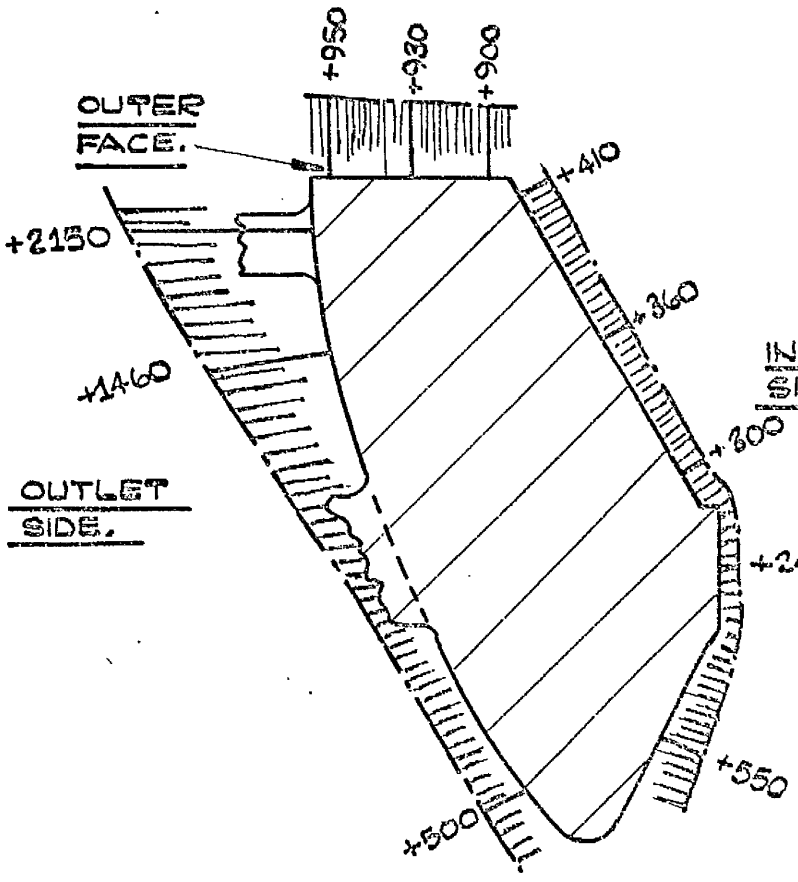

STRESSES ARE IN lb/in^2. + TENSILE.
(STRESS SCALE : 1 CM. = 1000 lb/in^2.)

FIG. 69. MEASURED CENTRIFUGAL CIRCUMFERENTIAL STRESSES ON TWO SECTIONS A AND B OF RIM OF 16½ IN. ALUMINIUM TURBO WHEEL, ROTATING AT 1300 R.P.M.

FULL SIZE.

and is significant.

All the measured circumferential stresses in Fig.69 are tensile, and the distributions over both sections exhibit the same feature, namely highest stresses on outlet side, lowest on inlet side. In section B, the highest stress occurs at the extreme outlet side fibre, the lowest stress at the extreme inlet side fibre— a situation close to repetition in section A. This feature signifies the presence of "ring inversion" moments exerted by the buckets on the rim sections, the moments acting in the planes of the sections. The resultant bending stresses produced on the rim sections are tensile to the outlet side, compressive to the inlet side, and are superimposed on the tensile direct stress in the rim.

It is now interesting and instructive to regard the centrifugal deformation of bucket and rim together, on the basis of the measured stresses on these two components, Figs.61 to 64, 68 and 69. From these, the centrifugal deformed condition is readily deduced. This is depicted in Fig.70.

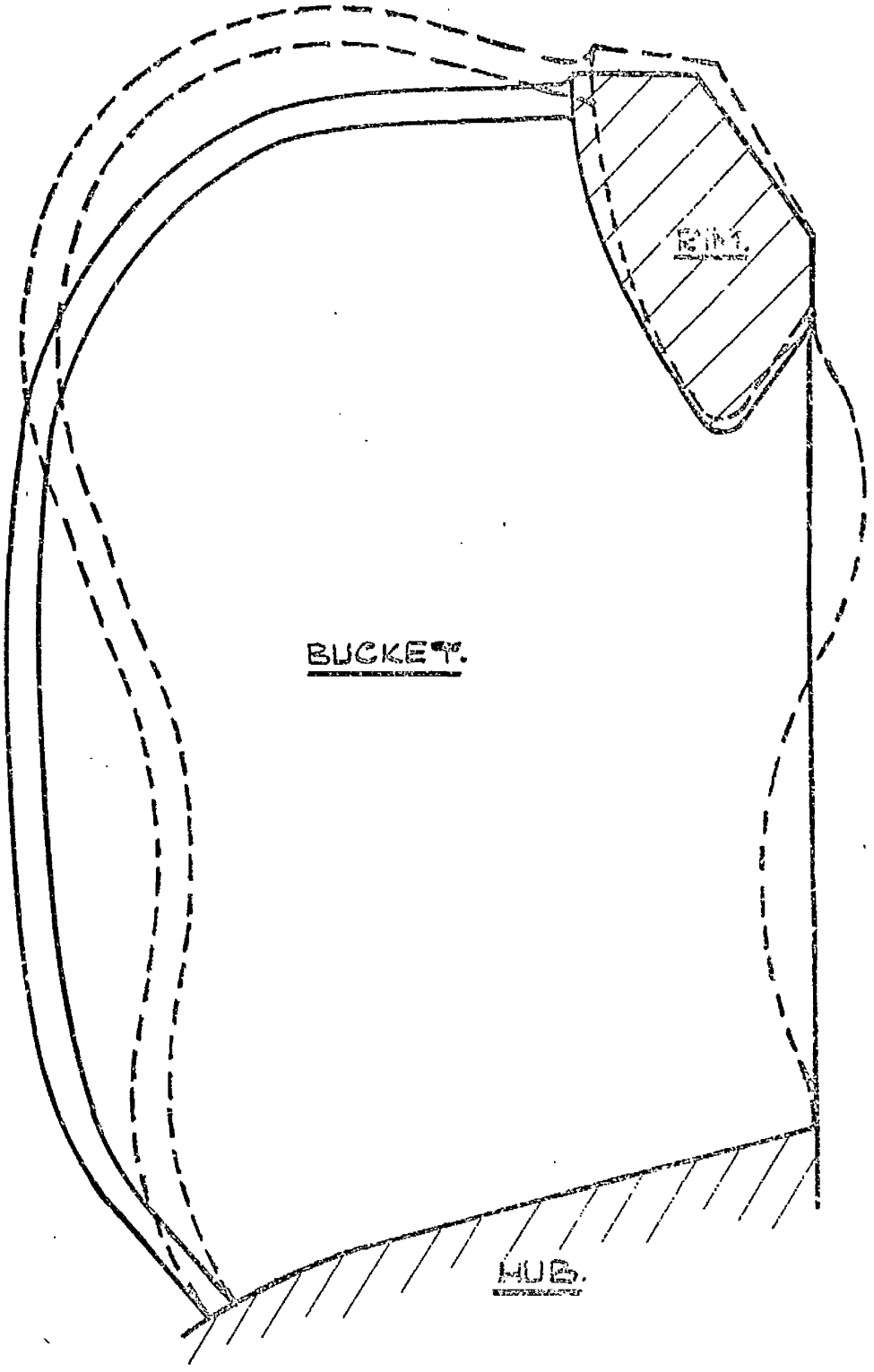

FULL LINES SHOW THE STATIONARY UNDEFORMED CONDITION.

DOTTED LINES SHOW THE (EXAGGERATED) CENTRIFUGAL DEFORMED CONDITION, AS DEDUCED FROM MEASURED STRESSES, FIGS. 61 TO 64, 68, 69.

FIG. 70. ILLUSTRATION OF CENTRIFUGAL DEFORMATION OF BUCKET EDGES AND OF RIM, OF 16½ IN. ALUMINIUM TURBO WHEEL, ROTATING AT 1300 R.P.M.

4B iv Centrifugal stresses on the hub

Fig.71 shows the centrifugal stresses which were measured on the hub of the wheel. The values indicated are mostly for circumferential stresses, the associated orthogonal stresses, where measured, being of comparatively negligible significance.

Save for the semi-axial compressive stress of - 280 lb/in^2, read from a single gauge between the buckets, all the stresses shown are tensile and are circumferential. All values are small in comparison with the corresponding bucket and rim centrifugal stresses. Towards the outlet side the stresses are higher than on the inlet side. This tends to confirm previous indications that the rim, in restraining radially outward displacement of the buckets, alleviates some of the bucket loading on the hub, particularly on the inlet side. The low inlet side values of + 110 lb/in^2 despite the recessed inlet side hub face, provide clear evidence of this. The result will also reflect, to a degree, the out-of-symmetry of bucket meridional sections (e.g. Fig.9), the centroids of which lie closer to the relatively thick outlet edge than to the thin inlet edge.

It is noteworthy that the highest measured centrifugal stress on the hub, + 570 lb/in^2 circumferential, occurs at a location adjacent to the bucket outlet edge junction, evidently a stress concentration region. The corresponding stress locally on the outlet edge is + 2600 lb/in^2, Fig.62, the highest stress measured on the unswept surfaces of the bucket edges.

On account of the relatively small magnitudes of these measured stresses, it is reasonable to assume that the maximum centrifugal stress at the hub bore will not be of a relatively high order and should be unlikely to exceed 1200 lb/in^2 tensile.

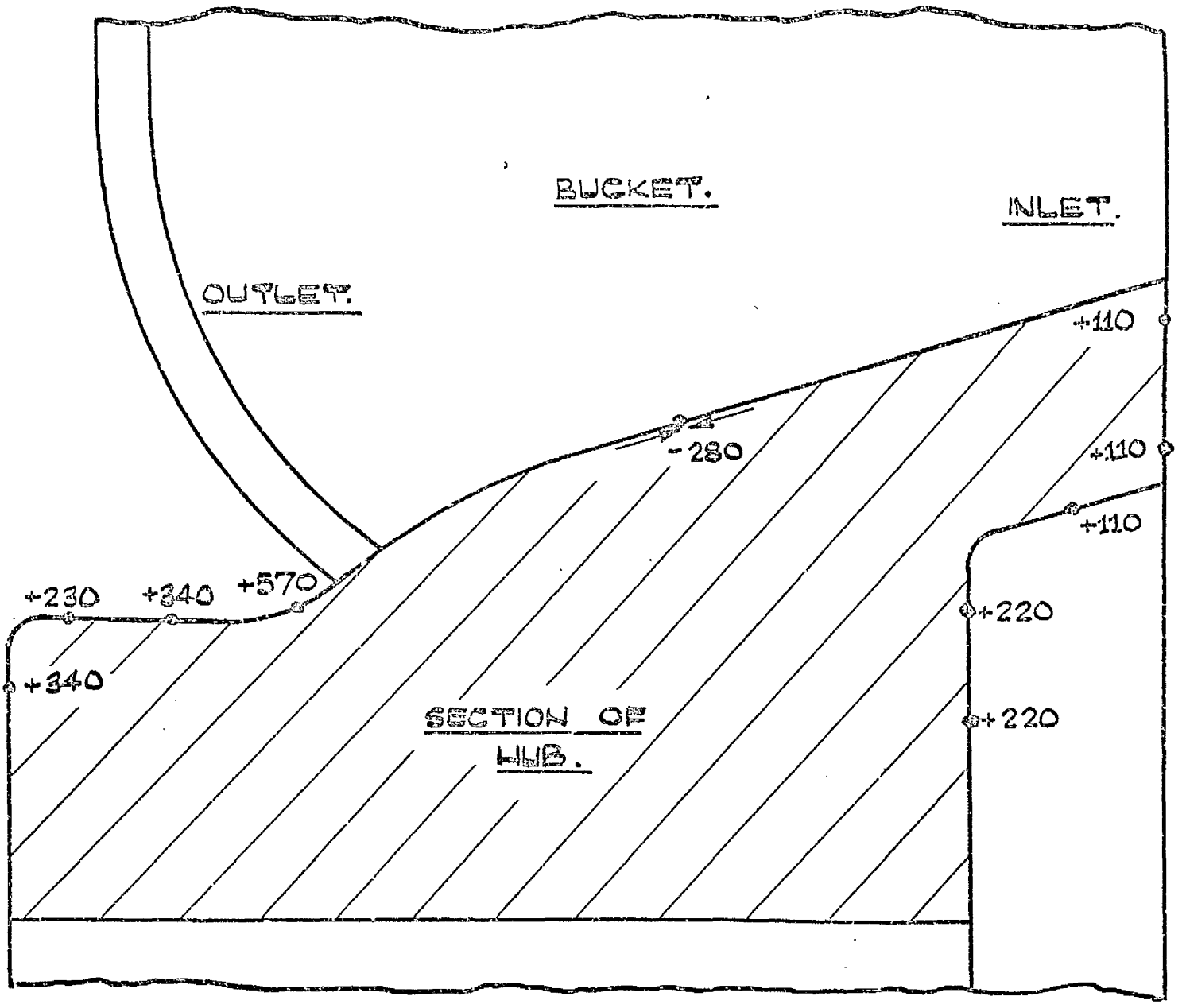

STRESSES ARE IN lb/in.^{2}, + TENSILE, AND ARE CIRCUMFERENTIAL WITH RESPECT TO THE AXIS OF THE WHEEL, UNLESS OTHERWISE INDICATED. ASSOCIATED ORTHOGONAL STRESSES ARE OF NEGLIGIBLE SIGNIFICANCE.

FIG. 71 MEASURED CENTRIFUGAL STRESSES ON HUB ON 16½ IN. ALUMINIUM TURGO WHEEL, ROTATING AT 1300 R.P.M.

FULL SIZE.

4B v Check on results by dynamic recording of centrifugal strains

As stated in section 4B i, centrifugal strain measurement on the $16\frac{1}{2}$ in. aluminium Turgo wheel was undertaken using steady-state, direct-reading strain meters. With these it was successfully completed. Throughout the tests, little or no vibration was apparent in the spinning rig, and, at constant speed, strain indication was very steady. This was attributed mainly to good dynamic-balancing of the wheel and to the relatively high damping capacity of cast aluminium. The latter factor was demonstrable by striking the edge of a bucket with a hammer, when a dull sound was emitted, as if wood or concrete had been struck. This was in direct contrast to the long sonorous musical note produced by a similar blow to a bronze Pelton bucket.

The steadiness of constant speed strain readings seemed somewhat remarkable in the light of dynamic stress recordings presented by EDEL[5], despite the fact that test conditions pertinent to the two cases were very different. The recordings are those of Fig. 4 and are from a strain gauge on the bracket of a Pelton bucket in a hydraulically working wheel. Vibrations of considerable stress amplitudes are evident, as might be expected from such a wheel running under jet loading.

On completion of centrifugal strain measurement with the steady-state meters, an opportunity arose of checking results by dynamic strain recording on an ultra-violet galvanometer recorder, to the manufacture of S.E. Laboratories Ltd. The frequency response of the galvanometers available with this instrument was such that strain amplitudes could be expected to be recorded accurately up to frequencies of 60 c/s. It was thought that, if vibrations were present in the spinning Turgo wheel, frequencies somewhat higher than 60 c/s might be encountered, so, together/

together with the recorded frequencies, moderately accurate strain amplitudes were anticipated.

Fig.72 depicts the dynamic recording circuit arrangement, which was very similar to that of the previous tests, Fig.57. The recorder required external initial balancing facilities, which were provided on the stationary side, by a measurable, variable shunt of 10^6 ohms maximum, arranged for switching over either ratio-arm of the rotating bridge, as required. By switching in or out a measured change in its resistance, the shunt could also be used to calibrate recordings.

The circuit of Fig.72 is suitable for recording the signal from only one active gauge per test run. By considerable alterations to the wiring on the rotating side, a circuit could have been arranged, capable of recording five active signals per run with the same slip ring unit. Alteration on the rotating side were undesirable however, so none were made, and, as it seemed necessary to check only a few gauges to obtain the information sought, the situation was considered tolerable with the circuit indicated. As shown on Fig.72, eight active "C" gauges on the wheel were selected and the appropriate connections made at the terminal board. These eight gauges included the two which had exhibited the highest tensile and compressive strains in the previous centrifugal strain measurements. The test equipment is shown in Fig.59(b), with the S.E.Laboratories dynamic strain recorder installed and preparations completed for a recording test run.

The check by recording was, in fact, confined to the two gauges which had shown highest tensile and compressive strains. During prior examination of the wheel, some taped gauge covers had been found showing signs of working loose. As these could not conveniently be replaced at the time, the test was limited to runs of short duration for these two gauges only, at maximum speeds around 900 r.p.m. These conditions were/

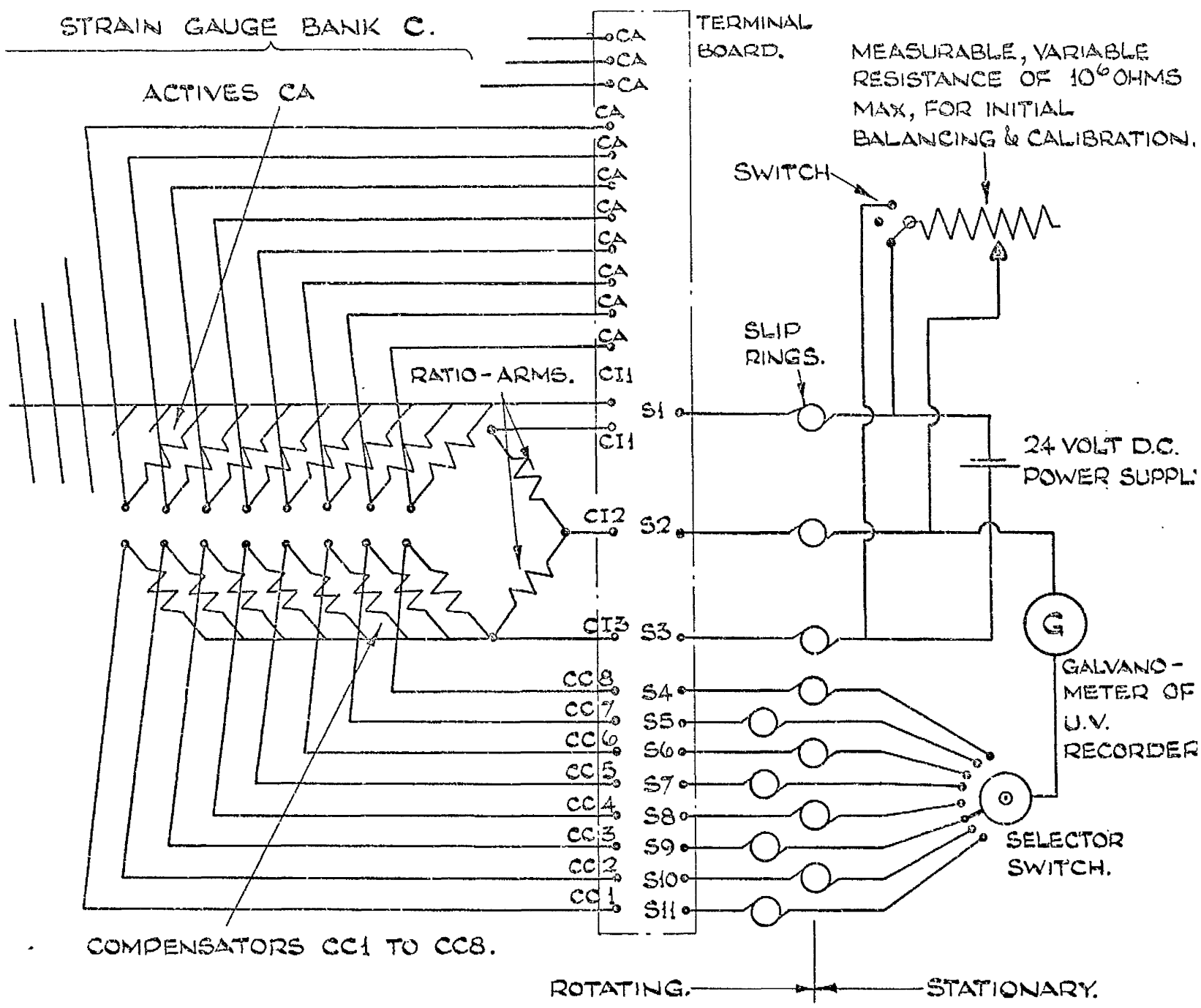

ACTIVE GAUGES CA ARE ON WHEEL.

COMPENSATORS CC1 TO CC8, AND RATIO-ARM GAUGES ARE ON SEGMENTED DISC.

FIG. 72. DIAGRAM OF STRAIN GAUGE CIRCUIT USED FOR CHECKING CENTRIFUGAL STRESSES IN $16\frac{1}{2}$ IN. ALUMINIUM TURGO WHEEL, BY DYNAMIC STRAIN RECORDING.
CIRCUIT IS SUITABLE FOR RECORDING OUTPUT OF ONLY 1 ACTIVE GAUGE PER TEST RUN, & WAS USED TO CHECK ONLY THE MOST SIGNIFICANT STRAIN, AND ONE OTHER.

were sufficient however, to provide useful confirmatory data.

Photographs of the centrifugal dynamic strain records from the two gauges are shown in Figs.73 and 74. The procedure pertinent to the records of the former Fig. was that initial balance of the galvanometer was obtained with the wheel stationary. The recorder paper was started to run at its lowest speed of 1.25 mm/sec., and a calibration "blip" was registered by switching the shunt. The wheel was then spun, speed increasing to about 900 r.p.m., at which it was held for several seconds. The wheel then coasted to a stop and recording ceased.

Both records of Fig.73 are very steady indeed, there being no evidence of fluctuations. The maximum strains recorded, $+ 130 \times 10^{-6}$ and $- 90 \times 10^{-6}$ confirm respectively the corresponding "maximum tensile gauge" and "maximum compressive gauge" centrifugal strains previously measured, and graphed in Fig.60.

For the records of Fig.74 which refers only to the "maximum tensile gauge", the strain zero was recorded on the paper after initial balancing. The paper was then stopped and the wheel was started and run up to about 900 r.p.m., at which the speed was held. With the galvanometer deflected to its "900 r.p.m. position" the paper was then run for a few seconds at high speed, and recording was completed. This was done for two high paper speeds, 50 mm/sec., and 100 mm/sec., to investigate for fluctuations in the strain reading.

Looking closely at Fig.74, only a very small regular fluctuation is observable. By measurements on the Fig., this fluctuation is found to occur at the rate of 1 cycle per wheel revolution, and may have its source in the slip ring unit.

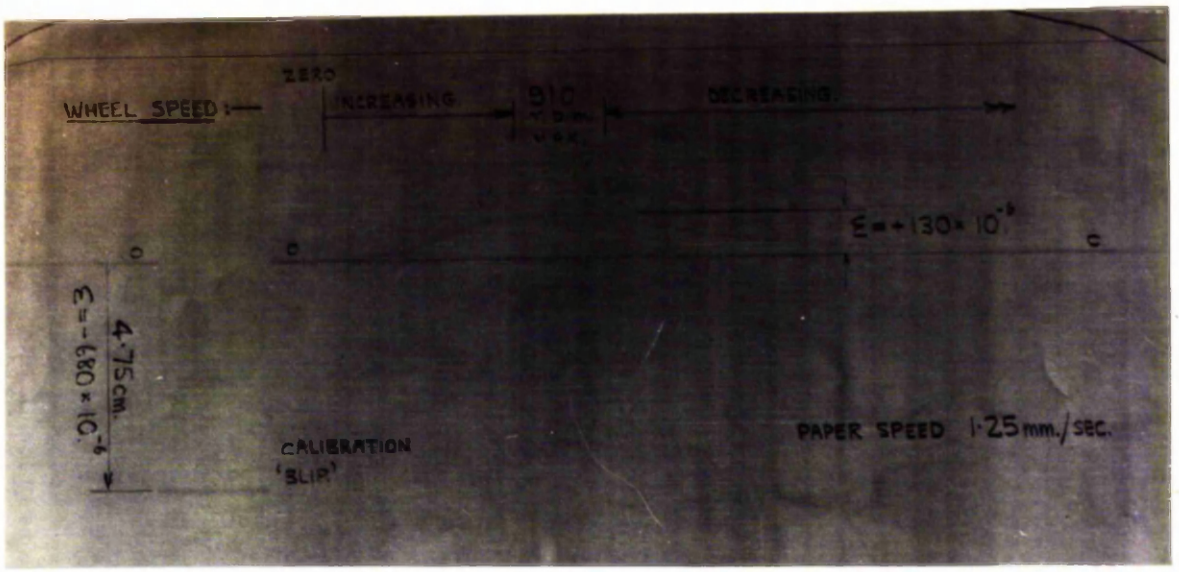

(a) DYNAMIC STRAIN RECORD FROM GAUGE EXHIBITING MAXIMUM TENSILE (+) STRAIN IN PREVIOUS TESTS.

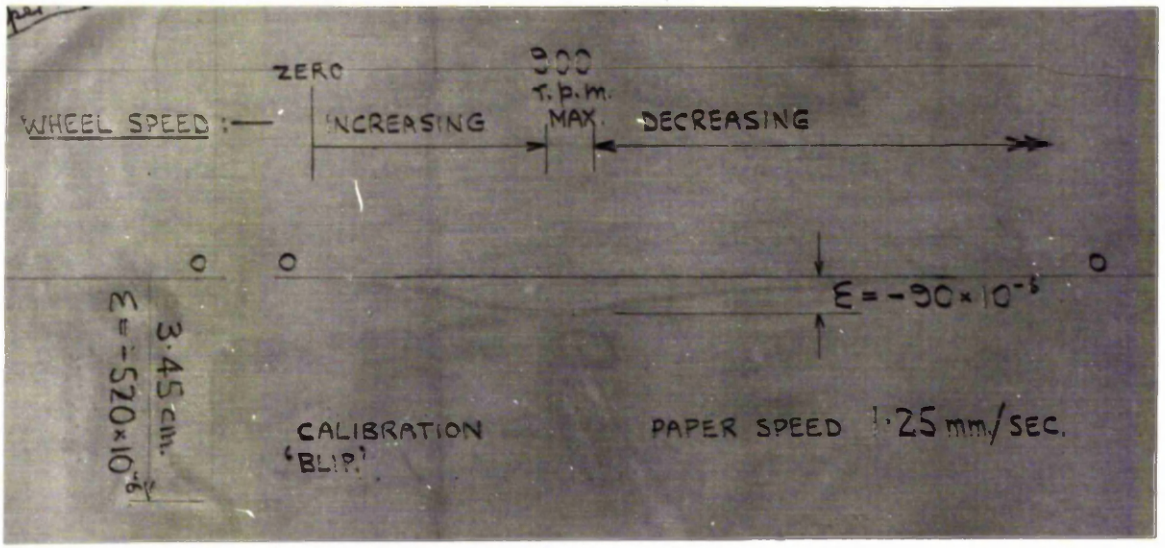

(b) DYNAMIC STRAIN RECORD FROM GAUGE EXHIBITING MAXIMUM COMPRESSIVE (-) STRAIN IN PREVIOUS TESTS.

FIG.73. CHECK ON MEASURED CENTRIFUGAL STRAINS BY DYNAMIC STRAIN RECORDING. PHOTOGRAPHS OF CENTRIFUGAL DYNAMIC STRAIN RECORDS FROM TWO STRAIN GAUGES ON $16\frac{1}{2}$ in. ALUMINIUM TURGO WHEEL. STRAINS AT MAXIMUM WHEEL SPEEDS CONFIRM THE CORRESPONDING STRAINS OF FIG.60.

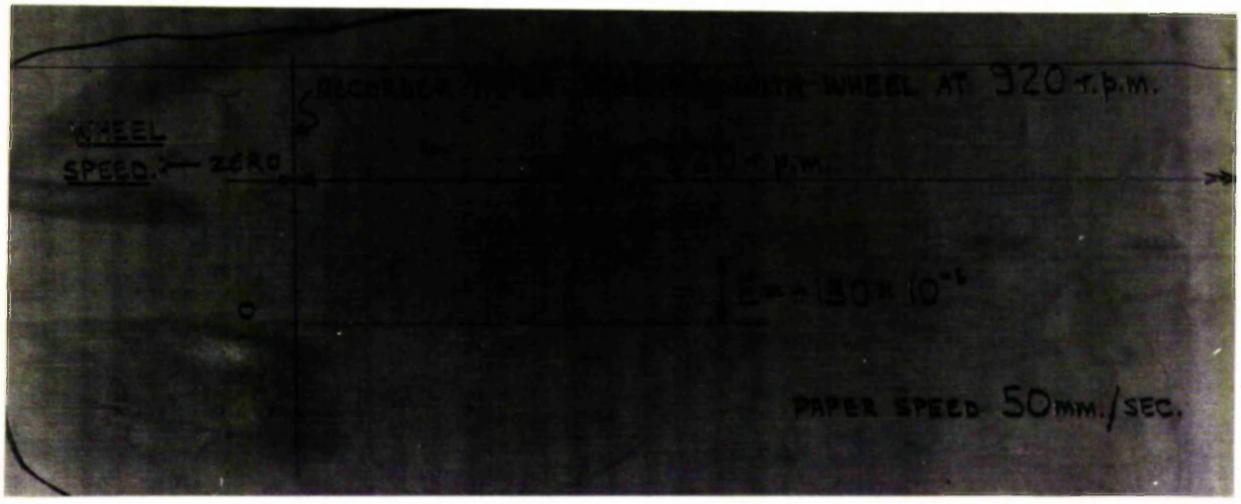

(a) RECORDING AT PAPER SPEED OF 50 m.m./sec.

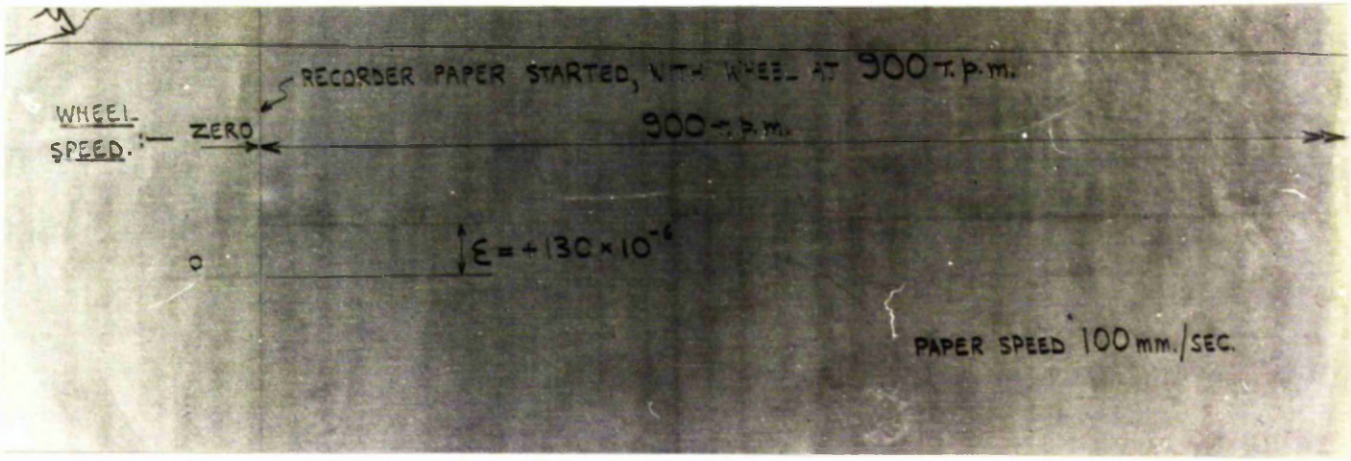

(b) RECORDING AT PAPER SPEED OF 100 m.m./sec.

FIG. 74. CHECK ON MEASURED CENTRIFUGAL STRAINS BY DYNAMIC STRAIN RECORDING. PHOTOGRAPHS OF CENTRIFUGAL DYNAMIC STRAIN RECORDS FROM GAUGE EXHIBITING MAXIMUM TENSILE (+) STRAIN ON $16\frac{1}{2}$ in. ALUMINIUM TURGO WHEEL. RECORDS ARE AT HIGH PAPER SPEEDS TO FACILITATE INVESTIGATION FOR FLUCTUATIONS.

4B vi Corresponding centrifugal stresses in $16\frac{1}{2}$ in. cast steel Turgo wheel

For rotors of identical geometry and size but of different linear-elastic materials with Poisson's Ratios ν of similar order, centrifugal stresses and actions are directly proportional to material density D and to the square of angular velocity ω.

Cast steel has three times the density of aluminium according to Table 1, so the centrifugal stresses and actions in a $16\frac{1}{2}$ in. cast steel Turgo wheel in service at the normal working speed of 1,300 r.p.m. are given by the values presented in Figs. 61 to 64, 66 to 69, 71, all multiplied by a factor of 3. The corresponding maximum measured centrifugal stress in the normal working cast steel wheel is thus 9480 lb/in^2 (4.2 T/in^2) tensile.

From Table 1, the overspeed is 2340 r.p.m. so the corresponding maximum measured centrifugal stress in the $16\frac{1}{2}$" cast steel Turgo wheel at overspeed, is given by :-

$$+ 9480 \times \left(\frac{2340}{1300}\right)^2 = 30,700 \text{ lb/in}^2, \ (13.7 \text{ T/in}^2) \text{ tensile.}$$

4C MEASUREMENT OF APPROXIMATE JET LOADING STRESSES IN $16\frac{1}{2}$ in. p.c.d. TURGO WHEEL

For the simulated jet loading test, the $16\frac{1}{2}$ in. aluminium Turgo wheel remained mounted in the spinning test rig. The slip ring unit was removed however, and an extension was fitted to the shaft on the inlet side so that the wheel could be drawn forward slightly for correct alignment with the bucket loading assembly. The appropriate wires relevant to the strain gauge circuit, which was left unaltered, were connected directly to the switch-box and steady-state, direct reading strain meter, sufficient length of cable being left to allow for at least one full revolution of the wheel.

An assembly was fitted on the outlet side of the wheel, for locking the shaft to the bedplate of the rig, with the wheel in any desired position. This arrangement was designed for quick application and release, and consisted of a bolted split sleeve lined with Ferodo brake material. The sleeve embraced the shaft at its greatest diameter and was grooved externally to fit into webs on the bedplate. On occasion, the effect of this device was reinforced by pinning the chain of the shaft coupling to the bedplate.

In parallel with the thoughts expressed in section 3C i, for lack of something better it was considered reasonable to assume that the pertinent working pressure distribution on a Turgo wheel bucket would resemble that depicted for a stationary Pelton bucket, in Fig. 29. It was obviously impracticable, by means other than hydraulic, to attempt to reproduce such a bucket loading or the corresponding one of Fig. 30. Since, in both cases, the greater fraction of total loading is concentrated in the region of the "hollow" of the bucket — a circumstance to be expected — it was decided to simulate jet action in this test by applying loading to a bucket mechanically, through/

through a pad bearing on the swept surface, only in the region of the "hollow", the resultant force on the pad to act roughly tangential to the pitch circle in the plane of the wheel.

The bucket loading pad was made by firstly casting cold-setting Araldite resin into the "hollow" of a correctly-positioned bucket on the locked wheel. When the resin pad had set, it was removed and a piece of $\frac{1}{4}$ in thick hard-rubber sheet was cut to suitable shape and bonded to the bucket-contact face. A suitably-shaped piece of 1/8 in thick steel plate was then bonded to the other face. It was considered that a point load applied perpendicularly and centrally to the steel surface of the completed pad, would be transmitted via the shaped Araldite and rubber, as a reasonably uniformly distributed loading on the bucket surface.

The appropriate loading was applied to the pad on a bucket of the locked wheel by the link/lever system shown in Fig.75. A bracket on the test rig frame served as fulcrum for the 10:1 lever, to the free end of which were hung dead-weights. The head of the loading link, Figs.75 and 76(a), was offset slightly from the plane of the lever, and was shaped to allow it to penetrate the wheel passages with ample clearance of buckets and rim. Final transmission of load from the head of this link to the steel face of the pad was through a $\frac{1}{4}$ in dia. ball bearing. The position of the loading pad on the bucket is shown in Fig.76(b), and is also indicated on the subsequent Figs.78 to 83, which present some of the relevant measured stresses.

When conducting strain measurements, loading and unloading of a bucket were performed incrementally. The maximum force applied on a bucket was 2000 lb, and corresponded to the resultant jet force tangential to the pitch circle in the plane of the wheel, on any of the three jet loaded buckets of the wheel running under normal working conditions (1013 B.H.P. at 1300 r.p.m. - Table 1). To cover the various conditions which/

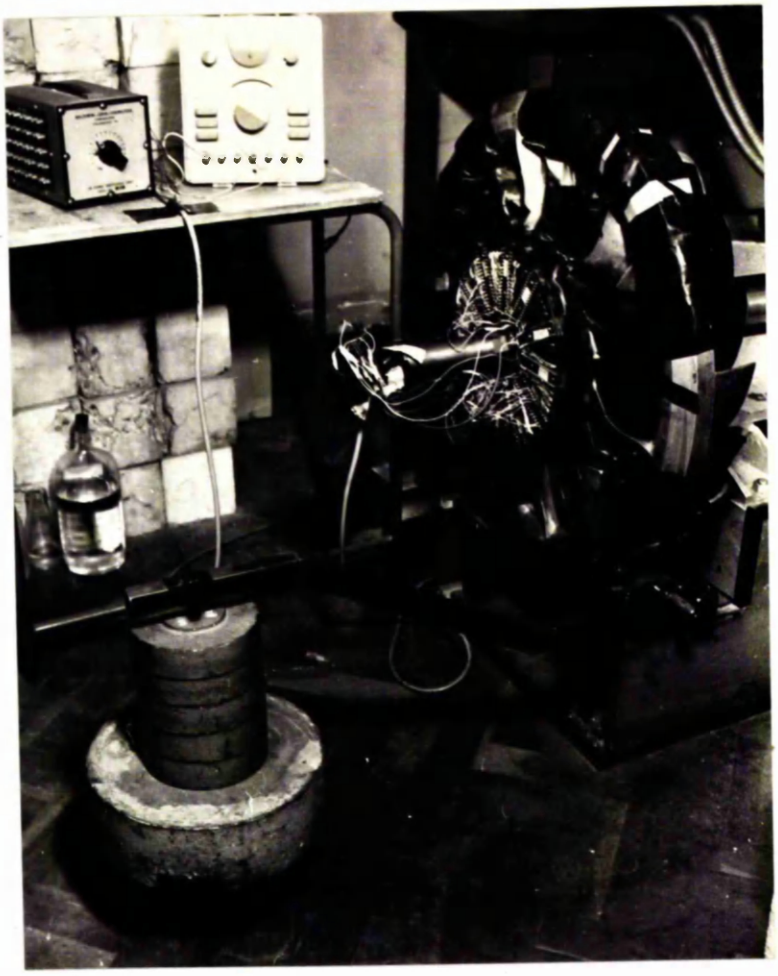

PHOTOGRAPH OF WHEEL, BUCKET LOADING ARRANGEMENT, WIRING AND STRAIN METER.

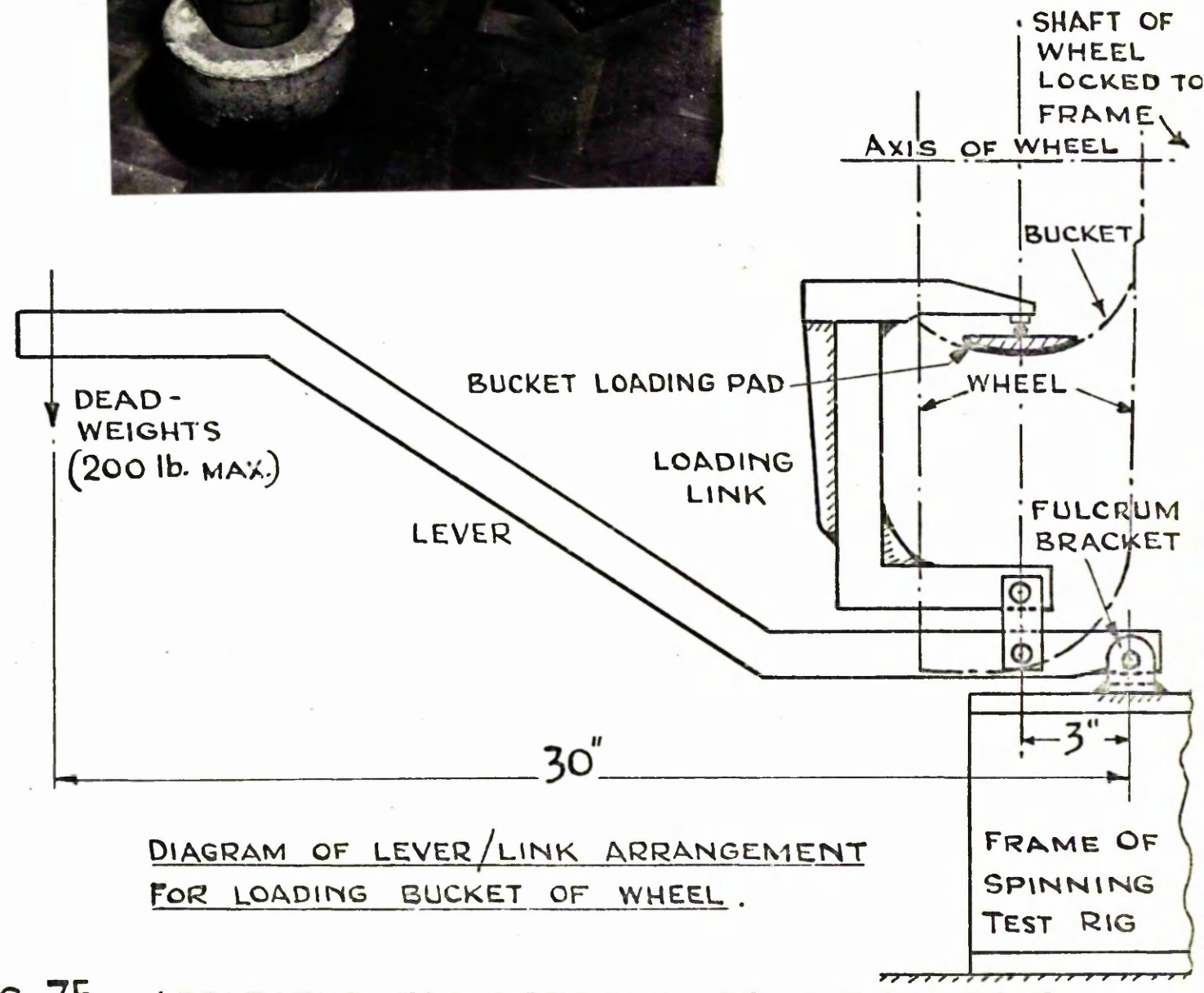

DIAGRAM OF LEVER/LINK ARRANGEMENT FOR LOADING BUCKET OF WHEEL.

FIG. 75. APPARATUS FOR APPROXIMATE JET LOADING TEST ON 16½ IN. ALUMINIUM TURGO WHEEL.

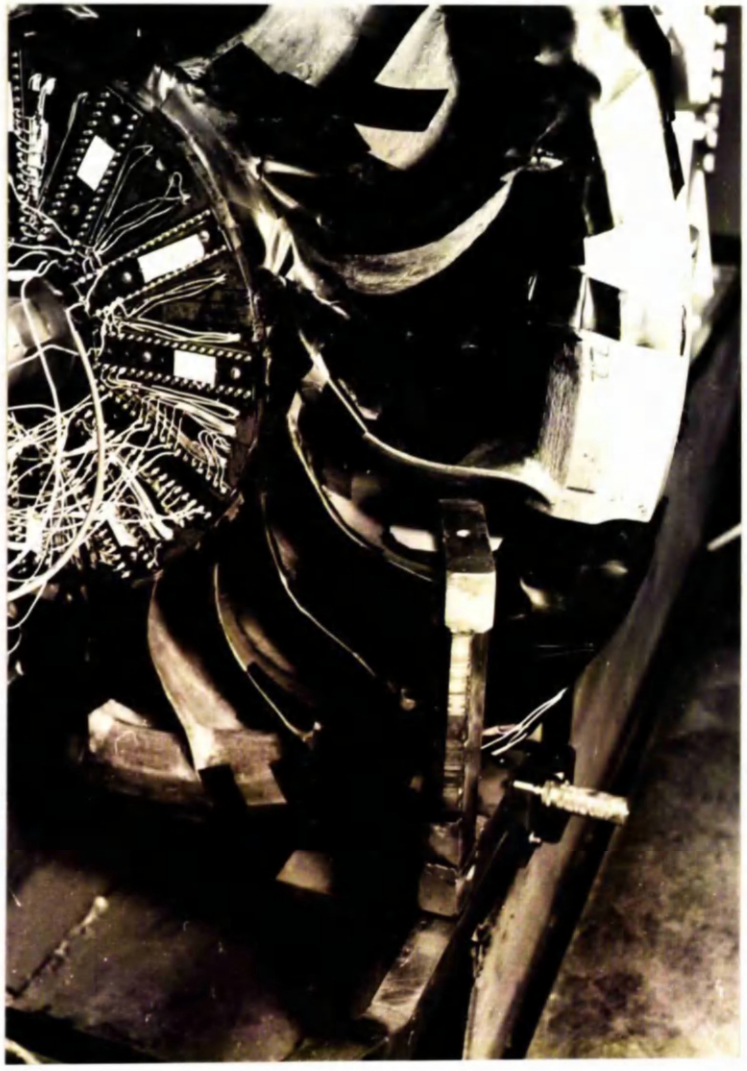

(a) VIEW SHOWING LOADING LINK AND LEVER. HEAD OF LINK IS OFFSET AT SLIGHT ANGLE TO PLANE OF LEVER, AND BEARS ON BUCKET LOADING PAD.

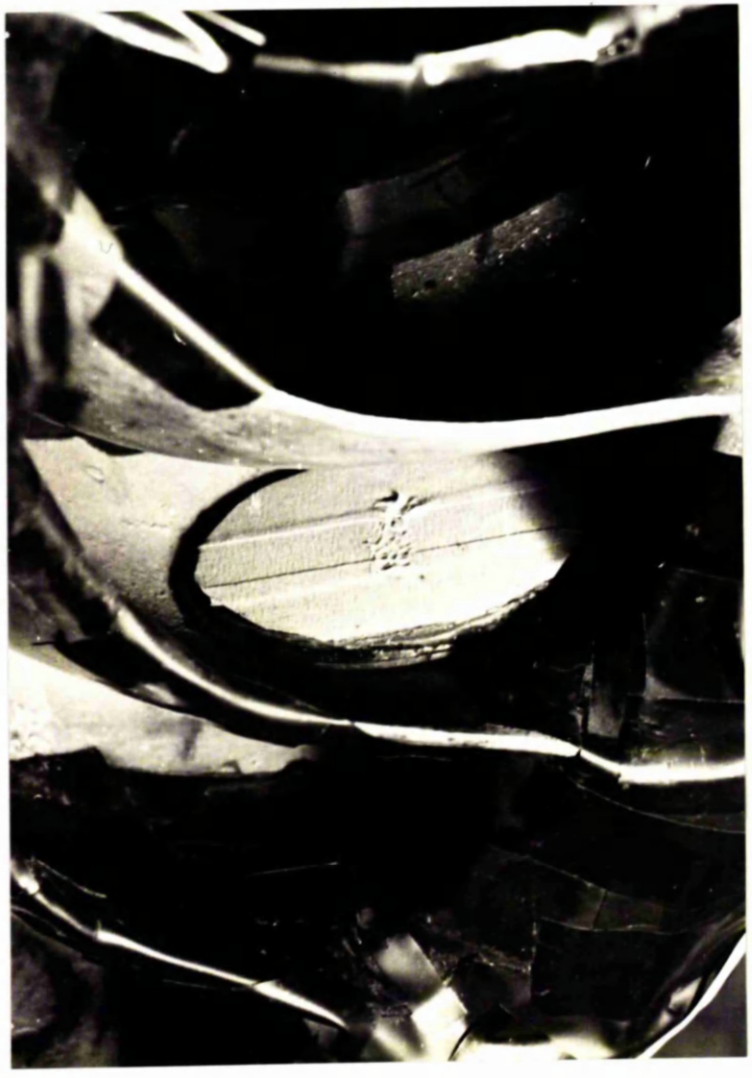

(b) VIEW SHOWING BUCKET LOADING PAD IN POSITION.

FIG. 76. APPARATUS FOR APPROXIMATE JET LOADING TEST ON $16\frac{1}{2}$ in. ALUMINIUM TURGO WHEEL. VIEWS ON INLET SIDE.

which required investigation, most of the 22 buckets were subjected to several loading test runs, in the fashion described, strains being measured on each run. It was necessary to measure the strains on a bucket directly loaded and also when acting as one of the supporting buckets for an adjacent or remote directly loaded bucket. Throughout the test, the variation of measured strain with applied load was found to be linear.

With regard to the directly loaded bucket, the experimental loading was probably not a close approximation to the corresponding actual jet loading, since the latter will almost certainly be distributed over all the swept surface of the bucket, somewhat as in Fig.29. It is possible that, on an actual working bucket, there may be significant pressure distribution near the edges, incurring significant magnitudes of stress locally. The measured directly loaded bucket stresses would therefore not be expected to be very closely representative of the corresponding actual jet loading values. On the other hand, the resultant of the experimental loading will resemble the actual jet loading resultant reasonably accurately, so that the stresses measured on a bucket due to its acting in a supporting capacity, would be expected to be reasonably close to their actual working counterparts. One of the early findings of this test was that corresponding directly loaded bucket stresses, and supporting bucket stresses, were commonly of comparable orders and should evidently be regarded, in general, as of equal significance.

4C i Approximate jet loading stresses on the buckets

During a revolution of a working Turgo wheel, a bucket will be one of the 3 adjacent jet loaded buckets, and then one of the 19 buckets acting only in support of the loaded 3, via the rim. A bucket therefore, will always be subjected to either of the following jet action loading conditions:-

(1) Direct jet loading, together with loading via the rim, deriving from the action of the bucket in support of the 2 adjacent jet loaded buckets.

(2) Loading via the rim, deriving from the action of the bucket in support of the 3 jet loaded buckets.

The supporting rôle of the bucket is thus a continuous one, but clearly of varying intensity. An indication of its relative importance is provided by Fig.77 which shows the variation of stresses measured at five edge locations on a given bucket, No.1, for a 2000 lb. simulated jet load applied in turn to each bucket including No.1. The buckets are numbered clockwise from No.1 looking on inlet, as per Fig.55(a) for example. The five graphs of Fig.77 are representative of the variations indicated at most of the many locations where strains were measured on a bucket.

Graph a relates both to the maximum measured stress due only to 2000 lb. direct simulated jet loading, and to the greatest maximum measured total stress which is due to direct loading and supporting. The value of the former is seen to be + 2910 lb/in.^{2}, while the value of the latter evidently comprises + 2910 lb/in.^{2} due to the direct loading, together with + 1390 lb/in.^{2} and + 970 lb/in.^{2} due respectively to the effects of 2000 lb. loadings on buckets 2 and 3, a total of + 5270 lb/in.^{2} by superposition. 45% of this, the greatest maximum total stress measured on the wheel, derives from the supporting rôle of the bucket. For the location graph/

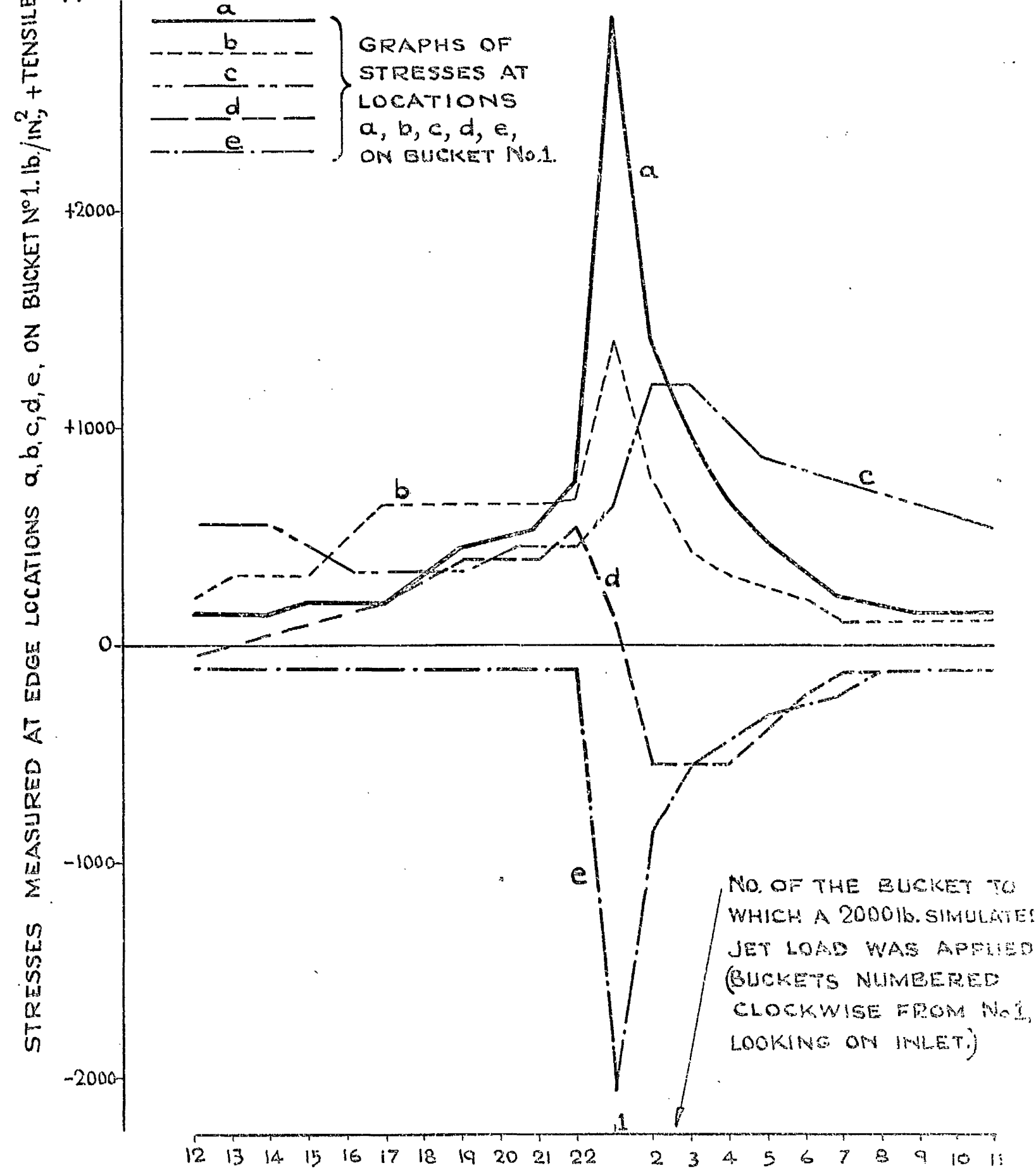

FIG. 77. APPROXIMATE JET LOADING TEST ON 16½ IN. ALUMINIUM TURGO WHEEL. VARIATION OF STRESSES MEASURED AT SOME LOCATIONS ON BUCKET No. 1 FOR A 2000 lb. SIMULATED JET LOAD APPLIED TO EACH BUCKET IN SUCCESSION.

graph b , the maximum total stress is evidently due to direct loading, together with the effects of loading on buckets 22 and 2, while for the locations, graphs c and d , the maximum total stresses occur when no direct loading acts on bucket No.1, but when the bucket acts solely in its supporting capacity, for 2000 lb loadings applied on each of the neighbouring buckets 2, 3 and 4.

The appreciable magnitudes of supporting bucket stresses are clear evidence of the relatively high flexibility of the buckets in the plane of the wheel. At location, graph c, on bucket No.1 for example, loading of the diametrically-opposite bucket No.12 produces a stress of the same order as that produced by corresponding direct loading on bucket No.1.

For a bucket subjected to 2000 lb direct simulated jet loading only, the measured edge stress distributions are depicted in Figs.78 and 79, and the stresses measured at points on the surfaces remote from the edges are presented in Figs.82 and 83. On the whole, the stresses on the swept surfaces of the edges, Fig.78, are higher than the corresponding ones on the unswept surfaces, Fig.79, thus demonstrating bending and membrane actions along the edges. The maximum measured stress on the directly loaded bucket, 2910 lb/in^2 tensile, occurs on the unswept surface of the outlet edge where it joins the hub— a stress concentration region, as may be seen in Fig.79. It is clear from Figs.78 and 79, that, over comparable regions, the general stress behaviour of one edge resembles that of the other.

During the test a cursory investigation was made of the effects of variations in the position of the applied loading on the bucket. It was found for example that, as was to be expected, a movement of the load pad nearer the inlet edge resulted in generally increased stresses on that edge and generally reduced stresses on the outlet edge.

On the meridional sections $\Theta = 92^\circ$, 111° of Figs.82 and 83, it is evident that the principal stresses are approximately circumferential and meridional./

meridional. The natures of these stresses indicate bending in the plane of the wheel, reducing the circumferential curvature and accompanied by meridional bending with increasing curvature. This local behaviour resembles the indications of the single bucket tests (section 4A i) Figs.46 and 48. The magnitudes of some of the principal stresses on sections $\Theta = 57^{\circ}, 74^{\circ}$, Figs.82 and 83, reflect the proximity of the applied loading, and their directions reflect the influence of the rim. Worthy of note are the appreciable bending stresses, tensile on swept surface, compressive on unswept surface of the bucket, and perpendicular to the rim, where it joins the bucket.

The results presented in Figs.78, 79, 82, 83 establish that the stresses on the bucket edges are the most significant, a finding matched by that of the investigations of the bucket stresses for the supporting rôle. The maximum total stresses therefore at all the edge locations, are presented as edge stress distributions in Figs.80 and 81. All the values have been obtained from graphs like those of Fig.77, so that they relate to a variety of conditions. At some locations on this bucket No.1 of Figs.80, 81, the maximum total is due to 2000 lb direct loading, plus supporting of similarly loaded adjacent buckets 2 and 3, say. At others the maximum occurs for direct loading plus supporting of loaded adjacent buckets 22 and 2, say. Yet again, there are one or two locations where the maximum total stress arises due to the supporting condition only, say for 2000 lb loadings on buckets 20, 21 and 22. The maximum total edge stresses are therefore greater everywhere than their components or counterparts due only to direct loading, shown in Figs.78 and 79. Respective comparison of these Figs. with Figs.80 and 81 illustrates that direct loading and the supporting rôle are of roughly equal importance with regard to the maximum total stresses.

In Figs.80 and 81, the maximum total stresses on average, are higher/

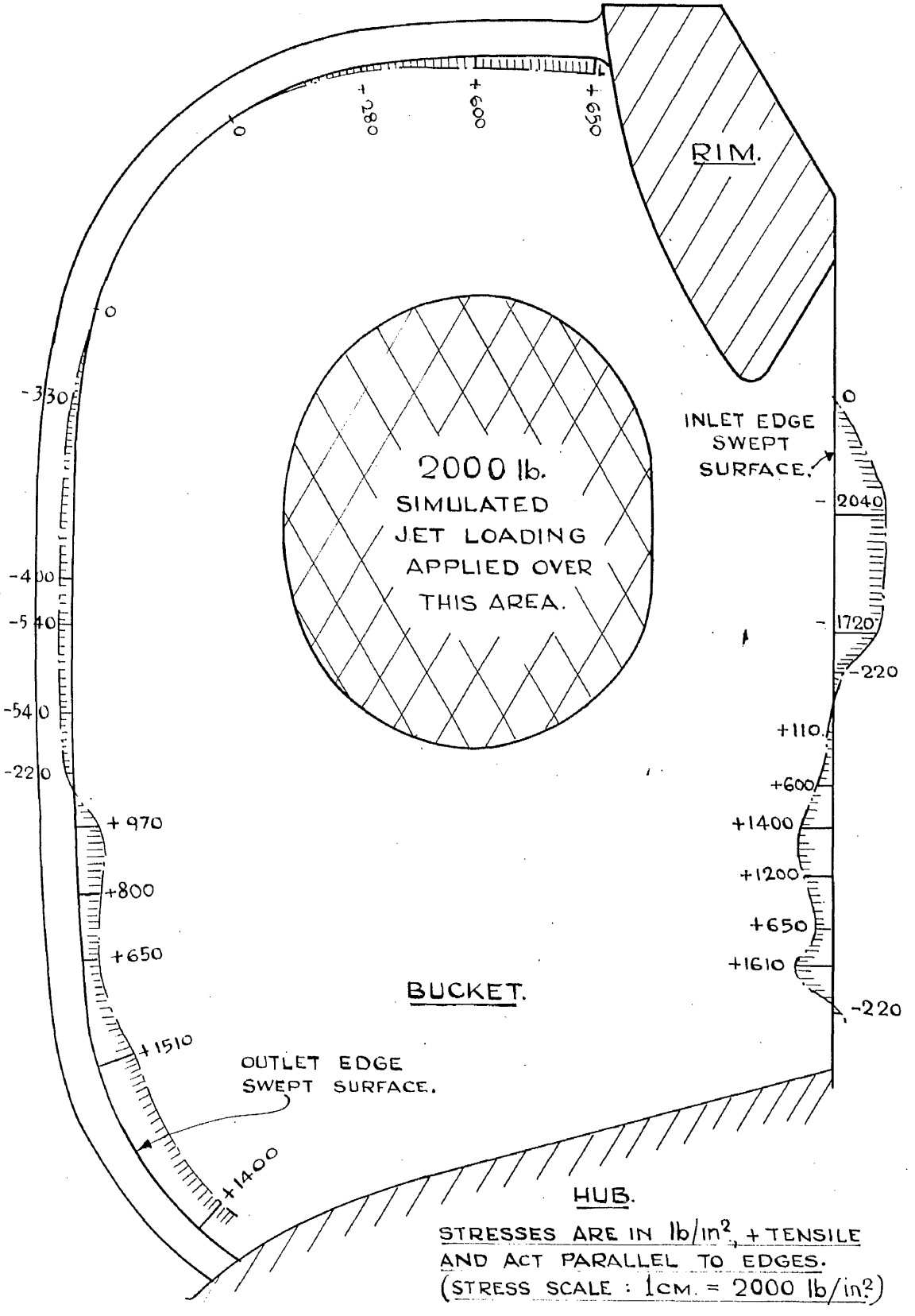

FIG. 78. MEASURED APPROXIMATE JET LOADING COMPONENT STRESSES ON THE SWEPT SURFACES OF THE INLET AND OUTLET EDGES OF A BUCKET OF THE 16½ IN. ALUMINIUM TURGO WHEEL. THE STRESSES PERTAIN TO A BUCKET CARRYING ONLY DIRECTLY APPLIED SIMULATED JET LOADING OF 2000 Lb., THE LOAD VALUE APPROPRIATE TO THE NORMAL WORKING CONDITION. FIG. 79 SHOWS STRESSES AT CORRESPONDING POINTS ON THE UNSWEPT SURFACES.

FULL SIZE.

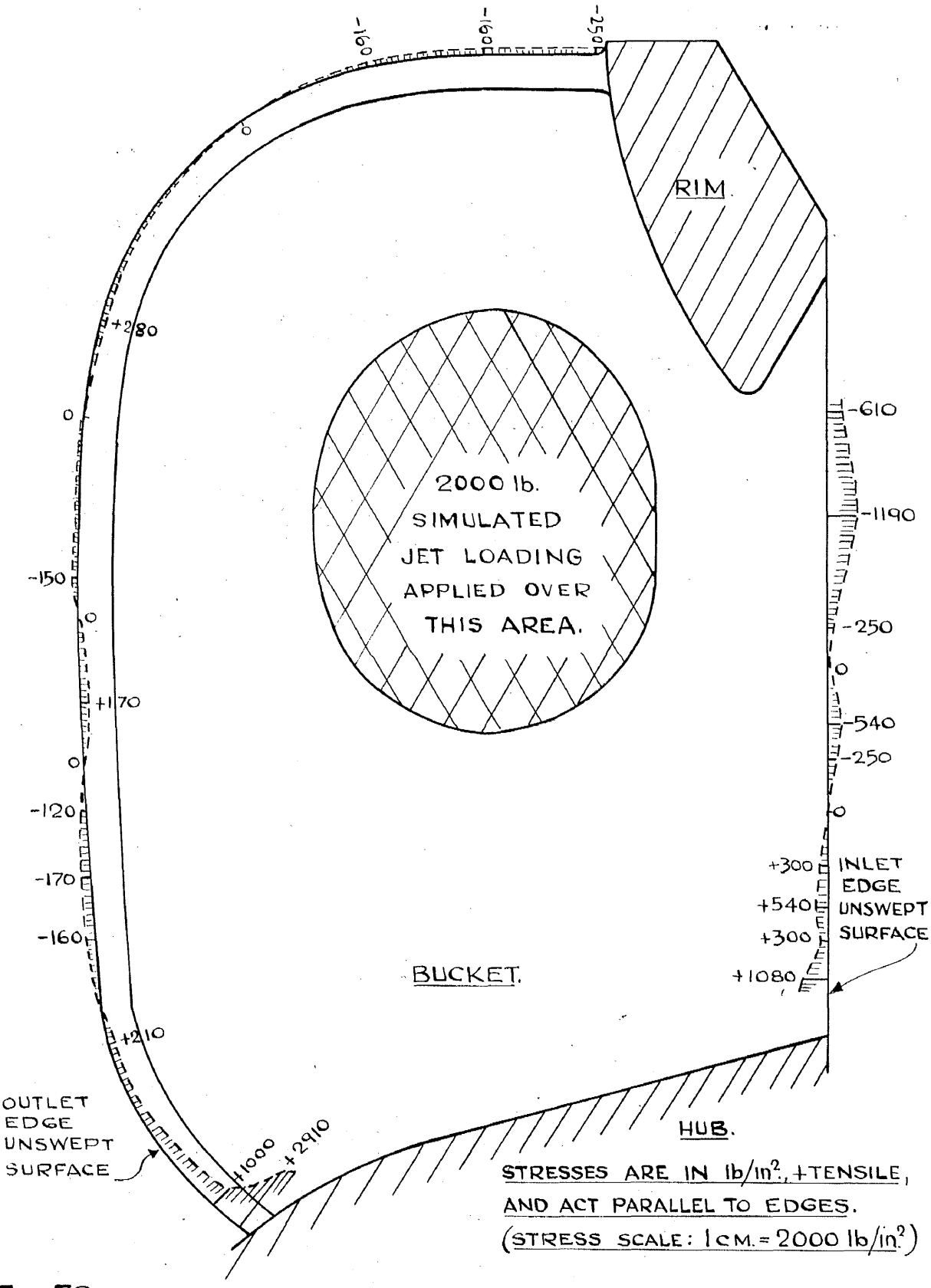

FIG. 79. MEASURED APPROXIMATE JET LOADING COMPONENT STRESSES ON THE UNSWEPT SURFACES OF THE INLET AND OUTLET EDGES OF A BUCKET OF THE 16½ IN. ALUMINIUM TURGO WHEEL. THE STRESSES PERTAIN TO A BUCKET CARRYING ONLY DIRECTLY APPLIED SIMULATED JET LOADING OF 2000 LB., THE LOAD VALUE APPROPRIATE TO THE NORMAL WORKING CONDITION.

FIG. 78 SHOWS STRESSES AT CORRESPONDING POINTS ON THE SWEPT SURFACES.

FULL SIZE.

Fig. 79.

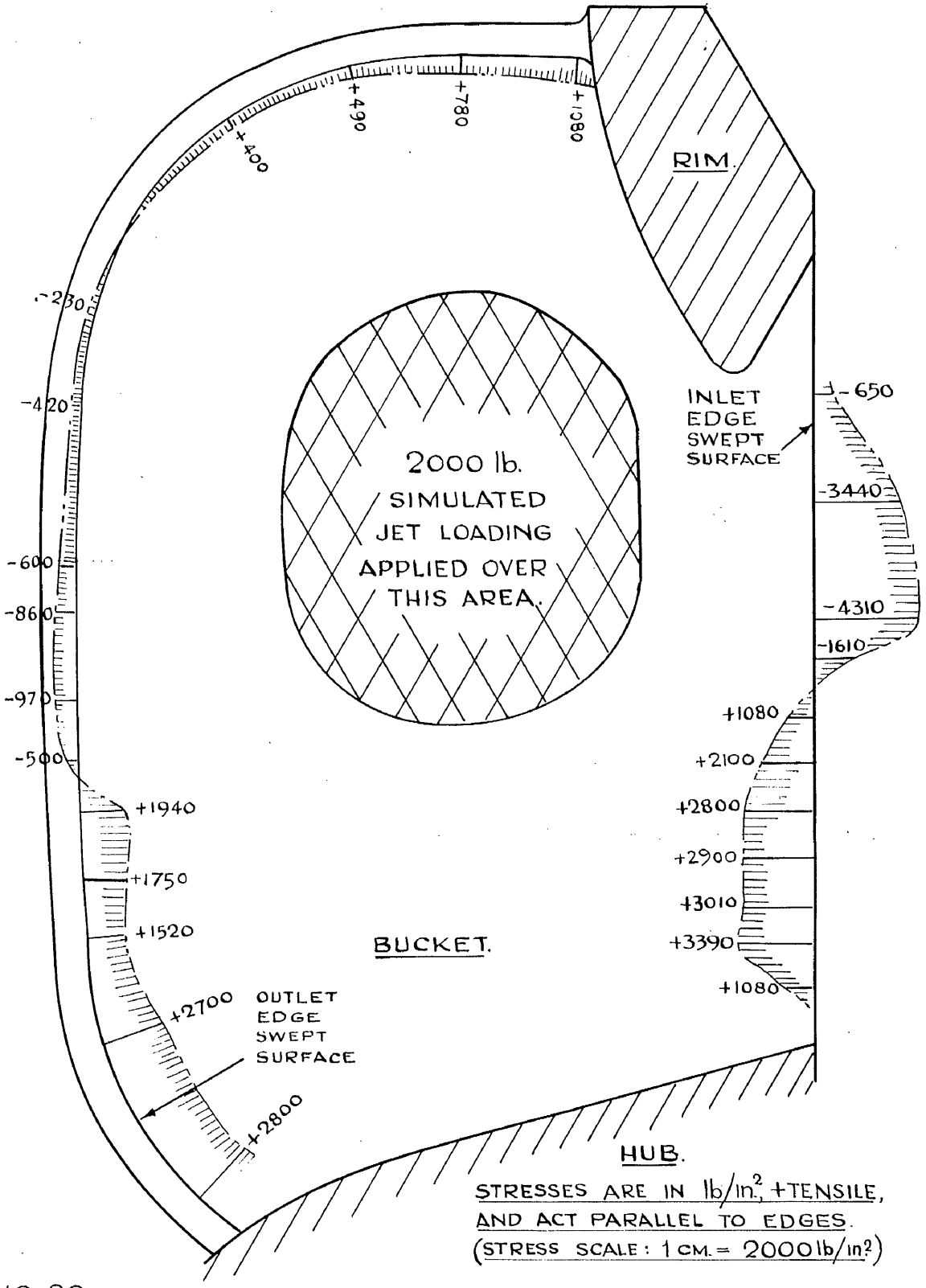

FIG. 80. MEASURED APPROX. JET LOADING MAXIMUM TOTAL STRESSES ON SWEPT SURFACES OF INLET AND OUTLET EDGES OF A BUCKET OF THE 16½" ALUMINIUM TURGO WHEEL. THE STRESSES PERTAIN MAINLY TO A BUCKET CARRYING DIRECTLY APPLIED SIMULATED JET LOADING, AND ACTING AS A SUPPORTING BUCKET FOR ONE OF THREE PAIRS OF ADJACENT DIRECTLY LOADED BUCKETS, AS APPROPRIATE. THE LOADING ON EACH OF THE 3 ADJACENT BUCKETS IS 2000 lb., CORRESPONDING TO THE NORMAL WORKING CONDITION.

FIG. 81. SHOWS STRESSES AT CORRESPONDING POINTS ON THE UNSWEPT SURFACES. FULL SIZE.

FIG. 80.

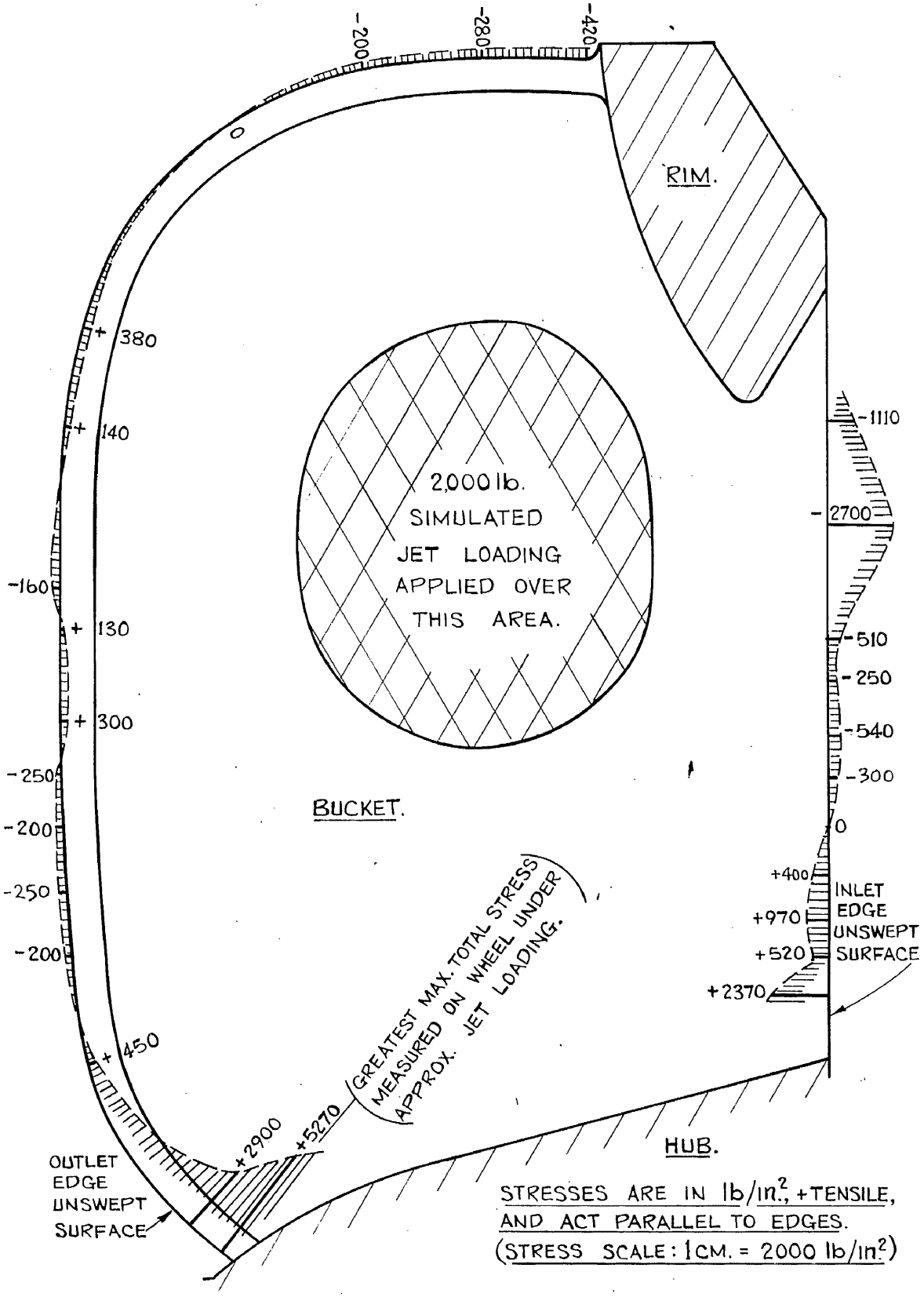

FIG. 81.

MEASURED APPROX. JET LOADING MAXIMUM TOTAL STRESSES ON UNSWEPT SURFACES OF INLET AND OUTLET EDGES OF A BUCKET OF THE 16½ IN. AL. TURGO WHEEL. THE STRESSES PERTAIN MAINLY TO A BUCKET CARRYING DIRECTLY APPLIED SIMULATED JET LOADING, AND ACTING AS A SUPPORTING BUCKET FOR ONE OF THREE PAIRS OF ADJACENT DIRECTLY LOADED BUCKETS, AS APPROPRIATE. THE LOADING ON EACH OF THE THREE ADJACENT BUCKETS IS 2000 lb., CORRESPONDING TO THE NORMAL WORKING CONDITION.

FIG. 80. SHOWS STRESSES AT CORRESPONDING POINTS ON THE SWEPT SURFACES.

FULL SIZE

Fig. 81.

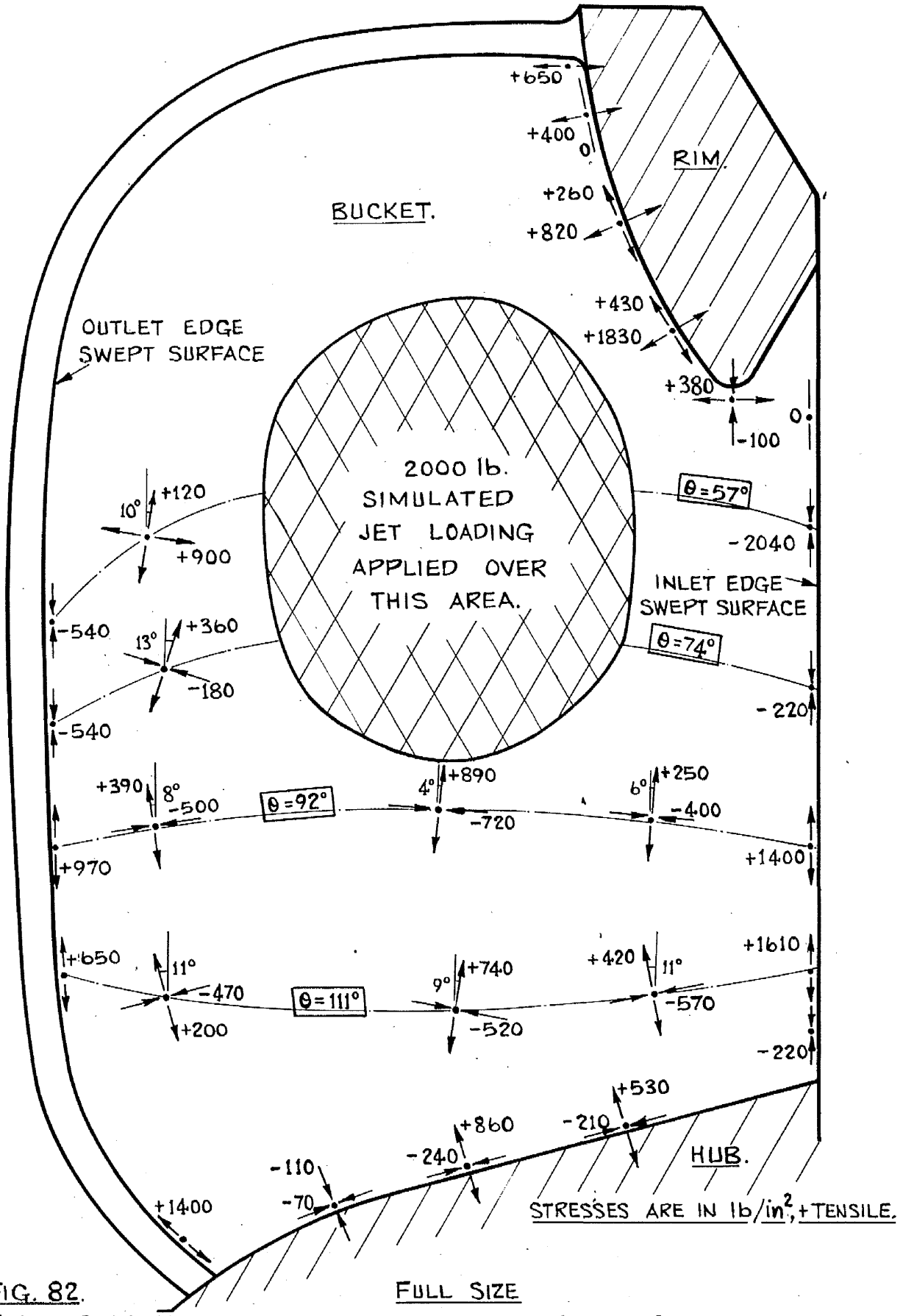

FIG. 82. FULL SIZE

MEASURED APPROXIMATE JET LOADING COMPONENT PRINCIPAL STRESSES ON SWEPT SURFACE OF BUCKET OF 16½ IN. ALUMINIUM TURGO WHEEL. THE STRESSES ARE MAINLY AT POINTS ON MERIDIONAL SECTIONS, AND AT RIM AND HUB JUNCTIONS, AND PERTAIN TO A BUCKET CARRYING ONLY DIRECT SIMULATED JET LOADING OF 2000 lb., THE LOAD VALUE APPROPRIATE TO THE NORMAL WORKING CONDITION.

FIG. 83. SHOWS PRINCIPAL STRESSES MAINLY AT CORRESPONDING POINTS ON UNSWEPT SURFACE.

FIG 82.

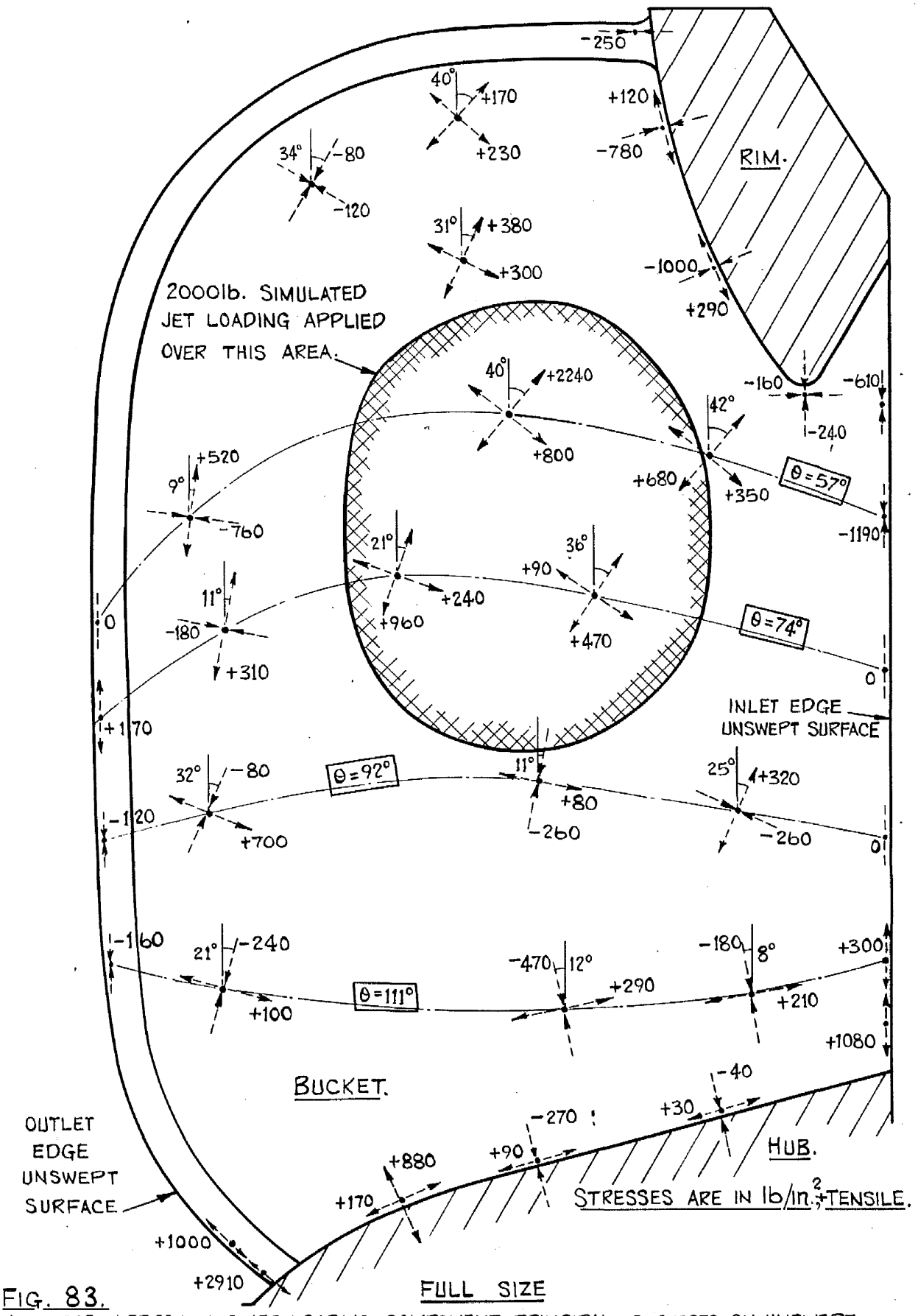

FULL SIZE

FIG. 83.

MEASURED APPROXIMATE JET LOADING COMPONENT PRINCIPAL STRESSES ON UNSWEPT SURFACE OF BUCKET OF 16½ IN. ALUMINIUM TURGO WHEEL. THE STRESSES ARE MAINLY AT POINTS ON MERIDIONAL SECTIONS, AND AT RIM AND HUB JUNCTIONS, AND PERTAIN TO A BUCKET CARRYING ONLY DIRECT SIMULATED JET LOADING OF 2000lb., THE LOAD VALUE APPROPRIATE TO THE NORMAL WORKING CONDITION.

FIG. 82. SHOWS PRINCIPAL STRESSES MAINLY AT CORRESPONDING POINTS ON SWEPT SURFACE.

FIG. 83.

higher on the inlet edge, than on the outlet edge. Nevertheless, the greatest maximum total stress, 5270 lb/in^2 tensile, which is the highest measured approximate jet loading stress on the wheel, occurs on the unswept surface of the outlet edge at its junction with the hub. The local maximum in this stress concentration area would be expected to be somewhat higher than this measured value. However, with inevitable reservations on account of the approximate nature of the loading in this test, it seems not unreasonable to assume that the highest measured total stress of 5270 lb/in^2 tensile provides an indication of the order of the actual maximum jet loading stress on the wheel.

No maximum total stress results are presented for any of the non-edge strain gauge locations on the bucket. Computations were undertaken for these values but at many rosette locations it was found that the gauges of the rosette showed maximum totals for differing loading conditions. Further analysis of such cases was not carried out. It was patently obvious from all the indicated magnitudes that nowhere remote from an edge, would a maximum total stress approach the order of 5000 lb/in^2.

The distributions with angle Θ (Fig.65) of the measured edge stresses, are presented in Figs.84 and 85. The former Fig. shows the component edge stresses for the bucket subjected only to 2000 lb direct simulated jet loading, i.e. for the stresses of Figs.78 and 79. The latter Fig. presents the maximum total edge stresses priorly indicated on Figs.80 and 81.

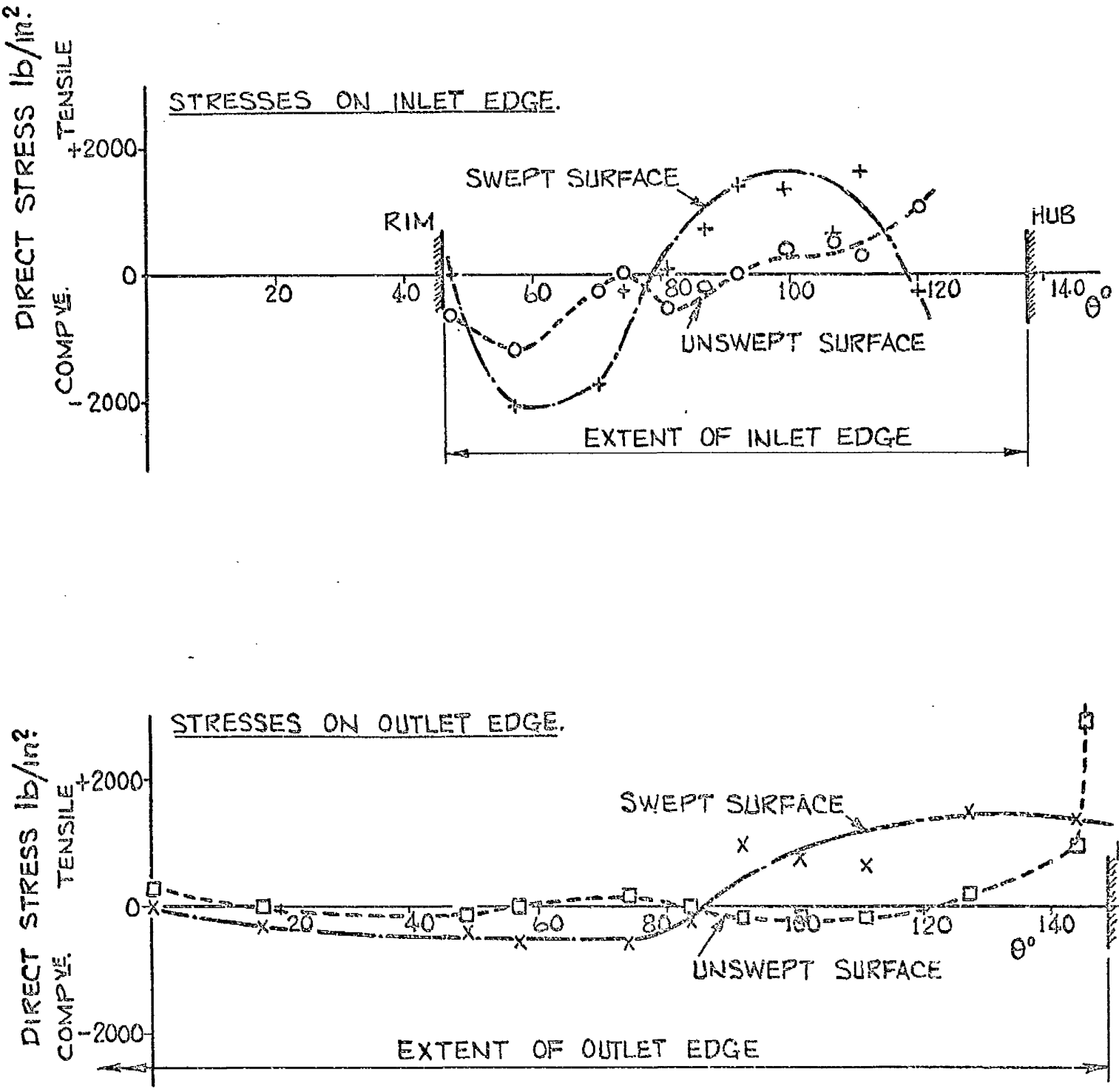

FIG. 84. DISTRIBUTION WITH θ (REF. FIG. 65) OF MEASURED APPROX. JET LOADING COMPONENT STRESSES ON SWEPT AND UNSWEPT SURFACES OF INLET AND OUTLET EDGES OF BUCKET OF 16½IN. AL. TURGO WHEEL. THE STRESSES PERTAIN TO A BUCKET CARRYING ONLY DIRECT SIMULATED JET LOADING OF 2000lb THE VALUE APPROPRIATE TO THE NORMAL WORKING CONDITION

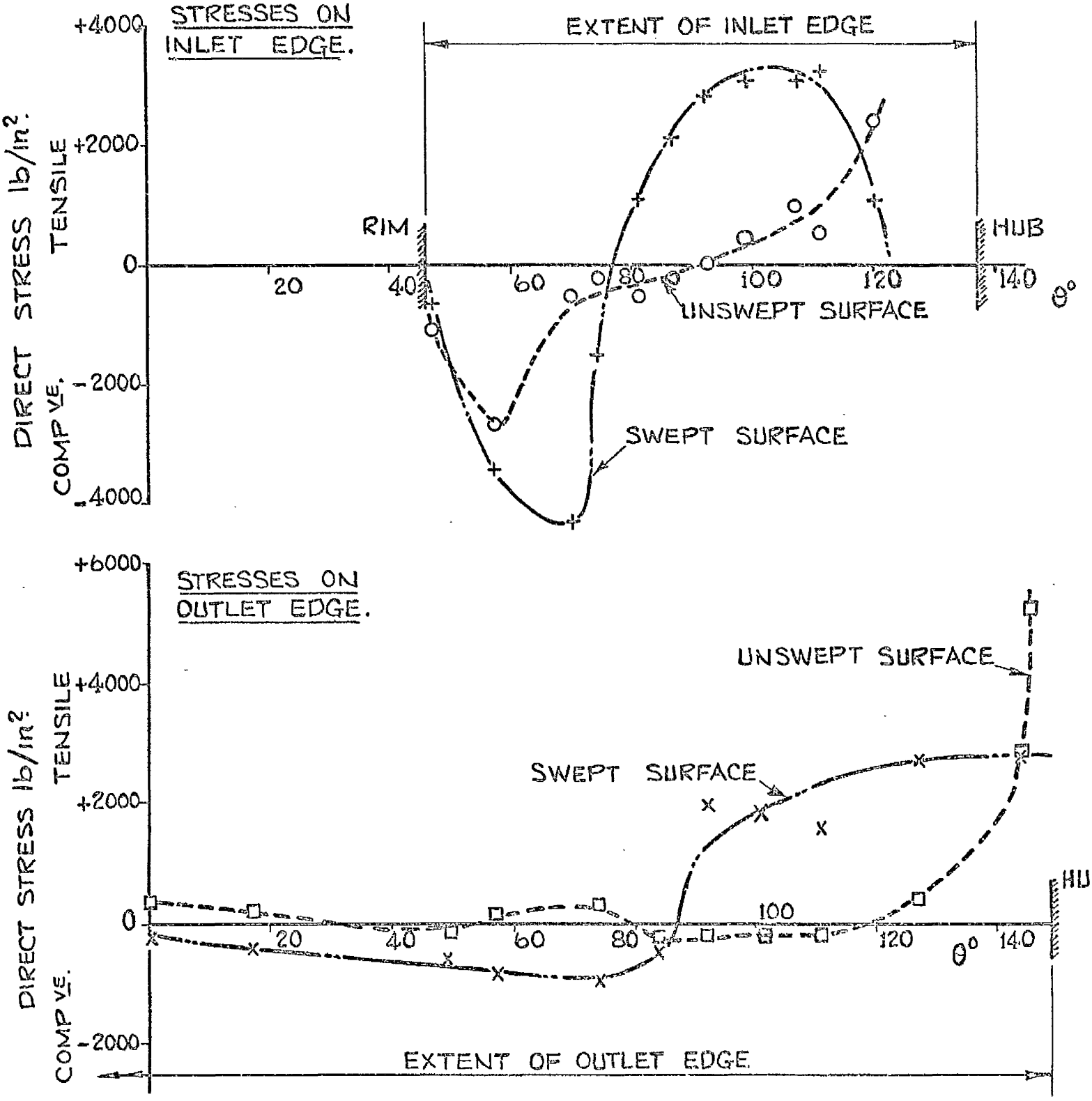

FIG. 85. DISTRIBUTION WITH θ (REF. FIG. 65) OF MEASURED APPROX. JET LOADING MAXIMUM TOTAL STRESSES ON SWEPT AND UNSWEPT SURFACES OF INLET AND OUTLET EDGES OF BUCKET OF 16½ IN. AL. TURGO WHEEL. THE STRESSES PERTAIN MAINLY TO A BUCKET CARRYING DIRECT SIMULATED JET LOADING AND ACTING AS A SUPPORTING BUCKET FOR ONE OF THREE PAIRS OF ADJACENT DIRECTLY LOADED BUCKETS, AS APPROPRIATE. THE LOADING ON EACH OF THE THREE ADJACENT BUCKETS IS 2000 lb., CORRESPONDING TO THE NORMAL WORKING CONDITION.

4C ii Approximate jet loading stresses on the rim

The stresses measured on the inlet side of the rim were found generally to be of a low order. This was the case for locations near a bucket carrying only 2000 lb direct simulated jet loading. It was also found that application of similar loadings to adjacent buckets, produced little additional stress effect at these locations, so that maximum total stresses on the inlet side were also low. The highest maximum total stress found there was + 250 lb/in^2. A similar situation was revealed on the rim outer face where a highest maximum total stress of + 450 lb/in^2 was measured at a location in way of the junction with the outlet edge of one of the buckets carrying 2000 lb simulated jet loading, and adjacent to 2 buckets similarly loaded.

Stresses of a much higher order were measured on the outlet side. This was perhaps to be expected since by far the greater portion of the long bucket-to-rim connection (see e.g. Fig.67) is on the rim outlet side, where the main transmission of loading from bucket to rim will take place. The stresses here were also found to vary considerably according to their locations relative to the bucket carrying the load, and variations not unlike some of those in Fig.77 were recorded. An indication of this may be seen in Fig.86, which shows the measured principal stresses on the outlet side of the rim between two buckets, each of which was subjected in its turn to 2000 lb loading. Alternatively, this Fig. may be taken as indicative of the principal stresses on each side of one loaded bucket.

On the side anti-clockwise from the loaded bucket (looking at inlet) the major principal stresses are all tensile and practically circumferential, the maximum being + 890 lb/in^2 for 2000 lb on the bucket only. In contrast, on the side clockwise of the loaded bucket, compression, also mainly/

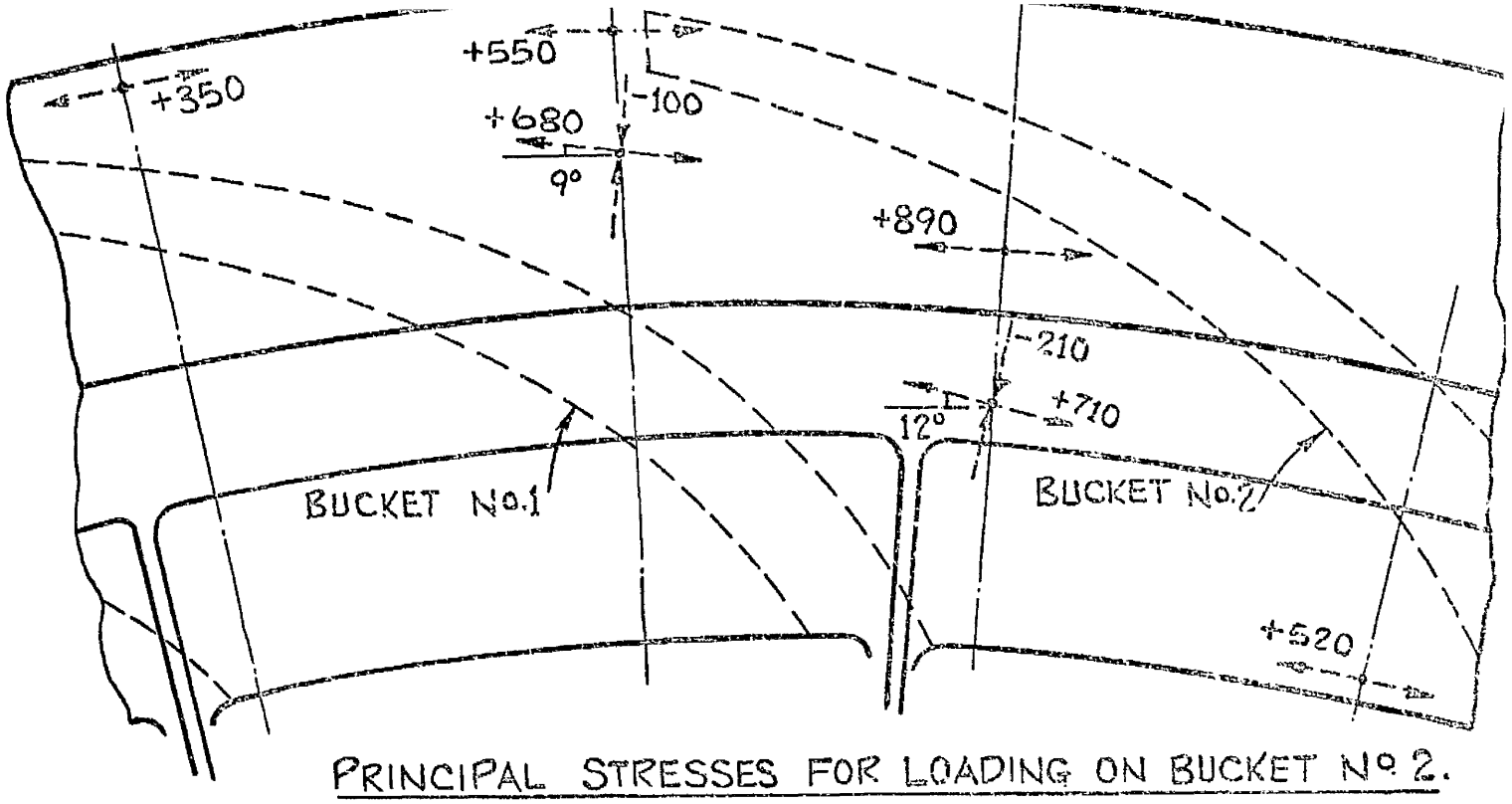

PRINCIPAL STRESSES FOR LOADING ON BUCKET No 2.

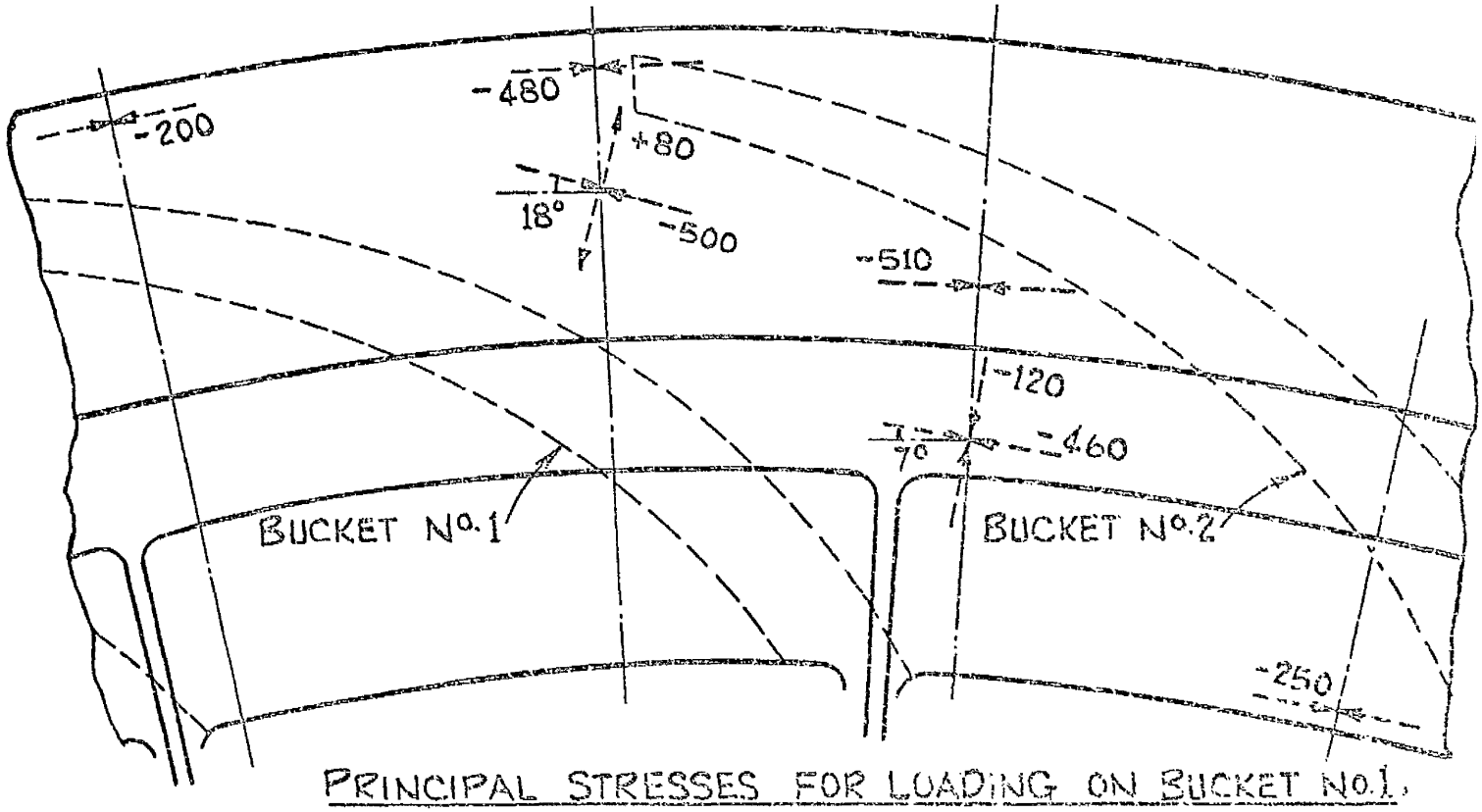

PRINCIPAL STRESSES FOR LOADING ON BUCKET No.1.

STRESSES ARE IN lb/in^2., + TENSILE.

FIG. 86. MEASURED APPROXIMATE JET LOADING COMPONENT PRINCIPAL STRESSES ON OUTLET SIDE OF RIM OF 16½in ALUMINIUM TURGO WHEEL., FOR BUCKETS NOS. 1 AND 2 SUBJECTED IN TURN TO 2000 lb. DIRECT SIMULATED JET LOADING ONLY.

mainly circumferential and of a lesser order, is the feature. These indications are consistent with the natures of the stresses on the loaded bucket at its junction with the rim, as shown on Figs. 82 and 83.

Of the maximum total stresses computed for outlet side locations, after the manner of Fig. 77, the highest value was 1950 lb/in^2 tension. This highest maximum total stress occurred on the outlet side at the location showing + 890 lb/in^2 stress in Fig. 86, and was, of course, due to 2000 lb simulated jet loading acting on each of the 3 adjacent buckets, say Nos. 2, 3 and 4.

4C iii Approximate jet loading stresses on the hub

Stresses were measured on the hub, only at locations at its junctions with a directly loaded bucket and with adjacent buckets. The values found were small, the highest maximum total stress measured being + 670 lb/in^2. This occurred in the circumferential direction (relative to the wheel axis) at a location between the bucket outlet edge/hub junctions of 2 adjacent buckets, these being 2 of a group of 3 buckets, each carrying 2000 lb simulated jet loading. This hub location, several of which are evident in Fig.56(b), adjoins the location on the unswept surface of the bucket outlet edge, where the highest maximum total stress in the wheel was measured, Fig.81.

4C iv Corresponding approximate jet loading stresses in $16\frac{1}{2}$ in. cast steel Turgo wheel

In members of identical geometry and size, but of different linear-elastic materials with Poisson's Ratio ν of similar order, identical stresses are induced by the same externally applied loadings. In such a pair of Turgo wheels, therefore, the same externally applied bucket loadings, whether due to water jet action on both wheels, or to mechanical action on both wheels, will produce identical stresses in the wheels.

Thus the approximate jet loading stresses in a $16\frac{1}{2}$ in. cast steel Turgo wheel are identical to their counterparts in the $16\frac{1}{2}$ in. aluminium wheel, as presented in Figs. 77 to 86 and in sections 4C i to 4C iii. The corresponding greatest measured maximum total approximate jet loading stress in the normal working cast steel wheel is then 5270 lb/in^2 (2.4 T/in^2) tensile.

4D COMPARISON AND COMBINATION OF CENTRIFUGAL AND APPROXIMATE JET LOADING STRESSES IN $16\frac{1}{2}$ in. p.c.d. TURGO WHEEL

The stress measurements show that the bucket edges are the critical locations of high stress, exhibiting the stress maxima. At corresponding points on the two surfaces at an edge, however, the stresses for a given loading are widely different, due to edge bending moments superimposed on membrane forces. The maximum centrifugal stress occurs on the swept surface of the outlet edge near the pitch-circle, while the maximum approximate jet loading stress occurs on the unswept surface of the same edge, where it joins the hub. For the cast steel wheel, from Figs.66 and 85, the measured maxima are as follows:-

Normal working conditions:
- Maximum centrifugal stress = + 3160 x 3 = + 9480 lb/in^2
- Greatest maximum total approximate jet loading stress = + 5270 lb/in
- $\therefore$ ratio, $\dfrac{\text{Max. centrifugal stress}}{\text{Greatest max. total approx. jet loading stress}} = 1.80$

Overspeed condition:- Maximum centrifugal stress = + 30,700 lb/in^2

Centrifugal stress is patently dominant at normal working conditions and is critically important at overspeed.

Under normal working conditions, the main action in respect of both centrifugal and jet loading stress maxima, is in-plane bending of the buckets. Both centrifugal and approximate jet loading measurements demonstrate the considerable flexibility of the bucket under this action, an important factor in relation to the supporting rôle played by the bucket in the jet-loaded wheel. The significance of this rôle is one of the main revelations of the approximate jet loading test.

The/

The combined centrifugal and approximate jet loading maximum total stresses on the bucket edges of the cast steel wheel are indicated in Fig.87. The values have been superimposed appropriately from Figs.66 and 85 and relate to the normal working condition. From Fig.87, the maximum combined measured stress at normal working, is seen to be about 13,100 lb/in^2 tensile, occurring on the unswept surface of the outlet edge where it joins the hub, for Θ = about 146°. The highest swept surface outlet edge value is + 11,400 lb/in^2 at Θ = about 92°, and the highest swept surface inlet edge value is + 10,600 lb/in^2 at about the same angle Θ. The corresponding maximum combined stress in the rim is + 7,650 lb/in^2, comprising + 6,450 lb/in^2 centrifugal stress (Fig.68) and + 1,200 lb/in^2 approximate jet loading maximum total stress. This maximum occurs circumferentially on the outlet side of the rim, at a bucket outlet edge junction.

These measured combined stresses are of relatively small order. Such would be expected in Turgo wheels in view of their operating conditions, and of their long trouble-free service record.

Mindful of the reservations which must be maintained in respect of the approximate nature of the jet loading test, the main conclusions from this chapter are summarised as follows:-

For the 16½ in.cast steel Turgo wheel:-

(1) Under normal working conditions centrifugal stress is predominant. The maximum measured centrifugal stress is + 9,480 lb/in^2. The greatest measured maximum total approximate jet loading stress is + 5,270 lb/in^2. At overspeed, the maximum measured centrifugal stress is + 30,700 lb/in^2. These maxima occur on the outlet edge of the bucket.

(2) For both centrifugal and approximate jet loading, the most significant stresses occur on the swept and unswept surfaces of the/

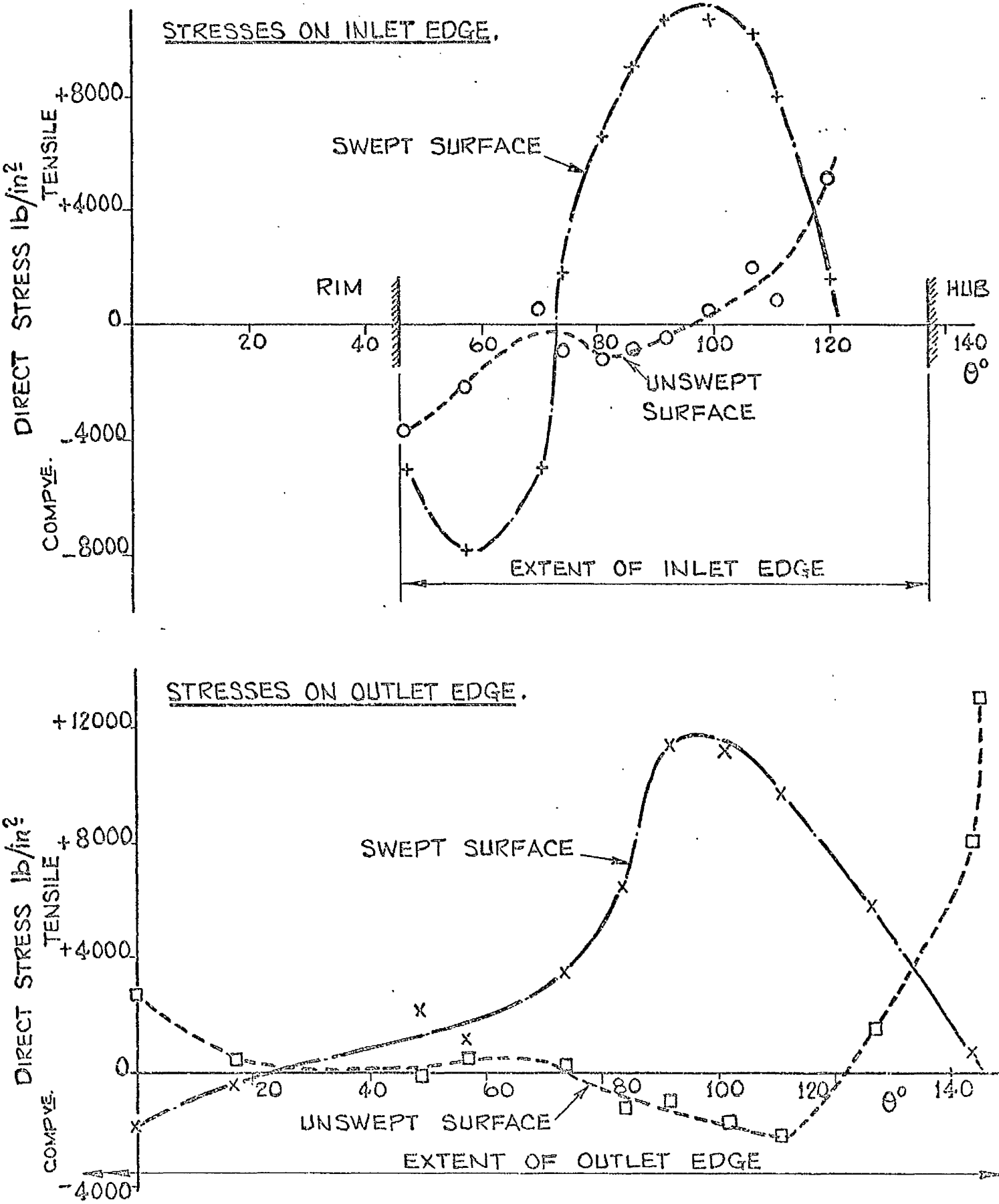

FIG. 87. DISTRIBUTION WITH θ OF THE COMBINED CENTRIFUGAL AND APPROXIMATE JET LOADING MAXIMUM TOTAL STRESSES MEASURED ON THE TWO SURFACES OF THE EDGES OF BUCKET OF THE 16½ IN. CAST STEEL TURGO WHEEL, UNDER NORMAL WORKING CONDITIONS. (FROM FIGS. 66 AND 8

the bucket edges, along which the stress distributions are quite distinctive. The surface stresses at the edges are the resultants of shell bending moment and membrane force actions along the edges.

(3) For both loadings, the most significant action on the bucket is bending in the plane of the wheel. The general shell behaviour of the bucket in a working wheel, is similar to that of a toroidal shell subjected to in-plane bending.

(4) Under jet action, the rôle played by a bucket in supporting adjacent directly loaded buckets, is an important one. Stresses in the bucket pertinent to this rôle, may be of consequence equal to that of stresses due to direct loading.

CHAPTER 5.

THEORETICAL ANALYSIS OF THE STRESSES AND DEFORMATIONS IN AN OPEN TOROIDAL SHELL SUBJECTED TO IN-PLANE BENDING.

THEORETICAL ANALYSIS OF THE STRESSES AND DEFORMATIONS IN AN OPEN TOROIDAL SHELL SUBJECTED TO IN-PLANE BENDING

From the previous chapters it is clear that the geometry of a Turgo wheel bucket resembles that of a portion of an open toroidal shell, and that the working stress behaviour of the bucket is roughly comparable to that of a toroidal shell sector subjected to bending in the plane of the shell. A shell theory treatment does not appear to have been given for the specific case of the open toroidal shell under in-plane bending. This contrasts with the well-documented corresponding case of the closed toroidal shell or pipe-bend, a case which first sustained theoretical onslaught in 1911.

It is rational to study the solutions relevant to the closed shell problem, as possible sources of a solution to the corresponding open shell case. Most of the significant theoretical papers on pipe-bends under in-plane bending are summarised and examined critically by TURNER AND FORD[58] who themselves present a theoretical solution superior in some respects to previous ones. It seems, however, that the basis of this solution would support a corresponding open shell solution less readily and with less generality than would that of the earlier closed shell analyses of REISSNER[49] and CLARK AND REISSNER[42]. These earlier authors advance a solution of the pipe-bend problem by means of the theory of thin elastic shells of revolution, and CLARK[8] in a later publication, generalises and extends the solution for closed shells of any reasonable curvilinear cross section and varying thickness. The shell of revolution approach, formulated in these papers of REISSNER and CLARK is readily applicable to the analysis of the open toroidal shell under in-plane bending as a general case. Indeed, CLARK'S[8] solution is eminently applicable as part of the open shell general/

general solution for the toroidal shells of relatively large curvatures comparable with the geometry of Turgo wheel buckets and with the geometry of Pelton buckets. As will be shown subsequently, a Pelton bucket somewhat resembles two identical open toroidal shell sectors rigidly connected on circumferential boundaries. Furthermore then, the shell of revolution approach promotes the extension of the analysis to include the case of a circumferentially-connected pair of identical open toroidal shells, subjected to in-plane bending.

The in-plane bending of an open toroidal shell considered as a sector of a shell of revolution, obeys theoretically the ordinary second order complex non-homogeneous differential equation characteristic of shells of revolution under axially symmetric loading. This equation is adopted by CLARK[8]. An asymptotic particular integral given by CLARK[8] also applies to the general solution of the open shell case. This particular integral approximates to the membrane solution over the greater portion of the shell. The complementary function is derived by an asymptotic method due to LANGER[60]. NAGHDI AND DE SILVA[61] indicate the applicability of this asymptotic method for solution of a homogeneous equation of general shell of revolution problems. The solution of the homogeneous equation describes the conditions and effects pertinent to the edges or boundaries of the shell. For the open toroidal shell then, the general solution is, for the most part, a synthesis of membrane and edge effect solutions, and so partially conforms to the pattern common in the approximate analysis of shells of revolution.

The main interest lies in open toroidal shells of large curvature and for these, asymptotic solutions of the differential equation are particularly advantageous and are of superior accuracy. Power series solutions on the other hand, would incur difficulties of convergence for the geometries of interest. Such solutions may not be practical at all, or may only be so, through/

through the use of a computer. The early publications by TUEDA[62] present a solution by power series for the closed toroidal shell bending case. The form of the solution is more directly applicable to the open shell than to the closed. It is however, restricted to uniform thickness, part-circular section toroidal shells. The open shell version of the TUEDA solution is practical only for relatively long radius toroidal shells, not comparable in curvatures with those of impulse water turbine buckets. For such shells, however, the writer has found it to indicate stress behaviour similar to that determined for the large curvature shells by asymptotic solutions, and similar in kind to that measured on Turgo wheel buckets.

A result from the open toroidal shell solution concerns the in-plane bending rigidity of the shell, in comparison with the rigidity which would be given by treatment with simple beam theory. This comparison has an exact parallel in the closed shell case, where the comparative rigidities are expressed as a ratio, namely the rigidity or flexibility factor. With regard to theoretical analysis of the working actions on a Turgo wheel bucket, the corresponding approximate open toroidal shell rigidity factor may be applied to parts of the beam theory calculations of Chapter 3, in a modification to convert the calculations to the more realistic and accurate shell basis.

5A GENERAL SOLUTION FOR OPEN TOROIDAL SHELL OF VARYING THICKNESS

It is assumed throughout that the shell has a plane of symmetry perpendicular to the axis of revolution and that the meridional cross-section is curvilinear, of the general shape shown in Fig. 88(a) or (b). Initially however, the cross-section is unspecified as to form and thickness.

Adopting the formulation and essentially the notation* of REISSNER AND CLARK[8, 42, 59], a sector of such an open toroidal shell, subjected to pure in-plane bending is considered, Fig. 88(c). The shell carries no surface loading and, under in-plane bending, has cylindrical neutral surface indicated by trace NS in the Fig. Considered as a problem of the theory of thin shells of revolution, except for the circumferential component of displacement, the displacements and the stress distributions are axisymmetric.

If r_N is the radius of the undeformed neutral surface, and θ its angle subtended at the axis, Fig. 88(d), and if $r_N - \Delta r_N$ and $\theta + \Delta\theta$ are the corresponding quantities for the deformed neutral surface, then the change in curvature due to applied moment m is given by:-

$$\Delta K = \frac{1}{r_N - \Delta r_N} - \frac{1}{r_N} = \frac{\Delta r_N}{r_N^2} \quad ,$$

neglecting products of small quantities.

Since the neutral surface remains unchanged in length:-

$$(r_N - \Delta r_N)(\theta + \Delta\theta) = r_N . \theta$$

Therefore, neglecting products of small quantities,

$$r_N . \Delta\theta = \theta . \Delta r_N$$

$$\therefore \Delta K = \frac{\Delta\theta}{\theta . r_N} \qquad (5A.1)$$

* See Nomenclature.

Although all other quantities are assumed to be independent of θ, the circumferential component of displacement v, is allowed to have the form:-

$$v = k r \theta \tag{5A.2}$$

at all points (r, θ) in the shell, k being a dimensionless constant.

At angle θ therefore, Fig.88(d), due to deformation, point B on the neutral surface is displaced circumferentially to B''. The circumferential displacement of B is thus given by:-

$$\begin{aligned} v_B = B'B'' &= k r_N \theta \\ &= (r_N - \Delta r_N).\Delta\theta \\ &= r_N.\Delta\theta \quad , \text{ neglecting products of small quantities.} \end{aligned}$$

$$\therefore \; k = \frac{\Delta\theta}{\theta} \tag{5A.3}$$

Hence, from equation (5A.1), change in curvature ΔK is given by:-

$$\Delta K = \frac{k}{r_N} \tag{5A.4},$$

where r_N is the radius of the cylindrical neutral surface, i.e. r_N is the radius at which the shell mid-surface circumferential strain $\varepsilon_{\theta M} = 0$, or where:-

$$N_\theta - \nu N_\xi = 0 \tag{5A.5},$$

in terms of the corresponding stress resultants in the shell, Fig.88(e). Subsequent to solution of the differential equation relevant to the shell theory treatment of this problem, stress resultants N_θ, N_ξ may be found, and so r_N may be determined from equation (5A.5) in any particular case.

Considering/

Considering the shell as part of a thin shell of revolution, a meridian of the mid-surface, Fig.88(a) and (b), may be represented in terms of the parameter ξ, by equations of the form:-

$$r = r(\xi) \quad , \qquad z = z(\xi) \tag{5A.6}$$

The meridian geometry is assumed to be such that r and z have continuous derivatives with respect to ξ up to at least third order, and also such that the quantity:-

$$\alpha = \left[(r')^2 + (z')^2 \right]^{\frac{1}{2}} \tag{5A.7}$$

Primes denote differentiation with respect to ξ, which is the independent variable thoughout.

From the general solution of the differential equation, in any particular case stress resultant N_θ and stress couple M_θ, Fig.88(e), may be found in terms of Ek. A relation between applied bending moment m and dimensionless constant k may then be obtained from the following equation which defines m :-

$$m = \int r N_\theta \alpha . d\xi - \int z' . M_\theta . d\xi \qquad * \tag{5A.8},$$

which reduces to:-

$$m = C_1 E k \tag{5A.9},$$

where C_1 is a constant for a particular shell.
From equation (5A.4) then:-

$$m = C_1 E r_N . \Delta K \tag{5A.10}$$

Now applying simple beam theory to the bending of the shell sector:-

$$m = EI . \Delta K$$

where I is the second moment of area of the meridional cross-section about/

* This is virtually the same equation as (4A.3)

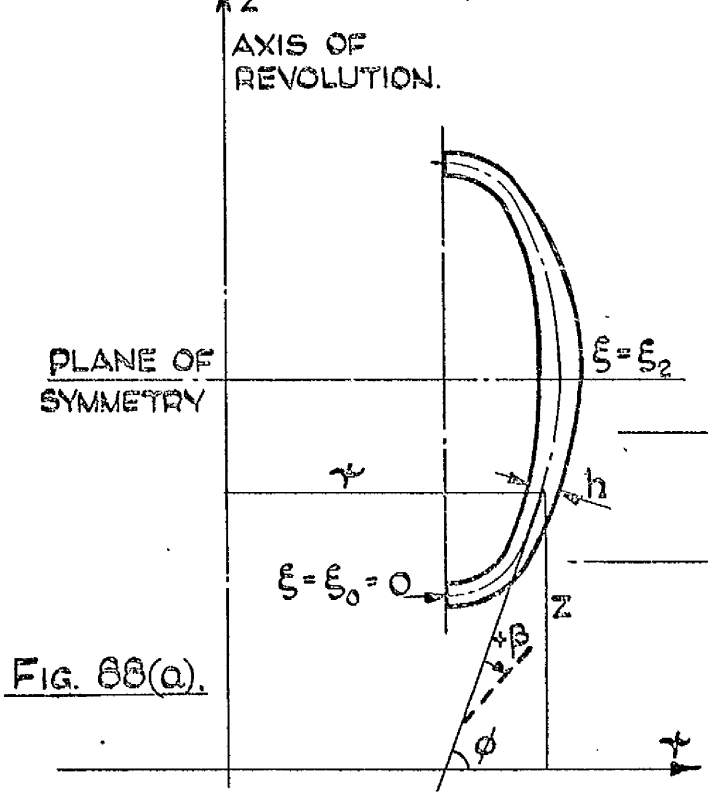

FIG. 88(a).

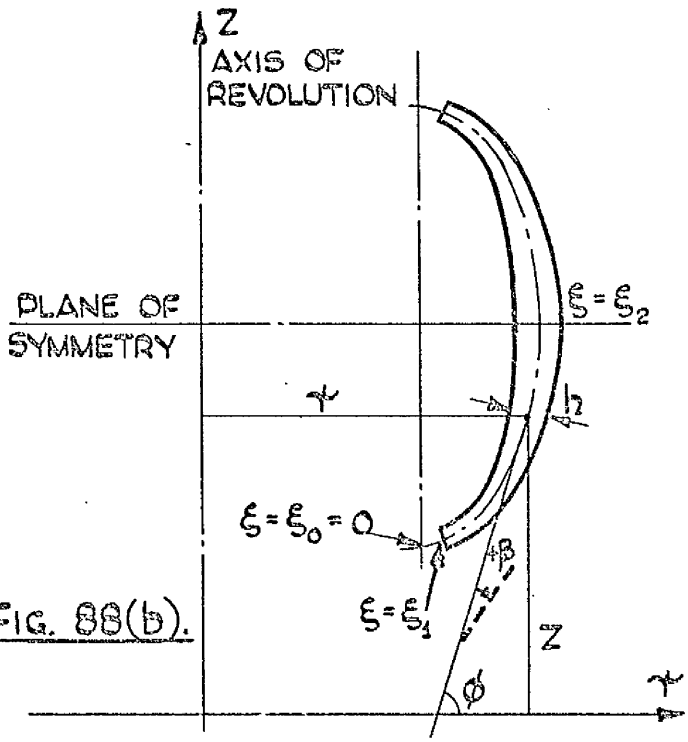

FIG. 88(b).

FIG. 88(a)(b). SHELL MERIDIONAL CROSS-SECTION SHOWING PARAMETER ξ AND CYLINDRICAL CO-ORDINATES r, Z PERTINENT TO THE MID-SURFACE. THE +VE DIRECTION OF ANGULAR DISPLACEMENT β IS ALSO SHOWN.

FIG. 88(e). ELEMENT OF SHELL SHOWING +VE DIRECTIONS OF STRESS RESULTANTS N_ξ, N_θ, Q AND STRESS COUPLES M_ξ, M_θ.

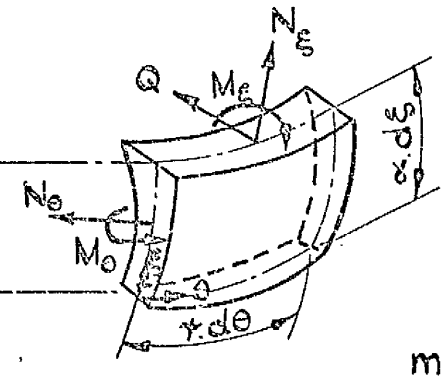

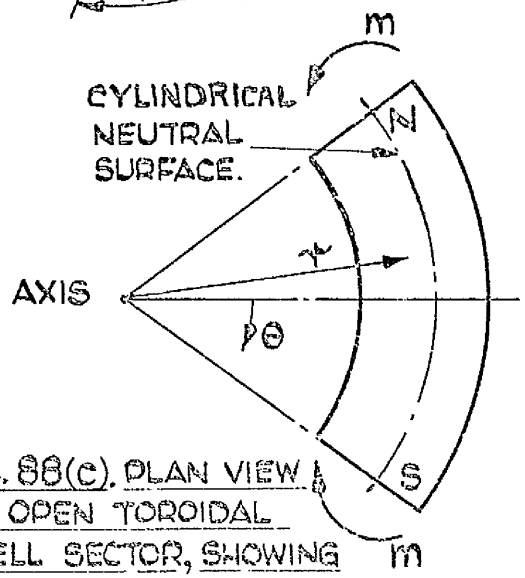

FIG. 88(c). PLAN VIEW OF OPEN TOROIDAL SHELL SECTOR, SHOWING APPLIED IN-PLANE BENDING MOMENT m.

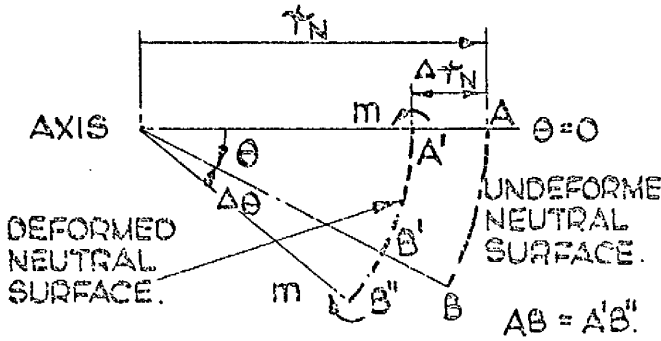

FIG. 88(d). DEFORMATION OF NEUTRAL SURFACE DUE TO BENDING MOMENT m. (SMALL DEFORMATION.)

FIG. 88. DIAGRAM SHOWING THE OPEN TOROIDAL SHELL SECTOR AND ITS CROSS-SECTION, AND INDICATING PARAMETERS RELEVANT TO THE ANALYSIS OF THE OPEN TOROIDAL SHELL SUBJECTED TO IN-PLANE BENDING MOMENT m.

(NOTATION THROUGHOUT IS ESSENTIALLY THAT OF REISSNER & CLARK (8,42,59))

about an axis through the centroid. Alternatively then, the shell theory equation (5A.10) may be written:-

$$m = \rho E I \Delta K \qquad (5A.11),$$

where ρ is a shell rigidity factor which has value unity for treatment by simple beam theory. In applying simple beam theory, the shell is treated as if it was a straight member. Equating (5A.10) and (5A.11) gives:-

$$\rho = \frac{C_1 r_N}{I} \qquad (5A.12)$$

If $\sigma_{S.MAX}$ is the maximum stress derived by shell theory, and $\sigma_{B.MAX}$ the corresponding maximum stress given by simple beam theory, then from the shell solution :-

$$\sigma_{S.MAX} = C_2 E k \qquad (5A.13),$$

where C_2 is a constant for a particular shell.

Now,

$$\sigma_{B.MAX} = \frac{m}{I} \cdot d \qquad (5A.14)$$

where d is the distance of the extreme fibre from the simple bending neutral axis. Expressing the maximum stresses as a ratio, from equations (5A.11), (5A.12), (5A.4) :-

$$\frac{\sigma_{S.MAX}}{\sigma_{B.MAX}} = \frac{C_2}{C_1} \cdot \frac{I}{d} \qquad (5A.15)$$

With reference to any particular shell, equations (5A.12) and (5A.15) concern quantities of practical interest. In respect of these then, the solution of the shell differential equation provides the values r_N, C_1 and C_2.

5A i Solution of the shell differential equation

The approximate non-homogeneous complex differential equation given by CLARK[8], governs the small deformational behaviour of a thin open toroidal shell of smoothly varying meridional section which has curvatures comparable to the in-plane curvature. The equation applies when the shell boundary is at $\xi = \xi_0 = 0$, Fig. 88(a) or at $\xi = \xi_1$ Fig. 88(b), and is written:-

$$Z'' - i\mu\Phi Z = f \qquad (5A.16),$$

where $Z = X + iY$.

For the shell under pure in-plane bending, the loading term f is given by:-

$$f = i\tau'\left(\frac{\alpha E h}{r}\right)^{\frac{1}{2}} k \qquad (5A.17)$$

In the coefficient $\mu\Phi$, μ is a large parameter defined by:-

$$\mu = \left[12(1-\nu^2)\right]^{\frac{1}{2}} \frac{\alpha_0 z_0''}{r_0 h_0} \qquad (5A.18)$$

where the zero subscript denotes the value of a quantity at $\xi = 0$, and function Φ is given by:-

$$\Phi = \frac{\alpha z'}{r h} \cdot \frac{r_0 h_0}{\alpha_0 z_0''} \qquad (5A.19)$$

It is characteristic that Φ vanishes at the isolated point where $z'(\xi) = 0$, or where a tangent to a meridian is perpendicular to the axis of revolution, Fig. 88(a) and (b). Parameter ξ is defined so that $\xi = 0$ corresponds to $\Phi = 0$, Φ being bounded from zero away from $\xi = 0$. For a curvilinear meridian the function Φ then has a first-order zero, to which case the solution is confined. By McLaurin's Expansion:-

$$\Phi = \xi + \left(\frac{1}{2}\frac{z_0'''}{z_0''} + \frac{\alpha_0'}{\alpha_0} - \frac{r_0'}{r_0} - \frac{h_0'}{h_0}\right)\xi^2 + \text{----------} \qquad (5A.20),$$

which form permits determination in the solution, of functions of Φ otherwise indeterminate at $\xi = 0$.

The stress resultants, stress couples, Fig. 88(e), and displacement of interest, Fig. 88(a) and (b), are determined in terms of the solution $Z = X + iY =$ Function of ξ, subject to appropriate boundary conditions, by the following relations:-

$$
\begin{aligned}
r N_\xi &= r' \left(\frac{C}{r\alpha}\right)^{\frac{1}{2}} Y , \qquad r Q = -Z' \left(\frac{C}{r\alpha}\right)^{\frac{1}{2}} Y , \\
\alpha N_\theta &= \left(\frac{\alpha C}{r}\right)^{\frac{1}{2}} \left[Y' - \frac{1}{2} \frac{(r/\alpha C)'}{(r/\alpha C)} Y \right] , \\
\alpha M_\xi &= \left(\frac{\alpha D}{r}\right)^{\frac{1}{2}} \left\{ X' + \left[\nu \frac{r'}{r} - \frac{1}{2} \frac{(r D/\alpha)'}{(r D/\alpha)} \right] X \right\} , \\
\alpha M_\theta &= \left(\frac{\alpha D}{r}\right)^{\frac{1}{2}} \left\{ \nu X' + \left[\frac{r'}{r} - \frac{\nu}{2} \frac{(r D/\alpha)'}{(r D/\alpha)} \right] X \right\} , \\
\beta &= \left(\frac{\alpha}{r D}\right)^{\frac{1}{2}} X ,
\end{aligned}
\qquad (5A.21)
$$

where $C = Eh$, $\quad D = \dfrac{Eh^3}{12(1-\nu^2)}$.

For the general solution of the basic differential equation (5A.16) a relevant approximate asymptotic particular integral is given by CLARK[8] as:-

$$Z(\xi) = \mu^{-\frac{2}{3}} . f(\xi) . T(\mu^{\frac{1}{3}} \Phi) \qquad (5A.22)$$

This particular integral is a good approximation for large μ, is valid at all ξ including $\xi = 0$, and reduces to the membrane solution away from $\xi = 0$. $T(\mu^{\frac{1}{3}}\Phi)$ is a function of argument $\mu^{\frac{1}{3}}\Phi$, related to a Lommel function. It is tabulated, together with its derivative.(9, 64)

Now taking the plane $z = 0$, as the plane of symmetry, Fig. 88(a) and (b), only the lower half of the shell need be considered. The boundary conditions relevant to in-plane bending of the shell are:-

at the free edge $\xi = 0$ or $\xi = \xi_1$:— $N_\xi = 0$ and $M_\xi = 0$,

giving from equations (5A.21),

$$Y(0,\xi_1) = 0 \quad \text{and} \quad \left\{X' + \left[\nu\frac{r'}{r} - \frac{1}{2}\frac{(r\,D/\alpha)'}{(r\,D/\alpha)}\right]X\right\}(0,\xi_1) = 0 \qquad (5A.23)$$

at the plane of symmetry $\xi = \xi_2$:— $Q = 0$ and $\beta = 0$,

giving from equations (5A.21),

$$Y(\xi_2) = 0 \quad \text{and} \quad X(\xi_2) = 0$$

$$\text{or} \quad Z(\xi_2) = 0. \qquad (5A.24)$$

Assuming that meridians of the shell have continuously turning tangents then r' vanishes at ξ_2. Loading term $F = f(\xi)$ contains r' as a factor, equation (5A.17), so that particular integral $Z(\xi)$, equation (5A.22), satisfies the boundary conditions at $\xi = \xi_2$. In general however, it cannot satisfy the boundary conditions at the free edge $\xi = 0, \xi_1$, so that the general solution of differential equation (5A.16) requires the complementary function, i.e. the solution of the corresponding homogeneous equation:-

$$Z'' - i\mu\Phi Z = 0 \qquad (5A.25),$$

which/

which pertains to effects at the shell edges. It is in this respect, deriving from a difference of conditions at one boundary, that the open and closed shell analyses differ.

An asymptotic solution of homogeneous equation (5A.25) may be found by a method developed by LANGER[60]. This method applies specifically to ordinary differential equations of such form, characterised by the vanishing of Φ at some isolated point $\xi_0 = 0$, to the degree ρ, where ρ is zero or a real positive constant. LANGER[60] shows that there may be associated with any such given equation, a related equation of the same type, which in this case, may be written:-

$$y''(\xi) + \left\{2i^3\left(\frac{\mu}{2}\right)\Phi - w(\xi)\right\}y(\xi) = 0 \qquad (5A.26)$$

The function $w(\xi)$ is bounded. Had there been a corresponding function in the coefficient of Z in the given equation (5A.25), that function would have been bounded also.

The related equation (5A.26), in respect of function $w(\xi)$, is such that its asymptotic solution is given explicitly in terms of Bessel functions of the first kind. The solution of the given equation for μ large, is then shown to be represented asymptotically by the known solution of the related equation. For Φ vanishing to the degree 1 at $\xi_0 = 0$, this is expressible by the following equality:-

$$\left[\begin{array}{c}\text{Solution}\\ \text{of}\\ \text{given equation}\end{array}\right] = \left[\begin{array}{l}\text{Solution of related}\\ \text{equation in terms}\\ \text{of Bessel functions}\\ \text{of the first kind.}\end{array}\right] + \sum_{n=1}^{\infty} \frac{S_n(\xi,\mu)}{\mu^{\frac{2}{3}n}} \qquad (5A.27),$$

where $S_n(\xi,\mu)$ is bounded in the range under consideration. The infinite series in inverse powers of $\mu^{2/3}$ converges uniformly for large μ. Thus an approximate solution to equation (5A.25) may be obtained, asymptotic in μ to an exact solution.

For a homogeneous equation general to the small deformation theory of/

of shells of revolution, and of which equation (5A.25) is a form, NAGHDI AND DE SILVA[61] indicate the LANGER [60] asymptotic solution using Bessel functions of the first kind. This is virtually the asymptotic solution of (5A.25) and for Φ vanishing to the degree 1 at $\xi_0 = 0$, may be written in the alternative form[63]:-

$$Z(\xi) = \left[\Phi^{-\frac{1}{2}} \int_{\xi_0}^{\xi} \Phi^{\frac{1}{2}}(\xi).d\xi\right]^{\frac{1}{2}} \left\{A_1 H_{\frac{1}{3}}^{(1)}(\eta) + B_1 H_{\frac{1}{3}}^{(2)}(\eta)\right\} \tag{5A.28}$$

where A_1, B_1 are constants. $H_{\frac{1}{3}}^{(1)}(\eta)$ and $H_{\frac{1}{3}}^{(2)}(\eta)$ are Hankel functions of order $\frac{1}{3}$ of the first and second kind respectively, of the complex argument η given by:-

$$\eta = (2i^3)^{\frac{1}{2}} \left(\frac{\mu}{2}\right)^{\frac{1}{2}} \int_{\xi_0}^{\xi} \Phi^{\frac{1}{2}}(\xi).d\xi \tag{5A.29}$$

This complementary function is a good approximation for large μ and is valid at all ξ including $\xi = \xi_0 = 0$. The following relations exist between the Hankel functions and the functions $h_1(z_1)$, $h_2(z_1)$ which, with their derivatives, are tabulated for complex arguments[65]:-

$$h_1(z_1) = \left(\frac{2}{3} z_1^{\frac{3}{2}}\right)^{\frac{1}{3}} . H_{\frac{1}{3}}^{(1)}\left(\frac{2}{3} z_1^{\frac{3}{2}}\right)$$

$$h_2(z_1) = \left(\frac{2}{3} z_1^{\frac{3}{2}}\right)^{\frac{1}{3}} . H_{\frac{1}{3}}^{(2)}\left(\frac{2}{3} z_1^{\frac{3}{2}}\right) \tag{5A.30}$$

The asymptotic general solution of governing differential equation (5A.16) is therefore given by the sum of equations (5A.28) and (5A.22). The relevant boundary conditions are formulated in equations (5A.23) and (5A.24). Thus, for the in-plane bending of an open toroidal shell of any reasonable continuously varying curvature and thickness defined by:-

$$r = r(\xi), \qquad z = z(\xi), \qquad h = h(\xi) \tag{5A.31}$$

approximate expressions for the various stresses and displacements can be obtained from the real and imaginary parts of $Z(\xi)$, together with equations (5A.21), (5A.8), (5A.12) and (5A.15). To express stresses and displacements as functions of ξ, the function Φ equation (5A.19), would require to be tabulated and the integral $\int_{\xi_0}^{\xi} \Phi^{\frac{1}{2}}(\xi).d\xi$ would require to be evaluated and tabulated. In most cases, the integral could readily be evaluated numerically and tabulated using a computer.

The function Φ and the associated integral depend on the exact shape of a meridian of the middle surface of the shell and on any variation in thickness. Nevertheless, it may be possible to derive general expressions for maximum stresses and other quantities of interest without assuming any specific shape for the open shell cross-section. This may be achievable by examining the dependence of the quantities of interest on the real and imaginary parts of the tabulated functions $h_1(z_1)$, $h_2(z_1)$, $T(\mu^{\frac{1}{3}}\Phi)$ and their derivatives, and by considering the natures of the variations [64, 65] in these real and imaginary components. Such a treatment has been applied by CLARK[8] to the corresponding general closed shell problem.

To illustrate the application of the solution to a particular shell form, an open toroidal shell of circular cross-section is selected. This is the most simple case and is the only one for which tabulated data relevant to function Φ and its dependents, have been published. The parabolic cross-section adopted in Chapter 3 to approximate a Turgo wheel bucket meridional section, is not treated. However, as may be seen from Fig.91, a section with a circular mid-surface meridian may be arranged to provide an approximation almost as good. The behaviour indicated for the in-plane bending of the circular section shell, would not be expected to differ very widely from that which might be determined in the closely corresponding parabolic section case. Moreover, as illustrated in Fig.107, Chapter 7, the/

the circular section may give a reasonably close approximation to the shape of the meridional section of a half Pelton bucket.

The parameter and independent variable ξ in equations (5A.6) and (5A.31) is taken as the central angle of the circular cross-section, Fig.89, this angle being the same as the tangent angle ϕ, Fig.88(a) and (b). The parametric equations of the mid-surface of the shell are therefore:-

$$r = a + b\sin\xi \quad , \qquad z = -b\cos\xi \tag{5A.32}$$

Assuming that continuously varying shell thickness h is defined by:-

$$h = h(\xi) = h_o\bar{h} \tag{5A.33}$$

where h_o is the thickness or the projected thickness at $\xi = 0$, Fig.89, then from equations (5A.32), (5A.7), (5A.33), (5A.18) and (5A.19) :-

$$\mu = \left[12(1-\nu^2)\right]^{\frac{1}{2}} \frac{b^2}{a h_o} \tag{5A.34}$$

and

$$\Phi = \frac{1}{\bar{h}}\left(\frac{\sin\xi}{1+\lambda\sin\xi}\right) \tag{5A.35}$$

where $\lambda = \frac{b}{a}$.

In shells of sections comparable with those of impulse water turbine buckets, b and a are of similar order, so that μ is large and λ may have values in the region of 1.

In equation (5A.28), the integral associated with Φ is:-

$$\omega = \int_{\xi_0}^{\xi} \Phi^{\frac{1}{2}}(\xi).d\xi = \int_0^{\xi} \Phi^{\frac{1}{2}}.d\xi = \int_0^{\xi} \left[\frac{1}{\bar{h}}\left(\frac{\sin\xi}{1+\lambda\sin\xi}\right)\right]^{\frac{1}{2}}.d\xi \tag{5A.36}$$

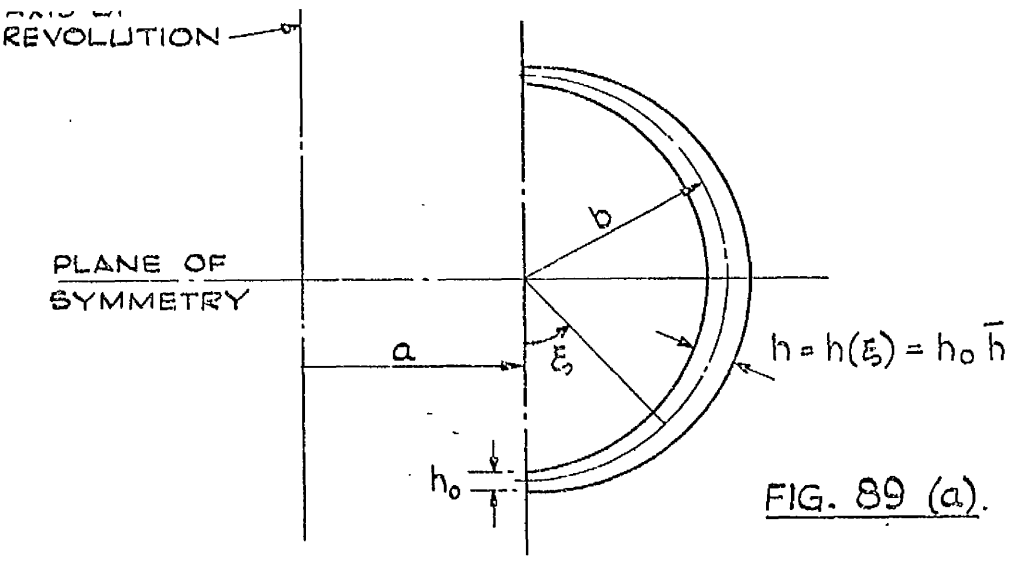

FIG. 89 (a).

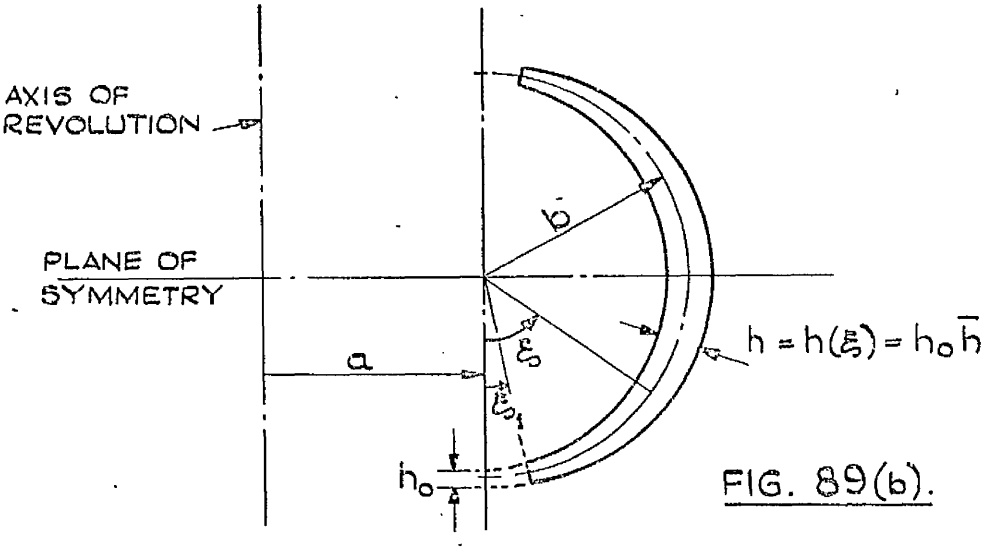

FIG. 89(b).

FIG. 89. OPEN TOROIDAL SHELL OF CIRCULAR MID-SURFACE MERIDIAN.

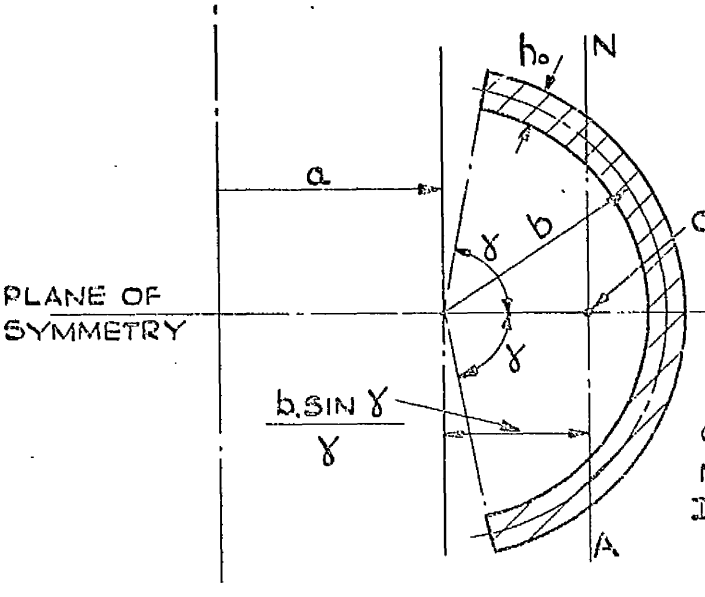

SECOND MOMENT OF AREA OF SECTION ABOUT NEUTRAL AXIS N.A. = I, WHERE

$$I = b^3 h_0 \left(\gamma + \tfrac{1}{2} \sin 2\gamma - \frac{2 \sin^2 \gamma}{\gamma} \right).$$

FIG. 90. OPEN TOROIDAL SHELL OF CIRCULAR MID-SURFACE MERIDIAN AND UNIFORM THICKNESS. PROPERTIES RELEVANT TO TREATMENT BY SIMPLE BEAM THEORY.

By equating complex argument y of the Hankel functions, equation (5A.29), to $\left(\frac{2}{3} z_1^{\frac{3}{2}}\right)$ and substituting for the Hankel functions in (5A.28) using relations (5A.30), the complementary function may be written in a more convenient form. This is given below in the general solution, with the particular integral for this case from equations (5A.22), (5A.17), (5A.32), (5A.33) and (5A.7). The general solution of the differential equation (5A.16) is:-

$$Z = \bar{Q}\left[(A_2+B_2 i)h_1(ix)+(C_2+D_2 i)h_2(ix)\right] + i\mu^{-\frac{2}{3}} bk(\lambda E h_0 \bar{h})^{\frac{1}{2}} \cos\xi (1+\lambda\sin\xi)^{-\frac{1}{2}} T(\mu^{\frac{1}{3}}\Phi) \tag{5A.37}$$

where $$z_1 = i\mu^{\frac{1}{3}}\left(\frac{3}{2}\omega\right)^{\frac{2}{3}} = ix \tag{5A.38}$$

i.e. argument z_1 of the modified functions is purely imaginary,

$$\bar{Q} = \frac{\left(\frac{3}{2}\omega\right)^{\frac{1}{6}}}{(\omega')^{\frac{1}{2}}} \tag{5A.39}$$

and A_2, B_2, C_2, D_2 are arbitrary constants obtainable from the boundary conditions. The functions $h_1(ix)$ and $h_2(ix)$ are tabulated for purely imaginary arguments also[64].

The form of the complementary function in solution (5A.37) is similar to that adopted by CLARK[9] in the analysis of an edge-loaded circular section toroidal shell of uniform thickness. The manner in which the varying thickness term $\bar{h}$ occurs in the governing differential equation and in the complementary function has an exact parallel in a treatment by LECKIE[66] of a symmetrically loaded spherical shell of varying thickness.

It is evident from equations (5A.36), (5A.38) and (5A.39), that for $\xi = 0$, ω and x are zero, and function $\bar{Q}$ is indeterminate. The latter may be defined there however, as $\lim_{\xi \to 0} \bar{Q}(\xi,\lambda) = 1$.

From/

From the solution (5A.37), X, Y and their derivatives are found to be:-

$$X = \bar{Q}\left[A_2 h_{1r}(ix) - B_2 h_{1i}(ix) + C_2 h_{2r}(ix) - D_2 h_{2i}(ix)\right] - \mu^{-\frac{2}{3}} bk(\lambda E h_0 \bar{h})^{\frac{1}{2}} \cos\xi (1+\lambda\sin\xi)^{-\frac{1}{2}} . T_i(\mu^{\frac{1}{3}}\Phi)$$

$$Y = \bar{Q}\left[A_2 h_{1i}(ix) + B_2 h_{1r}(ix) + C_2 h_{2i}(ix) + D_2 h_{2r}(ix)\right] + \mu^{-\frac{2}{3}} bk(\lambda E h_0 \bar{h})^{\frac{1}{2}} \cos\xi (1+\lambda\sin\xi)^{-\frac{1}{2}} . T_r(\mu^{\frac{1}{3}}\Phi)$$

$$\begin{aligned} X' = & -\frac{\mu^{\frac{1}{3}}}{\bar{Q}}\left[A_2 h'_{1i}(ix) + B_2 h'_{1r}(ix) + C_2 h'_{2i}(ix) + D_2 h'_{2r}(ix)\right] \\ & + \bar{Q}\left(\frac{\bar{Q}'}{\bar{Q}}\right)\left[A_2 h_{1r}(ix) - B_2 h_{1i}(ix) + C_2 h_{2r}(ix) - D_2 h_{2i}(ix)\right] \\ & - \mu^{-\frac{2}{3}} bk(\lambda E h_0)^{\frac{1}{2}}\left[\frac{d}{d\xi}\left\{(\bar{h})^{\frac{1}{2}}\cos\xi . (1+\lambda\sin\xi)^{-\frac{1}{2}}\right\}\right] . T_i(\mu^{\frac{1}{3}}\Phi) \\ & - \mu^{-\frac{1}{3}} bk(\lambda E h_0 \bar{h})^{\frac{1}{2}} \cos\xi (1+\lambda\sin\xi)^{-\frac{1}{2}} . \Phi' . T_i'(\mu^{\frac{1}{3}}\Phi) \end{aligned} \qquad (5A.40)$$

$$\begin{aligned} Y' = & \frac{\mu^{\frac{1}{3}}}{\bar{Q}}\left[A_2 h'_{1r}(ix) - B_2 h'_{1i}(ix) + C_2 h'_{2r}(ix) - D_2 h'_{2i}(ix)\right] \\ & + \bar{Q}\left(\frac{\bar{Q}'}{\bar{Q}}\right)\left[A_2 h_{1i}(ix) + B_2 h_{1r}(ix) + C_2 h_{2i}(ix) + D_2 h_{2r}(ix)\right] \\ & + \mu^{-\frac{2}{3}} bk(\lambda E h_0)^{\frac{1}{2}}\left[\frac{d}{d\xi}\left\{(\bar{h})^{\frac{1}{2}}\cos\xi(1+\lambda\sin\xi)^{-\frac{1}{2}}\right\}\right] . T_r(\mu^{\frac{1}{3}}\Phi) \\ & + \mu^{-\frac{1}{3}} bk(\lambda E h_0 \bar{h})^{\frac{1}{2}} \cos\xi (1+\lambda\sin\xi)^{-\frac{1}{2}} . \Phi' . T_r'(\mu^{\frac{1}{3}}\Phi) \end{aligned} ,$$

where prime $'$ means first derivative with respect to ξ, except for the functions $h_1(ix)$, $h_2(ix)$ and $T(\mu^{\frac{1}{3}}\Phi)$ where it means first derivative with respect to the argument of the function.

From equations (5A.23) and (5A.24), together with (5A.32), (5A.33), (5A.7) and (5A.21), the boundary conditions are:-

at $\xi = 0, \xi_1$:— $\quad Y = 0$,

and $$X' + \left[\frac{\nu\lambda\cos\xi}{1+\lambda\sin\xi} - \frac{1}{2}\frac{\frac{d}{d\xi}\{(\bar{h})^3(1+\lambda\sin\xi)\}}{(\bar{h})^3(1+\lambda\sin\xi)}\right]X = 0 \qquad (5A.41)$$

and at $\xi = \frac{\pi}{2}$:— $\quad X = 0$ and $Y = 0$ $\qquad (5A.42)$

Substituting from equations (5A.40) into these boundary condition equations, arbitrary constants A_2, B_2, C_2, D_2 may be found. Knowing these, stress resultants, stress couples and displacement may then be determined using equations (5A.21), (5A.40), (5A.32), (5A.33) and (5A.7). It is evident from these equations that in a numerical example, with $\bar{\Phi}$ and ω given, stress resultants and stress couples will be found in terms of Ek.

The expressions for stresses and displacement, for X, Y and their derivatives and for other important terms are ultimately dependent on Φ equation (5A.35) and on the evaluation of ω equation (5A.36), and so can be computed only when the expression for the varying thickness term $\bar{h} = \bar{h}(\xi)$ is known. For example $\bar{h}$ may be taken as:-

$$\bar{h} = 1 + W\xi \qquad (5A.43)$$

valid for $0 \leq \xi \leq \frac{\pi}{2}$, where W is a constant.

This term can describe a variety of thickness variations. Then:-

$$\Phi = (1+W\xi)^{-1}\left(\frac{\sin\xi}{1+\lambda\sin\xi}\right) \qquad (5A.44)$$

and $$\omega = \int_0^{\xi} (1+W\xi)^{-\frac{1}{2}} \left(\frac{\sin\xi}{1+\lambda\sin\xi}\right)^{\frac{1}{2}} . d\xi$$

(5A.45)

$$= \frac{2}{3}\xi^{\frac{3}{2}} - \frac{1}{5}(\lambda+W)\xi^{\frac{5}{2}} - \frac{2}{7}\left(\frac{1}{12} - \frac{1}{4}\lambda W - \frac{3}{8}\lambda^2 - \frac{3}{8}W^2\right)\xi^{\frac{7}{2}}$$

$$+ \text{----------} ,$$

in the region of $\xi = 0$, by McLaurin's Expansion and the Binomial Theorem.

Numerical integration of ω could be executed readily for a particular W, λ, or for various W, λ, computations and tabulations could be undertaken. The series form of ω, equation (5A.45), is necessary for the determination of terms otherwise indeterminate at $\xi = 0$. From equation (5A.39), the term $\left(\frac{\bar{Q}'}{\bar{Q}}\right)$ in equations (5A.40) is given by:-

$$\frac{\bar{Q}'}{\bar{Q}} = \frac{1}{6}\frac{\omega'}{\omega} - \frac{1}{2}\frac{\omega''}{\omega'} \qquad (5A.46)$$

$$= \frac{1}{5}(\lambda+W) + \left(\frac{1}{14} + \frac{1}{175}\lambda W - \frac{37}{175}\lambda^2 - \frac{37}{175}W^2\right)\xi$$

$$+ \text{----------} \text{ terms in } \xi^2, \xi^3, \text{ etc.},$$

in the region of $\xi = 0$.

In the foregoing, the general solution is presented for the analysis of an open toroidal shell of unspecified meridional shape and thickness variation, and the method of analysis is detailed for an open toroidal shell of circular meridian and varying thickness. Numerical solutions for such cases are subject to the availability of the particular functions Φ and ω in tabular form. No tables are available for any such functions. Although in certain cases, tables may be computed fairly readily, this will not be pursued/

pursued here. However, published tables relevant to Φ and ω for the circular section, uniformly thick toroidal shell are available, and for this reason and for simplicity, attention will now be turned to this case.

Although the case provides a somewhat remote representation of a Turgo wheel bucket meridional section, no essential difference would be expected in the in-plane bending behaviours of a varying thickness shell and a similar uniform thickness shell. Taking the uniform thickness as about the average value in the varying thickness shell, the latter may be simulated by a uniformly thick shell of similar curvatures and edge positions. The uniformly thick section is more directly comparable with a meridional section of a half Pelton bucket.

5B APPLICATION OF THE SOLUTION TO THE OPEN TOROIDAL SHELL OF CIRCULAR CROSS-SECTION AND UNIFORM THICKNESS

The solution for a circular section, uniform thickness shell is given by setting $\bar{h} = 1$ in equation (5A.33), and by setting $h = h_o$ or $\bar{h} = 1$ where appropriate, in previous and subsequent equations, h_o now being taken as the uniform thickness of the shell.

For this case, the complementary function of general solution (5A.37) is identical to that given by CLARK[9], who presents a relevant tabulation of ω for $0 \leq \xi \leq \pi/2$ and $0 \leq \lambda \leq 0{\cdot}5$. It is readily shown that the complementary function is also essentially identical to that of OSIPOVA AND TUMARKIN [64], who give a more accurate relevant tabulation * of $-u_{o.t.} = (3/2\,\omega)^{2/3}$, and of other relevant functions for $-\pi/2 \leq \xi \leq \pi/2$ and $0 \leq \lambda \leq 1$. Although no tabulation is available for $\lambda > 1$, it is evident that the solution, equation (5A.37), could apply to such cases, within limits. JENSSEN[67] applies CLARK'S [9] complementary function directly to a case in which $\lambda = 1$.

As indicated later, the tables of OSIPOVA AND TUMARKIN [64] can be used for the accurate determination of all the main functions necessary in numerical applications of the uniformly thick shell solution. The tables contain an extensive bibliography which features the publications of many Russian investigators in the field of toroidal shell theory.

For uniform thickness h_o, the relevant equations of the previous section become:- /

* Suffix O.T. denotes OSIPOVA AND TUMARKIN'S notation.

become:-

$$\Phi = \frac{\sin^p \xi}{1+\lambda \sin^p \xi} \quad ,$$

$$\omega = \int_0^{\xi} \left(\frac{\sin^p \xi}{1+\lambda \sin^p \xi} \right)^{\frac{1}{2}} . d\xi \quad , \tag{5B.1}$$

$$= \frac{2}{3}\xi^{\frac{3}{2}} - \frac{1}{5}\lambda \xi^{\frac{5}{2}} - \frac{2}{7}\left(\frac{1}{12} - \frac{3}{8}\lambda^2\right)\xi^{\frac{7}{2}} + \text{-------} \quad ,$$

in the region of $\xi = 0$,

$$x = \mu^{\frac{1}{3}} \left(\frac{3}{2}\omega\right)^{\frac{2}{3}} \quad , \qquad \bar{Q} = \frac{\left(\frac{3}{2}\omega\right)^{\frac{1}{6}}}{(\omega')^{\frac{1}{2}}} \quad , \qquad \omega' = \Phi^{\frac{1}{2}} \quad ;$$

from the general solution:-

$$X = \bar{Q}\left[A_2 h_{1r}(ix) - B_2 h_{1i}(ix) + C_2 h_{2r}(ix) - D_2 h_{2i}(ix)\right]$$

$$- \mu^{-\frac{2}{3}} bk (\lambda E h_0)^{\frac{1}{2}} \cos^p \xi (1+\lambda \sin^p \xi)^{-\frac{1}{2}} . \; T_i(\mu^{\frac{1}{3}} \Phi) \tag{5B.2}$$

$$Y = \bar{Q}\left[A_2 h_{1i}(ix) + B_2 h_{1r}(ix) + C_2 h_{2i}(ix) + D_2 h_{2r}(ix)\right]$$

$$+ \mu^{-\frac{2}{3}} bk (\lambda E h_0)^{\frac{1}{2}} \cos^p \xi (1+\lambda \sin^p \xi)^{-\frac{1}{2}} . \; T_r(\mu^{\frac{1}{3}} \Phi)$$

$$X' = -\frac{\mu^{\frac{1}{3}}}{\bar{Q}}\left[A_2 h_{1i}'(ix) + B_2 h_{1r}'(ix) + C_2 h_{2i}'(ix) + D_2 h_{2r}'(ix)\right]$$
$$+\bar{Q}\left(\frac{\bar{Q}'}{\bar{Q}}\right)\left[A_2 h_{1r}(ix) - B_2 h_{1i}(ix) + C_2 h_{2r}(ix) - D_2 h_{2i}(ix)\right]$$
$$+\mu^{-\frac{2}{3}} bk(\lambda E h_o)^{\frac{1}{2}} \frac{\sin\xi + \lambda\sin^2\xi + \frac{\lambda}{2}\cos^2\xi}{(1+\lambda\sin\xi)^{3/2}} \cdot T_i(\mu^{\frac{1}{3}}\Phi)$$
$$-\mu^{\frac{1}{3}} bk(\lambda E h_o)^{\frac{1}{2}} \frac{\cos^2\xi}{(1+\lambda\sin\xi)^{5/2}} \cdot T_i'(\mu^{\frac{1}{3}}\Phi). \qquad (5B.2)$$

$$Y' = \frac{\mu^{\frac{1}{3}}}{\bar{Q}}\left[A_2 h_{1r}'(ix) - B_2 h_{1i}'(ix) + C_2 h_{2r}'(ix) - D_2 h_{2i}'(ix)\right]$$
$$+\bar{Q}\left(\frac{\bar{Q}'}{\bar{Q}}\right)\left[A_2 h_{1i}(ix) + B_2 h_{1r}(ix) + C_2 h_{2i}(ix) + D_2 h_{2r}(ix)\right]$$
$$-\mu^{-\frac{2}{3}} bk(\lambda E h_o)^{\frac{1}{2}} \frac{\sin\xi + \lambda\sin^2\xi + \frac{\lambda}{2}\cos^2\xi}{(1+\lambda\sin\xi)^{3/2}} \cdot T_r(\mu^{\frac{1}{3}}\Phi)$$
$$+\mu^{-\frac{1}{3}} bk(\lambda E h_o)^{\frac{1}{2}} \frac{\cos^2\xi}{(1+\lambda\sin\xi)^{5/2}} \cdot T_r'(\mu^{\frac{1}{3}}\Phi)$$

where prime $'$ means first derivative with respect to ξ, except for the functions $h_1(ix)$, $h_2(ix)$ and $T(\mu^{\frac{1}{3}}\Phi)$ where it means first derivative with respect to the argument of the function;

for the boundary conditions:-

at $\xi = 0, \xi_1$ $\qquad Y = 0$

and $\qquad X' + \left(\nu - \frac{1}{2}\right)\frac{\lambda\cos\xi}{1+\lambda\sin\xi} X = 0$, $\qquad$ (5B.3)

at $\xi = \frac{\pi}{2}$ $\qquad X = 0$ and $Y = 0$ $\qquad$ (5B.4)

for/

for stress resultants, stress couples and displacement:-

$$N_\xi = \frac{(\lambda h_o)^{\frac{1}{2}} E^{\frac{1}{2}}}{a} \cdot \frac{\cos\xi}{(1+\lambda\sin\xi)^{3/2}}\, Y$$

$$Q = -\frac{(\lambda h_o)^{\frac{1}{2}} E^{\frac{1}{2}}}{a} \cdot \frac{\sin\xi}{(1+\lambda\sin\xi)^{3/2}}\, Y$$

$$N_\theta = \frac{(\lambda h_o)^{\frac{1}{2}} E^{\frac{1}{2}}}{b(1+\lambda\sin\xi)^{1/2}} \left[Y' - \frac{1}{2} \cdot \frac{\lambda\cos\xi}{1+\lambda\sin\xi}\, Y \right]$$

$$M_\xi = \frac{(\lambda h_o^3)^{\frac{1}{2}} E^{\frac{1}{2}}}{b\sqrt{12(1-\nu^2)}\,(1+\lambda\sin\xi)^{1/2}} \left[X' + \left(\nu - \frac{1}{2}\right) \frac{\lambda\cos\xi}{1+\lambda\sin\xi}\, X \right] \qquad (5B.5)$$

$$M_\theta = \frac{(\lambda h_o^3)^{\frac{1}{2}} E^{\frac{1}{2}}}{b\sqrt{12(1-\nu^2)}\,(1+\lambda\sin\xi)^{1/2}} \left[\nu X' + \left(1 - \frac{\nu}{2}\right) \frac{\lambda\cos\xi}{1+\lambda\sin\xi}\, X \right]$$

$$\beta = \left(\frac{\lambda}{h_o^3}\right)^{\frac{1}{2}} \frac{\sqrt{12(1-\nu^2)}}{E^{\frac{1}{2}}(1+\lambda\sin\xi)^{1/2}}\, X$$

In the tables of OSIPOVA AND TUMARKIN[64] the modified Hankel functions $h_1(i\chi)$, $h_2(i\chi)$ are termed Airy functions and, with their derivatives, are tabulated for $0 \leq \chi \leq 6$. The derivatives are with respect to χ. The function $T(\mu^{\frac{1}{3}}\Phi)$ is also given and is called/

called a generalised Airy function. The negative of this function and its derivative are tabulated for $0 \leq (\mu^{\frac{1}{3}}\Phi) \leq 6$. The nomination of these functions, their origin and their relation to Stokes' equation are discussed in ref.(65).

Other functions tabulated by OSIPOVA AND TUMARKIN[64] are related to all the other main functions, equation (5B.1), of the solution. For a numerical application, the complete calculation is conveniently executed by the use of these tables. The following list gives all the main functions pertinent to this analysis and their equivalents in terms of the functions tabulated in ref.(64). Suffix O.T. denotes OSIPOVA AND TUMARKIN'S notation and, except for the equivalents of functions $h_1(i\chi)$, $h_2(i\chi)$ and $T(\mu^{\frac{1}{3}}\Phi)$ previously mentioned, indicates a function tabulated for $-\frac{\pi}{2} \leq \xi \leq \frac{\pi}{2}$ and $0 \leq \lambda \leq 1$:—

TABLE 5

Main functions pertinent to this analysis and their equivalents in the tables of OSIPOVA AND TUMARKIN.[64]

Main functions pertinent to equations (5B.1) and (5B.2)	Equivalent functions in terms of those tabulated by OSIPOVA AND TUMARKIN.[64]
x	$\mu^{\frac{1}{3}} \cdot u_{o.T.}$
Φ	$\sin\xi / \varphi_{o.T.}$
$\bar{Q}$	$1 / (u'_{o.T.})^{\frac{1}{2}}$
$\bar{Q}\left(\frac{\bar{Q}'}{\bar{Q}}\right)$	$\frac{v'_{o.T.}}{\varphi_{o.T.}^{\frac{1}{2}}} - \frac{\lambda \cos\xi}{2\varphi_{o.T.}(u'_{o.T.})^{\frac{1}{2}}}$
$1+\lambda\sin\xi$	$\varphi_{o.T.}$
$h_{1r}(ix)$	$R(h_1)_{o.T.}$
$h_{1i}(ix)$	$I(h_1)_{o.T.}$
$h'_{1r}(ix)$	$I(h'_1)_{o.T.}$
$h'_{1i}(ix)$	$-R(h'_1)_{o.T.}$
$h_{2r}(ix)$	$R(h_2)_{o.T.}$
$h_{2i}(ix)$	$I(h_2)_{o.T.}$
$h'_{2r}(ix)$	$I(h'_2)_{o.T.}$
$h'_{2i}(ix)$	$-R(h'_2)_{o.T.}$
$T_r(\mu^{\frac{1}{3}}\Phi)$	$-R(e_0)_{o.T.}$
$T_i(\mu^{\frac{1}{3}}\Phi)$	$-I(e_0)_{o.T.}$
$T'_r(\mu^{\frac{1}{3}}\Phi)$	$-R(e'_0)_{o.T.}$
$T'_i(\mu^{\frac{1}{3}}\Phi)$	$-I(e'_0)_{o.T.}$

For a particular shell, after solving for constants A_2, B_2, C_2, D_2 by substitution from equations (5B.2) into the boundary condition equations (5B.3) and (5B.4), X, Y, X', Y' are found in terms of $E^{\frac{1}{2}}k$ for all ξ in the pertinent range, giving the stress resultants and stress couples, equations (5B.5) in terms of Ek. Then to relate the solution to the neutral surface position and to applied bending moment m, equations (5A.5) and (5A.8) are applied. In general the integrations in (5A.8) require to be evaluated numerically by Simpson's Rule or comparable method. Stresses and displacement throughout the shell may thus be found in terms of applied bending moment m. The shell rigidity factor and maximum stress ratio are obtainable by equations (5A.12), (5A.13) and (5A.15). Concerning the shell meridional section in relation to the comparable beam treatment, the neutral axis position and second moment of area I are indicated on Fig.90.

5C NUMERICAL APPLICATION OF THE ANALYSIS TO PARTICULAR CIRCULAR SECTION, UNIFORM THICKNESS OPEN TOROIDAL SHELLS ASSOCIATED WITH THE GEOMETRY OF IMPULSE WATER TURBINE BUCKETS

The equations pertinent to the circular section, uniform thickness shell have been applied mainly to the following two particular cases:-

Case I $a = 2.7"$, $b = 2.7"$, $h_o = 0.27"$, edge at $\xi = 13^o$, $\lambda = 1$, $\nu = 0.31$, $\mu = 32.9$.

Case II $a = 3.5"$, $b = 2.1"$, $h_o = 0.2$, edge at $\xi = 5^o$, $\lambda = 0.6$, $\nu = 0.3$ $\mu = 20.8$.

In the former case the geometry and material properties are associated with those of a bucket of a $16\frac{1}{2}$ in.p.c.d. aluminium or cast steel Turgo wheel. In the latter, the geometry and material properties are associated with those of a high tensile bronze half-bucket of a 21 in.p.c.d. Pelton wheel, as discussed in Chapter 7. Numerical results of the in-plane bending analyses of the two cases are presented here.

In selecting a uniformly thick, circular meridian shell to represent a bucket of the $16\frac{1}{2}$ in.Turgo wheel, two main criteria have to be reconciled. The uniform circular shell has to be as close a geometrical representation as possible, but requires to conform to proportions suitable for solution using existing tables, ref.(64). Comparing meridional and circumferential curvatures of the bucket sections, Fig.9, and from Figs.11 and 12, it is clear that $\lambda < 1$ is inappropriate. Taking $\lambda = 1$ then, and locating by Fig.12, the position of the axis of revolution relative to the meridional sections of Fig.11, the representative circular meridian may be drawn as shown on Fig.91. This gives $a = b = 2.7$ in. The thickness $h_o = 0.27$ in. is selected such that $b/h_o = 10$, being an acknowledged limit of the accurate applicability of thin shell theory. This gives the "thickest" associated/

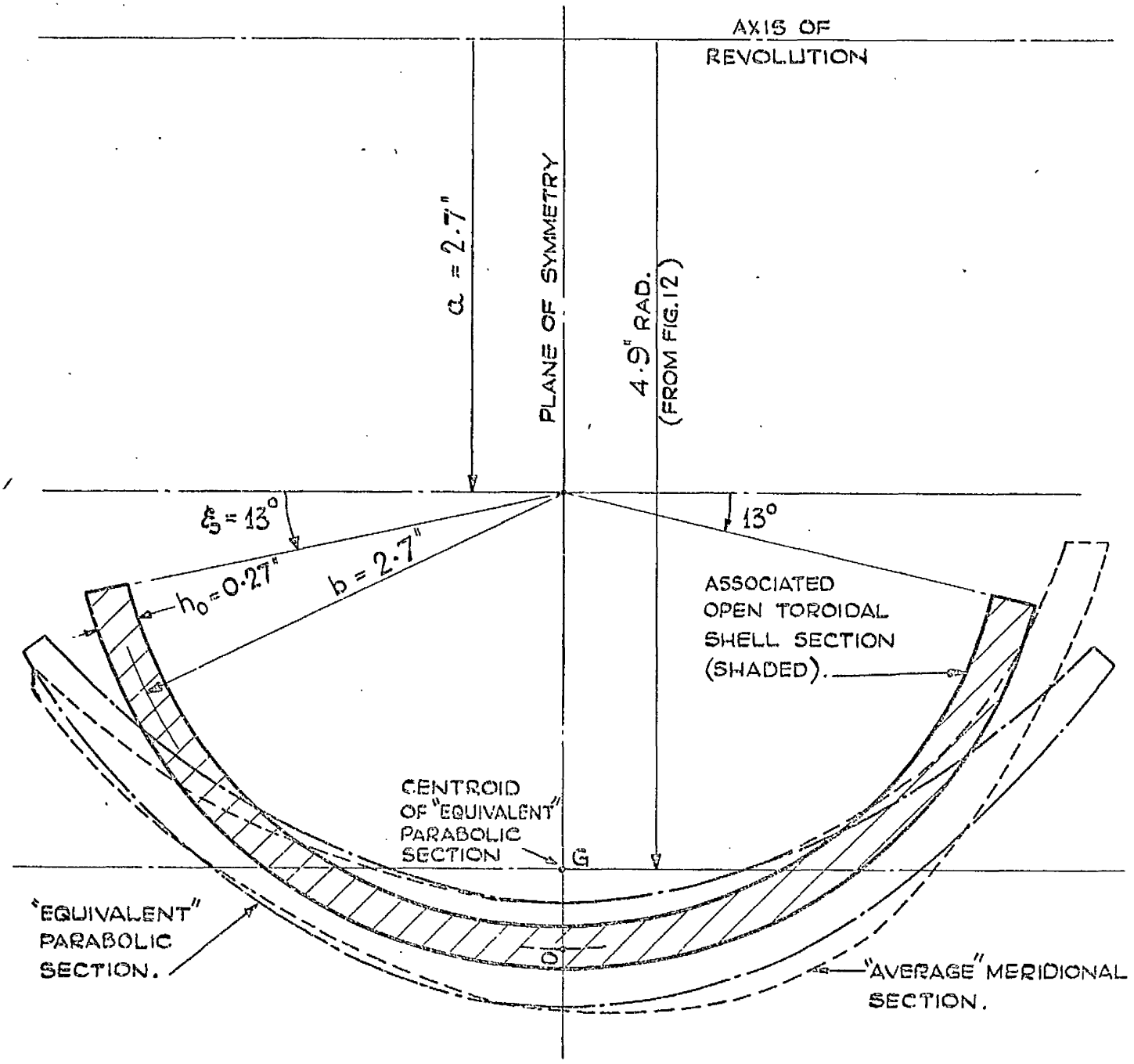

FIG. 91. COMPARISON OF THE "AVERAGE" MERIDIONAL SECTION AND "EQUIVALENT" PARABOLIC SECTION PERTINENT TO A BUCKET OF 16½" P.C.D. TURGO WHEEL, WITH MERIDIONAL SECTION (SHADED) OF THE ASSOCIATED CIRCULAR-MERIDIAN, UNIFORM THICKNESS, OPEN TOROIDAL SHELL (CASE I). (SEE FIGS. 11, 12 AND 89).

associated thin shell. Finally the edge angle $\xi = 13^{\circ}$ is taken as the nearest integer angle such that the second moment of area I of the uniform circular section approximates the corresponding quantity for the "equivalent" parabolic section. Although the associated uniform circular open toroidal shell, as shown in Fig.91, is a somewhat remote representation of a Turgo wheel bucket and of an "equivalent" parabolic section bucket, it is not an unreasonably remote one.

The analysis procedure which has been outlined previously, is facilitated in numerical applications, by adopting a tabular scheme under headings corresponding to each function given in the left-hand column of Table 5, together with headings X, Y, X', Y'. Tabulation is then undertaken for various ξ at short regular intervals in the range $\xi_{EDGE} \leq \xi \leq \frac{\pi}{2}$.

For Case I, the main results in the form of stress resultant $N_{\theta}/_{kE}$, stress couples $M_{\theta}/_{kE}$, $M_{\xi}/_{kE}$ and meridian rotation $\beta/_{k}$ are presented graphically in Fig.92, on a base of ξ, for $13^{\circ} \leq \xi \leq 90^{\circ}$. Stress resultants $Q/_{kE}$, $N_{\xi}/_{kE}$ are small and are not shown, although the latter has been determined over the ξ range. From $N_{\theta}/_{kE}$, $N_{\xi}/_{kE}$ and equation (5A.5), the cylindrical neutral surface occurs at:-

$$\xi = 39.7^{\circ}, \text{ giving } \quad r_N = 4.42 \text{ in.} \qquad (5C.1).$$

Applying equations (5A.32) and (5A.7) in equation (5A.8), the integrals in the last equation are evaluated by Simpson's Rule on the basis of the graphs of $N_{\theta}/_{kE}$ and $M_{\theta}/_{kE}$ versus ξ, Fig.92. It is then found from equations (5A.9), (5A.12) and Fig.90, that rigidity factor ρ is given by:-

$$\rho = 0.32 \qquad (5C.2).$$

Examination of Figs.92 and 88(e) reveals that the maximum stress occurs in/

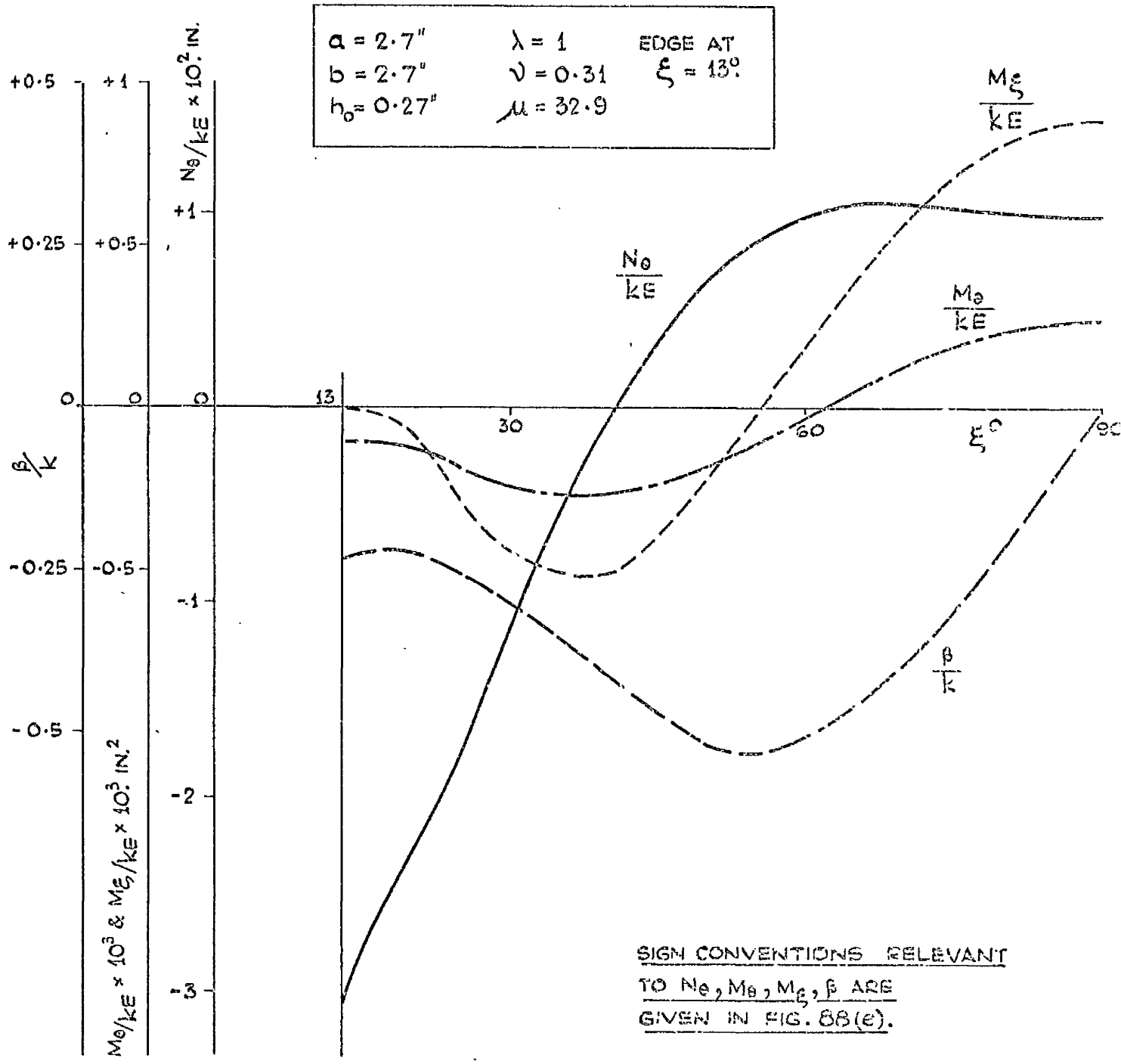

FIG. 92. APPLICATION OF OPEN TOROIDAL SHELL BENDING ANALYSIS TO CASE I, WHICH IS ASSOCIATED WITH 16½ P.C.D. TURGO WHEEL BUCKET. (SECTION ON FIG. 91). DISTRIBUTIONS OF N_θ/kE, M_θ/kE, M_ξ/kE, β/k WITH ξ FOR $13° \leq \xi \leq 90°$.

in the circumferential or Θ direction (i.e. parallel to the edge) at the edge $\xi = 13^{\circ}$ on the concave surface, corresponding to the swept surface of the bucket, Fig.91. The maximum stress is due to:-

$$\frac{N_\theta}{kE} = -3{\cdot}11 \times 10^{-2} \text{ in.} \quad \text{and} \quad \frac{M_\theta}{kE} = -0{\cdot}11 \times 10^{-3} \text{ in.}^2 \qquad (5C.3)$$

From the equivalent of equations (4A.1) and from (5A.15) and related equations, it is found that the maximum stress ratio is:-

$$\frac{\sigma_{s\,MAX.}}{\sigma_{\beta\,MAX.}} = 1.27 \qquad (5C.4)$$

The main results for Case II are similarly shown in Fig.93, for $5^{\circ} \leq \xi \leq 90^{\circ}$. Again by numerical integration in equation (5A.8), it is found for this case, that:-

$$k = 66{\cdot}98 \frac{m}{E} \qquad (5C.5)$$

Thus for subsequent use in Chapter 7, the stress resultants and stress couples are determinable in terms of applied moment m, and in particular, the meridian rotation β at the edge $\xi = 5^{\circ}$, Fig.93, is given by:-

$$\beta_{\xi=5^{\circ}} = -1.31\,k = -87.64 \frac{m}{E} \text{ radians} \qquad (5C.6)$$

From the evaluation of equation (5A.8) in both cases it is found that almost all of the resistance of the shells to applied in-plane bending moments m, is provided by membrane action, bending action accounting for less than 2%. Such proportions are not unexpected, bearing in mind the form of the general solution. Indirect comparison may be made with the proportions of about 80% membrane action, 20% bending action, determined experimentally for Turgo wheel buckets (Table 4, Chapter 4 and Table A6.2, Appendix 6).

The numerical accuracy of the analyses for both cases, Figs.92 and 93, is partly confirmed, since $\int_{\xi\,EDGE}^{\pi/2} N_\theta . d\xi = 0$ for both.

There/

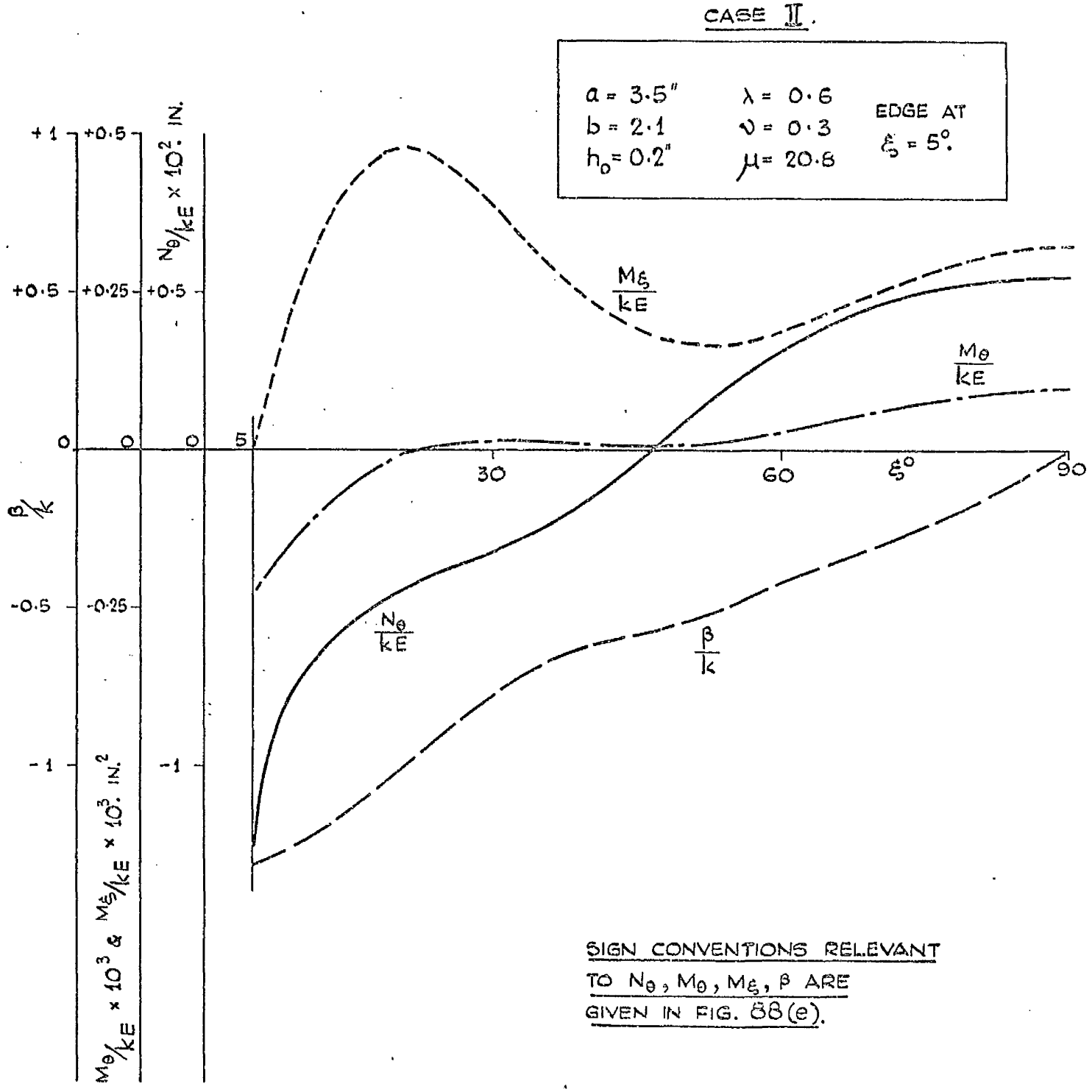

FIG. 93. APPLICATION OF OPEN TOROIDAL SHELL BENDING ANALYSIS TO CASE II, WHICH IS ASSOCIATED WITH 21 IN. P.C.D. PELTON WHEEL BUCKET (SECTION ON FIG. 10
DISTRIBUTIONS OF N_θ/kE, M_θ/kE, M_ξ/kE, β/k WITH ξ FOR $5° \leq \xi \leq 90°$.

There are evident differences in the natures of corresponding graphs for the two cases, this being due in the main, to the difference in the values of the edge angles. This has been revealed as the main cause, by less refined reworkings of Case I with edge angles of $\xi = 0$ and $\xi = 5^{\circ}$. From both reworkings, graphs fairly similar in natures to those of Case II, Fig.93, were obtained. It is plain that, particularly in respect of variations β and M_{ξ}, there is a difference in the relative intensities of the edge effects in the two cases. Near the edges, M_{ξ} is - ve for Case I but + ve for Case II. In both cases, however, M_{ξ} is + ve in the regions of the planes of symmetry $\xi = 90^{\circ}$, indicating meridional bending in these regions, tending to reduce the meridional curvatures, for applied moments m which tend to increase the in-plane curvatures of the shells, Fig.88(e), (c).

The characteristics of the results of both cases are of interest, in respect of stress behaviour of the shells in the circumferential or θ direction. The variations of the membrane stress resultants N_{θ} show a fair resemblance, that of Case II having the more pronounced edge effect. The natures of the circumferential edge couples M_{θ} in both cases (at $\xi = 13^{\circ}$ and $\xi = 5^{\circ}$ respectively) are such as to give bending and membrane stresses parallel to the edges, of similar signs on the concave (or swept) surfaces, and of dissimilar signs on the convex (or unswept) surfaces, (see Fig.91). These stress resultant and stress couple characteristics in the θ direction are partially illustrated in Fig.94, which iterates the sense of the application of in-plane bending moment m, basic to the derivation of the theory. Significant working stresses in a Turgo wheel bucket (and in a Pelton bucket, as is shown in Chapter 7) are associated mainly with in-plane bending moments acting in the sense opposite to that of m. Although direct quantitative comparison cannot be made between measured Turgo wheel bucket stresses and these stress/

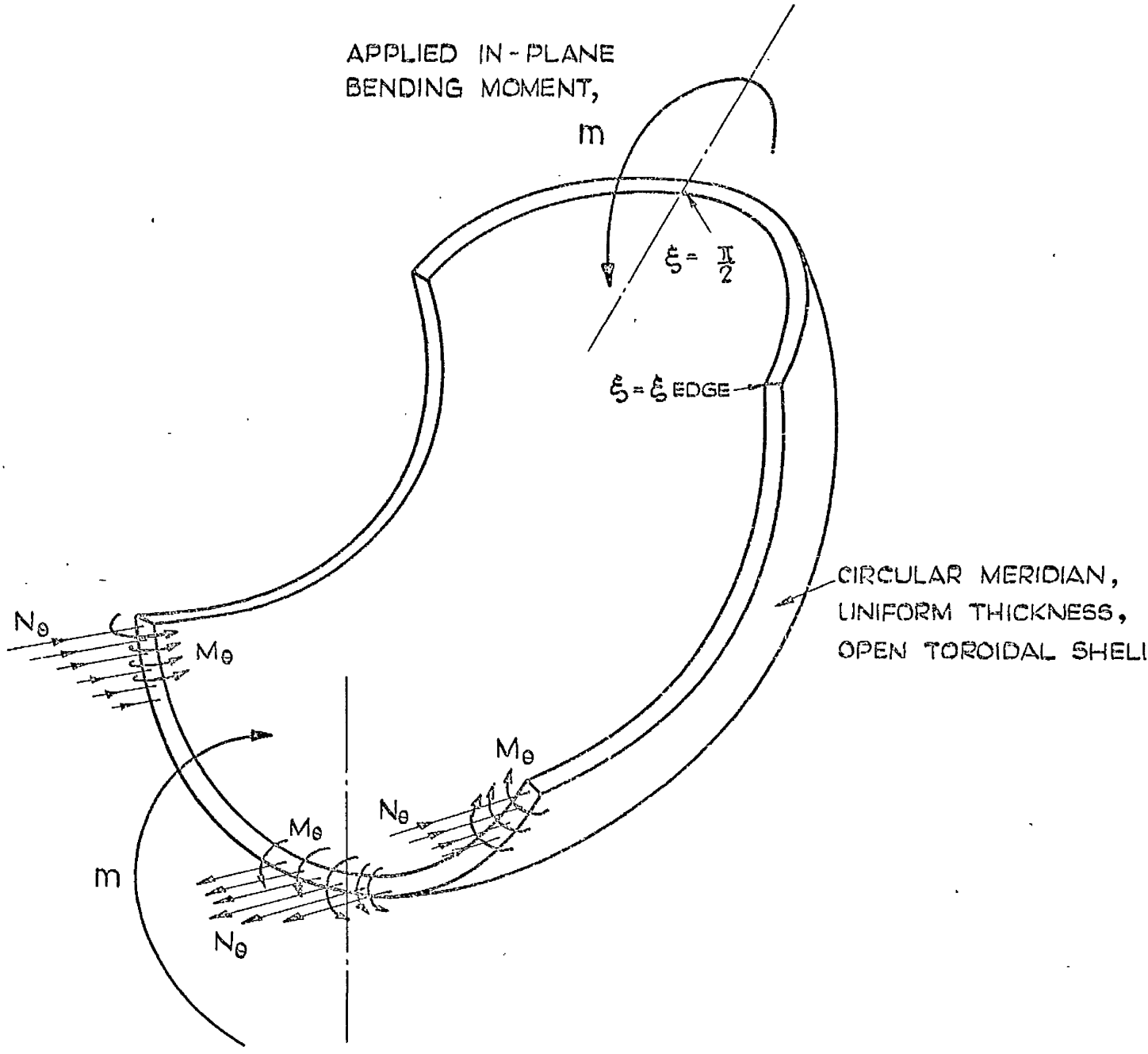

FIG. 94. PARTIAL ILLUSTRATION OF BEHAVIOUR OF CIRCUMFERENTIAL STRESS RESULTANTS N_θ, AND STRESS COUPLES M_θ AS INDICATED BY THE OPEN TOROIDAL SHELL BENDING ANALYSES, CASES I AND II, FIGS. 92 AND 93.

stress results of associated Case I, it is now helpful to consider the theory in relation to m applied in the sense opposite to that shown in Fig.94. Accordingly all the quantities in the results, Figs.92 and 93 will be regarded as having all the signs changed.

As may be seen in Fig.91, the portion of the Turgo wheel bucket meridional section towards the outlet edge, is that which resembles most closely the associated toroidal shell section. It is interesting to compare qualitatively, the measured N_θ curves of Figs. A6.3(c) and 51(b) over these portions of the bucket section (S_M = 4 in. or 5 in. to $S_{M\,MAX}$) with the theoretical N_θ curve (inverted for opposite m) for Case I, Fig.92, and, for additional interest, with the corresponding curve (inverted) for Case II, Fig.93. Taking into account that:-

(a) the bucket section pertinent to Fig.A6.3(c), although identical to the "average" meridional section of Fig.91, is subjected to considerable direct tensile force as well as to in-plane bending moment,

(b) the bucket section pertinent to Fig.51(b), although subjected only to pure in-plane bending moment, is larger than the "average" meridional section of Fig.91, but is geometrically similar to it,

qualitative comparison is good between measured N_θ and theoretical N_θ particularly for Case II with the lesser edge angle. It may be seen in Fig.91 that, for the outlet edge region, an edge angle smaller than 13° might be more appropriate geometrically.

From Figs.92 and 93 with all signs changed, circumferential and meridional total surface stresses have been determined at $\xi = \xi_{edge}$, $\xi = 90^\circ$ and at intermediate values of ξ . These are depicted in Fig.95 as principal stresses on the surfaces of meridional sections of the two shells and are there presented in a form facilitating qualitative comparison with measured principal stresses on meridional sections of Turgo/

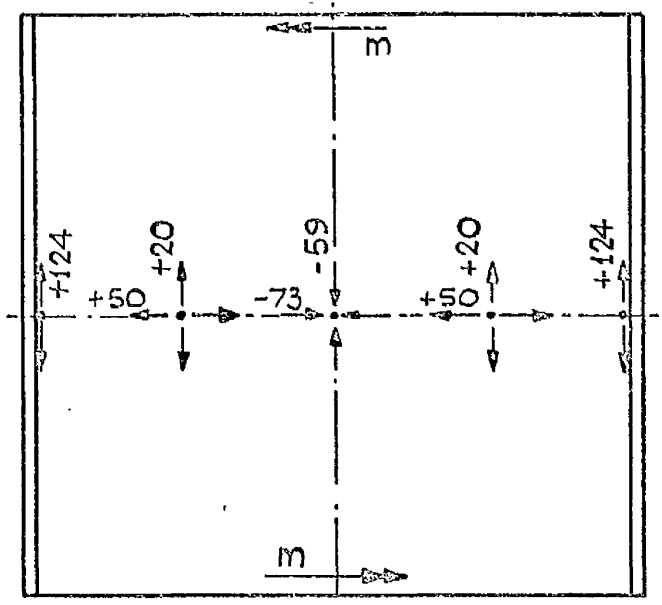

AT LOCATIONS ON CONCAVE (SWEPT) SURFACE.

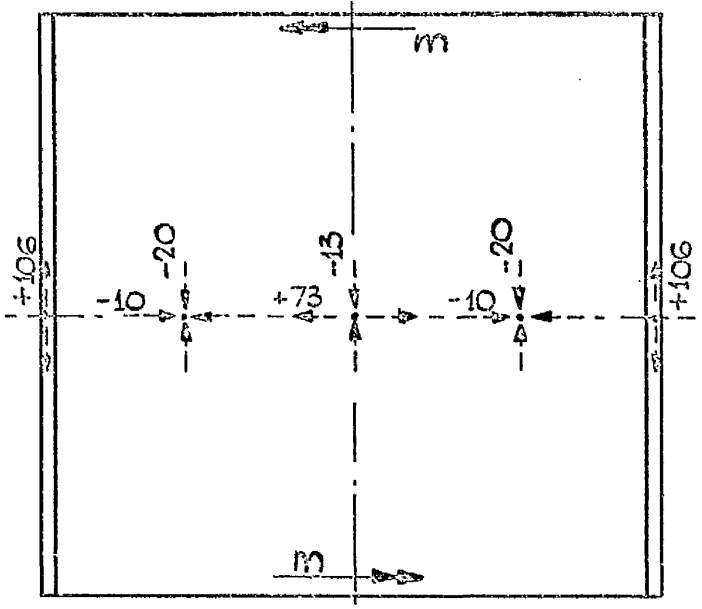

AT CORRESPONDING LOCATIONS ON CONVEX (UNSWEPT) SURFACE.

CASE I. VALUES ARE (MEMBRANE STRESS + BENDING STRESS) $\times 10^3/kE$, BASED ON FIG. 92. (+ TENSION, - COMPRESSION).

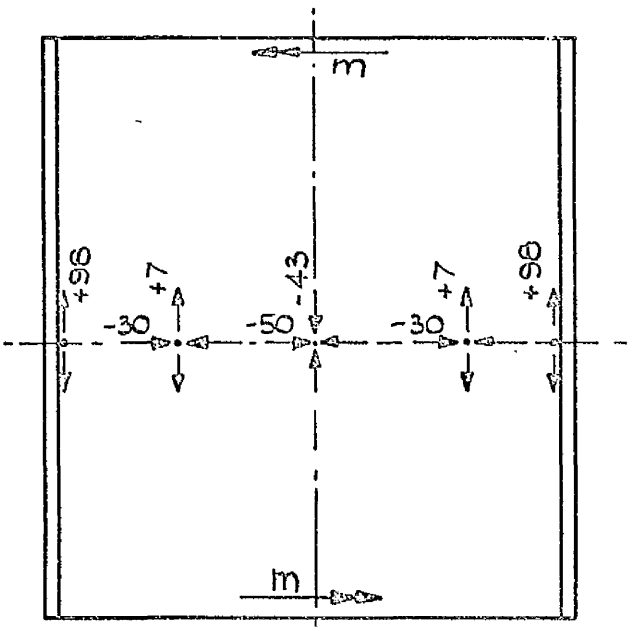

AT LOCATIONS ON CONCAVE (SWEPT) SURFACE.

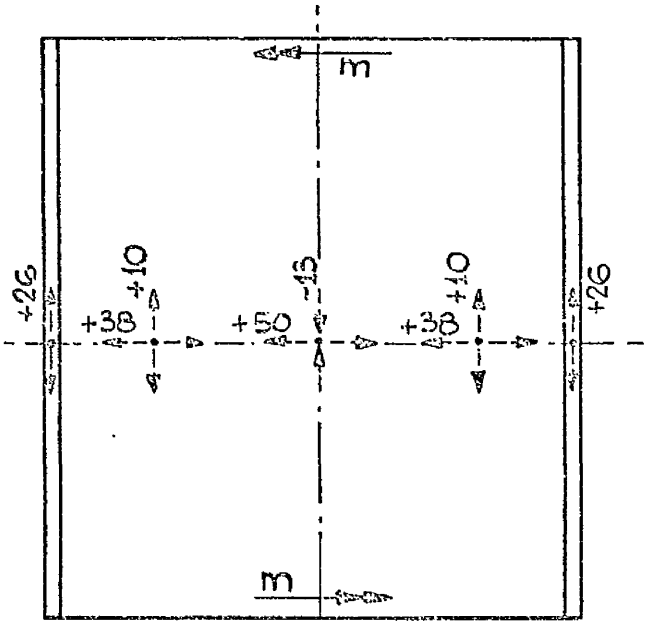

AT CORRESPONDING LOCATIONS ON CONVEX (UNSWEPT) SURFACE.

CASE II. VALUES ARE (MEMBRANE STRESS + BENDING STRESS) $\times 10^3/kE$, BASED ON FIG. 93. (+ TENSION, - COMPRESSION).

NOTE :- ON ACCOUNT OF DIRECTION OF APPLIED MOMENT m, SIGNS HERE ARE OPPOSIT TO THOSE OF THE CORRESPONDING QUANTITIES IN FIGS. 92 & 93.

FIG. 95. THEORETICAL PRINCIPAL STRESSES ON THE SURFACES OF MERIDIONAL SECTIONS OF OPEN TOROIDAL SHELLS, CASE I AND CASE II. VIEWS AND STRESS LOCATIONS CORRESPOND ROUGHLY TO THOSE OF FIG. 46, WITH WHICH QUALITATIVE COMPARISON MAY BE MADE.

Turgo wheel buckets. In particular, the experimental data of Fig.46 and perhaps to a lesser extent, that of Figs.63, 64 and 82, 83 are relevant. Comparing these experimental data with the theoretical principal stresses of Fig.95, it is evident that qualitative agreement is good.

Although quantitative comparison cannot rationally be made, it is worth noting that the proportions of bending stresses to membrane stresses at the edges, are much lower for the theoretical shell cases, than in the experimental bucket results. For the edges in Cases I and II, the ratios bending stress/membrane stress, are 0.08 and 0.58 respectively, while experimental ratios of 1.27 and 1.00 are found for the two edges of the Turgo wheel bucket, Fig.46. Higher theoretical ratios of 1.47 and 0.71 were found at the edges for the reworkings of Case I with edge angles of $\xi = 0$ and $\xi = 5^{o}$ respectively. The ratios all, of course, refer to bending and membrane stresses of the same sign on the concave or swept surfaces.

The membrane stress resultants N_{θ}/kE for both cases, are presented in Fig.96, replotted on the circular meridian sections. This is to illustrate more clearly how these circumferential membrane stress distributions compare with a linear stress variation pertinent to the application of simple beam theory.

The basis of the derivation of the shell theory developed in this chapter, is the consideration of a sector element of the shell, subjected to pure in-plane bending moment. The theory, however, is assumed to be applicable to cases of continuously varying in-plane bending moment.

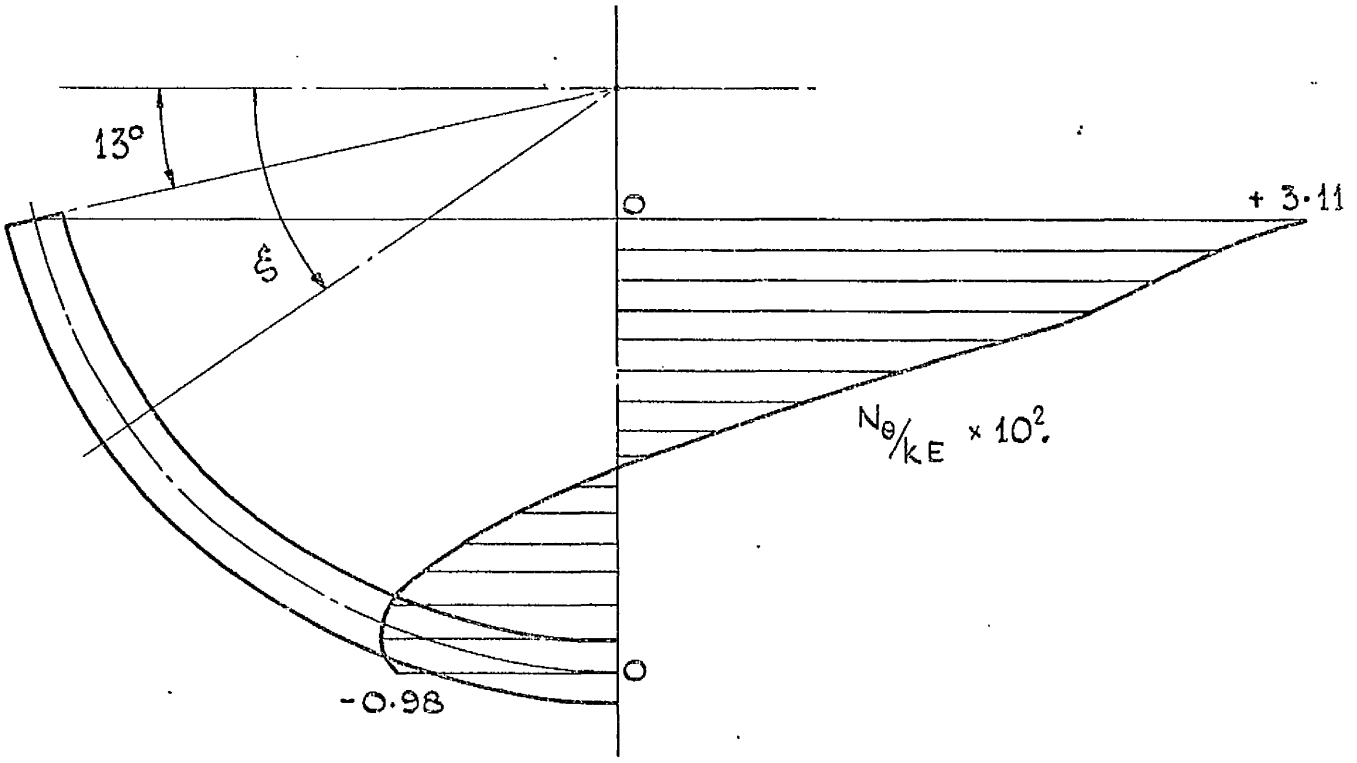

CASE I.- FROM FIG. 92, (SIGNS CHANGED).

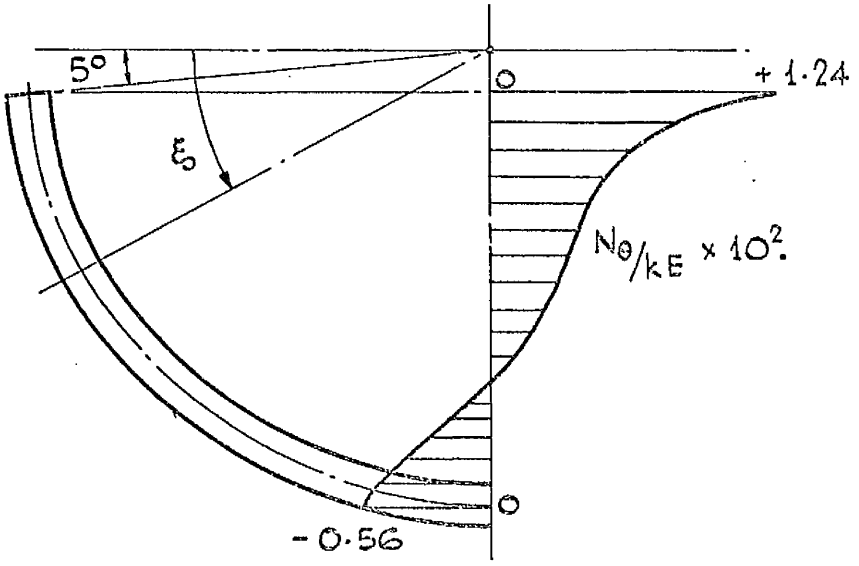

CASE II.- FROM FIG. 93, (SIGNS CHANGED).

FIG. 96. DISTRIBUTIONS OF CIRCUMFERENTIAL MEMBRANE STRESS RESULTANTS N_θ/kE, OVER THE CIRCULAR MERIDIAN SECTIONS OF OPEN TOROIDAL SHELLS, CASES I AND II.

CHAPTER 6.

THE TURGO IMPULSE WHEEL.
APPROXIMATE METHOD OF MODIFYING THEORETICAL ANALYSIS TO TAKE ACCOUNT OF THE SHELL BEHAVIOUR OF THE BUCKET.
COMPARISON OF THEORETICAL AND EXPERIMENTAL RESULTS.

6A APPROXIMATE METHOD OF MODIFYING THEORETICAL ANALYSIS TO TAKE ACCOUNT OF THE SHELL BEHAVIOUR OF THE BUCKET

The uniformly thick, circular section open toroidal shell, Fig.91, associated with the bucket of the $16\frac{1}{2}$ in. p.c.d. Turgo wheel and with the "equivalent" parabolic section bucket, has a rigidity factor $\rho = 0.32$, given by equation (5C.2) of the previous chapter. As would be expected, the shell is therefore appreciably less rigid or stiff under a given in-plane bending moment, than would be indicated by the application of simple beam theory. This finding calls to mind the relatively high in-plane flexibility of the Turgo wheel buckets, indicated by the experimental results of chapter 4.

Assuming now that rigidity factor $\rho = 0.32$ applies also to the "equivalent" parabolic section bucket, an approximate method is prompted whereby the beam theory treatment of chapter 3 may be modified to take into account the shell behaviour of the buckets. The basic approach of chapter 3 for determination of the working actions on a bucket, remains unaltered. In the calculations for the actions however, the modification entails the replacement of the "beam" flexural rigidity EI_{YY} by the corresponding "shell" flexural rigidity ρEI_{YY} throughout all the bucket in-plane bending terms. This type of modification is analogous to that applied in problems involving closed toroidal shells or pipe-bends, and playing a prominent rôle in pipework flexibility analysis.

Although in-plane bending is the most significant action on the bucket, the intensity of this action is dependent on the three-dimensional restraints exerted on the bucket by the offset rim. The modification of the beam theory treatment should therefore be carried a stage further, and the rigidity of the bucket as a shell should be considered for actions perpendicular to the plane of the wheel and of the open toroidal shell associated/

associated with the bucket, as well as for in-plane actions. In particular, the rigidity should also be considered for bending and torsion in transverse planes. No solution appears to have been given for the open toroidal shell subjected to moment action in a transverse plane.

VIGNESS[69] has analysed the case of the pipe-bend or closed toroidal shell under moment in planes perpendicular to the plane of the bend, and his findings may be used to deduce roughly what the corresponding open shell theoretical solution might indicate. His findings are that with regard to the bending moment in a transverse plane, the rigidity factor is exactly the same as for the in-plane bending case, and with regard to the twisting moment on the sections, the rigidity factor is unity, i.e. the torsional stiffness is the same for both beam theory and shell theory.

The crux of the shell theory in both open and closed cases is the deformation of the cross-section as a result of the circumferential or longitudinal stresses due to bending. For transverse bending moment on the closed shell, according to VIGNESS[69], the circular section deforms into an ellipse with principal axes at 45^{o} to the plane of the shell. By reasoning along lines similar to those of VIGNESS[69] in the corresponding open shell case, the meridional section would probably also deform into a shape like part of such an ellipse, one edge of the section moving nearer the axis of revolution of the shell, and the other edge receding from it. As a result of this deformation, the "shell" would be more flexible than the corresponding "beam". The second moment of area of the section relevant to the transverse bending moment is much greater than that relevant to the in-plane moment, whereas in the closed shell case the second moments of area are equal. From this viewpoint the open shell relationship might be expected to differ from that of the closed shell case, and/

and yet in both it is clear that the "shell" will be more flexible than the corresponding "beam". In any event, in view of the fact that, for an "equivalent" parabolic section bucket with which an open toroidal shell is associated, the strain energy due to bending in a transverse plane is invariably a very small proportion of the total strain energy (Table 2, section 3B iv, chapter 3) no significant error is incurred here by assuming that the relationship established for the closed shell case applies to the open shell case, i.e. for bending in a transverse plane the rigidity factor is the same as that for in-plane bending.

The torsional stiffness of the closed shell is indicated by VIGNESS[69] to be the same as that given by beam or simple torsion theory. This is reasonable since the torsional stiffness in the closed shell case is quite dissociated from the longitudinal stresses which induce deformation of the cross-section, and is related only to the shear stresses on the section. The open shell case, however, differs in that the "beam" torsional stiffness comprises two components, one due to St. Venant torsion therefore associated only with shear stress on the meridional section, the other due to warping restraint and therefore associated with circumferential or longitudinal direct stress as well as with shear stress. It is only in respect of this latter component, being related to longitudinal direct stress, that the "shell" torsional stiffness might be expected to differ from the "beam" torsional stiffness in the open shell case.

It is interesting to note from Table 2, for an associated "equivalent" parabolic section bucket, that, in the strain energy due to torsion with warping restraint, the St.Venant torsion component is invariably predominant, the strain energy due to that component being never less than 7 times that due to the corresponding warping restraint component. Lacking knowledge of the extent to which the warping restraint component of strain energy will be affected by the "shell" section deformation, since this/

this component is evidently relatively small here, it would seem that no appreciable error is incurred by neglecting this effect entirely and assuming that the "shell" torsional stiffness of the open shell is the same as that given by "beam" theory.

In summary then, the relationships established by VIGNESS[69] for the closed shell problem, are assumed to apply to the corresponding open shell case, that is to an open toroidal shell subjected to moment action in a transverse plane. These relationships are, that for bending moment in a transverse plane the rigidity factor is ρ, the same as for in-plane bending moment, and for twisting moment on the meridional sections the rigidity factor is unity. Assuming that these relationships also apply to the associated "equivalent" parabolic section bucket, the approximate method of modifying the beam theory calculations of chapter 3 to take account of bucket shell behaviour consists, in its final form, in replacing "beam" flexural rigidities EI_{YY} and EI_{ox} by the corresponding "shell" flexural rigidities ρEI_{YY} and ρEI_{ox} respectively, throughout all bucket in-plane and transverse plane bending terms. All other terms in the calculations remain unaltered.

In the centrifugal stress calculations for example, all the free rotating bucket displacement expressions of section 3B ii and all the assembly action displacement expressions of section 3B iv will be subject to these modifications in respect of bending flexural rigidities. Applied for the $16\frac{1}{2}$ in. cast steel Turgo wheel under normal working conditions, and taking rigidity factor $\rho = 0.32$ for the bucket, this will result in four simultaneous equations similar to, but differing numerically from, equations (3B.81) to (3B.84) inclusive. Solving these modified equations together with (3B.85) to (3B.88) inclusive, will then give the assembly actions relevant to the approximate shell basis treatment.

This modification procedure has been carried out for the numerical centrifugal/

centrifugal calculations of part 3B, and the following approximate shell basis assembly actions on the bucket have been found:-

$$F_{R2} = -1042.57 \text{ lb.}, \qquad F_{T2} = +101.83 \text{ lb.}, \therefore M_{P2} = (F_{T2} \cdot q) = +1361.12 \text{ lb in.}$$

$$M_{R2} = +241.64 \text{ lb in.}, \qquad M_{T2} = -388.02 \text{ lb in.} \qquad (6A.1)$$

The corresponding shell basis assembly actions, suffix 1, on the rim, have the same values as these but have opposite signs.

These actions, equations (6A.1), may be compared with the corresponding beam basis actions given subsequent to numerical equations (3B.81) to (3B.88) inclusive.

The resulting shell basis, total centrifugal in-plane bending moment $M_{\theta Y.TOT}$ and total centrifugal direct force $P_{\theta.TOT}$ have been determined for various θ, and their distributions with θ throughout the bucket are shown in Fig.97. The corresponding beam basis quantities are shown for comparison. In general, shell basis values are seen to be less than corresponding beam basis values.

While the rigidity factor of the "equivalent" parabolic section bucket may fairly reasonably be taken as that of the associated uniformly thick open toroidal shell, Fig.91, it would hardly be valid or meaningful to proceed to the determination of theoretical stresses on the same associated open toroidal shell basis. Such could only be considered for an associated open toroidal shell of varying thickness, simulating the bucket thicknesses fairly closely.

6B COMPARISON OF THEORETICAL AND EXPERIMENTAL RESULTS

Although the theoretical approach of chapter 3 is fairly approximate and of an order-of-magnitude character, the essential features of the Turgo wheel geometry and working loadings are contained therein. In its modified form, the approach also considers in essence, the shell behaviour of the bucket. Comparison of theoretical results with results obtained from the experimental stress analyses and presented in chapter 4, is therefore of much interest. This is now presented for the $16\frac{1}{2}$ in. cast steel Turgo wheel. It is called to mind that the relevant experimental results for centrifugal actions and stresses, are 3 times the corresponding results given for the aluminium wheel in chapter 4. Relevant experimental stresses for approximate jet loading are the same as those given for the aluminium wheel.

6B i Comparison of theoretical and experimental centrifugal actions and stresses

With regard to total in-plane bending moment and direct force actions on bucket meridional sections, the experimental results M_Y and P', Fig.67, have been transferred to Fig.97 for direct comparison with appropriate theoretical results. The accuracy of these experimental results from the wheel, may not be quite as good as that of the corresponding experimental results from the tests on single buckets, reference Table 3, section 4A ii, chapter 4. However, even allowing a maximum error of an order somewhat higher than the errors associated with the corresponding results in Table 3, agreement between the experimental results and the corresponding theoretical shell basis results on Fig.97, is remarkably good. If the experimental errors show the same trend as those of Table 3, then the plotted experimental points may be somewhat on the high side, thus further favouring the shell basis theory rather than the beam basis theory. It appears that the latter faithfully predicts the natures of the variations of actions $M_{\theta Y.TOT}$ and $P_{\theta.TOT}$ with θ, but, when unmodified, tends to overestimate these actions.

The theoretical free rotating in-plane bending moment curve M_θ, Figs.16 and 23, is repeated in Fig.97 for the following reasons:-

(1) M_θ is derived simply from co-planar statics, and is dependent only on the initially assumed bucket geometry. It is therefore very likely to correspond accurately to its counterpart on an actual bucket.

(2) The influence of the variation M_θ dominates all distributions with θ, of significant theoretical and experimental centrifugal stresses on the bucket.

Impressive evidence of the restraint exerted on the bucket by the rim, is/

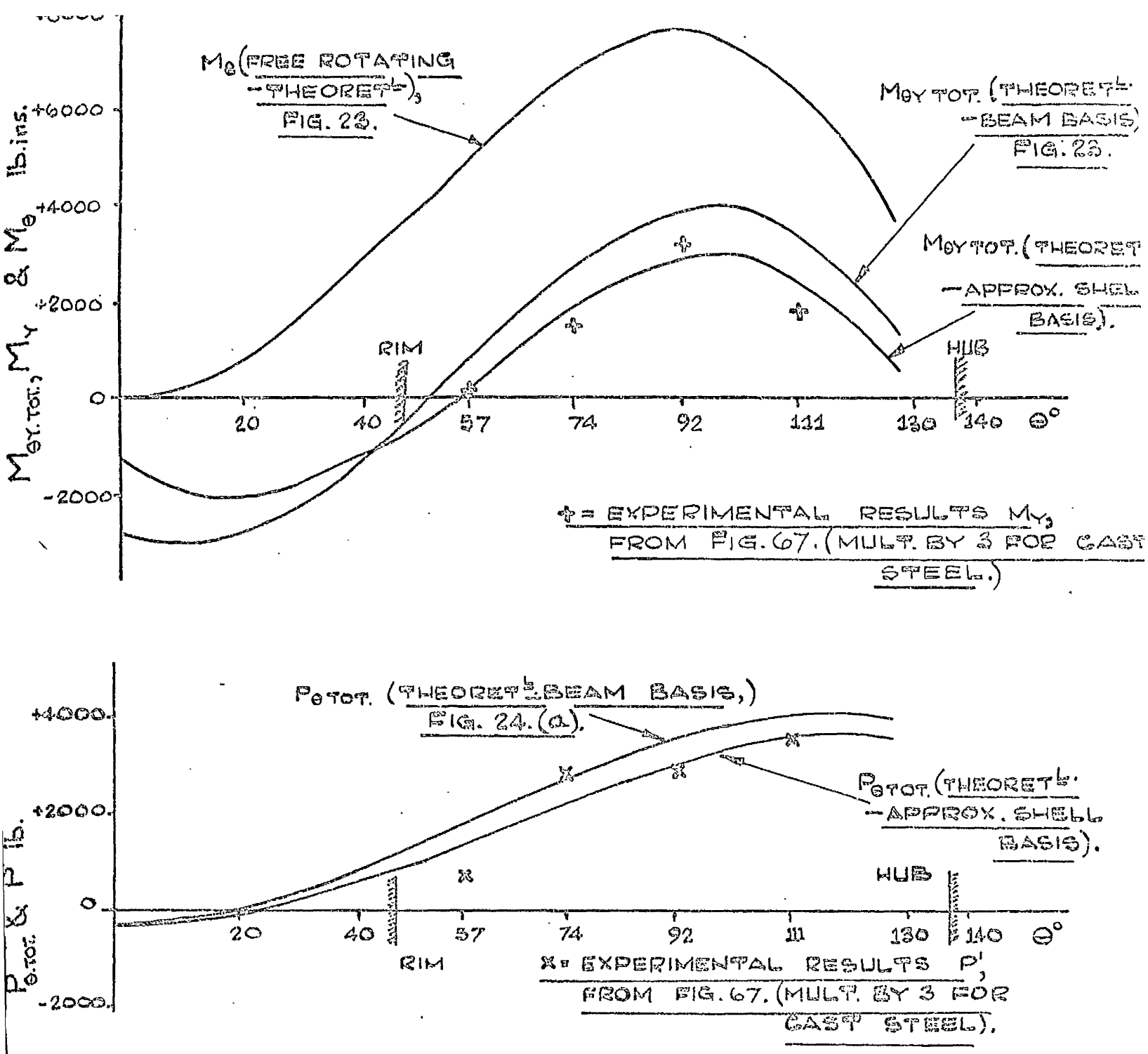

FIG. 97. DISTRIBUTIONS WITH θ OF CENTRIFUGAL ACTIONS ON MERIDIONAL SECTIONS OF BUCKET OF 16½ IN. CAST STEEL TURGO WHEEL AT NORMAL WORKING SPEED. COMPARISON OF IN-PLANE BENDING MOMENTS MθYTOT. THEORETICAL, BEAM (FIG 23.) AND APPROXIMATE SHELL BASES, AND MY EXPERIMENTAL (FIG. 67); AND OF DIRECT FORCES PθTOT THEORETICAL, BEAM (FIG. 24(a)) AND APPROXIMATE SHELL BASES, AND P' EXPERIMENTAL (FIG. 67).

is provided by the ordinates of the experimental points M_Y, Fig.97, in relation to the curve M_θ.

Characteristic of the shell behaviour of the bucket, as recorded by experiment, are the moments along the edges, resulting in markedly different edge stress values at corresponding points on swept and unswept surfaces. In consequence of this, comparison of the experimental edge stresses with the corresponding theoretical beam basis stresses of chapter 3, is rather difficult of interpretation in some respects. Fig.98 gives a comparison of the theoretical and experimental edge stresses. The most significant experimental values, (Fig.66), are plotted, being those on the swept surface, and the membrane experimental values are also plotted.

The experimental results substantiate several important aspects of the beam theory treatment. It is evident from Fig.98 that, in respect of bucket edge stresses, the theory correctly predicts the following:-

(1) The location of the maximum stress, at about $\Theta = 94^\circ$ on the outlet edge.

(2) Different distributions on the two edges, the outlet edge values being greater for the most part, than corresponding inlet edge values.

(3) The general natures of both swept surface and membrane distribution.

The fact that beam theory treatment also closely predicts the magnitude of the maximum stress in the wheel (+ 8750 lb/in^2, theoretical, + 9480 lb/in^2, measured) seems slightly fortuitous, although it may reflect the tendency of the theory to overestimate the magnitudes of significant actions $M_{\theta Y.TOT}$ and $P_{\theta.TOT}$ on the bucket. From the shell theory of chapter 5, the shell/beam maximum stress ratio, equation (5A.15) would always be expected to exceed unity. It would therefore be expected in general, that, for a given in-plane bending moment, a swept surface experimental edge stress value would exceed the corresponding value/

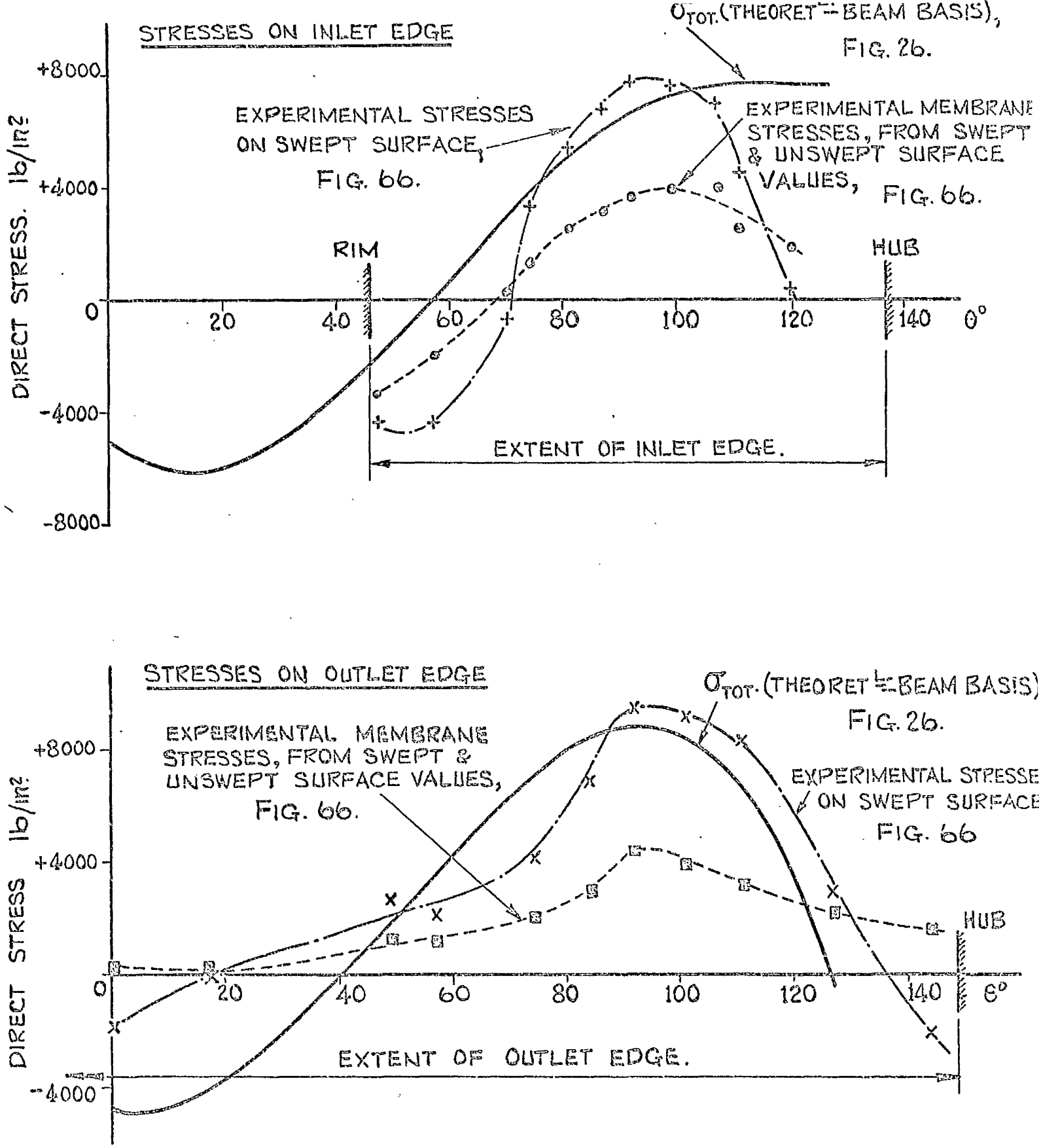

FIG. 98. DISTRIBUTIONS WITH θ OF CENTRIFUGAL STRESSES ON EDGES OF BUCKET OF 16½ IN. CAST STEEL TURGO WHEEL AT NORMAL WORKING SPEED. COMPARISON OF $\sigma_{TOT.}$ THEORETICAL BEAM BASIS (FIG. 26) AND CORRESPONDING EXPERIMENTAL STRESSES ON SWEPT SURFACE AND EXPERIMENTAL MEMBRANE STRESSES. (FIG. 66). FOR CAST STEEL, EXPERIMENTAL VALUES ARE x 3 THOSE ON FIG. 66.

value given by application of beam theory. On this basis, a difference greater than that found, might have been anticipated between the experimental and theoretical maximum stresses.

In the beam theory treatment, torsion warping restraint direct stress is a component in the differentiation of the two edge stress distributions, Figs.24(c) and 26. From the experiments on single buckets, section 4A iii, chapter 4 and Figs.52 to 54, it is reasonable to presume that experimental results Fig.98 are influenced by torsion warping restraint in some minor measure, although no such influence is detectable.

Prior to comparing theoretical and experimental stresses on the rim, it should be noted from equations (6A.1) of the previous section, that the theoretical rim stresses relevant to bucket beam theory treatment, are subject to modification as a result of altering the bucket flexural rigidities to take shell behaviour into account. Taking the modified actions, equations (6A.1), with signs changed, the "bucket shell basis" total theoretical rim stresses have been calculated. These are shown in Fig.99, together with the corresponding "bucket beam basis" theoretical values from Fig.27, and the corresponding circumferential experimental values from Fig.69. It is seen from Fig.99 that, on average, the experimental results rather favour the "bucket shell basis" theoretical results, but, in the light of the theoretical assumptions pertinent to the rim and its connection with the buckets, agreement between the experimental stresses and either set of theoretical stresses cannot but be regarded as remarkably good, both in respect of stress magnitudes and the natures of distributions.

Concerning stresses in the hub, the small order of the experimental values in Fig.71 is in accord with the theoretical predictions made in section 3B v, chapter 3.

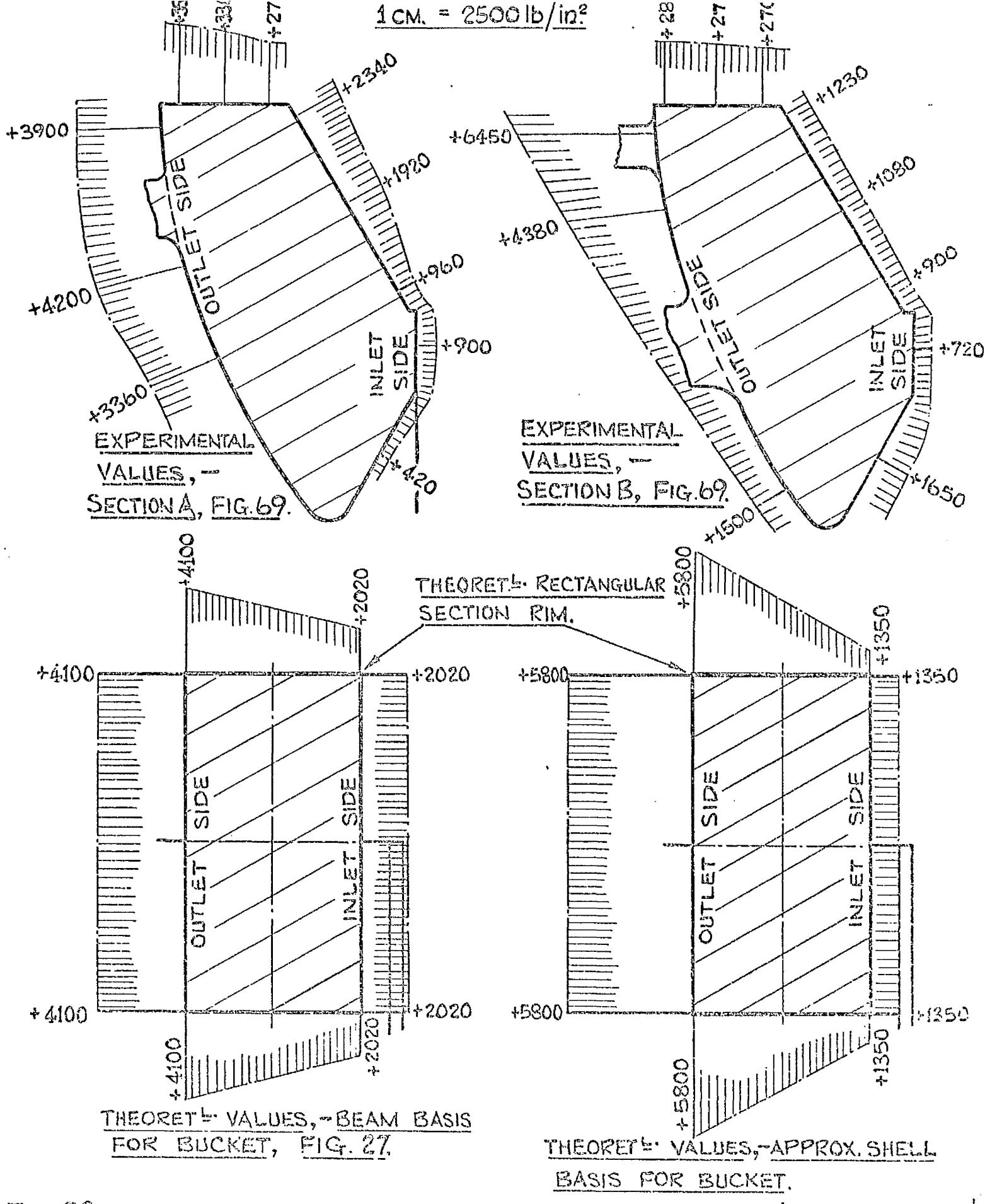

FIG. 99. CENTRIFUGAL CIRCUMFERENTIAL STRESSES (lb/in²) ON RIM OF 16½ C.S. TURGO WHEEL AT NORMAL WORKING SPEED. COMPARISON OF THEORETICAL (BEAM & APPROX. SHELL BASES) AND CORRESPONDING EXPERIMENTAL VALUES (≈3 THOSE ON FIG. 69).

6B ii Comparison of theoretical and experimental approximate jet loading stresses

There are two main features of the beam theory approximate jet loading stress analysis of chapter 3, rather at variance with associated conditions pertinent to the appropriate experimental results of chapter 4. These circumstances might be expected, in some measure, to influence adversely the correspondence of theory with experiment. The features are:-

(1) The assumed theoretical approximate jet loading Fig.30. As mentioned in chapter 4, this differs in distribution from the simulated jet loading applied in the experiments, Figs.76, 78, etc.

(2) The replacement in theory, of the actual restraint on the jet-loaded bucket at the rim, by the restraint of a 180° fully-fixed arch, section 3C iii, Figs.32 and 33.

Despite these points of difference, and despite the experimental revelation of the nature of the supporting rôle played by the bucket — a factor quite foreign to the postulates of section 3C iii, — there is a considerable degree of experimental support for several aspects of the theory. With regard to edge stresses, comparing appropriately the theoretical curves of Fig.37 with the experimental results Figs.84, 85, it is evident that the theory correctly predicts different distributions on the two edges, and the general natures of swept surface distributions. It correctly predicts the location of the maximum stress, on the outlet edge at its junction with the hub, and also closely predicts the magnitude of this maximum stress in the wheel, (+ 4800 lb/in^2., theoretical, + 5270 lb/in^2., measured). The accuracy of this last prediction is rather adventitious, but confirms that this theoretical approach is not entirely devoid of merit.

It is worth calling attention to the relatively high membrane stress indicated by experimental results Fig.84, in the maximum stress region, i.e./

i.e. on the outlet edge at $\Theta = 144^{\circ}$, near the edge/hub junction. This appreciable membrane stress may reflect the influence of torsion warping restraint in the maximum stress area.

Comparison of the conditions relevant to theoretical results Fig.37 and experimental results Fig.84 is of interest. Both sets refer to a bucket subjected only to approximate jet loading of 2000 lb resultant. The theoretical rim restraint condition Fig.37, is due to the 180° fully-fixed arch, while the corresponding experimental condition Fig.84, is of course, the actual one of restraint exerted by the rim supported by 21 unloaded buckets. The fact that in general, experimental stresses Fig.84, are considerably smaller than their theoretical counterparts Fig.37, tends to confirm the expectation expressed in section 3C iii, that the theoretical fully-fixed arch would offer less restraint than the actual system. The magnitudes of the theoretical stresses are more in accord with those of the corresponding experimental maximum total swept surface stresses, Fig.85.

A main disadvantage of the theoretical approach of chapter 3, however, is its lack of realism, especially in respect of its inability to predict bucket supporting stresses. A more realistic approximate theoretical treatment which overcomes this difficulty is detailed in Appendix 7. This is based on the ideas underlying the "unrealistically flexible restraint" case (section 3C v, Fig.39) wherein restraint of the loaded bucket at the rim, is assumed to be provided by two other co-linear buckets. In brief, this more realistic approach assumes that a loaded bucket is restrained at the rim by all the other 21 buckets, regarded as co-linear with the loaded one, and each exerting equal restraint. As in section 3C v, the pertinent restraining actions, and so their effects, are determined from results of the fully-rigid restraint case (Fig.39). Actions equal and opposite to the restraints on the loaded bucket, are carried/

carried by the 21 supporting buckets in equal measure, so actions on a bucket acting in a supporting capacity may be assessed.

In presenting the more realistic theoretical treatment, Appendix 7, its application to the wheel subjected to the originally assumed approximate jet loading, Fig.30, has been demonstrated. For comparison with experimental results however, the treatment has been applied for the wheel carrying the approximate jet loading as shown on Fig.100 — a loading assumed uniformly distributed over the hollow of the equivalent bucket and so corresponding more closely to the simulated jet loading of the experiments. In accordance with the explanation in Appendix 7, the ordinates of graph $M_{\theta Y2}$, Fig.101, are $\frac{21}{22}$ times the ordinates of the corresponding "fully-fixed support" graph, Fig.100. Graph $M'_{\theta Y.TOT}$ Fig.101, is then the summation of M_{θ} and $M_{\theta Y2}$ of the same Fig. Finally graph $M_{\theta Y.TOT}$ is given by:-

$$M_{\theta Y.TOT} = M'_{\theta Y,TOT} + \left(\frac{2}{21} \times M_{\theta Y2} \text{ with signs changed}\right),$$

all on Fig.101.

Thus approximate theoretical in-plane bending moment distributions $M'_{\theta Y.TOT}$ and $M_{\theta Y.TOT}$ are obtained, respectively for a bucket carrying direct jet loading only, and for a bucket carrying direct jet loading and acting in support of 2 other directly loaded buckets. The corresponding treatment in respect of direct force actions on the bucket is exactly similar to that for in-plane bending moments and is indicated in Fig.102. Fig.103 then presents distributions of the corresponding direct stresses on the edges of the bucket. Curve σ, for direct jet loading only, is obtained straightforwardly from curves $M'_{\theta Y.TOT}$ and $P'_{\theta.TOT}$, Figs.101, 102(b), and curve σ_{TOT} for direct loading and supporting, is found similarly from $M_{\theta Y.TOT}$ and $P_{\theta.TOT}$ of the same Figs. Fig.103 thus embodies the most significant results from this application of the more realistic approximate theoretical analysis for jet loading stresses.

The/

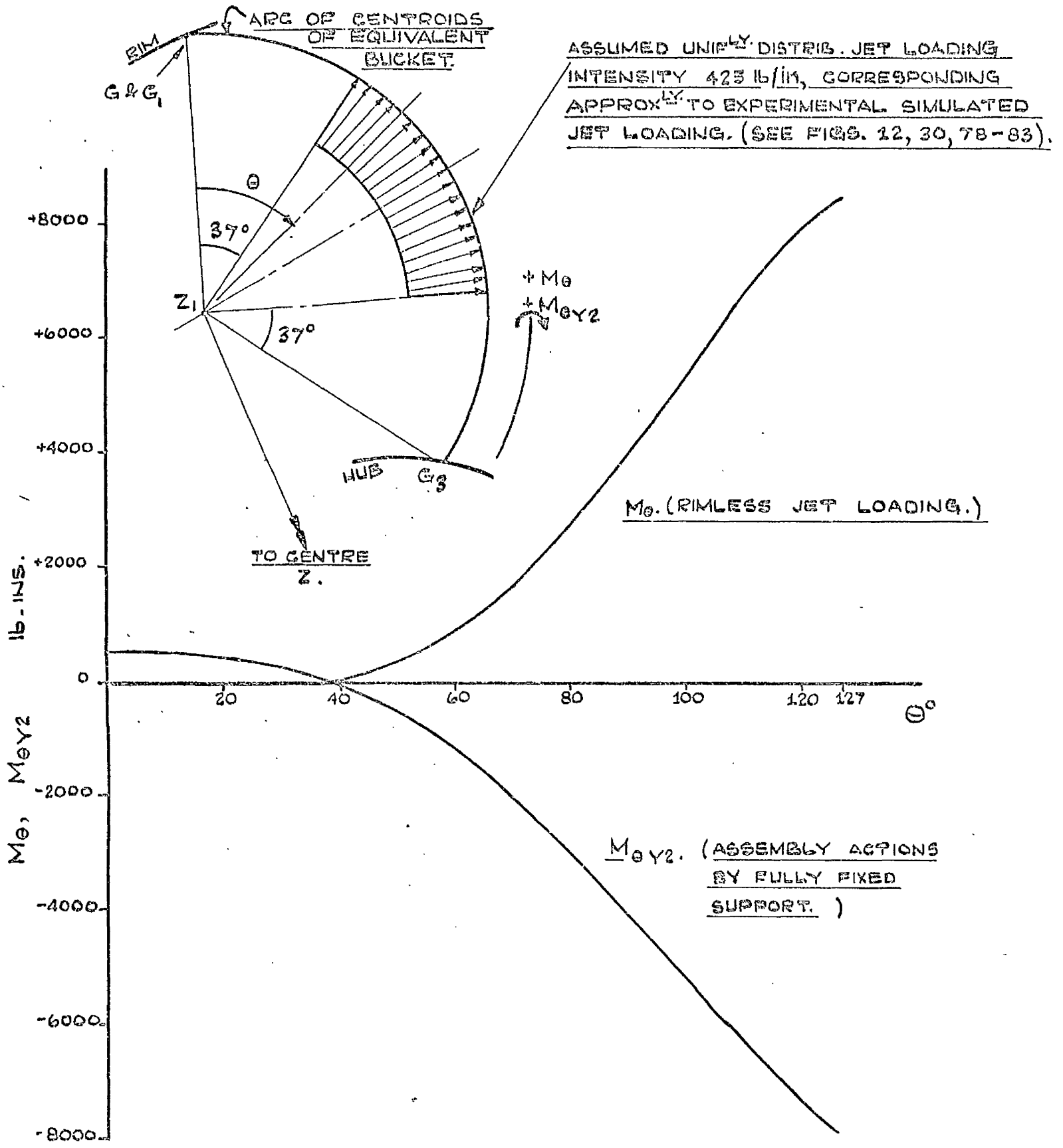

FIG. 100. DISTRIBUTIONS WITH θ OF IN-PLANE BENDING MOMENTS M_θ DUE TO RIMLESS JET LOADING (ASSUMED AS SHOWN), AND $M_{\theta Y2}$ DUE TO THE CORRESPONDING ASSEMBLY ACTIONS EXERTED, ASSUMING A FULLY RIGID SUPPORT AT THE BUCKET/RIM JUNCTION — ALL ON THE "EQUIVALENT" BUCKET OF THE 16½ IN. CAST STEEL TURGO WHEEL UNDER NORMAL WORKING CONDITIONS.

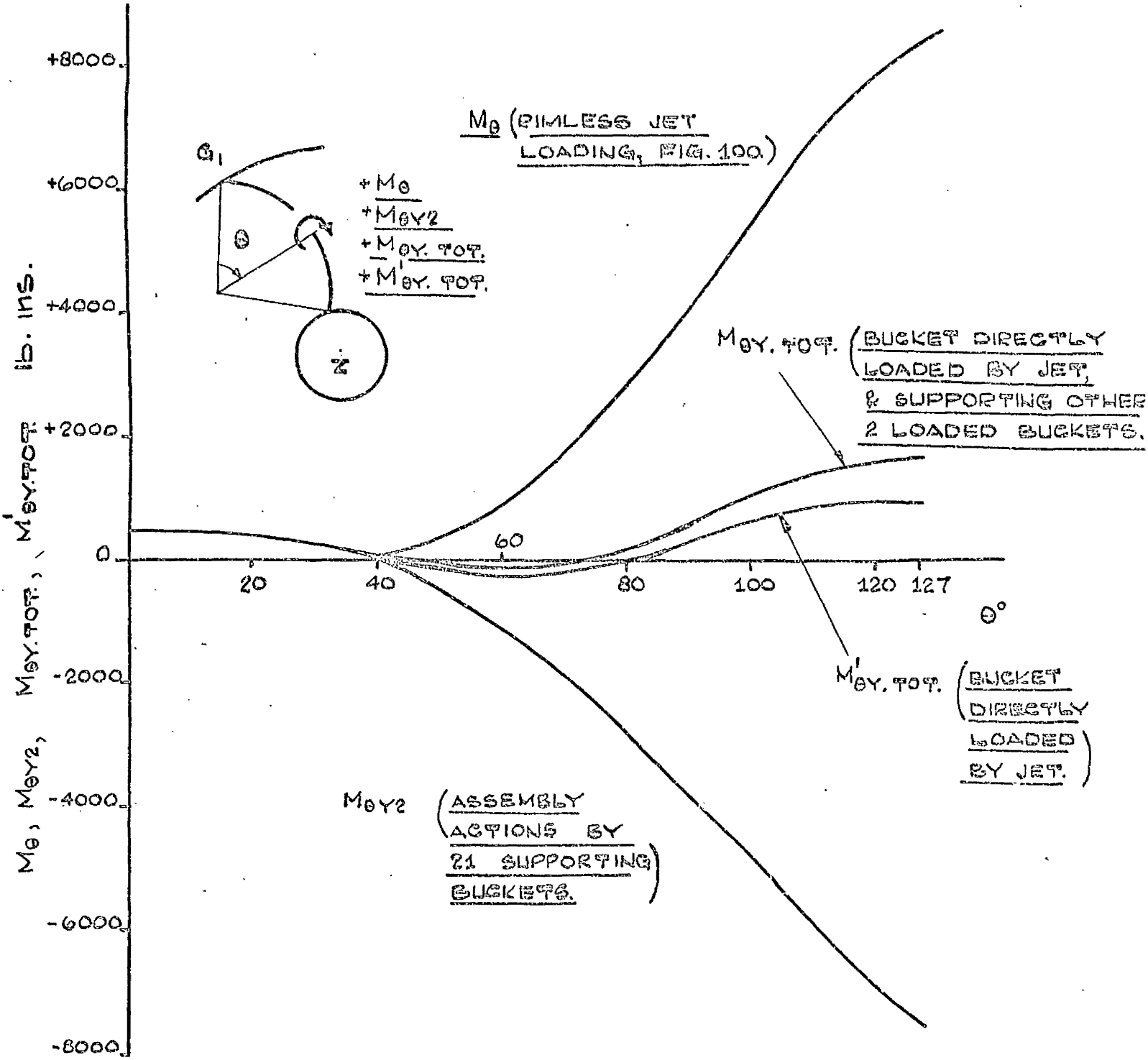

FIG. 101. DISTRIBUTIONS WITH θ OF IN-PLANE BENDING MOMENTS PERTINENT TO APPROX. JET LOADING, FIG 100, ON "EQUIVALENT" BUCKET OF 16½ IN. CAST STEEL TURBO WHEEL UNDER NORMAL WORKING CONDITIONS. CURVES $M_{\theta Y2}$, $M'_{\theta Y.TOT.}$ & $M_{\theta Y.TOT.}$ ARE DERIVED FROM MORE REALISTIC APPROX. THEORETICAL ANALYSIS OF THE JET LOADING STRESSES. (APPENDIX 7.)

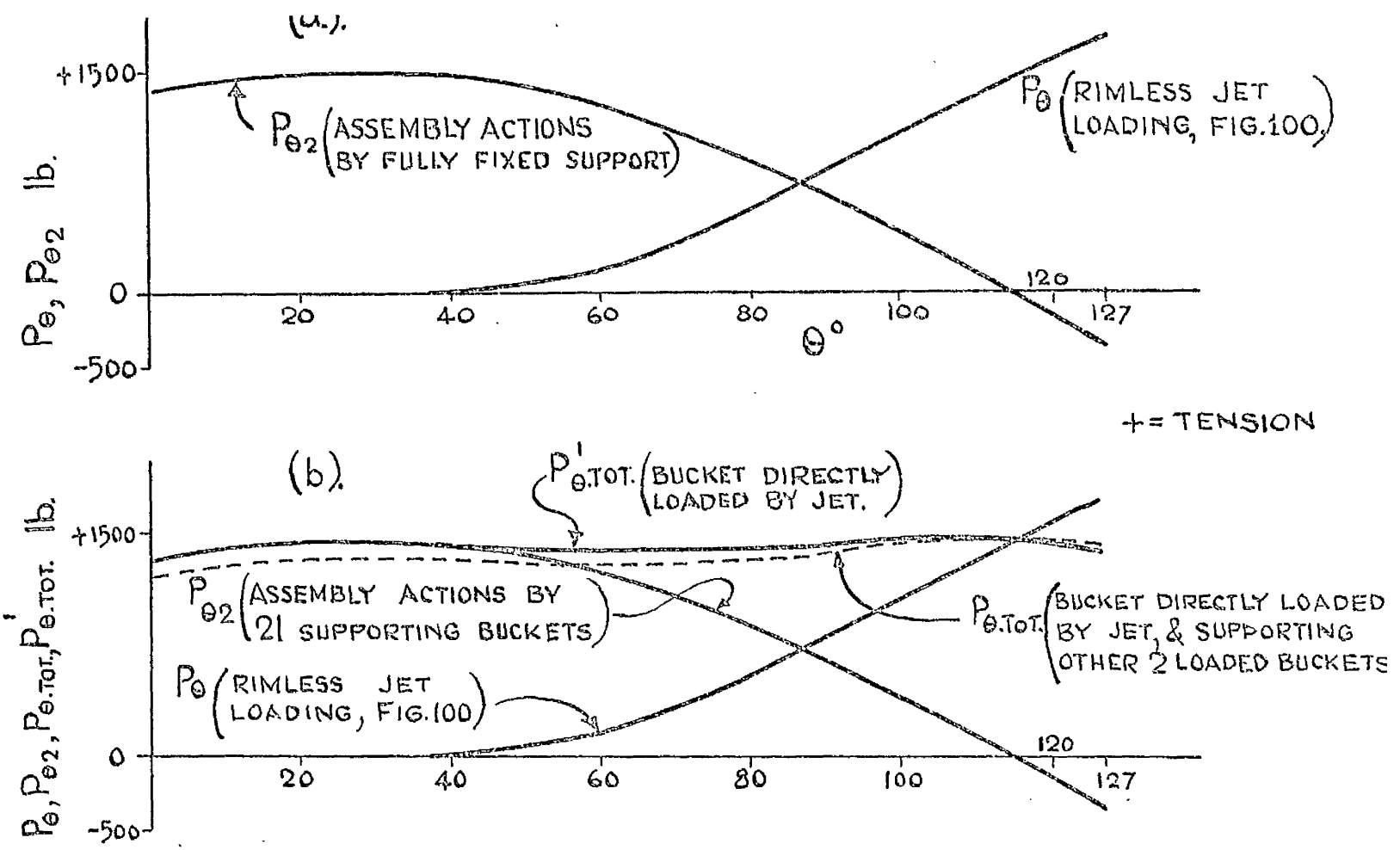

FIG. 102. DISTRIBUTIONS WITH θ OF DIRECT FORCES PERTINENT TO APPROX. JET LOADING, FIG. 100, ON "EQUIVALENT" BUCKET OF 16½ IN. C.S. TURGO WHEEL UNDER NORMAL WORKING CONDITIONS. (a) IS EQUIVALENT OF FIG. 100 FOR DIRECT FORCES $P_{\theta}, P_{\theta 2}$. (b) IS EQUIVALENT OF FIG. 101, CURVES $P_{\theta 2}$, $P'_{\theta.TOT.}$, $P_{\theta.TOT.}$ BEING DERIVED FROM MORE REALISTIC APPRO THEORETICAL ANALYSIS. (APPENDIX. 7).

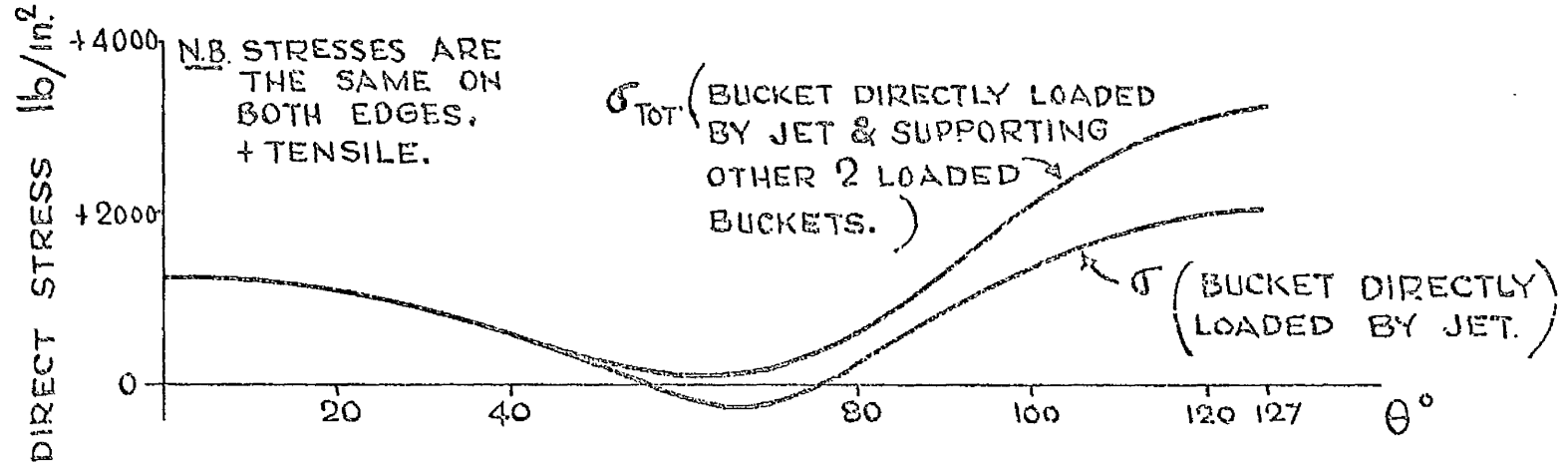

FIG. 103. DISTRIBUTIONS WITH θ OF APPROX. JET LOADING STRESSES ON EDGES OF "EQUIVALENT" BUCKET OF 16½ IN. C.S. TURGO WHEEL UNDER NORMAL WORKING CONDITIONS. STRESSES ARE DERIVED DIRECTLY FROM FIGS. 101, 102 (b) AND PERTAIN TO THE MORE REALISTIC APPROX. THEORETICAL ANALYSIS. (APPENDIX. 7).

The analysis gives identical stress distributions on both edges of the bucket.

Agreement with results of experiment is apparent forthwith, in respect of the significance of bucket "supporting" stresses in relation to stresses due to direct loading. In significant stress areas of the edges the theoretical results, Fig.103, show that about 40% of σ_{TOT} is due to the supporting rôle, a proportion well confirmed by corresponding experimental results, Figs. 84, 85.

Theoretical edge stress curves σ, σ_{TOT}, Fig.103, may be compared directly with corresponding experimental results, Figs.84, 85 respectively. For a bucket subjected only to direct jet loading, Fig.104 compares theoretical σ, Fig.103, with the appropriate swept surface and membrane experimental stresses from Fig.84. In Fig.105, theoretical σ_{TOT}, Fig.103, is compared with the corresponding swept and unswept surface experimental maximum total stresses, Fig.85, for a bucket mainly carrying jet loading and supporting other 2 jet loaded buckets.

From Figs.104, 105, it is seen that the more realistic theory correctly predicts the approximate general natures of swept surface and membrane edge stress distributions, and the location of maximum stress, an outlet edge/hub junction. However, it wrongly predicts an equal maximum stress at inlet edge/hub junction. On the whole, agreement between theory and experiment (swept surface values) is quite good in respect of significant magnitudes of edge stress. Since the theory considers only in-plane actions on the bucket, it might be expected to underestimate maximum stress and other significant stresses, but there is little general evidence to indicate that it does so. The theory, however, gives a maximum total stress of + 3280 lb/in^2, Fig.105, as against a measured maximum total stress of + 5270 lb/in^2. The latter value is pertinent to a stress concentration region of course, and would reasonably be expected to exceed the maximum value which an essentially simple approximate/

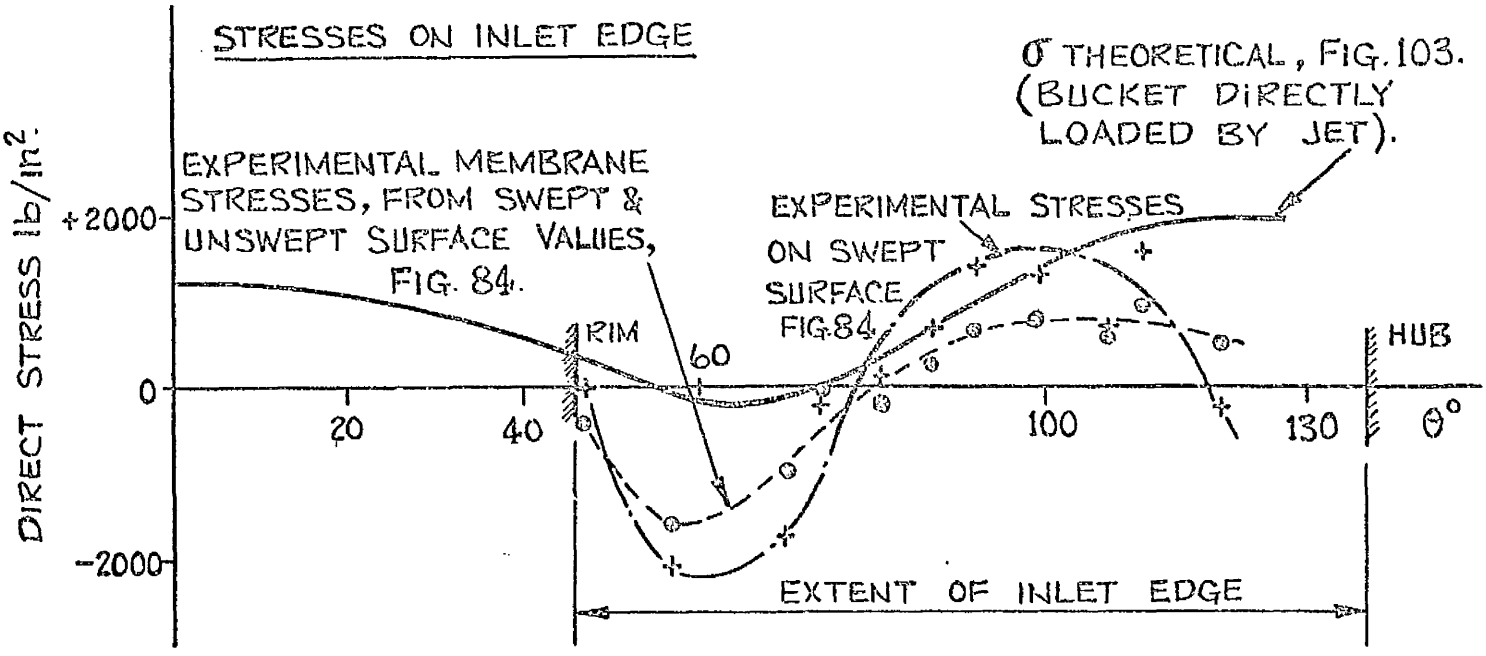

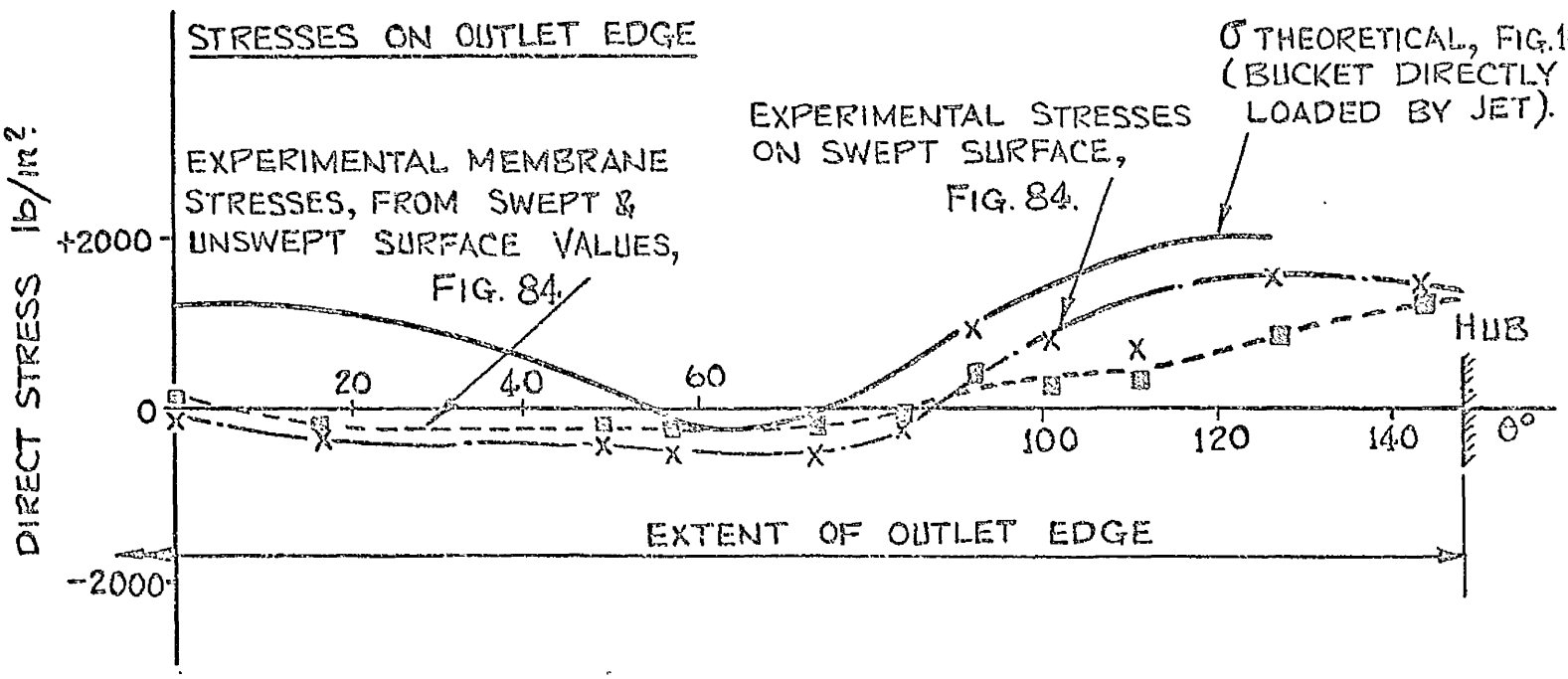

FIG. 104. DISTRIBUTIONS WITH θ OF STRESSES ON EDGES OF BUCKET OF 16½ IN. C.S. TURGO WHEEL, FOR BUCKET CARRYING ONLY DIRECT APPROXIMATE JET LOADING, PERTINENT TO NORMAL WORKING CONDITIONS. COMPARISON OF σ THEORETICAL (FIG. 103) DERIVED FROM MORE REALISTIC THEORY (APPENDIX 7) AND CORRESPONDING EXPERIMENTAL STRESSES ON SWEPT SURFACE AND EXPERIMENTAL MEMBRANE STRESSES, (FIG. 84)

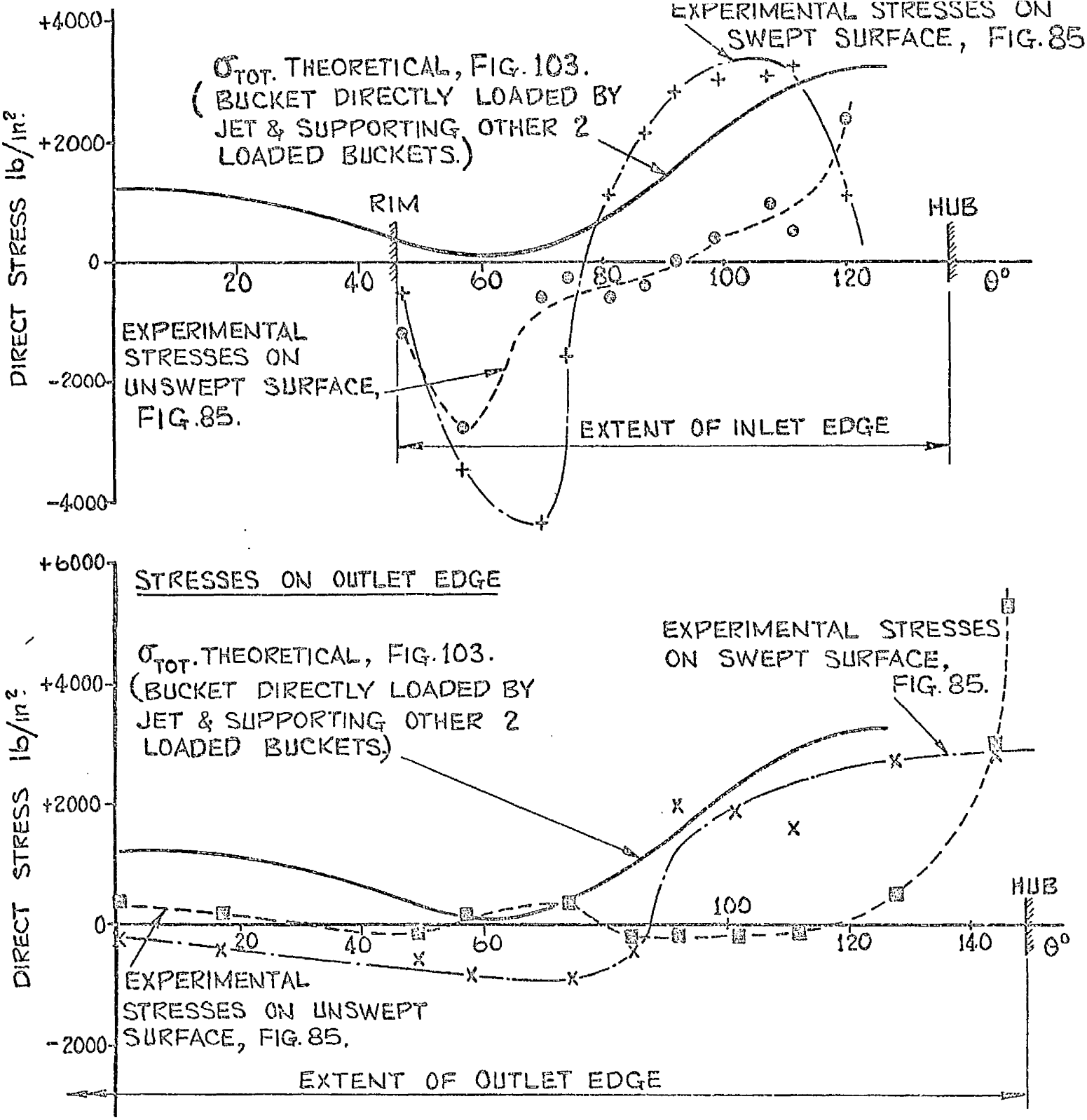

FIG. 105. DISTRIBUTIONS WITH θ OF APPROX. JET LOADING MAXIMUM TOTAL STRESSES ON EDGES OF BUCKET OF 16½ IN. C.S. TURGO WHEEL, MAINLY FOR BUCKET CARRYING DIRECT LOADING AND ACTING IN SUPPORT OF A PAIR OF DIRECTLY LOADED BUCKETS, AS APPROPRIATE TO NORMAL WORKING CONDITIONS. COMPARISON OF $\sigma_{TOT.}$ THEORETICAL (FIG. 103) DERIVED FROM MORE REALISTIC THEORY (APPENDIX 7) AND CORRESPONDING EXPERIMENTAL STRESSES ON SWEPT AND UNSWEPT SURFACES. (FIG. 85).

approximate theory is capable of providing. It may be observed that in both Figs.104 and 105, theoretical stress curves lie in relation to corresponding experimental curves much as do their counterparts for centrifugal loading, Fig.98.

6B iii Comparison of theoretical and experimental maximum stress ratios

It is useful to assess the approximate theoretical treatments in respect of their ability to predict the maximum stress ratio:-

$$\frac{\text{maximum centrifugal stress}}{\text{greatest maximum total approximate jet loading stress}},$$

pertinent to normal working conditions of the wheel.

The theoretical analyses, chapter 3, give:-

$$\text{maximum stress ratio} = \frac{+\,8750}{+\,4800} = 1.82$$

The theoretical analysis for centrifugal stresses, chapter 3, and the more realistic theoretical analysis for approximate jet loading stresses, previous section and Appendix 7, give:-

$$\text{maximum stress ratio} = \frac{+\,8750}{+\,3280} = 2.66$$

The experimental results, chapter 4, give:-

$$\text{maximum stress ratio} = \frac{+\,9480}{+\,5270} = 1.80$$

Both sets of approximate theoretical analyses thus correctly predict the dominance of centrifugal stress. As might be expected, the use of the more realistic approximate jet loading stress theory leads to an overestimate in this respect.

CHAPTER 7.

THE PELTON WHEEL.

APPLICATION OF SHELL THEORY TO DETERMINATION OF THE APPROXIMATE JET LOADING STRESSES AND DEFORMATIONS IN THE BUCKET.

COMPARISON OF THEORETICAL AND EXPERIMENTAL RESULTS.

Designs of Pelton buckets vary somewhat in detail. The essential geometrical features however, are all exhibited by Figs.2, 3, 5 and 114. The basic form is symmetrical about the splitter or inlet edge which is the junction of the two shell portions constituting the bucket. Invariably the inlet and outlet edges, Figs.107, 114, 115, lie practically in the same plane throughout. Mostly, a reinforcing rib is carried on the unswept surface of each half-bucket, Figs.2, 3, 5, 107, and runs in a direction parallel to the inlet edge. Fig.29(a) shows a section of the jet in relation to a bucket in a given position. Buckets are struck singly by the jet which, as is evident, acts in the plane of the wheel.

Large Pelton buckets, such as those of Fig.2, are frequently of varying shell thickness. Medium-sized buckets, however, are commonly of uniform shell thickness, as in Figs.5, 107, 114, 115. Only buckets of uniform shell thickness in unrimmed Pelton wheels are considered here.

For the shell portions of a bucket of a Pelton wheel, a rough indication of the proportions of maximum centrifugal stress to maximum jet loading stress may be obtained by comparison with conditions pertinent to a bucket of the equivalent Turgo wheel, both wheels being regarded as driven by the same jet, under normal working conditions. The following points of comparison are relevant:-

(1) The Pelton wheel is twice the p.c.d. of the equivalent Turgo wheel and rotates at half the speed of the Turgo wheel.

(2) The Pelton wheel has no rim and full jet force is exerted on a single bucket.

(3) The geometries of the buckets are considerably different. The Pelton bucket is the larger, and commonly carries a reinforcing rib.

Considering the experimental results of chapter 4 relating to the Turgo wheel bucket, it would seem on balance that in the shell portion of/

of the Pelton bucket under normal working conditions, centrifugal stress may not predominate and jet loading stress may be of equal or greater consequence.

The attitude of the Pelton bucket in relation to the wheel radius is also a factor. Fig.2 is typical and indicates that, with regard to bending of the bucket in the plane of the wheel, centrifugal action would probably be of less importance than the action of jet force, which is tangential to the pitch circle. The radial attitude of the Pelton buckets of Fig.2 may be contrasted with the corresponding attitude of the Turgo wheel buckets of Fig.55(a), (b), elucidated by Fig.65.

It seems likely then that, with regard to the maximum normal working stress in the shell of a Pelton bucket, jet action will predominate and give rise to this and other significant stresses mainly due to bending in the plane of the wheel. In respect of the buckets of a particular Pelton wheel, without giving reasons, PERRIG[4] considers that the maximum jet loading stress will be almost twice the maximum centrifugal stress, for normal working.

7A APPLICATION OF SHELL THEORY TO THE ANALYSIS OF THE APPROXIMATE JET LOADING STRESSES IN A PELTON BUCKET

The following main assumptions are made:-

(1) The bucket consists of two identical open toroidal shells of circular section and uniform thickness, rigidly connected to each other on circumferential boundaries, Fig.106(b). The junction of the toroidal shells represents the inlet edge, and the theoretical bucket is associated with the actual bucket geometry as indicated in the example which follows, Figs.107, 108.

(2) The only action exerted on the theoretical bucket is bending in the plane of the wheel. Each of the open toroidal shells is subjected to the same value of bending moment in the plane of the shell.

Fig.106 illustrates the basis of the shell analysis. Each open toroidal shell is subjected to pure in-plane bending moment m. In all respects, save that of circumferential displacement, the shell-pair system is rotationally symmetrical about the common axis of revolution. Now, if the shells were separated at the rigid joint and each was then loaded by bending moment m, Fig.106(d), the meridian rotations β_{edge} at the adjacent edges would freely occur. In the assembled and loaded condition then, it is clear that, on account of the rigidity of the joint, the effect of one shell on the other is fully to prevent this rotation β_{edge} taking place. Alternatively expressed, the only deformational discontinuity between the separated, loaded shells, Fig.106(d), is one of meridional rotation β_{edge}.

From symmetry, both rotational and in respect of the meridional cross-section Fig.106(c), it is apparent that, in the assembled condition, this/

this discontinuity is eliminated by meridional edge couples M_A, Fig.106(e), exerted by one shell on the other. On any one shell these edge couples M_A are, of course, a self-equilibrating, rotationally symmetrical system. Thus each open toroidal shell of the bucket, Fig.106(f), sustains externally applied in-plane bending moment m, together with couples M_A uniformly distributed along the inlet edge and such as completely to prevent rotation of a meridian at that edge.

From the foregoing, the analysis plainly falls into three parts:-

(1) The open toroidal shells are considered as free and separated, each taking in-plane bending moment m. The method of chapter 5, section 5B, is applied, culminating in the determination of stresses in terms of m, and, especially, in the determination of deformation β_{edge} in terms of m/E. It may be noted that solutions for small edge angles are appropriate since, for maximum efficiency in a Pelton wheel, inlet and outlet angles of the bucket edges are arranged so that the jet is deflected through 180° as nearly as possible.

(2) The shells are considered as assembled at the inlet edge rigid joint, by application of uniformly distributed edge couples M_A, such as to eliminate completely the meridian rotation β_{edge}. This involves application of the analytical treatment for a toroidal shell subjected to a uniformly distributed edge couple, a case which is well-documented. The treatment by CLARK[9] is appropriate, since his derived solution is in terms of the same independent variable ξ, as that of general solution, equation (5A.37), and is identical in form to the complementary function of equation (5A.37) applied for uniform thickness. Thus his solution shares certain functions with part (1) above. Using this treatment, β_{edge} is found in terms of M_A/E and so from (1), M_A is related to applied bending moment m. Thus the assembly stresses are found in terms of m.

(3) /

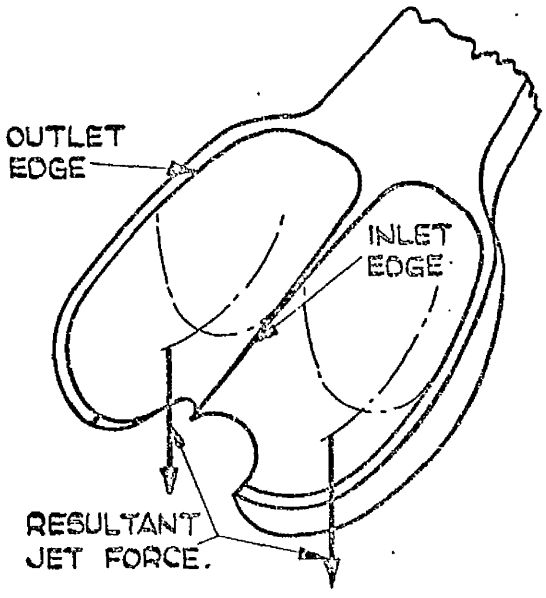

FIG.106(a). TYPICAL PELTON BUCKET. EACH HALF SUSTAINS BENDING IN THE PLANE OF THE WHEEL DUE TO JET FORCE.

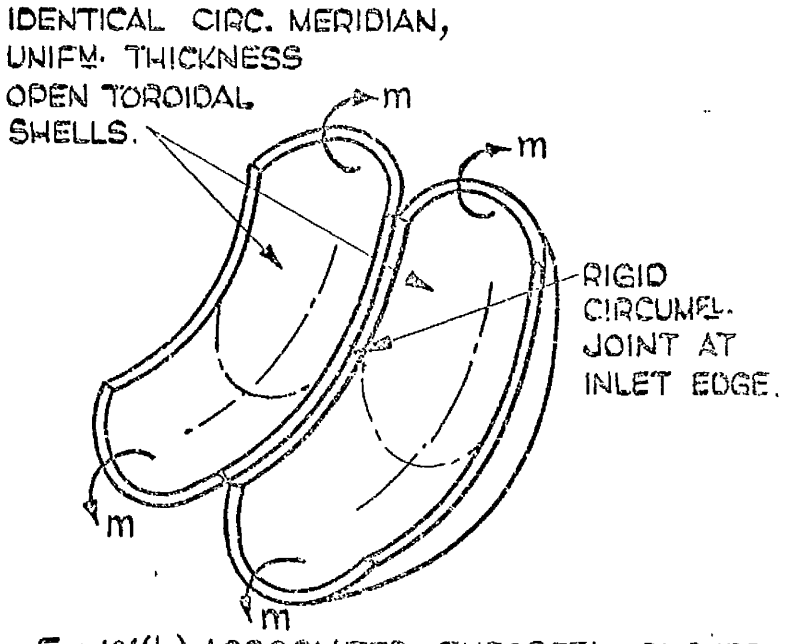

FIG.106(b). ASSOCIATED THEORETL. BUCKET ASSUMED FOR SHELL ANALYSIS. EACH HALF SUSTAINS PURE BENDING MOMENT m IN PLANE OF SHELL. SYSTEM IS ROTATLY. SYMMETL., SAVE FOR CIRCUMFL. DISPLT.

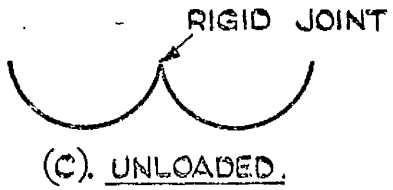

(c). UNLOADED.

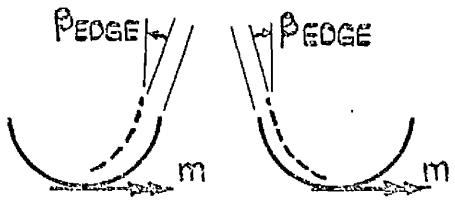

(d). OPEN TORL. SHELLS FREE & SEPARATED AT JOINT, EACH CARRYING m. JOINT EDGE DISCONTINUITY β EDGE IS SHOWN.

(e). SHELLS ASSEMBLED AT JOINT, EACH CARRYING m, ROTATLY. SYMMETL. EDGE COUPLES M_A ELIMINATE DISCONTY. β EDGE.

FIG.106(c),(d),(e). DIAGRAMMATIC MERIDL. SECTIONS OF THEORETICAL BUCKET.

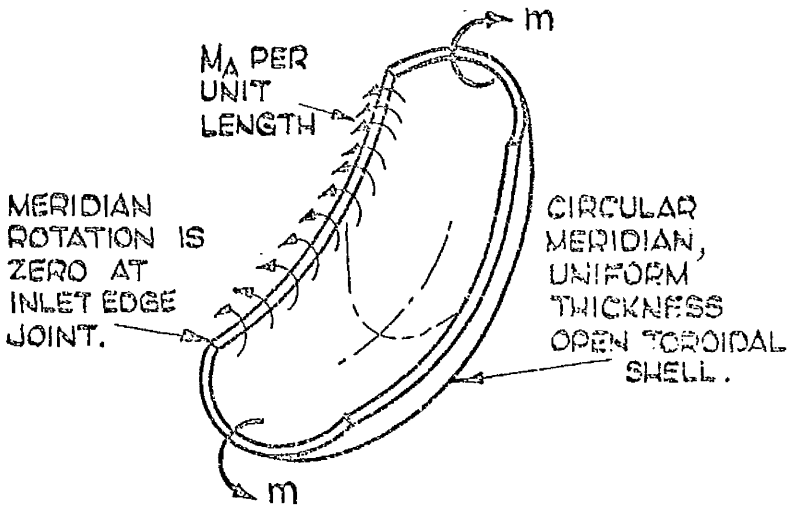

FIG.106(f). TOTAL ACTIONS SUSTAINED BY THEORTL. HALF BUCKET. ACTIONS AND STRESS DISTRIBNS. ARE ROTATLY. SYMMETL.

FIG. 106. DIAGRAM ILLUSTRATING CONCEPTS UNDERLYING APPLICATION OF SHELL THEORY TO DETERMINATION OF APPROX. JET LOADING STRESSES IN PELTON BUCKET.

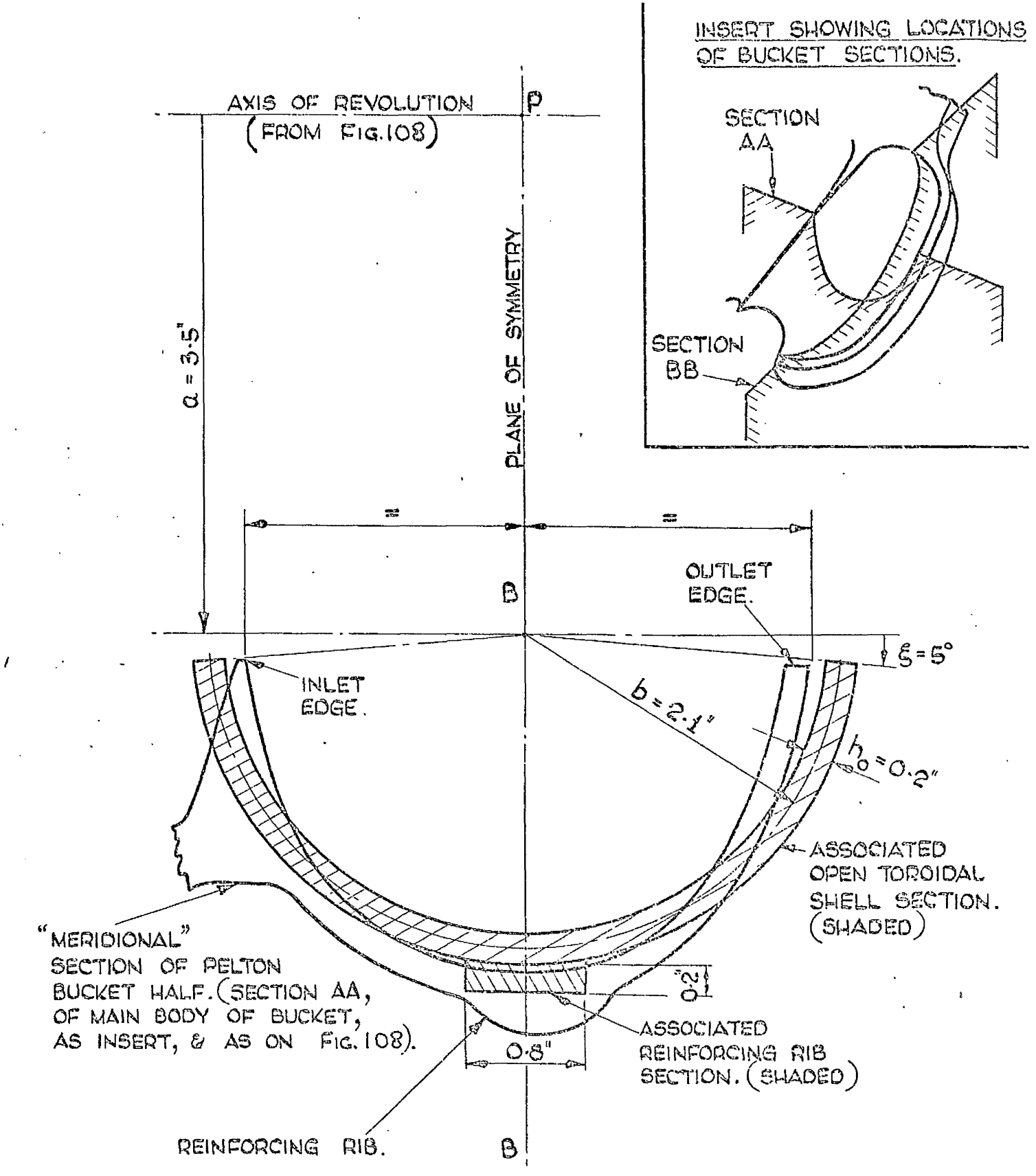

FIG. 107. COMPARISON OF "MERIDIONAL" SECTION FROM THE MAIN BODY OF HALF-BUCKET OF 21 IN. P.C.D. PELTON WHEEL, WITH MERIDIONAL SECTION (SHADED) OF THE ASSOCIATED CIRCULAR-MERIDIAN, UNIFORM THICKNESS, OPEN TOROIDAL SHELL. (CASE II, CHAPTER 5)

(3) The total stresses due to pure bending moment m on one half of the theoretical bucket, are then found by superimposing the stresses from (1) and (2). The total stresses are in terms of m.

The analysis is developed assuming rotational symmetry and pure in-plane bending. As mentioned subsequently, it is assumed further that, in its completed form as outlined, the analysis applies to cases of continuously varying in-plane bending moment.

For particular application of the analysis, and for related stress measurements, two high tensile bronze buckets, Fig.114, of a 21 in.p.c.d. Pelton wheel, were available. The geometries of these buckets were carefully examined using thickness gauges and templets. Except in way of the inlet edges and of the reinforcing ribs on the unswept surfaces, the buckets, which were virtually identical, of course, were found to be of uniform thickness 0.17 in. $\pm$ 5%, throughout the shell portions. Typical "meridional" and "circumferential" sections from the main shell portion of a half-bucket are shown on Figs.107, 108 respectively.

The swept surface profile of "circumferential" section, Fig.108, is symmetrical about line PA in way of which the profile is practically circular. The extent of this almost circular profile forming the "hollow" of the half-bucket, defines the main body, over which the edges, Fig.115, are sensibly parallel and the "meridional" section, Fig.107, is nearly constant. It is this main body of the half-bucket which approximates to the associated open toroidal shell, and within which the highest measured stress due to simulated jet loading, has been found.

The geometry of the open toroidal shell associated with the main body of the half-bucket is found by firstly producing the circular profile of the "hollow", Fig.108, to give arc FF, the centre P of which is then located. This is the centre of revolution of the toroidal shell, thus enabling the axis of revolution to be located relative to the "meridional" section/

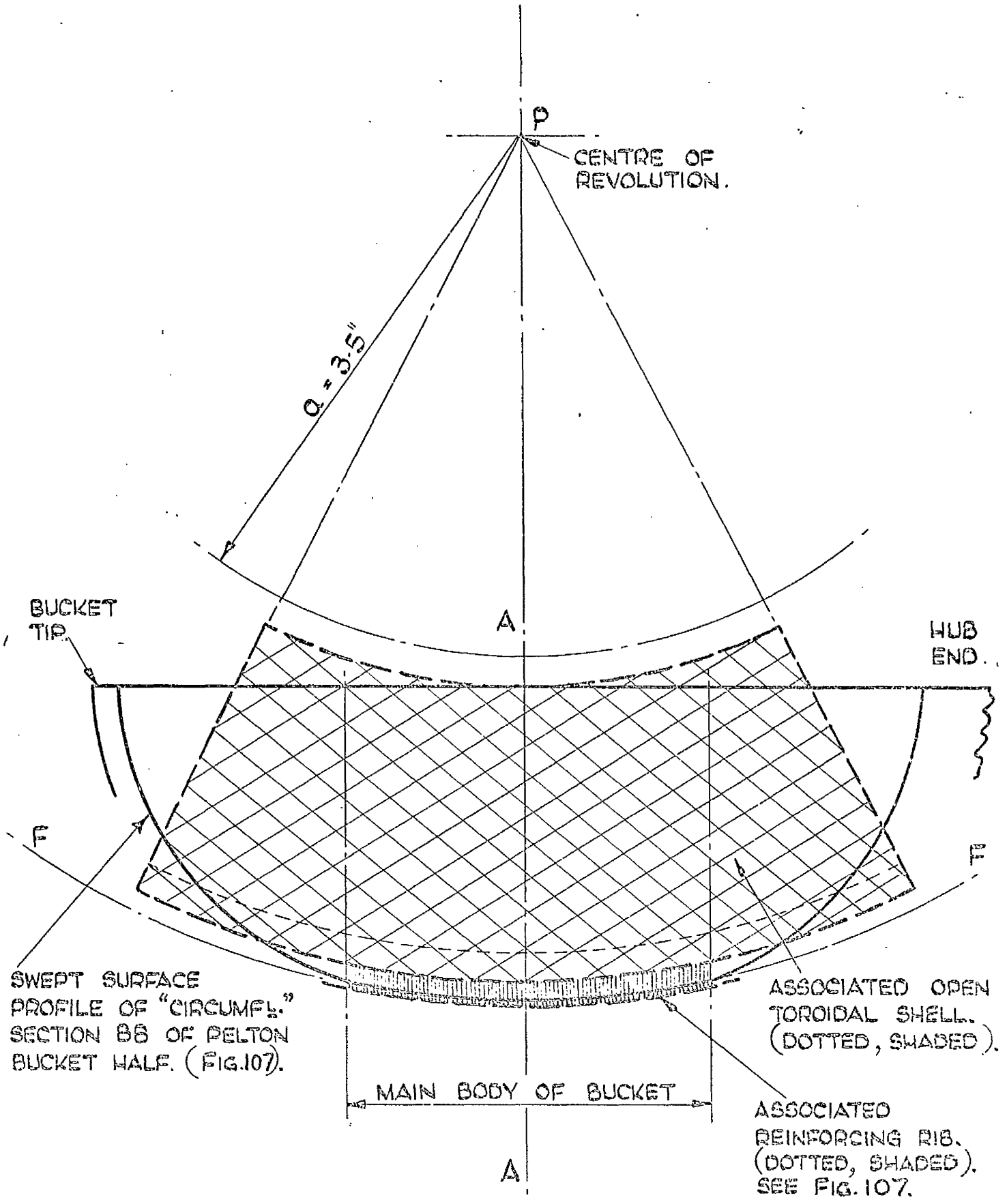

FIG.108. COMPARISON OF "CIRCUMFERENTIAL" SECTION ON "PLANE OF SYMMETRY" OF HALF-BUCKET OF 21 IN. p.c.d. PELTON WHEEL (FIG.107), WITH CIRCUMFERENTIAL VIEW (DOTTED, SHADED) OF ASSOCIATED CIRCULAR-MERIDIAN, UNIFORM THICKNESS, OPEN TOROIDAL SHELL. (CASE II, CHAPTER 5.)

section of the half-bucket on Fig.107. The "plane of symmetry" of the "meridional" section is established as shown. It is clear that the "meridional" section is not readily approximated by a circular form, which may be determined as a compromise in respect of the following criteria:-

(1) The circular centre-line should represent the "meridional" section centre-line in as reasonably balanced a manner as possible.

(2) The edge angle of the circular section should be an integer angle, closely simulating the actual inlet and outlet edge angles.

(3) The radii ratio $b/a = \lambda$ should correspond exactly to a value for which there exists direct tabulation of functions pertinent to the analysis.

The last criterion is relevant where the nature of the approximation justifies it. On these bases, the radii a and b are selected as shown in Fig.107, $a = 3.5$ in., $b = 2.1$ in., giving $\lambda = 0.6$, and the edge angle $\xi = 5^{\circ}$ is chosen. Thickness $h_o = 0.2$ in., is then selected, slightly more than the actual uniform thickness. This is partly in an attempt to compensate for the greater depth of the actual half-bucket section. Finally, the meridional section of the reinforcing rib is simulated by an associated rectangular section rib of about the same area and proportions, located at the convex or unswept surface, on the plane of symmetry. From Figs.107 and 108, it may be said that representation of the main body of the half-bucket by the associated reinforced open toroidal shell, is a reasonable procedure.

Concerning the associated open toroidal shell of these Figs.107, 108, with reinforcing rib temporarily disregarded, the first part of the shell theory application has already been completed. This refers to the separated open toroidal shell half-buckets, each subjected to in-plane bending moment m, Fig.106(d), and, taking Poisson's ratio $\nu = 0.3$ for bronze, the relevant numerical analysis corresponds to Case II, chapter 5, where the results are presented in section 5C and Fig.93.

For/

For bending moment m applied in the sense of Fig.106(b) and (d), the signs of stress resultant N_θ/kE, stress couples M_θ/kE, M_ξ/kE, and meridian rotation β/k, Fig.93, are all changed. From equation (5C.5):-

$$k = 66.98 \frac{m}{E} \qquad (7.1),$$

enabling $N_\theta, M_\theta, M_\xi$ to be found in terms of m, and from equation (5C.6):-

$$\beta_{\xi = 5^\circ} = + 87.64 \frac{m}{E} \text{ radians} \qquad (7.2),$$

for the relevant direction of m. By the sign convention, Fig.88(a), (b), the direction of $\beta_{\xi = 5^\circ}$ corresponds to that of β_{edge}, Fig.106(d). The rotationally symmetrical edge couples M_A therefore act as shown in Fig.106(e) and (f), for elimination of β_{edge}, and assembly of the half-buckets at the inlet edge rigid joint.

For the second part of the application of the shell theory, CLARK'S[9] analysis of the rotationally symmetrical edge couple case is used. Although this treatment shares certain functions with the analysis given in chapter 5, the basic formulations of the two solutions are rather different, so that corresponding quantities are differently expressed. In order to use the edge couple solution of CLARK[9] directly, the formulation and expressions pertinent to that solution are maintained. However in applying the solution throughout this chapter, the notation* used is largely common with that of chapter 5, and with section 5B in particular. The sign conventions pertinent to stress resultants, stress couples and displacement β are also common with those of chapter 5, being given in Fig.88(e), (a), (b). Where applicable, distinctions are clearly indicated between equations here and their counterparts in chapter 5.

The/

* see Nomenclature.

The solution is conveniently applied as illustrated in Fig.109, which also shows the sign conventions pertinent to displacements β and u. The halves of the shell are considered separated on the plane of symmetry, Fig.109(b), and edge couple M_A acts only on the lower one, causing displacements u_s, β_s at the separated boundary $\xi = \pi/2$. These displacements are the only deformational discontinuities between the halves and from symmetry, edge actions F_1, F_2, M_1, M_2, Fig.109(c), are necessary to eliminate them and effect assembly. The displacements relevant to the assembled loaded condition are indicated in Fig.109(d), from which the following displacement compatibility equations are evident:-

$$u_1 + u_s = u_2$$
$$\beta_1 + \beta_s = \beta_2 \qquad (7.3)$$

For equilibrium at $\xi = \pi/2$:-

$$F_1 + F_2 = 0$$
$$M_1 + M_2 = 0 \qquad (7.4)$$

With reference to Fig.109(c), (d), equations (7.3) may be re-written in terms of the individual displacements due to each of the assembly actions thus:-

$$u_{F_1} + u_{M_1} + u_s = u_{F_2} - u_{M_2}$$
$$\beta_{F_1} + \beta_{M_1} + \beta_s = -\beta_{F_2} + \beta_{M_2} \qquad (7.5)$$

But from equilibrium equations (7.4) and from symmetry, it is evident that:-

$$u_{F_1} = -u_{F_2}$$
$$u_{M_1} = -u_{M_2}$$
$$\beta_{F_1} = -\beta_{F_2}$$
$$\beta_{M_1} = -\beta_{M_2} \qquad (7.6)$$

Substituting/

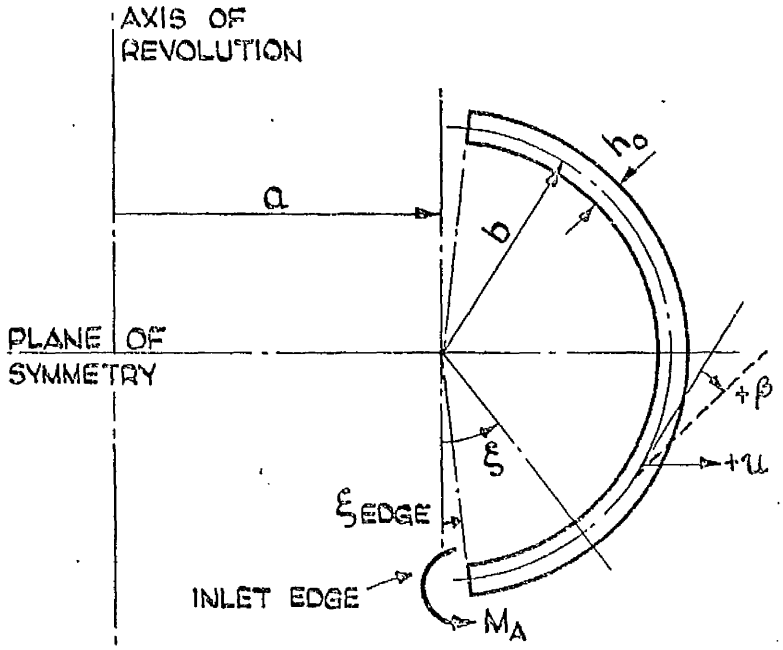

(a). COMPLETE MERIDL SECTION OF OPEN TOROIDAL SHELL, SHOWING EDGE COUPLE M_A, AND +VE DIRNS. OF RADIAL DEFORMN. u & MERIDIAN ROTN. β. ANALYSIS IS ALSO FULLY APPLICABLE FOR $\xi_{EDGE} = 0$.

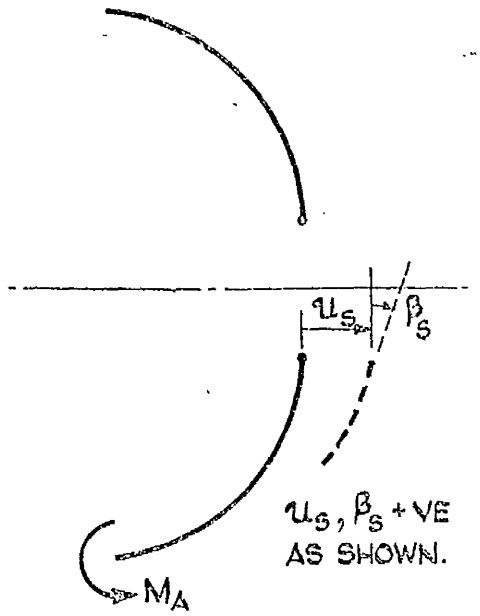

(b). SECTION HALVED AT $\xi = \frac{\pi}{2}$, M_A BEING CARRIED ONLY BY LOWER HALF AND CAUSING DEFORMNS. u_s, β_s: THESE ARE DEFORMN. DISCONTINUITIES BETWEEN HALVES AT $\xi = \frac{\pi}{2}$.

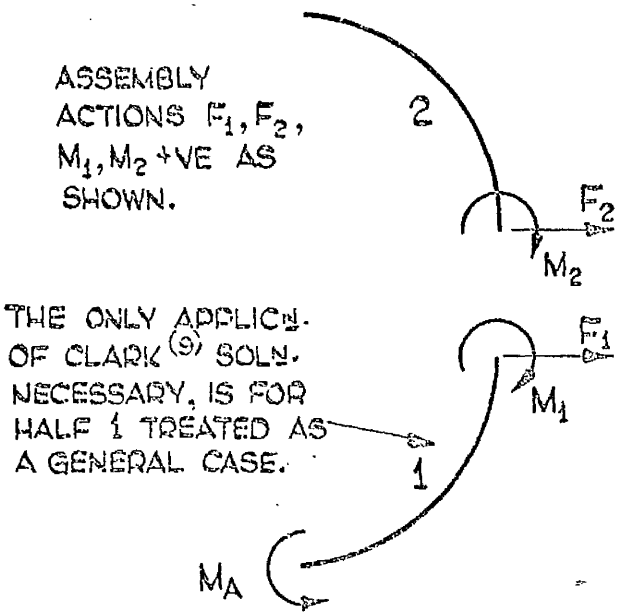

(c). DISCONTINUITY ASSEMBLY ACTIONS ON HALVES AT $\xi = \frac{\pi}{2}$, WITH LOADING M_A ALSO CARRIED.

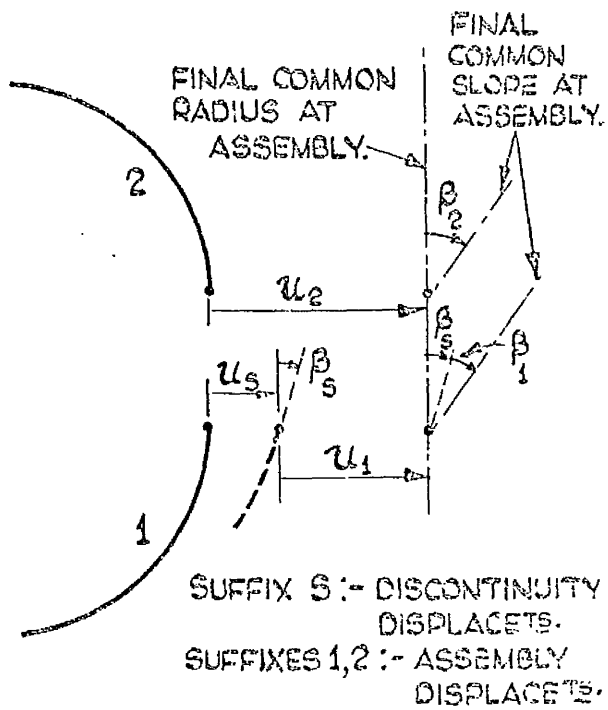

(d). ANALYSIS OF DISCONTINUITY & ASSEMBLY DISPLTS. FOR ASSEMBLY OF HALVES AT $\xi = \frac{\pi}{2}$, WITH M_A ACTING.

FIG. 109. DIAGRAM ILLUSTRATING METHOD OF ANALYSIS FOR THE CASE OF ROTATIONALLY SYMMETRICAL EDGE COUPLE M_A, FIG 106(f), MAKING USE OF CLARK (9) SOLUTION.

Substituting (7.6) into (7.5) gives:-

$$u_{F_1} = -\frac{u_s}{2}$$

$$\beta_{M_1} = -\frac{\beta_s}{2} \qquad (7.7)$$

Now from CLARK'S [9] solution, which applies also to the case of a uniformly distributed radial edge force, displacements u_{F_1}, β_{M_1} may be readily found as linear functions of F_1, M_1 respectively, and deformational discontinuities u_s, β_s may be readily found as linear functions of edge couple loading M_A. Then by equations (7.7) and (7.4) all the assembly actions F_1, F_2, M_1, M_2 are found in terms of M_A, thus, with reversion to the CLARK[9] solution, giving deformations and stresses anywhere in the shell, Fig.109(a), in terms of edge couple loading M_A.

From Fig.109(c), it is evident that only one application of the CLARK[9] solution is necessary, this being in respect of shell-half 1 treated as a general case subjected to loadings M_A, F_1, M_1 at the boundaries, as shown.

The relevant expressions which follow, are taken directly from CLARK[9]. For stress resultants, stress couples and displacement:-

$$N_\xi = \frac{h_o^2 E}{a\sqrt{12(1-\nu^2)}} \cdot \frac{\cos\xi}{1+\lambda\sin\xi} \cdot \Psi$$

$$Q = -\frac{h_o^2 E}{a\sqrt{12(1-\nu^2)}} \cdot \frac{\sin\xi}{1+\lambda\sin\xi} \cdot \Psi \qquad (7.8)$$

$$N_\theta = \frac{h_o^2 E}{b\sqrt{12(1-\nu^2)}} \cdot \Psi'$$

$$M_\xi = \frac{h_o^3 . E}{12b(1-\nu^2)}\left[\beta' + \frac{\nu\lambda\cos\xi}{1+\lambda\sin\xi}\beta\right]$$

$$M_\theta = \frac{h_o^3 . E}{12b(1-\nu^2)}\left[\nu\beta' + \frac{\lambda\cos\xi}{1+\lambda\sin\xi}\beta\right]$$

$$-u = \frac{a}{h_o E}(1+\lambda\sin\xi)(N_\theta - \nu N_\xi)$$

(7.8)

The formulation of these equations pertains only to the edge actions solution of CLARK[9]. The stress equations should not be confused with their counterparts, equations (5B.5). Both sets are essentially the same of course, but pertain to shell of revolution solutions formulated slightly differently.

In the above equations, the solution functions β and Ψ are given in terms of the independent variable ξ, by:-

$$\beta = (1+\lambda\sin\xi)^{-\frac{1}{2}}\bar{Q}\left[A_3 h_{1r}(ix) - B_3 h_{1i}(ix) + C_3 h_{2r}(ix) - D_3 h_{2i}(ix)\right]$$

$$\Psi = (1+\lambda\sin\xi)^{-\frac{1}{2}}\bar{Q}\left[A_3 h_{1i}(ix) + B_3 h_{1r}(ix) + C_3 h_{2i}(ix) + D_3 h_{2r}(ix)\right]$$

$$\beta' = -\frac{\mu^{\frac{1}{3}}}{\bar{Q}(1+\lambda\sin\xi)^{\frac{1}{2}}}\left[A_3 h'_{1i}(ix) + B_3 h'_{1r}(ix) + C_3 h'_{2i}(ix) + D_3 h'_{2r}(ix)\right] + R\beta$$

$$\Psi' = \frac{\mu^{\frac{1}{3}}}{\bar{Q}(1+\lambda\sin\xi)^{\frac{1}{2}}}\left[A_3 h'_{1r}(ix) - B_3 h'_{1i}(ix) + C_3 h'_{2r}(ix) - D_3 h'_{2i}(ix)\right] + R\Psi$$

(7.9)

where prime $'$ means first derivative with respect to ξ , except for the functions $h_1(ix), h_2(ix)$ where it means first derivative with respect to the argument of the function, and where:-

$$R = \frac{\bar{Q}'}{\bar{Q}} - \frac{\lambda\cos\xi}{2(1+\lambda\sin\xi)}$$

$$= -\frac{3}{10}\lambda + \left(\frac{1}{14} + \frac{101}{350}\lambda^2\right)\sin\xi + \text{------ terms in } \sin^2\xi, \sin^3\xi, \text{etc.}$$

in the region of $\xi = 0$.

$$x = \mu^{\frac{1}{3}}\left(\frac{3}{2}\omega\right)^{\frac{2}{3}}, \qquad \bar{Q} = \frac{\left(\frac{3}{2}\omega\right)^{\frac{1}{6}}}{(\omega')^{\frac{1}{2}}}, \qquad \omega = \int_0^{\xi}\left(\frac{\sin\xi}{1+\lambda\sin\xi}\right)^{\frac{1}{2}}.d\xi ,$$

(7.10)

and A_3, B_3, C_3, D_3 are arbitrary constants obtainable from the boundary conditions. The functions $x, \bar{Q}, \omega$ are identical to their counterparts in equations (5B.1), as also are functions $h_1(ix)$, $h_2(ix)$ to their counterparts in equations (5B.2). It is noteworthy however, that β should not be confused with its counterpart in equations (5B.5). As with section 5B, all relevant tabulation is available in OSIPOVA AND TUMARKIN[64].

For the general case under consideration, shell-half 1 of Fig.109(c), the boundary conditions are as follows:-

at $\xi = \xi_{edge}$:- $\quad M_\xi = M_A$, and $\quad N_\xi = Q = 0$,

at $\xi = \frac{\pi}{2}$:- $\quad M_\xi = M_1$, and $\quad Q = -F_1$,

giving from equations (7.8),

$$\frac{h_0^3 E}{12b(1-\nu^2)}\left[\beta' + \frac{\nu\lambda\cos\xi}{1+\lambda\sin\xi}\beta\right]_{\xi=\xi_{edge}} = M_A$$

$$\Psi_{\xi=\xi_{edge}} = 0 \qquad (7.11)$$

$$\frac{h_o^3 E}{12b(1-\nu^2)} \beta'_{\xi=\frac{\pi}{2}} = M_1$$

$$\frac{h_o^2 E}{a\sqrt{12(1-\nu^2)}(1+\lambda)} \Psi_{\xi=\frac{\pi}{2}} = F_1$$

(7.11)

Substituting for β, β', Ψ from equations (7.9), and solving the boundary condition simultaneous equations (7.11), give arbitrary constants A_3, B_3, C_3, D_3 in terms of edge actions M_A, F_1, M_1 of the form, e.g.

$$A_3 = {}_1A_3 M_A + {}_2A_3 F_1 + {}_3A_3 M_1 \qquad (7.12)$$

where ${}_1A_3$, ${}_2A_3$, ${}_3A_3$ are constants.

For a displacement or a stress at any point in the half-shell, due to one of the edge actions alone, the remaining two actions are each equated to zero and constants A_3, B_3, C_3, D_3 are thus in terms of the one action only. Substituting into equations (7.9) and (7.8), then gives the required quantity as a linear function of the action concerned. In this way, at $\xi = \pi/2$, displacements u_{F_1}, β_{M_1} are found in terms of F_1, M_1 respectively, and u_S, β_S are found in terms of M_A. The relation of F_1 and M_1 to applied loading M_A, follows from equation (7.7) and by substituting into equations of the type (7.12), constants A_3, B_3, C_3, D_3 are obtained as linear functions of M_A. Analysis for the lower half-shell, Fig.109(c), now continuous with the upper half at $\xi = \pi/2$, is thus complete and all quantities are readily determinable in terms of applied edge couple loading M_A. Clearly, analysis is also virtually complete for the upper half.

The procedure outlined on these last five pages, and the equations from (7.3) onward, refer to the second part of the application of shell theory/

theory to an open toroidal shell simulating an unreinforced Pelton half-bucket. Numerical treatment of this part is now undertaken in respect of the open toroidal shell which is associated with the Pelton half-bucket on Figs.107 and 108, (reinforcement meanwhile neglected), and for which the numerical results of the first part of the shell theory application, are given on Fig.93 with signs changed, and by equations (7.1) and (7.2). It is found for this case that, at $\xi = \pi/2$, Fig.109, the discontinuity assembly actions F_1, M_1 are given by:-

$$F_1 = -0.010\, M_A$$
$$M_1 = -0.038\, M_A \qquad (7.13)$$

Both F_1 and M_1 therefore, act in senses opposite to those shown in Fig.109(c). Proceeding now with all quantities in terms of applied edge couple loading M_A, it is found finally that the meridian rotation at the loaded edge $\xi = \xi_{edge} = 5^\circ$, Figs.109(a) and 107, is given by:-

$$\beta_{\xi=5^\circ} = -1537.40 \frac{M_A}{E} \quad \text{radians} \qquad (7.14)$$

To satisfy assembly of the two open toroidal shell half-buckets, Fig.106(e), at the inlet edge rigid joint, this edge rotation must be numerically equal to the corresponding rotation resulting from the first part of the shell theory application, i.e. as given by equation (7.2). Thus:-

$$87.64 \frac{m}{E} = 1537.40 \frac{M_A}{E}$$

giving
$$M_A = 0.057\, m \qquad (7.15)$$

Edge couple M_A, Fig.106(f), is thus found in terms of in-plane bending moment m, enabling all stresses due to M_A to be calculated in terms of m. The variations with ξ, of pertinent stress resultant and couples N_θ/m, M_θ/m, M_ξ/m are depicted in Fig.110. As would be/

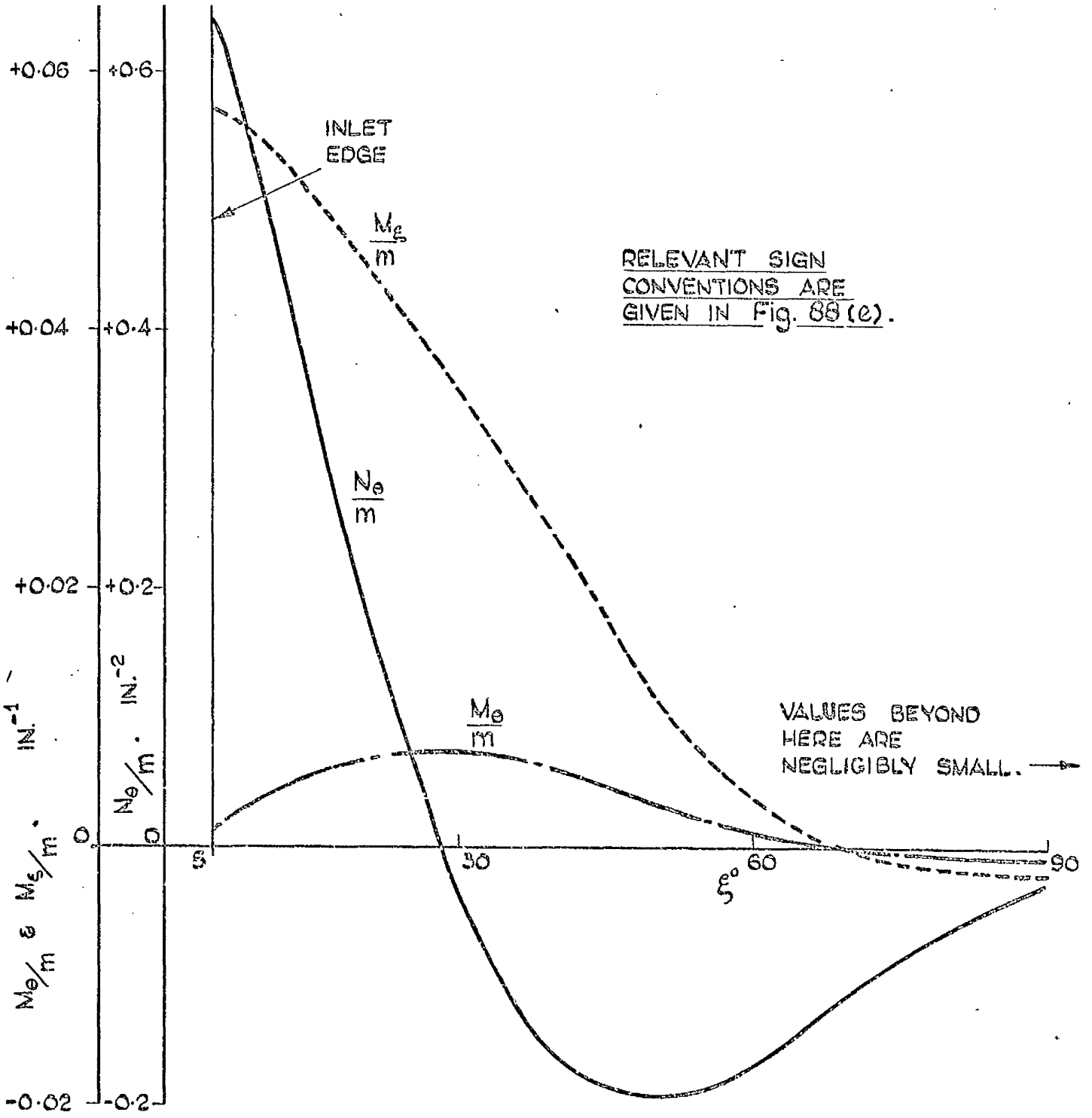

FIG. 110. APPLICATION OF CLARK[9] SOLUTION FOR THE CASE OF ROTATIONALLY SYMMETRICAL EDGE COUPLE $M_A = 0{\cdot}057m$ (FIG. 109) IN RESPECT OF OPEN TOROIDAL SHELL HALF-BUCKET, FIGS 107, 108 (REINFORCEMENT NEGLECTED) DISTRIBUTIONS OF N_θ/m, M_θ/m, M_ξ/m WITH ξ FOR $(\xi_{EDGE} = 5°) \leq \xi \leq 90°$.

be expected, the values are of most significance at and near the inlet edge where couple $M_A = 0.057m$ is applied, Fig.109(a). At $\xi = 90^o$, and in the upper half of the shell, Fig.109, the values are negligibly small.

The third and final part of this numerical application of the shell analysis consists in superposing the stresses resulting from the first and second parts, and embodied in Fig.93, with signs changed, equation (7.1) and Fig.110. The final total stress resultant and couples N_θ/m, M_θ/m, M_ξ/m, are shown in Fig.111, plotted against ξ over the full meridian of the open toroidal shell half-bucket. Stress resultant N_ξ/m has not been plotted as, throughout, it is negligible in comparison with the other quantities. Total surface stresses at any ξ are readily calculated from these graphs. It is found that the maximum stress occurs in the circumferential or θ direction on the swept surface at the inlet edge, i.e. at point A on Fig.111. With reference to points A, B, C on this Fig., the total surface stresses at the edges of the half-bucket are as follows:-

at A, inlet edge swept surface, $\sigma_\theta = +9.95\ m$

$\sigma_\xi = +8.55\ m$

at B, outlet edge swept surface, $\sigma_\theta = +6.59\ m$

at C, outlet edge unswept surface, $\sigma_\theta = +1.75\ m$ (7.16)

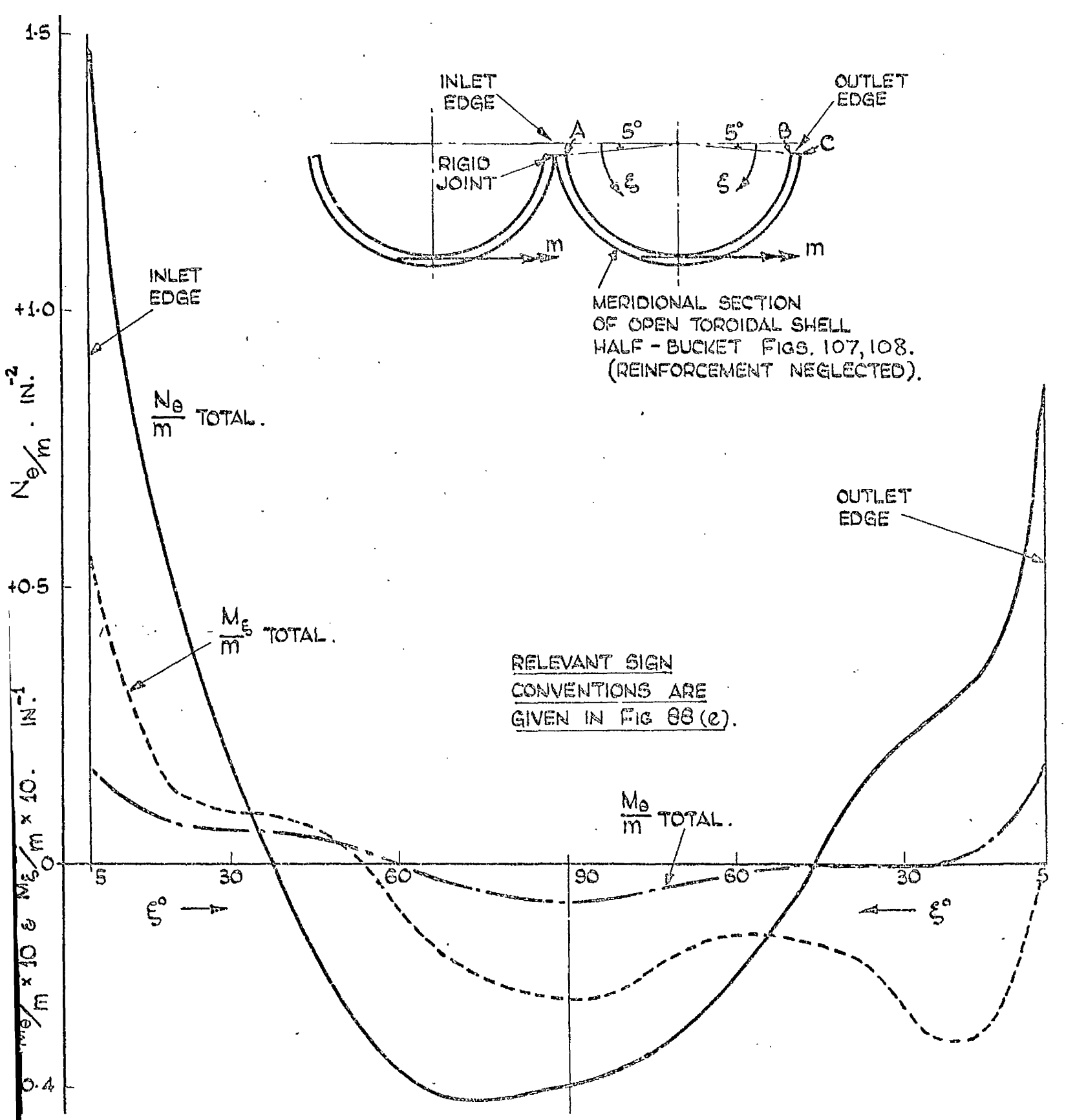

FIG. 111. SHELL HALF-BUCKET (REINFORCEMENT NEGLECTED) ASSEMBLED AT INLET EDGE AND CARRYING BENDING MOMENT m, AS ABOVE. DISTRIBUTIONS OF TOTALS N_θ/m, N_θ/m, M_ξ/m WITH ξ, OVER FULL MERIDIAN, OBTAINED FROM FIG 93, (SIGNS CHANGED), EQUATION (7.1) AND FIG. 110.

7A i Approximate theoretical analysis of the effectiveness of the "circumferential" reinforcing rib on a Pelton half-bucket

As has been mentioned, the Pelton bucket which is the subject of the numerical application of the shell theory, carries a "circumferential" reinforcing rib on the unswept surfaces of each half, Figs.107, 108. This has been disregarded in the previous section of the analytical treatment. In most, but not all designs, such reinforcement is present. In respect of its location and from the general bending nature of the problem, its reinforcing action would be expected to be fairly effective, and may be considered as tending to reduce the proportion of a total applied in-plane bending moment m_{TOT}, Fig.112, carried by the main shell body of the half-bucket.

The basis of the following approximate analysis is appropriate to simple bending theory of beams, and is illustrated in Fig.112. The main body of the half-bucket and the reinforcing rib are regarded as replaced by the associated open toroidal shell and the symmetrically located associated rectangular section rib respectively, e.g. as on Figs.107, 108. The associated reinforced open toroidal shell half-bucket is initially considered to be separated from its twin at the inlet edge. Referring to Fig.112, the total in-plane pure bending moment m_{TOT}, applied to a meridional section of the reinforced shell, is assumed to be distributed such that component m is taken by the shell, component m_R by the reinforcing rib, and the remaining component by couple $P(\ell_1 + \ell_2)$ such that forces P equal and opposite, act at point X on the neutral surface of the shell and at centroid Y of the rib. In both shell and rib, the stresses due to forces P are considered uniformly distributed over the sections. The theory of chapter 5 is relevant to the shell subjected to moment m, and simple beam theory is relevant to the rib under moment/

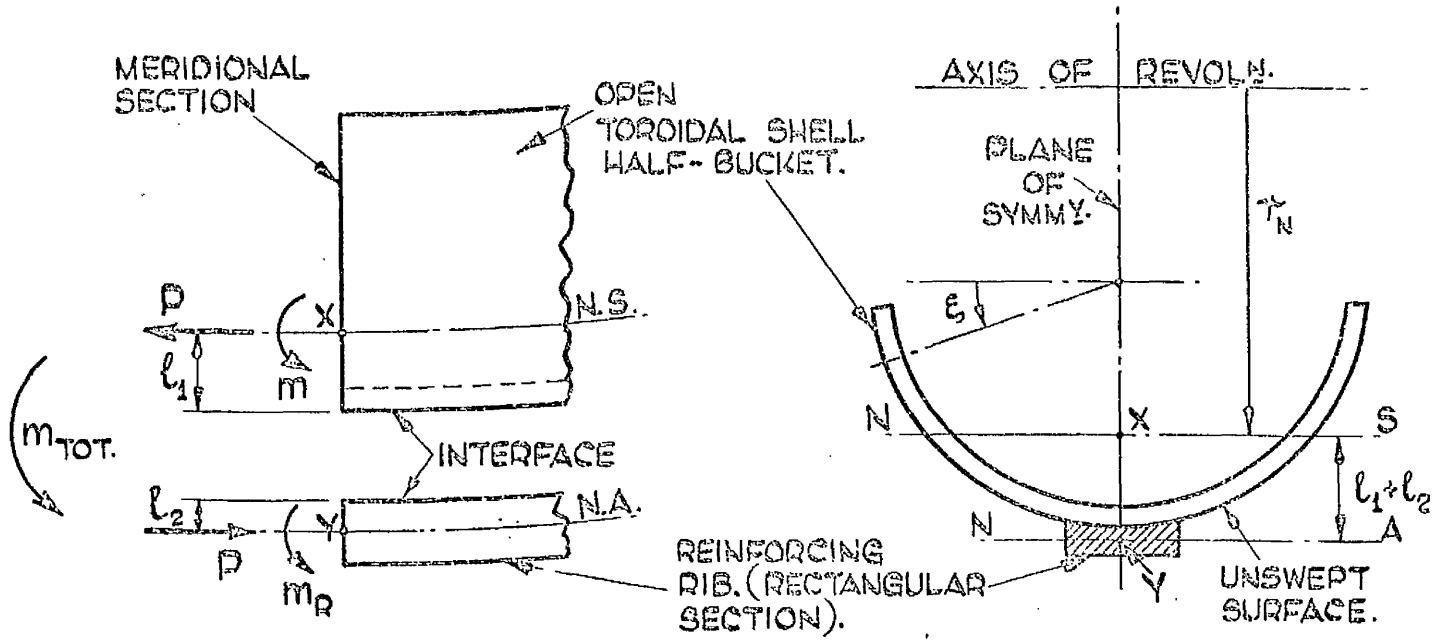

CONDITIONS ARE :-

$$m_{TOT.} = m + m_R + P(\ell_1 + \ell_2).$$

$$\varepsilon_S = \varepsilon_R \text{ AT INTERFACE.}$$

$$\Delta K_S = \Delta K_R \text{ AT INTERFACE.}$$

SUFFIX S = SHELL.
SUFFIX R = RIB.

FIG. 112. DIAGRAM ILLUSTRATING BASIS OF APPROX. THEORETICAL ANALYSIS FOR EFFECTIVENESS OF REINFORCING RIB ON PELTON HALF-BUCKET.

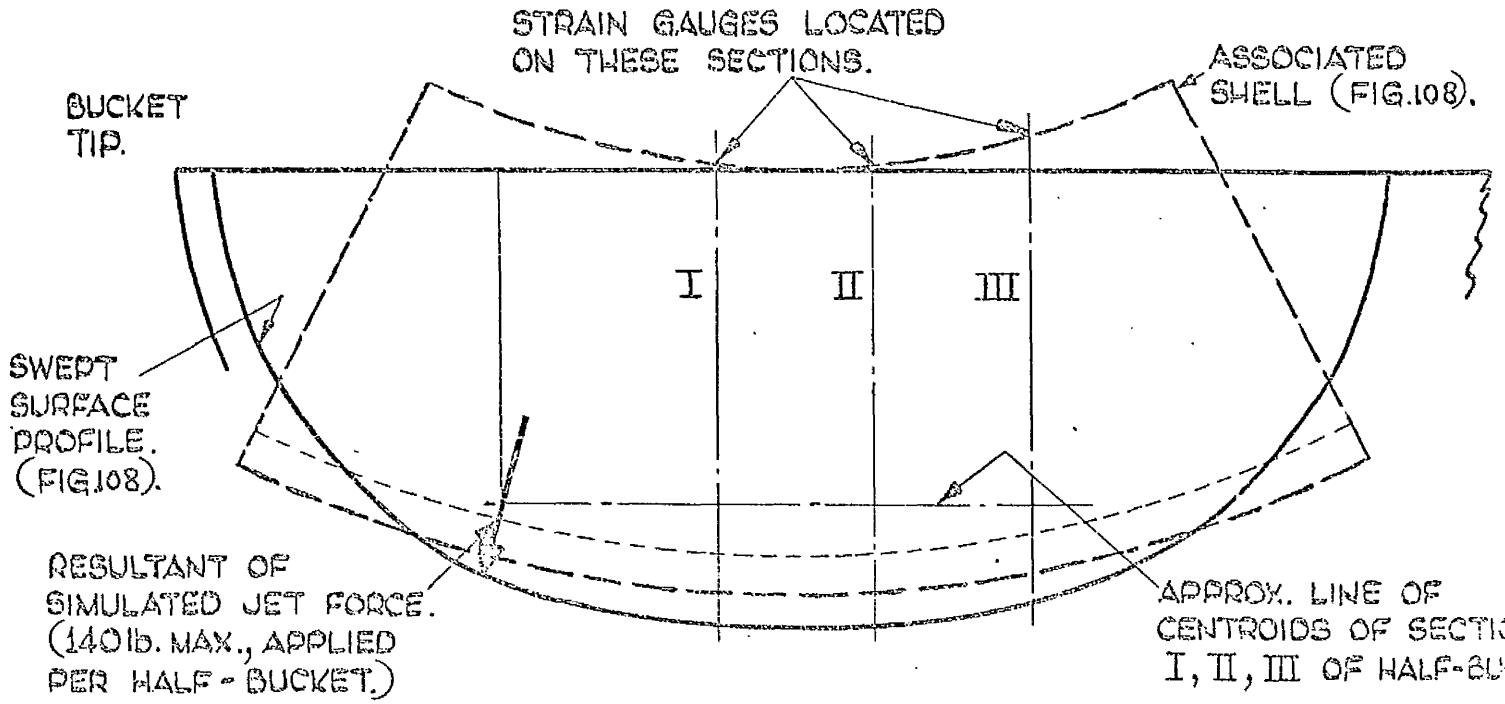

FIG. 113. LOCATION OF RESULTANT OF SIMULATED JET FORCE IN RELATION TO SECTIONS OF MAIN BODY OF PELTON HALF-BUCKET, AT WHICH STRAINS WERE MEASURED. (SEE FIGS. 108, 114).

moment m_R. For displacement compatibility at the interface, Fig.112, the circumferential strains in shell and rib must be equal and the changes in curvatures of shell and rib must be equal. Referring to Fig.112, all these conditions are embodied in the equations:-

$$m_{TOT} = m + m_R + P(\ell_1+\ell_2) \qquad (7.17)$$

$$\varepsilon_S = \varepsilon_R \qquad \text{at interface,} \qquad (7.18)$$

$$\Delta K_S = \Delta K_R \qquad \text{at interface,} \qquad (7.19),$$

where

$$\varepsilon_S = \varepsilon_{\substack{\theta \\ \xi=\frac{\pi}{2}}} = \frac{1}{E}\left(\sigma_\theta - \nu\sigma_\xi\right)_{\xi=\frac{\pi}{2}} ,$$

appropriate to the shell unswept surface,

and

$$\Delta K_S = \frac{\Delta r_N}{(r_N+\ell_1)^2} = \Delta K \frac{r_N^2}{(r_N+\ell_1)^2}$$

$$= k\frac{r_N}{(r_N+\ell_1)^2} ,$$

consistent with the formulation of the equation for ΔK, preceding equation (5A.1), and from equation (5A.4).

Reverting to chapter 5 for numerical application of this treatment to the case Figs.107, 108 it is noted that:-

$k = 66.98\frac{m}{E}$ from equation (5C.5).

Hence $\left(\sigma_\theta - \nu\sigma_\xi\right)_{\xi=\frac{\pi}{2}} = -1.84\ m$, on unswept surface, from Fig.93 with signs changed,

and $r_N = 5.01$, from Fig.93 and equation (5A.5).

Then/

Then with reference to Figs.107 and 112, application of equations (7.18), (7.19) above is, respectively, thus:-

$$-\frac{1.84\,m}{E} + \frac{P}{1.25\,E} = \frac{m_R \times 0.1}{\frac{1}{12} \times 0.8 \times 0.008\,E} - \frac{P}{0.16\,E}$$

$$66.98\frac{m}{E} \times \frac{5.01}{5.70}^2 = \frac{m_R}{\frac{1}{12} \times 0.8 \times 0.008\,E}$$

Solving these, together with equation (7.17), it is found that:-

$$m = 0.76\, m_{TOT} \qquad \text{and} \qquad P = 0.31\, m_{TOT}\,.$$

Thus the effect of the associated reinforcing rib Fig.107, is that the open toroidal shell itself, carries only 76% of the total applied in-plane bending moment m_{TOT}, together with a direct circumferential tensile stress equal to $+ 0.25\, m_{TOT}$ throughout. The shell itself may now be regarded as assembled to its twin at the inlet edge, and subjected to $m = 0.76\, m_{TOT}$, plus the direct stress. Then referring to equations (7.16) which give the final shell edge stresses for the assembled shells Fig.111, disregarding the reinforcing rib, these values are modified to take account of the reinforcement thus:-

at A, Fig.111, inlet edge swept surface, $\sigma_\theta = + 7.81\, m_{TOT}$

$\sigma_s = + 6.49\, m_{TOT}$ (7.20)

at B, Fig.111, outlet edge swept surface, $\sigma_\theta = + 5.26\, m_{TOT}$

at C, Fig.111, outlet edge unswept surface, $\sigma_\theta = + 1.58\, m_{TOT}$,

all for the associated reinforced open toroidal shell half-bucket, Figs.107, 108, assembled at inlet edge as on Fig.111, and subjected to in-plane bending moment m_{TOT}.

The effectiveness of the reinforcing rib may be gauged by comparing the stress maxima for the plain and reinforced shell assembled half-buckets, subjected to the same moment m_{TOT}. For the plain shell, m in

equations/

equations (7.16) equals m_{TOT}, so that for the case under examination:-

$$\frac{\sigma_{MAX.\ \text{reinforced shell half-bucket}}}{\sigma_{MAX.\ \text{plain shell half-bucket}}} = \frac{7.81}{9.95} = 0.79 \qquad (7.21)$$

This approximate assessment indicates that the reinforcement is fairly effective and is worthwhile.

This analysis, and that of the previous section, as has been mentioned therein, are derived on the assumption that the half-buckets are subjected to pure in-plane bending moment. It is now assumed further that, in their completed forms as presented, the analyses apply to cases of continuously varying in-plane bending moment.

7B MEASUREMENT OF APPROXIMATE JET LOADING STRESSES IN A BUCKET OF A 21 in.p.c.d. PELTON WHEEL. COMPARISON WITH THEORETICAL RESULTS.

More strain gauges were located on one of the two nominally identical bronze Pelton buckets than on the other. The latter played a secondary checking rôle and, during testing, gauges on one bucket served as compensators while the gauges on the other bucket were active. For the most part, gauges were located on the main body of the bucket at sections I, II, III, Fig.113. On both surfaces of the edges at all three sections, gauge pairs were mounted parallel and perpendicular to the edges and, on section III, rosettes were mounted at four points remote from the edges. All the locations explored for strains are evident from the results presented in Fig.115.

As in the Turgo wheel, so in the Pelton wheel, the intensity, the point of application and the direction of the resultant jet force on a bucket, are dynamic in character, under normal working conditions. Thus, in these tests, where the jet force was simulated by mechanical means with the bucket stationary, the loading may be considered roughly as pertinent to some instant during the dynamic cycle. The character of the simulated jet loading on the Pelton bucket was such that the loading may reasonably be considered as approximating to the working condition relevant to the maximum jet loading stress in the bucket.

The testing arrangements in respect of the bucket loading apparatus and strain measuring equipment, are illustrated in Fig.114. For loading, the bracket of the bucket was clamped in a vice, as shown, and equal forces were applied to the half-buckets via small pads, specially-formed weight-holders and deadweights. The forces were applied in the "hollows" of/

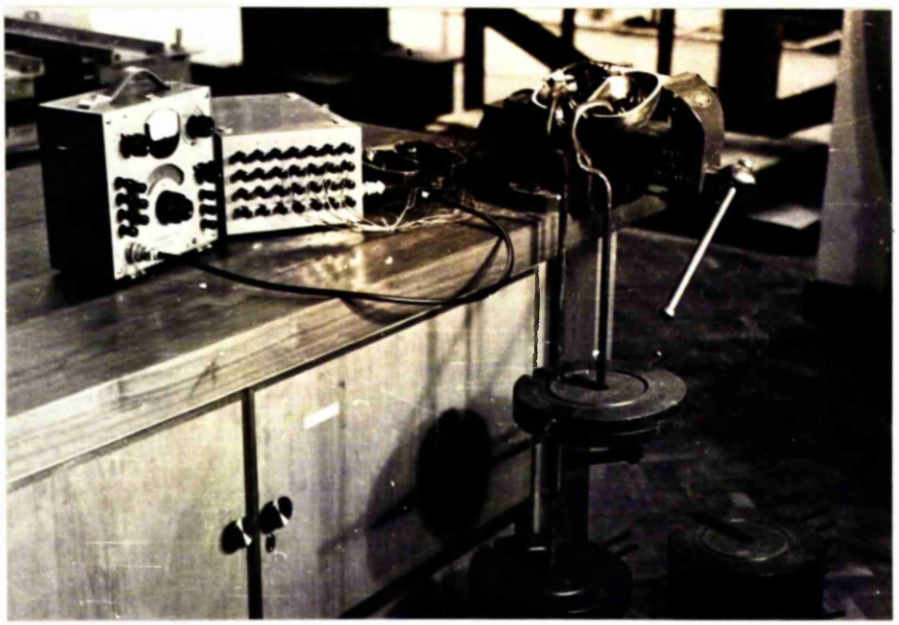

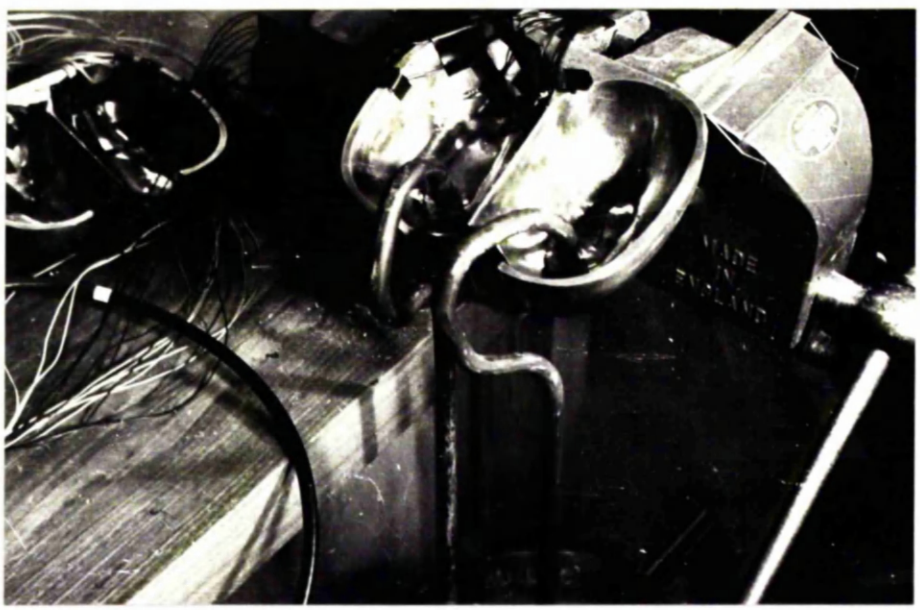

FIG.114. MEASUREMENT OF APPROXIMATE JET LOADING STRESSES IN A PELTON BUCKET. PHOTOGRAPHS SHOWING THE TWO BRONZE BUCKETS, THE STRAIN MEASURING EQUIPMENT, AND THE METHOD OF APPLICATION OF THE SIMULATED JET LOADING.

of the half-buckets, as nearly as possible in the planes of symmetry of the associated open toroidal shells, Fig.107. In relation to meridional sections at which strains were measured, the location and attitude of the resultant force on a half-bucket are shown in Fig.113. The force was positioned towards the bucket tip to produce a relatively high in-plane bending action on the main body of the half-bucket, and to correspond roughly with the resultant of the hydraulic loading depicted on Fig.29.

Using this method of loading, it was possible to apply a maximum force of 140 lb per half-bucket. As is evident from the measured values shown in Fig.115, this, and smaller loads, were perfectly adequate to produce ascurately measurable strains, and at all locations explored, the strain/load graphs were found to be linear. However, for this bucket in the 21 in. wheel at normal working conditions under the maximum rated head, the maximum resultant jet force per half-bucket is about 700 lb. In order to relate the test results to these normal working conditions therefore, the strains appropriate to the maximum applied test loading of 140 lb per half-bucket, have been multiplied by a factor of 5. Corresponding stresses have been determined using the values, for high tensile bronze:-

$$E = 16 \times 10^6 \text{ lb/in.}^2 \qquad \nu = 0.3$$

obtained from relevant literature. These measured simulated jet loading stresses, pertinent to the normal working condition of the bucket, are presented in Fig.115. They are the stresses shown on the upper half-bucket. All the values are well within the elastic limit of the bucket material.

For comparison, the corresponding theoretical jet loading stresses in the main body of the half-bucket, are shown on the lower half-bucket of Fig.115. These stresses have been determined from the analyses of the previous sections 7A and 7A i applied to this case of an in-plane bending moment varying continuously over the main body of the half-bucket, and so over/

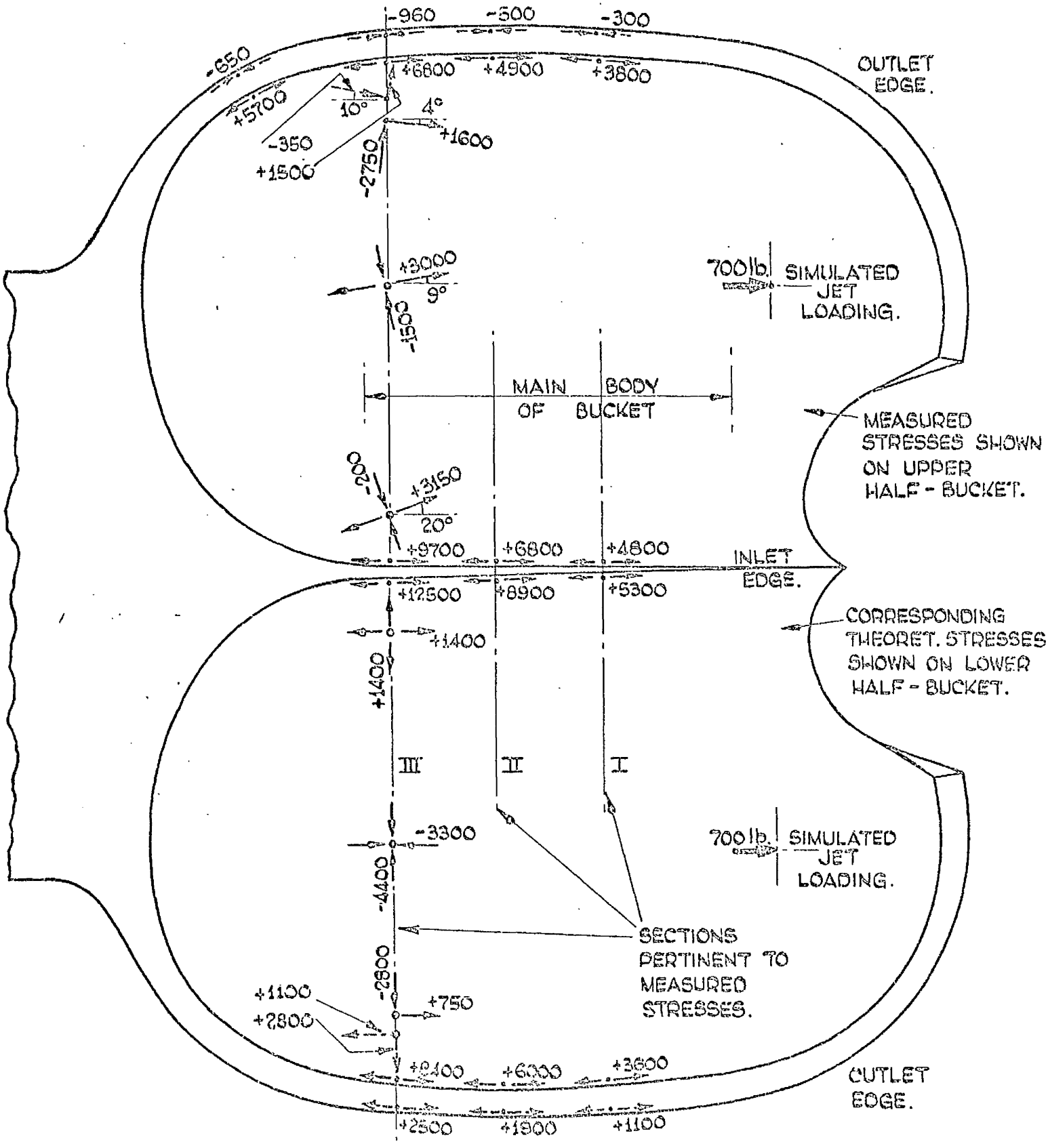

FIG. 115. MEASURED AND CORRESPONDING THEORETICAL PRINCIPAL STRESSES (lb/in^2) ON A BUCKET OF 21 in. p.c.d. PELTON WHEEL, UNDER SIMULATED JET LOADING, OF MAGNITUDE APPROPRIATE TO NORMAL WORKING CONDITIONS

over the associated reinforced open toroidal shell. From Fig.113, the value of the in-plane bending moment acting at any of the sections I, II, III, is given by the product of the simulated jet force and the perpendicular distance from the centroid of the section to the line of action of the force. This value is then taken as m_{tot} in the analytical sections 7A and 7A i, from which the appropriate theoretical stresses are readily determined. For example, at section III, Fig.113, for a simulated jet force of 700 lb per half-bucket, m_{tot} = 1610 lb.in., so that from equations (7.20), the maximum theoretical stress at the section is $\sigma_\theta = +7.81 \times 1610 = +12,500$ lb/in.^{2}, on the inlet edge.

On account of their greater significance, measured and theoretical stresses on the bucket edges are further compared in Fig.116, where the theoretical stresses are shown as edge surface stress distributions of linear form, in accordance with Fig.113. These stresses act parallel to the edges, of course. As was to be expected, the measured stresses perpendicular to the edges were found to be negligibly small. At the inlet edge, this finding is inevitably at variance with the theory, which shows a fairly high stress there in the ξ - direction, as may be seen from equations (7.20). This however, is a matter of little importance.

It is interesting to compare the measured edge stresses, Fig.116, with those measured by PERRIG[4], Fig.2, for a bucket without rims, subjected to simulated jet loading. Both sets of measured results, Figs.116 and 2, show approximately linear stress distributions on the inlet edges, with the maximum measured stresses located at the hub ends of the inlet edges. PERRIG'S[4] maximum stress is + 12,200 lb/in^2, compared with a maximum of + 9,700 lb/in^2, Fig.116. The measured stresses on the unswept surface of an outlet edge, are very small and tensile on Fig.2, but are very small and compressive on Fig.116. The buckets of Figs.2 and 116 are fairly different in design, and that of Fig.2/

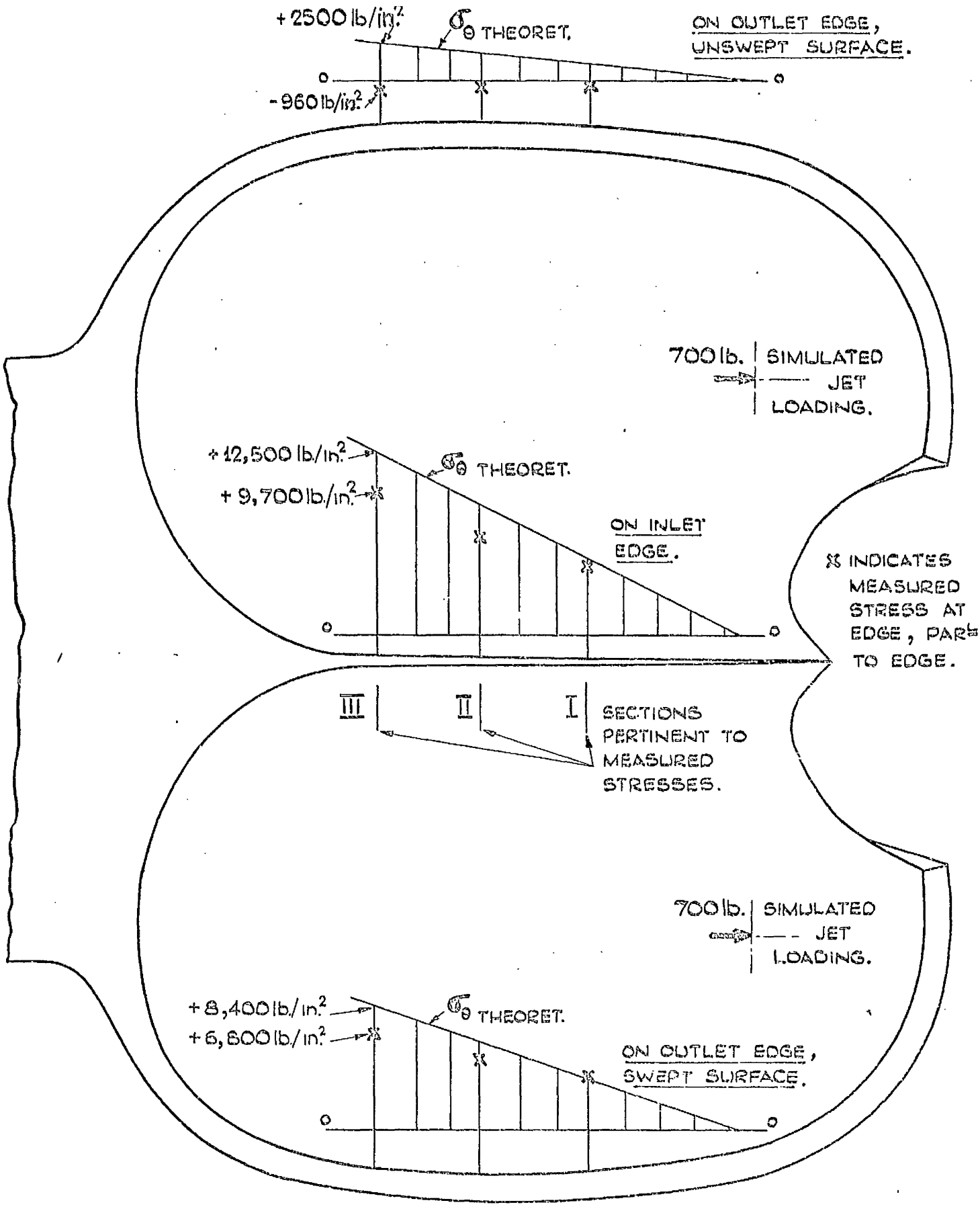

FIG. 116. COMPARISON OF MEASURED AND THEORETICAL STRESS DISTRIBUTIONS ON THE SURFACES OF THE EDGES OF A BUCKET OF 21 IN. P.C.D. PELTON WHEEL, UNDER SIMULATED JET LOADING, OF MAGNITUDE APPROPRIATE TO NORMAL WORKING CONDITIONS.

Fig.2 is three times as large as that of Fig.116.

For the non-edge principal stresses at section III, Fig.115, quantitative agreement between experimentand theory is best towards an outlet edge, but is not good on the whole. This is hardly surprising, since the actual and associated theoretical meridional cross-sections of the half-bucket, Fig.107, are rather a remote match, and corresponding non-edge locations thereon are difficult to define. Qualitative agreement between measured and theoretical stresses however, is reasonably good. It may be remarked that the measured stresses on section III of the Pelton half-bucket, Fig.115, show excellent qualitative correspondence with the stresses measured on a meridional section of the Turgo wheel bucket, Fig.48. The loadings relevant to both buckets are rather similar. The measured stresses on the meridional sections of both buckets, and the theoretical stresses indicated on the lower half-bucket of Fig.115, are in accord in exhibiting non-edge stresses of much lower values than the associated stresses on the swept surfaces of the edges.

The most significant measured and theoretical stresses on the Pelton bucket are those on the edges, Fig.116, and for those, agreement of experiment with theory is reasonably good. Since it is not possible to locate a strain gauge directly on the edge, it is not surprising that the measured values are, on the whole, less than their theoretical counterparts. In the main body of the bucket, measurement and theory both show stress maxima at the hub end of the inlet edge, the theoretical maximum being 29% in excess of the measured maximum. At this location, the actual and the theoretical bucket geometries are appreciably different, as may be seen in Fig.107. The actual inlet edge is sharp of course, and in way of this edge, the half-buckets are connected by a solid web. Nevertheless it seems likely that the actual stress behaviour on, and in the region of, the inlet edge will conform generally to the pattern of that assumed by the theory, and/

and embodied in Fig.106.

The effect of the sharpness of the inlet edge is difficult to assess, but it seems rather improbable that sharpness, of itself, would cause the stresses to be significantly higher than the corresponding ones on the swept surface of the outlet edge. It is noteworthy that, in the experimental results for Turgo wheel buckets, chapter 4, the highest stress on the sharp inlet edge is, in general, considerably lower than the corresponding highest stress on the blunt outlet edge.

CHAPTER 8.

IMPLICATIONS OF RESULTS IN RELATION TO THE DUTIES AND THE STRENGTH DESIGN OF TURGO IMPULSE WHEELS AND PELTON WHEELS.

IMPLICATIONS OF RESULTS IN RELATION TO THE DUTIES AND THE STRENGTH DESIGN OF TURGO IMPULSE WHEELS AND PELTON WHEELS

In foregoing chapters, approximate shell theoretical treatments have been developed, which explain the working stress behaviours of the buckets of impulse water turbines. Furthermore, and in especial, experimental and approximate theoretical analyses have been applied to determine stresses and deformations in particular sizes of impulse water turbines, at normal working conditions under particular maximum rated heads.

In the light of the possibility of adopting increased maximum head ratings, and in the light of the relationship of geometrical similarity which commonly exists between different-sized turbines of a kind, it is highly relevant now to consider the variations of normal working stresses with head and with size. These considerations, which are simple in essence and which produce satisfyingly simple results, are presented herein. It is an indication of the extent to which strength aspects of water turbine design have been neglected, that the author has searched the literature in vain, for evidence of such relatively simple but highly significant exercises having been undertaken, in respect of any type of water turbine.

Theoretical analyses are inherently approximate and, as has been previously mentioned, the experimental results are of the most direct significance. These latter give reliable magnitudes of important stresses. However the implications of experimental results in relation to strength design of the impulse water turbine, are best interpreted in the light of corresponding theory. This is particularly so when considering the results with a view to altering design for the express purpose of reducing significant working stresses. Recommendations for such design alterations must, of course, be realistic, and such as to involve little or no interference with the hydraulic characteristics of the turbine.

8A VARIATIONS OF NORMAL WORKING STRESSES IN IMPULSE WATER TURBINES WITH SIZE AND WITH HEAD

The following analyses apply to both Turgo impulse wheels and Pelton wheels. The analyses are on broad simple lines but, in essence, are similar to full dimensional analyses throughout rigorous theoretical treatments. As is evident from these subsequent considerations, the results deduced hereby, will be expected to be the same as those which would be given by the full detailed approach.

It is assumed that:-

(1) All impulse water turbines in a group of one kind, are geometrically similar.

e.g. for current design Turgo wheels, all dimensions of a $63\frac{1}{2}$ in. p.c.d. wheel say, are $S = \frac{63\frac{1}{2}}{16\frac{1}{2}}$ times the corresponding dimensions of a $16\frac{1}{2}$ in. p.c.d. wheel.

As thus defined, S in general, is the Dimension Ratio.

(2) The normal working conditions of all impulse water turbines in a group of one kind, are synonymous with the maximum efficiency conditions, i.e. all such turbines work at a constant velocity ratio:-

$$\frac{\text{wheel p.c. peripheral velocity}}{\text{jet velocity}} = \frac{v_w}{v_j} \doteq 0.5 .$$

For a given head, therefore a given jet velocity v_j, therefore a given wheel p.c. peripheral velocity v_w, the corresponding angular velocities ω of variously-sized wheels of a kind, are directly proportional to $\frac{1}{S}$:—

Centrifugal Force is directly proportional to (volume x ω^2 x radius),

i.e. to $S^3 \times \frac{1}{S^2} \times S$

i.e. to S^2.

Jet/

Jet Force is directly proportional to (jet mass flow x change in jet velocity),

i.e. to (nozzle area) x v_j x (dimensionless constant x v_j)

i.e. to S^2.

Now direct stresses σ, arise mainly due to internal direct forces F and bending moments M_B or, in shell notation, due to internal direct stress resultants N force/unit length, and stress couples M moment/unit length. All of these internal actions are directly proportional to Centrifugal Force and Jet Force. Hence comprehensively, and from above:

internal direct forces F are directly proportional to S^2,

internal bending moments M_B are directly proportional to $S^2 \times S$ i.e. to S^3,

internal stress resultants N are directly proportional to $\frac{S^2}{S}$ i.e. to S,

internal stress couples M are directly proportional to $\frac{S^2 \times S}{S}$ i.e. to S^2.

Therefore direct stresses σ are given by:-

$$\sigma = \frac{F}{\text{cross-sectional area.}} = \frac{M_B}{\text{section modulus.}} = \frac{N}{\text{thickness}} = \frac{6M}{\text{thickness}^2}$$

$$= \frac{\text{prop. to } S^2}{\text{prop. to } S^2} = \frac{\text{prop. to } S^3}{\text{prop. to } S^3} = \frac{\text{prop. to } S}{\text{prop. to } S} = \frac{\text{prop. to } S^2}{\text{prop. to } S^2}$$

= unaltered, and independent of S.

Thus, under the same head, all sizes of geometrically similar, normal working, impulse water turbines carry the same stresses.

For a given size of turbine, direct stress σ is directly proportional to Centrifugal Force and Jet Force.

Now Centrifugal Force is directly proportional to ω^2 for a given size of wheel,

i.e. is proportional to v_w^2,

i.e. is proportional to v_j^2.

Also Jet Force is directly proportional to v_j^2 for a given wheel (and therefore nozzle) size.

Therefore direct stress σ is directly proportional to v_j^2, and so direct stress σ is directly proportional to head.

Thus the normal working stresses in an impulse water turbine vary in direct proportion to the head.

These two simple but important findings above, may be summarised by the following statement:-

For all sizes of geometrically similar impulse water turbines working under the same head, at the same velocity ratio v_w/v_j, the stresses carried are the same. The stresses increase in direct proportion to the head, for velocity ratio remaining constant.

Although the statement applies for any constant velocity ratio v_w/v_j, its most important application in relation to service life is, of course, to the normal working condition, for which $v_w/v_j \fallingdotseq 0.5$. In general, an impulse water turbine will operate continuously at the normal working condition, for very long periods.

It is evident from the above simple analyses that, if the separate centrifugal and jet loading stresses be known, for a given wheel at a given speed, under a given jet force, then the stresses in the wheel at any other speed and at any other jet force may be readily found. More significantly, the stresses relevant to another geometrically similar wheel, at any speed and under any jet force, may also be readily deduced.

8B IMPLICATIONS OF RESULTS IN RELATION TO THE DUTIES AND STRENGTH DESIGN OF TURGO IMPULSE WHEELS

From the previous section, and from measured results quoted in chapter 4 and subsequently, Fig.117 has been derived, relating to the variations of the maximum normal working and overspeed stresses with head, for all sizes of geometrically similar current design cast steel Turgo wheels. Fig.117 thus represents some of the most important information sought in the stress investigations on the Turgo impulse wheel, and provides the essential stress data, in the light of which a decision may be reached concerning the adoption of a maximum rated head in excess of the present 700 ft.value. Such a decision would be taken, mindful of the experimental basis of Fig.117, as stated thereon, and of several other factors including the following:-

(1) At the present maximum rated head, the maximum and other significant normal working stresses as found by these investigations, are not high. At the locations of maximum and other significant stresses, the significant values are of a localised character, the stress values in the surroundings of these locations being of an appreciably smaller order.

(2) The maximum and other significant normal working stresses are partly of a cyclic nature (see Fig.122). At overspeed, the maximum and other significant stresses are steady and high. The overspeed condition, if it occurs at all, will do so only once or twice in the life of the wheel.

The experimental and approximate theoretical results prompt several fairly obvious suggestions for improvement from the strength viewpoint. Firstly, since centrifugal stress predominates, manufacture of wheels in bronze,/

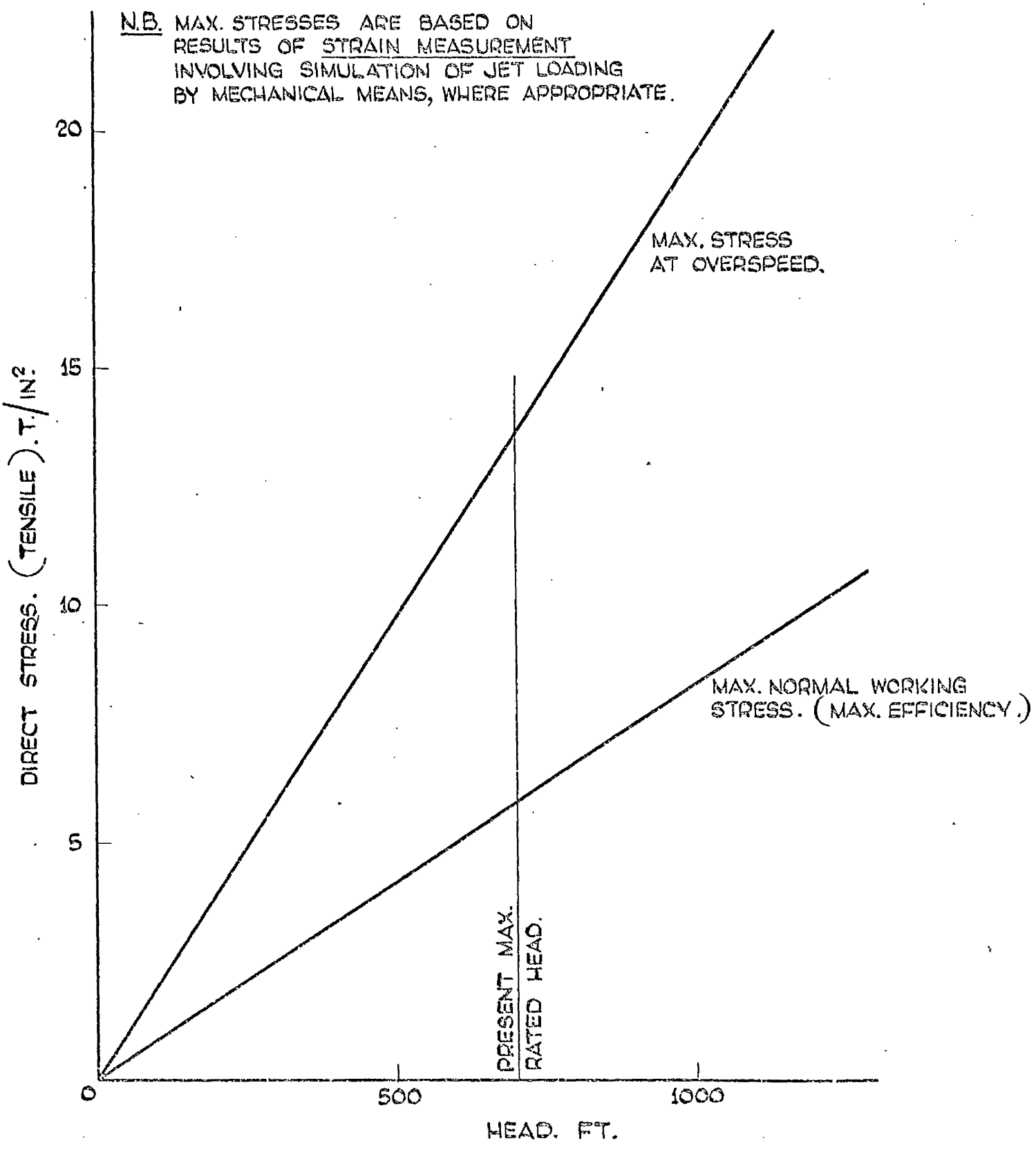

Fig. 117. VARIATIONS OF MAXIMUM NORMAL WORKING AND OVERSPEED STRESSES WITH HEAD, FOR ALL SIZES (GEOMETRICALLY SIMILAR) OF CURRENT DESIGN CAST STEEL TURGO WHEELS. NORMAL WORKING CONDITION REFERS TO CONSTANT RATIO (WHEEL p.c. VELOCITY / JET VELOCITY) = 0.5. OVERSPEED ≈ 1·8 × NORMAL WORKING SPEED.

bronze, which is almost 10% more dense than cast steel, is untenable. Also, it is not fanciful to recommend consideration of the use of lighter materials, like hard aluminium alloys. Secondly, in important stress concentration regions at the junctions of the bucket outlet edge with hub and with rim, generous fillets should be incorporated. In Fig.118, present design and recommended design, in respect of fillets at these stress concentrations, are contrasted. Thirdly, better surface finish should be achieved in areas of significant stress. Care should be taken to avoid or eliminate identations, scratches and nicks on the swept surfaces of bucket edges, and at the stress concentrations.

The results highlight the strength aspects of basic features of the wheel geometry. For instance, the highly essential part played by the rim has been amply demonstrated, with regard to both centrifugal and jet loading stresses. It is evident that alterations to dimensions and geometry could be firmly recommended for the purpose of achieving reductions in significant stresses, but such a course would be invalid in isolation from parallel considerations of possible effects on hydraulic characteristics. Suffice it that the strength effects of any appreciable design modification may be roughly assessed by application of the approximate theoretical treatments of chapter 3, section 6B ii of chapter 6, and Appendix 7.

Avoiding consideration of changes in respect of buckets, the strength effects of alterations pertinent to the rim may be worthy of some attention. Although in the existing design, the rôle taken by the rim is an effective one, it is likely that this would be enhanced if the rim were offset towards the inlet side to a less extent. For example, it may be instructive to apply the approximate theory to assess the effect of locating the equivalent existing rim on the line of centroids of the equivalent parabolic section bucket, Fig.12, although such an alteration in geometry would probably be too radical from the hydraulic standpoint.

A/

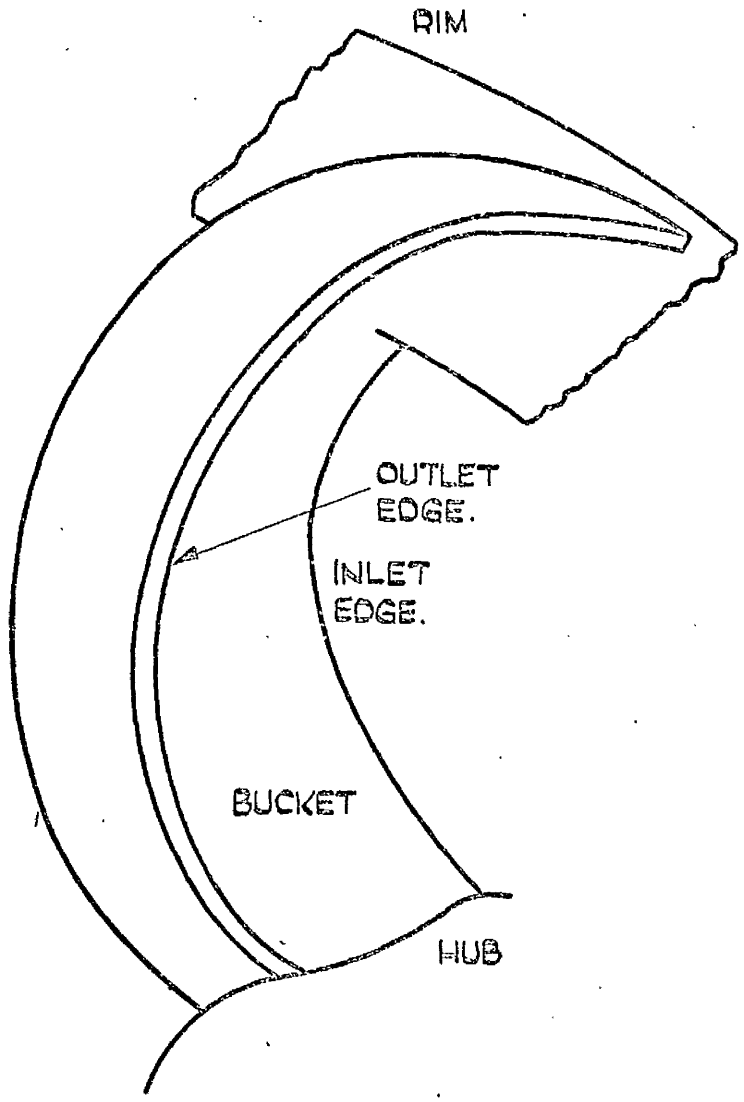

EXISTING DESIGN.
FILLETS AT OUTLET EDGE RIM & HUB JUNCTIONS ARE VERY SMALL.

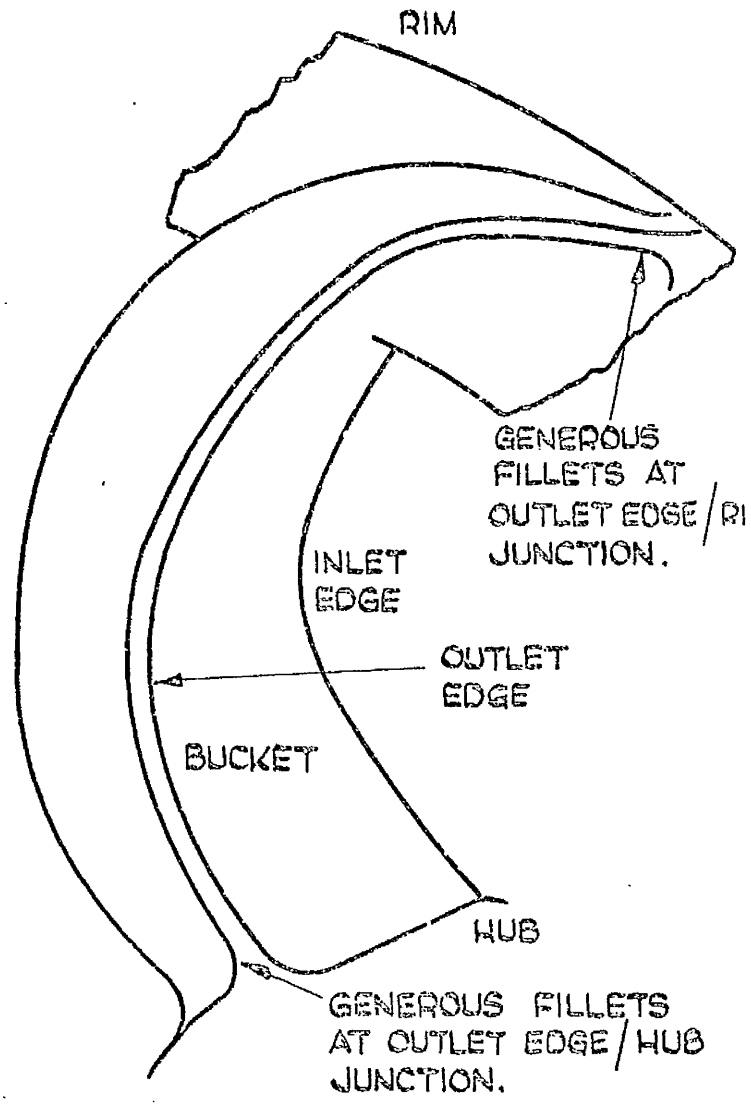

RECOMMENDED ALTERATIONS IN RESPECT OF FILLETS AT OUTLET EDGE RIM & HUB JUNCTIONS. FILLETS SHOULD BE $\frac{1}{4}$ IN. RADIUS AT LEAST, ON A $16\frac{1}{2}$ IN. p.c.d. WHEEL.

FIG. 118. COMPARISON OF EXISTING DESIGN (CURRENT) AND RECOMMENDED ALTERED DESIGN OF TURGO IMPULSE WHEEL, IN RESPECT OF FILLETS AT STRESS CONCENTRATION REGIONS, IN WAY OF JUNCTIONS OF BUCKET OUTLET EDGE WITH HUB AND WITH RIM.

A more realistic alternative may be to maintain the rim in its existing position, and to consider alterations in rim dimensions. From the results, it is unlikely that such alterations would affect bucket jet loading stresses to much extent, but they may have a fair influence on bucket centrifugal stresses. Both experiment and theory, Figs.70 and 99, reflect the flexibility of the rim in respect of rotation in the planes of cross-sections (theoretically, under assembly moment action M_T, Fig.13, and section 3B iii, chapter 3). In this particular respect, the existing rim may not be a very effective restraint on the bucket, as may be partially indicated by the tendency for bucket centrifugal stresses to be higher on the outlet edge than on the inlet. This aspect of the rim restraint might be improved by increasing the axial dimensions of the rim, an alteration which could be made, irrespective of hydraulic considerations, as is evident from Fig.119.

Concerning centrifugal stresses, an indication of the limit of the effects to be expected from increases in rim section sizes, may be obtained by assuming a rim much more massive than a bucket, so that in theory, the deformations of the massive rim under the assembly actions Fig.13 (and section 3B iii, chapter 3) may be taken as zero. For a rim of massive, but compact, almost symmetrical section, deformation in the free rotating condition, Fig.14 (and section 3B i, chapter 3) is independent of section dimensions. Such an application of the theory, section 3B v, chapter 3, involves the replacement by zero, of the terms δ_{R1}, ϕ_{P1}, ϕ_{R1}, ϕ_{T1} on the left-hand sides of equations (3B.81) to (3B.84) inclusive.

On this basis, for the $16\frac{1}{2}$ in.cast steel wheel at normal working speed, Fig.120 shows the resulting distribution of "massive" rim total centrifugal stresses on the bucket edges, as compared with the corresponding total stresses from Fig.26, pertinent to the bucket with the equivalent rim of the existing design. The "massive" rim total stress distribution/

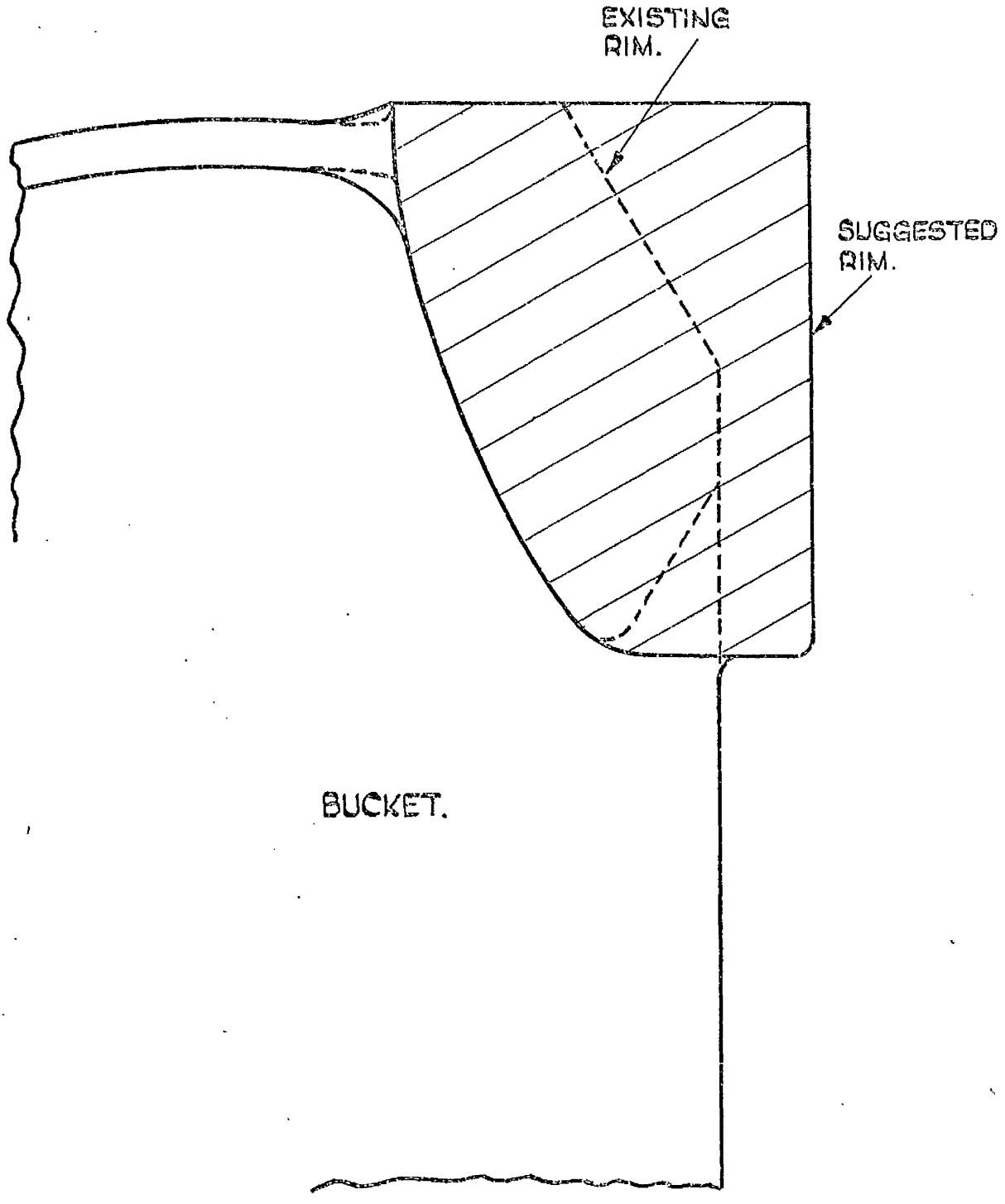

FIG. 119. CURRENT DESIGN TURGO IMPULSE WHEEL. SUGGESTED ALTERATION WITH REGARD TO INCREASE IN AXIAL DIMENSIONS OF RIM SECTION, TO ENHANCE RESTRAINT OF RIM ON BUCKETS. THIS ALTERATION HAS NO EFFECT ON HYDRAULIC CHARACTERISTICS. FULL SIZE FOR $16\frac{1}{2}$ IN. WHEEL.

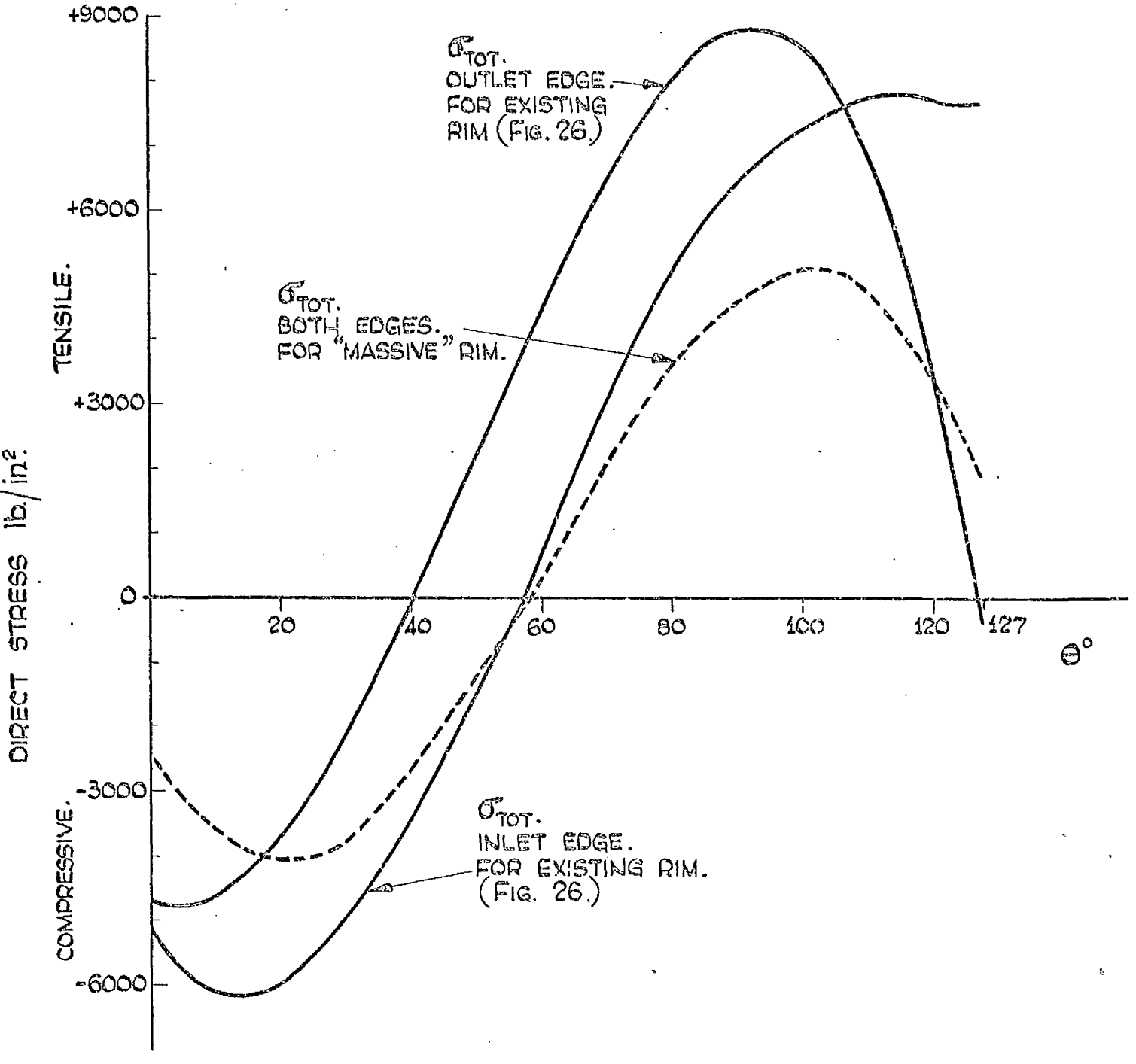

FIG. 120. DISTRIBUTION WITH θ OF THEORETICAL (CHAPTER 3) TOTAL CENTRIFUGAL STRESSES ON INLET AND OUTLET EDGES OF EQUIVALENT BUCKET OF 16⅝ IN. CAST STEEL TURGO WHEEL AT NORMAL WORKING SPEED. COMPARISON OF STRESSES FOR EXISTING RIM (FIG. 26), WITH STRESSES BASED ON ASSUMPTION OF A RIM "MASSIVE" IN RELATION TO BUCKETS.

distribution is the same for both edges of course, and shows considerably lower values than the distributions for the existing design. Even so, the "massive" rim values are appreciable and reflect characteristics of the rim, inherent and independent of its section dimensions, namely its free rotating deformation and its inability to restrain bucket linear tangential displacement.

8C IMPLICATIONS OF RESULTS IN RELATION TO THE STRENGTH DESIGN OF PELTON WHEELS

Some strength design recommendations proposed for the Turgo wheel are also applicable to the Pelton wheel. Although in the latter, centrifugal stresses are apparently of minor importance, for Pelton wheels also, the use of bronze as a manufacturing material should be abandoned in favour of cast steel or lighter materials. Also, concerning the surface finish of Pelton buckets, care should be exercised to avoid or eliminate notches and scratches, particularly on the swept surfaces of edges. It is worth mentioning that the general finish on swept surfaces of Pelton buckets, is invariably much superior to that on corresponding surfaces of Turgo wheel buckets. This is undoubtedly because Pelton bucket surfaces are much more easily accessible.

The approximate theoretical treatment of chapter 7, provides a means of rough assessment, from the strength viewpoint, of the effects of altering bucket dimensions and geometry. The bucket feature most appropriate for examination in this regard, is of course, the "circumferential" reinforcing rib. From section 7Ai and Fig.112, it is evident that the reinforcing effect of the rib is greatest when its depth is greatest. Quantitative assessment in this respect, is provided by Fig.121, which indicates results obtained by extending the numerical application analysis, section 7A i, to consideration of various depths of the reinforcing rib. Fig.121 shows the variation of ratio $\frac{\text{maximum stress in reinforced bucket}}{\text{maximum stress in plain bucket}}$ with depth of the reinforcing rib, for the theoretical Pelton bucket of Figs.107, 108, subjected to a given in-plane bending moment and having reinforcing rib of constant width 0.8 in. A deep reinforcing rib is clearly effective.

Inevitably/

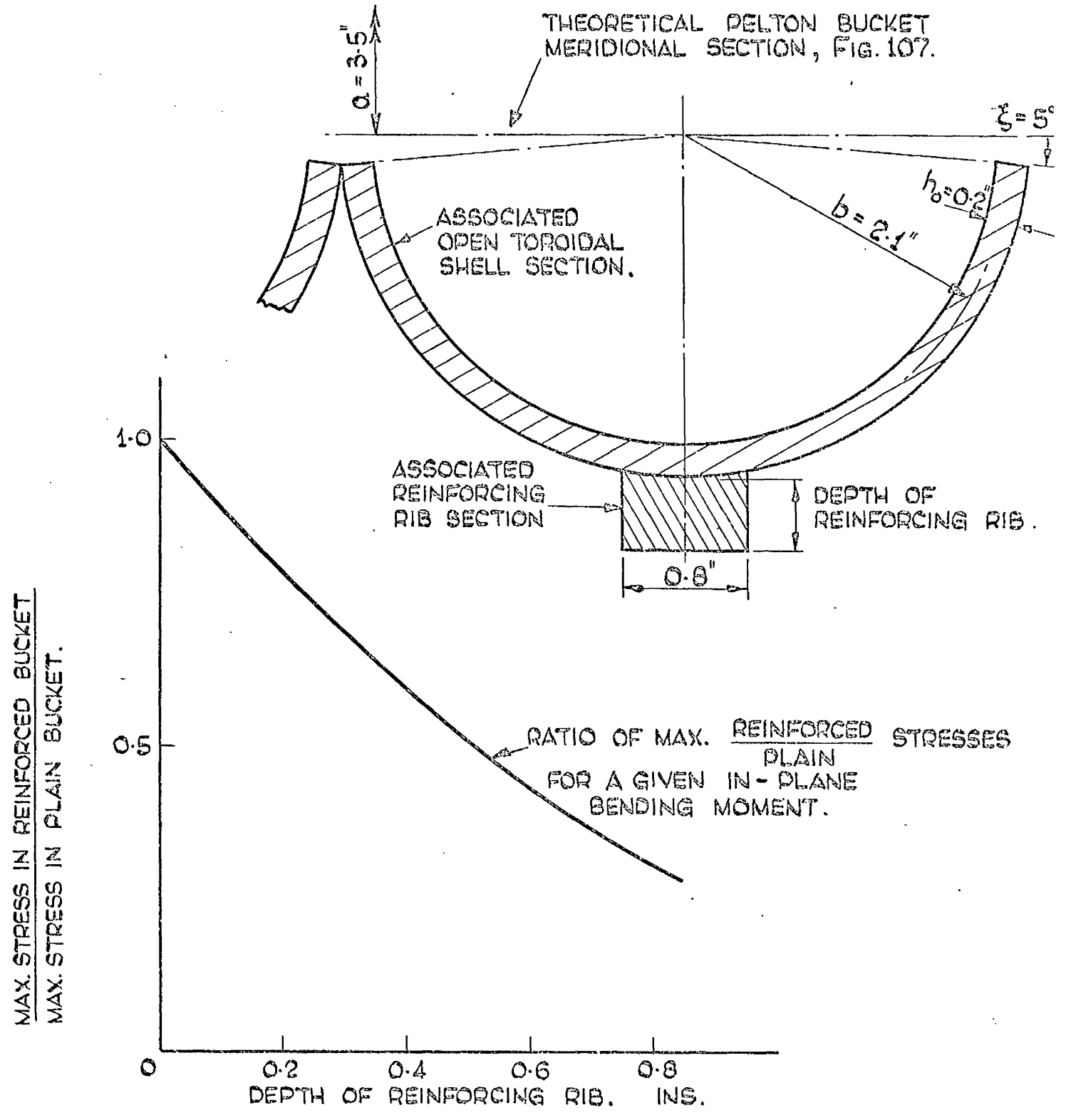

Fig. 121. THEORETICAL PELTON BUCKET OF FIGS. 107, 108 SUBJECTED TO A GIVEN IN-PLANE BENDING MOMENT. GRAPH SHOWING EFFECT OF REINFORCING RIB DEPTH ON MAXIMUM STRESS IN BUCKET, FOR CONSTANT REINFORCING RIB WIDTH.

Inevitably, hydraulic factors impose limits on reinforcing rib depth. For instance, the rib, Fig.121, relevant to the actual bucket, would possibly have a maximum permissible depth of around 0.5 in. The general inference from Fig.121 is clear however, - that design of a Pelton bucket should be such as to incorporate "circumferential" reinforcing ribs of the maximum depth (and width) permissible.

The results for the Turgo wheel, and the data of PERRIG[4], Fig.2, indicate that the use of rims on Pelton wheels will be highly beneficial from the strength aspect. If PERRIG'S[4] stress measurements for the rimmed Pelton wheel are accepted, and on the basis of Turgo wheel results, it is evident that this design modification alone might well produce a reduction of over 50% in maximum normal working bucket stress, or alternatively promote a commensurate increase in maximum rated head. Furthermore, it is likely that the predominant cyclic jet loading stress in the bucket would be the component most influenced in this way. It is useful to note that PERRIG[4] has shown the hydraulic characteristics of a Pelton wheel to be completely unaffected by the incorporation of rims round the buckets. The fact that rimmed Pelton wheels are so uncommon, implies that the unrimmed variety has proven more than adequately strong for the duties demanded of it.

8D COMMENTARY WITH REFERENCE TO FUTURE WORK DERIVING FROM THESE INVESTIGATIONS

With regard to theory, the solution developed in chapter 5 for the in-plane bending of a general open toroidal shell, has been applied only to shells of circular meridian and uniform thickness. Associated more directly with Turgo wheel bucket geometry, a case of a varying thickness, circular meridian shell would be a useful one to analyse initially, subsequent to preparing tables of the necessary functions. Following this, perhaps varying thickness shells of meridional curvatures other than circular, should be investigated using the theory.

However, apart from its relationship to the working stress and deformational behaviour of impulse water turbine buckets, the open toroidal shell in-plane bending problem is of intrinsic interest as an exercise in the development and application of shell theory. The corresponding transverse-plane bending and twisting problem, apparently lacking any solution, is in the same category. It would be irrational to regard the in-plane bending approximate solution, which is presented, as the most satisfactory and accurate solution obtainable within the confines of thin shell theory. Further work should be undertaken to explore improved general solutions, and perhaps to approach certain aspects of the problem afresh, from a different standpoint. In addition, direct experimental comparisons should be sought. As has been found with the corresponding closed shell problem, fully satisfactory experimental conditions may not be easy to achieve.

A feature common to solutions of the closed shell problem and to the solution given for the corresponding open shell problem, is that stress distributions are assumed invariant with circumferential angle Θ .

This/

This is one main respect, concerning which there are still discrepancies between theory and experiment for the closed shell problem, despite the many investigations which have been conducted.

Pursuing future developments in the theoretical analysis of working stresses and deformations in impulse water turbines, it is highly likely that assumed geometries and loadings will conform closest to reality, for solutions which will be derived using numerical analysis methods in conjunction with computers. Advances in computerised numerical analysis techniques must be made, before the undertaking of computer solutions for such complex problems could be considered feasible. It seems certain that such progress will be achieved. In this connection, the "finite element" technique of computerised theoretical stress analysis holds out some promise.

On the experimental side, for both Turgo wheel and Pelton wheel, knowledge of dynamic working pressure distributions on jet loaded buckets is entirely lacking. This knowledge is necessary to the correct understanding of the jet loading stress behaviour of these turbines. Highest priority must, of course, be given to the attainment of successful significant experimental stress analyses under actual working conditions. The related Russian work cited in chapter 1 has contributed little in this respect, and it appears that no such investigation, with strain gauges at important locations on bucket swept surfaces, has been successfully undertaken. Perfect protection of a strain gauge/wiring system against the effects of water jet action, may be achieved by relatively simple means, but to achieve it consistent with negligible interference to flow conditions is very difficult. Particular difficulty attaches in the case of strain gauges on edges of buckets of small or medium-sized impulse water turbines.

Without significantly affecting the stress behaviour on sufficiently large turbines, shallow recesses may be cut on swept surfaces, to accommodate/

accommodate strain gauges and wiring. Waterproofing materials are then applied to complete a perfectly flush surface. Russian investigators [15, 16, 20, 21, 22] have used this technique for working experimental stress analyses of large radial-flow and axial-flow water turbines.

In relation to working experimental stress analyses of impulse water turbines, the results herein are of value in several important respects. The locations, natures and approximate magnitudes of significant stresses are known. Furthermore, for the Turgo wheel, the theoretical and experimental results pertinent to the supporting rôle played by the bucket in respect of jet loading stresses, have a significant implication. On account of this rôle, the total dynamic working stresses recorded from a point on a bucket, will not in general, be resolvable into centrifugal and jet loading components on the basis of the working test data alone. For illustration, Fig.122 has been compiled from experimental results Figs.66 and 87, and in particular from experimental results Fig.77. From this last Fig., quantitative assessments may readily be made of some approximate working supporting bucket stresses, and their variations as the $16\frac{1}{2}$ in.cast steel wheel rotates. Thus for locations a, b, c, d, e on bucket No.1 of the wheel, Fig.77, variations of approximate total working stresses with wheel rotation may be determined, and so simulated recordings of "dynamic" total stresses may be drawn.

Two such simulated dynamic working stress recordings are shown in Fig.122, for the maximum stress location on the bucket (unswept surface of outlet edge at its junction with hub) and for a significant stress location on the bucket inlet edge. If experimental simulation of direct jet loading on a bucket has been reasonably representative of reality, these "recordings" will closely resemble corresponding actual dynamic working recordings, free from vibration effects. Working stress recordings are total, of course. It is evident then from Fig.122, that, from the recordings alone, accurate resolution/

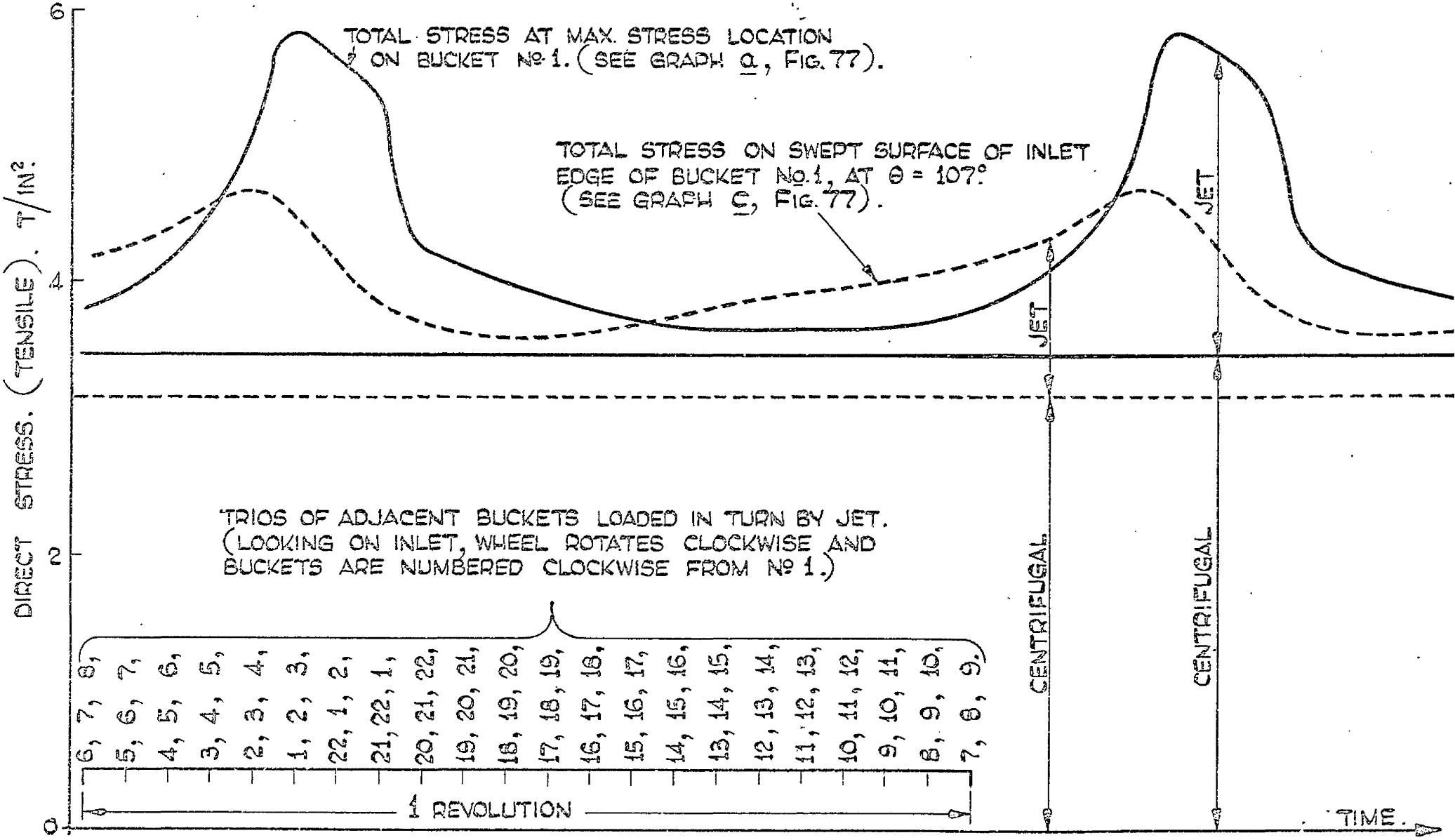

FIG. 122. SIMULATED RECORDINGS OF DYNAMIC TOTAL STRESSES AT MAXIMUM STRESS LOCATION AND AT ANOTHER SIGNIFICANT LOCATION ON BUCKET No. 1. OF 16½ IN. CAST STEEL TURGO WHEEL OPERATING AT NORMAL WORKING CONDITIONS, (700 ft. HEAD). "RECORDINGS" ARE COMPILED FROM MEASURED STRESSES, FIGS 66, 77 AND 87.

resolution into centrifugal and jet loading components is not possible. If the minimum total stress of a recording were taken as the centrifugal component, e.g. for the inlet edge location (dotted curve), this might evidently be excessive by an error of 14%. For correct interpretation of actual dynamic working stress recordings from a Turgo wheel, it is clear that the results of the centrifugal experimental stress analysis are essential.

The simulated recordings, Fig.122, may be compared with Fig.4 which shows actual dynamic working stress recordings from a point on the attachment bracket of a bucket on a Pelton wheel. The recordings of Fig.4, of course, show both the steady centrifugal stress component and the "peaked" jet loading stress component, in contrast to the continuously varying natures of the "recordings" of Fig.122.

APPENDIX 1

PROPERTIES OF THE "EQUIVALENT" PARABOLIC SECTION OF THE BUCKET PERTINENT TO THE APPROXIMATE THEORETICAL ANALYSES FOR CENTRIFUGAL AND JET LOADING STRESSES AND DEFORMATIONS IN A TURGO IMPULSE WHEEL

The general "equivalent" parabolic section of the bucket is shown referred to axes Ox and Oy in Fig.A1.1. The following is the nomenclature adopted for the pertinent properties of the section :-

s distance from origin O along parabola to point (x, y).

t thickness of section at s, where $t = mx + c$.

A area of section.

$\bar{x}$ distance from O along Ox to centroid G of section.

I_{YY} second moment of area of section about axis YY.

I_{ox} second moment of area of section about axis Ox.

I either I_{YY} or I_{ox} as appropriate.

l perpendicular distance from neutral axis YY or neutral axis Ox to a fibre of the section, as appropriate.

$\bar{Q}_x$ first moment of area about YY of the part of the section between $x = x$ and $x = b$, in the shear stress equation $\tau_x = \dfrac{V.(\bar{Q}_x)}{I_{YY}.2t}$, which applies for shearing force V acting in Ox.

K_x shear strain-energy coefficient of the section associated with shearing force V acting in Ox.

$\bar{Q}_y$ first moment of area about Ox of the part of the section between $x = x$ and $x = b$ for +ve y, in the shear stress equation $\tau_y = \dfrac{V.(\bar{Q}_y)}{I_{ox}.t}$, which applies for shearing force V acting through shear centre C_s, parallel to Oy.

K_y shear strain-energy coefficient of the section associated with shearing force V acting through shear centre C_s, parallel to Oy.

$\bar{Q}$ either/

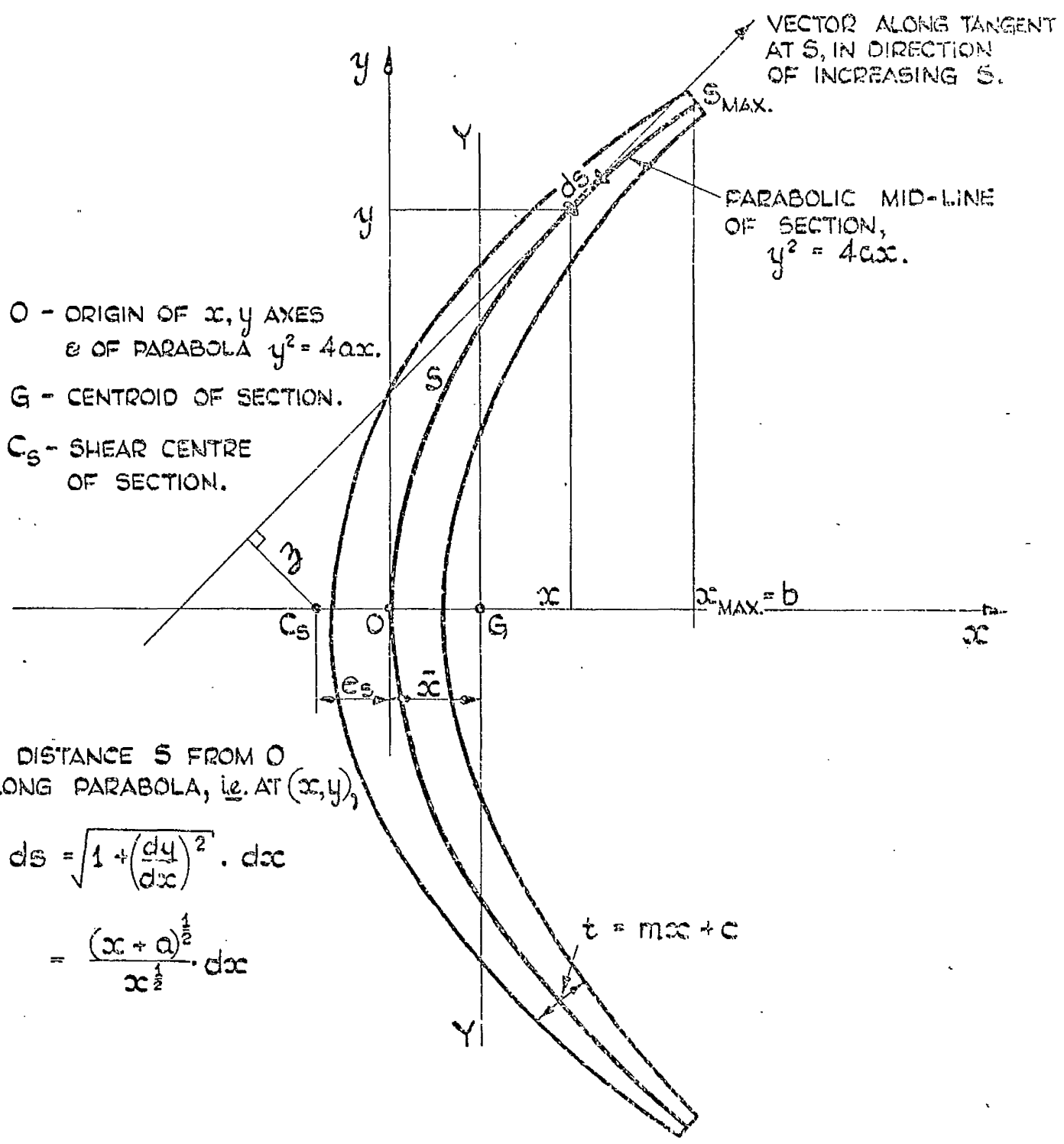

AT DISTANCE S FROM O ALONG PARABOLA, i.e. AT (x, y),

ELEMENT OF PARABOLA, $ds = \sqrt{1 + \left(\frac{dy}{dx}\right)^2} \cdot dx$

$$= \frac{(x + a)^{\frac{1}{2}}}{x^{\frac{1}{2}}} \cdot dx$$

Fig A1.1. GENERAL "EQUIVALENT" PARABOLIC SECTION OF BUCKET REFERRED TO ORTHOGONAL AXES Ox AND Oy, WITH THICKNESS t OF THE SECTION VARYING LINEARLY WITH x. THE FIGURE SHOWS THE BASIS ON WHICH THE PERTINENT PROPERTIES OF THE SECTION ARE DERIVED.

$\bar{Q}$ either $\bar{Q}_x$ or $\bar{Q}_y$ as appropriate.

e_s distance from O along the x-axis to shear centre C_s of section; lies to left of O as shown in Fig. A1.1 but is given +ve sign.

J St. Venant torsion constant of section.

w warping of the section due to non-uniform torsion.

Γ warping constant of section.

σ_z direct stress distribution in section due to warping restraint.

τ_z shear stress distribution in section due to warping restraint.

The properties of the parabolic section are derived as follows:-

$$A = 2\int_0^{S_{MAX}} t.ds = 2\int_0^b (mx+c)\frac{(x+a)^{\frac{1}{2}}}{x^{\frac{1}{2}}}.dx$$

$$= mb^{\frac{1}{2}}(b+a)^{\frac{3}{2}} + b^{\frac{1}{2}}(2c-\tfrac{1}{2}ma)(b+a)^{\frac{1}{2}} + a(2c-\tfrac{1}{2}ma)\log_e\left\{\frac{(b+a)^{\frac{1}{2}}+b^{\frac{1}{2}}}{a^{\frac{1}{2}}}\right\}$$

$$\bar{x} = \frac{2\int_0^{S_{MAX}} t.x.ds}{A} = \frac{2\int_0^b (mx+c)(x+a)^{\frac{1}{2}}x^{\frac{1}{2}}.dx}{A}$$

$$= \frac{1}{A}\left\{\tfrac{2}{3}mb^{\frac{1}{2}}(b+a)^{\frac{5}{2}} + b^{\frac{1}{2}}(c-\tfrac{7}{6}ma)(b+a)^{\frac{3}{2}} + \tfrac{1}{4}ab^{\frac{1}{2}}(ma-2c)(b+a)^{\frac{1}{2}} + \tfrac{1}{4}a^2(ma-2c)\log_e\left[\frac{(b+a)^{\frac{1}{2}}+b^{\frac{1}{2}}}{a^{\frac{1}{2}}}\right]\right\}$$

$$I_{YY} = 2\int_0^{S_{MAX}} tx^2.ds - A\bar{x}^2 = 2\int_0^b (mx+c)(x+a)^{\frac{1}{2}}x^{\frac{3}{2}}.dx - A\bar{x}^2$$

$$= \tfrac{1}{2}mb^{\frac{1}{2}}(b+a)^{\frac{7}{2}} + \tfrac{2}{3}b^{\frac{1}{2}}(c-\tfrac{17}{8}ma)(b+a)^{\frac{5}{2}} + ab^{\frac{1}{2}}(\tfrac{59}{48}ma-\tfrac{7}{6}c)(b+a)^{\frac{3}{2}} + 2a^2b^{\frac{1}{2}}(\tfrac{1}{8}c-\tfrac{5}{64}ma)(b+a)^{\frac{1}{2}} + 2a^3(\tfrac{1}{8}c-\tfrac{5}{64}ma)\log_e\left\{\frac{(b+a)^{\frac{1}{2}}+b^{\frac{1}{2}}}{a^{\frac{1}{2}}}\right\} - A\bar{x}^2$$

$$I_{ox} = 2\int_0^{s_{MAX}} t.y^2.ds = 2\int_0^b 4a(mx+c)(x+a)^{\frac{1}{2}}.x^{\frac{1}{2}}.dx$$

$$= 8a\left\{\tfrac{1}{3}mb^{\frac{1}{2}}(b+a)^{\frac{5}{2}} + \tfrac{1}{2}b^{\frac{1}{2}}(c-\tfrac{7}{6}ma)(b+a)^{\frac{3}{2}} + \tfrac{1}{8}ab^{\frac{1}{2}}(ma-2c)(b+a)^{\frac{1}{2}} + \tfrac{1}{8}a^2(ma-2c)\log_e\left[\frac{(b+a)^{\frac{1}{2}}+b^{\frac{1}{2}}}{a^{\frac{1}{2}}}\right]\right\}$$

$$= 4aA\bar{x}$$

$$\bar{Q}_x = 2\int_s^{s_{MAX}} t(x-\bar{x})ds = 2\int_x^b (mx+c)\frac{(x+a)^{\frac{1}{2}}}{x^{\frac{1}{2}}}(x-\bar{x})dx = f(x).$$

$$= -\tfrac{2}{3}mx^{\frac{1}{2}}(x+a)^{\frac{5}{2}} - (c-\tfrac{7}{6}ma-m\bar{x})x^{\frac{1}{2}}(x+a)^{\frac{3}{2}} - \left[\tfrac{1}{4}a(ma-2c)-\bar{x}(2c-\tfrac{1}{2}ma)\right]x^{\frac{1}{2}}(x+a)$$
$$-\left[\tfrac{1}{4}a^2(ma-2c)-a\bar{x}(2c-\tfrac{1}{2}ma)\right]\log_e\left\{\frac{(x+a)^{\frac{1}{2}}+x^{\frac{1}{2}}}{a^{\frac{1}{2}}}\right\}$$

$$K_x = \frac{A}{V^2}\int_0^A \tau_x^2.dA \quad \text{in general terms}$$

$$= \frac{A}{V^2}2\int_0^{s_{MAX}} \frac{V^2}{I_{YY}^2 4t^2}(\bar{Q}_x)^2 t.ds = \frac{A}{2I_{YY}^2}\int_0^b \frac{(\bar{Q}_x)^2(x+a)^{\frac{1}{2}}}{(mx+c)x^{\frac{1}{2}}}.dx$$

where $\bar{Q}_x = f(x)$ given previously.

This integral is best evaluated by Simpson's Rule in applications.

$$\bar{Q}_y = \int_s^{s_{MAX}} t.y.ds = \int_x^b 2a^{\frac{1}{2}}(mx+c)(x+a)^{\frac{1}{2}}.dx = g(x).$$

$$= 4a^{\frac{1}{2}}\left\{\tfrac{1}{5}m(b+a)^{\frac{5}{2}} - \tfrac{1}{3}(ma-c)(b+a)^{\frac{3}{2}} - \tfrac{1}{5}m(x+a)^{\frac{5}{2}} + \tfrac{1}{3}(ma-c)(x+a)^{\frac{3}{2}}\right\}$$

$$K_y = \frac{A}{V^2}\int_0^A \tau_y^2 . dA \quad \text{in general terms.}$$

$$= \frac{A}{V^2} 2\int_0^{s_{MAX}} \frac{V^2}{I_{ox}^2 t^2}(\bar{Q}_y)^2 t.ds = \frac{2A}{I_{ox}^2}\int_0^b \frac{(\bar{Q}_y)^2 (x+a)^{\frac{1}{2}}}{(mx+c)\,x^{\frac{1}{2}}} dx$$

where $\bar{Q}_y = q(x)$ given previously.

This integral is best evaluated by Simpson's Rule in applications.

$$e_s = \frac{1}{V} 2\int_0^{s_{MAX}} \tau_y . t.ds . \frac{dx}{ds}\left(y - x\frac{dy}{dx}\right)$$ by equating moment about O of the shear stress distribution τ_y over the section, to ($V \times e_s$).

$$= \frac{2}{V}\int_0^b \frac{V}{I_{ox}}(\bar{Q}_y) a^{\frac{1}{2}} x^{\frac{1}{2}} . dx = \frac{2a^{\frac{1}{2}}}{I_{ox}}\int_0^b (\bar{Q}_y) x^{\frac{1}{2}} . dx\,, \qquad \text{where } \bar{Q}_y = q(x)$$

given previously.

$$= \frac{4a}{I_{ox}}\left\{\begin{aligned}&\frac{4}{15}mb^{\frac{3}{2}}(b+a)^{\frac{5}{2}} - \frac{4}{9}(ma-c)b^{\frac{3}{2}}(b+a)^{\frac{3}{2}} - \frac{1}{10}mb^{\frac{1}{2}}(b+a)^{\frac{7}{2}} - \left(\frac{2}{9}c - \frac{43}{180}ma\right)b^{\frac{1}{2}}(b+a)^{\frac{5}{2}} \\ &- \left(\frac{5}{144}ma - \frac{1}{18}c\right)ab^{\frac{1}{2}}(b+a)^{\frac{3}{2}} - \left(\frac{5}{96}ma - \frac{1}{12}c\right)a^2 b^{\frac{1}{2}}(b+a)^{\frac{1}{2}} \\ &- \left(\frac{5}{96}ma - \frac{1}{12}c\right)a^3 . \log_e\left[\frac{(b+a)^{\frac{1}{2}} + b^{\frac{1}{2}}}{a^{\frac{1}{2}}}\right]\end{aligned}\right\}$$

e_s as given has +ve sign, but lies to the left of O in Fig. A1.1.

$$J = \frac{1}{3}\times 2\int_0^{s_{MAX}} t^3 . ds = \frac{2}{3}\int_0^b \frac{(mx+c)^3 (x+a)^{\frac{1}{2}}}{x^{\frac{1}{2}}} . dx$$

$$= \frac{1}{6}m^3 b^{\frac{1}{2}}(b+a)^{\frac{7}{2}} + \left(\frac{2}{3}m^2 c - \frac{17}{36}m^3 a\right)b^{\frac{1}{2}}(b+a)^{\frac{5}{2}} + \left(mc^2 - \frac{7}{6}m^2 ca + \frac{59}{144}m^3 a^2\right)b^{\frac{1}{2}}(b+a)^{\frac{3}{2}}$$

$$+\left(\frac{1}{4}m^2 ca^2 - \frac{1}{2}mc^2 a - \frac{5}{96}m^3 a^3 + \frac{2}{3}c^3\right)b^{\frac{1}{2}}(b+a)^{\frac{1}{2}}$$

$$+\left(\frac{1}{4}m^2 ca^2 - \frac{1}{2}mc^2 a - \frac{5}{96}m^3 a^3 + \frac{2}{3}c^3\right)a . \log_e\left\{\frac{(b+a)^{\frac{1}{2}} + b^{\frac{1}{2}}}{a^{\frac{1}{2}}}\right\}$$

$w = -\zeta \int_0^s z.ds$ by definition,[33,34] measuring s from the axis of symmetry where the warping is zero, and taking z +ve for the vector along tangent, pointing in the increasing $-s$ direction, clockwise about C_s. (as in Fig. A1.1).

ζ = angle of twist per unit length of twisting member.

$= \frac{d\phi}{k.d\Omega}$. (see Chapter 3, section 3Biv).

$$= -\zeta \int_0^s \frac{dx}{ds}\left[y - (x+e_s)\frac{dy}{dx}\right]ds$$

$$= -\zeta \int_0^x a^{\frac{1}{2}}(x^{\frac{1}{2}} - e_s x^{-\frac{1}{2}})dx = -\zeta 2a^{\frac{1}{2}}x^{\frac{1}{2}}\left(\frac{1}{3}x - e_s\right)$$

$$= -\zeta\, y\left(\frac{y^2}{12a} - e_s\right)$$

w is expressed in terms of y for generality over the whole section.

$$\Gamma = 2\int_0^{s_{MAX}} \left(\frac{w}{\zeta}\right)^2 t.ds \quad , \text{ by definition.} \qquad (33, 34).$$

$$= 2\int_0^b 4ax^{\frac{1}{2}}\left(\frac{1}{3}x - e_s\right)^2 (mx+c)(x+a)^{\frac{1}{2}}.dx$$

$$= 16a^3 \left\{ \frac{1}{90}\frac{m}{a^2}b^{\frac{1}{2}}(b+a)^{\frac{9}{2}} + \frac{1}{24}\left(\frac{1}{3}\frac{c}{a^2} - \frac{31}{30}\frac{m}{a} - 2\frac{e_s m}{a^2}\right)b^{\frac{1}{2}}(b+a)^{\frac{7}{2}} \right.$$

$$+ \frac{1}{18}\left(\frac{263}{240}m + \frac{17}{4}\frac{e_s m}{a} - \frac{17}{24}\frac{c}{a} + 3\frac{e_s^2 m}{a^2} - 2\frac{e_s c}{a^2}\right)b^{\frac{1}{2}}(b+a)^{\frac{5}{2}}$$

$$+ \frac{1}{4}\left(-\frac{121}{864}ma - \frac{59}{72}e_s m + \frac{59}{432}c - \frac{7}{6}\frac{e_s^2 m}{a} + \frac{7}{9}\frac{e_s c}{a} + \frac{e_s^2 c}{a^2}\right)b^{\frac{1}{2}}(b+a)^{\frac{3}{2}}$$

$$+ \frac{1}{8}\left(\frac{7}{288}ma^2 + \frac{5}{24}e_s ma - \frac{5}{144}ca + \frac{1}{2}e_s^2 m - \frac{1}{3}e_s c - \frac{e_s^2 c}{a}\right)b^{\frac{1}{2}}(b+a)^{\frac{1}{2}}$$

$$\left. + \frac{a}{8}\left(\frac{7}{288}ma^2 + \frac{5}{24}e_s ma - \frac{5}{144}ca + \frac{1}{2}e_s^2 m - \frac{1}{3}e_s c - \frac{e_s^2 c}{a}\right)\log_e\left[\frac{(b+a)^{\frac{1}{2}} + b^{\frac{1}{2}}}{a^{\frac{1}{2}}}\right] \right\}$$

$$\sigma_z = E.\frac{d^2\phi}{k^2 d\Omega^2}\left(\frac{-w}{\rho}\right), \quad \text{by definition.}^{(33,34)} \text{ (see Chapter 3, section 3Biv)}$$

$$= -E\frac{d^2\phi}{k^2 d\Omega^2} y\left(\frac{y^2}{12a} - e_s\right)$$

σ_z is expressed in terms of y for generality over the whole section.

$$\tau_z = -\frac{E}{t}.\frac{d^3\phi}{k^3 d\Omega^3}\int_0^s \left(\frac{-w}{\rho}\right) t.ds, \text{ by definition.}^{(33,34)} \text{ (see Chapter 3, section 3Biv}$$

$$= -\frac{E}{t}\frac{d^3\phi}{k^3 d\Omega^3}\left[\int\left(\frac{-w}{\rho}\right)t.ds + C'\right]$$

$$= -\frac{E}{(mx+c)}\frac{d^3\phi}{k^3 d\Omega^3}\left[-\int 2a^{\frac{1}{2}}\left(\frac{1}{3}x - e_s\right)(mx+c)(x+a)^{\frac{1}{2}}dx \quad + C'\right]$$

where constant C' is evaluated from the boundary condition $\underset{x=b}{\tau_z} = 0$.

$$= \frac{E\left(\frac{d^3\phi}{k^3 d\Omega^3}\right)4a^{\frac{1}{2}}}{(mx+c)}\left\{\frac{1}{21}m\left[\left(\frac{y^2}{4a}+a\right)^{\frac{7}{2}} - (b+a)^{\frac{7}{2}}\right] - \frac{1}{5}\left(\frac{2am}{3} - \frac{c}{3} + e_s m\right)\left[\left(\frac{y^2}{4a}+a\right)^{\frac{5}{2}} - (b+a)^{\frac{5}{2}}\right]\right.$$
$$\left. + \frac{1}{3}\left(\frac{a^2 m}{3} - \frac{ac}{3} + ae_s m - e_s c\right)\left[\left(\frac{y^2}{4a}+a\right)^{\frac{3}{2}} - (b+a)^{\frac{3}{2}}\right]\right\}$$

τ_z is expressed in terms of y for consistency with σ_z.

For the equivalent parabolic section bucket of the $16\frac{1}{2}$ in. wheel (see Fig.11), the definitive parameters have the following values:-

$a = 1.32$ in. $\quad b = 1.80$ in. $\quad m = -0.28 \quad c = 0.65$ in.

The properties of the parabolic section are then found to have the following values:-

A/

$$A = 3.39888 \text{ in.}^2$$

$$\bar{x} = 0.48798 \text{ in.}$$

$$I_{yy} = 0.76787 \text{ in.}^4$$

$$I_{qx} = 8.75735 \text{ in.}^4$$

$$K_x = 4.83889$$

$$K_y = 1.32853$$

$$e_s = 0.31706 \text{ in.}$$

$$J = 0.31842 \text{ in.}^4$$

$$\Gamma = 0.21062 \text{ in.}^6$$

APPENDIX 2

PROPERTIES OF THE "EQUIVALENT" RECTANGULAR SECTION OF THE RIM PERTINENT TO THE APPROXIMATE THEORETICAL ANALYSES FOR CENTRIFUGAL AND JET LOADING STRESSES AND DEFORMATIONS IN A TURGO IMPULSE WHEEL

The general "equivalent" rectangular section of the rim is shown referred to axes $X'X'$ and $Y'Y'$ in Fig.A2.1. The following gives the nomenclature adopted for the pertinent properties of the section, and presents their derivation:-

A_1 area of section. $A_1 = b_1 d_1$

$I_{x'x'}$ second moment of area of section about axis $X'X'$. $I_{x'x'} = \frac{1}{12} b_1 d_1^3$

$I_{y'y'}$ second moment of area of section about axis $Y'Y'$. $I_{y'y'} = \frac{1}{12} d_1 b_1^3$

$\bar{Q}_{y'}$ first moment of area about $X'X'$ of the part of the section between $y' = y'$ and $y' = d_1/2$, in the shear stress equation

$$\tau_{y'} = \frac{V_{y'} \cdot (\bar{Q}_{y'})}{I_{x'x'} \cdot b_1},$$

which applies for shearing force $V_{y'}$ acting in $Y'Y'$. $\bar{Q}_{y'} = 2 b_1 \left[\left(\frac{d_1}{4}\right)^2 - \left(\frac{y'}{2}\right)^2 \right]$.

$K_{y'}$ shear strain-energy coefficient of the section associated with shearing force $V_{y'}$ acting in $Y'Y'$.

$$K_{y'} = \frac{A_1}{V_{y'}^2} \int_0^{A_1} \tau_{y'}^2 \cdot dA_1 \quad = \frac{6}{5} \text{ for a rectangular section.}$$

$\bar{Q}_{x'}$ first moment of area about $Y'Y'$ of the part of the section between $x' = x'$ and $x' = b_1/2$, in the shear stress equation

$$\tau_{x'} = \frac{V_{x'} (\bar{Q}_{x'})}{I_{y'y'} \cdot d_1},$$

which applies for shearing force $V_{x'}$ acting in $X'X'$. $\bar{Q}_{x'} = 2 d_1 \left[\left(\frac{b_1}{4}\right)^2 - \left(\frac{x'}{2}\right)^2 \right]$.

$K_{x'}$ shear strain-energy coefficient of the section associated with shearing force $V_{x'}$ acting in $X'X'$.

$$K_{x'} = \frac{A_1}{V_{x'}^2} \int_0^{A_1} \tau_{x'}^2 \cdot dA_1 \quad = \frac{6}{5} \text{ for a rectangular section.}$$

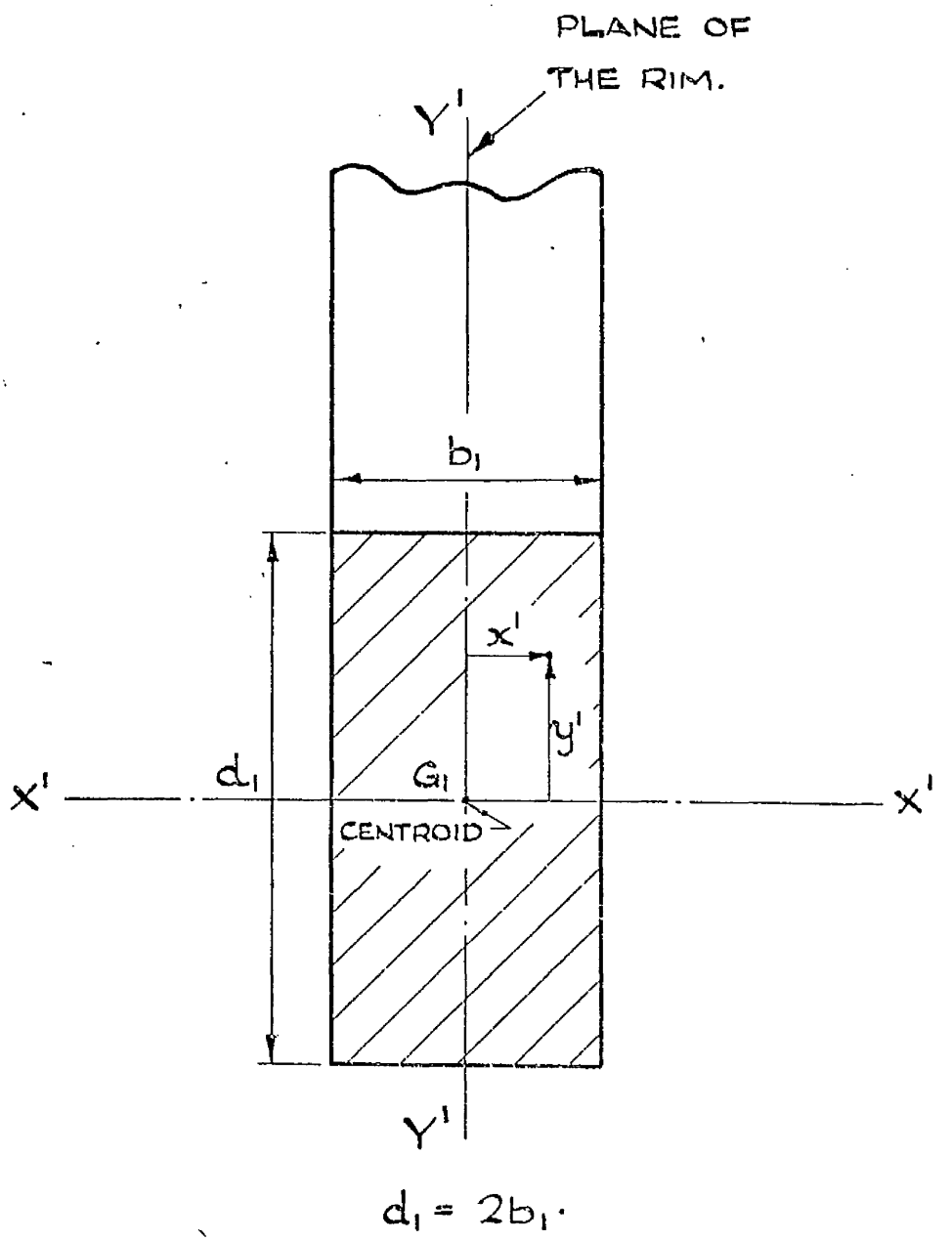

FIG. A2.1. GENERAL "EQUIVALENT" RECTANGULAR SECTION OF RIM REFERRED TO ORTHOGONAL AXES X'X' AND Y'Y'.

J_1 St. Venant torsion constant of section. $J_1 = 0.229\, d_1 b_1^3$, for a rectangular section[31] with $d_1/b_1 = 2$.

For the equivalent rectangular section rim of the $16\frac{1}{2}$ in. wheel, Fig.12, $b_1 = 1.25$ in. $d_1 = 2.5$ in.

giving the values for the section properties as follows:-

$$A_1 = 3.125 \text{ in}^2$$

$$I_{x'x'} = 1.62760 \text{ in}^4$$

$$I_{y'y'} = 0.40690 \text{ in}^4$$

$$K_{y'} = K_{x'} = \frac{6}{5}$$

$$J_1 = 1.11904 \text{ in}^4$$

APPENDIX 3

(a) SOLUTION OF THE NON-UNIFORM TORSION DIFFERENTIAL EQUATION FOR ASSEMBLY ACTION F_R ON THE BUCKET,

(b) DERIVATION OF THE NON-UNIFORM TORSION STRAIN-ENERGY COMPONENTS OF DISPLACEMENT $\delta_{T2}^{F_R}$ BY THE DUMMY LOAD METHOD, — BOTH PERTINENT TO THE APPROXIMATE THEORETICAL ANALYSES OF CHAPTER 3.

(a) For action F_R at the junction point on the bucket, Fig.21, the non-uniform torsion differential equation is given by (3B.36) :-

$$\frac{GJ}{k}\frac{d\phi}{d\Omega} - \frac{E\Gamma}{k^3}\frac{d^3\phi}{d\Omega^3} = F_R\left(M_3 \sin\Omega + N_3 \cos\Omega\right) \qquad \text{(A3.1)}$$

where $M_3 = d\frac{k}{q}\left\{\frac{h}{k}\sin\beta + \sin\alpha\right\}$

$$N_3 = d\frac{k}{q}\left\{-\frac{h}{k}\cos\beta + \cos\alpha\right\}$$

The equation is a fairly elementary third-order ordinary linear non-homogeneous differential equation with constant coefficients and as such, the general solution is given by the sum of the complementary function and the particular integral. The complementary function is the solution of the equation with R.H.S. = O, which solution may readily be shown to be given by:-

$$\phi = C_4 e^{K\Omega} + C_5 e^{-K\Omega} + C_6 \quad ,$$

where $K = \sqrt{\frac{H}{P}}$, $H = \frac{GJ}{k}$, $P = \frac{E\Gamma}{k^3}$

and C_4 , C_5 and C_6 are constants of integration.

Trying a particular integral of the form:-

$\phi = C_7 \sin\Omega + C_8 \cos\Omega$, where C_7, C_8 are constants, the particular/

particular integral is readily found to be given by:-

$$\phi = \frac{F_R(N_3 \sin\Omega - M_3 \cos\Omega)}{H+P}$$

The general solution of the differential equation is therefore given by:-

$$\phi = C_4 e^{K\Omega} + C_5 e^{-K\Omega} + C_6 + \frac{F_R}{H+P}(N_3 \sin\Omega - M_3 \cos\Omega).$$

The boundary conditions to which non-uniform torsion of the bucket is subject are as follows:-

At fully-fixed end $\Omega = 0$:- there is no angle of twist, $\therefore \phi_{\Omega=0} = 0$;

there is no warping of the section, $\therefore -\omega_{\Omega=0} = 0$,

$$\text{or } \left(\frac{d\phi}{d\Omega}\right)_{\Omega=0} = 0.$$

At free end $\Omega = \alpha$:- there is no warping restraint direct stress,

$$\therefore \sigma_{z_{\Omega=\alpha}} = 0, \text{ or } \left(\frac{d^2\phi}{d\Omega^2}\right)_{\Omega=\alpha} = 0.$$

Applying these conditions to the above solution, constants of integration C_4 , C_5 , C_6 , are found to be given by:-

$C_4 = F_R \times L_3$, where $L_3 = \dfrac{N_3 \sin\alpha - M_3 \cos\alpha - KN_3 e^{-K\alpha}}{K^2(H+P)(e^{K\alpha} + e^{-K\alpha})}$

$C_5 = F_R \times F_3$, where $F_3 = \dfrac{N_3 \sin\alpha - M_3 \cos\alpha + KN_3 e^{K\alpha}}{K^2(H+P)(e^{K\alpha} + e^{-K\alpha})}$

$C_6 = F_R \times S_3$, where $S_3 = \dfrac{-2(N_3 \sin\alpha - M_3 \cos\alpha) - KN_3(e^{K\alpha} - e^{-K\alpha}) + K^2 M_3(e^{K\alpha} + e^{-K\alpha})}{K^2(H+P)(e^{K\alpha} + e^{-K\alpha})}$

(b) /

(b) By application of the dummy load method, the non-uniform torsion strain-energy components of a general displacement of the bucket due to action F_R, Fig.21, are the last two terms of equation (3B.40):-

$$\int_0^{\alpha} \frac{GJ}{k}\left(\frac{d\phi}{d\Omega}\right)_{F_R} \cdot \frac{\partial}{\partial Q}\left[\left(\frac{d\phi}{d\Omega}\right)_{F_R+Q}\right] d\Omega \;+\; \int_0^{\alpha} \frac{E\Gamma}{k^3}\left(\frac{d^2\phi}{d\Omega^2}\right)_{F_R} \cdot \frac{\partial}{\partial Q}\left[\left(\frac{d^2\phi}{d\Omega^2}\right)_{F_R+Q}\right] d\Omega$$

To determine these components for tangential displacement $\delta_{T2}^{F_R}$ at the junction point, the torque $T_{\Omega 2}^{F_R+Q}$ due to F_R and to force Q tangentially at G_1 as shown dotted in Fig.21, is given by:-

$$T_{\Omega 2}^{F_R+Q} = F_R d \sin\psi_{\xi=\theta} + Qd\cos\psi_{\xi=\theta} = (F_R M_3 - QN_3)\sin\Omega + (F_R N_3 + QM_3)\cos\Omega ,$$

where M_3 and N_3 are as given for equation (A3.1).

The corresponding form of the non-uniform torsion differential equation is then:-

$$\frac{GJ}{k}\frac{d\phi}{d\Omega} - \frac{E\Gamma}{k^3}\frac{d^3\phi}{d\Omega^3} = (F_R M_3 - QN_3)\sin\Omega + (F_R N_3 + QM_3)\cos\Omega \qquad (A3.2),$$

which is of form exactly similar to equation (A3.1). The given solution of (A3.1) may then be taken as the solution of (A3.2), provided that coefficients $F_R M_3$ and $F_R N_3$ of (A3.1) are replaced throughout respectively by the corresponding coefficients $(F_R M_3 - QN_3)$ and $(F_R N_3 + QM_3)$ of (A3.2). The relevant constants of integration C_4' and C_5' in the solution of equation (A3.2) are then given by:-

$C_4' = F_R L_3 + Q L_4$, where L_3 is as given previously and,

$$L_4 = \frac{M_3\sin\alpha + N_3\cos\alpha - KM_3 e^{-K\alpha}}{K^2(H+P)(e^{K\alpha}+e^{-K\alpha})}$$

$C_5' = F_R F_3 + Q F_4$, where F_3 is as given previously and,

$$F_4 = \frac{M_3\sin\alpha + N_3\cos\alpha + KM_3 e^{K\alpha}}{K^2(H+P)(e^{K\alpha}+e^{-K\alpha})} .$$

Then/

Then,

$$\left(\frac{d\phi}{d\Omega}\right)_{F_R+Q} = K(F_R L_3 + Q L_4)e^{K\Omega} - K(F_R F_3 + Q F_4)e^{-K\Omega} + \frac{F_R N_3 + Q M_3}{H+P}\cos\Omega + \frac{F_R M_3 - Q N_3}{H+P}\sin\Omega \qquad (A3.3),$$

and,

$$\left(\frac{d^2\phi}{d\Omega^2}\right)_{F_R+Q} = K^2(F_R L_3 + Q L_4)e^{K\Omega} + K^2(F_R F_3 + Q F_4)e^{-K\Omega} - \frac{F_R N_3 + Q M_3}{H+P}\sin\Omega + \frac{F_R M_3 - Q N_3}{H+P}\cos\Omega \qquad (A3.4)$$

From these equations:-

$$\frac{\partial}{\partial Q}\left[\left(\frac{d\phi}{d\Omega}\right)_{F_R+Q}\right] = K L_4 e^{K\Omega} - K F_4 e^{-K\Omega} + \frac{M_3\cos\Omega - N_3\sin\Omega}{H+P}$$

and,

$$\frac{\partial}{\partial Q}\left[\left(\frac{d^2\phi}{d\Omega^2}\right)_{F_R+Q}\right] = K^2 L_4 e^{K\Omega} + K^2 F_4 e^{-K\Omega} - \frac{M_3\sin\Omega + N_3\cos\Omega}{H+P}$$

The expressions $\left(\frac{d\phi}{d\Omega}\right)_{F_R}$ and $\left(\frac{d^2\phi}{d\Omega^2}\right)_{F_R}$, are respectively obtained from equations (A3.3) and (A3.4) for $Q = 0$. All the derivatives under the integral signs of the non-uniform torsion strain-energy components are now available as functions of Ω. Multiplying the derivative functions as appropriate, integration is carried out straightforwardly. The non-uniform torsion strain-energy components of displacement $\delta_{Tz}^{F_R}$ are found to be:-

$$F_R H\Bigg\{\frac{K}{2}(L_3L_4e^{2K\alpha}-F_3F_4e^{-2K\alpha}) - K^2(L_4F_3+L_3F_4)\alpha - \frac{K}{2}(L_3L_4-F_3F_4)$$

$$+\frac{Ke^{K\alpha}}{(H+P)(K^2+1)}\left[(L_3M_3+L_4N_3)(K\cos\alpha+\sin\alpha)+(L_4M_3-L_3N_3)(K\sin\alpha-\cos\alpha)\right]$$

$$+\frac{Ke^{-K\alpha}}{(H+P)(K^2+1)}\left[(F_4N_3+F_3M_3)(K\cos\alpha-\sin\alpha)+(F_4M_3-F_3N_3)(K\sin\alpha+\cos\alpha)\right]$$

$$+\frac{2M_3N_3\sin 2\alpha+(M_3^2-N_3^2)(1-\cos 2\alpha)}{4(H+P)^2}$$

$$-\frac{K}{(H+P)(K^2+1)}\left[K(L_4+F_4)N_3+K(L_3+F_3)M_3-(L_4-F_4)M_3+(L_3-F_3)N_3\right]\Bigg\}$$

$$+F_R P\Bigg\{\frac{K^3}{2}(L_3L_4e^{2K\alpha}-F_3F_4e^{-2K\alpha})+K^4(L_4F_3+L_3F_4)\alpha-\frac{K^3}{2}(L_3L_4-F_3F_4)$$

$$-\frac{K^2e^{K\alpha}}{(H+P)(K^2+1)}\left[(L_4N_3+L_3M_3)(K\sin\alpha-\cos\alpha)-(L_4M_3-L_3N_3)(K\cos\alpha+\sin\alpha)\right]$$

$$+\frac{K^2e^{-K\alpha}}{(H+P)(K^2+1)}\left[(F_4N_3+F_3M_3)(K\sin\alpha+\cos\alpha)-(F_4M_3-F_3N_3)(K\cos\alpha-\sin\alpha)\right]$$

$$-\frac{2M_3N_3\sin 2\alpha+(M_3^2-N_3^2)(1-\cos 2\alpha)}{4(H+P)^2}$$

$$-\frac{K^2}{(H+P)(K^2+1)}\left[(L_4+F_4)N_3+(L_3+F_3)M_3+K(L_4-F_4)M_3-K(L_3-F_3)N_3\right]\Bigg\}$$

where $K, H, P, M_3, N_3, L_3, L_4, F_3$ and F_4 are all as given in this Appendix.

APPENDIX 4

BRITTLE LACQUER TECHNIQUE

Partly on account of the relatively low Young's Moduli of the experimental components, it was considered worthwhile to apply brittle lacquer techniques in attempts to obtain initial indications of tensile strain magnitudes and distributions. Of the relevant literature consulted, [37, 38, 39, 40], the work of LINGE[37], which has an extensive bibliography, was found particularly instructive. An apparently suitable lacquer was selected, a sample obtained and a satisfactory technique was developed.

The lacquer used was Brittle Lacquer RV519, obtained from Messrs. Robert Ingham Clark, 93-97 New Cavendish Street, London, W.1. This was an inoffensive varnish producing a good coating of light straw colour, free of air bubbles. It was capable of application by either spray or brush. In order to make the lacquer sufficiently strain-sensitive, the lacquered parts required stoving for a time in an oven or under infra-red lamps. The following was established as the general procedure:-

(1) The surfaces of interest and from six to eight cantilever calibration bars were thoroughly cleaned and degreased with Trichlorethylene. Aluminium bars, of which the cross-section and Young's Modulus were measured, were used as cantilever calibration specimens for determining the strain-sensitivity of the lacquer, this being the value of strain for initial cracking.

(2) Lacquer RV519 was brushed on, a procedure which required prior practice. At first, spraying had been attempted but found to be rather impracticable, especially in the case of the $16\frac{1}{2}$ in. Turgo wheel with its restricted access to some of the bucket surfaces. With the brush/

brush, a fast action was used, the brush being cleaned frequently in Trichlorethylene. Three coats were given, one being allowed to dry before a succeeding one was applied. This produced a correct coating thickness of 0.003 in.to 0.006 in.

(3) The lacquered parts were stoved in a closed oven for 40 hours at 105°F. It was found that the lacquer became more strain-sensitive the higher the stoving temperature and the longer the stoving time, but it also then became more prone to crazing, with risk of the lacquer being rendered useless. After slow cooling to ambient temperature, subsequent to stoving, the lacquered components were ready for loading.

(4) Half the number of calibration bars were tested by loading them as cantilevers, cracking of the lacquer being obtained for estimation of strain-sensitivity. The part of interest was then loaded appropriately and examined for cracking of the lacquer. Subsequently the remaining calibration bars were tested and cracking of the lacquer obtained. Throughout these tests on the part of interest and on the calibration bars, loads were applied in successively increasing increments, off-loading to zero and resting the lacquer for a few moments between each increment. This was done to minimise effects which might have been produced if the lacquer had tended to creep. It was found that the cracks which occurred in the lacquer were permanent and of good definition.

(5) In the calibration tests, for a given loading W_c on the cantilever bar, Fig.A4.1, the point on the cracked lacquer relevant to measurement of the strain-sensitivity, was taken as the point midway between the crack nearest the load and the fully-across crack nearest the load, as shown in the Fig. This was adopted on the recommendation of LINGE[37] as giving a more consistent and conservative/

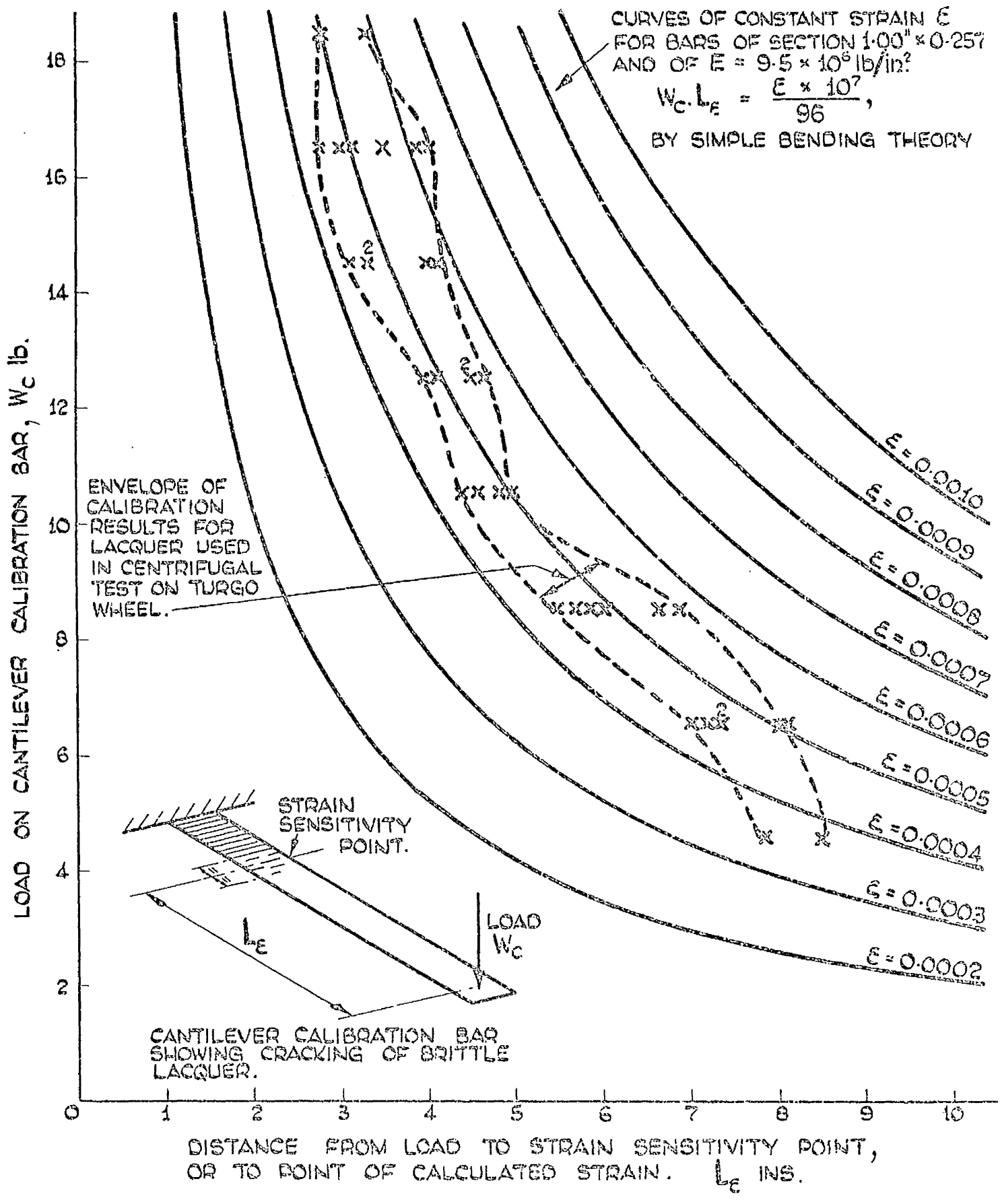

FIG. A4.1 GRAPH PERTINENT TO CANTILEVER CALIBRATION BARS, FOR DETERMINATION OF STRAIN-SENSITIVITY OF BRITTLE LACQUER. CURVES OF CONSTANT STRAIN ε ARE APPROPRIATE TO THE BARS USE THE PLOTTED POINTS REFER TO THE BRITTLE LACQUER USED IN THE CENTRIFUGAL TEST ON THE [illegible] ALUMINIUM TURBO WHEEL AND INDICATE A STRAIN-SENSITIVITY OF BETWEEN 0·0004 AND [illegible]

conservative indication of strain-sensitivity than that given by taking the strain-sensitivity point to be the crack nearest the load. Only when such crack was fully-across the bar was it taken as the strain-sensitivity point.

For each cantilever bar, locations l_ε of strain-sensitivity points were measured at about eight values of load W_c. The corresponding strain-sensitivity values were obtained straightway by plotting the results on a priorly constructed graph such as Fig.A4.1. This shows load W_c on the cantilever on a base of distance l_ε along the cantilever from the load point. By application of simple bending theory to the bars used, lines of constant strain ε on the bar have been drawn on this field for values in the range $0.0002 \leq \varepsilon \leq 0.0010$. By way of illustration a set of relevant calibration results is shown plotted on Fig.A4.1. This set refers to the lacquer used in the centrifugal test on the $16\frac{1}{2}$ in.Turgo wheel and shows that the strain-sensitivity was between 0.0004 and 0.0006. Such low order values are reckoned to be about as good as can reasonably be achieved. LINGE[37] draws notice to the tendency of the strain-sensitivity value to be lower in regions of low strain-gradient. This is exhibited by the results shown, where the strain-sensitivity at the low loads, and therefore low strain-gradients, tends to be of the order of 0.0004 or less, while at the high loads the value may be about 0.0006 or more.

Because of the possibility in the centrifugal test, of the wheel acting like a fan and subjecting the brittle lacquer to air draughts, a small preliminary test was carried out to investigate possible effects. Jets of air, from a hose connected to an air compressor, were applied to lacquered calibration bars before and during testing, but this was found neither to have any effect on strain-sensitivity nor to affect the tendency of the lacquer to craze. The air velocities available from the hose, however, were thought to have been somewhat smaller than some which might occur during spinning of the wheel.

APPENDIX 5

THE ROTATING WEDGE : A METHOD OF OBTAINING STRAIN-FREE LOCATIONS IN A CENTRIFUGAL FIELD

See pocket attached to inside of back cover of thesis.

APPENDIX 6

ANALYSIS OF MEASURED STRAINS TO DETERMINE CENTRIFUGAL ACTIONS ON FOUR MERIDIONAL SECTIONS OF BUCKET OF $16\frac{1}{2}$ in. ALUMINIUM TURGO WHEEL ROTATING AT 1,300 r.p.m.

Figs.63 and 64 indicate locations where centrifugal strains were measured, relevant to meridional sections of the bucket at $\Theta = 57^{\circ}$, 74°, 92° and 111°. From these strains, the stresses normal to the sections (i.e. the circumferential stresses) were calculated, and then analysed, according to the method outlined previously in section 4A ii, to determine direct force and bending moment actions on the sections.

A slight difference here, was that the moment actions were taken about axes YY and xx, the origin being G, the centroid of the equivalent parabolic section, and not G_M the centroid of each meridional section (see Fig.50 and e.g. Fig.A6.1(a)). The equivalent parabolic section is the same for all values of Θ, being that shown in Fig.11. Thus origin G was chosen as a datum common to all four meridional sections,— the datum appropriate to the direct comparison of the experimental results with corresponding theory. As would be expected, in all four sections G and G_M lie close together.

The full-size drawings of the sections and the graphs pertaining to the analyses, are presented as follows:-

For meridional section at $\Theta = 57^{\circ}$, Figs. A6.1 (a) to (d).
For meridional section at $\Theta = 74^{\circ}$, Figs. A6.2 (a) to (d).
For meridional section at $\Theta = 92^{\circ}$, Figs. A6.3 (a) to (d).
For meridional section at $\Theta = 111^{\circ}$, Figs. A6.4 (a) to (d).

In these Figs:- x corresponds to X_M of Fig.50(b), and section 4A ii,
Y corresponds to Y_M of Fig.50(b), and section 4A ii,
M_Y corresponds to M_{YM} of Fig.50(b), and section 4A ii,
P' corresponds to P_M of Fig.50(b), and section 4A ii,
M_x corresponds to M_{xM} of Fig.50(b), and section 4A ii.

The signs of M_Y, P' and M_x correspond respectively to the signs of M_{YM}, P_M and M_{xM} of Fig. 50(b).

The following table summarises the centrifugal actions on the meridional sections, derived from these analyses:-

Table A6.1

Experimental centrifugal actions on meridional sections of bucket of $16\frac{1}{2}$ in. aluminium Turgo wheel, rotating at 1,300 r.p.m.

Location of meridional section $\theta°$ (Figs. 9 and 12)	Centrifugal action on section		
	M_Y * lb.in.	P' * lb.	M_x * lb.in.
57	+ 40	+ 225	- 600
74	+ 500	+ 925	- 650
92	+ 1080	+ 940	- 1300
111	+ 580	+ 1190	- 1350

* In respect of natures and signs, these correspond respectively to M_{YM}, P_M, M_{xM}, Fig. 50(b).

With regard to in-plane bending moment M_Y on the sections, the proportions due to membrane and bending actions are given in Table A6.2:-

Table A6.2

Experimental centrifugal in-plane bending moment M_Y on meridional sections of bucket of $16\frac{1}{2}$ in. aluminium Turgo wheel, rotating at 1300 r.p.m. Proportions of membrane and bending actions.

Location of meridional section $\theta°$ (Figs. 9 and 12)	Percentage of M_Y taken by:-	
	membrane action $\int_0^{s_{MAX}} N_\theta . x . ds_M$	bending action $\int_0^{s_{MAX}} M_\theta . \sin\xi . ds_M$
57	+ 300	- 200
74	80	20
92	86	14
111	78	22

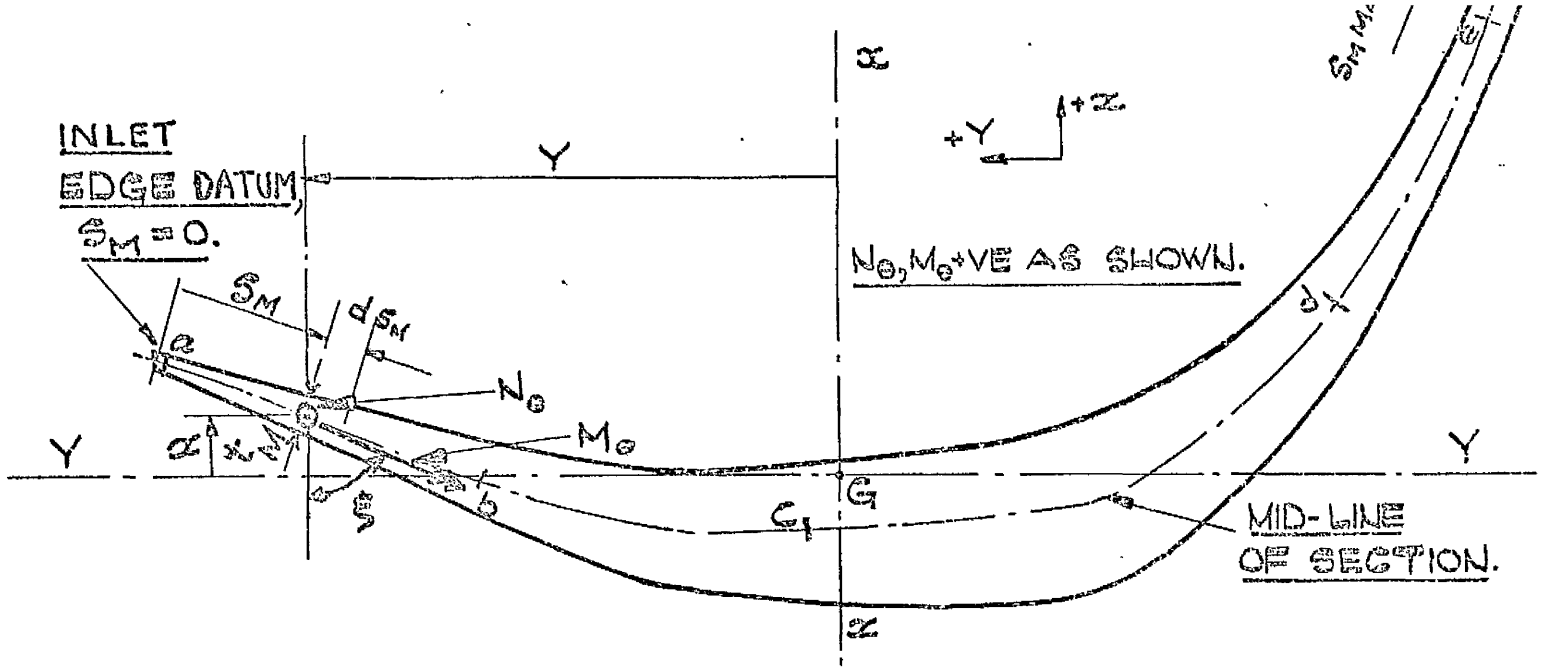

FIG A6.1(a). FULL SIZE DRAWING OF MERIDIONAL SECTION OF BUCKET OF 16½ IN. TURGO WHEEL, AT $\theta = 57°$. POINTS a, b, c, d, e CORRESPOND TO THE STRAIN GAUGE LOCATIONS SHOWN ON FIGS. 63 AND 64.

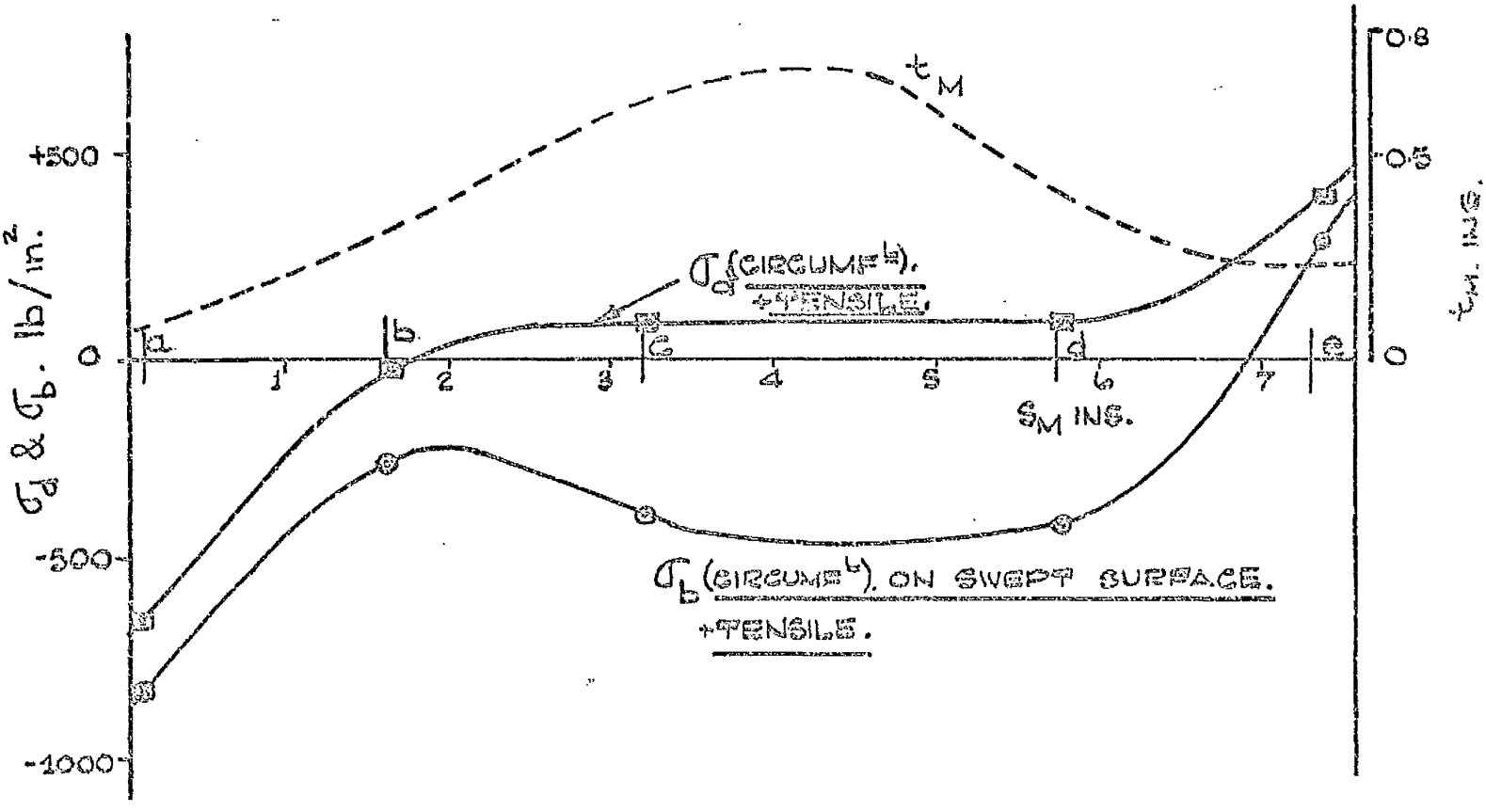

FIG A6.1(b). ANALYSIS FOR CENTRIFUGAL ACTIONS ON MERIDIONAL SECTION AT $\theta = 57°$, FOR 16½ IN. ALUMINIUM TURGO WHEEL ROTATING AT 1300 R.P.M. DISTRIBUTIONS OF t_M AND OF σ_d AND σ_b (DERIVED FROM MEASURED STRESSES) WITH s_M.

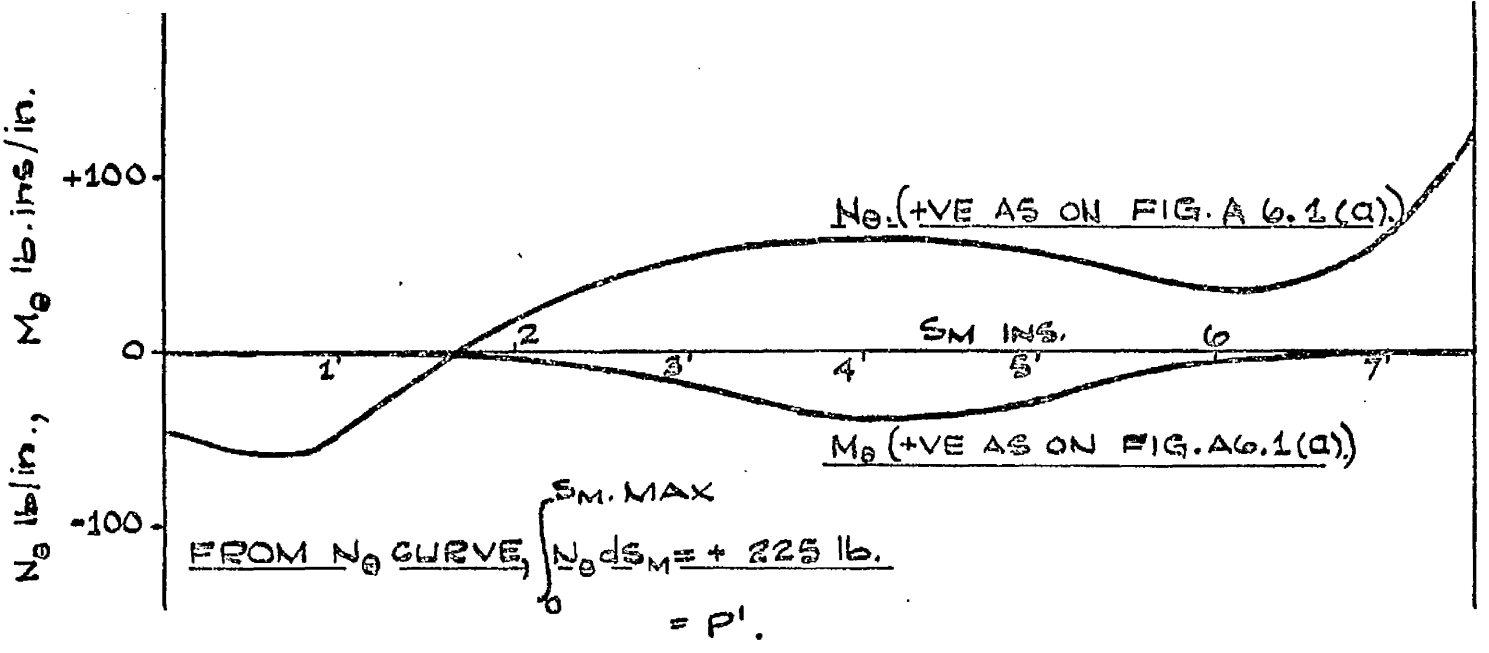

FROM N_θ CURVE, $\int_0^{S_{M.MAX}} N_\theta \, dS_M = +225$ lb.

$= P'$.

FIG A6.1(c). ANALYSIS FOR CENTRIFUGAL ACTIONS ON MERIDIONAL SECTION AT $\theta = 57°$. DISTRIBUTIONS OF N_θ AND M_θ WITH S_M, DERIVED FROM PREVIOUS FIG.

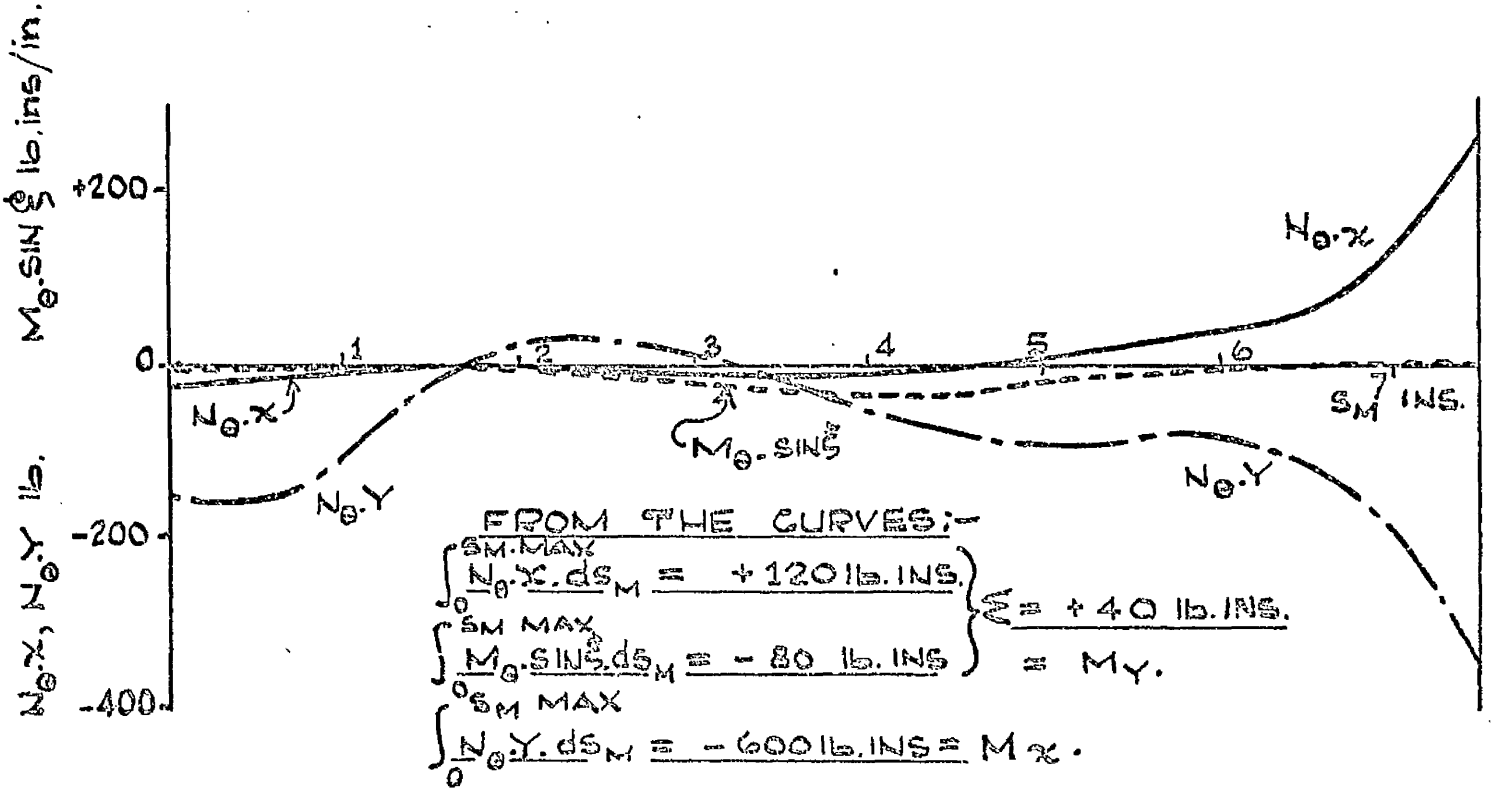

FROM THE CURVES:-

$\int_0^{S_{M.MAX}} N_\theta.X.dS_M = +1201$ lb. INS.

$\int_0^{S_{M\,MAX}} M_\theta.\sin\phi.dS_M = -80$ lb. INS

$\Sigma = +40$ lb. INS. $= M_Y$.

$\int_0^{S_{M\,MAX}} N_\theta.Y.dS_M = -6001$ lb. INS $= M_X$.

$M_\theta.\cos\phi \neq 0$, FOR ALL S_M.

FIG A6.1(d). ANALYSIS FOR CENTRIFUGAL ACTIONS ON MERIDIONAL SECTION AT $\theta = 57°$. DISTRIBUTIONS OF $(N_\theta.X)$, $(M_\theta.\sin\phi)$, $(N_\theta.Y)$ WITH S_M, DERIVED FROM PREVIOUS FIGS.

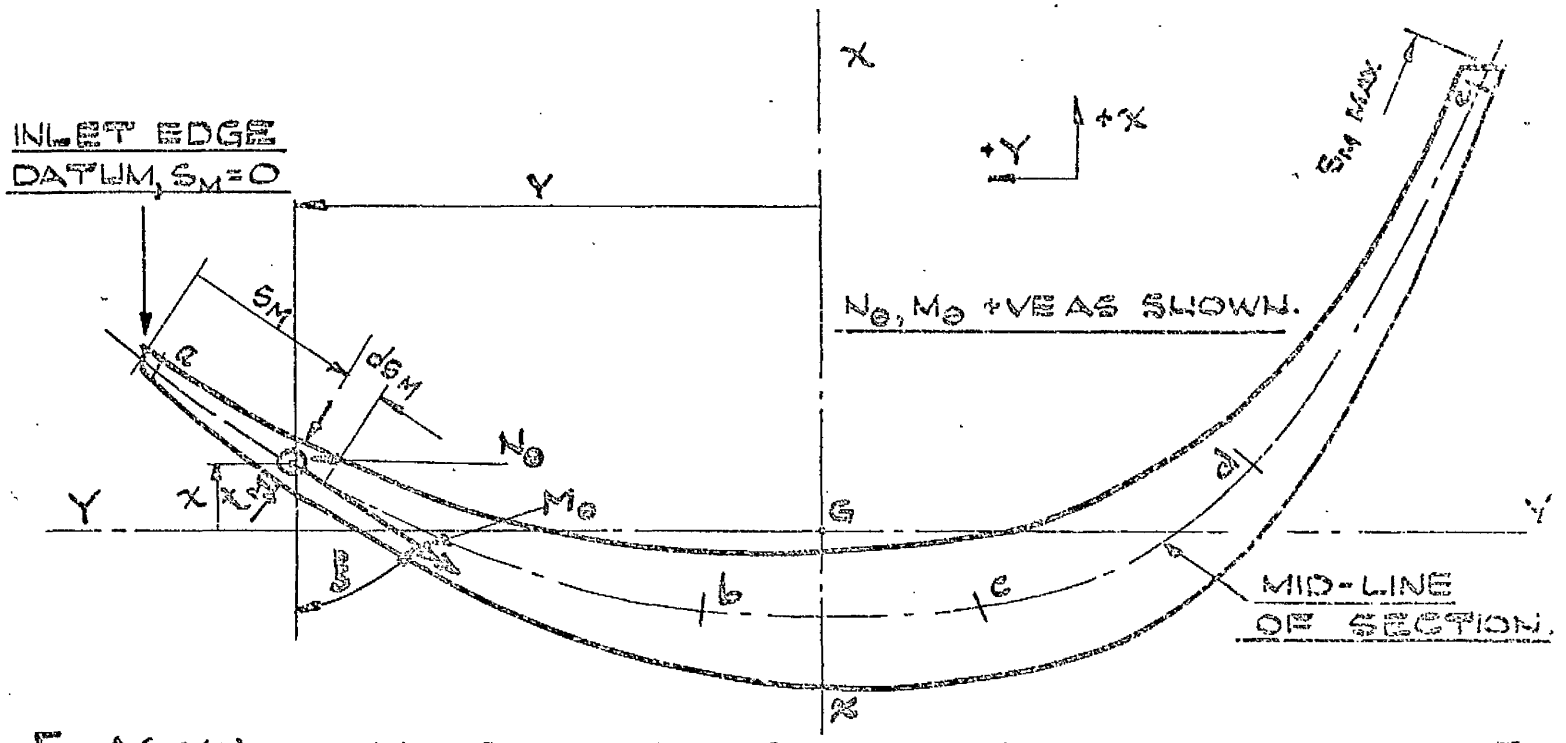

FIG A6.2(a). FULL SIZE DRAWING OF MERIDIONAL SECTION OF BUCKET OF 16$\frac{1}{2}$ IN TURGO WHEEL, AT $\theta = 74.5°$. POINTS a, b, c, d, e, CORRESPOND TO THE STRAIN-GAUGE LOCATIONS SHOWN ON FIGS 63 AND 64.

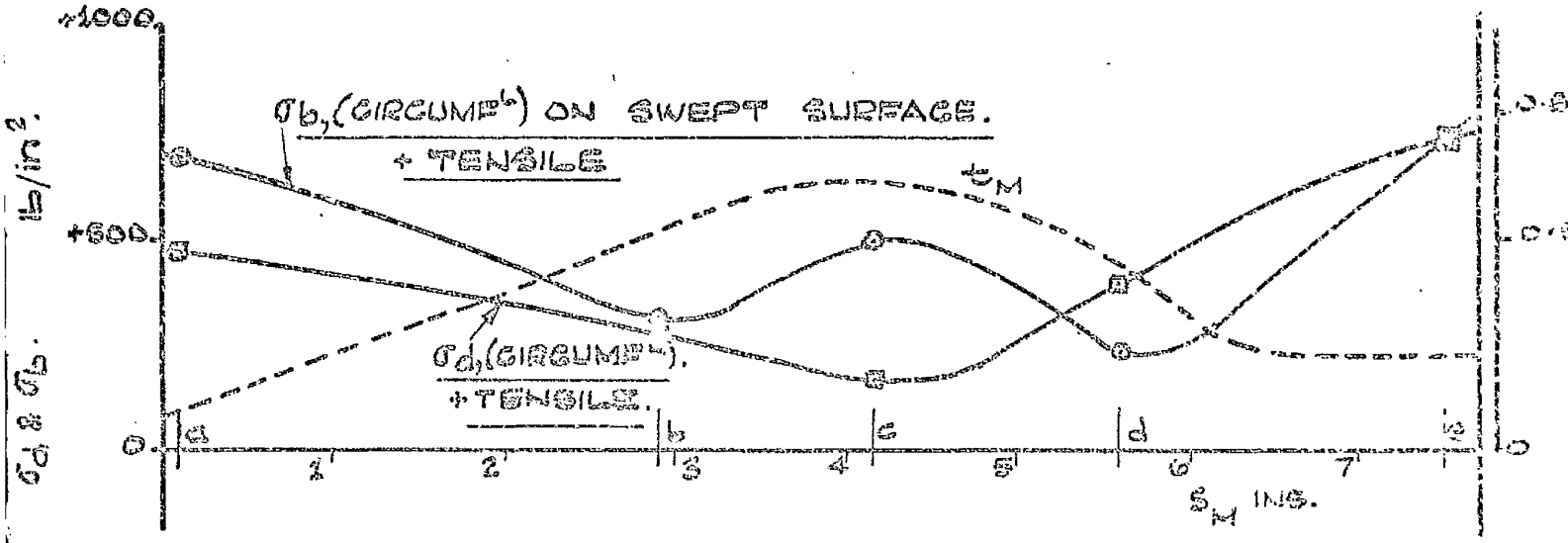

FIG A6.2(b). ANALYSIS FOR CENTRIFUGAL ACTIONS ON MERIDIONAL SECTION AT $\theta = 74.5°$, FOR 16$\frac{1}{2}$ IN ALUMINIUM TURGO WHEEL ROTATING AT 1300 R.P.M. DISTRIBUTIONS OF t_M AND OF σ_d AND σ_b (DERIVED FROM MEASURED STRESSES) WITH S_M.

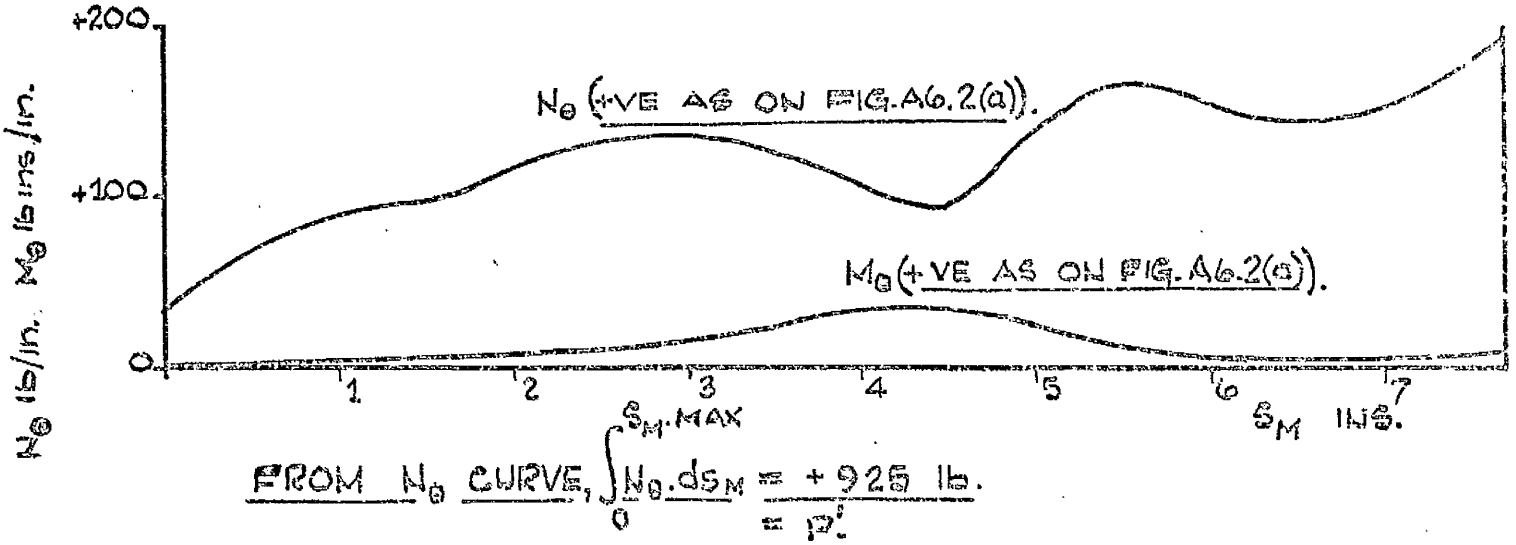

FROM N_θ CURVE, $\int_0^{s_{M.MAX}} N_\theta . ds_M$ = + 925 lb.
= p'.

FIG A6.2(c). ANALYSIS FOR CENTRIFUGAL ACTIONS ON MERIDIONAL SECTION AT $\theta = 74^0$. DISTRIBUTIONS OF N_θ AND M_θ WITH s_M DERIVED FROM PREVIOUS FIG.

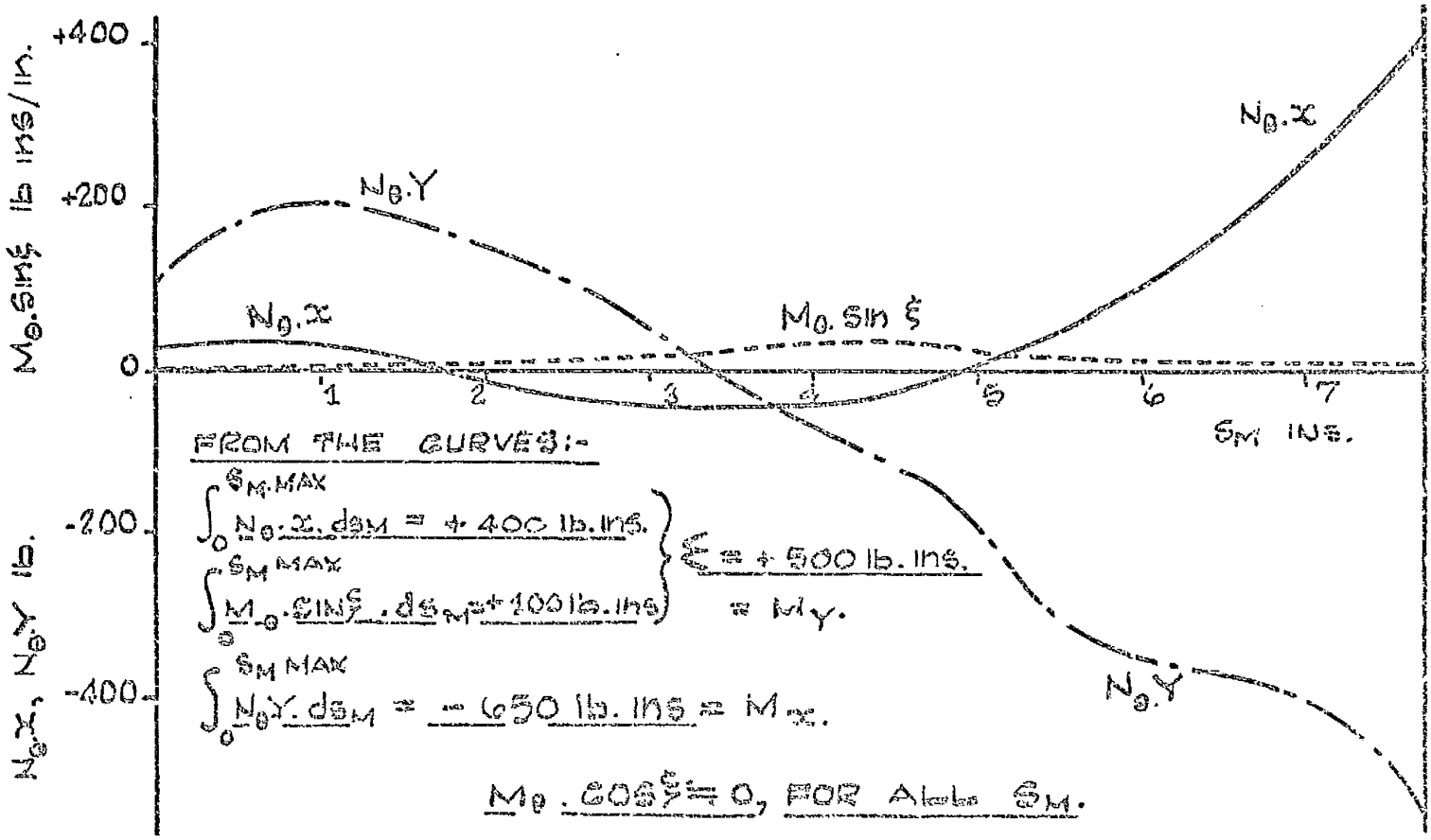

FROM THE CURVES:-

$\int_0^{s_{M.MAX}} N_\theta . x . ds_M$ = + 400 lb. ins.

$\int_0^{s_{M.MAX}} M_\theta . \sin\xi . ds_M$ = + 100 lb. ins

ξ = + 500 lb. ins. = M_Y.

$\int_0^{s_{M\,MAX}} N_\theta Y . ds_M$ = − 650 lb. ins = M_x.

$M_\theta . \cos\xi = 0$, FOR Also s_M.

FIG. A 6. 2(d). ANALYSIS FOR CENTRIFUGAL ACTIONS ON MERIDIONAL SECTION AT $\theta = 74^0$. DISTRIBUTION OF $(N_\theta . x)$, $(M_\theta . \sin\xi)$, $(N_\theta . Y)$ WITH s_M, DERIVED FROM PREVIOUS FIGS.

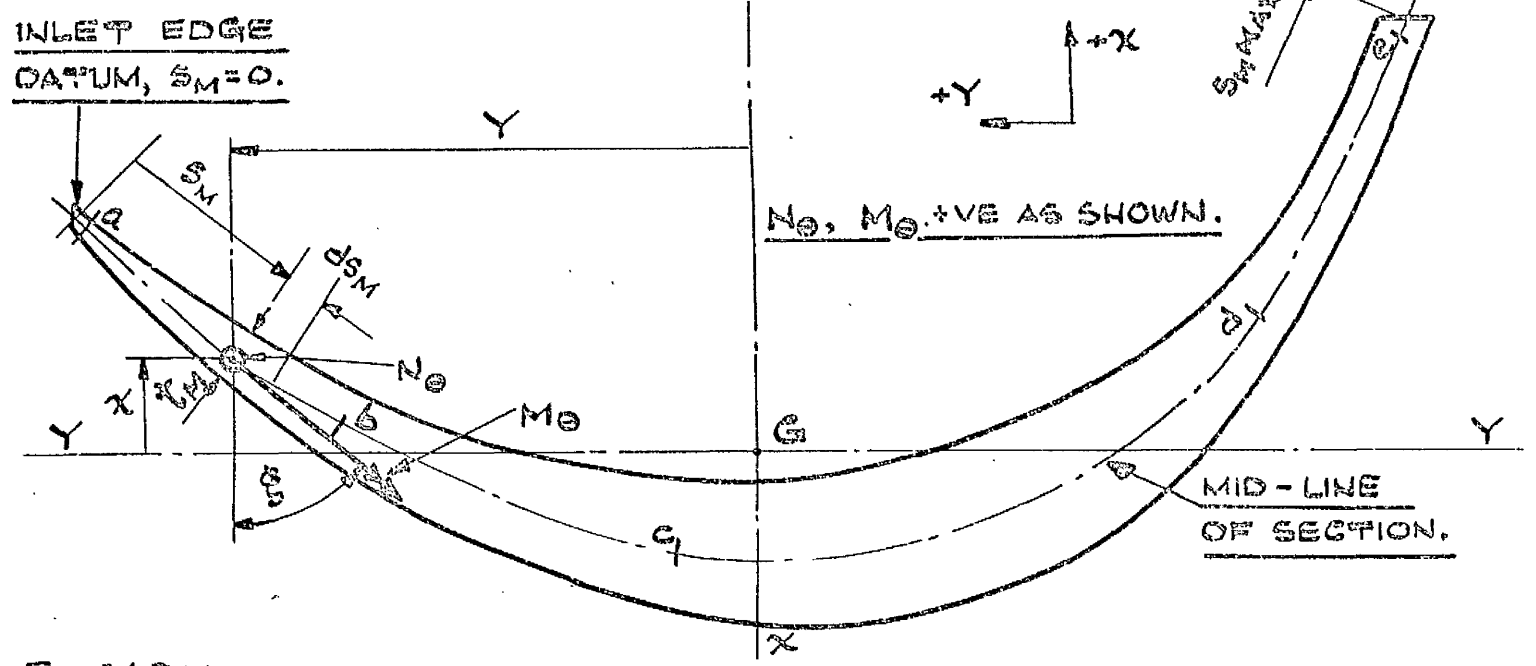

FIG. A6.3(a). FULL SIZE DRAWING OF MERIDIONAL SECTION OF BUCKET OF 16½ IN. TURGO WHEEL, AT $\theta = 92°$. POINTS a, b, c, d, e, CORRESPOND TO THE STRAIN-GAUGE LOCATIONS SHOWN ON FIGS. 63 AND 64.

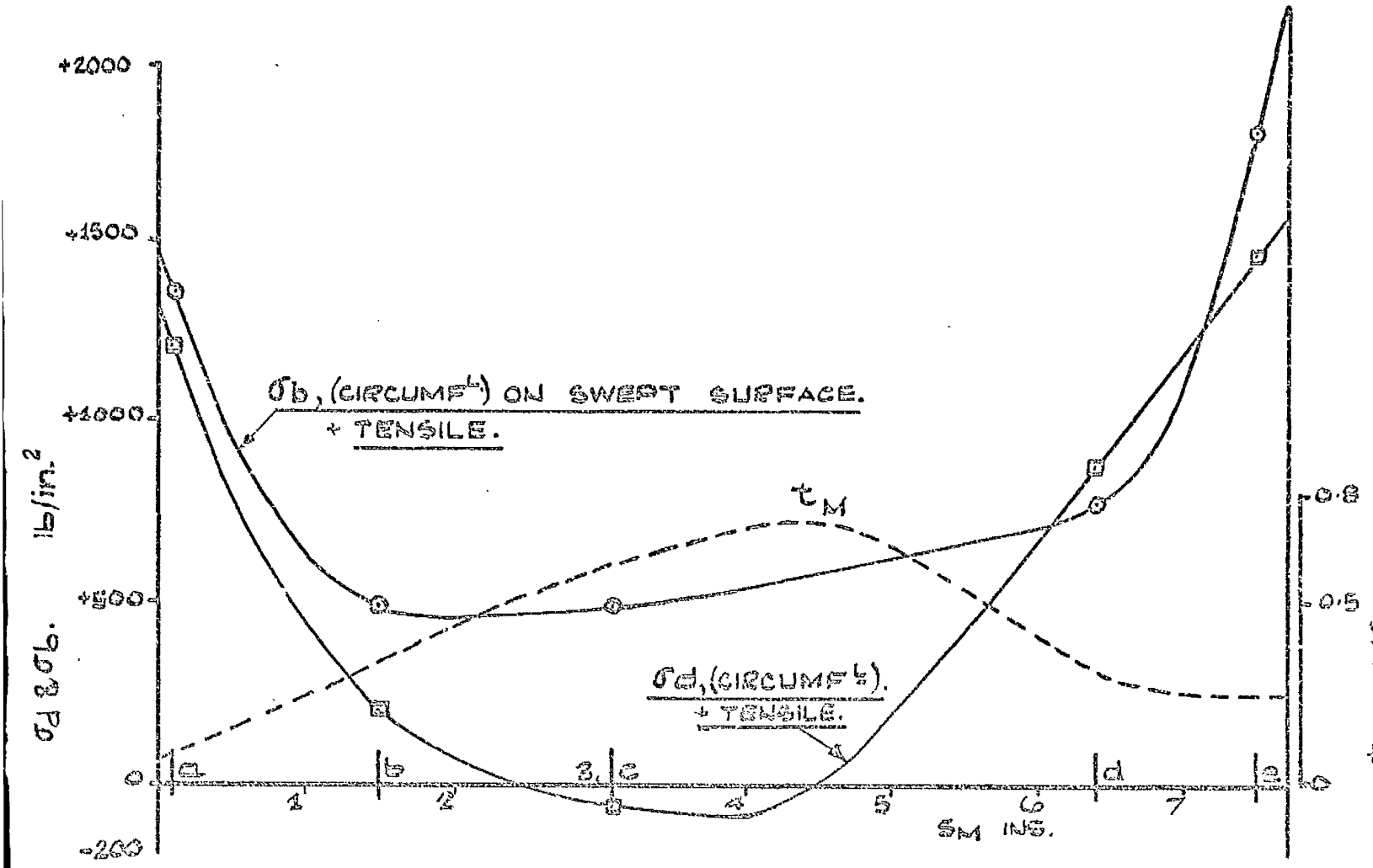

FIG A6.3(b). ANALYSIS FOR CENTRIFUGAL ACTIONS ON MERIDIONAL SECTION AT $\theta = 92°$, FOR 16½ IN. ALUMINIUM TURGO WHEEL ROTATING AT 1300 R.P.M. DISTRIBUTIONS OF t_M AND OF σ_d AND σ_b (DERIVED FROM MEASURED STRESSES) WITH S_M.

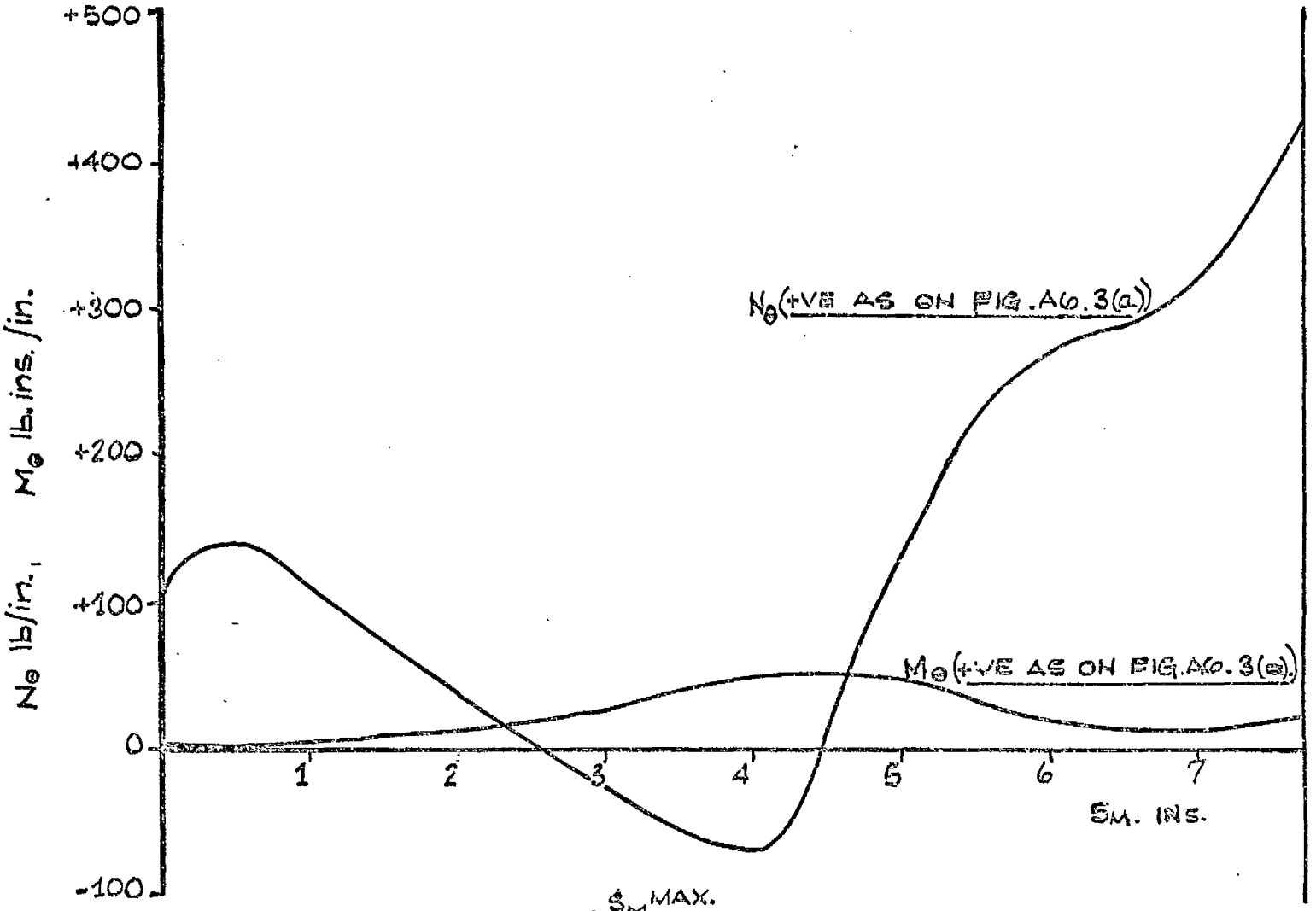

FROM N_θ CURVE, $\int_0^{S_M \text{MAX.}} N_\theta \cdot ds_M = +940$ lb. $= P'$.

FIG. A6.3(c). ANALYSIS FOR CENTRIFUGAL ACTIONS ON MERIDIONAL SECTION AT $\theta = 92°$. DISTRIBUTIONS OF N_θ AND M_θ WITH S_M, DERIVED FROM PREVIOUS FIG.

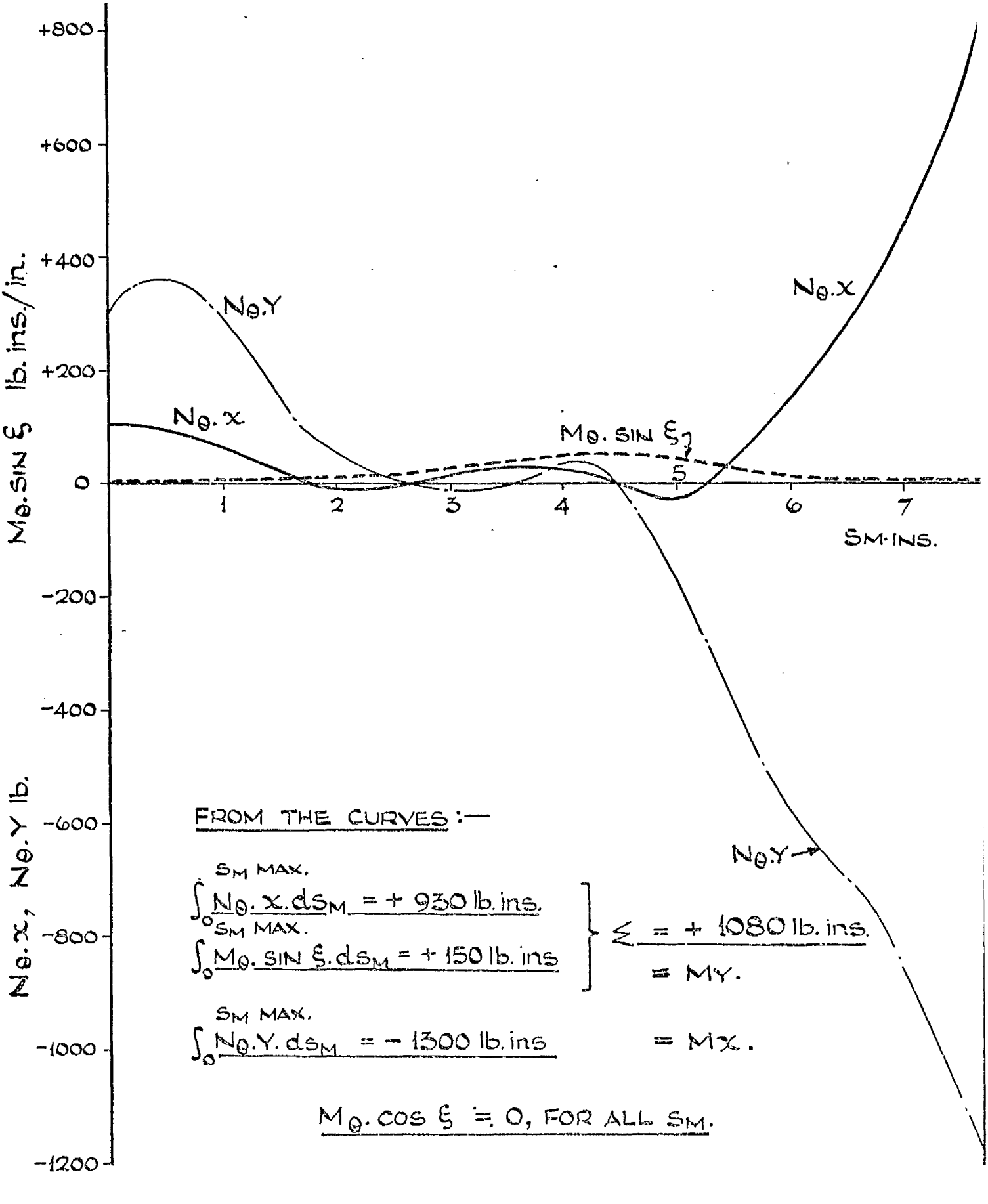

FIG. A6. 3(d) ANALYSIS FOR CENTRIFUGAL ACTIONS ON MERIDIONAL SECTION AT $\theta = 92°$. DISTRIBUTIONS OF $N_\theta.x$, $M_\theta.\sin\xi$, $N_\theta.Y$ WITH s_M, DERIVED FROM PREVIOUS FIGS.

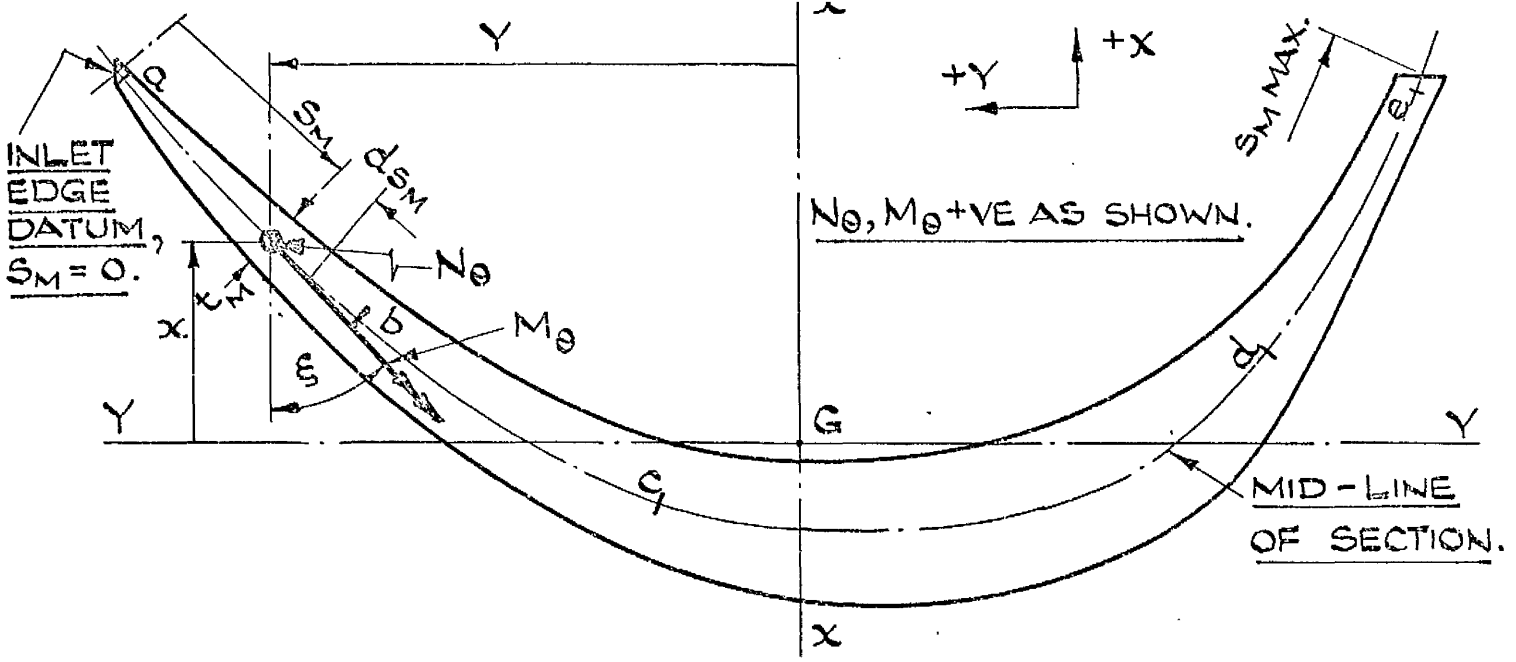

FIG. A6.4(a). FULL SIZE DRAWING OF MERIDIONAL SECTION OF BUCKET OF $16\frac{1}{2}$ IN. TURGO WHEEL, AT $\theta = 111°$. POINTS a, b, c, d, e CORRESPOND TO THE STRAIN-GAUGE LOCATIONS SHOWN ON FIGS. 63 AND 64.

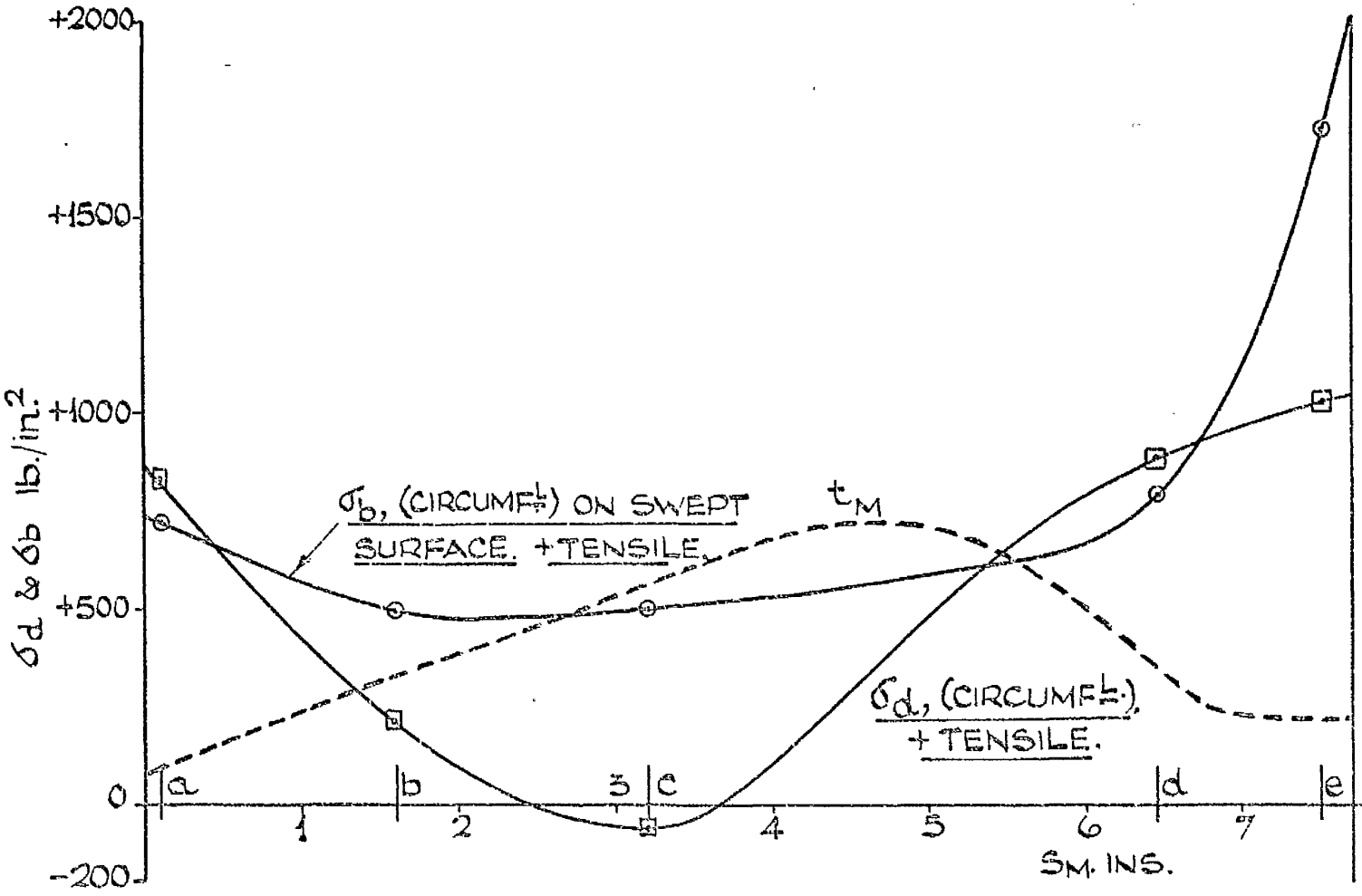

FIG. A6.4(b). ANALYSIS FOR CENTRIFUGAL ACTIONS ON MERIDIONAL SECTION AT $\theta = 111°$, FOR $16\frac{1}{2}$ IN. ALUMINIUM TURGO WHEEL ROTATING AT 1300 R.P.M. DISTRIBUTIONS OF t_M AND OF σ_d AND σ_b (DERIVED FROM MEASURED STRESSES) WITH S_M.

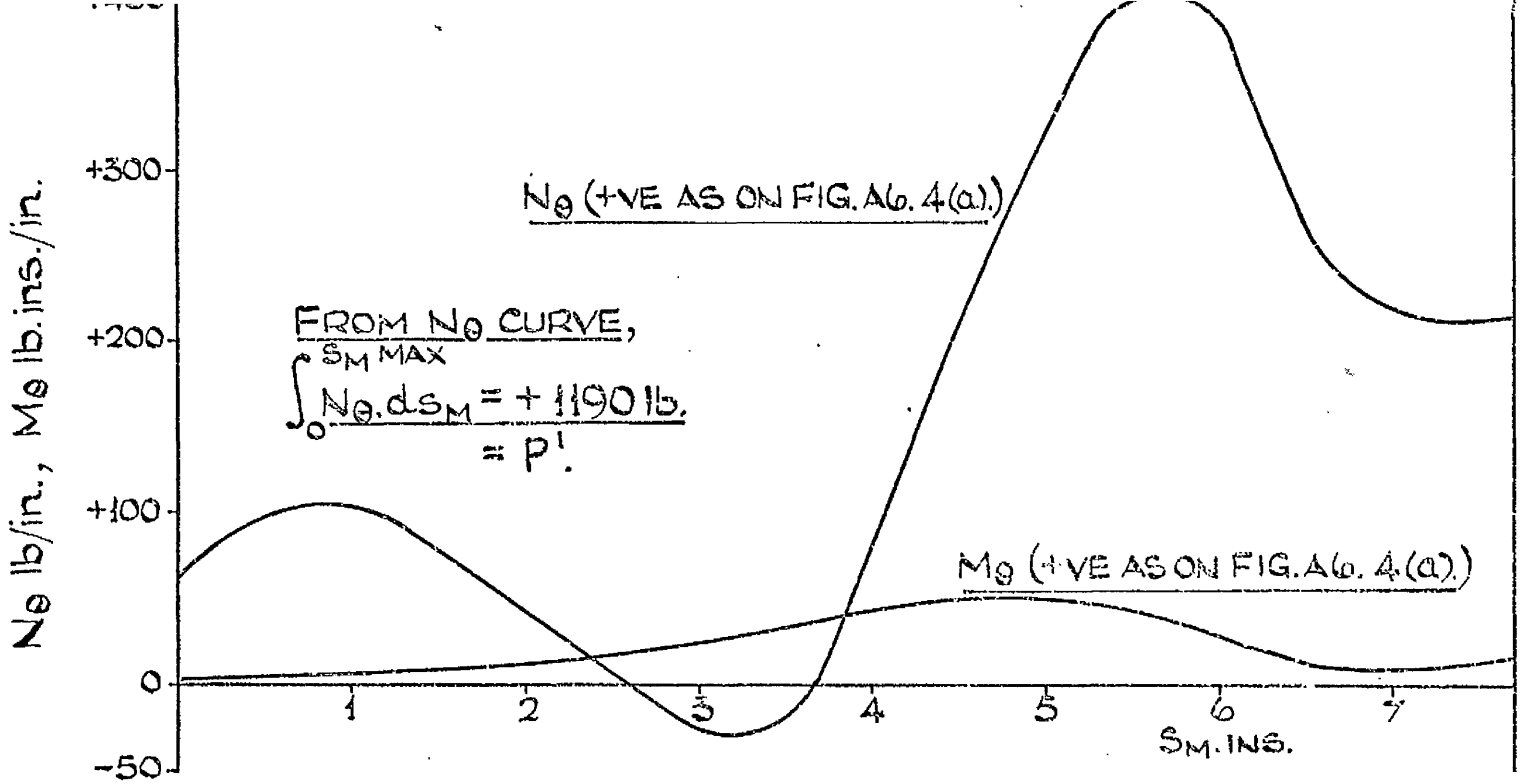

FIG. A6. 4(c). ANALYSIS FOR CENTRIFUGAL ACTIONS ON MERIDIONAL SECTIO AT $\theta = 111°$ DISTRIBUTIONS OF N_θ AND M_θ WITH S_M, DERIVED FROM PREVIOUS FIG.

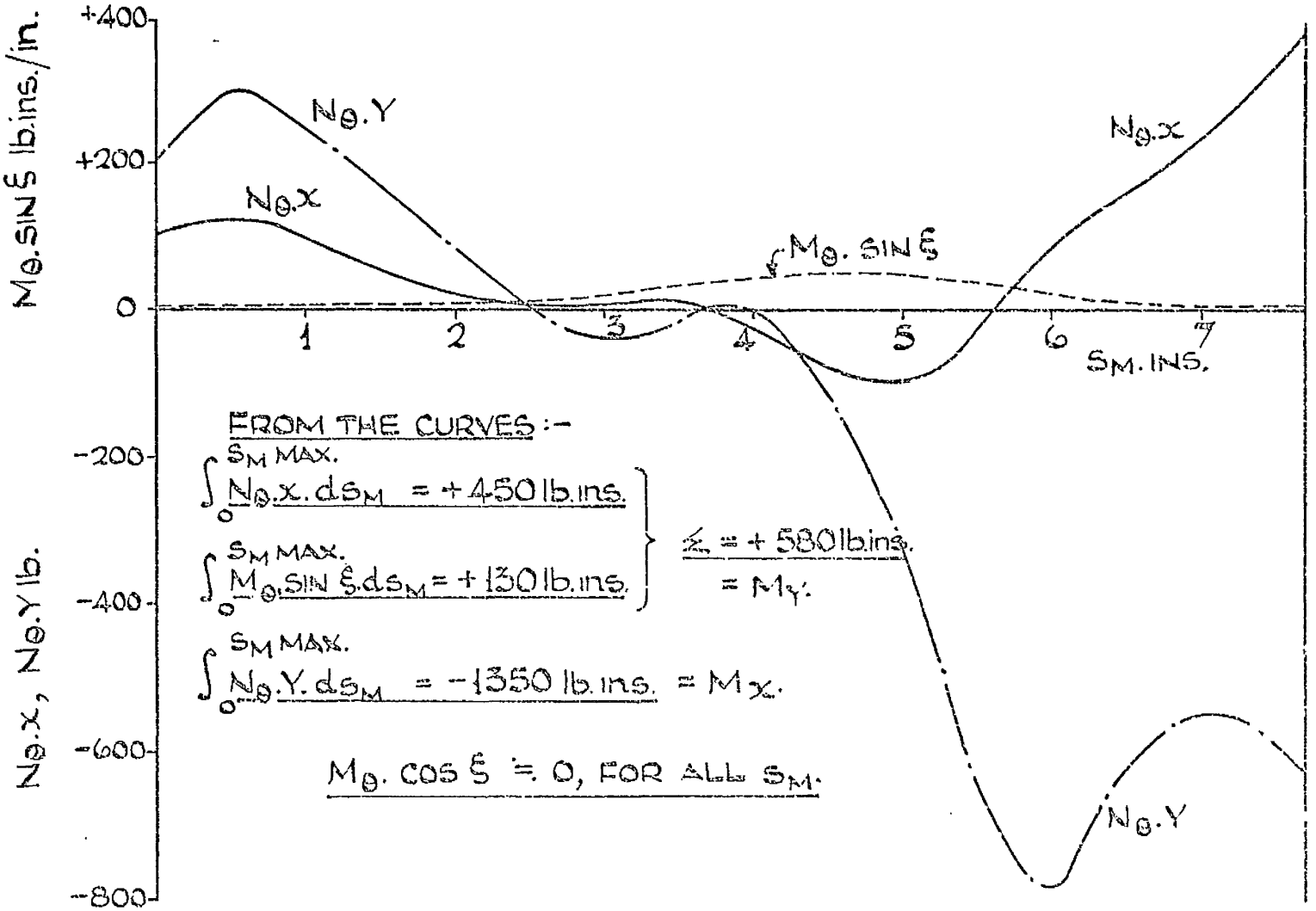

FIG. A6. 4(d). ANALYSIS FOR CENTRIFUGAL ACTIONS ON MERIDIONAL SECTION AT $\theta = 111°$ DISTRIBUTIONS OF $N_\theta . x$, $M_\theta . \sin\xi$, $N_\theta . Y$ WITH S_M, DERIVED FROM PREVIOUS FIGS.

APPENDIX 7

A MORE REALISTIC APPROXIMATE THEORETICAL ANALYSIS OF THE JET LOADING STRESSES IN THE BUCKETS OF THE TURGO IMPULSE WHEEL

From chapter 4, measurement of approximate jet loading stresses sustained by a bucket when directly loaded, and when acting as a supporting bucket for other loaded buckets, clearly shows that the theoretical treatment of the rim on the remainder of the wheel, as a 180^{o} fully-fixed arch (section 3C iii) bears little relation to the actual stress behaviour of the wheel under jet loading. Any agreement between results based on this theoretical treatment, and the corresponding experimental values is, to some extent, adventitious.

The restraint on a loaded bucket provided by the rim on the remainder of the wheel, may be treated theoretically by an approximate method more in accordance with the experimental indications and easy to develop from some previous considerations. Under jet action a bucket sustains stresses due to its being directly loaded and due to its acting as a supporting bucket for the rim which restrains other jet loaded buckets. In harmony with the essential simplicity of the approximate theoretical approaches of chapter 3, it is reasonable to make the following assumptions:-

(1) That in considering transmission of actions from a jet loaded bucket to supporting buckets, deformation of the rim itself may be neglected. The low average magnitude of relevant measured stresses in the rim (section 4C ii, Fig.86) lends support to this assumption.

(2) That the 3 buckets on which the jet impinges sustain identical stresses due to direct loading, and identical stresses in their rôles as supporting buckets. This latter part of the assumption infers that all the supporting buckets are assumed to carry the same stresses. Such a theoretical situation would arise if, subsequent to the rimless jet/

jet loaded condition (section 3C ii) the displacement discontinuities at the jet loaded bucket/rim junction were considered to be eliminated simply by bodily rotation of the rim, on the supporting buckets, about the axis of the wheel. Theoretical support for such a simplifying assumption is indicated by the nature of the rotational discontinuity Φ_{P2} (section 3C ii at the end) and by the fact that the major displacement discontinuity at the junction is that of tangential deflection, Δ_{T2}. Experimental support for the assumption, however, is not much in evidence in relevant results, Fig.77.

The inference that all the supporting buckets are assumed to be identically loaded at their points of junction with the rim, implies an approximate theoretical treatment on the same lines as that in which the restraint exerted on the jet loaded bucket by the rim on the remainder of the wheel, was considered to be due only to 2 co-linear buckets,— the "unrealistically flexible restraint" case of section 3C v. On the basis of the above assumptions, any 1 of the 3 buckets on which the jet impinges, may be considered to be restrained, at the bucket/rim junction point, by the remaining 21 buckets— all regarded as co-linear with the jet loaded bucket concerned, and as rigidly connected to it at the junction point. Similarly to the 2 co-linear supporting buckets case (section 3C v) the essential results for 21 co-linear supporting buckets may be derived from the results for fully-rigid restraint at the junction.

For the $16\frac{1}{2}$ in.cast steel Turgo wheel under normal working conditions, Fig.A7.1 shows M_θ due to rimless jet loading (for loading Fig.30), this curve coming directly from Fig.31, and $M_{\theta Y2}$ arising from the assembly actions exerted by a fully-fixed support at the bucket/rim junction. Superposition of the ordinates of these two curves gives curve II of Fig.39. By appropriate application of the assembly condition compatibility and equilibrium/

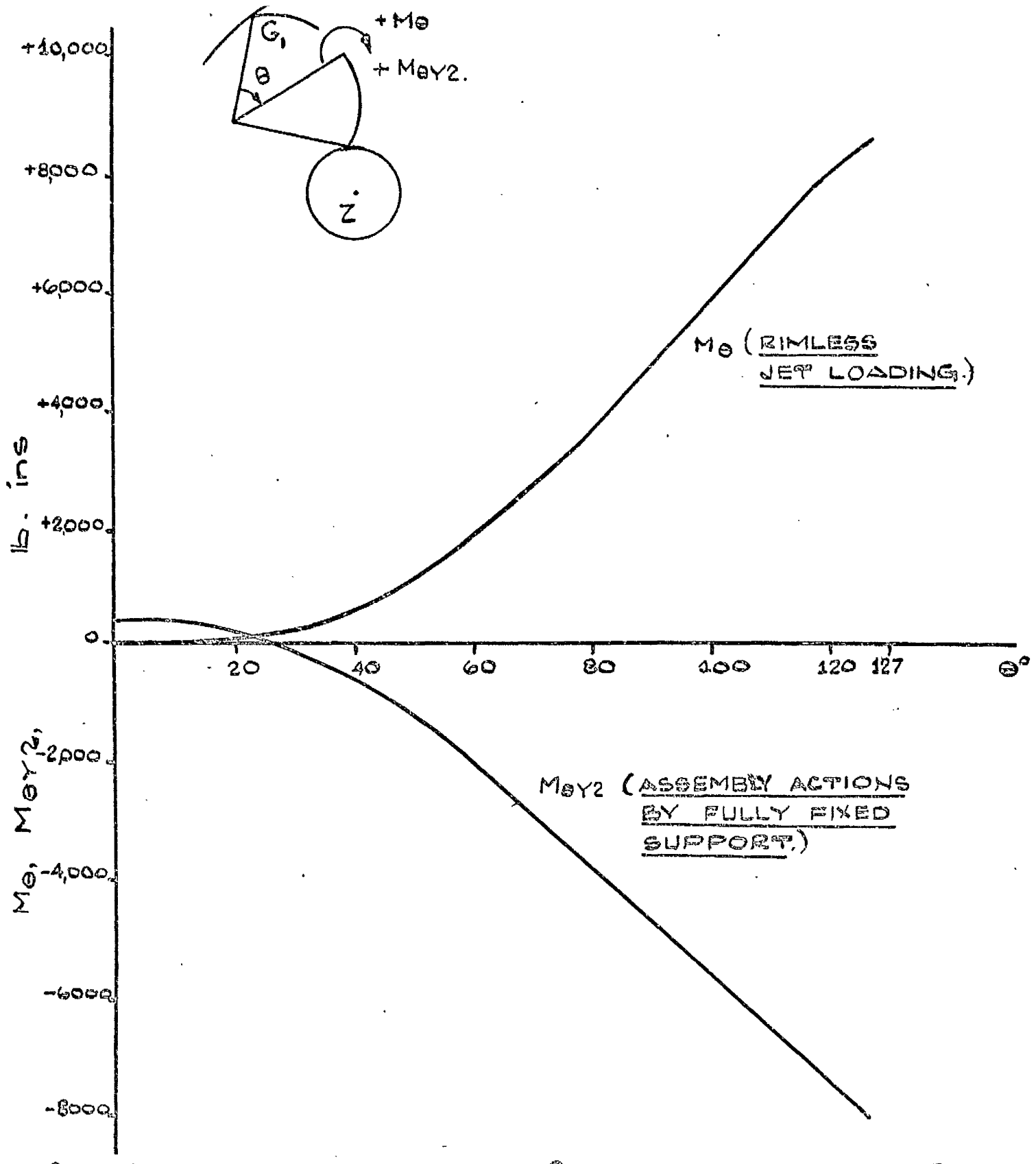

FIG. A 7.1. DISTRIBUTIONS WITH θ OF IN-PLANE BENDING MOMENTS Mθ DUE TO RIMLESS JET LOADING (FIG. 31) AND MθY2 DU TO THE CORRESPONDING ASSEMBLY ACTIONS EXERTED ASSUMING A FULLY RIGID SUPPORT AT THE BUCKE RIM JUNCTION - ALL ON THE "EQUIVALENT" BUCKET OF THE 162 IN. CAST STEEL TURGO WHEEL UNDER NORMAL WORKING CONDITIONS.

CURVE II, FIG. 39, IS THE RESULTANT OF THESE TWO CURVES

equilibrium equations (3C.40) to (3C.51) inclusive, to the case of 21 co-linear supporting buckets exerting restraint at the jet loaded bucket/ rim junction, the relevant assembly actions are readily found to be $\frac{21}{22}$ times the corresponding assembly actions for the fully-rigid restraint case. Hence, for in-plane bending, the resulting assembly action bending moment distribution on the jet loaded bucket, $M_{\theta Y2}$ (21 supporting buckets) has ordinates $\frac{21}{22}$x the corresponding ordinates of the $M_{\theta Y2}$ (fully-fixed support) curve of Fig.A7.1. The former $M_{\theta Y2}$ curve is thus readily obtained and is shown in Fig.A7.2. Superposition of its ordinates with those of curve M_{θ} (rimless jet loading) gives the total in-plane bending moment $M'_{\theta Y.TOT}$ on the bucket, due to its being directly loaded by the jet.

Since the jet impinges on 3 buckets however, any 1 of these 3 directly loaded buckets also acts as a supporting bucket, exerting restraint at the junction points of the other 2 directly loaded buckets. Now the bending moment distribution $M_{\theta Y2}$ of Fig.A7.2 arises from assembly actions exerted on the jet loaded bucket by the 21 supporting buckets. Equal and opposite total actions are exerted on the 21 supporting buckets by the jet loaded bucket. Therefore the in-plane bending moment distribution on any 1 supporting bucket, when acting with the other 20, in support of 1 directly loaded bucket, is found by multiplying by $\frac{1}{21}$, the corresponding ordinates of $M_{\theta Y2}$, Fig.A7.2, and changing the signs. For any of the buckets supporting 2 directly loaded buckets, the multiplying factor is then $\frac{2}{21}$, and for the case of any of the buckets acting solely in a supporting capacity, for the 3 directly loaded buckets, the factor is $\frac{3}{21}$.

The in-plane bending moment distribution on any 1 of the buckets acting in support of 2 loaded buckets, has been thus determined from Fig.A7.2. The values have been superimposed on the curve $M'_{\theta Y.TOT}$ for the bucket directly loaded only, to give the curve $M_{\theta Y.TOT}$, the total in-plane/

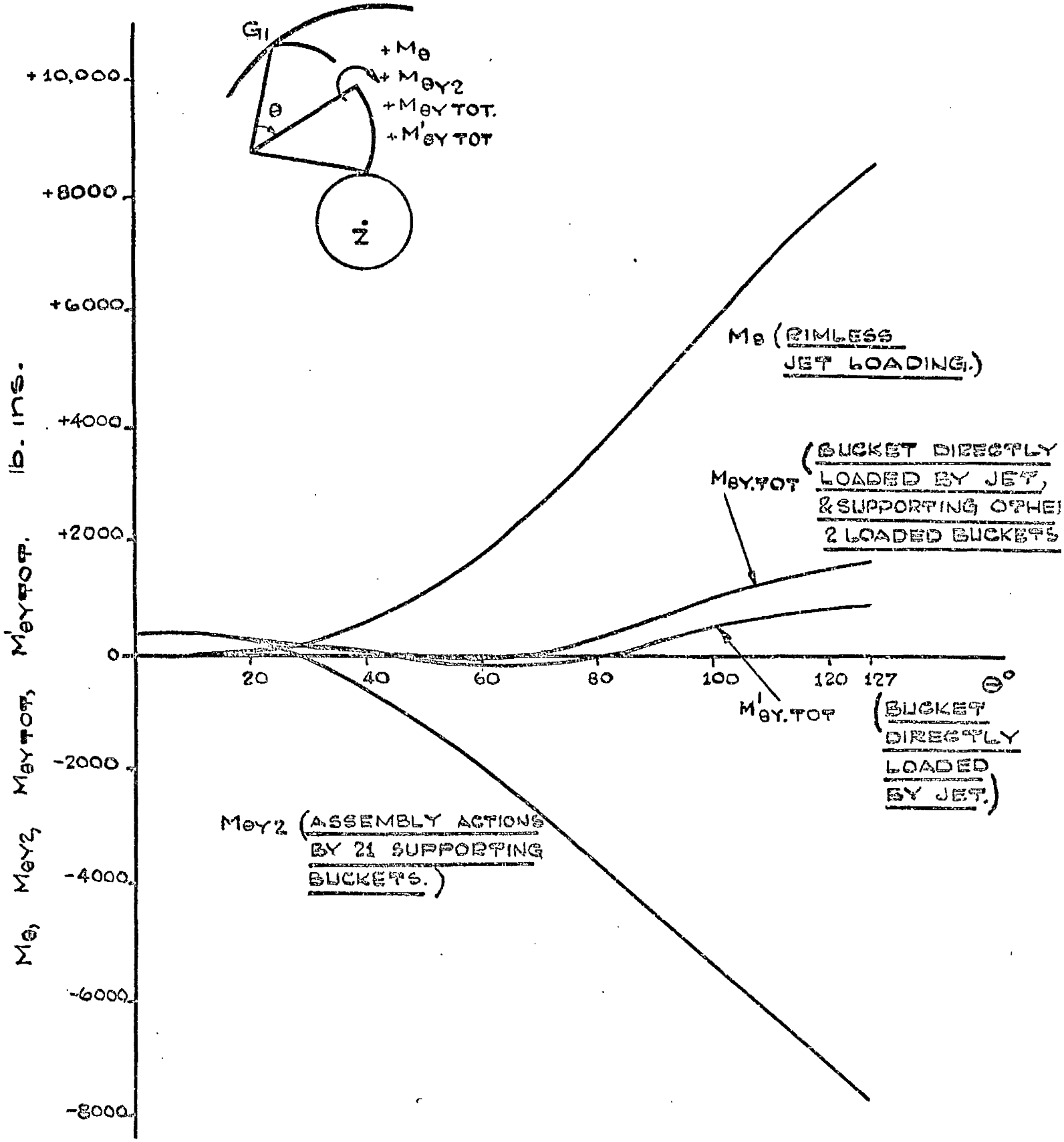

FIG. A7.2. DISTRIBUTIONS WITH θ OF IN-PLANE BENDING MOMENTS ON THE "EQUIVALENT" BUCKET OF THE 16½ IN. CAST STEEL TURGO WHEEL UNDER NORMAL WORKING CONDITIONS. THE CURVES $M_{\theta Y2}$, $M'_{\theta Y TOT}$, & $M_{\theta Y TOT}$ ARE DERIVED FROM THE MORE REALISTIC APPROXIMATE THEORETICAL ANALYSIS OF THE JET LOADING STRESSES.

in-plane bending moment due to direct jet loading on the bucket and due to the same bucket acting in support of the other 2 jet loaded buckets. It is clear from the values that, as might be expected, this latter condition of a bucket is a more severe one than that where the bucket is not directly loaded at all, but acts only in a supporting capacity, albeit for 3 loaded buckets. Corresponding stresses are readily calculated from the curves $M_{\theta Y.TOT}$ and $M'_{\theta Y.TOT}$ of Fig.A7.2.

The foregoing procedure is detailed for in-plane bending moment action on the bucket. The procedure relevant to the less significant direct force action is on exactly similar lines.

Although this approximate theoretical treatment for jet loading stresses is much more realistic than its equivalent in chapter 3, it considers only in-plane actions on the bucket, and so suffers from the disadvantage that identical stress distributions are predicted for the two edges of the bucket.

BIBLIOGRAPHY

1. Surber, A. and Schweizer, F. 'Strength investigations on components of hydraulic plants', Escher Wyss News, 1960, v.33, (nos.1, 2, 3) p.168.

2. Granovskiy, S. A., Orgo, V. M. and Smolyarov, L. G. 'Konstruktsii gidroturbin i raschet ikh detaley' (Water turbine construction and detail design), Mashgiz, Moscow-Leningrad, 1953.

3. Aronson, A. Ya. 'Primenenie teorii tonkikh sterzhney k raschetu rabochego kolesa radialnoosevoy turbiny' (Application of the theory of thin-walled beams to calculations concerning a radial-flow turbine), Sbornik LMZ No.4 (Gidroturbostroenie), Mashgiz, Moscow-Leningrad, 1957, p.182.

4. Perrig, A. 'Contributo allo studio delle sollecitazioni e delle corrosioni delle ruote Pelton' (Contribution to the study of the stresses and corrosion in a Pelton wheel), L'Elettrotecnica, Milan, 1934, v.21, no.16, p.357.

5. Edel, Yu. U. 'Kovshovye gidroturbiny, teoriya, issledovanie, raschet' (Pelton wheels, their theory, investigation and calculation), Mashgiz, Moscow-Leningrad, 1963.

6. Kovalev, N. N. and Kvyatkovskiy, V. S. 'Gidroturbinostroenie v SSSR'. (Water turbine construction in the U.S.S.R.), Gosenergoizdat, Moscow-Leningrad, 1957.

7. Gibson, A. H. 'Hydraulics and its applications'. Fifth edition, 1952, Constable and Co. Ltd., London.

8. Clark, R. A. 'Asymptotic solutions of toroidal shell problems', Quarterly of Applied Mathematics, 1958, v.16, p.47.

9. Clark, R. A. 'On the theory of thin elastic toroidal shells', Journal of Mathematics and Physics, 1950, v.29, p.416.

10. Löffler, K. 'Die berechnung von rotierenden scheiben und schalen' (The calculation of rotating discs and shells), 1961, Springer-Verlag, Berlin.

11./

11. Bibliography 17. References on or related to stresses in turbo-machine rotors. October, 1964, The British Hydromechanics Research Association, Harlow, Essex.

12. Nechleba, M. 'Hydraulic turbines, their design and equipment', 1957, Constable and Co., Ltd., London.

13. Quick, R. S. 'Problems encountered in the design and operation of impulse turbines', Transactions of the American Society of Mechanical Engineers, 1940, v.62, p.15.

14. Kustanovich, M. S. and Ignateva, T. N. 'Tensometricheskie issledovaniya napryazhennogo sostoyaniya modeli radialnoosevogo rabochego kolesa ot deistviya tsentrobezhnykh sil', (Strain gauge investigation for the stresses in a model mixed-flow turbine subjected to centrifugal forces), Sbornik LMZ No.4 (Gidroturbostroenie), Mashgiz, Moscow-Leningrad, 1957, p.177. (Department of Scientific and Industrial Research, Translation RTS 1532, December, 1960).

15. Prigorovskii, N. I., Preiss, A. K., Daichik, M. L., Bortkevich, V.I Kustanovich, M. S., and Komov, N. N. 'Napryazheniya i davleniya na detalyah gidroturbini Dneprovskoi GES po dannim naturnikh izmerenii' (Stresses and pressures, measured under working conditions, on parts of the turbine at the Dneiper Hydro-electric Station), Sbornik LMZ No.4 (Gidroturbostroenie), Mashgiz, Moscow-Leningrad, 1957, p.103. (Department of Scientific and Industrial Research, Translation RTS 1529, November, 1960).

16. Prigorovskii, N. I. 'Napryazheniya i deformatsii v detalyakh i uzlakh mashin' (Stresses and deformations in parts and fittings of machines), Mashgiz, Moscow, 1961.

17. Ruud, F. O. 'Stress analysis of hydraulic turbine parts', Engineering Monograph No.30, U. S. Department of the Interior. Bureau of Reclamation, Denver Colorado, July, 1962.

18. Osterwalder, J. 'Hydrodynamic forces on Kaplan turbine runner blades and their importance in stress analysis', Escher Wyss News, 1967, v.40, no.1, p.26.

19. Smirnov, V. I. 'Voprosy prochnosti lopasti vodyanoy turbiny' (Questions on the strength of a water turbine blade), University of Leningrad publication, Leningrad, 1954.

20. Rudashevskii, G. E., and Nemm, V. A. 'Issledovaniya davlenii i deformatsii v elementakh povorotnolopastnoi turbiny v ekspluatatsionnykh usloviyakh' (Investigation of pressures and deformations acting on components of axial-flow turbines under operating conditions), Sbornik LMZ No.4 (Gidroturbostroenie), Mashgiz, Moscow-Leningrad, 1957, p.127. (Department of Scientific and Industrial Research, Translation RTS 1530, January, 1961).

21. Kovalev, N. N. 'Essais effectués en U.R.SS sur des turbines hydrauliques en service' (Tests conducted in the U.S.S.R. on hydraulic turbines in service), La Houille Blanche, Aug.-Sept., 1958, p.467.

22. Kovalev, N. N., Prigorovskii, N. I., Rudashevskii, G. E., and Edel, Yu. U. 'Issledovanie davlenii i napryazhenii na lopasti rabochego kolesa gidroturbiny Narvskoi GES' (Investigation of pressures and stresses acting on the blades of hydraulic turbines at the Narva Hydro-electric Station), Energomashinostroenie, 1959, no.1, p.29. (Department of Scientific and Industrial Research, Translation RTS 1113).

23. Kovalenko, A. D. 'Oglyad doslidzhen z teoriy plastin i obolonok v rotorakh turbomashin' (Survey of studies in the theory of plates and shells in turbomachinery), Prikladna Mekhanika Viddiltekhnichnikh Nauk an U.R.S.R. (Ukraine), 1955, v.1, no.2, p.131.

24. Tumarkin, S. A. 'Raschet ventilyatorov na prochnost' (Calculations for the strength of fans), Trudy Tsentralnogo Aero-gidrodinamicheskogo Instituta, Moscow, 1940, no.496.

25. Hand-book, 'On the development of water power', Messrs. Gilbert Gilkes and Gordon Ltd., Kendal, England, 1956.

26. Crewdson, E. 'Design and performance of a new impulse water-turbine', Minutes of the Proceedings of the Institution of Civil Engineers, 1921-22, v.213, pt.1, p.396.

27. Lundgren, H. 'Cylindrical shells. v.1. cylindrical roofs' 1951, The Danish Technical Press, The Institution of Danish Civil Engineers, Copenhagen.

28. Gibson, J. E. 'The design of cylindrical shell roofs'. Second edition, 1961, E. and F. N. Spon Ltd., London.

29. Flugge, W. 'Stresses in shells'. 1960, Springer-Verlag, Berlin.

30. Biezeno, C. B. and Grammel, R. 'Engineering dynamics. vII. elastic problems of single machine elements'. 1956, Blackie & Son Ltd., London.

31. Timoshenko, S. P. 'Strength of materials', Part I and Part II, 1956, D. Van Nostrand Co., Inc., New York.

32. Roark, R. J. 'Formulas for stress and strain'. Fourth edition, 1965, McGraw-Hill Book Company, Inc., New York.

33. Timoshenko, S. P. and Gere, J. M. 'Theory of elastic stability'. 1961, McGraw-Hill Book Company, Inc., New York.

34. Argyris, J. H. 'The open tube', Aircraft Engineering, 1954, v.26, p.102.

35. Handbook of Aeronautics, No.1. 'Structural principles and data'. Fourth edition, 1952, Sir Isaac Pitman and Sons Ltd., London.

36. Pippard, A. J. S. 'Studies in elastic structures'. 1952, Edward Arnold & Co.,London.

37. Linge, J. R. 'Some developments and applications of brittle lacquer: Aircraft Engineering, 1958, v.30, p.94, p.142, p.173.

38. Perry, C. C. and Lissner, H. R. 'The strain gage primer', 1962, McGraw-Hill Book Company, Inc., London.

39. Dove, R. C. and Adams, P. H. 'Experimental stress analysis and motion measurement', 1964, Charles E. Merrill Books, Inc., Ohio.

40. Hendry, A. W. 'Elements of experimental stress analysis', 1964, Pergamon Press, London.

41. The M. W. Kellogg Co. 'Design of piping systems', 1956, John Wiley and Sons, Inc., New York.

42. Clark, R. A. and Reissner, E. 'Bending of curved tubes', Advances in Applied Mechanics, Academic Press Inc., New York, 1951, v.II, p.93.

43. Novozhilov, V. V. 'Thin shell theory', Second augmented and revised edition, 1964, P. Noordhoff Ltd., Groningen, The Netherlands.

44. Fessler, H. and Stanley, P. 'Stresses in torispherical drumheads: a photoelastic investigation', The Journal of Strain Analysis, 1965, v.1, no.1, p.69.

45. Fessler, H. and Rose, R. T. 'Photo-elastic investigation of stresses in the heads of thick pressure-vessels', Proceedings of the Institution of Mechanical Engineers, 1957, v.171, no.20, p.633.

46. Motsinger, R. N. 'A discussion and review of slip-ring instrumentation and design', Strain Gage Readings, 1960-61, v.3, no.1, p.3.

47. Ruge, A. C. 'The bonded wire gage torquemeter', Proceedings of the Society for Experimental Stress Analysis, 1945, v.1, No.2, p.68.

48. Manson, S. S., Meyer, A. J., Calvert, H. F. and Hanson, M.P. 'Factors affecting vibration of axial flow compressor blades', Proceedings of the Society for Experimental Stress Analysis, 1950, v.7, no.2, p.1.

49. Kemp, R. H., Morgan, W. C. and Manson, S. S. 'Advances in high temperature strain gages and their application to the measurement of vibratory stresses in hollow turbine blades during engine operation', Proceedings of the Society for Experimental Stress Analysis, 1951, v.8, no.2, p.209.

50. Kemp, R. H., Morgan, W. C. and Manson, S. S. 'High temperature strain gages and their application to measurement of vibratory stresses in turbo-supercharger buckets', Proceedings of the Society for Experimental Stress Analysis, 1947, v.5, no.1, p.90.

51. Burquest, M. O., Carpenter, J. E. and Sullivan, E. M. 'Structural dynamic tests of propeller blades in vacuo', Proceedings of the Society for Experimental Stress Analysis, 1958, v.15, no.2, p.85.

52. Drew, D. A. 'Developments in methods of measuring stresses in compressor and turbine blades on test beds and in flight', Proceedings of the Institution of Mechanical Engineers, 1958, v.172, p.320.

53. Hoffman, N. 'Messungen von mechanischen spannungen an umlaufenden teilen in fluggeräten' (Measurement of stresses in rotating members in flight), Selected Papers on Stress Analysis, Institute of Physics Conference, Delft 1959. Chapman and Hall Ltd., London, 1961, p.107.

54. Berger, R. A. and Brunot, A. W. 'Dynamic stress measurements in gas turbines', Proceedings of the Society for Experimental Stress Analysis, 1955, v.12, no.2, p.45.

55. Richards, D. G. 'Structural testing of aircraft propellers', Proceedings of the Society for Experimental Stress Analysis, 1956, v.13, no.2, p.49.

56. French, R. F. 'Mechanical evaluation of gas turbine blades in their actual centrifugal field', Proceedings of the Society for Experimental Stress Analysis, 1962, v.19, no.1, p.122.

57. Macduff, I. B. 'The rotating wedge: a method of obtaining strain-free locations in a centrifugal field', The Journal of Strain Analysis, 1965, v.1, no.1, p.20.

58. Turner, C. E. and Ford, H. 'Examination of the theories for calculating the stresses in pipe bends subjected to in-plane bending Proceedings of the Institution of Mechanical Engineers, 1957, v.171, p.513.

59. Reissner, E. 'On bending of curved thin-walled tubes', Proceedings of U.S. National Academy of Sciences, 1949, v.35, p.204.

60. Langer, R. E. 'On the asymptotic solutions of ordinary differential equations, with an application to the Bessel functions of large order' Transactions of the American Mathematical Society, 1931, v.33, p.23

61. Naghdi, P. M. and De Silva, C. N. 'On the deformation of elastic shells of revolution', Quarterly of Applied Mathematics, 1954, v.12, p.369.

62. Tueda, M. 'Mathematical theories of Bourdon pressure tubes and bending of curved pipes', Memoirs of the College of Engineering, Kyoto Imperial University, Japan, 1934-35, v.8, p.102, and 1936, v.9, p.132.

63. McLachlan, N. W. 'Bessel functions for engineers', Second edition 1955, Clarendon Press, Oxford.

64. Osipova, L. N. and Tumarkin, S. A. 'Tables for the computation of toroidal shells' (translated by M. D. Friedman), 1965, P. Noordhoff Ltd., Groningen, The Netherlands.

65. Annals of the Harvard University Computation Laboratory, v.II, 'Tables of the modified Hankel functions of order one-third and of their derivatives', 1945, Harvard University Press, Cambridge, Massachusetts.

66. Leckie, F. A. 'Asymptotic solutions for the spherical shell subjected to axially symmetric loading', Proceedings of Symposium on Nuclear Reactor Containment Buildings and Pressure Vessels; Royal College of Science and Technology, Glasgow, 1960, Butterworths, London.

67. Jenssen, O. 'Asymptotic integration of the differential equation for a special case of symmetrically loaded toroidal shells', Journal of Mathematics and Physics, 1960-61, v.39, p.1.

68. Timoshenko, S. P. and Woinowsky-Krieger, S. 'The theory of plates and shells', Second edition, 1959, McGraw-Hill Book Compan Inc., New York.

69. Vigness, I. 'Elastic properties of curved tubes', Transactions of the American Society of Mechanical Engineers, 1943, v.65, no.2, p.105.

ACKNOWLEDGMENTS

The work on which this thesis is based, was carried out in the Department of Mechanics of Materials, Mechanical Engineering Group, University of Strathclyde, Glasgow.

The author wishes to record his thanks to -

Professor A.S.T. Thomson, D.Sc., Ph.D., A.R.C.S.T., M.I.C.E., F.I.MECH.E., F.R.S.E.

Dr. J. M. Harvey, M.S., Ph.D., A.R.C.S.T., C.ENG., M.I.MECH.E.

for their continued interest and encouragement, and to -

Mr. Ian Tullis,

The directors and staff of Messrs. Gilbert Gilkes and Gordon, Ltd., Kendal,

for their invaluable assistance in connection with the experimental work.

FIG. 9.

MANUFACTURING DRG OF 16½ IN. P.C.D. TURGO IMPULSE WHEEL SHOWING DIAMETRAL SECTIONS OF HUB & RIM & SECTIONS OF BUCKET.

22 BUCKETS.

FULL SIZE.

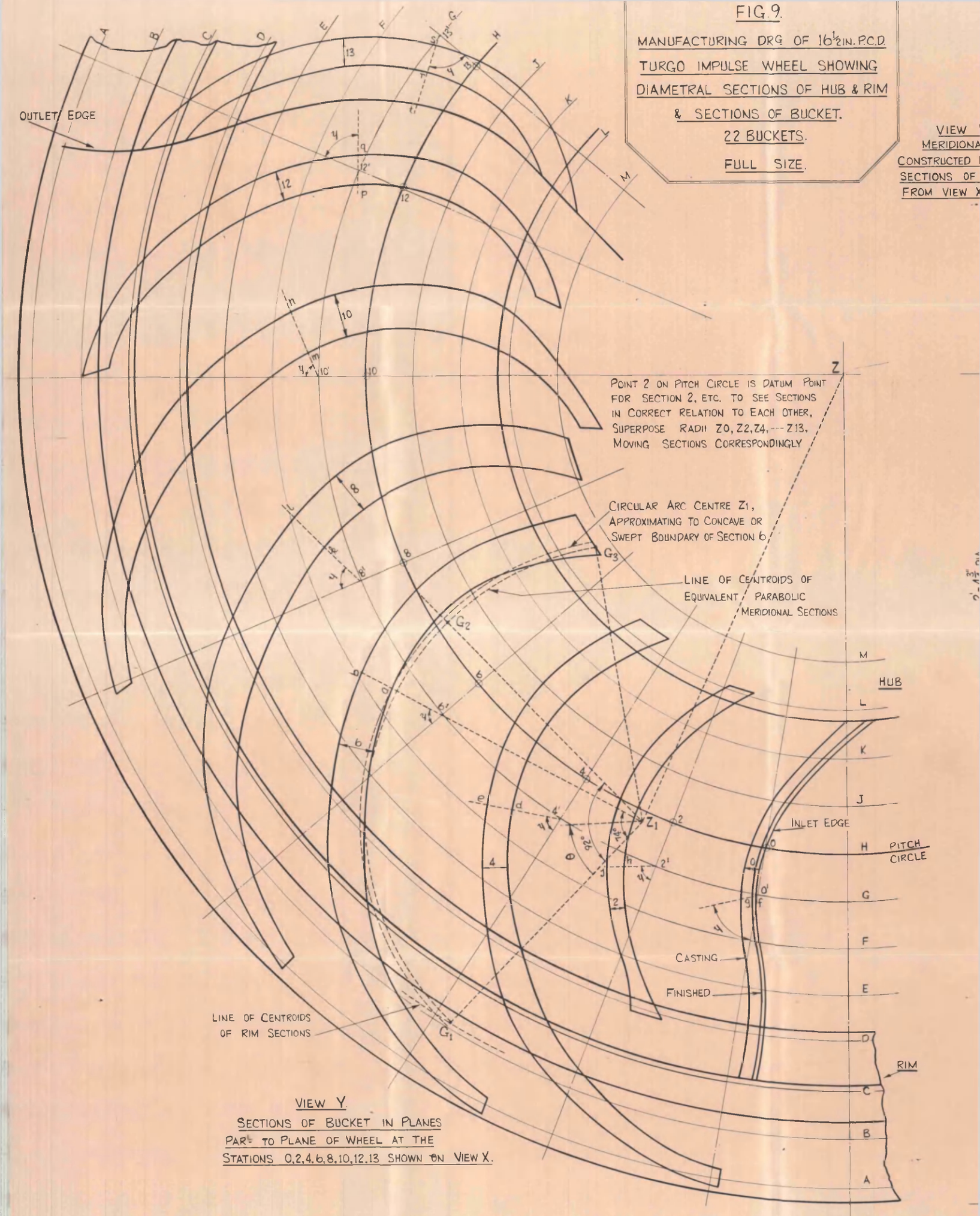

VIEW Y.

SECTIONS OF BUCKET IN PLANES PARL TO PLANE OF WHEEL AT THE STATIONS 0, 2, 4, 6, 8, 10, 12, 13 SHOWN ON VIEW X.

VIEW
MERIDIONA
CONSTRUCTED
SECTIONS OF
FROM VIEW X